STUDY OF THE IRRADIATION EFFECT ON ELECTRICAL PROPERTIES OF MAGNETIC OXIDES

THESIS

SUBMITTED TO THE SAURASHTRA UNIVERSITY, RAJKOT

FOR THE DEGREE OF

DOCTOR OF PHILOSOPHY

IN

PHYSICS

By

MANISHA C. CHHANTBAR
M. Sc., M. Phil (Physics)

GUIDE
Dr. Hiren H Joshi
M. Sc., Ph. D.

Professor
Department of Physics
Saurashtra University
Rajkot – 360 005
Gujarat- INDIA

July-2009

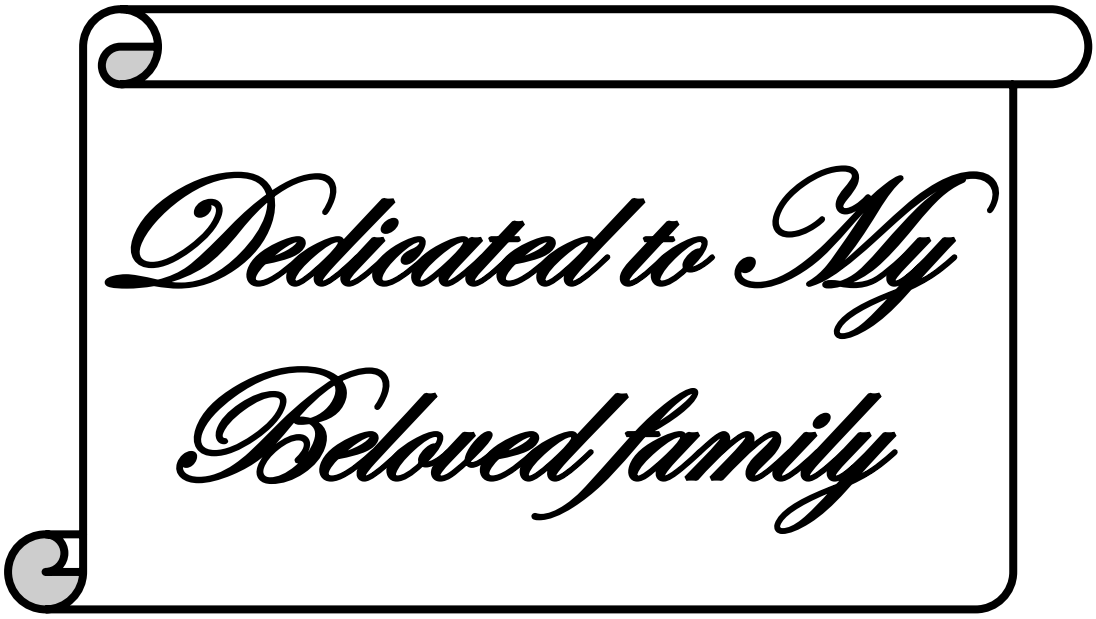
Dedicated to My
Beloved family

Statement under O.Ph.D.7 of Saurashtra University

The work presented in this thesis is my own work carried out under the supervision of *Prof. H. H. Joshi* leads to some important contributions in physics supported by necessary references.

Date: **(M. C. Chhantbar)**
Place: Rajkot

This is to certify that the present work submitted for the Ph.D. degree in Physics of Saurashtra University, Rajkot, by Ms. Manisha C. Chhantbar has been the result of about seven years of work under my supervision and is a valuable contribution in the field of Condensed Matter Physics.

Date:
Place: Rajkot

(H. H. Joshi)
Professor
Department of physics,
Saurashtra University,
Rajkot

ACKNOWLEDGEMENT

At this juncture of fulfilling my desire of satisfactory completion of the present work, I curtsy before Almighty God to express my deep gratitude for the divine grace. I prostrate to my most affectionate parents and I express my deepest sense of gratitude for their blessings, external inspiration, care and love without that I would not have been able to venture into this work.

At this blissful event, I am highly obliged to my respected guide Prof. Hiren H. Joshi, Department of Physics, Saurashtra University, Rajkot, for introducing me to this promising field of swift heavy ion irradiation study of ferrites and his inspiring guidance at every stage of my research work. His association as a research guide is undoubtedly valuable but I am also impressed by his optimistic, active and enthusiastic personality.

I am highly grateful to Dr. Ravikumar, Scientist, Inter University Accelerator Centre, New Delhi; our collaborator in the project work, for his kind help, guidance and constant encouragement during the course of this work. It's my destiny and privilege to have an opportunity to work with him.

I am thankful to the Inter University Accelerator Centre, New Delhi for providing me financial support in the form of research fellowship as well as irradiation experimental facility throughout the course of work. The research work presented in this thesis has been carried out under the UFUP project No. 34315. I wish to express my special thanks to Dr. Anjana Dogra, Dr. Surender Sharma, Dr. Shalendra Kumar, Dr. D. K. Shukla and Pelletron group at IUAC for helping me during the irradiation experiment.

I extend my heart-felt thanks to Dr. G. J. Baldha and Dr. K. B. Modi for their constructive suggestions, co-operation and clean motivation through out the progress of this work.

I sincerely thank Prof. K. N. Iyer, Head, Department of Physics, Saurashtra University, Rajkot for his educating remarks and for the freedom I got in the department and laboratory during this work. I am pleased to acknowledge the support received from Profs. M. J. Joshi, D. G. Kuberkar and Drs. H. P. Joshi, J. A. Bhalodia, Department of Physics, Saurashtra University, Rajkot.

I am grateful to Prof. Ajay Gupta for providing the Mössbauer facility and Dr. Alok Banerji for providing VSM facility at IUC DAEF Indore. The X-ray diffractometer facility provided by Dr. Lalla, IUC DAEF Indore, is gratefully acknowledged.

I am extremely thankful to Prof. R. V. Upadhyay, Department of Physics, Bhavnagar University, Bhavnagar for providing XRD and Mössbauer facility. I am also thankful to Dr. Debnarayan Jana and Dr. Sanjay Chattopadhyay from Physics Department, Calcutta University, Kolkatta, W.B for providing Mössbauer facility. The IR and XRD facility provided by IUAC, New Delhi scientists Mr. Fouran Singh and Mr. Pavan kulriya and EDAX facility provided by SICART, V.V. Nagar is also gratefully acknowledged. I thank Prof. Ali Yousif, Sultan Qaboos University, Muscat, Oman for extending the low temperature Mössbauer facility.

I have great pleasure to acknowledge my senior colleagues Dr. K. H. Jani and Dr. U. N. Trivedi for their valuable help during my work. I placed on record my sincere thanks to my research colleagues Dr. Malini Agrawal, Ms. Pooja Sharma, Ms. Daxaben Joshi, Mr. Ashish Tanna, Dr. Niraj Pandya, Mr. Ritweej Ranjan for their self-less and untiring co-operation in my thesis work and their company making my time cheerful during the laboratory work. I express my thanks to the workshop staff and non-teaching staff of Physics Department, Saurashtra University, Rajkot for their kind cooperation.

It gives me pleasure to express my special thanks to Mr. L. R. Parulkar, Assistant Director, GSLDC, Vyara and Dr. G. Mank, Director, Physics Section, International Atomic Energy Agency, Vienna, Austria for his persistent encouragement and supporting me during the entire duration of my course.

I wish to express my deepest sense of gratitude to my family members Deepak and his wife Nita, Kaushik and his wife Rina for their unfailing help, encouragement, love and affection throughout the work.

Date:

Place: Manisha C. Chhantbar

CONTENTS

CHAPTER: 4

Structural, Magnetic and Mössbauer Characterizations: Experimental Techniques

CHAPTER: 5

Electrical and Dielectric Properties: Theory and Experiments

CHAPTER: 6 Section-A

Results & Discussion

- ***50 MeV Li^{3+} ions irradiation of $Li_{0.5(1+x)}Ti_xAl_{0.1}Fe_{2.4-1.5x}O_4$***

CHAPTER: 6 Section-B

Results & Discussion

❖ ***50 MeV Li^{3+} ions irradiation of $Li_{0.5(1+x)}Ti_xCr_{0.1}Fe_{2.4-1.5x}O_4$***

CHAPTER: 6 Section-C

Results & Discussion

❖ ***50 MeV Li^{3+} ions irradiation of $MnAl_xCr_xFe_{2-2x}O_4$***

CHAPTER: 6 Section-D

Results & Discussion

❖ ***50 MeV Li^{3+} ions irradiation of $CuAl_xCr_xFe_{2-2x}O_4$***

ABSTRACT

During last two decades considerable research work has been carried out on the effect of swift heavy ion irradiation (SHI) on the structural and physical properties of magnetic insulators. Ferrites the magnetic oxides are homogeneous ceramic materials composed of various oxides; Iron oxide is their main constituent. The crystallographic and magnetic changes in bulk samples induced by irradiation are known for various kinds of radiation, such as fast neutron, low energy ions, high energy ions for different kinds of ferrites structure, such as spinels, garnets and hexa-ferrites. Two models of microscopic energy transfer mechanism, thermal spike and the ionic spike have been used to establish the relevant parameters governing the basic energy transfer process in irradiation of materials.

It has been shown through the study of swift heavy ion (SHI) irradiation of magnetic insulators that irradiation of solids with the energetic particle beams leads to the creation of a wide variety of defect states (points defects, clusters of defects, phase change like amorphization of crystal) leading to the modifications on their physical properties It has been demonstrated that in the ion energy regime for which the electronic energy loss (S_e) dominates over the nuclear energy loss (S_n), above specific energy threshold, the damage created by the high electronic excitation induced by SHI in insulators results in formation of the defected regions.

In the S*pinel* structure which is basically an *fcc* Oxygen cage in which there are two different types of interstitial sites present, namely, tetrahedral (A) and octahedral (B), which are occupied by different metal ions. In general, the superexchange magnetic interactions between these metal ions, limited only to the nearest neighbours, are antiferromagnetic and sensitive to the site occupancy of magnetic ions and their crystallographic positions. Therefore, it is an important issue to elucidate the SHI induced modifications in the spinel ferrites owing to the complications caused by the added role of the rearrangement or displacement of cations through transfer mechanisms in the interstitial sites and high sensitivity of superexchange interactions to any change in the direction and length of bonds.

The study of electric and dielectric behaviour stands equal importance, as magnetic properties from both applied and fundamental research point of view. The polycrystalline ferrite are very good dielectric materials. This is possible because in

the process of polycrystalline ferrites synthesis, when the ferrite powder is sintered under slightly reducing conditions, the divalent iron ion formed in the body leads to high conductivity grains. When such material is cooled in an oxygen atmosphere, it is possible to form layers of very law conductivity over its constituent grains. Almost all the ferrites in the polycrystalline form have such high conductivity grains separated by low conductivity layers so that they behave as inhomogeneous dielectric materials. As such the dielectric properties of ferrites are dependent on several factors including the method of preparation, sintering temperature, sintering atmosphere, chemical composition, microstructure etc. When radiant energy act on the ferrite materials, there electrical and dielectric properties may change and a new electrical and dielectric phenomenon may be developed.

The present thesis work includes on SHI irradiation studies on the following spinel ferrite systems:

1. $Li_{0.5(1+x)}Ti_xAl_{0.1}Fe_{2.4-1.5x}O_4$ (x = 0.0 to 0.3, step – 0.1)
2. $Li_{0.5(1+x)}Ti_xCr_{0.1}Fe_{2.4-1.5x}O_4$ (x = 0.0 to 0.3, step – 0.1)
3. $MnAl_xCr_xFe_{2-2x}O_4$ (x = 0.0 to 0.8, step – 0.2)
4. $CuAl_xCr_xFe_{2-2x}O_4$ (x = 0.0 to 0.8, step – 0.2) [Slow-Cooled & Quenched]

Lithium ferrite $Li_{0.5}Fe_{2.5}O_4$ in the spinel structure is a low - cost material which is generally useful for microwave-device and memory-core applications. Lithium ferrite is a high-resistivity, low mobility semiconductor that has low eddy current losses. Modifications of the properties of $Li_{0.5}Fe_{2.5}O_4$ due to substitution of different divalent, trivalent and tetravalent (Zn, Ti…) ions, which are dependent upon the nature and number of substituted ions, are of fundamental importance for microwave devices. In order to understand the effect of Ti^{4+} substitution in the presence of small amount of Al^{3+} (non-magnetic) and Cr^{3+} (magnetic) for Fe^{3+} on the structural, magnetic, electrical and dielectric properties of $Li_{0.5}Fe_{2.5}O_4$, the spinel solution series $Li_{0.5(1+x)}Ti_xAl_{0.1}Fe_{2.4-1.5x}O_4$ (x = 0.0 to 0.3, step – 0.1) and $Li_{0.5(1+x)}Ti_xCr_{0.1}Fe_{2.4-1.5x}O_4$ (x = 0.0 to 0.3, step – 0.1) have been synthesized. The compounds were synthesized by standard ceramic technique by using Fe_2O_3, Li_2CO_3, Al_2O_3 Cr_2CO_3 and TiO_2 AR grade (Thomas-Backer) materials. The chemical stoichiometry and monophase structure formation was confirmed by Energy dispersive X-ray analysis (EDAX) and powder X-ray diffractometry. All samples were irradiated with a 50 MeV Li^{3+} ion beam at fluence of 5 x 10^{13} ions/cm^2 at Inter

University Accelerator Centre, New Delhi. The electronic energy loss, the nuclear energy loss and the range of 50 MeV Li^{3+} ions in these ferrites materials are calculated using SRIM-2003 software. The structural parameters such as lattice constant, X-ray density, porosity, cation distribution, oxygen positional parameter, inter-ionic distances and bond angels have been determined before and after irradiation for better understanding of electrical and dielectric behaviour.

The X-ray diffraction patterns of unirradiated and irradiated specimens show all the Bragg reflections could be indexed for the *fcc* spinel structure and the peak positions are shifted to lower Bragg angle (2θ) values in the case of irradiated samples. This indicates expansion of the unit cell. The compositional increase in lattice parameter for unirradiated and irradiated specimens is due to the larger cationic radius of the replacing cation Ti^{4+} (0.68 Å) than the replaced cation Fe^{3+} (0.64 Å) in the spinel lattice. It is also found that the compositional increase in the cell edge parameter (a) is greater for the irradiated samples than the unirradiated ones. The cation distributions deduced through XRD intensity analysis, magnetization and ^{57}Fe-Mössbauer spectroscopy for the unirradiated and irradiated samples, clearly indicate the redistribution of the cations in the A- and B-sites induced by SHI-irradiation for both the systems.

The Mössbauer spectra for irradiated samples of $Li_{0.5(1+x)}Ti_xAl_{0.1}Fe_{2.4-1.5x}O_4$ system exhibit central paramagnetic doublet superimposed on magnetic sextet which is attributed to the partial formation of paramagnetic centres and rearrangement of the cations in the lattice due to swift heavy ion irradiation but no appreciable influence of SHI-irradiation has been observed in the Mössbauer spectra of $Li_{0.5(1+x)}Ti_xCr_{0.1}Fe_{2.4-1.5x}O_{4+}$ ferrites. The hyperfine interaction parameters deduced through Mössbauer spectroscopy is identified that the line width for the $Li_{0.5(1+x)}Ti_xAl_{0.1}Fe_{2.4-1.5x}O_4$ is not much influenced by SHII but it gives rise to central enhancement, while no central enhancement is observed but the line widths are much influenced in case of $Li_{0.5(1+x)}Ti_xCr_{0.1}Fe_{2.4-1.5x}O_4$.

The magneton number (i.e. Saturation magnetization per formula unit) values have been experimentally found through high field magnetization. The variation of the magneton number as function of Ti-concentration (x) for before and after irradiation can be explained satisfactory on the basis of Neel's collinear spin ordering model. The Nèel temperatures have been determined through thermal variation of low-filed AC-susceptibility measurements.

The IR spectral analysis is used to obtain band positions in order to calculate force constant for unirradiated and irradiated samples. The IR spectrum shows the presence of two absorption bands (higher frequency band ν_1 and lower frequency band ν_2) along with some shoulders/splittings in the range of 400-800 cm^{-1}, which is assigned to intrinsic vibrations of the tetrahedral group and octahedral group, respectively for the both systems. The shifting of main absorption bands ν_1 and ν_2 and more splitting is observed in the case of irradiated samples with respect to unirradiated ones. Elastic moduli and Debye temperature is determined through IR spectral analysis and observed change in elastic moduli with titanium concentration suggests weakening and strengthening of interatomic bonding, respectively both the systems before and after irradiation.

The electrical parameters such as the activation energy, Fermi energy, charge carrier concentration and mobility have been determined and a probable conduction mechanism in the both systems has been suggested. The thermoelectric power measurement is established the present samples are p-type semiconductors and probable conduction mechanism is due to the hole transfer from the Fe^{3+} to Fe^{4+} and Cr^{3+} to Cr^{4+} for $Li_{0.5(1+x)}Ti_xCr_{0.1}Fe_{2.4-1.5x}O_4$ system and Fe^{3+} to Fe^{4+} for $Li_{0.5(1+x)}Ti_xAl_{0.1}Fe_{2.4-1.5x}O_4$ system at octahedral sites. The dielectric behaviour has been studied by measuring the dielectric constant, complex dielectric constant, dielectric loss tangent and a. c. resistivity in the frequency range 100Hz-1MHz at selected temperatures. The variation of ε', ε'' and tanδ with frequency reveals the dispersion due to Maxwell-Wagner type interfacial polarization in agreement with Koop's phenomenological theory for unirradiated and irradiated samples.

The structural, magnetic, electric and dielectric properties of the pre- and post SHI-irradiated specimens can be explained in the light of defect states and rearrangement of cations in the lattice sites.

The spinel ferrite system $MnAl_xCr_xFe_{2-2x}O_4$ (x = 0.0 to 0.8, steps 0.2) has studied for its structural, magnetic, electrical and dielectric properties for before and after irradiation. The XRD has confirmed that all specimens are single-phase cubic spinel and cell edge parameter decreases with Al-Cr content (x), which is due to the replacement of larger ion by smaller ion in the lattice. The well-characterized samples were irradiated with 50 MeV Li^{3+} ions with fluence values 1x 10^{13} ions/cm^2 using 15UD Pelletron accelerator at Inter University Accelerator Centre, New Delhi. All X-

ray diffraction patterns of the irradiated samples are seen to shift towards lower Bragg angle indicating expansion of the unit cell. The cell edge parameter of all the compositions are found to increase after subjected to the swift heavy ion irradiation. This is due to the migration of Mn^{2+}, largest cation present in the system, to the tetrahedral site after irradiation.

The observed variation of saturation moment and Nèel's moment found from cation distribution shows collinear type of magnetic ordering. The observed saturation moment of Mn-ferrite is found to increase after SHI-irradiation and attains value almost near to the Nèel's moment suggesting the modification of magnetic micro structure due to SHII. The oblate type of deformation of $3d^5$ shell is reflected in the X-ray diffraction and Mössbauer spectroscopy. The decrease in T_c is found with increase in Al-Cr Content (x) for both unirradiated and irradiated samples.

The change in IR band positions and intensity is observed as a function of Al-Cr content (x) before and after irradiation. The IR spectra of irradiated ferrites show more splitting of main absorption bands ν_1, ν_2 as well as ν_{sh} for the samples with $x \geq 0.4$, while at higher concentrations $x = 0.6$ and 0.8 no shoulders/splitting are observed. This may be due to the generation of small fraction of Jahn-Teller effect of the ions (Fe^{2+}, Cr^{4+}, Mn^{3+}) at A- and B-sites, where the Jahn Teller effect can cause a local distortion of the cubic spinel lattice. The shifting of main absorption bands ν_1 and ν_2 after irradiation towards high frequency is also due to the irradiation induced mixed valence of Fe-ions. The change in the structural parameters after the SHII has also affected the elastic constants of the system.

The compositional variation of electrical resistivity is explained on the basis of clusters of Mn^{3+} ions and microstructural factors such as grain size, porosity and gain boundary area before and after irradiation. The electrical resistivity as a function of temperature follows the conventional semiconducting behaviour and obeys the well known Arrhenius relation of the compositions $x \leq 0.4$ under investigations. For the compositions with $x = 0.6$ and 0.8, the anomalous electrical behaviour (metallic conductivity) of resistivity in the temperature range 300-500K is occurred. The activation energy is found to higher than the ionization energy 0.1 eV and electron-transition energy of 0.2 eV, which suggest the polaron hopping mechanism in present system. The polaron radius (r_p) and jump lengths (L_A, L_B) for unirradiated and

irradiated samples are decreased with increasing Al-Cr content (x) due to the reduction of the size of the unit cell.

The behaviour of a. c. resistivity, the dielectric properties real and imaginary part of the dielectric constant and dielectric loss tangent have also been carried out as function of temperature and frequency, which is discussed by invoking the Rabinkin and Novikova model of dielectric polarization. The dielectric behaviour of ferrites is explained on the basis of dielectric polarization process which is similar to that of the conduction mechanism is mainly by the hopping conduction mechanism. The changes occurred after irradiation in electric and dielectric properties is due to the alteration of polarizability by formation of point/clusters of defects in the system. The contribution of grain and grain boundaries in electrical conduction and the change in hopping and relaxation process of charge carriers is studied by impedance spectroscopy and electrical modulus.

The copper ferrite, having interesting electric and magnetic properties, is distinguished from the other ferrites by the fact that it undergoes a structural phase transition accompanied by a reduction in the crystal symmetry due to the co-operative Jahn-Teller effect and also the crystal structure of Cu^{2+} containing spinels is sensitive to the thermal history of the samples. Therefore, we have prepared $CuAl_xCr_xFe_{2-2x}O_4$ system by using standard ceramic route to study the influence of heat treatment as well as irradiation effect on structural, magnetic, electrical and dielectric properties.

The substitution of non-magnetic Al^{3+} in $CuFe_2O_4$ may lead to collapse of long range magnetic ordering and the presence of Cr^{3+} may enhance the disorder in the system. Five samples of Al^{3+} and Cr^{3+} substituted $CuFe_2O_4$ system was prepared: $x \leq 0.8$, in steps 0.2. One set of the samples was quenched from the final sintering temperature to liquid nitrogen temperature and other one was furnace cooled to room temperature. All slow-cooled and quenched samples were irradiated using a 50 MeV Li^{3+} ion beam at fluence of 5×10^{13} ions/cm^2.

The XRD patterns for all the samples show tetragonal deformation. The study showed that the distribution of cations is sensitive to the heat treatment of the materials. The SHII reduces the tetragonal distortion in both the cases and significantly modifies the cation distribution in case of quenched sample. The lattice constants “a” and “c” are found to decrease after the SHII in both the specimens indicated overall unit cell contraction after the SHII. The quenched samples show

higher values of saturation magnetization σ_s compared to the slow-cooled ones due to the effect of thermal history on the cation distribution. No remarkable change has been observed in the magnetization after the specimens subjected to the SHII. The SHII affects the micro-magnetic properties like "Mössbauer hyperfine interactions" significantly compared to the bulk properties like saturation magnetization. The variation in T_c value after the SHII in case of both the SC and QC samples are due to variation in cation distributions and disorder. The IR spectra results as irradiation shifts ν_1 and ν_2 to higher frequencies, due to the creation of a large ionic radius of Fe^{2+} induced by irradiation on both octahedral and tetrahedral sites.

The present system provides the most probable mechanism for n-type conduction is electron hopping between $Fe^{3+} \Leftrightarrow Fe^{2+}$ and $Cu^{2+} \Leftrightarrow Cu^{1+}$ ions and the activation energy in order to 0.2 eV is supported the electron transition such as $Fe^{3+} \Leftrightarrow Fe^{2+}$ and $Cu^{2+} \Leftrightarrow Cu^{1+}$. The value of charge carrier concentration n_c is found to higher for all SC and QC irradiated samples as compared to unirradiated samples due to the more charge carriers developed by electronic rearrangement of cation under irradiation. The rise in temperature dependence dielectric properties is results of enhanced build up the space charge polarization with temperature increases. Before and after irradiation all samples reveal an abnormal dielectric behaviour as a function of temperature and frequency, which is explained in the light of the Rezlescu model. This suggests that the abnormal dielectric behaviour of the ferrites containing copper is due to the collective contribution of the two types of carriers, p- and n, to the polarization.

CHAPTER: 1

Introduction

1.1 Introduction

1.2 Literature Survey and Aim of the present work

References

1.1 Introduction

Interaction of radiant energy with matter, especially Swift Heavy Ion (SHI) irradiation, is extremely important problem from the viewpoint of theory and practice. In the past few years a broad development of nuclear engineering, the use of radioactive isotopes, accelerators of elementary particles put forward more often the problem of action of various kinds of ionizing radiation on materials. Elementary charged particles and electromagnetic radiation with high energy interact with an electronic shell or the atomic nuclei of the substances passing through them. These interactions results in an elastic and inelastic scattering of the particles attended by excitation and ionization of the atoms, as well as the initiation of nuclear reactions and also disturbance in the structure of matter, the so-called radiation damage. Two models of microscopic energy transfer mechanism; thermal spike [1.1-1.3] and the ionic spike [1.4, 1.5] have been used to establish the relevant parameters governing the basic energy transfer process.

The term swift heavy ion (SHI) here refers to the energetic ions having energy in the range of a few tens of million electron volts (MeV) to giga electron volts (GeV). During last two decades considerable research work has been carried out on the effect of swift heavy ion irradiation (SHI) on the structural and physical properties of magnetic insulators like ferrites. The crystallographic and magnetic changes in bulk samples induced by irradiation are known for various kinds of radiation, such as fast neutron, low energy ions, high energy ions for different kinds of ferrites structure, such as spinels, garnets and hexa-ferrites.

It has been shown through the study of swift heavy ion (SHI) irradiation of magnetic insulators that irradiation of solids with the energetic particle beams leads to the creation of a wide variety of defect states (points defects, clusters of defects, phase change like amorphization of crystal) leading to the modifications on their physical properties. It has been demonstrated that in the ion energy regime for which the electronic energy loss (S_e) dominates over the nuclear energy loss (S_n), above specific energy threshold, the damage created by the high electronic excitation induced by SHI in insulators results in formation of the defected regions.

In the S*pinel ferrite* structure which is basically an *fcc* Oxygen cage in which there are two different types of interstitial sites present, namely, tetrahedral (A) and octahedral (B), which are occupied by different metal ions. In general, the

superexchange magnetic interactions between these metal ions, limited only to the nearest neighbours, are antiferromagnetic and sensitive to the site occupancy of magnetic ions and their crystallographic positions. Therefore, it is an important issue to elucidate the SHI induced modifications in the spinel ferrites owing to the complications caused by the added role of the rearrangement or displacement of cations through transfer mechanisms in the interstitial sites and high sensitivity of superexchange interactions to any change in the direction and length of bonds.

The study of electric and dielectric behaviour stands equal importance, as magnetic properties from both applied and fundamental research point of view. The polycrystalline ferrite are very good dielectric materials. This is possible because, in the process of preparation of ferrites in the polycrystalline form. When the ferrite powder is sintered under slightly reducing conditions, the divalent iron ion formed in the body leads to high conductivity grains. When such material is cooled in an oxygen atmosphere, it is possible to form layers of very law conductivity over its constituent grains. Almost all the ferrites in the polycrystalline form have such high conductivity grains separated by low conductivity layers so that they behave as inhomogeneous dielectric materials. As such the dielectric properties of ferrites are dependent on several factors including the method of preparation, sintering temperature, sintering atmosphere, chemical composition, microstructure etc. When radiant energy act on the ferrite materials, there electrical and dielectric properties may change and a new electrical and dielectric phenomenon may be developed.

Many experimental results have been reported on the new properties of spinel and garnet ferrimagnetic oxides after irradiation by various kinds of particles like electrons, γ-photons, fast neutrons, protons, low energy ion and high energy ions.

Irradiation of magnetic oxides by heavy ions was first investigated by Hansen et al [1.6, 1.7] on epitaxial thin film of garnet, $Y_3Fe_5O_{12}$. These authors showed by Mössbauer spectroscopy and magnetic measurements that heavy ions (Xe, U) left in their wakes amorphized which appeared to be paramagnetic. The irradiation of ferrites $Bi_2Fe_4O_9$, $Y_3Fe_5O_{12}$, $BaFe_{12}O_{19}$ and AFe_2O_4 (A= Fe, Zn, Ni, Mg) have been studied by C. Houpert et al [1.8] by 3.0 GeV Xenon ions creates paramagnetic cylinder of nearly amorphous matter around the path of the ions. The latent tracks are continuous for $Bi_2Fe_4O_9$, $Y_3Fe_5O_{12}$, $BaFe_{12}O_{19}$, $NiFe_2O_4$ and $MgFe_2O_4$ and discontinuous for Fe_3O_4 and $ZnFe_2O_4$ emphasizing the existence of a threshold energy

deposition. Track production mechanism based on coulomb explosion spike and stastical ion spike concepts is proposed above the threshold. Magnetic oxides MFe_2O_4, exhibiting spinel structure, with M= Mg^{2+}, Ni^{2+}, Fe^{2+} and Zn^{2+} have been irradiated by 3.1 GeV Xenon ions in the range of fluences (10^{11} – 5 x 10^{12} inos/cm^2). The effect of the high electronic excitation induced in the spinel structure has been investigated [1.9] by Mössbauer spectroscopy.

The improved properties of the bubble ferrimagnetic garnets by low energy ion implantation have been established in 1971 [1.10]. In 1984, Pascard [1.11] proposed a linear law for irradiated materials corresponding to a model based on the transformation of Fe^{3+} into Fe^{2+}. The garnet and spinel structure have been extensively studied in the field of irradiation effects induced by swift heavy ions. With the used of heavy ions like Ar, Xe, Kr, Pb and U for irradiation [1.12-1.14], study on the defect morphologies, variation of effective track radii, recrystallization etc. have been deduced using high resolution electron microscopy (HRTEM), Mössbauer spectroscopy and magnetic measurements. In most of the materials, heavy ion irradiation induces specific anisotropy [1.15], a specific volume of increase of the matter and orientation of the magnetization.

Zinc ferrite, $ZnFe_2O_4$, has been irradiated by GeV heavy ions (Kr, Xe, Pb, U) and the induced chemical and physical modifications have been investigated by F. Studer et al [1.16] by means of magnetization measurements, Mössbauer spectroscopy and high resolution electrons microscopy. Xe, Pb and U ion irradiation leads to amorphized latent tracks, while Kr ion irradiation produced Moiré's characteristics lattice disorientations. In both cases, relaxation phenomena involve atomic displacements and a subsequent distribution of ferric ions over tetrahedral and octahedral sites. The result is the creation of a new magnetic ordering and spontaneous magnetization which can reach 2 μ_B at 300K.

The study of the heavy ion irradiation induced change in the magnetic properties of Fe_3O_4 [1.17] has led to the hypothesis that magnetic domain wall could be pinned by the extended defects.

The effect of fast neutron irradiation on saturation magnetization η_B, for different spinel ferrites: Mn-Zn , Ni-Zn ferrites [1.18] and $NiFe_2O_4$ [1.19]. In the case of spinel structure (Mn-Zn, Ni-Zn and $NiFe_2O_4$), the changes are interpreted by a

statistical redistribution of cations over unequivalent sites: thus nickel ions can move from octahedral to tetrahedral sites and cause an increase in η_B.

Electrical conduction in γ - irradiated and unirradiated Zinc iron ferrites [1.20] and Fe_3O_4, $CdFe_2O_4$, $Co_xZn_{1-x}Fe_2O_4$ [1.21] have reported.

1.2 Literature Survey and Aim of the present work

Lithium and substituted lithium ferrites have been found to be excellent materials in high density recording media, absorbers and microwave devices due to their low cost, high saturation magnetization, high Curie temperature and hysteresis loop properties, offering performance advantages over other spinel structures [1.22]. Substituted lithium ferrites have attained considerable importance owing to their attractive magnetic and electrical properties. Titanium and zinc-substituted lithium ferrites are the most widely used materials. The incorporation of titanium in the lithium ferrite $Li_{0.5}Fe_{2.5}O_4$ necessitates adjustment of both monovalent lithium and trivalent iron.

The crystallographic and magnetic characteristics of the lithium ferrite aluminates have been investigated [1.23, 1.24]. The Mössbauer spectroscopic studies [1.25] of lithium aluminates have shown the central quadrupole doublet superimposed on a magnetic sextet and its intensity was sensitive to Al concentration.

Mössbauer studies of system $Li_{0.5+0.5x}Ti_xFe_{2.5-1.5x}O_4$ with x ranging from 0 to 1.2 are obtained at 300K and 78K by Pran Kishan et al [1.26]. They have observed that the well defined hyperfine Zeeman spectra for samples with $x \leq 0.6$ at 300K and for $x \leq$ at 78K and resolved into two sextets corresponding to octahedral and tetrahedral sites. The samples with x = 0.2 to 0.6 show a central doublet at both the temperatures which is attributed to the presence of superparamagnetic clusters. Relaxation effects are observed for the samples with x = 0.8 and 1.0 at 300K and with x = 1.0 and 1.2 at 78K, while the sample with x = 1.2 at 300K exhibit paramagnetic behaviour. There is no change observed in isomer shift with increasing Ti^{4+} substitution. The same system has been investigated by A. A. Yousif et al [1.27] using X-ray diffraction and Mössbauer spectroscopy (300 and 77K) and S. A. Mazen et al [1.28] have studied IR absorption and dielectric properties of the same system. IR absorption spectra were used for analyzing the compositions. Three bands were observed in the IR spectra. The band at around 600 cm^{-1}(ν_1^*) and

another one around 400 cm^{-1} (ν_2^*) were assigned to the tetrahedral and octahedral complexes, respectively. A small band (ν_3) at around 335 cm^{-1} indicated the octahedral divalent metal-oxygen bond in these complexes. The threshold frequency for the electronic transition seems to increase with increasing Ti^{4+} content, namely with decreasing Fe^{3+} concentration. The AC conductivity and dielectric properties (loss tangent, dielectric constant and dielectric loss) have been measured at various frequency and temperatures. At room temperature (RT), the AC conductivity exhibits dispersion in the frequency range from 3 x 10^2 Hz to 5 x 10^5 Hz. The variation of loss tangent with frequency at RT shows a peak in the range (2-6) x 10^5 Hz. The electrical conduction mechanism was explained in terms of the electron hopping model. Temperature and frequency effects tend to increase dielectric constant and dielectric loss.

Gorter [1.29] has shown from the study of magnetic properties of Li-Cr ferrites that some of the lithium ions occupy octahedral sites and fraction of lithium ions migrate to tetrahedral sites whereas Cr^{3+} ions replace Fe^{3+} ions at both the sites. Analysis of Mössbauer ^{57}Fe spectra and Infrared spectra have been made for $Li_{0.5}Fe_{2.5-x}Cr_xO_4$ ferrite samples for $0 \leq x \leq 2.0$ with x varying in steps of 0.2 [1.30]. They have showed presence of hyperfine field at A and B site for Cr^{3+} concentration (x) up to 1.2. A ferromagnetic relaxation occurs when x is increased to 1.6 which is followed by paramagnetic transition when x approaches 2.0. The decrease in the internal magnetic field with increase in Cr^{3+} concentration has been explained from super transferred hyperfine field whereas relaxation effect in Mössbauer spectra has been explained on the basis of domain wall displacement. Infrared spectra of these ferrites showed absorption bands in the range 400-800cm^{-1}. The variation in absorption bands of IR spectra with increase in Cr^{3+} concentration indicated presence of ordering and disordering of cations and possible presence of Fe^{2+} ions. The study of the distribution of Cr^{3+} ions in same system has been reported by the NMR method [1.31].

Mössbauer spectroscopy studies on the $Li_{0.5+0.5x}Cr_{0.3}Ti_xFe_{2.2-1.5x}O_4$ system at 300K and 78K disclosed that for a low Ti^{4+} concentration the spectrum displayed a Zeeman Pattern for concentration higher than 0.4 a central quadrupole appeared together with the magnetic sextet. The intensity of the doublet increased when the Ti

concentration was increased. Consequently, the spectrum collapsed into a central quadrupole doublet. This behaviour was assigned to the existence of magnetic cluster for high Ti-concentration [1.32]. In the case of LiFeTiO4 ferrites, studies conducted at 4.2K with and without an external magnetic field of 4T showed that the direction of the resultant magnetization is due to mainly to the tetrahedral Fe^{3+} moments [1.33].

The effect of substitution of Fe^{3+} by non-magnetic Al^{3+} and magnetic Cr^{3+} in $Li_{0.5}Fe_{2.5}O_4$ on its structural and magnetic properties, the spinel system $Li_{0.5}Al_xCr_xFe_{2.5-2x}O_4$ was studied by U. N. Trivedi et al [1.34] by means of X-ray diffraction, high field magnetization, low field a.c. susceptibility and ^{57}Fe Mössbauer spectroscopy. They have reported that the system exhibits canted spin structure and a central paramagnetic doublet was found superimposed on magnetic sextet in the Mössbauer spectra (x>0.5).

Diamagnetically substituted Li-ferrites have attained considerable importance to their attractive magnetic and electrical properties and potential microwave applications. Therefore, the substituted Li-ferrites are found to be good substitutes for Garnets in microwave devices due to their low costs, high resistivity and low eddy current losses. Among them, West and Blankenship [1.35] determined the resistivities for the series $(Li_{0.5}Fe_{0.5})_{1-x}ZnFe_2O_4$. Electrical properties of $Li_{0.5-x/2}Zn_xFe_{2.5-x/2}O_4$ have reported by Davydov et al [1.36] and Kishan et al [1.37]. Rezlescu [1.38] have studied the resistivity and Curie point of lithium zinc ferrites as a function of composition and in relation to the ion on octahedral sites. It was observed that the resistivity increased with increasing concentration of zinc ions in the ferrite. In contrast, in many other spinel ferrites the resistivity decreases with the introduction of Zn ions. This behaviour was explained in terms of an increase in Fe^{2+} concentration caused by the evaporation of zinc during sintering. The electrical conductivity and thermoelectric power of some lithium-titanium ferrites with small amount of manganese and zinc have been studied by Manjula et al [1.39] as a function of temperature in the range of 300-550K. The samples have a general compositions of $Li_{0.45+x/2}Mn_{0.1}Zn_{0.1}Ti_xFe_{2.35-3x/2}O_4$ where x = 0.36, 0.46, 0.56, 0.66 and 0.76. They are reported the conductivity shows two different regions with a large variation in the activation energies. The possible mechanisms with respect to ionic conduction and electron hopping are discussed with the support of thermoelectric power measurements. The resistivity of

the of the ferrites $(Li_{0.5}Fe_{0.5})_{1-x}Cu_xFe_2O_4$ (x = 0.2, 0.4, 0.6, 0.8 and 1) has been measured in the temperature range of 300 to 1000K by A. B. Naik et al [1.40]. Three distinct regions have been observed in logρ vs $10^3/T$ curves for all the samples. They have reported that the conduction in the first region is due to impurities and impurity phases. In the second and third regions it is due to ordered and disordered state of the material. The transition from the first region to the second region is due to lowering of symmetry and long range ordering of Li ions for low content of Cu whereas it is due to phase transition, i.e. tetragonal to cubic, for high content of Cu. The transition from second to third region is due to magnetic transition, i.e. ferrimagnetic to paramagnetic state. These transition temperatures are nearly equal to Curie temperature of the materials. The resistivity behaviour reflects the magnetic ordering that takes place in these ferrites.

The electrical conductivity of mixed lithium-cadmium ferrites having the compositional formula $Li_{0.5-x/2}Cd_xFe_{2.5-x/2}O_4$ (where x = 0.2, 0.4, 0.6, 0.8 and 1.0) sintered at 1200, 1250 and 1300^oC have been investigated by D. Ravinder [1.41] from room temperature to well beyond the Curie temperature by two probe method. The porosity and activation energy were calculated and it was found that the electrical conductivity is progressively increasing with increase of sintering temperature while porosity and activation energy decrease continuously. The conduction mechanism in these ferrites can be explained on the basis of hopping mechanism. Infrared spectra have been analyzed by S. S. Bellad et al [1.42] of the same system in the frequency range 200-800 cm^{-1}. The IR spectra revealed four absorption bands along with the shoulders for the samples with x = 0 to 0.3. For x > 0.3, the x>0.3, last bands viz. ν_3 and ν_4 got converted into shoulders. The IR bands along with their shoulders shifted gradually towards the lower frequency side with the addition of cadmium, which have been attributed to the increase in the lattice parameter. The shoulders appeared in the spectrum have been attributed to the presence of Fe^{2+} ions in excess amount in the samples. Radha et al [1.43] have studied the Li-Cd ferrites for their frequency and composition dependence of dielectric behaviour. Composition dependence of the elastic moduli of mixed Li-Cd ferrites have been studied by Ravinder [1.44].

The transport properties of trivalent substituted Li-ferrites have been investigated by A. A. Satter et al [1.45]. The electrical resistivity and thermoelectric power of $Li_{0.5}Fe_{2.5-x}R_xO_4$ (R = Al, La, Sm, and Gd; x = 0.0 and 0.1) have been

studied. The electrical resistivity is found to have a direct relation with the ionic radius of the substituted R ions.

The conduction mechanism in Mg^{2+} and Al^{3+} substituted $Li_{0.5}Fe_{2.5}O_4$ with general formula $Mg_xAl_{2x}Li_{0.5(1-x)}Fe_{2.5(1-x)}O_4$ (x = 0.0, 0.2, 0.5, 0.6 and 0.7) has been studied by M. P. Pandya et al [1.46] by means of compositional and temperature dependent d. c. resistivity, thermoelectric power and I-V characteristics measurements. It is found that ferrites are electronic conductors. For x = 0.0 and 0.2 conduction is due to holes, while for x = 0.5, 0.6 and 0.7 it is due to electrons. Thermal variation of mobilities and activation energies have been determined through d. c. resistivity measurements conformed the small polarons. The switching phenomena have revealed in the sample with x = 0.0. The same system has studied on structural [1.47], magnetic [1.48], far-infrared absorption spectroscopy [1.49].

A systematic study of far-infrared spectra of Ti^{4+} and Zr^{4+} substituted Li-Zn ferrites [1.50] and Li-Co ferrites [1.51] have reported. A systematic investigation on compositional variation of lattice parameter, Curie temperature and dc resistivity as a function of temperature and applied field of the Li-Sb ferrites substituted Cr^{3+} was done by Radhapiyari et al [1.52].

Many scientists have studied the dispersion in the dielectric constant as well as the tangent of the dielectric loss angle and their strong dependence on the polarization processes [1.53, 1.54]. The dependence of dielectric properties of mixed ferrites of Li-Zn, on the composition and frequency, has been studied out by Ravinder [1.55]. The frequency and composition dependence of dielectric behaviour of mixed Li-Cd ferrites [1.56] have reported. The DC and AC resistivity, dielectric constant and dielectric loss tangent of Zn-substituted Li-Mg ferrites having the general formula $Li_xMg_{0.4}Zn_{0.6-2x}Fe_{2+x}O_4$ (where x = 0.0 to 0.3 step-0.05) have been investigated by A. M. Shaikh et al [1.57] as a function of composition, temperature and frequency. They reported that the compositional variation of DC resistivity and dielectric constant show the inverse trend with each other. High frequency dielectric behaviour of Li-Mg ferrites [1.58] have been studied at room temperature. Plots of dielectric constant vs. frequency show a normal dielectric behaviour and frequency dependence of loss tangent is found to be abnormal, giving a peak at certain frequency for all mixed Li-Mg ferrites have reported.

Many researchers have studied Mössbauer spectroscopy of $Li_{0.5}Fe_{2.5-x}Ga_xO_4$ system [1.59], anisotropy paradox of Co^{2+} ions in lithium ferrite [1.60],

Magnetocrystalline anisotropy in iron defect LiZnTiMn ferrites [1.61], Magnetic anisotropy and Mössbauer spectra in disorder lithium-zinc ferrites [1.62], Elastic properties of mixed Li-Cu ferrites [1.63] and microwave absorption properties of Ce-substitued lithium ferrite [1.64].

Moreover, the effect of γ-irradiation on some physical properties of rare earth ferrite on the general formula $Li_{0.5+z}Co_zYb_xFe_{2.5-2z-x}O_4$, (z= 0.1, x = 0.0 to 0.2 step-0.025) have been discussed by M. A. Ahmed et al [1. 65]. The temperature dependence of the polarization and resistance has studied in the range (300K≤ T ≤ 700K) at different frequencies (10 kHz ≤ f ≤ 1 MHz). The relaxation time and the activation energy were calculated for γ does of 1 and 3 Mrad. Also, a comparison was made between the ac resistance, before and after irradiation, the samples with different Yb concentration (0.0≤ x ≤0.2). The result after irradiation with a 1 Mrad dose of γ-rays showed that the resistance at the critical concentration decreases from 800 to 25 kΩ, at room temperature.

The effect of laser irradiation on the electrical properties of $Li_{0.5+z}Co_zDy_xFe_{2.5-2z-x}O_4$ ferrite (0.0 ≤ x ≤ 0.2, z = 1) has been studied [1.66] in the temperature range 300K ≤ T ≤ 750K at frequencies of 10kHz-5MHz, using a LIMO-IR diode, at wavelength of 808 nm. It was found that laser irradiation increase the polarization, the resistivity and the paramagnetic region. As a result of electronic rearrangement and lattice defects, small polaron and cluster were created.

Influence of 50 MeV lithium ion irradiation effect on hyperfine interaction of $Cr_{0.5}Li_{0.5}Fe_2O_4$ system has been investigated by Mössbauer spectroscopy [1.67]. The Mössbauer spectrum of irradiated samples shows no paramagnetic doublet contribution and the hyperfine fields corresponding to the Fe^{3+} in the octahedral (B) and the tetrahedral (A) site are very well separated. That is the observed superimposed A and B sites in unirradiated sample are split into separate lines after Li irradiation. Further an increase of the intensity of the lines (2) - (5) with respect to (1) – (6) signals an orientations of the hyperfine magnetic field towards a direction perpendicular to the ion path due to the irradiation induced strain by the latent tracks.

In view of the above consideration, the present thesis reports the Swift heavy ion irradiation effects of Ti^{4+} substitution in the presence of small amount of Al^{3+} (non-magnetic) and Cr^{3+} (magnetic) for Fe^{3+} on the structural, magnetic and electrical properties of $Li_{0.5}Fe_{2.5}O_4$.

The Manganese ferrite ($MnFe_2O_4$) was reported to be 81% normal by Hasting and Corliss [1.68], Harission [1.69] tried to explain the net moment of 4.6 μB per molecule by invoking the valence fluctuations (i.e. $Mn^{2+} \Leftrightarrow Mn^{3+}$ and $Fe^{3+} \Leftrightarrow Fe^{2+}$). But, Lotgering [1.70] concluded through the electrical conductivity and Seebeck effect measurements on Fe_3O_4-$MnFe_2O_4$-Mn_2O_4-$Mn_2Fe_2O_4$, that the presence of Mn_{2+} on B-site in $MnFe_2O_4$ is very unlikely. This controversy was resolved by Satya Murthy et al [1.71] through neutron diffraction study and established that Mn^{2+} is in the divalent state. It has been found that $MnCr_2O_4$ is normal spinel and it exhibits 'Spiral' type of magnetic ordering [1.72]. The neutron diffraction study of $MnAl_2O_4$ [1.71] has shown 9% degree of inversion. This means that the substitution of Al^{3+} on B-site in $MnFe_2O_4$ may leads to collapse of long range ordering on increasing Al^{3+} while the presence of Cr^{3+} in $MnFe_2O_4$ would compensate this effect and may also enhance the B-B interactions. In view of this, it was thought to study irradiation effects on the structural, magnetic and electrical properties of Mn-ferrite with simultaneous substitution of non-magnetic Al^{3+} and magnetic Cr^{3+} for Fe^{3+}.

Effect of 50 MeV Li^{3+} ion irradiation induced modifications in structural and dielectric properties of In^{3+} substituted Mg-Mn ferrite [1.73] and Al^{3+} substituted Mg-Mn ferrite [1.74] systems have studied. Mössbauer studies of 190 MeV Ag ion irradiated $NiMn_{0.05}Fe_{1.95}O_4$ ferrite [1.75] and $NiMn_{0.05}Ti_xMg_xFe_{1.95-2x}O_4$ ferrite [1.76] systems have reported.

Copper ferrite, $CuFe_2O_4$ is rather unique among the spinel for two reasons: firstly, its cation distribution over the non-equivalent sites is variable and strongly dependent on the temperature. Secondly, the presence of Cu^{2+} ions leads to severe Jahn-Teller type distortions of the sites [1.77]. For this reason, the non-equivalent sites are more distinct than in other spinels.

The ferrimagnetic spinel copper ferrite shows remarkable variation of its structure and consequently, of its magnetic properties depending on heat treatment [1.78-1.82]. The lattice of the low temperature phase is distorted to tetragonal symmetry and above 630K it is cubic. The stable low-temperature phase of $CuFe_2O_4$ is an inverse spinel, i.e. the cupric ions populate mainly octahedral sites (B-sites) while the ferric ions are found on B sites as well as on tetrahedral sites (A-sites) in about equal amounts. Quenching originate a cubic phase which is stable at lower temperatures [1.83-1.86].

The Mössbauer spectrum of $CuFe_2O_4$ has been reported by several authors [1.87-1. 90]. Tetragonal and cubic $CuFe_2O_4$ has studied [1.91] by Mössbauer effect technique at room temperature and at 4.2 K with and without applied field. The results demonstrated that tetragonal $CuFe_2O_4$ is an inverse spinel of Neel collinear arrangements and that cubic copper ferrite is not completely inverse with a cation distribution dependent on the heat treatment.

The Al-substituted disordered spinel series $CuFe_{2-x}Al_xO_4$ (x = 0.0-1.6) has been studied [1.92] by X-ray diffraction, Magnetization, ac susceptibility and Mössbauer measurements. The variation of the saturation magnetic moment per formula unit measured at 77K and 300K wit the Al content is satisfactory explained on the basis of Neel collinear spin ordering model for x = 0.0 – 1.0. The Mössbauer spectra at 300K have been fitted with two sextets in the ferrimagnetic state corresponding to Fe^{3+} at the tetrahedral (A) and octahedral (B) sites for $x \leq 0.8$. Mössbauer results conform a collinear ferrimagnetic structure for x = 0.0-0.6 and suggest non-collinear behaviour $x \geq 0.8$. The Curie temperature decreases nearly linear with increase of al concentration from x = 0.0 to 1.2. The structural study on Al^{3+} substituted Cu-ferrite [1.93] has shown the absence of tetragonal distortion for lower Al content and higher B-site occupancy of Al^{3+} ions.

The introduction of Cr^{3+} ions gives rise to strong B - B interaction [1.94]. Many studies have been carried out on $CuCr_2O_4$ [1.95, 1.96], $CuCr_xFe_{2-x}O_4$ [1.97, 1.98, 1.99]. The results show that Cr and Cu are in the charge state Cr^{3+} and Cu^{2+}, respectively. When Cr^{3+} is progressively replaced by Fe^{3+} ions, the crystal structure becomes a cubic spinel structure and its Neel temperature rises. However, some of them are complex spectra of ferrous ions. In an attempt to studied superexchange interactions in Cu-Cr ferrites [1.100] using Mössbauer and infrared spectra, a series of the samples $CuCr_xFe_{2-x}O_4$, $0 \leq x \leq 1$ has been prepared. The dielectric constant and dielectric loss were measured by M. A. El Hiti et al [1.101] of the same system at different frequencies and temperatures from room temperature to 600K. The results have been revealed that the dielectric loss decrease with increasing frequency and Cr substitution. The dielectric decreases with both increasing frequency and Cr substitution at room temperature. At moderate temperatures, the dielectric constant shows a dispersion peak and this peak shifted to higher frequency with increasing temperature. The results have been explained in the light of the fact that the dielectric

polarization process is similar to that of conduction and the appearance of the dispersion peak is related to the contribution of two types of charge carriers.

Electrical conductivity of Cr-substituted copper ferrites having the chemical formula $Cu_{1-x}Cr_xFe_2O_4$ (where x = 0.1 - 0.5 step of 0.1) studied by D. Ravinder et al [1.102]. Various compositions have been investigated as a function of composition and temperature.

The effect of thermal history on the structural and magnetic properties of the quenched and slow-cooled powdered samples of the spinel system $CuAl_xCr_xFe_{2-2x}O_4$ for compositions with x = 0.2, 0.4, 0.6 and 0.8 has been investigated [1.103] by means of XRD, high field (6T) magnetization, low field dc magnetization, ac susceptibility and Mössbauer spectroscopy. The results have been explained on the basis of random canting of spins model and domain wall kinetics.

Aim of the present work is to study the influence of heat treatment or thermal history as well as swift heavy ion irradiation on the structural, magnetic and electrical properties of Al^{3+} and Cr^{3+} co-substituted $CuFe_2O_4$.

Some work has been reported in the literature on the magnetic ordering in Zn-substituted slow-cooled and quenched $Zn_xCu_{1-x}FeCrO_4$ [1.104, 1.105], effect of Zn-substitution on some structural properties of $CuFeCrO_4$ [1.106], compositional and temperature dependent electrical behaviour of Zn-substituted copper-ferri-chromates [1.107], Infrared spectral studies of Zn-substituted CuFeCrO4 spinel ferrite system [1.108], Elastic behaviour of Zn-substituted copper ferri chromates [1.109], Gamma irradiation effects on the electrical conductivity of pure and Cu-doped Fe_3O_4 spinel [1.110], Laser induced structural and transport properties changes in Cu-Zn ferrites [1.111].

The interest in the SHI irradiation on ferrites is because of the effect of irradiation on the magnetic interaction, especially the superexchange interactions that ate highly sensitive to any change in the bond length, bond angle and the cation distribution in the ferrite materials. SHI irradiation is good sources to generate defects that can further be responsible for the cation redistribution and strain/stress in the lattice structure thereby modify the structural, magnetic and electrical properties.

In this regard the present thesis work includes on SHI irradiation studies on the following spinel ferrite systems:

1. $Li_{0.5(1+x)}Ti_xAl_{0.1}Fe_{2.4-1.5x}O_4$ (x = 0.0 to 0.3, step – 0.1)
2. $Li_{0.5(1+x)}Ti_xCr_{0.1}Fe_{2.4-1.5x}O_4$ (x = 0.0 to 0.3, step – 0.1)

3. $MnAl_xCr_xFe_{2-2x}O_4$ (x = 0.0 to 0.8, step – 0.2)
4. $CuAl_xCr_xFe_{2-2x}O_4$ (x = 0.0 to 0.8, step – 0.2) [Slow-Cooled & Quenched]

The polycrystalline samples of all the above-mentioned spinel solid solutions were synthesized by double sintering ceramic technique. The compositional stoichiometry of all the final products was ascertained by Energy Dispersive Analyses of X-rays. The X-ray diffractometry was employed to confirm single face structure and to deduce the structural parameters. The structural, magnetic and electrical characterization of the prepared bulk samples have been performed using different techniques. The relevant theoretical background and experimental details for the various parameters related to microstructural, magnetic and electrical behaviour of the ferrite system have been discussed in chapter 4 and chapter 5, respectively. The details of sample synthesis have been given in the chapter 2 and chapter 3 includes the theoretical concept of the swift heavy ion irradiation.

Irradiation experiments were performed in high vacuum chamber, with typical vacuum maintained at 1 x 10^{-6} mbar after purity and structural conformation of all above mention bulk samples. The specimens of $Li_{0.5(1+x)}Ti_xAl_{0.1}Fe_{2-2x}O_4$, $Li_{0.5(1+x)}Ti_xCr_{0.1}Fe_{2-2x}O_4$, $CuAl_xCr_xFe_{2-2x}O_4$ were irradiated in vacuum with 50 MeV Li^{3+} ions with fluence of 5 x 10^{13} ions/cm^2 and $MnAl_xCr_xFe_{2-2x}O_4$ were irradiated in vacuum with 50 MeV Li^{3+} ions with fluence of 1 x 10^{13} ions/cm^2 using 15 UD Pelletron accelerator at Inter University Accelerator Centre (formerly known as a Nuclear Science Centre), New Delhi.

The knowledge of the cation distribution is essential to understand the physical properties of spinel ferrites. All the XRD patterns were analyzed and indexed by using powder-X software and the distribution of cations in the tetrahedral and octahedral sites for all the unirradiated and irradiated systems was found by XRD intensity analysis using a computer programme developed in C-language in our laboratory. Unirradiated and irradiated samples were studied by means of high field and low temperature (77K) magnetization, thermal variation of low field AC susceptibility, Mössbauer spectroscopy.

The compositional, frequency and temperature dependent electrical and dielectric behaviour have been studied of the unirradiated as well as irradiated all the systems. The samples were characterized by electrical measurements such as thermoelectric power, DC and AC resistivity, dielectric constant and dielectric loss

(loss tangent) as a function of frequency in the range 100 Hz – 1MHz and temperature range 300K to 800K using impedance analyzer.

References

1.1 F. Desauer, Z. Physik **38** (1923) 12, Sol St. Phys. **2** (1956) 305

1.2 F. Seitz and J. S. Koehler, Sol St. Phys. **2** (1956) 305

1.3 G. Szenes, Phys. Rev **B51** (1995) 8026

1.4 R. L. Fleischer, P. B. Price and R. M. Walker, J. Appl. Phys. **36** (1865) 3645

1.5 R. E. Johnson, W. L. Brown, Nucl. Instr. Meth. Phys. Res. **B198** (1982) 103

1.6 P. Hansen, H. Heitmann and P. H. Smit Phys. Rev. B. **26** (1982) 3539

1.7 H. Heitmann and P. Hansen, J. Appl. Phys. **53** (1982) 7321

1.8 C. Houpert, M. Hervieu, D. Groult, F. Studer and M. Toulemonde, Nucl. Instr. Meth. Phys. Res. **B32** (1988) 393

1.9 F. Studer, H. Pascard, D. Groult, C. Houpert, N. Nguyen and M. Toulemonde, Nucl. Instr. Meth. Phys. Res. B**32** (1988) 389

1.10 R. Wolfe, J. C. North, R. L. Barms, M. Robinson, H. J. Levinstein, Appl. Phys. Lett. **19** (1971) 298

1.11 H. Pascard, Phys. Rev. B **30** (1984) 2299

1.12 F. Studer, Ch. Houpert, D. Groult, M. Toulemonde, Radi. Eff. & Defect in Solids **110** (1989) 55

1.13 F. Studer and M. Toulemonde, Nucl. Instr. and Meth. B **65** (1992) 560

1.14 A. Meftah, F. Brisard , J. M. Costantini, M. Hage-Ali, J. P. Stoquert, F. Studer, M. Toulemonde, Phys. Rev. B **48** (1993) 920

1.15 M. Toulemonde, G. Fuchs, N. Nguyen, F. Studer, D. Groult, Phys. Rev. B **35** (1987) 6560

1.16 F. Studer, Ch. Houpert, D. Groult, J. Yun Fan, A. Meftah and M. Toulemonde, Nucl. Instr. Meth. Phys. Res. B **82** (1993) 91

1.17 S. Meillon, F. Studer, M. Hervieu and H. Pascard, Nucl. Instr. Meth. Phys. Res. B**107** (1996) 363

1.18 Yu G. Chukalkin, B. N. Goshchitskii, S. F. Dubinin, S. K. Sidorov, V. V. Petrov, V. D. Parkhomenko, V. G. Vologin, Phys. Stat. Sol. (a) **28** (1975) 345

1.19 V. V. Petrov, Yu G. Chukalkin, B. N. Goshchitskii, Sov. Phys. Solid State **22** (1980) 339

1.20 M. A. Mousa and M. A. Ahmed, Journal of Material Science **23** (1988) 3083-3087

1.21 M. A. Mousa, A. M. Summan, M. A. Ahmed and A. M. Badawy, J. Mater. Sci. **24** (1989) 2478

1.22 X. W. Qi, J. Zhou, Z. X. Yue, Z. L. Gui, L. T. Li, Mater. Sci. & Eng. B-Solid State Materials for Advanced Technology **99** (2003) 278

1.23 J. A. Sehulke and G. Blasse, J. Phys. Chem. Solids **24** (1963) 1651

1.24 D. Striker and R. Roy, J. Amer. Ceram. Soc. **44** (1961) 225

1.25 P. Raj and S. K. Kulshreshtha, J. Phys. Chem. Solid **31** (1970) 9

1.26 Pran Kishan, Chandra Prakash, J. S. Baijal and K. K. Laroia, Phys. Stat. Sol. (a) 84 (1984) 535

1.27 A A Yousif, M E Elzain, S A Mazen, H H Sutherland, M H Abdalla and S F Masour, J. Phys.: Condensed. Matter **6 (**1994) 5717

1.28 S. A Mazen, F. Metawe and S. F. Mansour, J. Phys. D: Appl. Phys. **30** (1997) 1799

1.29 E. W. Gorter, Philips Res Repts (Netherlands) **9** (1954) 403

1.30 Navdeep K. Gill and R. K. Puri, Ind. J of Pure & Appl. Phys **23** (1985) 71-73

1.31 G. N. Abelyashev, V. V. Mal'nev, V. N. Seleznev, N. A. Sergeev and Yu. V. Fedotov, Sov. Phys. Solid State **33(6)** (1991) 1059

1.32 K. Deeppik, P. Sumitra, J. S. Baijal, K. Prom and P. Chandra, J. Phys. C: Solid state Phys. **21** (1988) 6169

1.33 K. S. Kulshreshtha, J. Magn. Magn. Mater. **53** (1986) 345

1.34 U. N. Trivedi, K. B. Modi and H. H. Joshi, PRAMANA-J. Phys. **58 (5-6)** (2002) 1031

1.35 R. G. West and A. C. Blankenship, J. Am. Ceram. Soc. **50** (1967) 343

1.36 L. A. Davydov, S. A. Plotinnikov and M. F. Bryzhina, Sov. Phys. Sloid State **7** (1965) 596

1.37 P. Kishan, D. R. Sagar and P. Swarup, J. Less Com. Met. **108** (1985) 345

1.38 N. Rezlescu, Rev. Roum. Phys. **15** (1970) 619

1.39 R. Manjula, V. R. K. Murthy, and J. Sobhandari, J. Appl. Phys. **59(8)** (1986) 2929

1.40 A. B. Naik, S. A. Patil and J. I. Pawar, Ind. J. of Pure & Appl. Phys. **27** (1989) 149

1.41 D. Ravinder, Mater. Lett. **40** (1999) 198

1.42 S. S. Bellad, R. B. Pujar & B. K. Chougule, Ind. J. of Pure & Appl. Phys. **36** (1998) 598-601

1.43 K. Radha and D. Ravinder, Ind. J. of Pure & Appl. Phys. **33** (1995) 74

1.44 D. Ravinder, J. Appl. Phys. **75(10)** (1994) 6121

1.45 A. A. Sattar, A. H. wafik and H. M. El-Sayed, J. Mater. Sci. **36** (2001) 4703

1.46 M. P. Pandya, K. B. Modi and H. H. Joshi, J. Mater. Sci. **40** (2005) 5223

1.47 K. B. Modi, J. D. Gajera, M. C. Chhantbar, K. G. Saija, G. J. Baldha and H. H. Joshi, ibid. **57** (2003) 4049

1.48 G. J. Baldha, K. G. Saija, K. B. Modi, H. H. Joshi and R. G. Kulkarni, Mater. Lett. **53** (2002) 233

1.49 K. B. Modi, J. D. Gajera, M. P. Pandya, H. G. Vora and H. H. Joshi, PRAMANA-J. of Phys. **62(5)** (2004) 1

1.50 R. S. Patil, S. V. Kakatkar, A. M. Sankpal, S. R. Sawant, S. S. Suryavanshi, U. R. Ghodake and R. K. Kamat, Ind. J. of Pure & Appl.Phys. **32** (1994) 193

1.51 K. Mohan and Y. C. Venudhar, J. Mater. Sci. Lett. **18** (1999) 13

1.52 L. Radhapiyari, Ch Chivayi, P. Sumitra and H. Sarma, Ind. J. Phys. **73** (1999) A175

1.53 R. S. Patil, S. V. Kakatkar, S. A. Patil, P. K. Maskar and S. R. Sawant, Phys. Status Solidi a **126** (1991) K185

1.54 R. S. Patil, S. V. Kakatkar, P. K. Maskar, S. A. Patil, and S. R. Sawant, Ind. J. of Pure & Appl. Phys. **29** (1991) 589

1.55 D. Ravinder, J. Mater. Sci. Lett. **11** (1992) 1498

1.56 K. Radha and D. Ravidner, Ind. J. of Pure & Appl. Phys. **33** (1995) 74

1.57 A. M. Shaikh, S. S. Bellad, B. K. Chougule, J. Magn. & Magn. Mater. **195** (1999) 384

1.58 D. Ravinder, P. Vijaya Bhasker Reddy, Mater. Lett. **57** (2003) 4344

1.59 S. K. Kulshreshtha, J. Mater. Sci. **20** (1985) 3900

1.60 Gerald F. Dionne, J. Appl. Phys. **57(1)** (1985) 3727

1.61 A. Iglesias, J. Balmaseda, A. Gonzalez Arias, J. Mater. Res. **17(7)** (2002) 1702

1.62 Z. C. Xu, J. Appl. Phys. **93(8)** (2003) 4746

1.63 D. Ravinder and P. Vijaya Bhaskar Reddy, Mater. Lett. **57** (2003) 4575

1.64 Chang Sun and Kangning Sun, Solid State Commun. **141** (2007) 258

1.65 M. A. Ahmed and Samiha T Bishay, J. Phys. D: Appl. Phys. **34** (2001) 1339

1.66 M. A. Ahmed and S. T. Bishay, Radi. Eff. & Def. in Solid **160(9)** (2005) 417

1.67 S. G. Parmar, Ravikumar and R. G. Kulkarni, Hyper. Inter. **160** (2005) 235

1.68 J. M. Hasting and L. M. Corliss, Phys. Rev. **104** (1956) 328

1.69 S. E. Harrison, C. J. Kriessman and S. R. Pollack, Phy. Rev. **110** (1958) 844

1.70 F. K. Lotgering , J. Phys. Chem.. Solids, **25** (1964) 95

1.71 N. S. Satya Murthy, L. Madhav Rao, R. J. Begam, M. g. Natera and S. I. Yusuf, J. de Phys. **32** (1971) C1-318

1.72 J. M. Hastings and L. M. Corliss, Phys. Rev. **126** (1962) 556

1.73 M. Singh, Anjana Dogra and Ravi Kumar, Nucl. Instr. Meth. Phys. Res. B **196** (2002) 315

1.74 Anjana Dogra, M. Singh and Ravi Kumar, Nucl. Instr. Meth. Phys. Res. B **207** (2003) 296

1.75 Anjana Dogra, S. K. Srivastava, M. Singh, N. Kumar, P. Sen and Ravi Kumar, Radi. Measur. **26** (2003) 667

1.76 Anjana Dogra, M. singh, N. Kumar, P. Sen and Ravikumar, Nucl. Instr. Meth. Phys. Res B**212** (2003) 190

1.77 A. M. Kapitonov, M. Smokotin, Phys. Status Solidi **A34** (1976) K47

1.78 L. Well, F. Bertaut and L. Bochirol, J. Phys. Radium **11** (1950) 208

1.79 H. M. O'Bryan, H. J. Lewinstein and R. C. Sherwood, J. Appl. Phys. **37** (1966) 1438

1.80 M. Ohnishi and T. Teranishi, J. Phys. Soc. Japan **16** (1961) 35

1.81 K. P. Bielov, A. N. Goriaga and L. T. Antoschina, Fiz. tverd. Tela **15** (1973) 10

1.82 J. Pietrzak, I. Onyszkiewcz and J. Kubiak, Mater. Sci. Techn. Univ. Wroclaw **3** (177) 21

1.83 H. Ohnishi, T. Teranishi and S. Miyahara, J. Phys. Soc. Japan **14** (1958) 106,

1.84 T. Inoue and S. Iida, J. Phys. Soc. Japan **13** (1958) 656,

1.85 I. Onyszkiewicz, N. T. Malafayev, A. A. Murakhowsky and J. Pietrazak, conf. CMEA countries Physics of Magnetic Materials, Jaszowiec, Poland (1980) p.6,

1.86 J. Kubiak and J. Pietrzak, Phys. Stat. Sol. **(a) 67** (1981) 103

1.87 B. J. Evans, S. S. Hafner and G. M. Kalvins, Phys. Lett. **23** (1966) 24

1.88 B. J. Evans and S. S. Hafner, J. Phys. Chem. Solids **29** (1968) 1573

1.89 W. R. Cares and J. W. Hightower, J. Catalysis **39** (1975) 36

1.90 V. U. Patil and R. G. Kulkarni, Solid State Commun. **31** (1979) 551

1.91 J. Janicki, J. Pietrzak, A. Porebska and J. Suwalski, Phys. Stat. Sol. **(a)72** (1982) 95

1.92 R. G. Kulkarni, Bimal S. Trivedi, H. H. Joshi and G. J. Baldha, J. Magn. Magn. Mater. **150** (1996) 375

1.93 V. D. Murumkar, K. B. Modi, K. M. Jadhav, G. K. Bichile, R. G. Kulkarni, Mater. Lett. **32** (1997) 281

1.94 V. A. M. Barbers, Progress in spinel Ferrites, Elsevier, Amsterdam, 1995

1.95 G. Wyckoff, Crystal Structures, Vol-3 (Interscience, New York, 1965) p. 86

1.96 E. Prince, Acta Cryst. **10** (1957) 554

1.97 A. Gerard, F. Grandjean, J. Phys. C: Solid State Phys. **12** (1979) 4601

1.98 H. N. Ok and Y. K. Kim, Phys. Rev. B **36** (1987) 5120

1.99 H. N. Ok, K. S. Back and E. J. Choi, Phys. Rev. B **40** (1989) 84

1.100 M. A. Amer, M. A. Ahmed, M. K. El-Nimr and M. A. Mostafa, Hyper. Inter. **96** (1995) 91

1.101 M. A. El Hiti, M. A. Ahmed, M. M. Mosaad and S. M. Attia, J. Magn. Magn. Mater. **150** (1995) 399

1.102 D. Ravinder, K. Sathi Reddy, P. Mahesh, T. Bhaskar Rao, Y. C. Venudhar, J. Alloy & Comp. **370** (2004) L17

1.103 Uday. N. Trivedi, K. B. Modi, Darshan C. Kundaliya, Amish G. Joshi, H. H. Joshi and S. K. Malik, J. Alloys & Comp. **369** (2004) 58

1.104 Kunal B Modi, V. T. Thanki and H. H. Joshi, Ind. J. Phys. **70A (4)** (1996) 497

1.105 Kunal B Modi, H. H. Joshi and R. G. Kulkarni, Ind. J. Pure & Appl. Phys. **34** (1996) 92

1.106 K. B. Modi, P. V. Tanna, S. S. Laghate and H. H. Joshi, J. Mater. Sci. Lett. **19** (2000) 1111

1.107 Kunal B Modi and H. H. Joshi, Ind. J. Phys., **76A (6)** (2002) 543

1.108 M. C. Chhantbar, U. N. Trivedi, P. V. Tanna, H. J. Shah, R. P. Vara, H. H. Joshi and K. B. Modi, Ind. J. Phys. **78A (3)** (2004) 321

1.109 K. B. Modi, Journal of Materials Science **39** (2004) 2887

1.110 M. A. Mousa, J. Radioanal . Nucl. Chem. Lett. **118(1)** (1987) 33

1.111 M. A. Ahmed, A. A. I. Khalil, S. Solyman, J. Mater. Sci. 42 (2007) 4098

CHAPTER: 2

Spinel Ferrites: Crystal Structure, Chemistry, Magnetic interactions and Synthesis

---

2.1 Introduction

Material science and engineering plays an imperative role in this modern age of science and technology. Various kinds of materials like Metallic Materials, Magnetic Materials, Ceramics, Polymers, Composites, Semiconductors, and Bio-Materials are used in industry, housing, clothing, agriculture, transportation, communication etc. to meet the plant and individual requirements. Among different materials, Magnetic materials play very important role in almost all equipment and instruments using modern technology such as ferrite magnets in TV, memory cores in computers, permanent magnet in motors, superconducting magnets in particle accelerators. There would be no audio/video equipment without the development of suitable magnetic materials. Magnetic materials are functional materials. They are sometimes used in large quantities (many tones), such as for the core materials in power transformers. One of such well known magnetic material family is 'ferrites'.

2.2 Ferrites

Ferrites are homogeneous ceramic materials composed of various oxides being Iron oxide (Fe_2O_3) their main constituent. Ferrites materials are known for a long time now and have been exploited for a number of communication and defense applications. In spite of the development in the technology of ferrite materials, the scientist still prefer to examine the structure and transport properties of these materials in systematic manner to understand the fundamental physics, which evolve correlations between various characteristics.

The history of ferrites (magnetic oxides) began centuries before the birth of Jesus Christ with the discovery of stones that would attract iron. The most plentiful deposits of these stones were found in the district of "Magnesia" in Asia Minor, hence the mineral's name became "Magnetite (Fe_3O_4)" much later, and the application of magnetite was as "Lodestone" meaning "way stone" used by early navigators to locate magnetic North. In 1600 William Gilbert published *De Magnete*, the first scientific study of magnetism.

The term "ferrite" is derived from the Latin "ferum", meaning iron and different things to different scientists. To metallurgists ferrite means pure iron. To geologists, ferrites are a group of minerals based on iron oxide. To electrical engineers, ferrites are also a group of minerals based on iron oxide, but ones that have particular useful properties: magnetic properties and dielectric properties.

Ferrites are useful in the electronics industry due to a combination of two key characteristics: (i) high magnetic permeability, which concentrate the magnetic-flux density, and (ii) high electrical resistivity, which limits the amount of electric current flow in the ferrite. Thus, ferrites exhibit low energy losses are efficient and function at high frequencies (1MHz to 1GHz). These qualities make ferrites good design devices for the manufacture of small high-frequency electronic components. Some of the more common use of ferrite includes magnetic devices, power transformer and chokes, inductors and tuned transformers, pulse and wide-band transformers, magnetic deflection systems, recording heads, rotating transformers and shield beads. Ferrites are manufactured in several different shapes like toroids, beads, rods, cylinders, blocks and multihole and in different sizes.

2.2.1 Classification of Ferrites

Depending on nature of the magnetic behaviour, the ferrites can be classified in to hard and soft ferrites. Hard ferrites retain their magnetism once they are magnetized. It is hard to demagnetized them, whereas soft ferrites can easily be magnetized and demagnetized. Barium and strontium ferrites are widely studied hard ferrites whereas nickel-zinc and manganese-zinc ferrites are the most used soft ferrites. Considering the crystal structure and magnetic ordering, ferrites can be classified into four different types [2.1] namely Spinel, Garnet, Magnetoplumbite and Orthoferrites as given in Table 2.1.

Table 2.1: Different types of ferrites with their structures, general formulae and examples

Type	Structure	General Formula	Examples
Spinel	Cubic	$A^{II}Fe_2O_4$	A^{II}- Mn, Zn, Ni, Mg, Co etc.
Garnet	Cubic	$Ln_3{}^{III}Fe_5O_{12}$	Ln^{III}- Y, Sm, Eu, Gd, Tb, Dy, Ho, Er, Tm and Lu
Magnetoplumbite	Hexagonal	$A^{II}Fe_{12}O_{19}$	A^{II}- Ba, Sr
Orthoferrites	Pervoskite	$Ln^{III}FeO_3$	Ln^{III} – same as garnets

Out of the four types of ferrites mentioned above the simplest ferrite is the spinel type and form a major class. The Spinel and Garnet are soft ferrites whereas Magnetoplumbite and the Orthoferrites are hard ferrites.

2.2.2 Crystal structure and Chemistry of Spinel Ferrites

The term spinel ferrite is named after the mineral spinel $MgAl_2O_4$, since both have the same structure. The crystal structure of spinel was first determined independently by Bragg [2.2] and Nishikawa [2.3]. The majority of spinel compounds belong to the space group O_h^7 (Fd3m). Formerly, only the spinels containing Iron were designated as spinel ferrite but now the term has been broadened to include all the ferrimagnetic involving spinel structure, which may or may not contain Iron. The spinel structure can be represented as $M'M''_2X_4$, where X represents oxygen or one chalcogenic bivalent anion (S^{2-}, Se^{2-}, Te^{2-}) and M' and M'' are metallic ions. The valences have to fulfill the electroneutrality requirements. Due to large electronegativity of Oxygen, the ionic type of bonds prevails in almost all oxide spinels. There are Z = 8 formula units or 'molecules' per cubic unit cell of spinel structure, each of which consist of 32 anions and 24 cations, for a total of 56 atoms. The crystallographic structure is formed by a nearly closed packed face cubic *(fcc)* array of anion with two in equivalent sites for cations. These differ in oxygen coordination; four oxygen ions surround tetrahedral cationic sites and octahedral sites by six oxygen ions. These are also called A and B sites, respectively.

There are 96 interstices between the anions in the cubic unit cell; however, in $M'M''_2X_4$ compounds only 24 are occupied by cations. Of the 64 tetrahedral interstices that exist between the anion, 8 are occupied by cations. The remaining 16 cations occupy half of the 32 octahedral interstices. The geometry of the occupied interstitial sites is shown in Fig. 2.2, where the primitive cell contains two formula units is shown [2.4].

The crystal structure is best described by subdividing the unit cell into eight octants, with edge ½ a ('a' is edge of the unit cell) as shown in Fig 2.1. The location of oxygen ions and metal ions in every octant then can be easily described.

The position of oxygen anions is identical in all the octants. Each octant contains four oxygen ions on the body diagonals and they lie at the corners of a tetrahedron (Fig. 2.2). Each oxygen ion is located at a distance equal to one forth of the length of the body diagonal from alternate corners of the octant. The array of oxygen ions as a whole in the crystal constitutes a *fcc* lattice with edge = a/2 and thus, there are four such interpenetrating fcc oxygen lattices. But the position of metal ions are identical only in the octants sharing the common edge or corner and

are different in the octants sharing common faces as shown in Fig. 2.1. So to get the complete picture of the positions of metal ions it is suffice to show any two adjacent octants (Fig. 2.2). In one of the octants, an occupied tetrahedral site is located at the centre and four more sites on the corners of the octant.

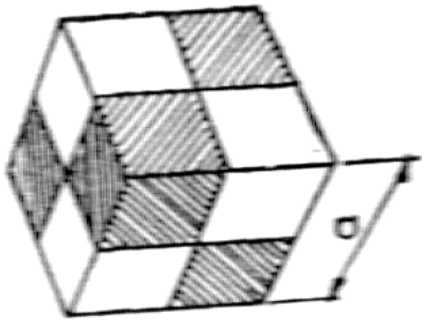

Fig. 2.1 Eight octants of a unit cell of spinel ferrite. The location of metal ions in four shaded and unshaded octants are identical

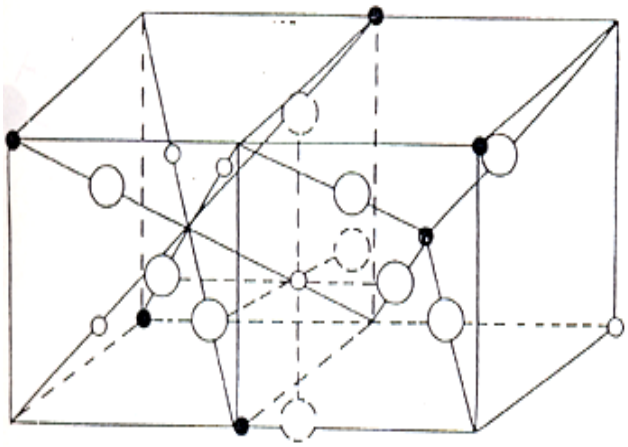

Fig. 2.2 The geometry of the occupied interstitial sites in spinel structure

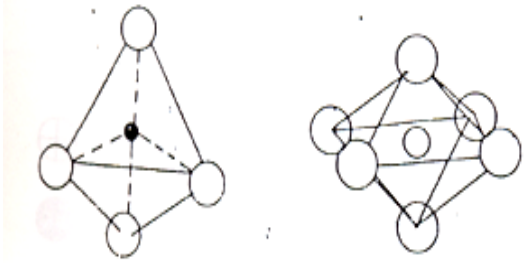

Tetrahedral (A) site Octahedral (B) site

In adjacent octant, that central site is not occupied, but owing to translation symmetry, half of the corner sites are occupied. Thus, the occupied tetrahedral sites form two interpenetrating *fcc* lattices, having a edge a, which are displaced with respect to each other, over a distance $a\sqrt{3}/4$ in the direction of the body diagonal of a cube. Each tetrahedral ion is surrounded by four other tetrahedral ions, which lie in

the corners of a regular tetrahedron. There are twelve nearest neighbour octahedral ions for every tetrahedral ion.

Each octant contains four octahedral metal ions and these are situated at sites analogous to those of the oxygen ions, i.e., at one quarter length of the body diagonal from the other ends of the four body diagonals of the octant. Octahedral metal ions form four interpenetrating *fcc* lattices, with edge 'a', which are displaced with respect to each other, over a distance $a\sqrt{2}/4$ in the direction of the face diagonals of a cube. The environment of an octahedral ion by the other octahedral ions is not cubic, as in the case of an individual tetrahedral ion. Each octahedral ion forms part of the two regular tetrahedral of octahedral ions, having the ion under consideration as common one. Each octahedral ion is surrounded by six nearest neighbour tetrahedral ions.

Each oxygen ion is surrounded by one tetrahedral ion (A ion) and three octahedral ions (B ions) as shown in Fig. 2.3. This unit can be regarded as the basic component of the spinel lattice. Each A ion belongs to four such units and each B ion six. The direction of OA is that of the body diagonal of a cube and the directions OB are along the cube edges.

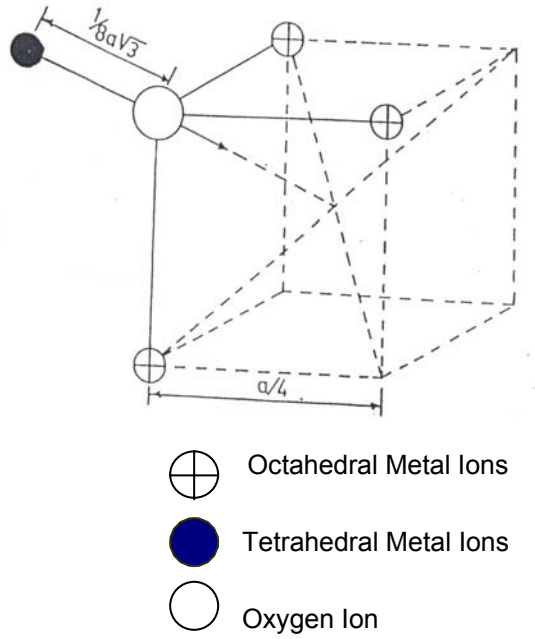

Fig: 2.3 Basic component of a spinel lattice

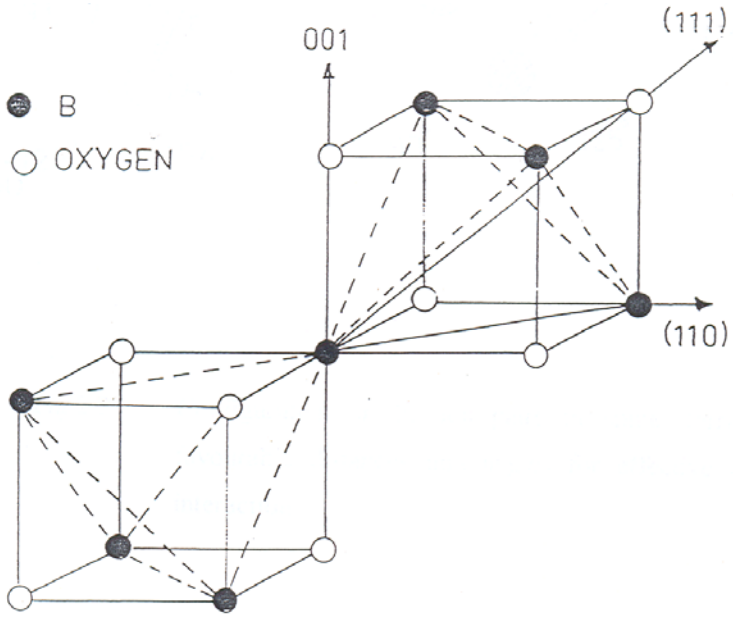

Fig.2.4 Indication of the direction in which the oxygen ion is moved if u>3/8

Description of the atomic positions in spinel is dependent on the choice of setting for the origin in the Fd3m space group. Two different equipoints with point symmetries $\bar{4}\,3m$ and $\bar{3}\,m$ are possible choice for the unit cell origin. Moreover, the origin can be assigned to either a vacant site or an occupied lattice site. Table 2.2 lists the arrangement of lattice sites along the unit –cell body diagonal for four possible choices of origin.

Table 2.2: Lattice sites along the Cube Body diagonal in the ideal conventional Unit Cell of Spinel

Fractional coordinates along body diagonal of unit cell	**Origin at $\bar{4}\,3m$**			**Origin at $\bar{3}\,m$**		
	Equipoint	**Origin on A-site**	**Origin on tetrahedral vacancy**	**Equipoint**	**Origin on B-site**	**Origin on octahedral vacancy**
0,0,0	8a	A-site cation	Tetrahedral vacancy	16c	B-site cation	Octahedral vacancy
1/8,1/8,1/8	16c	Octahedral vacancy	B-site cation	8a	Tetrahedral vacancy	A-site cation
¼,1/4,1/4	8a	A-site cation	Tetrahedral vacancy	32e	Anion X	Anion x
3/8,3/8,3/8	32e	Anion X	Anion X	8b	A-site cation	Tetrahedral vacancy
1/21/2,1/2	8b	Tetrahedral vacancy	A-site cation	16d	Octahedral vacancy	B-site cation
5/8,5/8,5/8	16d	B-site cation	Octahedral vacancy	8b	A-site cation	Tetrahedral vacancy
¾,3/4,3/4	8b	Tetrahedral vacancy	A-site cation	32e	Anion X	Anion X
7/8,7/8,7/8	32e	Anion X	Anion X	8a	Tetrahedral vacancy	A-site cation

The positions of anions and cations in Centro-symmetric representation are given by Wyckoff [2.5] in the following notation

32 (e) Oxygen coordinates	(u, u, u) ($\bar{u}$, $\bar{u}$, $\bar{u}$)	(u, ¼ - u, ¼ - u) ($\bar{u}$, ¼ - u, ¼ - u)	(¼ - u, u, ¼ - u) (¼ - u, $\bar{u}$, ¼ - u)	(¼ - u, ¼ - u, u) (¼ - u, ¼ - u, $\bar{u}$)
16(d) Octahedral	½, ½, ½	½, ¼, ¼	¼, ½, ¼	¼, ¼, ½
8(a) Tetrahedral	⅛, ⅛, ⅛	⅞, ⅞, ⅞		

The coordinates of remaining ions are obtained by *fcc* translations:
(0, 1/2, 1/2), (1/2, 0, 1/2), (1/2, 1/2, 0)

The symmetry of the structure is cubic and belongs to the space group O_h^7 (Fd3m). A small displacement defined by a single parameter u of the anions, from their ideal positions is allowed along the corresponding body diagonal which enables a better matching of anion positions to the relative radii of A and B cations. Anions, in spinel usually are dilated away from their ideal ccp positions. This dilation has several important crystallographic implications, which include changes in bond lengths, bond angles, interstice volumes and the symmetries of coordination.

In an ideal spinel, the lattice is perfect, that is u = 3/8. However, slight deviations from perfection must occur from ideal value of u because of the presence of cations. Assuming the hard sphere model, the radii of A and B sites are given in terms of 'u' and 'a' and the radius of the anion r (O^{2-}) as follows.

$$r_A = (u - 0.25)\, a\, (1.73) - r\,(O^{2-})$$

$$r_B = (0.625 - u)\, a - r\,(O^{2-})$$

As 'u' increases from its ideal value, anions move away from the tetrahedrally coordinated A-site cations along the ⟨111⟩ directions, which increase the volume of each A-site interstice while the octahedral B-sites become correspondingly smaller. For given spinel compounds, the anion sublattice expands or contracts by varying u, until the A- and B-site volumes match the radii of the constituent cations. The symmetry of regular tetrahedra that are associated with A-sites is unchanged by the anion-lattice dilation; however, B-sites suffer reduced symmetry. Changes in site symmetries with anion dilation are reflected in bond-angle variations with 'u'. These structural variations have important implications for the materials properties.

Both translational and local symmetries corresponding to the O_h^7 space group strictly apply only if each sublattice contains only one kind of cations, i.e. if all M' ions in M' M''$_2$ X_4 are in tetrahedral and all M'' ions are in octahedral positions. The spinel is then called *normal spinel*. We also have so called *inverse spinel* structure in which half the cations M'' are in A positions and the rest, together with the M' ions, are randomly distributed among the B positions. There are many examples of intermediate cases between a normal and an inverse spinel where a fraction of M' and M'' are inverted, that is M' occupies B positions and M'' occupies A positions. They are termed as *partially inverse spinels*. Therefore, in order to characterize the spinel structure fully, a further parameter is needed describing the degree of inversion. The formula may be explicitly written as,

$$(M'_{1-\delta}\ M''_{\delta})\ [M'_{\delta}\, M''_{2-\delta}]\ X_4,$$

where δ is known as inversion parameter, and is equal to zero in case of normal spinel and one in case of inverse spinel. As a part of convention, the cations at tetrahedral (A) sites are written in parenthesis and those at octahedral (B) sites in square brackets.

The electroneutrality leads to three basic types, according to the cation valency combinations. Three are,

$M'^{2+}\ M''^{3+}\ O_4$: (2-3 spinel), e.g. $NiFe_2O_4$, $CuFe_2O_4$

$M'^{4+}\ M''^{2+}\ O_4$: (4-2 spinel), e.g. $GeFe_2O_4$, $TiFe_2O_4$

$M'^{6+}\ M''^{1+}\ O_4$: (6-1 spinel), e.g. $MoLi_2O_4$, WAg_2O_4

It is found that practically any cation with radius within the limits 0.4 to 1Å may be incorporated into the spinel structure and most of them can occur in both octahedral and tetrahedral positions. The smallest cations with valency ≥ 4, however, are found in the tetrahedral coordination only, while the monovalent cations occurring mainly in 6-1 spinels are confined to the octahedral sites. Besides the geometrical factors, the distributions of cations among A and B positions is influenced by many other factors.

Crystal field splitting of energy levels and Jahn-Teller Effect:

With respect to the magnetic properties, the interest is primarily in transition metal ions particularly those of $3d^n$ group. The outer d-electrons of these ions may be regarded as practically localized in almost all oxide spinels so that the crystal (or ligand) field theory applies. This theory says that the low lying energy levels are decisive for the magnetic behaviour. The origin of the ligand field splitting of levels is attributed to both the electrostatic crystal field and the covalency between the cation

and the surrounding anions (ligands). Both these effects contribute to the stabilization of cations in the given surrounding. Crystal or ligand field stabilization energy = lowering of the ground level with respect to the ground level of the free ion. In an octahedral environment, the five d orbitals on a transition metal atom are no longer degenerate but split into two groups, the t_{2g} group of lower energy and the e_g group of higher energy as shown in Fig. 2.5. If possible, electrons occupy orbitals singly, according to Hund's rule of maximum multiplicity. For d^4 to d^7 atoms or ions, two possible configurations occurs, giving low spin and high spin states; these are shown for a d^7 ion in Fig. 2.6. In these, the increased energy, Δ required to place an electron in an e_g orbital, and hence maximize the multiplicity, has to be balanced against the repulsive energy or pairing, P, which arises when two electrons occupy the same t_{2g} orbital. The magnitude of Δ depends upon the ligand or anion to which the metal ion is bonded: for week field anions (ligands), Δ is small and the high spin state configuration occurs, and vice versa for strong field ligands. For magnitude of Δ, generally $\Delta(5d)>\Delta(4d)>\Delta(3d)$. Consequently the high spin behaviour is rarely observed in the 4d and 5d series.

In many transition metal compounds, the metal coordination is distorted octahedral and the distortions are such that the two axial bonds are either shorter than or longer than the other four bonds. The Jahn-Teller effect [2.6, 2.7] is responsible for these distortions in d^9, d^7 (low-spin) and d^4 (high-spin) ions. Consider the d^9 ion Cu^{2+} whose configuration is $(t_{2g})^6 (e_g)^3$. One of the e_g orbitals contains two electrons and the other contains one. The singly occupied orbital can be either d_z^2 or d_x^2-$_y^2$ and in a free ion situation both would have the same energy. However, since the metal coordination is octahedral the e_g levels, with one doubly and one singly occupied orbitals, are no longer degenerate. The e_g orbitals are high energy orbitals (relative to t_{2g}) since they point directly towards the surrounded ligands and the doubly occupied orbital will experience stronger repulsion and hence have somewhat higher energy than the singly occupied orbital. This has the effect of lengthening of the metal-ligand bonds is the directions of the doubly occupied orbital, e.g. if the d_z^2 orbital is doubly occupied, the two metal-ligand bonds along the z axis will be longer than the other four metal-ligand bonds. The energy level diagram for this later situation is shown in Fig. 2.7. Lengthening of the metal-ligand bond along the z-axis leads to a lowering of the d_z^2 orbital. The distorted structure is stabilized by an amount $(1/2)\delta 2$ relative to the

regular octahedral arrangement and, hence, the distorted structure becomes the observed, ground state.

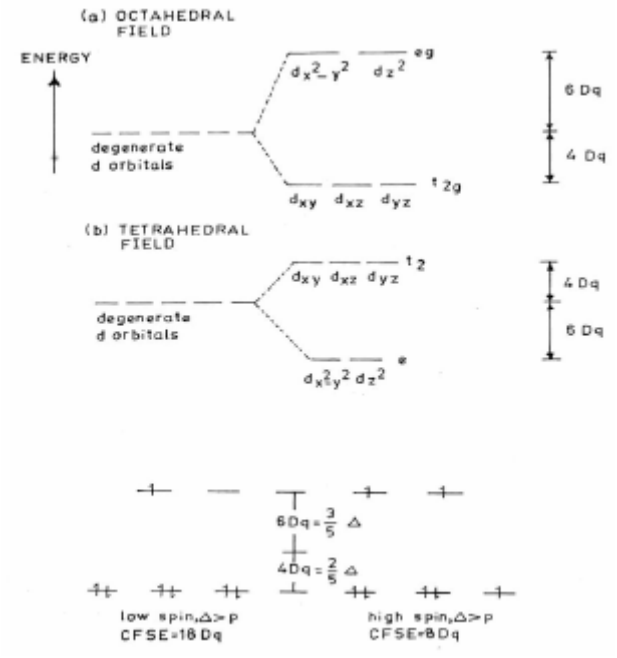

Fig. 2.5 Crystal field splitting of energy level and spin states in octahedral coordination

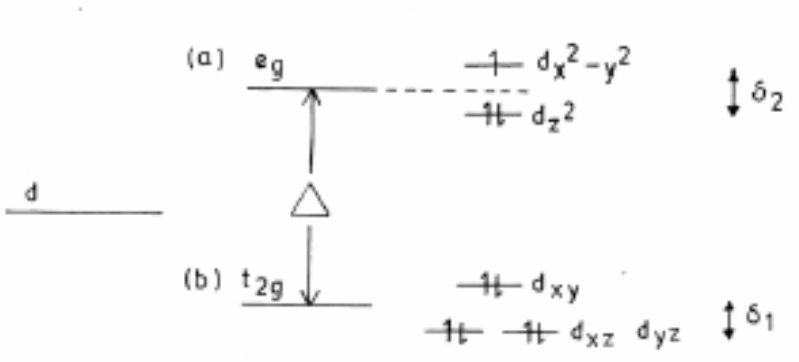

Fig. 2.6 Energy level diagram for the d-levels in an ion experiencing a Jahn-Teller distortion

In the oxide spinels, the cooperative Jahn-Teller effect is frequently encountered. The necessary condition for this to appear is the presence of transition metal ions which have an orbitally degenerate electronic ground state. The interaction between the degenerate states and the lattice vibrations leads to an effective coupling between electronic states on different cations. When this coupling is sufficiently strong and the concentration of active cations exceeds a certain critical value, the electronic states order and simultaneously a structural phase transition from cubic to

lower symmetry appears. Thus, Jahn-Teller effect refers to the condition in which a crystal lattice is distorted from the cubic to tetragonal configuration as a consequence of the possession of some 3d orbitals of fewer electrons than other orbitals. This condition results in an electrostatic imbalance that has the effect of repelling some oxygen anions more than others. In effect, these anions are pushed further away, thus producing the charge from cubic to tetrahedral symmetry. The phase with lower symmetry is stable only below a critical temperature. In the B-site, there are two ions, namely Mn^{3+} and Cu^{2+} both having doubly degenerate ground state of e_g type, which exhibit the Jahn-Teller effect. The corresponding distortion is always tetragonal with c/a>1. The $CuFe_2O_4$ having the degree of inversion, $0.06<\delta<0.24$ exhibits Jahn-Teller effect with c/a ratio ~ 1.06 [2.8].

Chemistry of Ferrites

The oxides spinels are commonly prepared at elevated temperatures by a direct solid-state reaction between the simple oxides. The relevant temperature range is about 800°C to 1500°C, depending on the type of cations. The thermodynamic stability of spinels compared to the constituent oxides is given by Gibbs free energy formation (ΔG) fir the reaction,

$$M' O + M''_2 O_3 \rightarrow M' M''_2 O_4$$

The largest contribution to the crystal energy in oxide spinels comes from the Coulomb energy of the charged ions (Madelung energy),

$$E_c = (-e^2 / a) A_M$$

where, e is the charge of electron, a is the lattice parameter and A_M the Madelung constant. The Madelung constant, A_M can be expressed as a function of the mean electric charge q_A of the cations in tetrahedral positions and of the oxygen parameter u. With increasing A_M the stability of the spinel increases. Therefore, owing to its dependence on q_A, the Coulomb energy generally plays an important role in the equilibrium distribution of cations among tetrahedral and octahedral positions, even though in some cases other energy contributions may become important.

According to the formula, $(M'_{1-\delta}M''_{\delta})\ [M'_{\delta}M''_{2-\delta}]\ O_4$, oxide spinels may have various degrees of inversion. If the energy difference between two limiting cases $\delta = 1$ and $\delta = 0$ is not very large, we expect the distribution of cations to be random at high temperature due to the prevailing influence of entropy term-TS in the free energy. When the temperature is lowered, the spinel tends to be more or less normal

or inverse depending on the sign and amount of energy corresponding to the interchange of cations M', M'' in different sublattices. The equilibrium distribution will be given by the requirement that the Gibbs free energy is minimum, i.e.

$$dG/d\delta = \{(dH/d\delta) - T(dS/d\delta)\} = 0$$

If one restricts to configurational entropy of cations and assumes total randomization in both sublattices, S may be approximated by,

$$S = N_k [-\delta \ln \delta + 2 (\delta-1) - (\delta+1) \ln (\delta+1)]$$

Defining further $\Delta P = dH/d\delta$, we find

$$\delta = (1+\delta)/(1- \delta)^2 = \exp (-\Delta P/RT)$$

which determines the equilibrium value of δ at temperature T. Generally, ΔP depends on δ and frequently a linear expression $\Delta P = H_o + H_1 \delta$ is used to describe the experimental results. Here, H_o and $H_o + H_1$ may be interpreted as energies connected with interchange of ions M', M'' from different sublattices in the case completely normal and inverse distribution, respectively.

When $\Delta P<5$ kCal/mol, a partially inverted spinel is usually observed. Otherwise, the energy difference between the normal and inverse structures is sufficient for the spinel to attain either normal or inverse structure. Once again the main contributions to ΔP come from Madelung energy, Born repulsion energy and further from polarization and ligand field effects. On the basis of systematic studies of cation distribution in various spinels it has been recognized that some regularities exist in them pointing to the possibility to connect the distribution to individual site preference of cations. In such case, The energy ΔP can be expressed as a difference $\Delta P = P(M') - P(M'')$, of individual preference energies P of cations M' and M''. Once P(M') and P(M'') are known for all relevant cations, the distribution of ions in arbitrary spinel could be predicted. The values of P(M) for different spinels are shown in Fig. 2.7.

Chemistry, crystal structure and microstructure determine the engineering material characteristics of ferrites. Many desirable combinations of chemical ingredients and basic structure cannot be obtained because some ions are incomplete with certain crystal structures despite the best efforts of materials scientists. Microstructure includes the size and number of voids, size of grains, and presence of grain boundary phases, grain shape and orientation.

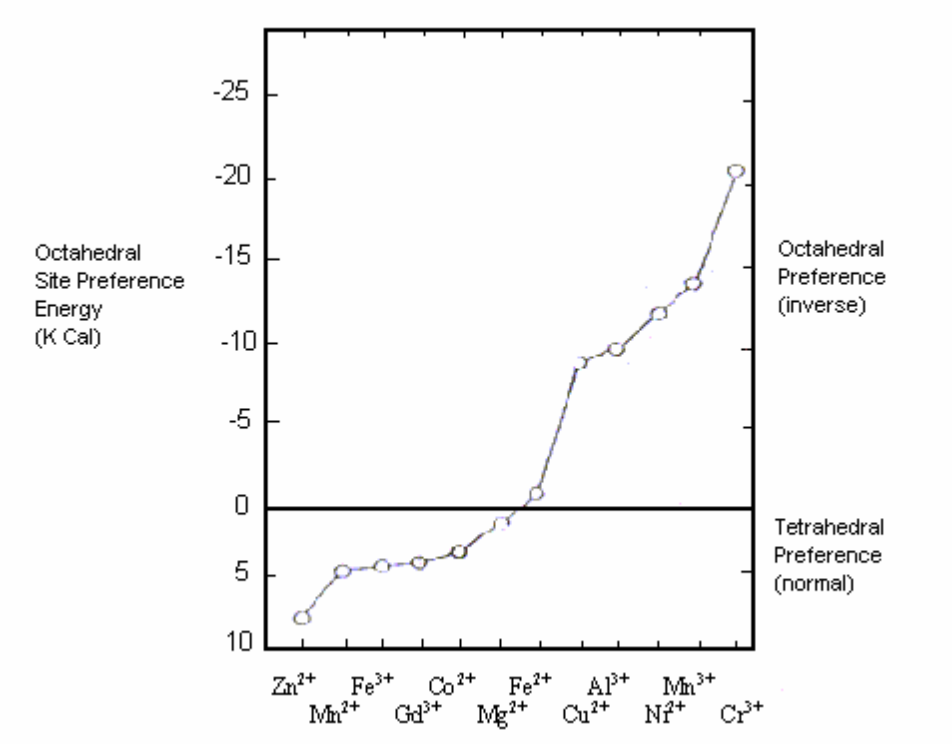

Fig. 2.7 Cation site preference energy for various transition metal ions

In essence, microstructure is the architecture of the materials that is, how the various phases and crystalline are put together, their particular patterns and arrangements, and how these are joined. Ferrite microstructures are extremely sensitive to processing because the pre-reaction and grinding of raw materials, forming technique employed, sintering time, and temperature and cooling conditions influence crystal composition and size, and also the size and volume of pores.

2.2.3 Magnetic properties of Ferrites

After having appraised the crystallographic and some other associated aspects of spinel ferrites, we shall now review their magnetic behaviour in some details, which is the one part of the present work.

The origin of magnetism and ultimately of the magnetic properties of materials essentially always result form the spin and orbital motion of electrons, the magnetic moment of electrons, and the resulting magnetic moment of atoms and ions.

Atomic magnetic moment is due to the motion of electrons in their orbits and due to their spin motion. The atomic magnetic moment is given in the unit, Bohr magneton μ_B. One Bohr magneton is given by

$$\mu_B = \frac{eh}{4\pi mc} = 9.21 \times 10^{-21} \text{ erg. Orsted}^{-1}$$

Where, h is the Planck's constant and e, m are the electron's charge and mass respectively, c is the velocity of light.

Although the orbital motion of electrons may contribute to the atomic magnetic moment when the atom is in Free State, when it is a part of solid the contribution of orbital motion is often very small and negligible. For the present case of spinel ferrite, the cations are subjected to the very intense inhomogeneous electric field which influences the orbital angular momentum partly due to the large radius of 3d shell and partly due to the lack of outer electrostatic shell to screen the 3d shell whose unpaired electrons are responsible for net magnetic moment. The spin angular momentum is however, not affected by the influence of anion field.

The quenching of the orbital momentum can be pictured as follows: The orbital angular momentum assumes definite orientation relative to the crystal lattice under the influence of the electric field of anions which has the symmetry of the crystal. This orbit-lattice coupling is so strong that the angular momentum vector direction and so the angular magnetic moment is locked in a particular direction and does not respond to the applied external magnetic field.

The atom with a resultant spin quantum number S gives the spin magnetic moment as follows,

$$\mu = g\sqrt{s(s+1)}\ \mu_B$$

g = Lende's splitting factor

The oxide spinels represent a classical example of a crystal structure, which allows a special type of magnetic order called ferrimagnetism. In fact, spinels were first materials where the existence of such magnetic ordering was recognized by Neel [2.9]. He coined the word ferrimagnetism and elaborated the molecular field theory to account for this type of order. Until the discovery of ferrimagnetism, the magnetic properties of the few magnetic spinels then known, such as magnetites, were classified as ferromagnetics. The difficulty, however, was to understand the low magnetic moment and the deviations from the Curie-Weiss law. The departures from the ferromagnetic behaviours were excellently explained by Neel Through a simple yet elegant theory.

Ferrimagnetism can be considered as a special case of antiferromagnetism or perhaps vice versa. Because at least two unequal and anti parallel systems of atomic moments exist which give rise to spontaneous magnetization.

The simplest case is of a two-sublattices system. Here, neglecting the minor differences we may consider all the octahedrally coordinated sites to compose one sub-lattice (B) and in similar manner all the tetrahedrally coordinated sites to compose (A) sub-lattice. These both are crystallographically nonequivalent and when both contain paramagnetic ions in sufficiently high concentration the ferrimagnetism may occur.

The ferrimagnetism, however, is a broad class and includes materials with more than two sub-lattices and other configurations of moments, rather complicated, like triangular and spiral etc.

The intense short-range electrostatic field causes the interactions, which are responsible for the magnetic ordering. These interactions are quantum mechanical in origin and are related to the overlap of the charge distributions of the atoms concerned.

The exchange interaction coupling the spins of pair of electrons is given as proportional to the scalar product of two spin vectors.

$\varepsilon_{ij} = -2 \cdot J_{ij} S_i S_j$

where J_{ij} is the exchange constant given as

$$J_{ij} = \int \Psi_i^*(1) \cdot \Psi_j^*(2) \cdot \left(\frac{2}{r_{12}} + \frac{2}{r_{ij}} - \frac{1}{r_{i1}} - \frac{1}{r_{j2}} - \frac{1}{r_{12}} - \frac{1}{r_{ji}} \right) \cdot \Psi_i(2) \cdot \Psi_j(1) dv_1 dv_2$$

where 1, 2 refer to two electrons; i,j refer to two atoms; r's are the distances. The magnitude and sign of the exchange integral decide the type and strength of the magnetic ordering. The ferromagnetism results from strong parallel coupling of spins having large, positive J vales. The semi empirical calculations to decide the type of ordering depending on the type of the ions and distances between them were given by Slater [2.10].

2.2.3.1 Magnetic Interactions in Spinel Ferrites

The interaction causing magnetic ordering in spinels, however, are not the same as described above. In spinels the cations are situated at large distance and have anions as their nearest neighbours. These anions obscure the direct overlap of the cations' orbitals sometimes partially and at times completely. Moreover, the ratio of

the distance between two cations to the diameter of the concerned electron orbit comes about 2.5 indicating a moderate to week positive interaction favouring weak ferromagnetic type of ordering [2.11]. But experimental evidence favour strong interactions of negative type, as evident from the observed high magnetic transition temperatures of spinel ferrites. So, it is unlikely that the interactions are dependent on direct coupling of cations spins. On the other hand since anions possess no magnetic moments the direct coupling with anions are also ruled out.

A "superexchange" mechanism was proposed by Kramer [2.12] for such cases and was developed by Anderson [2.13-2.16] and Van Vleck [2.17]. The superexchange mechanism between cations operates via the intermediate anions. The superexchange mechanism was explained by Anderson considering a simple example of MnO. In the ground state there cannot be any spin coupling of oxygen (S=0) possible with cations. But in the excited state, oxygen gives a p electron from a 2p pair, which becomes a temporary part of any one of the Mn ions. The consequence of the process is the emergence of net spin on the oxygen ion due to which it can then after interact with the other Mn ion by direct exchange. If the separation is not very large the interaction will be negative favouring antiparallel of spins in the two Mn ions. The spinel ferrites also undergo the same indirect interactions, which is responsible for the strong negative coupling of the cation spins in the above case. The p orbital of the oxygen anion overlaps with cation d orbital which accepts an electron from oxygen's p shell. The p electron will occupy the next available place in d orbital of cation according to the Hund's rule i. e. if 3d is less than half filled the p electron will be placed parallel to the electrons already present in 3d shell. But if 3d is equal to or more than half full the later will be placed antiparallel to the net magnetization. If both the cations are same type, the Hund's rule applying to both the cations will orient the net spins on both 3d shell antiparallels since 2p electrons are paired according to Pauli Exclusion Principle.

The sign and the strength of the super exchange interactions depend, however, upon the bond angle and the bond distances involving the two cations and an intermediary anion. The bond angles are the angle formed between the bonds connecting the intervening anion with two cations. Several authors including Slater [2.18], Nagmiya [2.19], Goodenough [2.20] and Kanamori [2.21] have discussed the various types super exchange interactions considering the symmetry properties of electron orbitals. Goodenough [2.22] and Kanamori came up with some predictions

concerning the sign and strength of super exchange interactions in their semi-empirical rules.

The Magnetic orbitals involved in the super exchange interactions in spinel are the T_{2g} and E_g orbitals of 3d metal ins and P_x, P_y and P_z orbitals, which are highly directional, of intermediary anion. The T_{2g} orbitals consist of d_{xy}, d_{yz} and d_{zx} while E_g orbitals consist of d_z^2 and $d_{x^2-y^2}$.

The semi empirical rules given by Goodenough and Kanamori are:

(a) When the two cations have lobes of magnetic orbitals directed towards the anion as to involve a reasonably large overlap (i.e. the 3d orbitals are non-orthogonal with d_z^2 type orbitals each with one d electrons and pointing directly towards the legand ions in 180^o configuration) the exchange is antiferromagnetic type because the antiparallel electrons gain energy by spreading into overlapping orbitals.

(b) When the participating cation orbitals are of the d_{xy} type, for example, each with one d electron and interacting with the P orbital of the legand in 180^o configuration, the exchange interaction is antiferromagnetic type but the strength is not as large as in 1.

(c) In 90^o configuration of the above orbitals along with d_x^2 orbitals each with one electron, the P orbital making σ bond with one cation is making π bond with another cation in this configuration. One expects strong overlapping and an antiferromagnetic exchange interaction.

(d) When magnetically filled cation orbital is in contact with an empty cation orbital via the intervening legand ion, the exchange is ferromagnetic. But it is not as strong as the antiferromagnetic exchange.

Few more qualitative conclusions drawn are:

1. From the orbital symmetry of cation-anion-cation configuration one yields $J_{d8}>J_{d5}>J_{d3}$ for 180^o configuration $J_{d5}>>J_{d8}$ for 90^o configuration. J_{d3} can either be ferro or antiferro in nature.
2. From the valance state of the cation $J_{trivalent}>J_{divalent}$.

The higher charge on any cation increases the covalent nature of bond and results in greater overlap of orbitals giving stronger exchange interaction. The role of the legand ion is more obscure but generally it is observed that exchange interaction decreases with increasing electron negativity.

We refer now ourselves to the possible configuration in the spinel structure. We can identify basically three types of super exchange interaction to operate in spinels:

- J_{AB} exchange interaction namely the inter sub-lattice interaction between cations on A and B sub-lattices.
- J_{AA}, J_{BB} exchange interaction namely the intra sub-lattice interaction operating among the cations on A sites and B sites.

Fig. 2.8 gives the possible M-O-M (where A or B) configurations involving these three exchange interactions. Since the exchange forces are of short range in character the interactions including the next nearest are only considered. The hatched circles represent the B-site cations and small circles represent A-site. Relative magnitude of radii and distance shown are approximately correct.

We point our some configurations on the basis of our discussion so for and knowing the nature of the exchange forces. The Table 2.3 lists the various distances involved in these configurations. The configurations shown have at least one short distance (p or q) and other distances are not larger than r, s, t.

Among them AB configurations only pqc configuration is favorable since the (M-O) distance as well as angle (M-O-M) (~126^o) is favorable for having strong exchange interaction. The other AB configurations such as pre and tqe have much favorable angle (~154^o and 180^o respectively) but with one very large (M-O) distance. So one cannot expect reasonable exchange interaction between them. Among the B-B configurations, the (M-O) distance is small for ppb configuration but angle (90^o) is unfavorable. Other configuration are ptb and pab both, the angle and distance, are unfavorable. For ptb the angle (~126^o) is favorable but one (M-O) distance is unfavorable. Thus, overall BB interactions are expected to stay lower in strength than AB interactions.

Among the AA configurations, only one configuration is shown, rqd, having both the (M-O) distances much larger (~3.9 A) than any BB or AB distance. Besides, for the BB interactions there is a possibility of direct exchange since B-cations direct their T_{2g} orbitals towards each other which is not the case for AA interaction. Thus AA is expected to be the weakest of all.

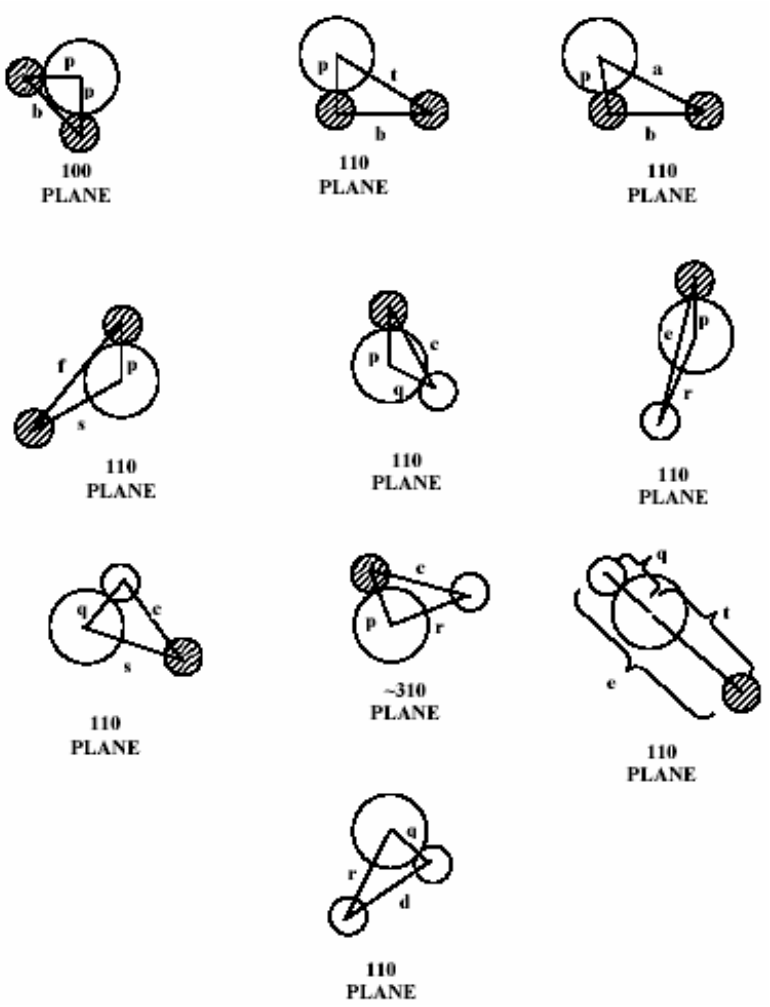

Fig. 2.8 Near neighbour configurations in spinel lattice

Table 2.3: Ionic distances in the spinel lattice

$\Delta u = u - 0.25$

Distance between Cation and Anion	Distance between Cation and Cation
$p = a\ \{1/16 - (\Delta u/2) + 3\Delta u^2\}^{-1/2}$	$b = (1/4)\ a\ 2^{1/2}$
$q = a.3^{1/2}(\Delta u + (1/\Delta u))$	$c = (1/8)\ a\ 11^{1/2}$
$r = a\ \{11/64 + (\Delta u/4) + 3\Delta u^2\}^{-1/2}$	$d = (1/4)\ a\ 3^{1/2}$
$s = a\ \{3/16 + (\Delta u/2) + 3\Delta u^2\}^{-1/2}$	$e = (3/8)\ a\ 3^{1/2}$
$t = a\ (1/4 - \Delta u).3^{-1/2}$	$f = (1/4)\ a\ 6^{1/2}$

Now let us apply the conclusion of semi empirical rules of Goodenough and Kanamori to the configurations we have pointed out. We see that direct application is possible only for the BB interactions with M-O-M angle to be 90^o. The case of A-B interaction with M-O-M angle of 126^o is more complicated. The usual way is to interpolate between the 180^o and 90^o configurations assuming rather arbitrarily that the change is smooth. If the sings of the 180^o and 90^o configurations happens to be opposite than the interpolation scheme is not reliable.

The AA interactions, as we have seen, are the weakest of all and really do not influence the ordering due to another interactions. This is true, off course, only when there are sufficient numbers of magnetic ions present on both the sites and that is implied throughout in our above discussion.

Based upon the G. K. rules and the interpolation, the following tables predicted the interactions between the nearest pairs in the B sub-lattice and inter sub-lattice interactions between the A and B sub-lattices for different d electron populations.

J_{BB} (nn) (prediction a 1a G.K. rules	
$d^3 - d^3$	+ or –*
$d^5 - d^5$	- weak
$d^8 - d^8$	+
$d^3 - d^8$	- weak
$d^5 - d^8$	+ or –*
$d^3 - d^5$	- weak

A-B	180°	90°	125° interpolation
$d^2 - d^3$	- weak	-or + weak	Uncertain
$d^5 - d^3$	+ weak	- medium(weak)	- uncertain
$d^5 - d^5$	-strong	-medium	-
$d^5 - d^8$	-strong	- medium(weak)	-
$d^7 - d^3$	+weak	- medium(weak)	- uncertain
$d^7 - d^5$	-strong	- medium(weak)	-
$d^7 - d^8$	-strong	-or + weak	-

The above tables are very rough guidelines and should not be relied upon totally. The best recourse is experiments. The most comprehensive being the Neutron inelastic scattering by measuring the magnon dispersion curves.

But in general for spinel we find that $|J_{AB}| >> |J_{BB}| > |J_{AA}|$ with J_{AB}, J_{BB} and J_{AA} all being negative.

2.2.3.2 Magnetic Ordering in Spinel Ferrites

Neel theory of ferrimagnetism:

Consider the simplest case of two sub-lattices, which have anti parallel and unequal magnetic moments. The inequality may be due to

1. Different elements in different sites
2. Same elements in different ionic states
3. Different crystalline fields leading to different effective moments for ions having the same spin.

Neel's model is briefly outlined below which is based on a simplified model composed of identical magnetic ions divided unequally between the A and B sub-lattices.

Let there be n identical magnetic ions per unit volume with fraction λ located on A sites and ν (=1 - λ) on B sites. Let μ_A and μ_B the average moments of an A ion and B ion in the direction of field at temperature T. Though A and B ions are identical, μ_A and μ_B are not because they feel different fields in different sites.

Let $M_A = n\mu_A$ and $M_B = n\mu_B$

The Molecular field acting on both sub-lattices is

$$H_{mA} = \gamma_{AB} (\lambda\alpha M_A - \nu M_B)$$

$$H_{mB} = \gamma_{AB} (\beta\alpha M_B - \nu M_A)$$

Where $\alpha = \gamma_{AA}/\gamma_{AB}$ and $\beta=\gamma_{BB}/\gamma_{AB}$, γ_{AA}, γ_{AB} and γ_{BB} are the Weiss constants

The above equations yield the expression for mass susceptibility as follows which is derived from the solving the equations above Tc

$$\frac{1}{\chi} = \frac{T}{C} + \frac{1}{\chi_o} + \frac{b}{T - \theta'}$$

Where $\frac{1}{\chi_o} = \gamma_{AB}\rho\ (2\lambda\nu - \alpha\lambda^2 - \beta\nu^2)$

$b = \gamma^2_{AB}\rho^2\ C\lambda\nu[\lambda\ (1+\alpha) - \nu\ (1+\beta)]^2$

$\theta' = \gamma_{AB}\rho\, C\lambda\nu\, (2+\alpha+\beta)]$

Where ρ is density and C is is Curie constant for the material. From equating $\chi = 0$ in the above equation for negative value of Weiss constants the Neel temperature can be given as $T_N = \gamma_{AB}\rho C/2[\alpha\lambda+\beta\nu+\{(\alpha\lambda-\beta\nu)^2+4\lambda\nu\}^{1/2}]$

The equation for the mass susceptibility actually represents a hyperbola and physically meaningful part of it is shown in Fig. 2.9. The curve cuts the temperature axis at θ_p which is called paramagnetic Curie point. It is in good agreements with the experimental observed susceptibility v/s temperature which differentiates ferrimagnetics form ferromagnetics.

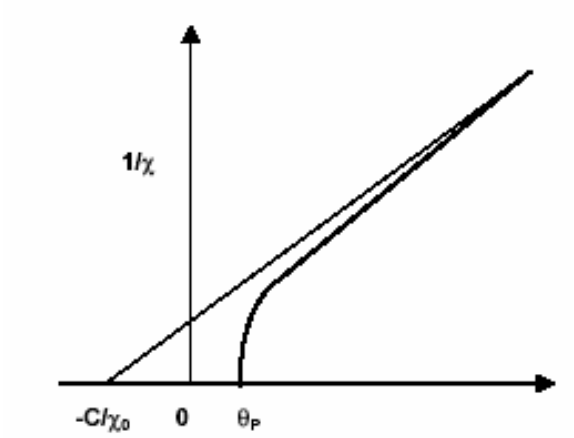

Fig. 2.9 Variation of inverse susceptibility with Temperature (K) below T_c

In the ferrimagnetic region each sub-lattice is spontaneously magnetized by the molecular field acting on it. But the two sub-lattice magnetizations are opposite to each other. The observable magnetization is

$|M| = |M_B| - |M_A|$

Each sub-lattice magnetizations are governed by the same relation as ferromagnetics. In terms of specific magnetization, they are given by

$$\frac{\sigma_A}{\sigma_o} = B\left(J, \frac{\mu_H H_{mA}}{kt}\right)$$

$$\frac{\sigma_A}{\sigma_o} = B\left(J, \frac{\mu_H H_{mB}}{kt}\right)$$

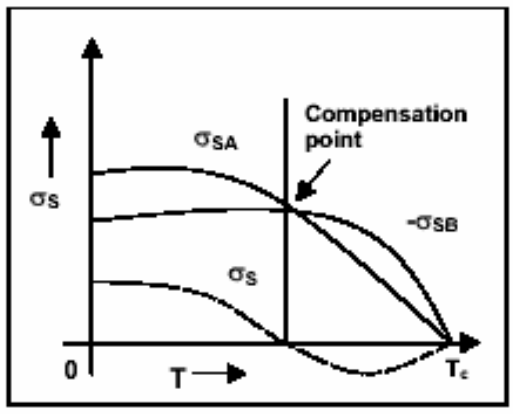

Fig. 2.10 Anomalous Magnetization v/s temperature curve for ferrimagnets

where k is Boltzmann's constant and B is Brillouin function.

These sub-lattice magnetizations will have different temperature response because effective molecular field acting on them are different. This suggests the possibility of having anomalous net magnetization versus temperature curves. For most ferrimagnetics the curves show simple behaviour but in few cases there may be a compensation point or a maximum in the curve at some temperature. The shape of the curve depends on γ, λ, ν and α. There is an interesting possibility of the net magnetization reversing its sign. The situation is depicted in Fig. 2.10 where, at some temperature below T_c both the $| M_B | = | M_A |$ and of opposite sign. So M disappears at that point, which is called compensation point. Gorter [2.23] observed these types of behaviour in Li-Cr system.

Shortcoming of the Neel model

1) saturation magnetization values in many ferrites are found to be much lower than those predicted by Neel model
2) Some M v/s T curves have finite slopes at 0oK and cannot be explained by Neel model
3) It is based on the assumption that strong negative AB predominates over AA and BB interactions, which is not applicable to each and every case.

Yafet-Kittel theory of ferrimagnetism:

Yafet-Kittel [2.24] were the first to find the solution of the difficulties encountered in Neel model. They considered further sub-division of A and B sites and departure from the notion of co-linear arrangement of spins which was central in Neel's model. They promoted triangular type of spin structure to account for the observed facts.

In the dilute limit of magnetic concentration, the strong antiferromagnetic interactions among the anion on B-sites further splits the sub-lattice into two sub-lattice of titled spins in response of their tendency to be simultaneously anti-parallel to both their A and B site neighbours. In the simplest case, the moments on the B site cations will form sub-lattice, in each of which the moments are parallel. But moments in one sub-lattice, make an angle with the moments in the other sub-lattice. The resultant moment is, however, anti-parallel to A site moments.

The Y-K arrangements can explain beautifully some observed low value of magnetization in Zn-Ni and Zn-Mn ferrite.

The Y-K model yields the following equation for Calculations of net magnetization

$M = 2[M_B \cos\psi_{Y.K.}] - M_A$

The Y. K. spin configuration gives rise To a magnetic reflection at normally forbidden (200) position as well as at normal spinel positions in magnetic Neutron Scattering experiments. So, transition to Y-K configuration can be confirmed by Neutron diffraction experiment. Satyamurthy et al [2.25] found this type ordering in Ni-Zn ferrites.

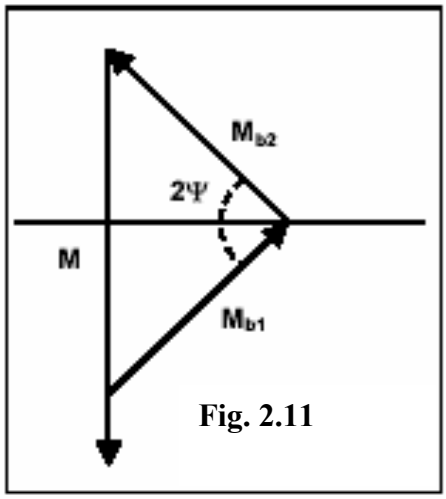

Fig. 2.11

Helical and Spiral spin configuration:

Yashomori [2.26], Villain [2.27] and Kaplan [2.28] independently suggested the possible existence of helical or spiral spin configuration which is favourable in some systems in some situation. In such type of configuration, the spin direction gradually rotates with some definite angle. The Neutron diffraction study of some spinels shows there is a contribution to fundamental spinel reflection due to the axial component of spins and the rotating components give rise to satellite reflections. Corliss [2.29] found it in $MnCr_2O_4$.

Fig. 2.12 shows the dependence of the energy of the ground state E on a factor $w = 4J_{BB}S_b/3J_{AB}/S_A$ as given by different theory of magnetic ordering in a spinel.

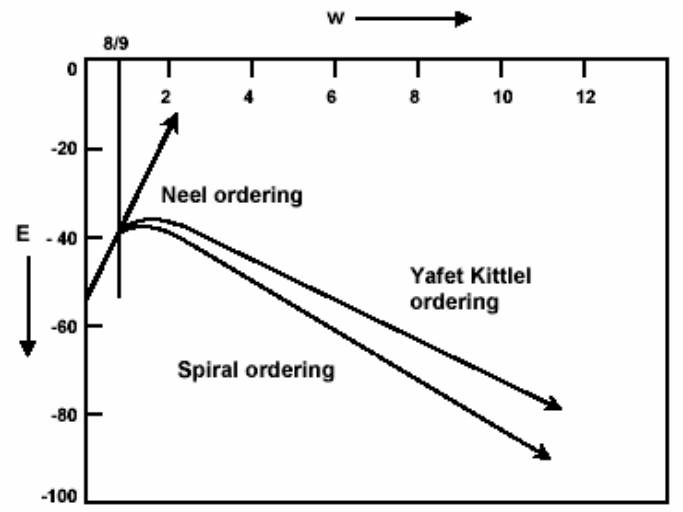

Fig. 2.12 Dependence of the energy of the ground state energy E on $w = 4J_{BB}S_b/3J_{AB}/S_A$ as given by different theories of magnetic ordering in spinel.

An overview of statistical models of spin canting:

Soon after the launching of Neel's two sub-lattice model to explain ferrimagnetic in spinel ferrites, large number of spinel ferrites were found having significant departure from the predicting of Neel's model. Those were the ferrites with non-magnetic substitution.

Neel himself proposed a statistical linkage approach to quality his arguments to account for observed variation. The theoretical efforts to account for the observed facts have since then been counting and have been diversified into three major branches of treatment.

1) An exchange linkage approach in which the number of magnetic nearest neighbours determines whether the given magnetic ions will order and contributes to the ferrimagnetism (Neel, Gellio).
2) A uniform canting approach (Yafet and Kittle, Kaplan)
3) A localized canting approach in which individual moments on one sub-lattice are canted at different angles depending on specifies of local magnetic environment (Geller, Patton and Liv).

We have already discussed the uniform canting models such as Yafet and Kittle model. Spiral spin configuration model etc. Now we shall briefly review some statistical models developed so far simultaneously in a different branch of treatment. First we shall overview the exchange linkage stastical model.

Statistical theory in substituted ferrites:

A number of ferrimagnetic spiels show the observed value of saturation magnetization much lower than that predicted by Neel's theory. The Y. K. approach explains many of them on the basis of the change in the configuration of spins. But it is not evident in all the compounds. Many of them do not reflect any sign of Y. K. type ordering in any of their experimental data.

As early as the time when Neel launched his two-sublattice model he soon found the failure of his model to account for the observed value of saturation magnetization in Ni-Zn system. Neel proposed that qualitatively the observed variation can be accounted for by assuming that a B site magnetic ion with less than two linkages with A magnetic ions, did not contribute to ferrimagnetism [2.30].

Gellio elaborated this basic idea in his treatment. According to him an indefinitely long chain of M_A - O - M_B linkages in ferrite breaks with the

incorporation of non-magnetic ions in the lattice. The statistics developed by Gellio assumes: If a magnetic ion doesn't interact with at least two magnetic ions in different coordination, it doesn't take part in cooperative process.

The limitations of Gilleo model

1) In the derivation of the above expression it is tacitly assumed that the character of superexchange interactions doesn't change with the dilution. So it is valid only when all the magnetic ions are identical.
2) It doesn't tell any thing about the effect of low temperature.
3) It doesn't throw light on the excluded regions whether they contribute to paramagnetic behaviour or there is any other type of ordering taking place.

Localized Canting Spin Approach:

The early model developed by Geller and others [2.31-2.36] were based on random canting of localized moment in a given sub-lattice. The central postulate was of the variation of exchange constants in a local environment.

The basic difference of localized canting treatment of Geller from the Gellio's statistical linkage approach and from uniform canting approach of Y. K. and spiral type of model is as follows: The Gellio's statistical model has a basis in random distribution of incomplete super exchange interactions. So the observed magnetization is assumed due only to the reason that some magnetic ions do not take part in super exchange interaction. So the exchange interactions are not propagated throughout the lattice. An effect of which is measured by applying statistical approach. But no change in the character of super exchange interaction is considered due to the presence of the diamagnetic ions. The uniform canting approach on the other hand does take into consideration the change in the character of the exchange interaction but it is taken to occur throughout the lattice in uniform way. This approach also doesn't take due consideration of the influence of local environment on exchange interactions. Geller's treatment takes into account the essential parts of both the above treatments. It takes the statistical approach of Gellio along the due change in exchange interactions because of local environment.

In the early model of Geller [2.37] the canting is assumed random. And randomness of canting essentially should be taken, in his words, in the same sense that the distribution of ions within the substituted sub-lattice is random. Rosencwaig [2.38, 2.39] presented a localized variant of Yafet Kittle calculations and obtained

local effective molecular field and local canting angles. White [2.40] and Dickof [2.41] subsequently refined the Rosencwaig calculation to yield random average local canting angle. It is given by

$$\mathrm{Cos}\theta_{\mathrm{Y.K.ave}} = \frac{M_A}{M_B}\left(\frac{J_{AB}}{J_{BB}}\right)$$

Patton and Liu [2.42] provided the mathematical formulation of random localized canting by considering many quantities on a site to site basis, which were taken on average basis in earlier treatment, and maid it more quantitative. The treatment yields the results as follows

$$\mathrm{Cos}\theta_{\mathrm{L.AV.}} = \frac{\langle n_{B1A}\rangle |J_{AB1}|}{\langle n_{BB}\rangle |J_{B1B2}|}$$

n_{ij} denote the magnetic ion concentration on particular sub-lattice sites. They were able to explain the observed variation in saturation magnetization with concentration in Li-Zn spinels.

2.3 Reaction kinetics - Synthesis of Spinel Ferrites

Various methods are available for preparing solids; the methods adopted depending to a certain extent on the form of the desired product. A crystalline solid may take the form of either a single crystal or polycrystalline powder. In addition, fine particle (nano-sized) or thin film can be prepared by special preparative techniques [2.43, 2.44]. It is important to make materials of known compositions and properties in reproducible manner. The apparently simple method of preparation though requires a great deal of art. Good amount of care is to be taken at each stage of preparation.

The present thesis deals with the synthesis of polycrystalline spinel ferrite materials. In order to produce polycrystalline ferrites the firing temperature, sintering duration and furnace atmosphere play very important role because they influence the cation distribution, the valence state of cations and the amount of oxygen into the lattice of final product.

There are different methods to synthesize polycrystalline spinel ferrite materials, namely

- Ceramic method (Solid-State reaction)
- Wet Chemical method
- Sol-gel method
- Combustion method

- Citrate precursor method
- Hydrothermal synthesis

Out of these methods, Polycrystalline spinel ferrites may usually be prepared by solid-state reaction route (Ceramic method) [2.45] at elevated temperatures in a sintering process commonly employed in the ceramic industry [2.46]. The constituent ferrites or compounds that form are taken in the correct proportions and are sintered at the temperature in 800^{o}C to 1500^{o}C range. The stochiometric spinel ferrites may be written as $MO.Fe_2O_3$, and the reaction forming this from the solid constituent oxides is simply

$MO + Fe_2O_3 \rightarrow MFe_2O_4$

In the ceramic technique it is necessary to heat a mixture of powders to much higher temperature, often 1000^{o}C to 1500^{o}C for reaction to occur at an appreciable rate. This means that both thermodynamic stability and kinetic factor are important in solid state reaction: thermodynamic considerations show whether or not a particular reactions should occur by considering the changed in free energy that are involved; kinetic factors determines the rate at which the reaction occurs. The starting chemicals used for the preparation of ferrite material are pure, anhydrous powder of oxides, carbonates or nitrates of the selected elements [2.47].

The solid state reaction route can be divided into four steps in the preparation:

(1) Preparation of materials to form an intimate mixture with the metal ions in the ratio which they will have in the final product

(2) Pre-sintering - heating of this mixture to form the ferrites

(3) Powdering of the prepared material and pressing or forming into the required shape and size

(4) Sintering to form the final body

For the synthesis of magnetic oxides through solid state reaction, highly pure oxide powders would be the obvious starting materials to use. These oxides ingredients should be dried thoroughly prier to weighing. Fine grained materials should be used if possible in order to maximize surface areas and hence reaction rates. After the reactants have been weighed out in the required amounts, they are mixed together. For manual mixing of starting materials, this may be done with an agate mortar and pestle or electric grinder. Homogenization of the mixture is aided greatly by adding sufficient amount of volatile organic liquid like acetone to form paste.

During the process of grinding and mixing the organic liquid gradually volatizes and after 10-15 minutes it has usually evaporated completely. Grinding of chemical powders for several hours is necessary for the better homogeneity of the powder.

The resulting fine homogeneous mixture of oxides is subsequently dried and calcined. During calcination raw materials such carbonates and oxides react to form spinel. If starting materials are other than pure oxides, at moderate temperature of $200^{o}C$ for few hours. This causes partial reaction of the constituents, which also increase the homogeneity and reduces shrinkage during the final sintering.

The resulting mass is then pressed into a desired shape. The compacted material is again presintered at nearly $800^{o}C$ for few hours. The presintering is followed by crushing and milling to ensure the greater homogeneity. Again the material is palletized then it undergoes final sintering at $1100^{o}C$ for appropriate duration of time depending on the constituents used.

For the subsequent reaction at high temperature, it is necessary to choose a suitable container material, which is chemically inert to the reactants under the heating conditions used. Various inert refractory inorganic materials are used for container, such as crucibles of Al_2O_3, stabilized ZrO_2 & SiO_2. Sometimes these containers are prone to attack at high temperature especially by Alkali oxides. The heat treatment to be used depends upon the form and reactivity of reactants.

The furnace atmosphere plays critical role during the final sintering in determining the total oxygen content of the final product. The chemical stability against the oxidizing or reducing influence of the atmosphere doesn't greatly affect if the incorporated cations have fixed valences that cannot be changed within wide limits of the oxygen pressure. However, in the case of transition metal ions this certainty is not a plausible approach. The stoichiometry of ideal spinel depends on both temperatures T and the partial oxygen pressure pO_2. Most ferrites have the tendency to give off the oxygen, as the equilibrium pressure in reaction (pO_2) is often higher than the atmospheric pressure. This equilibrium pressure increases with increase in temperature. If this deviation exceeds some critical value, the spinel structure may be unstable. The chemical reaction involved is $6Fe_2O_3 \rightarrow 4Fe_3O_4 + O_2$ (Fe_3O_4 contains Fe^{2+} and Fe^{3+}). The formation of ferrous ions thus occurs along with the deficiency of oxygen in the final product.

The problem, however, is not much serious in ferrite when sintering temperature is fixed between 1000^{o}C to 1200^{o}C with appropriate duration of sintering and slow cooling is usually a safe guard against this problem. The slow cooling tends to reoxydize any divalent ions formed. The quenching is done only when the high temperature phase has to be preserved. All the spinel ferrites studied in the present thesis have been synthesized by double sintering ceramic technique.

2.4 Sample Preparation

In the present course of work, the following bulk samples of spinel ferrite systems were synthesized by usual double sintering ceramic technique

(1) $Li_{0.5(1+x)}Ti_xAl_{0.1}Fe_{2.4-1.5x}O_4$ (x = 0.0 to 0.3 with step of 0.1)

(2) $Li_{0.5(1+x)}Ti_xCr_{0.1}Fe_{2.4-1.5x}O_4$ (x = 0.0 to 0.3 with step of 0.1)

(3) $CuAl_xCr_xFe_{2-2x}O_4$ (x = 0.0 to 0.8 with step of 0.2) (Slow-Cooled & Quenched)

(4) $MnAl_xCr_xFe_{2-2x}O_4$ (x = 0.0 to 0.8 with step of 0.2)

Fig. 2.14 shows the flow chart of the different steps used for the sample preparation in solid state reaction route.

The starting materials were analytical reagent grade powders of Fe_2O_3, Li_2CO_3, Al_2O_3, TiO_2 Cr_2O_3; all 99.9 % pure supplied by Thomas & Backer used for the polycrystalline samples of $Li_{0.5(1+x)}Ti_xAl_{0.1}Fe_{2.4-1.5x}O_4$ (x = 0.0 to 0.3 with step of 0.1) and $Li_{0.5(1+x)}Ti_xCr_{0.1}Fe_{2.4-1.5x}O_4$ (x = 0.0 to 0.3 with step of 0.1) system. The oxides of different molecular weights were taken in proportion according to the required stoichiometry of the structure and total required yield of 10 gm of final product. They were first mixed intimately and ground to obtain a very fine powder of good homogeneity. The mixture was then presintered at 850^{o}C for 24 hours in air atmosphere. During presintering to ensure that all the carbon is liberated from the mixture in the form of CO_2. It is necessary because of alkaline carbonates. Also it is known that for constant sintering temperature, a lower value of oxygen partial pressure leads to the formation of ferrites. The presintered mixture was again well ground and resulting fine powder was then palletized in cylindrical shape of 1 cm in diameter. The binder used was the mixture of Polyvinyl Alcohol (PVA), which evaporates at 300^{o}C. The Pellet prepared by compressing the fine powder with application of the pressure of about 3 tones. The pellets were finally sintered in air at 1000^{o}C for 24 hours.

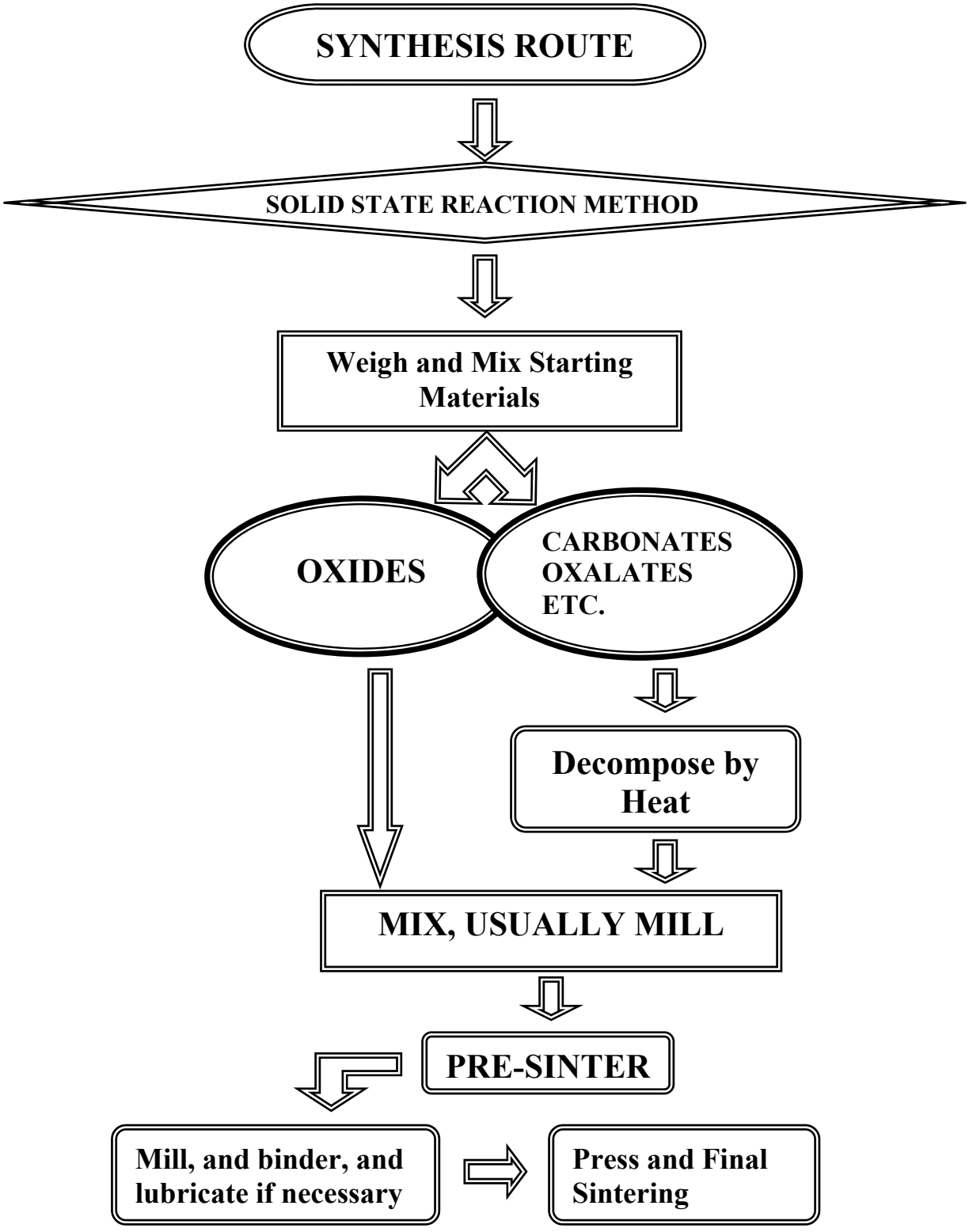

Fig. 2.14 Flow chart of the stages in ferrite preparation

After that there were slowly cooled to room temperature in the furnace, Thus the spinel ferrites samples of this system were prepared in the form of cylindrical pellets.

2. The samples of the spinel solid solution series $CuAl_xCr_xFe_{2-2x}O_4$ (x = 0.0 to 0.8 with step of 0.2) were prepared by above mentioned standard ceramic technique. The starting materials were AR grade oxide powders of the constituent metals: CuO, Fe_2O_3 (Thomas & Backer), Cr_2O_3 (BDH), Al_2O_3 (BDH). One set of the samples (0.0, 0.2, 0.4, 0.6 and 0.8) was quenched from the final sintering temperature (1100^{o}C) to liquid nitrogen temperature and the other one was furnace-cooled to room temperature.

3. The five samples of spinel oxide system $MnAl_xCr_xFe_{2-2x}O_4$ (x = 0.0 to 0.8 with step of 0.2) were prepared by using same technique. The starting materials were AR grade Fe_2O_3 (Thomas & Backer), $MnCo_3$ (Ranabaxy), Cr_2O_3 (BDH), Al_2O_3 (BDH). The $MnCO_3$ gets converted into Mn-oxide at around 500oC during presintering of the mixture. The presintering temperature and final sintering temperature were 1000^{o}C and 1200^{o}C for 24 hours, respectively.

All the final products were characterized by Energy dispersive X-ray Analysis (EDAX) and X-ray diffraction to ascertain purity and surety of their chemical compositions and formation of single phase spinel structure. The experimental details for both of these techniques are given in the Chapter-4.

Irradiation experiments were performed in high vacuum chamber, with typical vacuum maintained at 1 x 10^{-6} mbar after purity and structural conformation of all above mention bulk samples. The specimens of $Li_{0.5(1+x)}Ti_xAl_{0.1}Fe_{2-2x}O_4$, $Li_{0.5(1+x)}Ti_xCr_{0.1}Fe_{2-2x}O_4$, $CuAl_xCr_xFe_{2-2x}O_4$ were irradiated in vacuum with 50 MeV Li^{3+} ions with fluence of 5 x 10^{13} ions/cm^2 and $MnAl_xCr_xFe_{2-2x}O_4$ were irradiated in vacuum with 50 MeV Li^{3+} ions with fluence of 1 x 10^{13} ions/cm^2 using 15 UD Pelletron accelerator at Inter University Accelerator Centre (formerly known as a Nuclear Science Centre), New Delhi.

The targets in the form of thin layer of ferrite material having thickness of about 20 mg/cm^2 for irradiation experiments were prepared by spreading fine ferrite powders in a aluminium ring of 1 cm diameter on a thin aluminium foil, and uniform thickness was achieved by fixing the powder using liquid GE Varnish for the Mössbauer studies and the ferrite pellets were cut and polished to the required size as determined by using the SRIM-98 software for the SHI irradiation experiments for the

other electrical and magnetic measurements. The porosity of the samples was maintained around 10%.

The projected range (R_p), electronic energy loss (S_e) and nuclear energy loss (S_n) of 50 MeV Li^{3+} ions in all the compounds calculated using the SRIM-2003 are as follows:

1. 235 μm, 12.6 eV/Å and 6.77x 10^{-3} eV/Å for the $Li_{0.5(1+x)}Ti_xAl_{0.1}Fe_{2.4-1.5x}O_4$ system
2. 231 μm, 12.8 eV/Å and 6.88x 10^{-3} eV/Å for the $Li_{0.5(1+x)}Ti_xCr_{0.1}Fe_{2.4-1.5x}O_4$ system
3. 215 μm, 13.8 eV/Å and 7.48x 10^{-3} eV/Å for the $CuAl_xCr_xFe_{2-2x}O_4$ system
4. 223 μm, 13.2 eV/Å and 7.10x 10^{-3} eV/Å for the $MnAl_xCr_xFe_{2-2x}O_4$ system

The detail study of irradiation experiments and the plots of variation of electronic energy loss and nuclear energy loss with energy and depth of incident 50 MeV Li^{3+} ion in these entire compounds are explained in Chapter- 3.

References

2.1 B. Viswanathan and V. R. K. Murthy, Ferrite Technology: Science and Technology, Narosa Publishing House (1990)

2.2 W. H. Bragg, "The structure of the spinel Group of Crystals", Philos. Mag., **30 (176)** (1915) 305-15

2.3 S. Nishikawa, "Structure of Some Crystals of Spinel Group", Proc. Math. Phys. Sco. Tokyo, **8** (1915) 199-209

2.4 J. Smit and H. P. J. Wiin, Ferrites- Physical Properites of Ferrimagnetic Oxides in Relation to Technical Applications, (N. V. Philips Gloeilampenfabrieken, Eindhoven, Holland, (1959) P. 136-176

2.5 R. W. G. Wyckoff, Crystal Structure, **1 & 2**, (Interscience New York, 1951)

2.6 H. A. Jahn and E. Teller, Proc. Proc. R. Soc., London Ser., **A161** (1937) 220

2.7 J. B. Goodenough, Annual Rev. Materials Science **28** (1998) p. 1-27

2.8 H. Ohnishi and T. Teranishi, J. Phys. Soc. Japan, **16** (1961) 35

2.9 L. Neel, Ann. Phys. **3** (1948) 137

2.10 J. C. Slater, Phys. Rev. **35** (1930) 509

2.11 J. C. Slater, Phys. Rev. **36** (1930) 57

2.12 H. A. Kramer, Physica **1** (1934) 182

2.13 P. W. Anderson, Phys. Rev. **115** (1959) 2,

2.14 P. W. Anderson, Solid State Physics **14** (1963) 99

2.15 P. W. Anderson, Magnetism, Eds. G. T. Rado and H. Shull, **1** (1963) 25, (Academic Press, New York,)

2.16 P. W. Anderson and H. Hassgawa, Phys. Rev. **100** (1955) 675

2.17 J. H. Van Vleck, J. Phys. Radium **12** (1951) 262

2.18 J. C. Slater, Quart, Porf. Rept. M. I. T. July **1** (1953) 15
and October **1** (1953) 15

2.19 T. Nagamiya, K. Yoshida and R. Kubo, Advan. Phys. **4** (1955) 1

2.20 J. B. Goodenough and A. L. Loeb, Phys. Rev. **98** (1955) 391

2.21 J. Kanamori, J. Phys. Chem. Solids, **10** (1959) 87

2.22 J. B. Goodenough, Phys. Rev. **117** (1960) 1442

2.23 H. W. Gorter, Philps Res. Repts. **9** (1954) 295

2.24 Y. Yafet and C. Kittel, Phys. Rev. **87** (1952) 290

2.25 N. S. Satya Murthy, M. G. Materu, S. I. Yussef, R. J. Begum and C. V. Srivastava, Phys. Rev. **181** (1969) 969

2.26 A. Yoshomori, J. Phys. Soc. Japan, **14** (1959) 807

2.27 J. Villain, Phys. Chem. Solids **11** (1959) 303

2.28 T. A. Kaplan, Phys. Rev. **116** (1960) 888

2.29 J. M. Hastings and L. M. Corliss, Phys. Rev. **126** (1962) 556

2.30 L. Neel, C. R. Acad. Sci. Paris 230 (1950) 375

2.31 S. Geller, J. Phys. Chem. Solids **16** (1960) 21,

2.32 S. Geller, J. Appl. Phys. **37** (1966) 21,

2.33 S. Geller, Phys. Rev. **181** (1969) 21,

2.34 S. Geller, Physics of magnetic garnets (Bologna: Tipografia Compositori 1978

2.35 S. Geller, H. J. Williams, G. P. Espinosa and R. C. Sherwood, Bell syst. Tech. J. **63** (1964) 565

2.36 S. Geller, H. J. Williams, R. C. Sherwood and G. P. Espinosa, J. Appl. Phys. **33S** (1962) 1195

2.37 S. Geller, J. Phys. Chem. Solids **16** (1960) 21

2.38 A. Rosencwaig, Can. J. Phys. **48** (1970) 2857,

2.39 A. Rosencwaig, Can. J. Phys. **48** (1970) 2868

2.40 G. O. White, C. A. Edmondson, R. B. Goldfarb and C. E. Patton, J. Appl. Phys. **50** (1979) 2381

2.41 P. A. Dickof, P. J. Schurer and A. H. Morrish, Phys. Rev. B **22** (1980) 115

2.42 C. E. Patton and Y. Liu, J. Phys. C. Solid State Phys. **16** (1983)

2.43 A. Word and D. Bellavance, "Preparative methods in Solid State Chemistry" Ed. P. Hagenmuller, Academic Press (1972),

2.44 H. Schafer, "Preparative Solid State Chemistry: The present position", Angew. Shem. Chem. Int'l Ed. **10** (1971) 43

2.45 H. Schmalzried, "Solid State Reactions", Verlag Chemie, (1971

2.46 C. J. Kriessman and N. Goldberg, Magnetism, Eds. G. J. Radio and H. Shul, **3**, 555, (Academic Press, New York, 1963)

2.47 R. W. Cahn, P. Haasen, E. J. Kramer, "Material Science and Technology" VCH Weinheim & New york **11** (1994) & **17A** (1994)

CHAPTER: 3

Swift Heavy Ion Irradiation

3.1 Introduction

In ion irradiation, energetic ions are directed on a target material to initiate changes in its physical, structural and transport properties. This method of materials modification is non-equilibrium in nature, hence interesting, and a wide class of materials like metals, semiconductors, ceramics, insulators, polymers and biological samples has been found sensitive to the technique. Study of the process of irradiation has two broad aspects:

- Study of nature of interaction and qualitative nature of damage created by the process and
- Quantify the damage created under controlled conditions.

These studies would help in diverse research goals: to induce grain refinement, provide nucleation sites, form precipitates, create amorphous phase and variety of other stochiometric or structural alterations of materials. The above-mentioned studies are bulk changes of materials whereas one could also think of surface modification, which is an important part of materials research. Surface modification can be achieved using techniques such as ion implantation, ion beam mixing, low-energy ion deposition and ion beam annealing. Fortunately, numerous material characterization techniques and ion beam techniques like Rutherford Backscattering Spectrometry (RBS), Elastic Recoil Detection (ERD), Secondary Ion Mass Spectroscopy (SIMS), Nuclear Reaction Analysis (NRA), Heavy Ion Backscattering Spectrometry (HIBS), Low Energy Time-of-Flight Elastic Recoil Detection (TOF-ERD), Particle Induced X-ray Emission (PIXE), X-ray Fluorescence (XRF) and Nondestructive Detection of Plastic Explosives available for material characterization and developed ultra clean materials. Each technique can add to the general understanding of implantation effects.

In the last decade, focus has been shifted to the fundamentals of ion-solid interaction. This shift is due to increasing need to utilize beams to modify materials for specific applications. The interaction of the ion beam with solid is a non-equilibrium process. When an energetic ion penetrates a target; it loses its energy via two nearly independent processes:

(i) Inelastic collisions of the highly charged energetic ions with atomic electrons of the matter [electronic energy loss $(dE/dx)_e$] and

(ii) Elastic scattering from nuclei of atom of the matter [nuclear energy loss $(dE/dx)_n$]

In the inelastic collision (cross section 10^{-16} cm^2) energy is transferred from the projectile to atom of the matter through excitation and ionization of their surrounding electrons. The amount of electronic energy loss in each collision varies from few eV/Å to a few keV/ Å. For a swift heavy ion (SHI) moving at a velocity comparable to the Bohr velocity of electron, this is the dominant mechanism for transfer of energy to the material causing the modification of its properties. The nature of modification depends upon the electrical, thermal and structural properties of the target material, the mass of the projectile ion and irradiation parameters [3.1].

3.2 Irradiation Study of Solids

The irradiation of solid material with high-energy ions is extremely important from the fundamental physics as well as from material engineering point of view. A large number of reports dealing with the effects of low energy heavy ions on semiconductor materials are available in the literature, however relatively a few reports are available describing effects of high energy heavy ions on semiconducting materials and devices [3.2-3.4], ceramic insulators [3.5], insulating materials [3.6] ferroelectrics ceramics [3.7], organic crystals [3.8].

V N. Bhoraskar [3.9] has carried out a systematic study by exposing crystalline silicon, porous silicon, gallium arsenide and silicon diode samples to 50-80 energy silicon and oxygen ions in fluence range of the order of 10^{13} to 10^{14} ion/cm^2. It is observed that a large number of defects are produced in the surface region of each of the irradiated semiconductor sample through the energy deposited in the surface region through electronic loss is three orders of magnitude greater than that of nuclear collisions.

S. J. Zinkle [3.5] has reported the radiation –induced microstructural changes in ceramic insulators (Al_2O_3, MgO, Si_3N_4, and $MgAl_2O_4$). The relative influence of ionizing and displacive radiation was studied by systematically varying the mass and energy of the bombarding ions between 1 MeV H^+ and 4 MeV Zr^{3+} ions. The implanted ion exerted a strong influence on the overall microstructural evolution of the irradiated ceramics. Numerous microstructural features (e.g. amorphization, Colloids) were produced in the implanted ion region, which could not be produced in irradiated regions that were well separated from the implanted ions. The

microstructural evolution in regions well separated from the implanted ions was found to depend strongly on the mass and energy of the bombarding ion. Light ion irradiation produced a significant enhancement in point defect diffusion compared to heavy ion irradiation at the same damage rate. Similarly, irradiation with a given ion at a higher flux generally produced an increased amount of observable diffusion.

Quanli Hu et al [3.6] have reported irradiation effect on breakdown phenomena of insulating materials. Irradiation effect of γ and electron on breakdown phenomena for three different compositions of Aluminium Nitride (AIN) samples (99 wt% AIN+0.9 wt%0), (94.9 wt % AIN + 4.3 wt% Y_2O_3), (59.5 wt % AIN + 40% BN) was studied by comparing the incubation time before breakdown. They have found that the breakdown is enhanced after γ - irradiation and suggests that the accumulation of the electrons produced by γ-irradiation at defect could increase the local electrical field. For electron irradiation the slight suppression of breakdown was found presumably because of the local heating from interaction of electron and intrinsic defects.

Interaction of ferroelectrics ceramics with energetic ions is capable of inducing deep buried disorder and new types of defects have expected to be produced. The dynamics of the defects are expected to be influenced by many nonlinear mechanisms like creation of oxygen vacancies, interstitial cation vacancies etc. Jaimon Yohannan et al [3.7] were carried out on solid solution of pure barium sodium niobate (BSN) as well as Nd-doped BSN ceramic samples irradiated using 100 MeV Fe heavy ion beam with a fluence of 1 x 10^{13} ions/cm^2. Dielectric measurements were carried at in the temperature range 30^{o}C-400^{o}C at 1MHz for pristine and irradiated samples. It was observed that the dielectric behaviour changes with heavy ion irradiation.

Sharada G. Prabhu et al [3.8] have studied dielectric properties of non-linear organic crystal of acetoacetanilide before and after irradiation. Crystals are irradiated by 120 MeV Ag^{13+} heavy ion beam with different fluences 7.3 x 10^{10}, 1.7 x 10^{11}, 1.4 x 10^{12} ion/cm^2. The variation of dielectric constant, dielectric loss, ac conductivity and loss factor of both unirradiated and irradiated samples are measured at different fluences. The defects produced due to irradiation caused an increase in dielectric constant. At higher fluences, i.e. 10^{12} ions/cm^2, the defects are found to get annealed out.

3.3 Mechanism for Track Formation

The defects (point defects, clusters of defects, phase change like amorphization of a crystal) created in the wake of a single heavy ion in the considered matter is called latent track [3.10]. Track formation is clearly related to high electronic stopping powers. Of course, no clear limit between a low and a high electronic stopping regime can be proposed and this threshold value must depend on the nature of the target material. The mica was the first material in which latent tracks have been observed [3.11]. The efficiency of heavy ions to induce damage was measured in different classes of materials such as Polymers, alkali-halides, Silicates, Magnetic insulators, Organic conductors, and also in metallic and amorphous alloys.

❖ Track Characteristics

In general, to observe tracks after SHI-irradiation, one of the following processes can be employed:

(i) State of strain and chemical Reactivity of Tracks

- Tracks have been observed directly in a number of materials by first irradiating and then thinning the samples sufficiently for viewing in the electron microscope where tracks appear as dark diffraction – contrast lines whose behaviour indicates that the region around a track is strained.
- The samples are selectively etched and then observed under the microscope, etch channels or pits are formed at charged particle tracks as a result of the accelerated rate of solution of the damage region
- Tracks have been revealed by precipitation along the damage material in silver chloride and glass samples

Each of the above three accessible methods for displaying tracks indicates them to be composed of strained and chemically reactive material and are continuous microscopic scale.

(ii) Classes of Materials in which Tracks are formed

Tracks may be formed in almost any sort of insulating materials-crystalline, Glassy or Polymeric but have not been observed in good conductors.

(iii) Geometry of Tracks

The tracks must be continuous on a macroscopic scale. If they are discontinuous on an optical scale, the etch pits would be rough sided and often irregular in shape, which they normally are not.

(iv) Energy Loss needed to Form Tracks

Tracks are formed by any particle whose energy loss per unit length exceeds a critical value $(dE/dx)_e$ that is a quantity characteristic of the irradiated material.

Several theoretical models have been proposed to explain the appearance of tracks induced in matter by the slowing down of energetic ions in the electronic stopping power regime like,

(i) Coulomb Spike Model or Ionic Spike Model [3.12, 3.13]

(ii) Thermal Spike Model

First proposed by F. Desauer - [3.14]

Reconsidered for Metals by F. Seitz & J. S. Koehler - [3.15]

Extended to Insulators by G. Szene - [3.16]

and a more refined model putting forward a statistical deposition of electronic stopping power [3.17] or the role of target inner-shell electron excitation as a source of local intense ionization which triggers the damage process [3.18, 3.19].

3.3.1 Coulomb Spike Model or Ionic Spike Model

In the coulomb spike model the coulomb repulsion between ionized lattice atoms is dependent on the time screening by returning electrons. It is assumed that an energetic ion along its path creates a cylindrical region of highly ionized matter. Repulsive electrostatic forces act during the period before electronic neutrality is restored and give rise to a violent explosion. The coulomb explosion will be significant only if the charge neutralization time exceed 10^{-14}s for light target atom. In the course of time, the ionic spike arises within 10^{-14}-10^{-13}s. This phenomenon leads to a localized destruction of the lattice. Schiwietz et al [3.20] showed that the coulomb explosion cannot be efficient in carbon structures such as diamond, graphite, and amorphous carbon, because the electronic charge neutralization is too fast in these materials, and life of the repulsive states is not long enough to initiate the coulomb explosion.

3.3.2 Thermal Spike Model

The application of the thermal spike model to irradiation phenomena is an old idea. The first one was the thermal spike model proposed by F. Desauer [3.14] and reconsidered for metal by F. Seitz and J. S. Koehler [3.15]. The same model was especially extended for the analysis of latent track formation in insulators by G. Szenes [3.16]. In this model the energy is first deposited on the electrons of the target

by the projectile. In a first step this energy is shared between electrons and in a second step, is transferred to the lattice interaction leading to a large increase of temperature along the ion path [3.21].

The basic assumption of all thermal spike models is that around the trajectory of the high-energy ion a high-temperature region is formed in the material. In the following, all temperatures refer only to the phonon system. It is assumed that when the temperature exceeds the melting point of the crystal a melt is formed. Due to its small diameter, the cooling rate of the melt may reach 10^{13}-10^{14} K/s that results in an amorphous structure when the melt solidifies.

- The peak temperature of the spike T_p first grows up to its maximum value within a very short time ($<10^{-12}$ s) and then it decreases and the spike broadens as a result of heat conduction. We shall measure the time t from that moment when T_p is the maximum in the phonon system.
- Let us denote by T_{tg}, T_m, T(r , t) the target temperature, the melting point and the temperature at a distance r from the ion trajectory, respectively. If ΔT (r , t) is the temperature increase in the thermal spike then T (r , t) = T_{tg} + ΔT (r , t).

One of the main assumption of this model is that ΔT (r, t) can be approximated by a Gaussian distribution:

$$\Delta T (r , t) = Q [\pi a^2 (t)]^{-1} \exp\{-r^2/a^2(t)\} \qquad \text{.....(3.1)}$$

Where a^2 (t) depends on thermal diffusivity. The value of Q can be obtained from the balance of energy $Q = (gS_e - L\rho\pi R^2)(\rho c)^{-1}$, where gS_e is the fraction of energy deposited in the thermal spike, R = R (t) is the radius of the melted zone, c, ρ and L are the mean specific heat, the density and latent heat of the phase transition, respectively. In the following, the approximation $gS_e >> L\rho\pi R^2$ will be used. This is usually valid for materials in which latent track formation can be observed.

A second assumption of the model is that the volume of the amorphous phase formed along the ion trajectory is proportional to the maximum volume of the melt. In the following, the proportionality factor is taken equal to 1.

- To reach the melting point the temperature in the thermal spike should be increased by $T_o = T_m - T_{tg}$. The size of the melted region may increase or decrease as the thermal spike broadens.

- The maximum value $R = R_o$ can be obtained from the condition $dr/dt = 0$ at $\Delta T = T_o$. A short calculation leads to a very simple result: if the temperature at $r = a(t)$ is denoted by T_a, then $R = R_o$ when $T_a = T_o$.
- The width of the temperature distribution a (t) monotonically increases and T_a decreases with time in the cooling spike.
- If initially $T_o > T_a$ at $t = 0$ [$R(o) < a(o)$], $T_o = T_a$ never fulfills and the melted zone will have its maximum diameter at $t = 0$.
- If $T_o < T_a$ at $t = 0$ [$R(o) > a(o)$] then the melted zone expanded up to $t = t'$ when $T_o = T_a$ [$R_o = R(t') = a(t')$] and further it shrinks for $t > t'$.

The two behaviors are described by expressions, obtained from eq. (3.1) by introducing the conditions for maximum [3.22].

$$R_o^2 = a^2(o) \ln (S_e/S_{et}), \qquad 2.7 \geq S_e/S_{et} \geq 1 \qquad \text{.....(3.2a)}$$

$$R_o^2 = [a^2(o)/2.7] (S_e/S_{et}), \qquad S_e/S_{et} \geq 2.7 \qquad \text{.....(3.2b)}$$

$$S_{et} = \rho \pi c a^2(o) T_o/g \qquad \text{.....(3.3)}$$

Thus, the track radius and the electronic stopping power are related through two remarkably simple equations.

- According to Equation (3.2a) at low electronic stopping power there is a threshold S_{et} below which no amorphization is predicted. At this point $T_p = T_o$. Eq. (2a) describes a logarithmic variation of the damage cross section $A = \pi R_o^2$ in the $1 < S_e/S_{et} < 2.7$ range.
- Expression (2b) is an equation of a straight line for $S_e/S_{et} > 2.7$ going through the origin. There is a smooth transition between the logarithmic and linear regimes.
- At $S_e = 2.7 S_{et}$, Eqs. (3.2) provide the same value for R_o^2. The g parameter does not figure explicitly in eqs. (3.2). It affects the variation of R_o^2 through S_{et}.
- The slopes of the linear and logarithmic expressions differ only in a numerical factor. This is an additional requirement of the model besides the threshold behaviour and the existence of a logarithmic and a linear regime.
- Since R_o is obtained from a maximum condition, Eqs. (3.2) do not contain the time as a variable. Whatever is the time interval, short or long, necessary to reach the maximum size of the melted zone, it does not affect R_o. This is the reason why thermal diffusivities do not figure explicitly in the equations,

which is a great advantage of the model. The parameter which is related to thermal diffusivities is a (o). However, it can be obtained from fitting.

3.4 Damage (Track and Defects) Morphology

The damage (defect and track) induced in magnetic insulators (i.e. ferrites like spinels, garnets and hexaferrites) by swift heavy ion irradiation in the electronic slowing down regime has been extensively studied during the past decade. The damage induced in magnetic oxides was investigated for a wide range of electronic stopping power (dE/dx) and ion energies. Several oxides [3.23, 3.10] were irradiated. The damage induced by swift heavy ion irradiation was measured using several physical-characterization techniques like Mössbauer spectroscopy, saturation magnetization measurements, channeling Rutherford backscattering, infrared absorption and electrical resistivity measurements versus the fluence for specific values of dE/dx. For each physical characterization, specific analysis is necessary to determine the damaged volume fraction C. From the damaged volume fraction C, one can calculate a damage cross section 'A' deduced from Poisson's law $C = 1 - \exp(-A\varphi t)$ where φt is the ion fluence. Depending on the material and on the value of the electronic stopping power (dE/dx) the damage cross section varies between 10^{-17} to 10^{-12} cm^2 [3.10].

Studer et al [3.23] have linked the damage morphology to the damage efficiency $\epsilon = A/(dE/dx)$. To correlate damage efficiency and morphology one needs a direct observation of the defects. Electron microscopy and especially high resolution electron microscopy appeared as valuable tool for this purpose. Fig. 3.1 show general behaviour of the damage efficiency as observed in magnetic insulators [3.24]. In the upper part of the figure have the evolution of the damage efficiency versus (dE/dx). In the lower part the damage morphology corresponding to the five specified ranges as indicated (the beam direction is parallel to the continuous latent track as observed in the range V).

- In range I the damage results only from the nuclear elastic collisions.
- At $dE/dx \geq T_e$ the damage induced by inelastic collisions overcomes the nuclear elastic collisions one. The defect morphology is then spherical.
- At $dE/dx \geq T_s$ a percolation of the extended spherical defects leads to discontinues cylindrical defects

- At $dE/dx \geq T_c$ the cylindrical defects become continues but the damage is inhomogeneous inside the cylinder of defects.
- At $dE/dx \geq T_m$ (range V) the defects are cylindrical and homogeneous inside the cylinder defects.
- The values of T_i (i = e, s, c, m) are dependent on the specific materials.

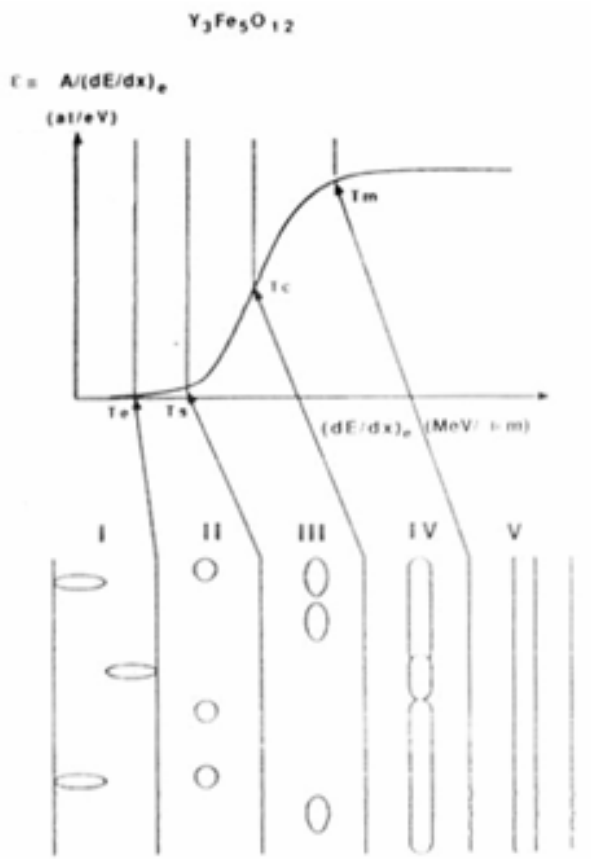

Fig. 3.1 General behaviour of the damage efficiency as observed in magnetic insulators [3.24].

Hourpert et al [3.25] have studied the latent track morphology evolution versus dE/dx for different materials like $Y_3Fe_5O_{12}$, $BaFe_{12}O_{19}$, $NiFe_2O_4$, $MgFe_2O_4$, the following descriptions on defect evolution and defect morphology is proposed

(I) For 4.5 < dE/dx < 7 keV/nm spherical defects appear with a radius of the other of 1.5 nm.

(II) For 7 < dE/dx < 14 keV/nm, the spherical defects percolate and discontinues cylindrical defects appear with radii of the order of 1.5 nm.

(III) For 14 < dE/dx < 20 keV/nm, the cylindrical defects percolate and the latent track radius start to increase from 1.5 nm to 3.1nm.

(IV) For dE/dx > 20 keV/nm, the latent track is long and cylindrical

Using medium and high resolution transmission electron microscopy and chemical etching of the latent track, an electronic stopping power evolution of the damage morphology has been observed leading to the definition of an effective radius R_e of the latent track which can be linked to the damage (amorphous) cross section A by the relation $A = \pi R_e^2$ [3.26-3.28]. Moreover there is a direct correlation between these values and the damage morphology.

In the representation of R_e versus dE/dx, R_e is equal to the observed radius only if the damage cross section A is higher than 10^{-13} cm^2. On the contrary for $A<10^{-13}cm^2$ the extracted R_e is only an effective cylindrical radius in which the amorphous phase of discontinuous defects is concentrated [3.10]. Effective radius R_e verses dE/dx and the corresponding damage morphology in $Y_3Fe_5O_{12}$ is given in Fig. 3.2 [3.29]. Four different regimes appears for the different values of R_e.

- Range II: For $R_e < 0.56$; $A < 10^{-14}$ cm^2, the electronic damage overcomes the nuclear damage. The extended defects are nearly spherical with a diameter of 3 nm.
- Range III: For $0.56 < R_e < 1.8$ nm; $10^{-14} < A < 10^{-13}$ cm^2, by overlapping spherical effect, cylindrical defects of 3 nm diameter appear.
- Range IV: For $1.8 < Re < 3.1$ nm; $10^{-13} < A < 3 \times 10^{-13}$ cm^2, the cylindrical effect overlap and the chemical etching of latent tracks begin to be efficient.
- Range V: For $Re > 3.1$ nm; $A > 3 \times 10^{-13}$ cm^2, the defects are long cylinders of amorphous material and the damage is homogeneous inside the cylinder.

The range I where the damage arise from nuclear collisions ($A \approx 10^{-19}$-10^{-16} cm^2) is not represented on the figure. Knowing the damage cross section A or R_e, the latent track damage morphology can be deduced. It is only the link between the absolute value of R_e and dE/dx which is a specific characteristic of each materials. Moreover the velocity of the incident ion has a direct influence on the damage production; the lower the velocity, the higher the damage [3.10].

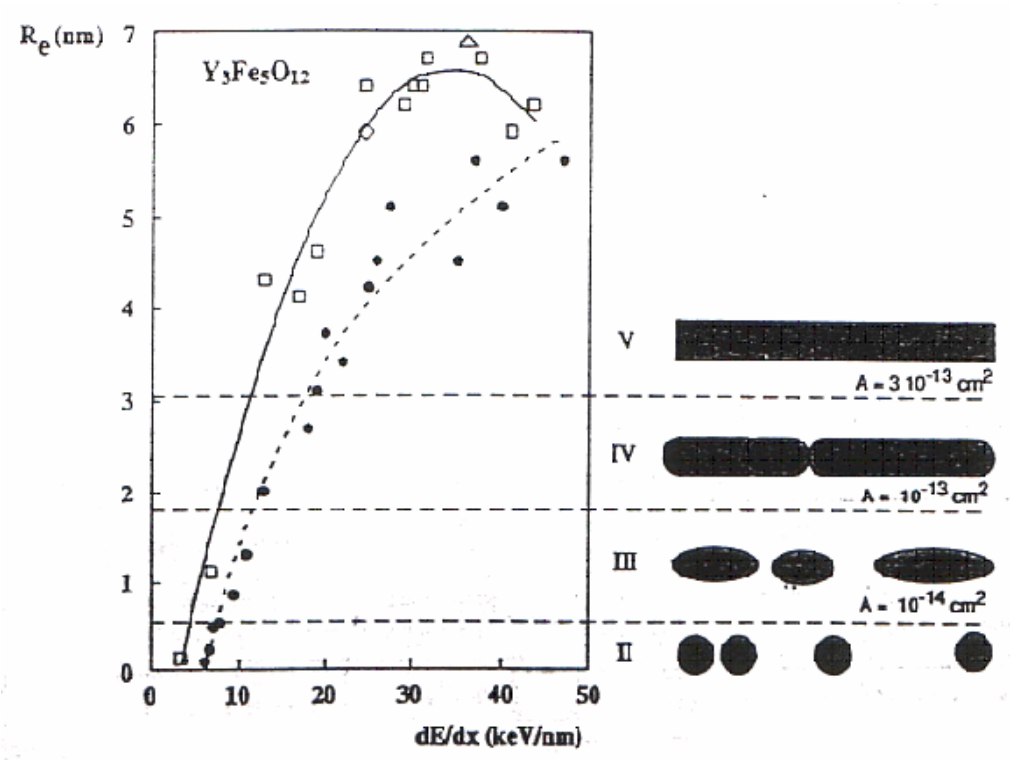

Fig. 3.2 Effective radius R_e versus dE/dx and the corresponding damage morphology in $Y_3Fe_5O_{12}$. Black dot corresponds to the high velocity regime around (10-20 MeV/amu) and open marks corresponds to the low velocity regime (around 5 MeV/amu). The lines are only drawn to guide the eyes [3.10]**.**

3.5 Irradiation Study of Ferrites

Irradiation by various kinds of particles like electrons, γ-photons, fast neutrons, protons, low energy ion and high energy ions on magnetic oxides causes micro-structural defects and disorder, which affect magnetic, electrical and dielectric properties. The work available in the literature deals with irradiation effects on various properties of polycrystalline, single crystal, thin films and nanoparticles of magnetic oxides like ferrites. In materials like $Y_3Fe_5O_{12}$, $BaFe_{12}O_{19}$ and $NiFe_2O_4$, the magnetic properties are very sensitive to the irradiation-induced disorder, which results in a decrease of the saturation magnetization [3.30, 3.31]. Mössbauer spectroscopy experiments have verified [3.32] that a paramagnetic phase induced. The damage induced in magnetic insulators by high energy heavy ion irradiation has the form of latent track, in general a cylindrical volume of amorphous material extending along the ion path. Such latent tracks have been observed by electron microscopy, especially high resolution electron microscopy in magnetic oxides a garnet and a

magnetoplombite $BaFe_{12}O_{19}$ [3.33-3.34, 3.30]. The effect of high electronic excitation induced by xenon ions (3.1 GeV) in magnetic oxides with spinel structure MFe_2O_4 with M = Mg^{2+}, Ni^{2+}, Fe^{2+} and Zn^{2+}, has been studied a large range of fluencies (10^{11} to 5 x 10^{12} Xe/cm^2) [3.35] by magnetic measurements, Mössbauer spectroscopy and HREM. The behaviour of spinel oxides under heavy ion irradiation [3.35] indicate that continuous trails of damage, called discontinuous latent tracks, have been observed in $NiFe_2O_4$ and Mg Fe_2O_4. Conversely, electron microscopy has shown that the spinel $ZnFe_2O_4$ and the Magnetite Fe_3O_4 compounds exhibits no discontinuous latent tracks, but extended spherical defects aligned along the ion wakes [3.35]. The magnetic properties of the magnetite Fe_3O_4 irradiated by high energy Pb ions have been investigated by magnetization measurements [3.36]. In low fluence regime, an increase of the coercivity due to a pinning of magnetic domain boundaries by columnar defects has evidenced. The induced damage and resulting stress strongly affect the magnitude and the direction of the magnetization via magnetostrictive effects. A phenomenological model was applied to reproduce the fluence evolution of the saturation magnetization, assuming relaxation of the stress induced around the core of defects of the tracks by overlapping effects at high fluence

Irradiation of thin epilayers of yttrium iron garnet (YIG) was performed at room temperature with 50 MeV ^{32}S, 50 MeV ^{63}Cu and 235 MeV ^{84} Kr, for which the energy loss in the target was mainly due to electronic excitation and ionization [3.37]. The resulting damage was studied by HRXRD and HRTEM. Recrystallization of 50 MeV ^{63}Cu tracks was observed in YIG, leading to grain size around 10nm, while no recrystallization was found for 235 MeV ^{84}Kr tracks. This recrystallization process is thought to be triggered by the dense electronic excitation produced by the ion beam, just like the amorphization. The effect of irradiations with swift heavy ions (3.8 GeV ^{129}Xe or 6.0 GeV ^{208}Pb) on magnetic properties of single crystal plates of yttrium iron garnet (111)-YIG:Si ($Y_3Fe_{4.94}Si_{0.06}O_{12}$) and barium hexaferrite (00.1)-BaM ($BaFe_{12}O_{19}$ or (00.1)-BaM : Co,Ti ($BaFe_{9.1}Co_{1.4}Ti_{1.5}O_{19}$) have been studied in the electronic slowing down regime and above the threshold (≈ 20 keV nm^{-1}) of formation of continuous and homogenous cylindrical amorphous tracks reported [3.38].

γ- Irradiation effects on the electrical conductivity of pure and Cu-doped Fe_3O_4 spinel has investigated and the effect of γ- irradiation on the conductivity

values, activation energy and type of defects has been discussed by M. A. Mousa [3.39]. The behaviour of the D.C. conductivity and the number of jumping vacancies per second in the different compositions of $Ni_{0.65}Zn_{0.35}Cu_xFe_{2-x}O_4$ before and after γ-irradiation of 10^6 rad were determined [3.40]. The action of γ-irradiation has displaced some atoms from their equilibrium positions and many vacancies are located there, leading to lower resistivity. Ahmed and Bishay [3.41] studied the effect of γ-irradiation on the electrical properties of Li-Co ferrites doped with rare earth ions. The results showed that, irradiation doses had high effect on electrical properties of the samples. These causes inflection in the dielectric properties from decreasing the polarization at 1 Mrad to increasing it at 3 Mrad while activation energy decreases with increasing dose due to the increase in electron exchange interaction. M. A. Ahmed et al [3.42, 3.43] is carried out to study the effect of γ-irradiation on both structural and electrical properties of Ti-substituted Mg-Ti ferrites doped with a constant concentration of rare earth element (Er). The results found that the ratio Fe^{2+}/Fe^{3+} plays a dominant role in the decrease of the crystal size due to irradiation damage with γ-rays. The effect of γ-irradiation on the structural and electrical properties of rare earth ferrites of the general formula $Co_{0.5}Zn_{0.5}Ce_yFe_{2-y}O_4$ ($0.0 \leq y \leq 0.2$) has discussed [3.44]. The results showed that the electrical conductivity and dielectric constant are highly dependent on both Ce and radiation dose. The numbers of ferrous ion at octahedral sites play a dominant role in the change of the crystal size due to irradiation effect. The effect of Q-switched Nd: YAG laser irradiation with wavelength of 1064 nm on the structural and transport properties of the samples Cu1-xZnxFe2O4 has been studied and mention the change in ac conductivity is attributed to the creation of lattice vacancies after laser irradiation [3.45]. They have reported that the decrease of the ac conductivity and the dielectric constant after laser irradiation with 18000 shots due to formation of traps, which decrease the number of carriers.

Influence of 190 MeV Ag ion irradiation on structural and magnetic properties and oxygen content of $NiMn_{0.05}Ti_xMg_xFe_{1.95-2x}O_4$ ($x = 0.0, 0.2$) ferrite thin film have been studied for different fluencies from $5x10^{10}$ to $1x10^{12}$ ions/cm^2 by Anjana Dogra et al [3.46]. The XRD pattern of the film showed the texturing along (111) plane in the irradiated films. For undoped film $NiMn_{0.05}Fe_{1.95}O_4$, the magnetization showed a decrease with increase in the ion fluence due to amorphization of the system. Whereas

for the substituted thin film of $NiMn_{0.05}Ti_{0.2}Mg_{0.2}Fe_{1.55}O_4$ the saturation magnetization value increases up to the fluence value of 1 x 10^{11} ions/cm^2 due to the defects induced texturing of the film under irradiation. Film irradiated with higher fluence showed a decrease in magnetization due to trapped magnetic moments in the defects created by irradiation.

In recent years, attention has been devoted towards the swift heavy ion irradiation induced modifications in the ferrite nanoparticles. 100 MeV Si^{+7} ion irradiation induced modification in the structural and magnetic properties of $Mg_{0.95}Mn_{0.05}Fe_2O_4$ nanoparticles [3.47] have been studied and the enhancement of saturation magnetization after irradiation was explained on the basis of SHI irradiation induced modifications in surface states of the nanoparticles. The results of the comparative study of unirradiated and irradiated ball milled $Ni_{0.65}Zn_{0.375}In_{0.25}Ti_{0.025}Fe_{1.70}O_4$ and co-precipitated $Mn_{0.75}Zn_{0.18}Fe_{2.07}O_4$ ferrite nanoparticles were explained in terms of ion induced disorder [3.48].

3.6 Pelletron

The main building at Inter University Accelerator Center houses the Pelletron tower, beam hall and the laboratory complex. The 50 meter tall tower is made of heavy concrete for radiation shielding. The 15UD Pelletron [3.49], a versatile heavy ion tandem electrostatic accelerator is installed in a vertical configuration in an insulating tank of 26.5 meter height and 5.5 meter diameter. The accelerator tank is filled with an insulating, gas sulphur hexafluroride (SF_6) maintained at a pressure of 6-7 atmosphere. A schematic of the tank is shown in Fig. 3.3. In this machine the negative ions are produced and preaccelerated to ~ 300 keV by Cesium sputter ion source known as SNICS (Source of Negative Ions by Cesium sputtering) (Now it has been replaced by MCSNICS (Multi Cathode SNICS)). The ions are mass analyzed by dipole magnet called injector magnet and are turned vertically downward direction. The ions then enter the strong electric field inside the accelerator. A terminal shell, about 1.52 meter in diameter and 3.61 meter in height, is located at the center of the tank which can be charged to a high voltage (~15MV) by a pellet charging system. The negative ions on traversing through the accelerating tubes from the column top of the tank to the positive terminal get accelerated. On reaching the terminal they pass through a stripper (foil or gas) that removes some electrons from the negative ions thus transforming the negative ions into the positive ions. For very heavy ions

(A>50), the lifetimes of the carbon foils used in stripper are limited to a few hours due to radiation damage. Therefore a gas filled canal or a combination of the gas stripper followed by a foil striper is used for heavy ions. The transformed positive ions are then repelled away from the positively charged terminal and are accelerated to ground potential to the bottom of the tank.

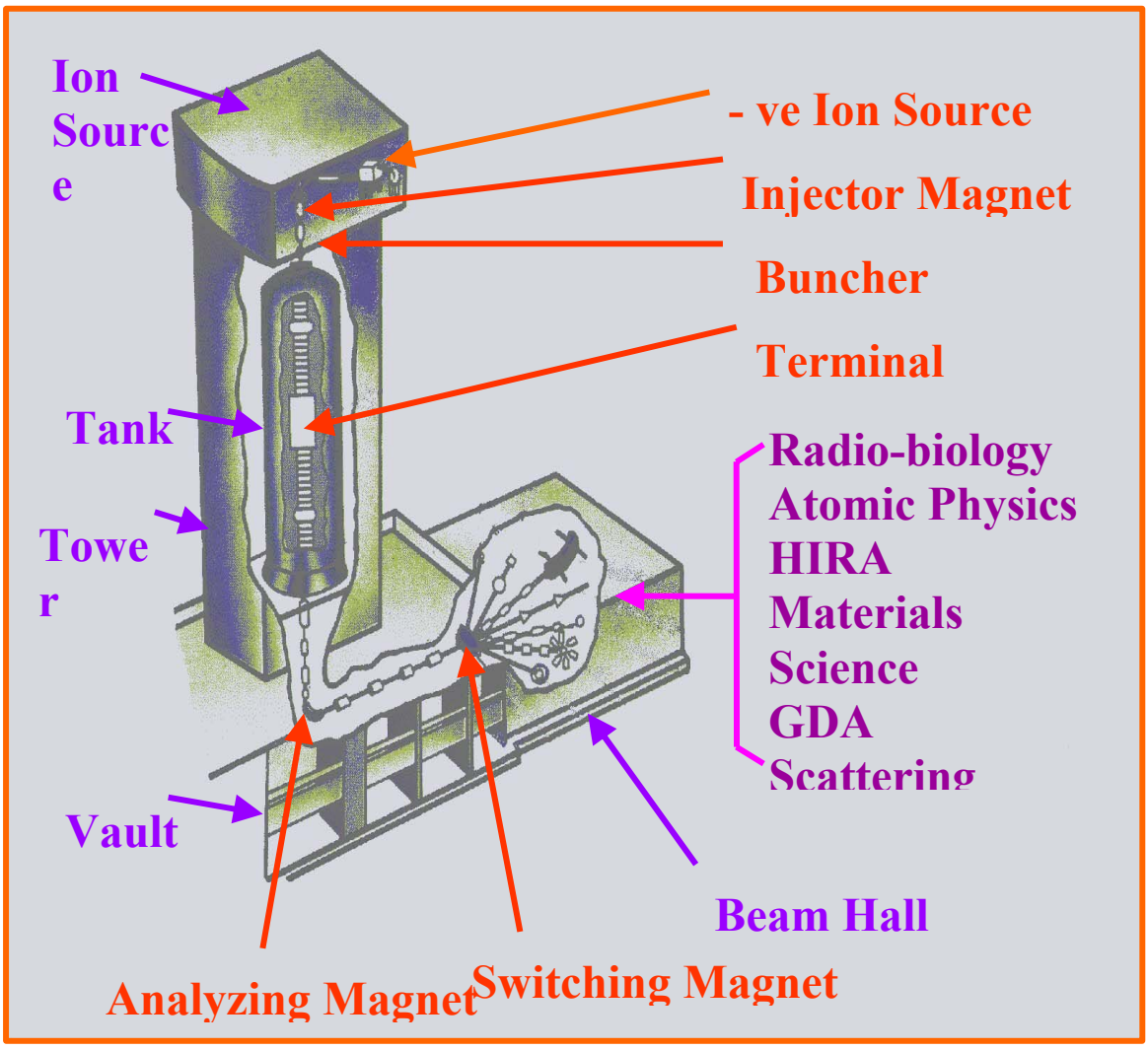

Fig.3.3 The Pelletron Accelerator at IUAC

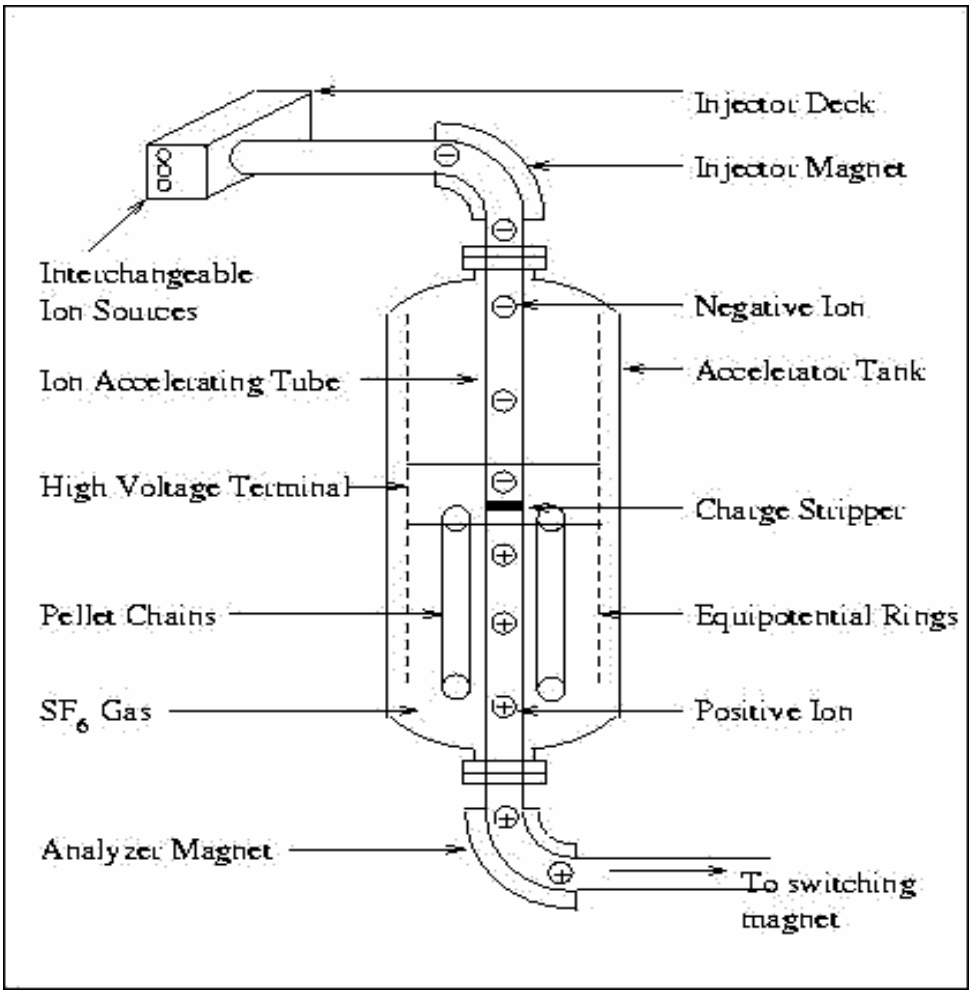

Fig. **3.3** Schematic Diagram of 15 UD Pelletron at IUAC, New Delhi

In this way same terminal potential is used twice to accelerate the ions. Therefore this accelerator is called a tandem Pelletron accelerator. The final energy of the emerging ions from the accelerator is given by

$$E_i = [E_{decpot} + (1+q_i)\ V] \qquad \ldots (3.4)$$

Where E_i is the energy of the in having a charge state q_i after stripping, V is the terminal potential in MV and E_{decpot} is the deck potential of the SNICS source. On existing from the tank, the ions are bent into horizontal plane by analyzing magnet. This magnet works as an energy analyzer and depending on the dipole magnetic field, ions of particular energy travel in the horizontal direction. The switching magnet diverts the high-energy ion beam into desired beam line of the beam hall. The ion beam is kept centered and focused using steering magnets and quadrupole triplet magnets. The beam line of the accelerator is in ultra vacuum condition (~10^{-10} mbar). The beam is monitoring by beam profile meter (BPM) and the current is observed by

means of Faraday cups. The entire machine is computer controlled and is operated from the control room. The accelerator can accelerate an ion from Proton to Uranium from few MeV to hundreds of MeV (200 MeV) depending on the ion.

3.6.1 Material Science Beam Line

The accelerated beam from the Pelletron is brought to the beam hall and switched to any one of the seven beam lines using the switching magnet. The Material Science beam line is at 15° to the right with respect to the zero degree beam line (Fig.3.4). This beam line houses three chamber- high vacuum chamber, ultra high vacuum chamber and goniometer chamber. The high vacuum chamber is a cylindrical shaped multiport stainless steel chamber.

Fig.3.4 Photograph of Material Science Beam Line

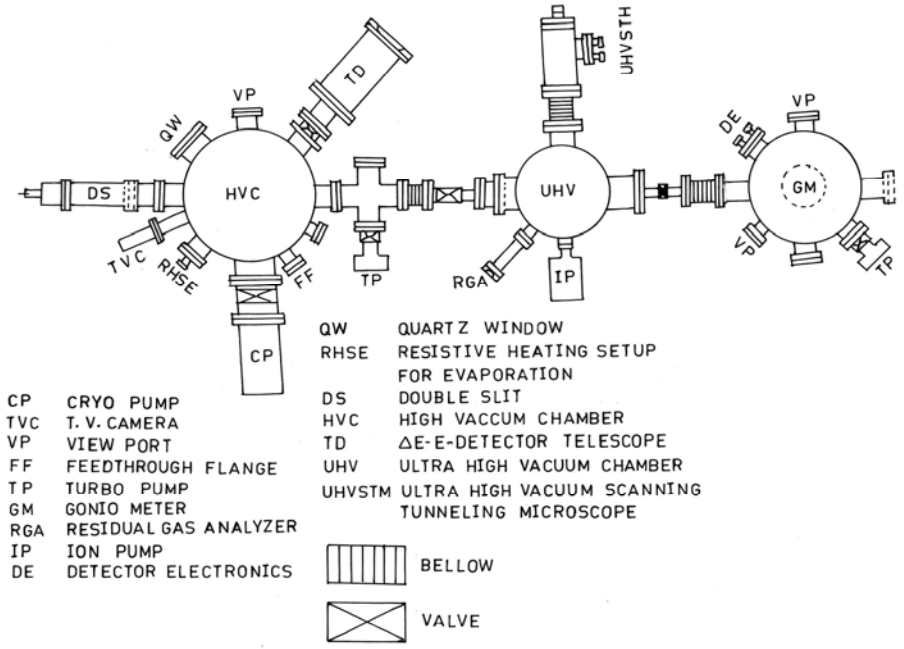

Fig. 3.4 Schematic Diagram Material Science Beam Line

Most of the irradiation experiments are performed in high vacuum chamber. A typical vacuum of 1 x 10^{-6} mbar is generally maintained during irradiation. The samples to be irradiated are mounted on the four sides of the target ladder (on copper block). The whole body of the ladder is made stainless steel and a perforated square copper block is brazed at the end of the ladder. The target ladder is mounted through a Wilson seal from the top flange of the chamber. This top flange is connected to the chamber through a flexible bellow that can expand up to 11cm from its minimum position. A stepper motor in conjunction with suitable mechanical assembly is used to control the up and down motion of the ladder. The beam on the ladder can be observed by observing the luminescence of the beam on the quartz crystal mounted on all sides of the ladder.

After the observation of the beam on the quartz, the samples to be irradiated are brought to the same position as that of the quartz by moving the ladder in the desirable position. A CCD camera is attached to one of the ports of the chamber for viewing the sample and the quart position. The positions can be monitored using close circuit television (CCTV) in the data acquisition room. The magnetic scanner that can sweep the beam (25mm in y-direction and 10mm in x-direction) ensures the sample ladder, which is kept at a negative potential of 120 V. This enclosure suppresses the

secondary electrons coming out of sample during irradiation. An opening in the suppressor allows the ion beam to fall on the sample. The total number of particles/Charges falling on the sample can be estimated by a combination of the current integrator and the pulse counter (Faraday cup) from which the irradiation fluence can be measured.

The second chamber, UHV chamber contains facilities like in-situ scanning tunneling microscopy (STM) for in-situ surface studies and residual gas analyzer (RGA) for ion beam induced desorption. Third chamber is the goniometer chamber, which incorporates the in-situ X-ray reflectivity (XRR), large area position sensitive detector for Elastic recoil detector analysis (ERDA) and other channeling facilities.

The irradiation experiments were performed in high vacuum chamber, with a typical vacuum maintained at 1 x 10-6 mbar. The reason for requiring vacuum is to avoid any collision of the particle (beam) with gas molecules. The samples to be irradiated were mounted on the four sides of the target ladder (on copper block), which were separated from each other by a distance of about 1cm.

The counts calculated for the fluence for each sample was calculating using the following relation

$$n\ (dose) = I(nA) \times t / 1.6 \times 10^{-19} \times q$$

or

$$\text{Number of Counts} = \text{dose} \times q \times 1.6 \times 10^{-19} / \text{Pulsed Height}$$

3.7 SRIM Calculations

SRIM is a group of programs, which calculate the stopping, and range of ions (10 eV - 2 GeV /amu) into matter using a quantum mechanical treatment of ion-atom collisions (we shall always refer to the moving atom as an *"ion",* and all target atoms as *"atoms"*). During collisions, the ion and atom have a screened Coulomb collision, including exchange and correlation interactions between the overlapping electron shells. The ion also has long-range interactions with target atoms creating electron excitations and plasmons within the target. These are described by including a description of the target's collective electronic structure and interatomic bond structure when the calculation is setup. The charge-state of the ion within the target is described using the concept of effective charge, which includes a velocity dependent charge state and long range screening due to the collective electron sea of the target. A full description of the calculation is found in the tutorial book [3.50]. This book

presents the physics of ion penetration of solids in a simple tutorial manner, and then presents the source code for SRIM programs with a full explanation of its physics. Further chapters document the accuracy of SRIM and show various applications.

❖ Tables of the Stopping and Range of Ions in Matter

This function quickly creates Tables of the stopping and range of ions in matter over a wide band of ion energies. These tables are useful to set up the full Monte Carlo TRIM program, so that the target thickness is adequate to contain all the ions. The target may be a complex compound, but may only contain one layer (the target is considered homogeneous and of infinite thickness).

➢ Tables of Stopping Powers

The stopping powers tabulated are identical to those used in TRIM. The stopping powers are reported as electronic energy loss (to the target electrons) and as nuclear energy loss (to the target nuclei). These are the traditional components of the ion's energy loss. The nuclear energy loss may lead to recoiling target atoms, which will also have a component of electronic energy loss, however this secondary energy loss to the target electrons is not considered.

➢ Tables of Ion Ranges

The ranges of ion are calculated using the transport equation approach developed by J. P. Biersack, which he called PRAL (Projection RAnge ALgorithm) [3.51, 3.50]. This method allows the rapid calculation of ion ranges over a large band of ion energies. The ranges are quite accurate, usually within 5% if those found using TRIM (which is the most accurate method of calculating ranges). The range straggling values are less accurate, and are tabulated for reference.

❖ TRIM

TRIM (The Transport of Ions in Matter) is the most comprehensive program included in the SRIM software. It is a Monte-Carlo calculation, which follows the ion into the target, making detailed calculations of the energy transferred to every target atom collision. TRIM will accept complex targets made of compound materials with up to eight layers, each of different materials. It will calculate both the final 3D distribution of the ions and also all kinetic phenomena associated with the ion's energy loss: target damage, sputtering, ionization, and phonon production. All target atom cascades in the target are followed in detail. The programs are made so they can be interrupted at any time, and then resumed later. Plots of the calculation may be

saved, and displayed when needed (it takes 5 seconds to begin viewing a saved calculation). This calculation is made very efficient by the use of statistical algorithms, which allow the ion to make jumps between calculated collisions and then averaging the collision results over the intervening gap. TRIM results from the original work by J. P. Biersack on range algorithms [3.52] and the work by J. F. Ziegler on stopping theory [3.50].

3.7.1 Variation of S_e & S_n with energy and depth in ferrites

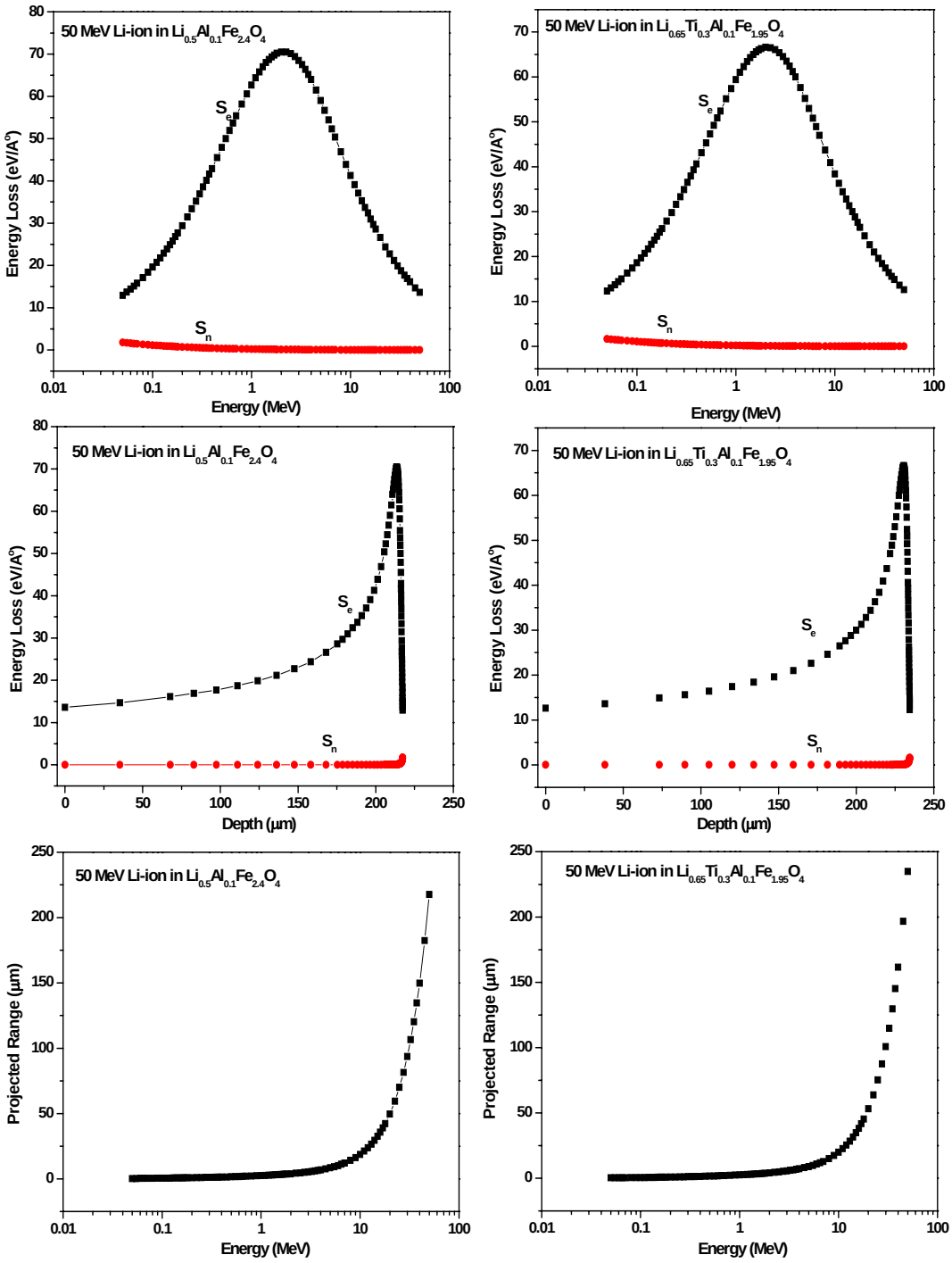

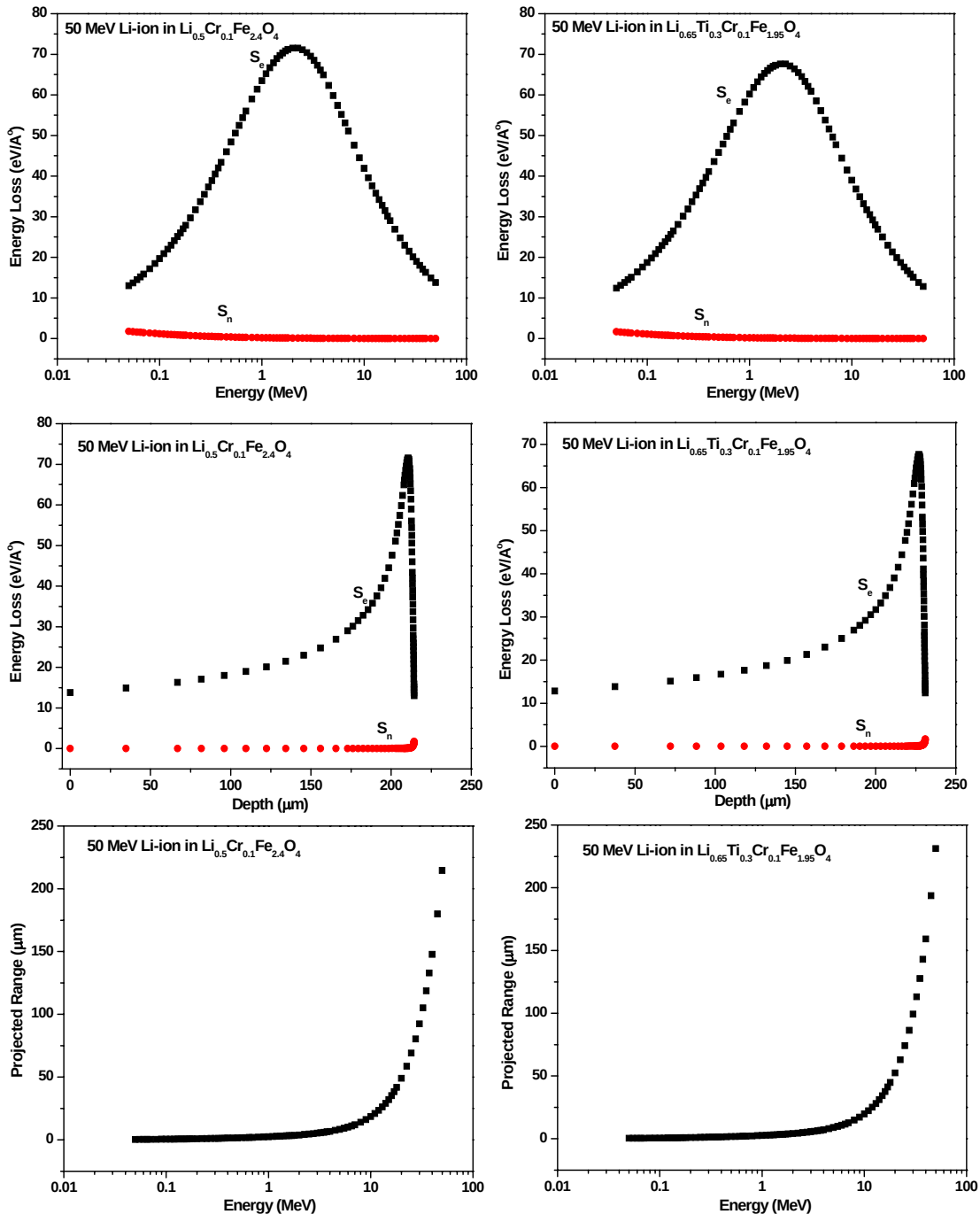
50 MeV Li-ion in Li0.5Cr0.1Fe2.4O4
Se
Sn
Energy Loss (eV/A°)
Energy (MeV)
50 MeV Li-ion in Li0.65Ti0.3Cr0.1Fe1.95O4
Se
Sn
Energy Loss (eV/A°)
Energy (MeV)
50 MeV Li-ion in Li0.5Cr0.1Fe2.4O4
Se
Sn
Energy Loss (eV/A°)
Depth (μm)
50 MeV Li-ion in Li0.65Ti0.3Cr0.1Fe1.95O4
Se
Sn
Energy Loss (eV/A°)
Depth (μm)
50 MeV Li-ion in Li0.5Cr0.1Fe2.4O4
Projected Range (μm)
Energy (MeV)
50 MeV Li-ion in Li0.65Ti0.3Cr0.1Fe1.95O4
Projected Range (μm)
Energy (MeV)

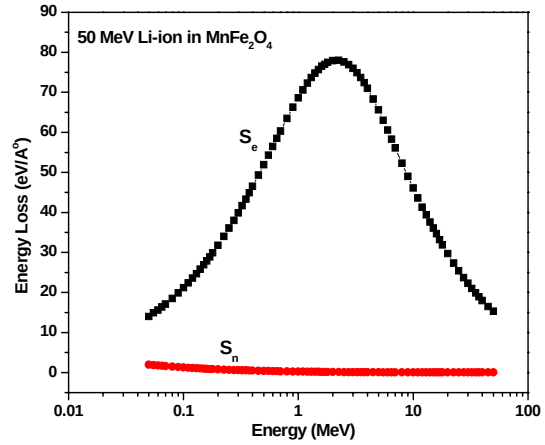
50 MeV Li-ion in MnFe2O4
Se
Sn
Energy Loss (eV/A°)
Energy (MeV)

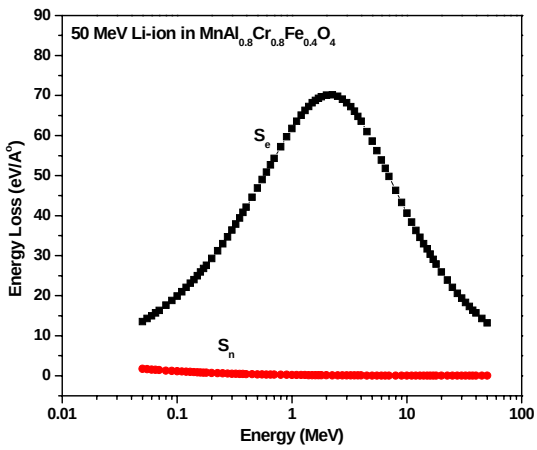
50 MeV Li-ion in MnAl0.8Cr0.8Fe0.4O4
Se
Sn
Energy Loss (eV/A°)
Energy (MeV)

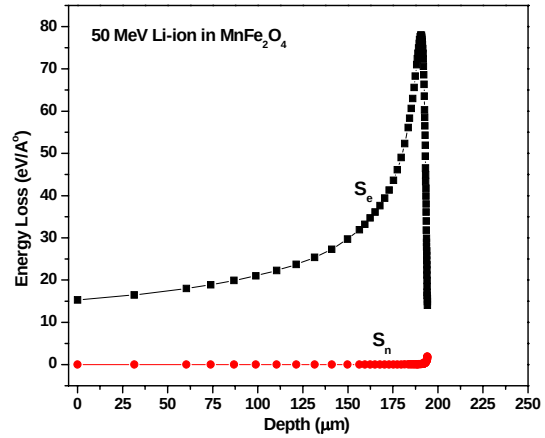
50 MeV Li-ion in MnFe2O4
Se
Sn
Energy Loss (eV/A°)
Depth (µm)

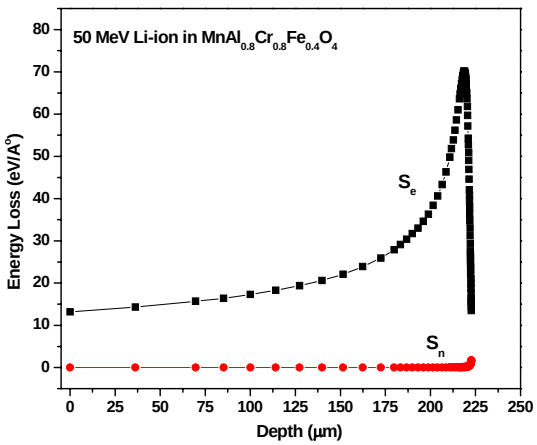
50 MeV Li-ion in MnAl0.8Cr0.8Fe0.4O4
Se
Sn
Energy Loss (eV/A°)
Depth (µm)

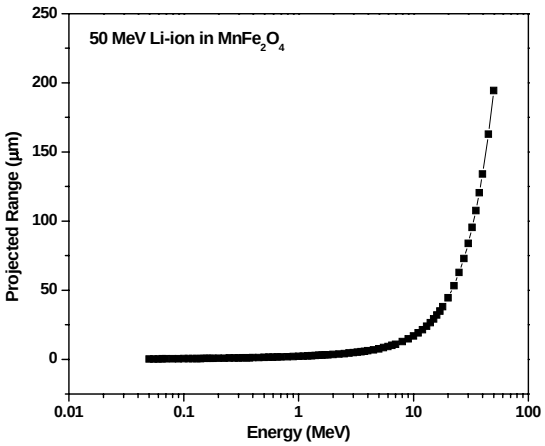
50 MeV Li-ion in MnFe2O4
Projected Range (µm)
Energy (MeV)

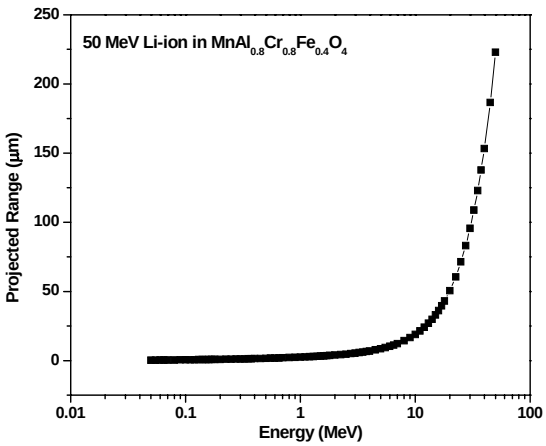
50 MeV Li-ion in MnAl0.8Cr0.8Fe0.4O4
Projected Range (µm)
Energy (MeV)

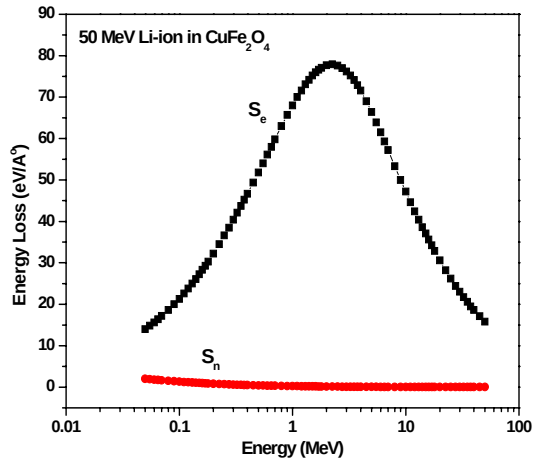
50 MeV Li-ion in $CuFe_2O_4$
S_e
S_n
Energy Loss (eV/A°)
Energy (MeV)

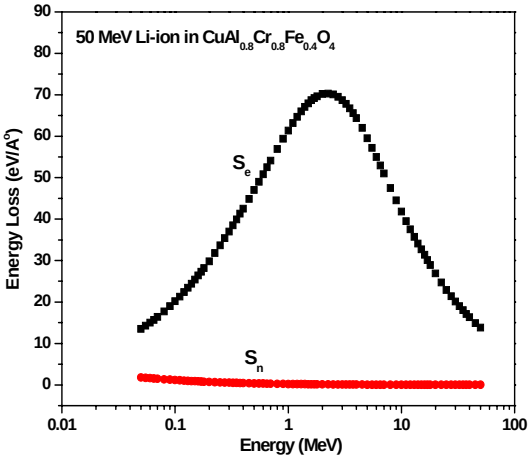
50 MeV Li-ion in $CuAl_{0.8}Cr_{0.8}Fe_{0.4}O_4$
S_e
S_n
Energy Loss (eV/A°)
Energy (MeV)

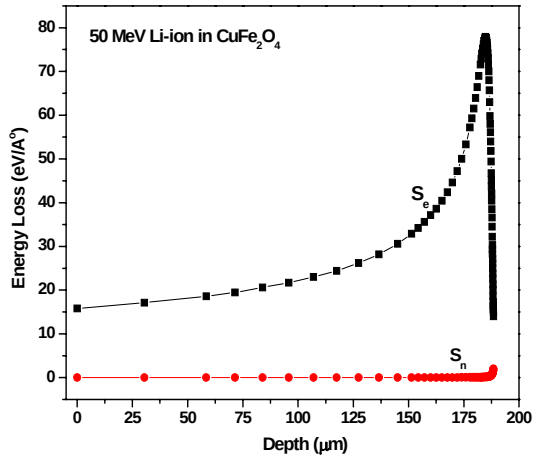
50 MeV Li-ion in $CuFe_2O_4$
S_e
S_n
Energy Loss (eV/A°)
Depth (μm)

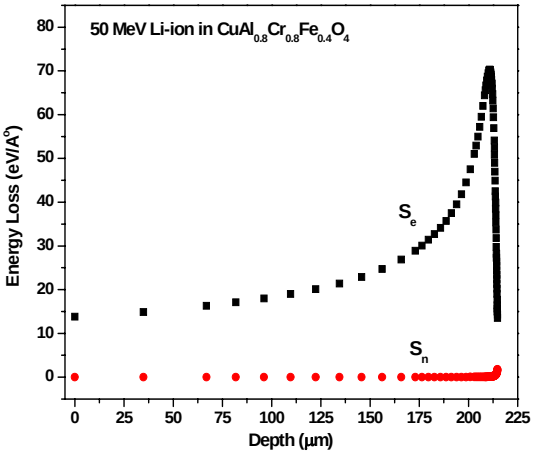
50 MeV Li-ion in $CuAl_{0.8}Cr_{0.8}Fe_{0.4}O_4$
S_e
S_n
Energy Loss (eV/A°)
Depth (μm)

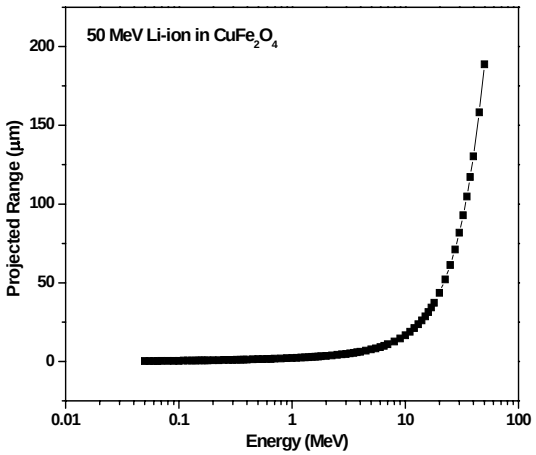
50 MeV Li-ion in $CuFe_2O_4$
Projected Range (μm)
Energy (MeV)

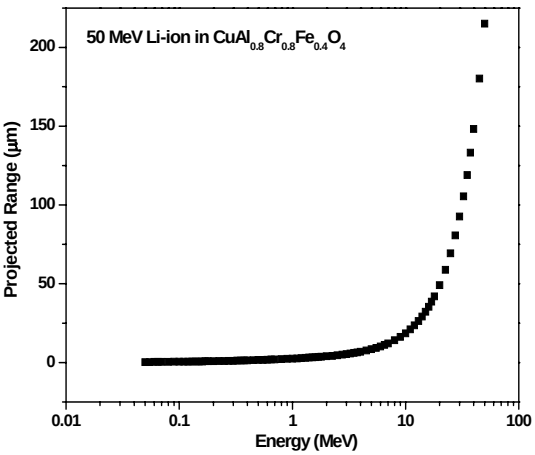
50 MeV Li-ion in $CuAl_{0.8}Cr_{0.8}Fe_{0.4}O_4$
Projected Range (μm)
Energy (MeV)

3.7.2 Table of Sample Calculations using SRIM –2003 software (Output of SRIM Calculations)

==========

Calculation using SRIM-2003
SRIM version ---> SRIM-2003.20
Calc. date ---> November 29, 2006

==========

Disk File Name = SRIM Outputs\Lithium in $Li_{0.5+0.5x}Ti_xAl_{0.1}Fe_{2.4-1.5x}O_4$ (x=0.3)

Ion = Lithium [3] , Mass = 7.016 amu

Target Density = 3.2879E+00 g/cm3 = 7.1264E+22 atoms/cm3

======= Target Composition ========

Atom Name	Atom Numb	Atomic Percent	Mass Percent
Li	3	009.29	002.32
Ti	22	004.29	007.40
Al	13	001.43	001.39
Fe	26	027.86	055.99
O	8	057.13	032.90

==========

Bragg Correction = 0.00%
Stopping Units = eV / Angstrom
See bottom of Table for other Stopping units

Ion Energy	dE/dx Elec.	dE/dx Nuclear	Projected Range	Longitudinal Straggling	Lateral Straggling
50.00 keV	1.230E+01	1.652E+00	3018 A	1292 A	1161 A
55.00 keV	1.301E+01	1.560E+00	3287 A	1356 A	1233 A
60.00 keV	1.371E+01	1.480E+00	3550 A	1415 A	1300 A
65.00 keV	1.438E+01	1.408E+00	3806 A	1470 A	1363 A
70.00 keV	1.502E+01	1.344E+00	4056 A	1520 A	1422 A
80.00 keV	1.627E+01	1.235E+00	4539 A	1609 A	1531 A
90.00 keV	1.744E+01	1.144E+00	5002 A	1687 A	1629 A
100.00 keV	1.857E+01	1.067E+00	5446 A	1756 A	1718 A
110.00 keV	1.965E+01	1.001E+00	5873 A	1816 A	1799 A
120.00 keV	2.068E+01	9.438E-01	6285 A	1870 A	1874 A
130.00 keV	2.168E+01	8.935E-01	6683 A	1919 A	1942 A
140.00 keV	2.265E+01	8.489E-01	7068 A	1963 A	2006 A
150.00 keV	2.358E+01	8.091E-01	7442 A	2003 A	2065 A
160.00 keV	2.448E+01	7.732E-01	7805 A	2040 A	2120 A
170.00 keV	2.536E+01	7.408E-01	8158 A	2074 A	2171 A
180.00 keV	2.622E+01	7.113E-01	8501 A	2105 A	2220 A
200.00 keV	2.785E+01	6.596E-01	9164 A	2162 A	2309 A
225.00 keV	2.979E+01	6.056E-01	9950 A	2223 A	2407 A

250.00 keV	3.160E+01	5.607E-01	1.07 um	2275 A	2495 A
275.00 keV	3.332E+01	5.226E-01	1.14 um	2320 A	2572 A
300.00 keV	3.494E+01	4.898E-01	1.21 um	2360 A	2643 A
325.00 keV	3.647E+01	4.613E-01	1.27 um	2395 A	2706 A
350.00 keV	3.792E+01	4.363E-01	1.34 um	2427 A	2765 A
375.00 keV	3.931E+01	4.141E-01	1.40 um	2455 A	2819 A
400.00 keV	4.062E+01	3.942E-01	1.46 um	2481 A	2869 A
450.00 keV	4.306E+01	3.602E-01	1.57 um	2529 A	2959 A
500.00 keV	4.528E+01	3.321E-01	1.68 um	2570 A	3038 A
550.00 keV	4.731E+01	3.084E-01	1.79 um	2606 A	3108 A
600.00 keV	4.916E+01	2.882E-01	1.89 um	2638 A	3172 A
650.00 keV	5.085E+01	2.706E-01	1.98 um	2666 A	3230 A
700.00 keV	5.240E+01	2.553E-01	2.08 um	2692 A	3284 A
800.00 keV	5.513E+01	2.296E-01	2.26 um	2742 A	3379 A
900.00 keV	5.742E+01	2.090E-01	2.43 um	2786 A	3463 A
1.00 MeV	5.935E+01	1.921E-01	2.60 um	2824 A	3538 A
1.10 MeV	6.096E+01	1.779E-01	2.77 um	2859 A	3606 A
1.20 MeV	6.230E+01	1.658E-01	2.93 um	2890 A	3668 A
1.30 MeV	6.340E+01	1.554E-01	3.08 um	2919 A	3726 A
1.40 MeV	6.430E+01	1.463E-01	3.24 um	2946 A	3780 A
1.50 MeV	6.502E+01	1.382E-01	3.39 um	2972 A	3832 A
1.60 MeV	6.558E+01	1.311E-01	3.54 um	2996 A	3880 A
1.70 MeV	6.600E+01	1.247E-01	3.69 um	3019 A	3927 A
1.80 MeV	6.631E+01	1.190E-01	3.84 um	3042 A	3971 A
2.00 MeV	6.661E+01	1.091E-01	4.14 um	3098 A	4055 A
2.25 MeV	6.653E+01	9.894E-02	4.51 um	3174 A	4154 A
2.50 MeV	6.609E+01	9.063E-02	4.89 um	3247 A	4248 A
2.75 MeV	6.539E+01	8.369E-02	5.27 um	3318 A	4338 A
3.00 MeV	6.449E+01	7.781E-02	5.65 um	3388 A	4425 A
3.25 MeV	6.347E+01	7.275E-02	6.04 um	3458 A	4511 A
3.50 MeV	6.236E+01	6.835E-02	6.43 um	3527 A	4595 A
3.75 MeV	6.120E+01	6.448E-02	6.84 um	3597 A	4679 A
4.00 MeV	6.000E+01	6.106E-02	7.25 um	3668 A	4763 A
4.50 MeV	5.759E+01	5.525E-02	8.10 um	3905 A	4931 A
5.00 MeV	5.523E+01	5.052E-02	8.98 um	4146 A	5102 A
5.50 MeV	5.297E+01	4.658E-02	9.90 um	4391 A	5277 A
6.00 MeV	5.084E+01	4.324E-02	10.86 um	4642 A	5457 A
6.50 MeV	4.886E+01	4.037E-02	11.86 um	4898 A	5643 A
7.00 MeV	4.701E+01	3.789E-02	12.90 um	5161 A	5836 A
8.00 MeV	4.371E+01	3.378E-02	15.10 um	6113 A	6242 A
9.00 MeV	4.088E+01	3.051E-02	17.47 um	7051 A	6679 A
10.00 MeV	3.842E+01	2.786E-02	19.98 um	7986 A	7146 A
11.00 MeV	3.629E+01	2.565E-02	22.66 um	8923 A	7645 A
12.00 MeV	3.441E+01	2.378E-02	25.48 um	9867 A	8175 A
13.00 MeV	3.275E+01	2.218E-02	28.46 um	1.08 um	8736 A
14.00 MeV	3.127E+01	2.080E-02	31.58 um	1.18 um	9327 A
15.00 MeV	3.003E+01	1.958E-02	34.83 um	1.27 um	9947 A
16.00 MeV	2.880E+01	1.851E-02	38.23 um	1.37 um	1.06 um
17.00 MeV	2.759E+01	1.755E-02	41.77 um	1.47 um	1.13 um
18.00 MeV	2.651E+01	1.670E-02	45.46 um	1.57 um	1.20 um

20.00 MeV	2.462E+01	1.522E-02	53.28 um	1.94 um	1.35 um
22.50 MeV	2.264E+01	1.373E-02	63.86 um	2.48 um	1.55 um
25.00 MeV	2.099E+01	1.251E-02	75.32 um	2.98 um	1.77 um
27.50 MeV	1.960E+01	1.150E-02	87.63 um	3.48 um	2.01 um
30.00 MeV	1.839E+01	1.065E-02	100.78 um	3.97 um	2.26 um
32.50 MeV	1.735E+01	9.926E-03	114.76 um	4.47 um	2.53 um
35.00 MeV	1.642E+01	9.296E-03	129.56 um	4.96 um	2.81 um
37.50 MeV	1.561E+01	8.744E-03	145.16 um	5.46 um	3.11 um
40.00 MeV	1.487E+01	8.258E-03	161.55 um	5.97 um	3.42 um
45.00 MeV	1.362E+01	7.438E-03	196.65 um	7.83 um	4.08 um
50.00 MeV	1.258E+01	6.773E-03	234.82 um	9.57 um	4.80 um

Multiply Stopping by	for Stopping Units
1.0000E+00	eV / Angstrom
1.0000E+01	keV / micron
1.0000E+01	MeV / mm
3.0416E-02	keV / (ug/cm2)
3.0416E-02	MeV / (mg/cm2)
3.0416E+01	keV / (mg/cm2)
1.4032E+00	eV / (1E15 atoms/cm2)
5.7436E-02	L.S.S. reduced units

==========

==========

Calculation using SRIM-2003
SRIM version ---> SRIM-2003.20
Calc. date ---> November 29, 2006

==========

Disk File Name = SRIM Outputs\Lithium in $MnAl_xCr_xFe_{2-2x}O_4$ (x=0.8)

Ion = Lithium [3] , Mass = 7.016 amu

Target Density = 3.4580E+00 g/cm3 = 7.1295E+22 atoms/cm3

======= Target Composition ========

Atom Name	Atom Numb	Atomic Percent	Mass Percent
Mn	25	014.29	026.88
Al	13	011.43	010.56
Cr	24	011.43	020.35
Fe	26	005.71	010.92
O	8	057.14	031.30

==========

Bragg Correction = 0.00%
Stopping Units = eV / Angstrom
See bottom of Table for other Stopping units

Ion Energy	dE/dx Elec.	dE/dx Nuclear	Projected Range	Longitudinal Straggling	Lateral Straggling
50.00 keV	1.354E+01	1.743E+00	2778 A	1144 A	1035 A
55.00 keV	1.428E+01	1.646E+00	3027 A	1201 A	1099 A
60.00 keV	1.498E+01	1.561E+00	3272 A	1254 A	1160 A
65.00 keV	1.566E+01	1.486E+00	3510 A	1303 A	1217 A
70.00 keV	1.632E+01	1.418E+00	3744 A	1347 A	1271 A
80.00 keV	1.758E+01	1.302E+00	4196 A	1428 A	1370 A
90.00 keV	1.878E+01	1.206E+00	4630 A	1499 A	1460 A
100.00 keV	1.991E+01	1.125E+00	5047 A	1561 A	1542 A
110.00 keV	2.100E+01	1.055E+00	5450 A	1616 A	1616 A
120.00 keV	2.205E+01	9.946E-01	5839 A	1666 A	1685 A
130.00 keV	2.305E+01	9.414E-01	6215 A	1711 A	1749 A
140.00 keV	2.402E+01	8.943E-01	6580 A	1751 A	1808 A
150.00 keV	2.496E+01	8.523E-01	6935 A	1789 A	1863 A
160.00 keV	2.587E+01	8.145E-01	7280 A	1823 A	1914 A
170.00 keV	2.675E+01	7.802E-01	7616 A	1854 A	1963 A
180.00 keV	2.761E+01	7.491E-01	7944 A	1883 A	2008 A
200.00 keV	2.925E+01	6.945E-01	8576 A	1936 A	2092 A
225.00 keV	3.119E+01	6.376E-01	9329 A	1994 A	2185 A
250.00 keV	3.301E+01	5.902E-01	1.00 um	2043 A	2268 A
275.00 keV	3.474E+01	5.500E-01	1.07 um	2086 A	2342 A
300.00 keV	3.637E+01	5.155E-01	1.14 um	2124 A	2409 A
325.00 keV	3.792E+01	4.854E-01	1.20 um	2158 A	2470 A
350.00 keV	3.939E+01	4.590E-01	1.26 um	2188 A	2526 A
375.00 keV	4.079E+01	4.356E-01	1.32 um	2215 A	2578 A
400.00 keV	4.213E+01	4.147E-01	1.38 um	2240 A	2626 A
450.00 keV	4.463E+01	3.789E-01	1.49 um	2287 A	2712 A
500.00 keV	4.691E+01	3.492E-01	1.60 um	2326 A	2789 A
550.00 keV	4.900E+01	3.243E-01	1.70 um	2361 A	2857 A
600.00 keV	5.093E+01	3.030E-01	1.79 um	2392 A	2918 A
650.00 keV	5.270E+01	2.845E-01	1.89 um	2419 A	2975 A
700.00 keV	5.434E+01	2.683E-01	1.98 um	2444 A	3026 A
800.00 keV	5.723E+01	2.414E-01	2.15 um	2494 A	3118 A
900.00 keV	5.970E+01	2.197E-01	2.32 um	2536 A	3199 A
1.00 MeV	6.180E+01	2.019E-01	2.48 um	2574 A	3271 A
1.10 MeV	6.357E+01	1.869E-01	2.64 um	2607 A	3337 A
1.20 MeV	6.506E+01	1.742E-01	2.79 um	2638 A	3396 A
1.30 MeV	6.630E+01	1.632E-01	2.94 um	2666 A	3452 A
1.40 MeV	6.733E+01	1.536E-01	3.09 um	2692 A	3504 A
1.50 MeV	6.816E+01	1.452E-01	3.24 um	2717 A	3552 A
1.60 MeV	6.882E+01	1.377E-01	3.38 um	2740 A	3599 A
1.70 MeV	6.933E+01	1.310E-01	3.52 um	2763 A	3643 A
1.80 MeV	6.971E+01	1.250E-01	3.67 um	2784 A	3685 A
2.00 MeV	7.014E+01	1.146E-01	3.95 um	2839 A	3765 A
2.25 MeV	7.018E+01	1.039E-01	4.31 um	2912 A	3859 A
2.50 MeV	6.980E+01	9.516E-02	4.66 um	2982 A	3947 A
2.75 MeV	6.912E+01	8.787E-02	5.02 um	3050 A	4031 A

3.00 MeV	6.823E+01	8.169E-02	5.38 um	3118 A	4113 A
3.25 MeV	6.719E+01	7.637E-02	5.75 um	3184 A	4193 A
3.50 MeV	6.605E+01	7.175E-02	6.12 um	3251 A	4272 A
3.75 MeV	6.483E+01	6.769E-02	6.50 um	3318 A	4350 A
4.00 MeV	6.358E+01	6.409E-02	6.89 um	3385 A	4428 A
4.50 MeV	6.104E+01	5.800E-02	7.69 um	3612 A	4584 A
5.00 MeV	5.855E+01	5.302E-02	8.52 um	3841 A	4743 A
5.50 MeV	5.615E+01	4.888E-02	9.39 um	4075 A	4905 A
6.00 MeV	5.389E+01	4.538E-02	10.30 um	4314 A	5071 A
6.50 MeV	5.178E+01	4.237E-02	11.24 um	4558 A	5243 A
7.00 MeV	4.981E+01	3.976E-02	12.23 um	4807 A	5421 A
8.00 MeV	4.629E+01	3.544E-02	14.30 um	5713 A	5796 A
9.00 MeV	4.326E+01	3.202E-02	16.53 um	6605 A	6199 A
10.00 MeV	4.063E+01	2.923E-02	18.92 um	7492 A	6630 A
11.00 MeV	3.835E+01	2.691E-02	21.45 um	8383 A	7091 A
12.00 MeV	3.634E+01	2.495E-02	24.12 um	9279 A	7581 A
13.00 MeV	3.456E+01	2.327E-02	26.94 um	1.02 um	8100 A
14.00 MeV	3.298E+01	2.182E-02	29.89 um	1.11 um	8647 A
15.00 MeV	3.167E+01	2.054E-02	32.98 um	1.20 um	9221 A
16.00 MeV	3.036E+01	1.941E-02	36.20 um	1.29 um	9821 A
17.00 MeV	2.907E+01	1.841E-02	39.57 um	1.39 um	1.04 um
18.00 MeV	2.793E+01	1.751E-02	43.07 um	1.48 um	1.11 um
20.00 MeV	2.593E+01	1.597E-02	50.49 um	1.84 um	1.25 um
22.50 MeV	2.385E+01	1.440E-02	60.53 um	2.34 um	1.44 um
25.00 MeV	2.211E+01	1.312E-02	71.41 um	2.83 um	1.64 um
27.50 MeV	2.063E+01	1.206E-02	83.10 um	3.30 um	1.86 um
30.00 MeV	1.937E+01	1.117E-02	95.59 um	3.77 um	2.10 um
32.50 MeV	1.826E+01	1.041E-02	108.88 um	4.24 um	2.35 um
35.00 MeV	1.729E+01	9.747E-03	122.93 um	4.71 um	2.61 um
37.50 MeV	1.642E+01	9.169E-03	137.75 um	5.18 um	2.88 um
40.00 MeV	1.565E+01	8.659E-03	153.33 um	5.66 um	3.17 um
45.00 MeV	1.433E+01	7.799E-03	186.68 um	7.43 um	3.79 um
50.00 MeV	1.323E+01	7.101E-03	222.96 um	9.09 um	4.46 um

Multiply Stopping by	for Stopping Units
1.0000E+00	eV / Angstrom
1.0000E+01	keV / micron
1.0000E+01	MeV / mm
2.8919E-02	keV / (ug/cm2)
2.8919E-02	MeV / (mg/cm2)
2.8919E+01	keV / (mg/cm2)
1.4026E+00	eV / (1E15 atoms/cm2)
5.7678E-02	L.S.S. reduced units

==========

==========

Calculation using SRIM-2003
SRIM version ---> SRIM-2003.20
Calc. date ---> December 24, 2006

==========

Disk File Name = SRIM Outputs\Lithium in $CuAl_xCr_xFe_{2-2x}O_4$ (x = 0.8)

Ion = Lithium [3] , Mass = 7.016 amu

Target Density = 3.6703E+00 g/cm3 = 7.2613E+22 atoms/cm3

======= Target Composition ========

Atom Name	Atom Numb	Atomic Percent	Mass Percent
Cu	29	014.29	029.83
Al	13	011.43	010.13
Cr	24	011.43	019.53
Fe	26	005.71	010.48
O	8	057.14	030.03

==========

Bragg Correction = 0.00%
Stopping Units = eV / Angstrom
See bottom of Table for other Stopping units

Ion Energy	dE/dx Elec.	dE/dx Nuclear	Projected Range	Longitudinal Straggling	Lateral Straggling
50.00 keV	1.354E+01	1.804E+00	2701 A	1168 A	1046 A
55.00 keV	1.430E+01	1.705E+00	2945 A	1227 A	1112 A
60.00 keV	1.503E+01	1.618E+00	3183 A	1281 A	1174 A
65.00 keV	1.574E+01	1.540E+00	3415 A	1332 A	1232 A
70.00 keV	1.642E+01	1.471E+00	3643 A	1378 A	1287 A
80.00 keV	1.773E+01	1.351E+00	4084 A	1462 A	1388 A
90.00 keV	1.897E+01	1.252E+00	4506 A	1535 A	1479 A
100.00 keV	2.015E+01	1.169E+00	4913 A	1599 A	1562 A
110.00 keV	2.129E+01	1.097E+00	5305 A	1656 A	1637 A
120.00 keV	2.238E+01	1.034E+00	5684 A	1708 A	1707 A
130.00 keV	2.342E+01	9.793E-01	6050 A	1754 A	1772 A
140.00 keV	2.443E+01	9.307E-01	6406 A	1796 A	1831 A
150.00 keV	2.541E+01	8.872E-01	6751 A	1835 A	1887 A
160.00 keV	2.635E+01	8.480E-01	7087 A	1870 A	1940 A
170.00 keV	2.726E+01	8.126E-01	7413 A	1902 A	1989 A
180.00 keV	2.815E+01	7.804E-01	7732 A	1932 A	2035 A
200.00 keV	2.984E+01	7.238E-01	8348 A	1987 A	2120 A
225.00 keV	3.182E+01	6.648E-01	9080 A	2046 A	2214 A
250.00 keV	3.366E+01	6.156E-01	9778 A	2097 A	2298 A
275.00 keV	3.538E+01	5.739E-01	1.04 um	2142 A	2374 A
300.00 keV	3.698E+01	5.380E-01	1.11 um	2181 A	2442 A
325.00 keV	3.849E+01	5.068E-01	1.17 um	2216 A	2504 A
350.00 keV	3.991E+01	4.793E-01	1.23 um	2247 A	2562 A

375.00 keV	4.125E+01	4.550E-01	1.29 um	2276 A	2615 A
400.00 keV	4.251E+01	4.332E-01	1.35 um	2302 A	2664 A
450.00 keV	4.486E+01	3.960E-01	1.45 um	2351 A	2754 A
500.00 keV	4.701E+01	3.651E-01	1.56 um	2393 A	2834 A
550.00 keV	4.899E+01	3.391E-01	1.66 um	2429 A	2905 A
600.00 keV	5.082E+01	3.169E-01	1.76 um	2462 A	2970 A
650.00 keV	5.251E+01	2.976E-01	1.85 um	2491 A	3029 A
700.00 keV	5.409E+01	2.808E-01	1.94 um	2518 A	3084 A
800.00 keV	5.692E+01	2.526E-01	2.12 um	2570 A	3182 A
900.00 keV	5.935E+01	2.300E-01	2.29 um	2615 A	3268 A
1.00 MeV	6.144E+01	2.114E-01	2.45 um	2655 A	3345 A
1.10 MeV	6.322E+01	1.958E-01	2.61 um	2691 A	3415 A
1.20 MeV	6.473E+01	1.825E-01	2.76 um	2723 A	3479 A
1.30 MeV	6.601E+01	1.710E-01	2.91 um	2753 A	3539 A
1.40 MeV	6.707E+01	1.610E-01	3.06 um	2781 A	3594 A
1.50 MeV	6.794E+01	1.522E-01	3.21 um	2807 A	3647 A
1.60 MeV	6.865E+01	1.444E-01	3.35 um	2831 A	3696 A
1.70 MeV	6.921E+01	1.374E-01	3.49 um	2855 A	3744 A
1.80 MeV	6.964E+01	1.311E-01	3.64 um	2877 A	3789 A
2.00 MeV	7.016E+01	1.201E-01	3.92 um	2934 A	3875 A
2.25 MeV	7.032E+01	1.090E-01	4.27 um	3008 A	3976 A
2.50 MeV	7.006E+01	9.984E-02	4.63 um	3079 A	4070 A
2.75 MeV	6.949E+01	9.220E-02	4.98 um	3148 A	4161 A
3.00 MeV	6.871E+01	8.573E-02	5.34 um	3215 A	4248 A
3.25 MeV	6.776E+01	8.016E-02	5.71 um	3282 A	4334 A
3.50 MeV	6.670E+01	7.531E-02	6.08 um	3348 A	4418 A
3.75 MeV	6.556E+01	7.106E-02	6.45 um	3415 A	4501 A
4.00 MeV	6.438E+01	6.729E-02	6.84 um	3482 A	4583 A
4.50 MeV	6.195E+01	6.090E-02	7.63 um	3702 A	4749 A
5.00 MeV	5.954E+01	5.569E-02	8.45 um	3925 A	4916 A
5.50 MeV	5.721E+01	5.134E-02	9.30 um	4151 A	5086 A
6.00 MeV	5.500E+01	4.767E-02	10.19 um	4381 A	5260 A
6.50 MeV	5.292E+01	4.451E-02	11.11 um	4617 A	5440 A
7.00 MeV	5.098E+01	4.177E-02	12.07 um	4858 A	5625 A
8.00 MeV	4.748E+01	3.724E-02	14.10 um	5726 A	6014 A
9.00 MeV	4.445E+01	3.365E-02	16.27 um	6581 A	6429 A
10.00 MeV	4.181E+01	3.072E-02	18.59 um	7435 A	6873 A
11.00 MeV	3.950E+01	2.829E-02	21.05 um	8291 A	7345 A
12.00 MeV	3.747E+01	2.623E-02	23.64 um	9155 A	7846 A
13.00 MeV	3.566E+01	2.447E-02	26.37 um	1.00 um	8375 A
14.00 MeV	3.405E+01	2.294E-02	29.24 um	1.09 um	8932 A
15.00 MeV	3.271E+01	2.160E-02	32.23 um	1.18 um	9515 A
16.00 MeV	3.138E+01	2.042E-02	35.34 um	1.27 um	1.01 um
17.00 MeV	3.007E+01	1.936E-02	38.59 um	1.36 um	1.08 um
18.00 MeV	2.891E+01	1.842E-02	41.98 um	1.45 um	1.14 um
20.00 MeV	2.686E+01	1.680E-02	49.15 um	1.79 um	1.28 um
22.50 MeV	2.472E+01	1.515E-02	58.84 um	2.28 um	1.47 um
25.00 MeV	2.294E+01	1.381E-02	69.32 um	2.74 um	1.68 um
27.50 MeV	2.142E+01	1.269E-02	80.59 um	3.20 um	1.90 um
30.00 MeV	2.011E+01	1.176E-02	92.62 um	3.65 um	2.14 um

32.50 MeV	1.897E+01	1.095E-02	105.40 um	4.10 um	2.39 um
35.00 MeV	1.797E+01	1.026E-02	118.93 um	4.55 um	2.65 um
37.50 MeV	1.708E+01	9.650E-03	133.18 um	5.01 um	2.93 um
40.00 MeV	1.628E+01	9.113E-03	148.15 um	5.47 um	3.22 um
45.00 MeV	1.492E+01	8.209E-03	180.20 um	7.16 um	3.84 um
50.00 MeV	1.378E+01	7.475E-03	215.04 um	8.76 um	4.51 um

Multiply Stopping by	for Stopping Units
1.0000E+00	eV / Angstrom
1.0000E+01	keV / micron
1.0000E+01	MeV / mm
2.7247E-02	keV / (ug/cm2)
2.7247E-02	MeV / (mg/cm2)
2.7247E+01	keV / (mg/cm2)
1.3772E+00	eV / (1E15 atoms/cm2)
5.6796E-02	L.S.S. reduced units

==========

References

3.1 J. P. Singh, R. Singh, S. Ghosh, A. Tripathi, D. Kabiraj, S. Gupta, T. Som, Ravi Kumar, S. K. Arora, K. Asokan, D. K. Avasthi, D. Kanjilal, N. C. Mishra and G. K. Mehta, Nucl. Inst. Meth. Phys. Res. B **156** (1999) 206

3.2 J. Schultz, C. Jagadish, M. C. Ridgway, R. G. Eliman and J. C. William, Phys. Rev. B **44** (1991) 9118

3.3 T. A. Railkar, S. V. Bhoraskar, S. D. Dhole and V. N. Bhoraskar, J. Appl. Phys. **74** (1993) 4343

3.4 Y. Zhu, Z. X. Cai, R. C. Budhani, M. Suenaga and D. O. Welch, Phys. Rev. B **48** (1993) 6436

3.5 S. J. Zinkle, Nucl. Instr. Meth. Phys. Res. B **91** (1994) 234

3.6 Quanli Hu, Satoral Tanaka, Toshiaki, Yoneoka and Victor Grishmanov, Nucl. Instr. Meth. Phys. Res. B **141** (1998) 404

3.7 Jaimon Yohannan, K. Nandakumar and Ravi Kumar, Nucl. Instr. Meth. Phys. Res. B **156** (1999) 227

3.8 Sharada G. Prabhu, P. Mohan Rao, D. K. Avasthi and Shiuli Gupta, Nucl. Inst. Meth. Phys. Res. B **174** (2001) 159

3.9 V N. Bhoraskar, Bull. Mater. Sci. **20(4)** (1997) 385

3.10 M. Toulemonde, S. Bouffard and F. Studer, Nucl. Inst. Meth. Phys. Res. B **91** (1994) 108

3.11 E. C. M. Silk and R. s. Barnes, Philo. Mag. **4** (1959) 970

3.12 R. L. Fleischer, P. B. Price and R. M. Walker, J. Appl. Phys. **36** (1865) 3645

3.13 R. E. Johnson and W. L. Brown, Nucl. Instr. Meth. Phys. Res. B **198** (1982) 103

3.14 F. Desauer, Z. Physik **38** (1923) 12

3.15 F. Seitz and J. S. Koehler, sol. St. Phys. **2** (1956) 305

3.16 G. Szene, Phys. Rev. B **51** (1995) 8026

3.17 E. Dartyge and P. Sigmund, Phys. Rev. B **32** (1985) 5429

3.18 T. A. Tombrello, Nucl. Instr. Meth. Phys. Res. B **2 (1-3)** (1984) 555

3.19 T. A. Tombrello, Int. J. Mass Spect. Ion Pro. **126** (1993) 11

3.20 G. Schiwietz, E. Luderer, G. Xiao and P. L Grande, Nucl. Instr. Meth. Phys. Res. B **175-177** (2001) 1

3.21 M. Toulemonde, Ch. Dufour, Z. Wang and E. Paumier, Nucl. Instr and Meth B **112** (1996) 26

3.22 G. Szenes, Mater. Sci. Forum **97-99** (1992) 647

3.23 F. Studer, C. Houpert, H. Pascard, R. Spohr, J. Vetter, Jin-yun Fan and M. Toulemonde, Radiat. Eff. Def. Sol. **116** (1991) 59

3.24 F. Studer and M. Toulemonde, Nucl. Instrum. Meth. Phys. Res. B **65** (1992) 560

3.25 C. Houpert, F. Studer, D. Groult and M. Toulemonde, Nucl. Instr. and Meth. B **39** (1989) 720

3.26 M. Toulemonde and F. Studer, Philos. Mag. **58** (1988) 799

3.27 D. Groult, M. Hervieu, N. Nguyen and B. Raveau, J. Sol. State. Chem. **76** (1988) 248

3.28 A. Timm and B. Strocka, Nucl. Instr. and Meth. B **12** (1985) 479

3.29 A. Meftah, F. Brisard, J. M. Costantini, M. Hage-Ali, J.P.Stoquert, F. Studer and M. Toulemonde, Phys. Rev. B **48** (1993) 920

3.30 F. Studer, D. Groult, N. Nguyen and M. Toulemonde ,Nucl. Instr. Meth. B **19/20** (1987) 856

3.31 G. Fuchs, F. Studer, E. Balanzat, D. Groult, J. C. Jousset and B. Raveau, Nucl. Instrum. Methods B **12** (1985) 471

3.32 M. Toulemonde, G. Fuchs, N. Nguyen, F. Studer and D. Groult, Phys. Rev. B **35** (1987) 6560

3.33 G. Fuchs, D. Groult, M. Hervieu, N. Nguyen, F. Studer, M. Toulemonde and B. raveau, Proc. 3rd Eur. Conf. on soild state chemistry, Rogensburg (1986)

3.34 G. Fuchs, F. Studer, E. Balanzat, D. Groult, M. Toulemonde and J. C. Jousset, Europhys. Lett. **3** (1987) 321

3.35 F. Studer, H. Pascard, D. Groult, C. Houpert, N. Nguyen and M. Toulemonde, Nucl. Instr. and Meth. B **32** (1988) 389

3.36 A. Fnidiki, F. Studer, J.Teillet, J. Juraszek, H. Pascard and S. Meillon, Eur. Phys. J. B **24** (2001) 291

3.37 J. M. Costantini, F. Ravel, F. Brisard, M. Caput and C. Cluzeau, Nucl. Instru. Meth. Phys. Res. B **80/81** (1993) 1249

3.38 J. M. Costantini, F. Studer and J. C. Peuzin, J. Appl. Phys. **90(1)** (2001) 126-135

3.39 M. A. Mousa, J. Radional. Nucl. Chem. Lett. **118 (1)** (1987) 33

3.40 N. Z. Darwish, Phase Transitions **53** (1995) 69

3.41 M. A. Ahmed and S. T. Bishay, J. Phys. D: Appl. Phys. **34** (2001)1339

3.42 M. A. Ahemed, E. Ateia, G. Abdelatif and F. M. Salem, Mater. Chem. Phys. **81** (2003) 63

3.43 M. A. Ahmed, E. Ateia and F. M. Salen, J. Mater. Sci. **42** (2007) 3651

3.44 E. Ateia, Egypt. J. Solids. **29(2)** (2006) 317

3.45 M. A. Ahmed, A. A. I. Khalil and S. Solyman, J. Mater. Sci. **42** (2007) 4098

3.46 Anjana Dogra, Ravi Kumar, S. A. Khan, V. V. Siva Kumar, N. Kumar and M. Singh, Nucl. Instru. Meth. Phys. Res. B **225** (2004) 283

3.47 Ravi Kumar, S. K. Sharma, Anjana Dogara, V. V. Siva Kumar, S. N. Dolia, A. Gupta, M. Knobel and M. Singh, Hyper. Inter. **160** (2005) 143

3.48 B. P. Rao, K. H. Rao, P.S.V.Subbh Rao, A. Mahesh Kumar, N. S. Gajbhiye and O. F. Caltun, Nucl. Instru. Meth. Phys. Res. B **244** (2006) 27

3.49 D. Knjilal, S. Chopra, M. M. Narayanan, I. S. Iyer, V. Jha, R. Joshi and S. K. Datta, Nucl. Instr. and Meth. A **238** (1993) 97

3.50 J. F. Ziegler, J. P. Biersack and U. Littmark, "*The Stopping and Range of Ions in Matter*", Pergamon Press, vol. 2-6, New York, 1985 (new edition in 2003)

3.51 J. P. Biersack and J. F. Ziegler, "The Calculation of Ion Ranges in Solids with Analytic Solutions", 157-176, in "Ion Implantation Techniques", H. Ryssel and H. Glawischnig, Springer Verlag, Berlin (1982)

3.52 J. P. Biersack and L. Haggmark, Nucl. Instr. and Meth. **174** (1980) 257

CHAPTER: 4

Structural, Magnetic and Mössbauer Characterizations: Experimental Techniques

---

4.1 Introduction

This chapter presents relevant background and the theoretical concepts for the experimental and characterization techniques used in the present work. The chapter comprises various sections describing in detail the experimental techniques employed to evaluate micro- structural and magnetic properties.

4.2 Structural Characterizations

4.2.1 X-ray Diffraction

The products of solid state reaction or semi-wet route are usually in the form of a powder or a sintered polycrystalline piece. The X- ray diffraction which is an important and useful technique in Solid state Physics, has been in use since the early part of this century for the finger print characterization of crystalline materials and for the determination of their crystal structures [4.1, 4.2]. The X-rays are electromagnetic radiations of wavelength ~ 1Å. By analogy with the diffraction of light by an optical grating, crystals with their regularly repeating structure, should be capable of diffracting radiation that has a wave length similar to the inter atomic separation ~ 1 Å. Three types of radiations are used for crystal diffraction studies; X- rays, electrons and neutrons. Of these, X-rays are by far the most useful but electron and neutron diffraction both have important specific applications. The X- ray wavelength commonly employed is the characteristics Kα radiation, λ = 1.5418 Å, emitted by Copper. There are two approaches used to treat X- ray diffraction by crystals

(i) The Laue equations

(ii) Bragg's law

The Laue equations provide a rigorous and mathematically correct way to describe diffraction by crystals. The drawback is that they are cumbersome. The alternative theory of diffraction based on Bragg's law is much simpler and is used almost universally in Solid State Physics [4.3]. The Bragg's law is an easiest example of scattering, yielding structural information through scattering of X- rays from a set of partially reflecting equally spaced parallel planes, it's intensity being modulated by constructive or destructive interference. For an infinite set of such planes the only surviving reflection is one for which there is constructive interference between waves reflected by each set of neighboring planes. Thus, the difference in path length

between waves reflected from adjacent planes separated by a distance d must be an integral multiple of the wavelength, λ. This leads to the Bragg's law,

$$n\lambda = 2\,d\sin\theta$$

where,

n = order of diffraction

λ = wavelength of the target used

d = inter-planner distance

θ = incident and reflection angle

The plane spacing equation for the cubic system is,

$$\frac{1}{d^2} = \frac{(h^2 + k^2 + l^2)}{a^2}$$

where, (h, k, l) are Miller indices and a is lattice constant. By combining the Bragg's law with the plane spacing equation for the cubic system,

$$\frac{\sin^2\theta}{s} = \frac{\lambda^2}{4a^2}$$

where, $s = (h^2 + k^2 + l^2)$

Since the sum 's' is always integral and $\lambda^2/4a^2$ is a constant for any one pattern, the problem of indexing the pattern of a cubic substance is one of finding a set of integers s , which will yield a constant quotient when divided one by one into the observed $\sin^2\theta$ values. Once the proper integers are found, the indices (hkl) of each Bragg reflection can be written down by inspection. A computer program has been developed in our laboratory for indexing powder X-ray diffraction patterns.

The basic principles involved in the structure determination have already been discussed briefly. We saw that the crystal structure of a substance determines the diffraction pattern of that substance or more specifically, that the shape and size of the unit cell determine the angular positions of the diffraction lines and the arrangement of the atoms within the unit cell determines the relative intensities of the lines. It is interesting to study the relation between atom position and intensity [4.4]. The problem is complex because of the many variables involved. We have to consider how X-rays are scattered by a single electron, then by an atom, and finally by all the atoms in the unit cell. In this process we shall define the atomic scattering factor and structure factor.

When an electron is subjected to the X-rays, it will undergo the oscillatory motion, which causes emission of an electromagnetic radiation of the same frequency as that of the incident X-rays. This is an example of coherent scattering and scattering intensity is given by the popular Thomson equation,

$$I_{SC} = I_0 \frac{K}{r^2}\left(\frac{1+\cos^2 2\theta}{2}\right)$$

Where, K is a constant 7.94×10^{-30} m^2, r is the distance from the scatterer. Let us calculate the scattered intensity in the forward direction where the polarization factor is always unity. Suppose that r is 1 cm then $I_{sc}/I_o \approx 10^{-26}$ which is feeble even in forward directions and it falls off in other directions as the angle between the incident and scattered radiation increases. It shows that the scattered intensities are much lesser than the intensity of the incident radiation. The Thomson equation can give the exact intensity of scattered ray provided one knows the intensity of the incident ray. Since it is hard to calculate the exact values of the scattered and incident radiation therefore, for all practical purposes the relative values of diffracted radiation are considered. So, except the last term, called polarization factor, others can be omitted. The polarization factor enters the equation simply because the incident radiation is unpolarized. The incoherent scattering which also takes place to some extent is called the Compton scattering and doesn't contribute to the interference.

When X-rays interact with an atom, all such contributions from individual electrons add up to give rise to final intensity. In forward direction, it is just the simple addition of all the scattered intensities from individual electrons. But in other directions it is not so. This is because the scattered rays from different electrons are perfectly in phase in forward direction. But as the angle increases the phase difference gives rise to only partial interference. The atomic scattering factor or form factor (f_n) is the measure of this efficiency, therefore,

$$f = \frac{\text{Amplitude of the wave scattered by an atom}}{\text{Amplitude of the wave scattered by an electron}}$$

The atomic scattering factor for any atom in forward direction is Z (atomic number). It decreases with θ. It also depends upon the wavelength of the incident beam. The shorter the wavelength smaller will be the $\mathbf{f_n}$ in actual calculation it involves sinθ rather than θ. It depends on the quantity (sin θ)/(λ). Its dependence on this quantity for Cu is shown in Fig. 4.1

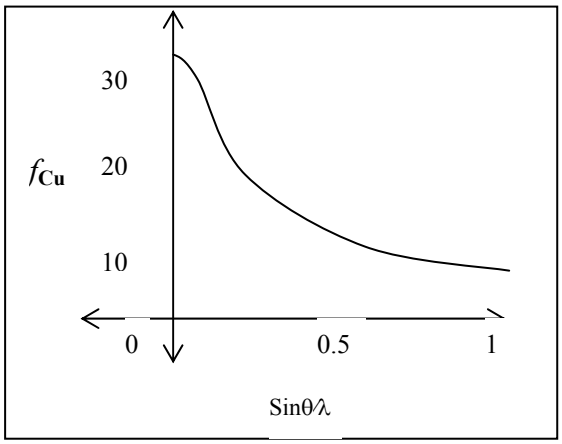

Fig. 4.1 Variation of Atomic Scattering factor as a function of (sin θ)/(λ) for copper.

This scattered rays from an atom combines with the scattered rays from other atoms in unit cell. We have just seen that scattering from an individual atom is given by form factor, which is direction dependent. Let us see how the form factors of the scattered rays from different atoms in a unit cell combine with each other. It is given by the structure factor**,**

$$F_{hkl} = \sum_{i}^{N} f_n \cdot e^{2\pi i(hx+ky+lz)}$$

where, x, y, z are fractional atomic coordinates in a unit cell, f_n is atomic scattering factor of the pertaining atom. The summation is over all the N atoms in unit cell. In general, F is a complex number and expresses both the phase as well as amplitude of the resultant scattered wave.

Intensities of the diffracted lines in powder spectra:

In addition to the atomic scattering factor and structure factor there are several other parameters affecting the relative intensities of Bragg reflection lines are:

Multiplicity factor (P): It is the number of different planes in a form having the same spacing. It depends on the crystal system.

Lorentz factor (L): It is defined as follows $L = 1/(4\sin^2\theta\cos\theta)$. It is a geometrical factor. It combines with the polarization factor and finally we have a lorentz-polarization factor as $\frac{1+\cos^2 2\theta}{\sin^2\theta.\cos\theta}$

Temperature factor: It enters because of the thermal vibration of the atoms at given temperature. For powder sample it is given by e^{-M}, where M is a factor depending on the mean square displacement of the atom in the direction normal to the reflecting planes. It is angle-independent for powder samples. So for the purpose of relative intensity calculation it can be omitted.

The final equation for intensity is given as, $I = |F|^2.P. \left(\frac{1+\cos^2 2\theta}{\sin^2\theta.\cos\theta}\right) e^{-M}$

The subject is discussed in detail in [4.5].

Table 4.1 Structure factors for an ideal spinel

(hkl)	F
(111)	$4 (-\sqrt{2}\, b_A + 2\, b_B)$
(220)	$-8b_A$
(311)	$4 (-\sqrt{2}\, b_A - 2\, b_B)$
(222)	$16 (b_B - 2b_0)$
(400)	$8 (-b_A + 2b_B + 4b_0)$
(331)	$4 (\sqrt{2}b_A - 2b_B)$
(422)	$8b_A$
(333), (511)	$4 (\sqrt{2}b_A + 2b_B)$
(440)	$8 (b_A + 2b_B + 4b_0)$
(531)	$4 (\sqrt{2}b_A - 2b_B)$

X-ray diffractometer:

There are several methods of getting the X –ray diffraction using a crystal specimen, such as Laue method, rotating – crystal diffractometer method, powder diffractometer method etc. The powder diffractometer in particular is relevant to the present study. In this method the crystal to be investigated is in the form of fine powder. Each particle of this powder is a tiny crystal oriented totally at random with respect to the incident X – ray beam. The method is of immense importance since it can take polycrystalline specimen and thus it is not necessary to have a single crystal, which is not always possible to grow. This method has widened the horizons of the utilization of X – ray diffraction tool in great number of cases where single crystals were not available.

The geometrical diagram of the diffractometer based on this method is in the diagram and three main components are discussed in brief.

X-ray tube: The X-ray tube is a high vacuum, sealed off unit, usually with a copper, iron or molybdenum target. During the process of X-ray generation, the target is cooled by the water circulation. The generated X-rays beam is passed through thin beryllium window.

Detector: In addition to photographic film, the Geiger counter, the proportional counter, the scintillation counter and some times semiconductors are used in X-ray detection. The Scintillation counter is widely used. They have shortest dead time of around 0.25 μsec and have nearly uniform and high quantum efficiency throughout the important wavelength region.

Goniometer: It comprises of two circular tracks. On outer track the X-ray tube is usually made fixed. Detector is mounted on the arm moving on outer track. The sample holder is fixed on the inner track. The inner track rotates at half the angular distance than the outer arm. The movement of both the inner track and outer arm is controlled by mechanical motors.

Since the mass of powder is equivalent to a single crystal rotated not only about the one axis but in fact, about all possible axes, it has simplified to get signature of all the planes in one shot. The specimen for this method is a flat thin layer of powdered sample on a glass or a silicon single crystal holder. The randomness in the orientations of small crystals (or crystallites in the case of polycrystalline material) with respect to each other is such that there is a presence of all possible orientations of crystals.

In other words, there is a presence of a set of all permissible (hkl) planes with different d value and oriented parallel to flat surface of the specimen. Assume that the size of each crystal is such that it possesses enough number of planes necessary for perfect constructive and destructive interference. Now for any incident X-rays beam at angle θ, the detector is set at angle 2θ with respect to the incident beam. At a particular value of 2θ, the d spacing of any of the (hkl) planes fulfilling the Bragg's

condition will give constructive interference and all other (hkl) planes will give perfect destructive interference.

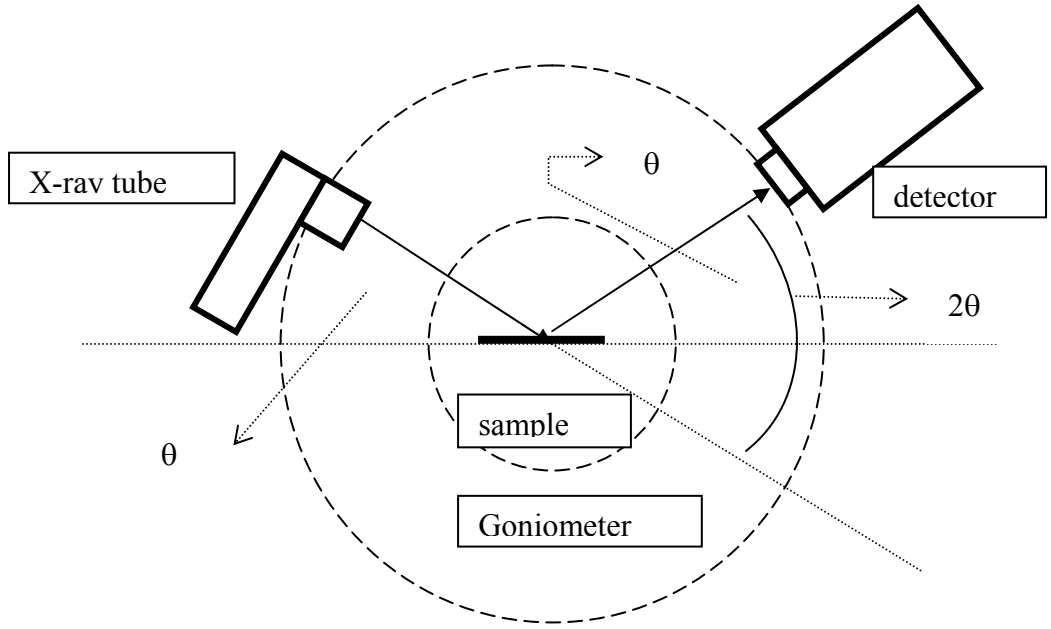

Fig. 4.2 X-ray diffractometer

If the specimen and detector are now moved in such a way that the specimen rotates half the angular distance than the detector in the same angular direction, the incident angle θ can be changed and each time the presence of Bragg peak can be detected. Thus, whole spectra of diffracted intensities by various planes at different angles will be traced. The experimental particulars regarding the X-ray diffractometer along with data acquisition electronics is discussed at length in [4.3].

The X-ray diffractograms contained the information regarding the peak positions and the intensity counts of respective peaks along with the plot and other instrumental information. The first hand task is to confirm the monophase structure. The spinel ferrites possess the cubic *fcc* structure and so all the peaks are first indexed according to that structure. The indexing provides instant check of the formation of monophase *fcc* structure. A computer program was written in BASIC language for this purpose that does the indexing of the X-ray peaks according to *fcc* structure and determines the cell edge parameter by using the Nelson Relay method [4.3].

Once single phase is confirmed after indexing, one determines the distribution of cations among lattice sites in the spinel ferrite structure from the given X-ray intensity data. The programs developed for the intensity calculation can extract the required information from the X-ray data to reasonably good extent particularly when

only the peaks positions and relative intensities are available. The total intensity of the peak is an area under the curve rather than peak height. This fact is more crucial at higher angle peaks as the peak width increases with increase in 2θ. The relative heights of the peaks then become misleading.

4.2.2 Energy Dispersive Analysis of X-rays (EDAX)

If the element is bombarded with the X-ray of high enough energy, it will emit its 'characteristic lines'. In most cases they are the K_α and K_β lines. They are called the characteristic lines to emphasize that the wavelength of them are fixed and characteristic to the emitting element. The phenomena are called the fluorescence. It provides a basis for a method of chemical analysis. If the different elements in the sample are bombarded with X-ray they will emit their characteristic lines of different wavelengths thus providing identification of the elements. The X-ray spectrometer is used for this purpose in two different modes.

1. **Wavelength dispersive:** In this mode the wavelength of the emitted radiation from sample are analyzed by diffracting the radiations through a single crystal of known d value and obtaining the wavelength distribution.
2. **Energy dispersive:** In this mode diffraction of the radiation is not involved in the process of analyzing on the basis of their energies rather than their wavelengths.

Fluorescence Spectroscopy:

Suppose that monochromatic primary radiation of constant intensity and wavelength λ is incident on an element, which has K absorption edge λ_k. As we decrease λ, the fluorescence will not occur until λ is just shorter than λ_k where the fluorescence intensity will be maximum. For further decrease in λ, the fluorescence intensity will decrease in much the same manner as absorption coefficient.

There are many other phenomena occurring along with the fluorescence. They are ejection of an Auger electron, coherent and incoherent diffracted radiations. The auger effect plays crucial role when the emitter is any light element. The probability of fluorescence emission is much less in such case. The other radiations contribute to the background in energy dispersive spectrum.

The wavelength range generally used in fluorescence extends from 0.2Å to 20Å. The lower limit is generally imposed by the maximum voltage that can be applied to the tube. The radiation of 0.2 Å wavelength would cause the K

fluorescence in Hf (Z = 72). For heavier elements than Hf, we can use the L rather than K fluorescence. The upper limit on wavelength depends upon the equipment used. It is imposed due to the large absorption of long wavelength fluorescence caused by just anything if encounters, such as air, counter wind etc. The more important is the absorption by the elements it self in this limit, particularly for the lighter elements. In case of the lighter elements, the fluorescence radiation comes only from the surface because the fluorescence radiation coming out from the interior is absorbed by the element atoms. Thus, the total fluorescence intensity is only meager. This puts limit on the detection of the lighter elements. Generally, commercial spectrometer detect F (Z = 13), which is the lower limit of detection of elements.

Design of the Spectrometer:

The essential parts of the Energy Dispersive spectrometer are shown in the diagram below (Fig 4.3). It consists of i). The X – ray tube, ii) Specimen, iii) Si (Li) counter & a FET preamplifier, both cooled by liquid Nitrogen and iv) Multichanel Analyzer (MCA).

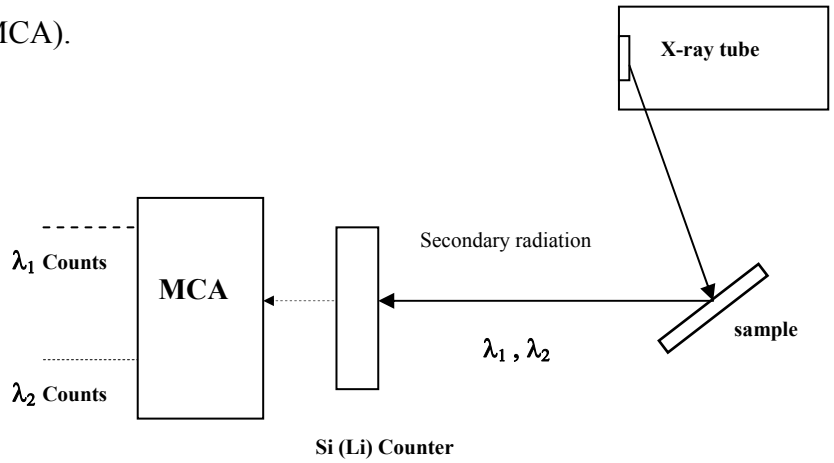

Fig. 4.3 Energy Dispersive spectrometer

The sample specimen is bombarded with X – rays of enough high energy generated from the X – ray tube. The fluorescence radiation, emitted by the sample comprising of various wavelengths according to the various elements present in the sample is analyzed and various wavelengths are separated on the basis of their energies by means of a Si (Li) counter and a multichanel analyzer (MCA).

The counter produces the pulses proportional in height to the energies in the incident beam and MCA sorts out the various pulse heights. The excellent energy resolution of the Si (Li) counter with FET preamplifier [4.6] and the ability of the MCA to perform rapid pulse height analysis make the spectrometer to measure the

intensities of all the spectral lines from the sample in about a minute, unless there are elements in very low concentration are to be determined. The extended treatment of apparatus for energy dispersion is given elsewhere [4.6].

Chemical analysis:

The energy dispersive spectrometer is used to make a rapid chemical analysis qualitatively. It can also be used for a semi quantitative, if not quantitative, analysis. The energy dispersive spectrum one gets from this spectrometer is the intensity (in counts) v/s energy spectrum. The energies in keV cover all the K and L lines emitted by the samples. The analysis is done with the help of the computer software. There is a table or chart of the energies of all K and L lines arranged in consequent manner of all the elements. The information from it is retrieved by the computer for assigning any energy peak in the diagram with the respective element. Thus, from the peak energy the elements present in the sample can be detected. The semi quantitative analysis can be done with calculating the total number of counts recorded for a particular energy. This examination is difficult to do manually since all the energy peaks may not be well separated and may be diffused with each other. Since the analysis needs the total area under the curve and not the height of the peak, it is difficult to separate the contributions of each peak. But computer software simulates the peaks with different areas under the curve and it checks their resultant effect when merged. It can separate out the contribution from each peak in this manner. The relative concentrations of the elements can be known, if not the absolute, from this analysis. The detailed treatment on quantitative analysis in energy dispersion method is given elsewhere [4.7, 4.8]. All the samples of the present study were characterized with EDAX at SICART, V. V. Nagar (Gujarat state, India).

4.2.3 Infrared Spectroscopy

Infrared spectroscopy has been widely used for structural and compositional analysis of organic, inorganic and polymeric materials and played and important role in quality control of raw materials. IR spectroscopy deals with changes in vibrational motion (stretching and bending) of atoms in a molecule which leads to net change in dipole moment and results in absorption of IR radiation. These motions are greatly influenced by masses of atoms, their geometrical arrangement and the strength of their chemical bonds. Infrared radiation spans a section of the electromagnetic spectrum having wavenumbers from roughly 12,500 to 10 cm^{-1} or wavelengths from

0.78 to 1000μm. It is bound by the red end of the visible region at higher frequencies and the microwave region at low frequencies. In accordance with both applications and instrumentation involved, the IR spectral region (12,500 – 10 cm^{-1}) is conveniently divided into near-IR (12,500 to 4000 cm^{-1}), mid-IR (4000 to 400 cm^{-1}) and far-IR (400 to 10 cm^{-1}). The main significance of this division is that most fundamental molecular vibrations occur in mid-IR making this region richest in chemical information while overtones and combination of fundamental vibrations especially those involving hydrogen atoms appear in near-IR. On the other hand, far-IR region contains vibrations involving heavy atoms, lattice modes of solids and some rotational absorption of small molecules.

IR absorption positions are generally presented as either wavenumbers ($\bar{\upsilon}$) or wavelengths (λ). Wavenumbers defines the number of waves per unit length. Thus, wavenumbers are directly, proportional to frequency, as well as the energy of the IR absorption. The wavenumber unit (cm^{-1}, reciprocal centimeter) is more commonly used in the modern IR instruments that are linear in the cm^{-1} scale. In contrast, wavelengths are inversely proportional to frequencies and their associated energy. Wavenumber and wavelengths can be interconverted using the following equation:

$$\bar{\upsilon} \text{ (in cm}^{-1}) = \frac{1}{\lambda(in\mu m)} x10^4$$

IR absorption information is generally presented in the form of a spectrum with wavelength or wavenumber as the x-axis and absorption intensity or percent transmittance as the y-axis.

Transmittance, *T*, is the ratio of radiant power transmitted by sample (*I*) to the radiant power (I_0). Absorption (*A*) is the logarithm to the base 10 of the reciprocal of transmittance (*T*).

$$A = \log_{10} (1/T) = -\log_{10} T = -\log_{10} I/I_0$$

The transmittance spectra provide better contrast between intensities of strong and week bands because transmittance ranges from 0 to 100%T whereas absorption ranges from infinity to zero. The analysis should be aware that the same sample will give quite different profiles for the IR spectrum, which is linear in the wavenumber, and the IR plot, which is linear in the wavelength. It will appear as if some IR bands have been constructed or expanded [4.9].

At temperature above absolute zero, all the atoms in molecules are in continues vibrations with respect to each other. When the frequency of a specific vibration is equal to the frequency of IR radiation directed on the molecule, the molecule absorbs the radiation.

Each atom has three degree for freedom, corresponding to the motions along any of the three Cartesian coordinate axes (x, y, z). A polyatomic molecule of n atoms has 3n total degree of freedom. However, 3 degree of freedom required to describe, translation, the motion of the entire molecule through space. Additionally, 3 degree of freedom corresponds to the rotation of the entire molecule. Therefore, the remaining 3n-6 degrees of freedom are true, fundamental vibrations for nonlinear molecules. Linear molecules possess 3n-5 fundamental vibrational modes because only 2 degrees of freedom are sufficient to describe rotation. Among the 3n-6 and 3n-5 fundamental vibrations (also known as normal modes of vibration), those that produce a net change in dipole moment may result in an IR activity and those that give polarizability changes may give rise to Raman activity. Naturally, some vibrations can be both IR and Raman active.

The total number of observed absorption bands is generally different from the total number of vibrations. It is reduced because some modes are not IR active and a single frequency can cause more than one mode of motion to occur. Conversely, additional bands are generated by the appearance of overtones (integral multiples of the fundamental frequencies), combinations of fundamental frequencies, difference of fundamental frequencies, coupling interactions of two fundamental absorption frequencies, and coupling interactions between fundamental vibrations and overtones or combination bands (Fermi resonance). The intensities of overtone, combination and difference bands are less than those fundamental bands. The combination and blending of all the factors thus create a unique IR spectrum for each compound.

The major type of molecular vibrations are stretching and bending. Infrared radiation is absorbed and the associated energy is converted into these types of motions. The absorption involves discrete, quantized energy levels. However, the individual vibrational motion is usually accompanied by other rotational motions. These combinations lead to the absorption bands, not the discrete lines, commonly observed in the mid IR region [4.9].

Instrumentation

A typical spectrometer mainly comprises of components like radiation source, optical path and monochromator, radiation detector and sample. These components are briefly described below [4.10]:

Source: The source is always some form of filament which is maintained at red-or white-heat by an electric current. Two common sources are the Nernst filament, consisting of spindle of rare earth oxides (ZrO_2 + Y_2O_3) about 1 inch long and 0.1 inch in diameter, and the Globar (SiC) filament a rod of carborundum, somewhat thicker and longer than the Nernst. The Nernst requires to be pre-heated before it will conduct electricity, but once red-heat is reached the temperature is maintained by the current.

Optical path and monochromator: The beam is guided and focused by mirrors aluminized or silvered on their surfaces. Normally a focus is produced at the point where the sample is to be placed. Ordinary lenses and mirrors are not suitable as glass absorbs strongly over most of the frequencies used. Normally, highly polished IR transparent mineral salt windows such as, NaCl (transparent above 650 cm^{-1}) and KBr (transparent above 400 cm^{-1}) are used to contain a sample, or protect to the detector. For aqueous samples, AgCl and CaF_2 sample cell can be used. These are infra – red transparent above 400 and 1200 cm^{-1}, respectively. A rotatable grating is usually used to disperse the radiation, having largely superseded rotatable prisms, which have poorer resolving power. Where the latter are still in use, the prism is usually made of NaCl or KBr.

Detector: Two main types are in common use, one sensing the heating effect of the radiation, the other depending on photoconductivity. In both greater the effect (temperature or conductivity rise) at a given frequency, the greater the transmittance (and the less the absorbance) of the sample at that frequency. An example of the temperature method is to be found in Golay cell, thermocouples or bolometers. Pyroelectric detectors such as, deuterated triglycine sulphate (DTGS) which are specialized thermal detectors are in common use in FT spectrometers. Liquid nitrogen cooled Mercury cadmium telluride (MCT), Indium antimonide (InSb etc., are some example photoconductive detectors used in IR spectroscopy. These have a faster response time and sensitivity, compared even with, for example, the DTGS.

Sample: Sample is held between plates of polished mineral salt such as NaCl, KBr or AgCl. For sample preparation following procedures is normally employed for gas, liquid and solid samples.

- Gas: Glass cells either 5 or 10 cm long fitted with rock salt windows are used for gaseous samples at pressures of up to 1 atmosphere or greater. Special long-path cell, in which the radiation is repeatedly reflected up and sown the cell, may be used for gases at low pressure, perhaps than 100 Torr.
- Liquid: Pure liquids are studied in thickness of about 0.01 mm, while solutions are usually 0.1-10 mm thick, depending on the dilution. Carbon tetrachloride, carbon disulfide, chloroform etc are used as solvents.
- Solid: Two methods are generally followed: (a) Mull Method and (b) KBr pellet method. In former method a solid sample is thoroughly grounding along with a weakly absorbing, non-volatile liquid normally Nujol to form a thick paste, called a mull which can then be held between salt plates in the same way as a pure liquid or solvent. It is very important that the sample be ground to a very fine particle size to reduce light scattering and salt plate scratching. Nujol is transparent in the infrared except for narrow bands at 2900, 1450 and 1375 cm^{-1}. An alternative mulling liquid, which does not absorb in these regions, is a perfluorokeroscene, such as, Fluorolubs S.

  In KBr pellet method, the solid is finely ground with pure, dry KBr, the mixture is pressed in a hydraulic press to form a transparent pellet, and the spectrum of pellet is measured. It is important that the solid be extremely finely divided and well mixed. The pellet is usually pressed in a special die that can be evacuated in order to avoid entrapped air, which causes cloudiness in the pellet. A major advantage of this method is that KBr has no absorptions in the IR above 250 cm^{-1}, so that an unimpeded spectrum of the compounds is obtained.

Types of Instruments: In simple terms, IR spectra are obtained by detecting changes in transmittance (or absorption). Most commercial instruments separate and measure IR radiation using dispersive Infrared spectrometers or Fourier-transform spectrometers.

Modern Fourier transform IR (FTIR) spectrometers are superior to the dispersive IR spectrometers on several counts, noticeable among them are the

multiplex (or Fellgett) and throughput (Jacquinot) advantages. With these advantages measurements of transmission, reflection or even emission spectra has become significantly faster and with higher sensitivity than ever before. It has enormously increased the range of applications and the materials amenable to study.

FTIR spectrometers are based upon Michelson interferometer Fig. 4.4 shows schematics of this spectrometer. To obtain an IR absorption spectrum, one mirror of the interferometer moves to generate interference in the radiation reaching the detector. Since all wavelengths are passing through the interferometer, the interferogram is a complex pattern. The absorption spectrum as a function of wavenumber (cm^{-1}) is obtained from the Fourier transform of the interferogram, which is a function of mirror movement. This design does not have the reference cell of dispersive instrument, so reference spectrum is recorded and stored in memory to subtract from the sample spectrum [4.11].

IR Experimental details:

The IR study was carried out for the following unirradiated and irradiated systems:

- $Li_{0.5(1+x)}Ti_xAl_{0.1}Fe_{2-2x}O_4$ (x = 0.0 to 0.3 with step of 0.1)
- $Li_{0.5(1+x)}Ti_xCr_{0.1}Fe_{2-2x}O_4$ (x = 0.0 to 0.3 with step of 0.1)
- $CuAl_xCr_xFe_{2-2x}O_4$ (x = 0.0 to 0.8 with step of 0.2) (Slow-Cooled & Quenched)
- $MnAl_xCr_xFe_{2-2x}O_4$ (x = 0.0 to 0.8 with step of 0.2)

The FTIR studies of the system $Li_{0.5(1+x)}Ti_xAl_{0.1}Fe_{2-2x}O_4$ and $Li_{0.5(1+x)}Ti_xCr_{0.1}Fe_{2-2x}O_4$ were carried out at Department of chemistry, Saurashtra University, Rajkot. The IR spectra for the system $CuAl_xCr_xFe_{2-2x}O_4$ and $MnAl_xCr_xFe_{2-2x}O_4$ were recorded on the FTIR spectrometer at Inter University Accelerator Centre, New Delhi and Regional sophisticated Instrumentation Centre, Indian Institute of Technology (IIT), Chennai.

All the samples were used to carry out the infrared spectroscopic studies in the KBr medium. The infrared spectrum was recorded in the wave number range of 400-4000 cm^{-1} and the powder samples were used in study.

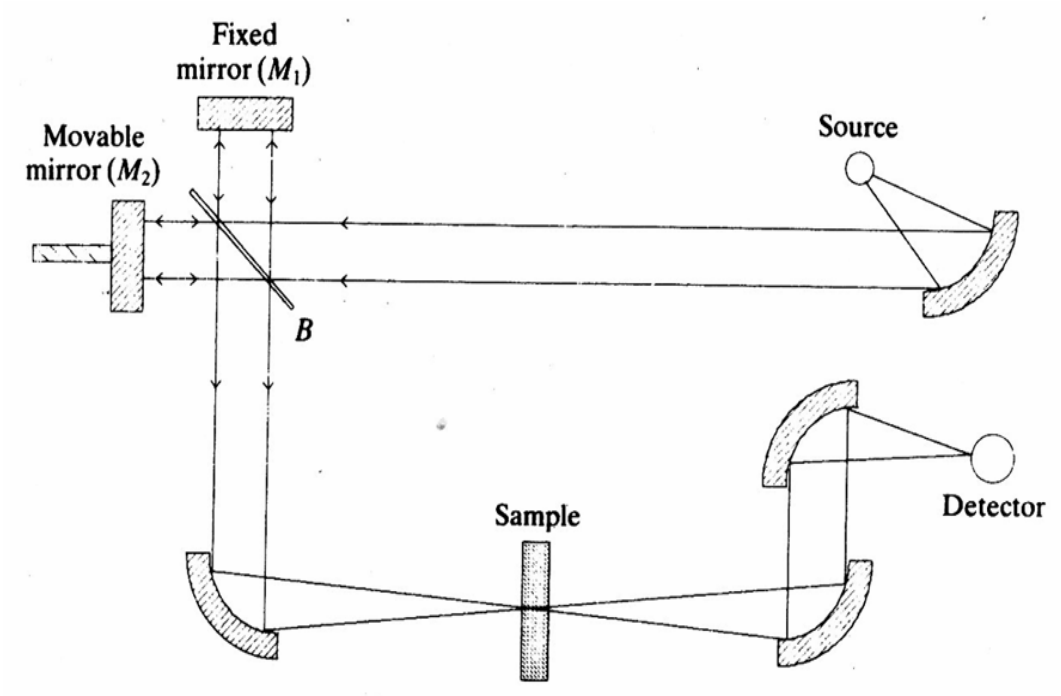

Fig. 4.4 Schematic diagram of FTIR spectrometer; B is beam splitter

Photograph of Fourier-transform IR (FTIR) spectrometer

4.3 Magnetic Characterizations [Magnetometry]

The experimental study of magnetic materials requires (a) a means of producing the field which will magnetize the material, and (b) a means of measuring the resulting effect on the material. It is important to know magnetic properties like saturation magnetization, Hysteresis loop, magnetic susceptibility a magnetic material. The magnetic behaviour of magnetic materials provides information about spin structure, anisotropy and phase transitions.

The magnetic properties of materials are determined first and foremost by the magnetic moment of electrons, atoms, and ions in the material. The magnetic response of electrons and of atoms and ions can exhibit a wide variety of behaviour in materials due to the wide range of interactions that can occur between the magnetic moments and their environment.

The macroscopic constitute relationships between the magnetic field the magnetic induction of flux density and the magnetization are presented first.

The magnetization is a quantity descriptive to the extent to which any material is magnetized. The magnetization of a material is expressed in terms of density of net magnetic dipole moments μ_{total} in the material. A vector quantity called the magnetization M is defined by,

$$M = \mu_{total}/V,$$

where, V is the volume of material

Then, the total magnetic field B in the materials is given by

$$B = B_0 + \mu_0 M,$$

where, μ_0 is the magnetic permeability of space and B0 is the externally applied magnetic field. Another way to deal with the magnetic field which arises from magnetization of materials is to introduce a quantity called magnetic field strength H. It can be defined by the relationship,

$$H = B_0/\mu_0 = B/\mu_0 - M,$$

and is has the value of unambiguously designating the driving magnetic influence from external current in a material, independent of the material's magnetic response. The relationship for B above can be written in the equivalent form,

$$B = \mu_0 (H + M),$$

H and M will have the same units, in M.K.S unit system, amperes/meter. In c.g.s. unit system it's unit is erg/orstead.cm^3. However, more often it is referred to as emu/cm^3,

where emu is called electromagnetic unit of dipole moment. Sometimes it is more convenient to refer to the extent of magnetization to the mass rather than volume, which is called specific magnetization σ.

$$\sigma = M/\rho$$

emu/gm in c.g.s and $A.m^2/kg$ in M.K.S.

When magnetic fields inside of materials are calculated using Ampere's law or the Biot-savart's law, then the μ_0 in those equations is typically replaced by just μ with the definition,

$$\mu = K_m\mu_0$$

where, K_m is called the relative permeability. If the material does not respond to the external magnetic field by producing any magnetization, the $K_m = 1$. Another commonly used magnetic quantity is the magnetic susceptibility, which specifies how much the relative permeability differs from one.

Magnetic Susceptibility, $\chi_m = K_m - 1$

Materials may be classified by their response to externally applied fields as diamagnetic, paramagnetic or ferromagnetic. These magnetic responses differ greatly in strength. Diamagnetism is property of all materials and opposes applied magnetic fields, but is very week. Paramagnetism, when present is stronger than diamagnetism and produces magnetization in the direction of the applied field, and proportional to the applied field. Ferromagnetic effects are very large and produce magnetizations sometimes orders of magnitude greater than the applied field and as such are much larger than either diamagnetic or paramagnetic effects. For paramagnetic and diamagnetic materials the relative permeability is nearly 1 and the magnetic susceptibility close to zero while for ferromagnetic materials, these quantities may be very large.

4.3.1 Saturation Magnetization

The aim of magnetometry is to measure the saturation magnetization (either intrinsic or induced by applied field) of a material. This can be achieved in a number of ways utilizing various magnetic phenomena. The various types of magnetometers fall within two categories:

[1] Measuring the force acting on a sample in an inhomogeneous magnetic field:

- Magnetic balance
- Magnetic Pendulum

[2] Measuring the magnetic field produced by a sample:

- Hysteresis loop technique
- Vibrating Sample Magnetometer (VSM)
- Superconducting Quantum Interference Devices (SQUID)

Hysteresis loop technique

The saturation magnetization measurements on the bulk samples of the unirradiated and irradiated systems $Li_{0.5(1+x)}Ti_xAl_{0.1}Fe_{2-2x}O_4$, $Li_{0.5(1+x)}Ti_xCr_{0.1}Fe_{2-2x}O_4$ and $MnAl_xCr_xFe_{2-2x}O_4$ were carried out on An alternating current electromagnet type high field (5 kOe) hysteresis loop tracer at Department of Physics, Saurashtra University, Rajkot. A block cum diagram and photograph of hysteresis loop tracer shown in Fig. 4.5 [4.12, 4.13]. The essential components of this loop tracer is a laminated silicon iron C-core used as an electromagnet that produces the alternating magnetic field when energized by the main supply. The maximum pick field obtainable with this type of iron core in a 4 mm pole gap is 5 kOe. The energizing coil of the electromagnet is wound on a suitable former and magnet is tuned to the main supply frequency (50 Hz) with fixed capacitor of 1 μF. The pick up coil is made of two rings on which thousands turns with 46 SWG super enameled copper wires are

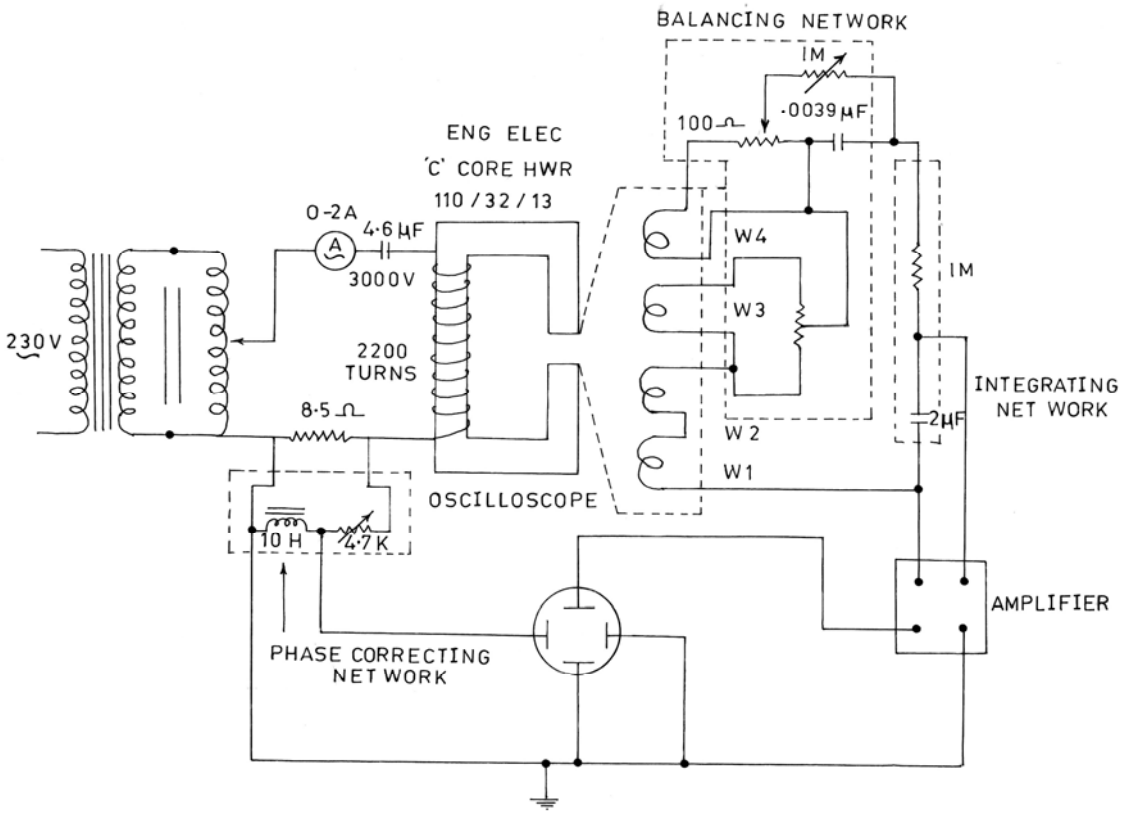

Fig. 4.5 Block cum Circuit diagram of Hysteresis loop tracer

wound. These are held one above the other in a vertical frame which is fixed vertically on flat plate that can freely move in and out of the pole gap. For any desired magnetic field a good balance of the pick up coil can be achieved by adjusting the potentiometers connected to the pick up coil circuit. The main advantage of this type of hysteresis loop tracer is that with a quick transfer of a sample, pre cooled in liquid nitrogen bath, in to the pick up coil, changes in hysteresis of the sample as it warms up from 77K to room temperature can be watched or photographed from the oscilloscope screen. Apart from two fixed temperatures to room temperature and 77K, others at which a hysteresis loops are observed can not be accurately estimated. Distortion free hysteresis loops can be obtained only for samples that can develop a pick magnetic moment of 1 emu or more. The instrument was calibrated by using Ni-powders and magnetization per formula unit in Bohr magneton (μ_B) was calculated by using per gram saturation magnetization and molecular weight of the composition.

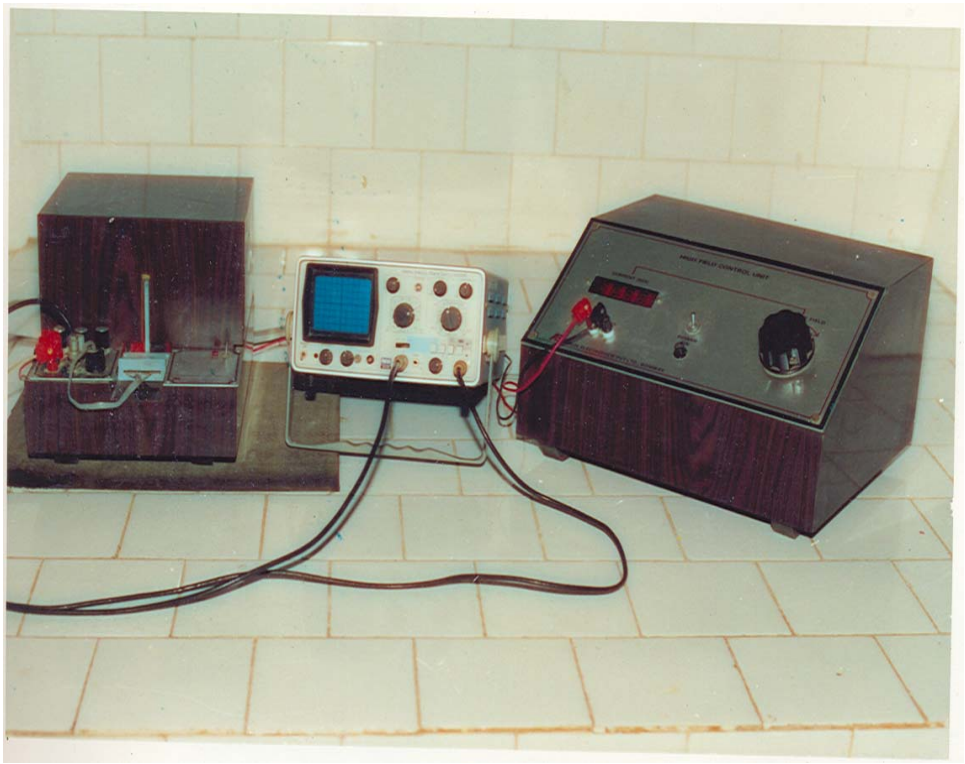

Photograph of Hysteresis loop tracer

Vibrating Sample Magnetometer (VSM)

DC magnetic measurements determine the equilibrium value of the magnetization in a sample. The sample is magnetized by constant magnetic field and

the magnetic moment of the sample is measured, producing a DC magnetization curve M (H). The moment is measured by force, torque or induction techniques, the last being the most common in modern to set instruments. Inductive measurements are performed by moving the sample relative to a set of pick up coils, either by vibration or one-shot extraction. In conventional inductive magnetometers, one measures the voltage induced by the moving magnetic moment of the sample in a set of copper pick up coils.

The Vibrating Sample Magnetometer (VSM) is the basic instrument for characterizing magnetic materials. The basic principle of operation for a vibrating sample magnetometer is that a changing magnetic flux will induce a voltage in pickup coil. The time –dependent induced voltage is given by the following equation:

$$V_{Coil} = \frac{d\Phi}{dt} = \left(\frac{d\Phi}{dz}\right)\left(\frac{dz}{dt}\right)$$

In above equation, Φ is the magnetic flux enclosed by pickup coil, z is the vertical position of sample with respect to the coil, and t is the time. For sinusoidally oscillating sample position, the voltage in base on following equation:

$$V_{Coil} = 2\pi f C m A \sin(2\pi f t)$$

In above equation, C is a coupling constant, m is the DC magnetic moment of the sample, A is the amplitude of the oscillation, and f is the frequency of the oscillation. The acquisition magnetic moment measurement involves measuring the coefficient of the sinusoidal voltage response from the detection coil.

The values of saturation magnetization of the unirradiated and irradiated samples of $CuAl_xCr_xFe_{2-2x}O_4$ (x = 0.0 to 0.6 with step of 0.2) were measured by using the Quantum Design Vibrating Sample Magnetometer (VSM) (14 Tesla) for the present study was the Physical Properties Measurements system (PPMS) instrument at the laboratory of magnetism , UGC-DAE CSR, Indore Centre, Indore. The specifications of the instrument are summarized as follows:

- external magnetic Field: Up to 1.5KOe field
- Temperature range: 80 - 300K
- Sensitivity better than $5x10^{-6}$ emu

The operating principle for the PPMS VSM is shown in Fig. 4.6. The samples is attached is the end of a sample rod that is driven sinusoidally. The centre of oscillation is the positioned in the vertical centre of a gradiometer pickup coil. The precise position and amplitude of oscillations is controlled from the VSM motor module using and optical linear encoder signal readback from the VSM linear motor transport. The voltage induced in the pickup coil is amplified and lock –in detected in the VSM detection module. The VSM detection module uses the position encoder signal as a reference for the synchronous diction. This encoder signal is obtained from the VSM motor module, which interpret the raw encoder signals from VSM linear motor transport. The VSM detection module detects the in-phase and quadrature-phase signal from the encoder and from amplified voltage from the pickup coil. These signals are averaged and sent over the CAN bus to the VSM application running on the PC.

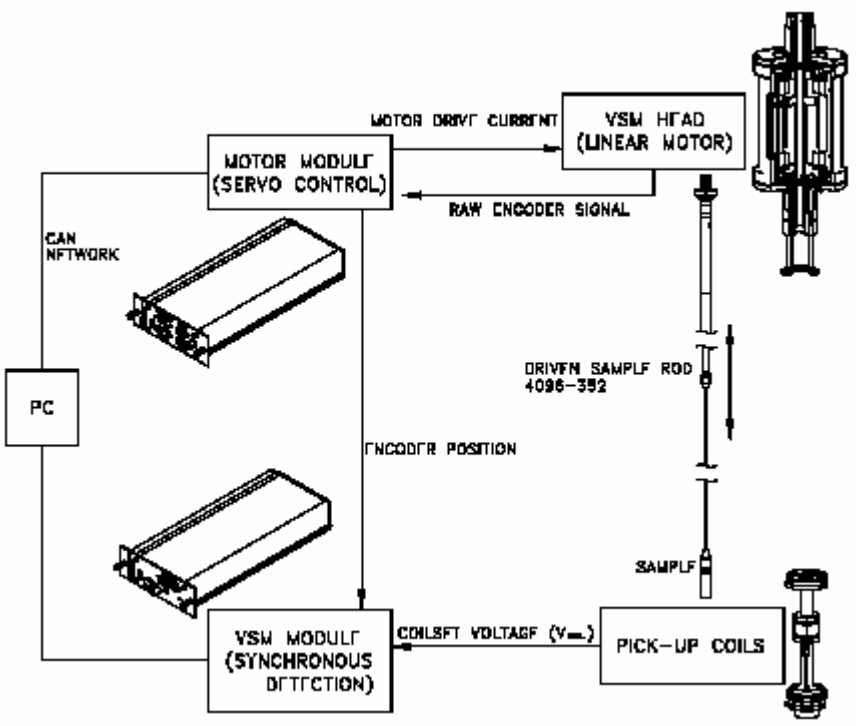

Fig. 4.6 The operating principle for the PPMS VSM

Photograph of Experimental Set up of PPMS VSM

4.3.2 Low field AC susceptibility

AC magnetic measurements, in which an AC applied is applied to a sample and the resulting AC moment is measured, are an important tool for characterizing many materials. Because the induced sample moment is time-dependent, AC measurements yield information about magnetization dynamics, which are not obtained in DC measurements, where the sample moment is constant during the measurement time.

AC magnetometry:

In AC magnetic measurements, a small AC drive magnetic field cause a time-dependent moment in the sample. The field of the time-dependent moment induces a current in the pickup coils, allowing measurement without sample motion. The detection circuitry is configured to detect only in a narrow frequency band, normally at the fundamental frequency (that of the AC drive field). In order to understand what is measured in AC magnetometry, first consider very low frequencies, where the measurement is most similar to DC magnetometry. In this case, the magnetic moment of the sample follows the *M (H)* cure that would be measured in DC experiments. As

long as the AC field is small, the induced AC moment is $M_{AC} = (dM/dH)$. H_{AC} sin (ωt) where H_{AC} is the amplitude of the driving field, ω is the driving frequency and $\chi = dM/dH$ is the slope of the M (H) curve, called the susceptibility. The susceptibility is the quantity of interest in AC magnetometry. χ is called the Mass susceptibility and has unit emu/g Oe in c.g.s. and weber. meter/ampere kg in M. K. S.

As the DC applied magnetic field is changed, different parts of the *M (H)* curve are accessed, giving a different susceptibility. One advantage of the AC measurements is already evident: the measurement is very sensitive to small changes in *M (H)*. Since the AC measurement is sensitive to the slope of *M (H)* and not to the absolute value, small magnetic shift can be detected even when the absolute moment is large. At higher frequencies than those considered above, the AC moment of the sample does not follow along the DC magnetization curve due to dynamic effects in the sample. For this reason, The AC susceptibility is often known as the dynamic susceptibility. In this higher frequency case, the magnetization of the sample may lag behind the drive field, an effect that is detected by the magnetometer circuitry. Thus, the AC magnetic susceptibility measurement yields two quantities: the magnitude of the susceptibility, χ, and its out of phase component (relative to the drive signal). The AC susceptometry, very sensitive to thermodynamic phase changes, is often used to measure transition temperature, which allows one to probe all the interesting magnetic phenomena [4.14].

The thermal variation of the low field AC susceptibility of these ferrites samples was obtained by using the instruments, which consist of (i) magnetic field unit (ii) magnetization unit and (iii) temperature unit. The magnetic field is produced by a double (Primary and secondary) coil set up i.e. Helmholtz coil, operating at a frequency of 263 Hz with rms field varying between 0 to 10 Oe. The two coils are oppositely wound relative to each other producing uniform magnetic field along the axis perpendicular to the coils. For the magnetization measurement a pick up coils is provided at the centre of a Helmholtz coil.

The temperature variation from RT to 800 K was achieved using a platinum wire wound silica tube, which act as a furnace to heat the sample. The over heating of the coil is avoided by water circulars system as a precaution against the burning or leaking of the coil. The temperature was sensed by platinum-Rhodium thermocouple

calibrated against the current in the heating element. Variable current was provided to the heating element by a variable power supply.

The sample tube is held in such a way that the sample material can be located in the middle of the pick up coil. By applying the current to the Helmholtz coil, the change in magnetization of the sample produces EMF in the pick up coil. The signal is then digitized by an analog to digital converter (ADC) and then fed to a digital panel meter. The clock diagram and the photograph of the susceptibility instrument are shown in the Fig. 4.7. The susceptibility measurements in the present study were taken for all the samples at temperature ranging from RT to 800K.

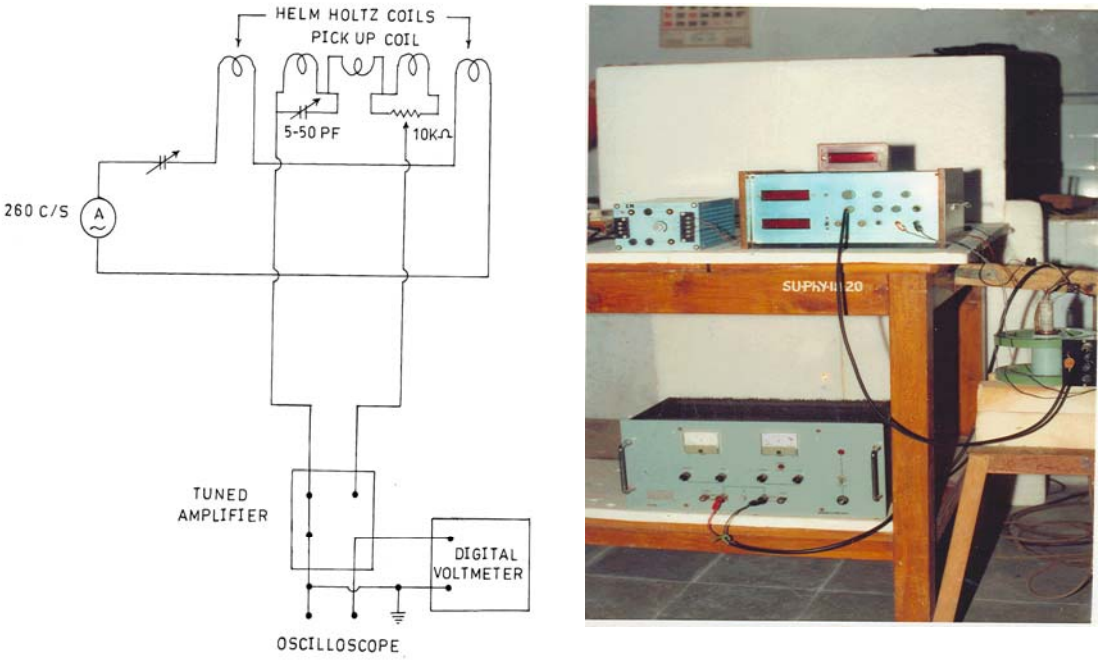

Fig. 4.7 Block cum circuit diagram and Photograph of AC Susceptibility Apparatus

4.4 Theory and Instrumentation - Mössbauer Spectroscopy

The Mössbauer spectroscopy is a versatile technique that can be used to provide information in many areas of science such as physics, chemistry, Biology and Metallurgy. It can be give very precise information about the chemical, structure, magnetic and time dependent properties of a material. Key to the success of the technique is the discovery of recoilless gamma rays emission and absorption, now referred to as the "Mössbauer effect"

Nuclei in atoms undergo a variety of energy level transitions, often associated with the emission or absorption of a gamma ray. In a free atom, the nucleus recoils, due to conservation of momentum, resulting in the emitted gamma ray being of lower energy than the nuclear transition energy. The same is observed in absorption where the absorbing nucleus recoils; meaning the energy of the resonantly absorbed photon has to be greater than that of the transition. Thus, in these circumstances, resonant emission or absorption doesn't occur. In 1957 Rudolph Mössbauer discovered the phenomenon of Recoil-Free Nuclear Resonance Fluorescence [4.15]; a phenomenon later to become commonly known as the "Mössbauer effect".

Mössbauer spectroscopy is a spectroscopic technique based on the Mössbauer effect. In its most common form, Mössbauer Absorption Spectroscopy, a solid sample is exposed to a beam of gamma radiation, and a detector measures the intensity of the beam that is transmitted through the sample, which will change depending on how many gamma rays are absorbed by the sample. The atoms in the source emitting the gamma rays are the same as the atoms in the sample absorbing them. It is thanks to the Mössbauer effect that a significant fraction of the gamma rays emitted by the atoms in the source do not lose any energy due to recoil and thus have almost the right energy to be absorbed by the target atoms. The gamma-ray energy is varied by accelerating the gamma-ray source through a range of velocities with a linear motor. The relative motion between the source and sample results in an energy shift due to the Doppler effect.

In the resulting spectra, gamma-ray intensity is plotted as a function of the source velocity. At velocities corresponding to the resonant energy levels of the sample, some of the gamma-rays are absorbed, resulting in a drop in the measured intensity and a corresponding dip in the spectrum. The number, positions, and intensities of the dips (also called peaks) provide information about the chemical environment of the absorbing nuclei and can be used to characterize the sample.

In order for Mössbauer absorption of gamma-rays to occur, the gamma-ray must be of the appropriate energy for the nuclear transitions of the atoms being probed, which is almost always achieved by having the same atoms of the same isotope in both the source and the target. Also, the gamma-ray energy should be relatively low, otherwise the system will have a low recoil-free fraction (see Mössbauer effect) resulting in a poor signal-to-noise ratio. Only a handful of elemental isotopes exist for which these criteria are met, so Mössbauer spectroscopy

can only be applied to a relatively small group of atoms including: ^{57}Fe, ^{129}I, ^{119}Sn, and ^{121}Sb. Of these, ^{57}Fe is by far the most common element studied using the technique.

The isotope with the strongest recoilless resonant absorption is Fe^{57}. Since the vast majority of the work reported in the Mössbauer literature is for iron, we restrict our discussion to that isotope. Fig.1 shows the decay of Fe^{57} from its parent Co^{57}. Of all the excited Fe^{57} nuclei, about 10% will emit a 14.4 keV gamma ray via a magnetic dipole transition from the metastable I = 3/2 state to I = 1/2 the ground state (I is the nuclear spin). The ratio of recoil-free 14.4 keV photons to all the 14.4 keV photons emitted is f, the recoil-free fraction of the source. f varies with the properties of the solid and decreases monotonically with increasing temperature. The linewidth of the emitted radiation is limited in theory by t, the mean life of the I = 3/2 state. In Fe^{57}, t = 1.4×10^{-7} sec, and the energy distribution is given by a Lorentzian with a fullwidth at half maximum of $\Gamma_{nat} = 4.7 \times 10^{-9}$ eV (Lang, 1970). The intensity per unit energy of the Mössbauer radiation is many orders of magnitude greater than the background radiation, and we shall henceforth refer to the gamma beam as if it were 100% Mössbauer radiation unless we specifically note otherwise. We shall also assume that the nuclear levels of the source are not split, and the energy distribution of the beam is given by a single Lorentzian. To use our Mössbauer source as a spectroscopic tool we must be able to vary its energy over a significant range. This is accomplished by Doppler shifting the energy of the gamma beam. Moving the source at a velocity of 1 mm/sec toward the sample will increase the energy of the photons by 14.4 keV (v/c) = 4.8×10^{-8} eV or ten natural linewidths.

The "mm/sec" is a convenient Mössbauer unit and is equal to 4.8×10^{-8} eV for Fe^{57}. A Mössbauer spectrometer consists of a source which may be moved relative to the sample and a counter to monitor the intensity of the beam after it has passed through the sample. The Mössbauer spectrum is a plot of the counting rate against the source velocity, i.e., the beam energy.

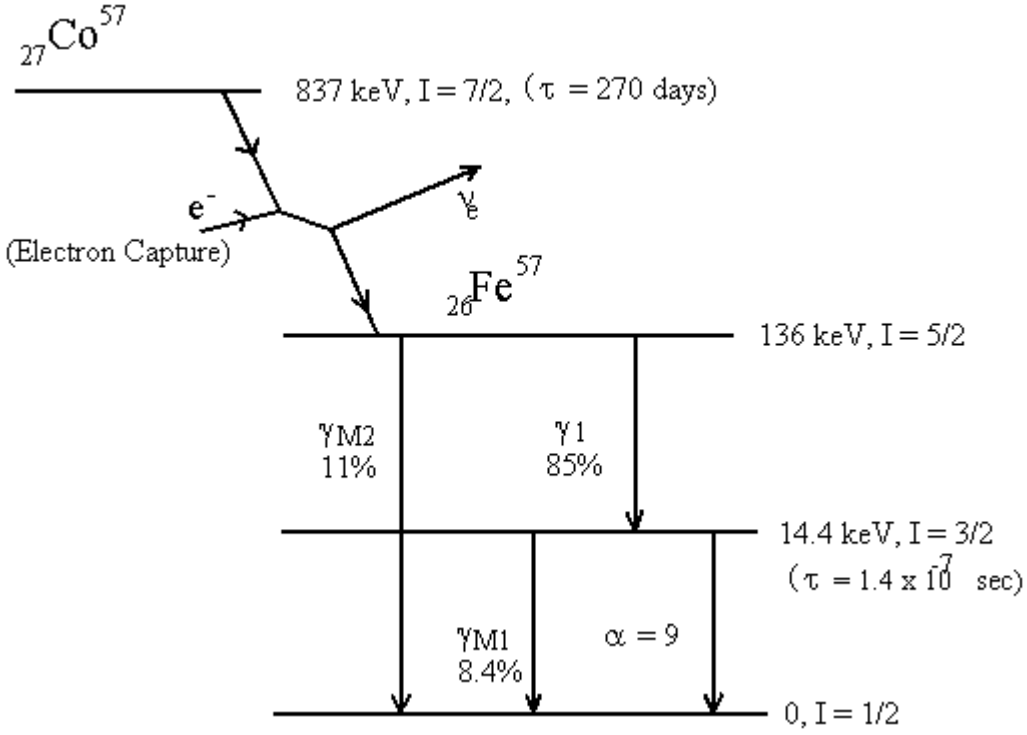

Fig. 4.8 Energy level scheme of Fe^{57}. Mössbauer spectroscopy involves the 14.4 keV transition. Intensities are given in % of decays.

The two main obstacles in the path of achieving nuclear resonant emission and absorption are the recoil energy shift and the thermal Doppler shift. Fig. 4.9 shows an isolated atom in the gas phase undergoing a nuclear transition from an excited state, E_e, to the ground state, E_g.

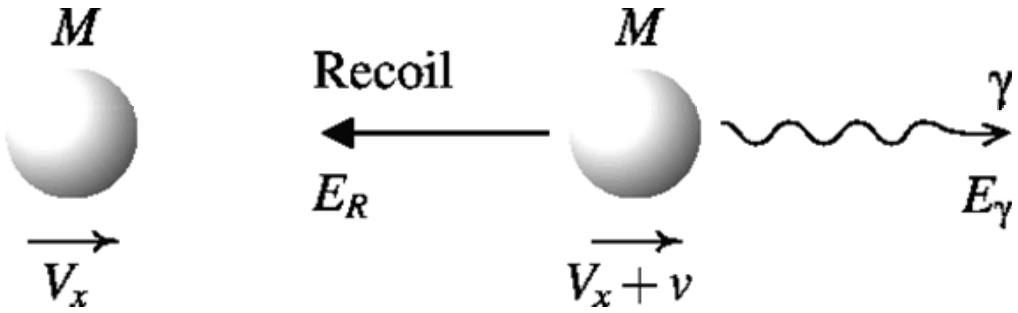

Fig. 4.9 Recoil in a free nucleus during gamma ray emission

The recoil kinetic energy of the free nucleus, E_R, is proportional to the mass of the nucleus, M, and the energy of the emitted gamma ray, E_γ, and is given by

$$E_R = \frac{E_\gamma^2}{2Mc^2}$$

The gamma ray energy will also be broadened into a distribution by the Doppler-effect energy, $E_D = M\nu.V_x$, which is proportional to the initial velocity, V_x, from the random thermal motion of the atom, and ν from the recoil of the nucleus. This can be expressed as

$$\overline{E}_D = E_\gamma \sqrt{\frac{2\overline{E}_k}{2Mc^2}}$$

where $\overline{E}_k$ is the mean kinetic energy per translational degree of freedom of a free atom [4.16].

Heisenberg Natural Linewidth also broadens the lineshape. The uncertainty in the mean lifetime of the excited state, Δt, is related to the uncertainty in the energy of the excited state, ΔE, by the Heisenberg uncertainty principle

$$\Delta E \Delta t \geq \hbar$$

Typical values of the linewidth broadening due to this are of the order of 10^6 times less than that due to E_R and $\overline{E}_D$ for isolated atoms and can be neglected in this case.

The same equations apply for absorption. This leads to a distribution of emitted and absorbed gamma ray energies as shown in Fig. 4.10. The resonance overlap is extremely small and so practically useless as the basis of a technique. The overlap is shown shaded and not to scale as it is extremely small.

The Mössbauer effect occurs when atoms are in a solid lattice or matrix. The chemical binding energies in solids (1-10 eV) are much greater than free atom recoil energies, E_R. The mass, M, recoiling then becomes effectively that of the entire crystal, which can be of the order of 10^{15}greater than a single atom. It can be seen from equations that E_R and E_D will now be negligible in this case.

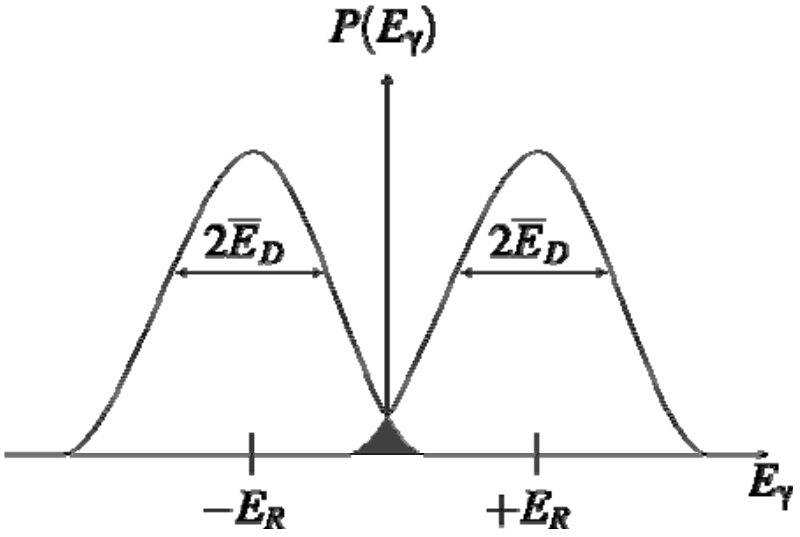

Fig. 4.10 Gamma ray energy distributions for emission and absorption in free atoms

However, although the nucleus is bound within the lattice it is still free to vibrate. The recoil energy can still be transferred to the lattice as a quantised lattice vibration, or phonon. If the recoil energy is less than the lowest quantised vibrational mode then a recoil-free event will occur. The probability of such an event is governed by the recoil-free factor, f, which is given as

$$f = \exp\left(\frac{-E_\gamma^2 \left\langle x^2 \right\rangle}{\hbar c^2} \right)$$

where $\left\langle x^2 \right\rangle$ is the mean square vibrational amplitude of the emitting or absorbing nucleus[4.16]. It can be seen that f decreases exponentially with the square of the gamma ray energy; this is why the Mössbauer effect is only detected in isotopes with a very low lying excited state. The other dependent factor, $\left\langle x^2 \right\rangle$, is a function of both the binding strength and temperature. The optimum f factor, and hence the best signal/noise ratio, is obtained for isotopes with very low lying excited states at temperatures well below their Debye Temperature, θ_D. A good example is ^{57}Fe, with Mössbauer gamma ray energy of 14.41 keV and a θ_D of 470K, allowing strong signals to be recorded at room temperature.

Earlier the Heisenberg Natural Linewidth (HNL) was ignored as being totally negligible compared to E_R. However, in recoil-free events E_R is 0 and hence the HNL becomes the major limit on the resolution of the gamma ray energies.

This spread in energies of width Γ_s is 4.67 x 10^{-9} eV in ^{57}Fe. Compared to the Mössbauer gamma ray energy of 14.41keV for this isotope this gives a resolution of ~1 in 10^{12}. This is an incredibly high level of energy resolution and is of the order of nuclear hyperfine interactions. Hence, the Mössbauer effect can be used to probe the electronic environment of a sample via the hyperfine interactions.

The technique of Mössbauer spectroscopy involves using the gamma rays emitted from the nuclei of a radioactive source to probe those in the sample to be studied. The source contains the parent nucleus of the Mössbauer isotope, embedded in a rigid matrix to ensure a high f factor. The gamma rays emitted from this are passed through the material being investigated and those transmitted through the absorber are detected and counted.

If the nuclei in the source and absorber are in the exact same environment (ie the energy of the nuclear transition is equal in both nuclei) the gamma rays will be resonantly absorbed and an absorption peak will be observed.

In order to probe the energy levels in nuclei in different environments we must scan the energy of the Mössbauer gamma ray. This is achieved by moving the source relative to the absorber. The Doppler effect produces an energy shift in the gamma ray energy allowing us to match the resonant energy level(s) in the absorber.

The simplest case is shown in Fig. 4.11. The spectrum recorded is a plot of transmission intensity versus source velocity in mms. The x-axis, through the Doppler effect on the gamma ray energy, is effectively an energy scale. The lineshape of the recorded peak in a thin sample is theoretically a Lorentzian, with a FWHM of twice the uncertainty in the energy of the excited state, Γ.

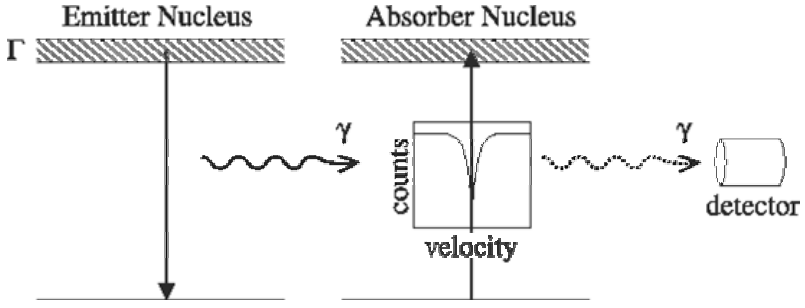

Fig. 4.11 Example Mössbauer spectrum showing the simplest case of emitter and absorber nuclei in the same environment. The uncertainty in the energy of the excited state, Γ, is shown exaggerated.

Hyperfine Interactions:

The interaction between a nucleus and its surrounding environment is known as a hyperfine interaction. These interactions are very small compared to the energy levels of the nucleus itself but the extreme energy resolution of the Mössbauer effect enables these interactions to be observed. The hyperfine interactions may shift energy levels or lift their degeneracy. Both of these variations will affect the shape of a Mössbauer spectrum.

The nuclear Hamiltonian can be expressed as

$$\mathcal{H} = \mathcal{H}_0 + \mathrm{E}_0 + \mathrm{M}_1 + \mathrm{E}_2 + \ldots..$$

where $\mathcal{H}_0$ represents all of the terms of the Hamiltonian other than the hyperfine interactions. E_0 refers to the electric monopole interactions, M_1 the magnetic dipole interactions and E_2 the electric quadrupole interactions.

These effects will be discussed in turn with reference to their physical causes and their effects on the Mössbauer spectrum lineshapes and positions.

Center Shift:

The Center Shift (CS) of a Mössbauer spectrum, which sets the centroid of the spectrum, is composed of two factors: the Chemical Isomer Shift, δ, and the Second Order Doppler Effect (SODS), meaning that

$$CS = \delta + SODS$$

Chemical Isomer Shift (δ):

The Isomer Shift arises due to the non-zero volume of the nucleus and the electron charge density due to s-electrons within it leading to an electric monopole (Coulomb) interaction which alters the nuclear energy levels. The volume of the nucleus in its ground and excited states are different and the s-electron densities are affected by the chemical environment. This relationship between s-electron density and nuclear radius is given by

$$\delta = \frac{2}{3}\pi Z e^2 \left\{ \left|\psi_s(0)_E\right|^2 - \left|\psi_s(0)_A\right|^2 \right\} \left\{ \left\langle R_e^2 \right\rangle - \left\langle R_g^2 \right\rangle \right\}$$

where $\left\langle R_g^{\,2} \right\rangle$ and $\left\langle R_e^{\,2} \right\rangle$ are the mean square radii of the ground and excited nuclear states, $|\psi_S(0)_E|^2$ and , $|\psi_S(0)_A|^2$ are the electron densities at the emitting and absorbing nuclei and Z is the atomic number [4.16].

Any difference in the s-electron environment between emitter and absorber thus produces a shift in the resonance energy of the transition. This shift cannot be measured directly and so a suitable reference is necessary, such as a specific source or an absorber. In all of the results presented in this thesis isomer shifts are quoted relative to α-Fe at room temperature (any isomer shifts quoted from other work which use a different calibration material are quoted relative to α-Fe in this thesis for consistency).

The Isomer Shift is good for probing the valency state of the Mössbauer atom. As the wavefunctions of the s-electrons penetrate into outer shells, changes in these shells will directly alter the s-electron charge density at the nucleus. For example, Fe^{2+} and Fe^{3+} have electron configurations of $(3d)^6$and $(3d)^5$ respectively. The ferrous ions have less s-electron density at the nucleus due to the greater screening of the d-electrons. This produces a positive Isomer Shift greater in ferrous iron than in ferric.

Second Order Doppler Shift (SODS):

The Second Order Doppler Shift (SODS) is a temperature-dependent effect on the center shift of a Mössbauer spectrum. Above 0 K atoms in a lattice oscillate about their mean position. The frequency of this oscillation is of the order of 10^{12} meaning that the average displacement during the lifetime of a Mössbauer event is zero. However, the second term in the Doppler shift depends on υ^2 leading to the mean square displacement being non-zero. This energy shift is given by

$$\frac{\delta E_\gamma}{E_\gamma} = -\frac{\left\langle \upsilon^2 \right\rangle}{2c^2}$$

For ^{57}Fe in the high temperature limit this gives a change of +0.07 mms^{-1} for a decrease of 100K [4.16].

Electric Quadrupole Splitting:

A nucleus that has a spin quantum number I > ½ has a non-spherical charge distribution. The magnitude of the charge deformation, Q, is given by

$$eQ = \int \rho r^2 (3\cos^2\theta - 1) d\tau$$

where e is the charge on the proton, ρ is the charge density in a volume element dτ at a distance τ from the center of the nucleus and making an angle θ to the nuclear spin quantisation axis. The sign of Q indicates the shape of the deformation. Negative Q is due to the nucleus being flattened along the spin axis, an elongated nucleus giving positive Q [4.16].

An asymmetric charge distribution around the nucleus causes an asymmetric electric field at the nucleus, characterized by a tensor quantity called the Electric Field Gradient (EFG) ∇E. The electric quadrupole interaction between these two quantities gives rise to a splitting in the nuclear energy levels. The interaction between nuclear moment and EFG is expressed by the Hamiltonian

$$H_{Eq} = -\frac{1}{6} eQ\nabla E$$

where ∇E may be written as

$$\nabla E_{ij} = -\frac{\partial^2 V}{\partial x_i \partial x_j} = -V_{ij}$$

$$\{x_i, x_j\} = \{x, y, z\}$$

where V is the electrostatic potential.

There are two contributions to the EFG (i) lattice contributions from charges on distant ions and (ii) valence contributions due to incompletely filled electron shells. If a suitable coordinate system is chosen the EFG can be represented by three principal axes, V_{xx}, V_{yy} and V_{zz}, and. If an asymmetry parameter is defined using these axes as

$$\eta = \left(\frac{V_{xx} - V_{yy}}{V_{zz}} \right)$$

where $|V_{xx}| \geq |V_{yy}| \geq |V_{zz}|$ so that $0 \leq \eta \leq 1$, the EFG can be specified by two parameters: V_{zz} and η.

The Hamiltonian for the quadrupole interaction can be rewritten as

$$H_{Eq} = \frac{e^2 qQ}{4I(2I-1)} \left[3I_z^2 - I(I+1) + \frac{\eta}{2}(I_+^2 + I_-^2) \right]$$

where I_+ and I_- are shift operators and I_z is a spin operator[4.16].

The excited state of ^{57}Fe has a spin I = 3/2. The EFG has no effect on the I = ½ ground state but does remove degeneracy in the excited state, splitting it into two sub-states $m_I = \pm ½$ and $m_I = \pm 3/2$ where the $m_I = \pm 3/2$ states are higher in energy for positive V_{zz}. The energy eigenvalues for I = 3/2 have exact solutions given by

$$E_{Eq} = \frac{e^2 qQ}{4I(2I-1)}\left[3m_I^2 - I(I+1)\right]\left(1+\frac{\eta^2}{3}\right)^{\frac{1}{2}}$$

Whilst the energies for higher spin states require analytical methods to calculate the energies.

The now non-degenerate excited states give rise to a doublet in the Mössbauer spectrum as illustrated in Fig. 4.12. The separation between the lines, Δ, is known as the quadrupole splitting and is given by

$$\Delta = \frac{e^2 qQ}{2}\left(1+\frac{\eta^2}{3}\right)^{\frac{1}{2}}$$

with the line intensities being equal for polycrystalline samples. Texture or orientation effects can lead to asymmetric doublets. As the nuclear quadrupole moment is fixed the magnitude and sign of Δ gives information about the sign of the EFG and magnitude of η.

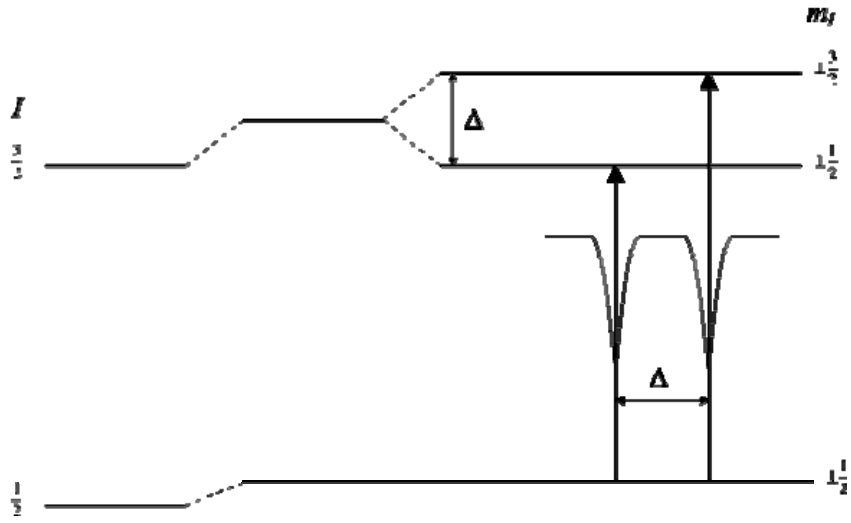

Fig. 4.12 The effect on the nuclear energy levels for a 3/2 → ½ transition, such as in ^{57}Fe or ^{119}Sn, for an asymmetric charge distribution. The magnitude of Quadrupole splitting Δ is shown

Magnetic Hyperfine Splitting:

Magnetic hyperfine splitting is caused by the dipole interaction between the nuclear spin moment and a magnetic field ie Zeeman splitting. The effective magnetic field experienced by the nucleus is a combination of fields from the atom itself, from the lattice through crystal field effects and from external applied fields. This can be considered for now as a single field, H, whose direction specifies the principal z axis.

The Hamiltonian for the magnetic hyperfine dipole interaction is given as

$$\mathcal{H} = -\mu.H = -g\mu_N I.H$$

where μ_N is the nuclear Bohr magneton, μ is the nuclear magnetic moment, I is the nuclear spin and g is the nuclear g-factor [4.16].

This Hamiltonian yields eigenvalues of $E_M = - g\mu_N H m_I$

where m_I is the magnetic quantum number representing the z component of I (ie m_I = I, I-1,….,-I). The magnetic field splits the nuclear level of spin I into (2I+1) equispaced non-degenerate substates. This and the selection rule of $\Delta m_I = 0, \pm 1$ produces splitting and a resultant spectrum as shown in Fig. 4.13 for a $3/2 \rightarrow 1/2$ transition.

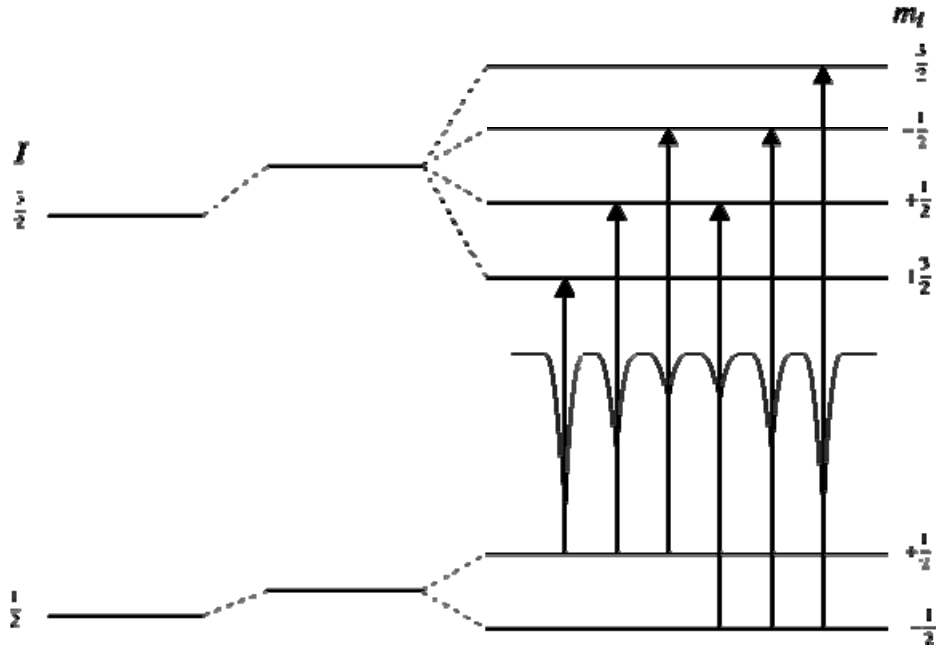

Fig. 4.13 The effect of magnetic splitting on nuclear energy levels in the absence of quadrupole splitting. The magnitude of splitting is proportional to the total magnetic field at the nucleus

This splitting is a combination of a constant nuclear term and a variable magnetic term, influenced by the electronic structure. The magnetic field at the nucleus has several terms associated with it. A general expression is

$$H = H_0 - DM + \frac{4}{3}\pi M + H_S + H_L + H_D$$

Where H_0 is the value of magnetic field at the nucleus due to an external magnetic field, -DM is the demagnetising field, $4/3\pi M$ is the Lorentz field, H_s is the Fermi contact term, H_L is the orbital magnetic term and H_D is the dipolar term. The demagnetising field and Lorentz field are usually negligible compared to the other terms.

H_s is produced by the polarisation of electrons whose wavefunctions overlap the nucleus, ie s-electrons. This polarisation is due to unpaired electrons in the d or f orbitals and gives an imbalance in spin density at the nucleus from the difference in interaction between the unpaired electrons with s-electrons of parallel or antiparallel spin to its own. This can be expressed formally as

$$H_S = -\frac{8\pi}{3}\mu_0\mu_B \sum \left\{ \left|\psi_{s\uparrow}(0)\right|^2 - \left|\psi_{s\downarrow}(0)\right|^2 \right\}$$

H_L arises from the net orbital moment at the nucleus caused by the orbital motion of electrons in unfilled shells and given by

$$H_L = \frac{2\mu_0\mu_B}{4\pi}\left\langle r^{-3}\right\rangle (L)$$

In transition metals L is usually quenched by interactions with the crystal field, but it can be substantial in Rare Earth ions.

H_D arises from the dipolar interaction between the nucleus and the spin moment of 3d or 4f electrons and can be expressed as

$$H_D = -2\mu_B \langle S \rangle \left\langle r^{-3} \right\rangle \left\langle 3\cos^2\theta - 1 \right\rangle$$

In transition metal compounds with cubic symmetry this has zero magnitude but can be substantial in Rare Earths.

Combined Magnetic and Quadrupole Interactions:

When dealing with quadrupole or magnetic splitting separately with chemical isomer shifts the recorded spectrum has uniform shifts of resonance lines with no change in their relative separations. However, both the quadrupolar and magnetic

interactions depend upon angle and so when they are both present the interpretation of the spectrum can be complex.

The situation can be simplified a great deal if two assumptions are made

1. The electric field gradient is axially symmetric with its principal axis, V_{zz}, at an angle θ to the magnetic axis
2. The strength of the quadrupole interaction is much less than the magnetic interaction, ie $e^2qQ << \mu H$.

The solution to the Hamiltonian can then be solved by treating the quadrupole interaction as a perturbation so that the resultant energy levels are given by

$$E = -q\mu_N H m_I + (-1)^{|M_I|} + \frac{\frac{1}{2}e^2qQ}{4}\left(\frac{3\cos^2\theta - 1}{2}\right)$$

giving a spectrum as in Fig. 4.14 [4.16].

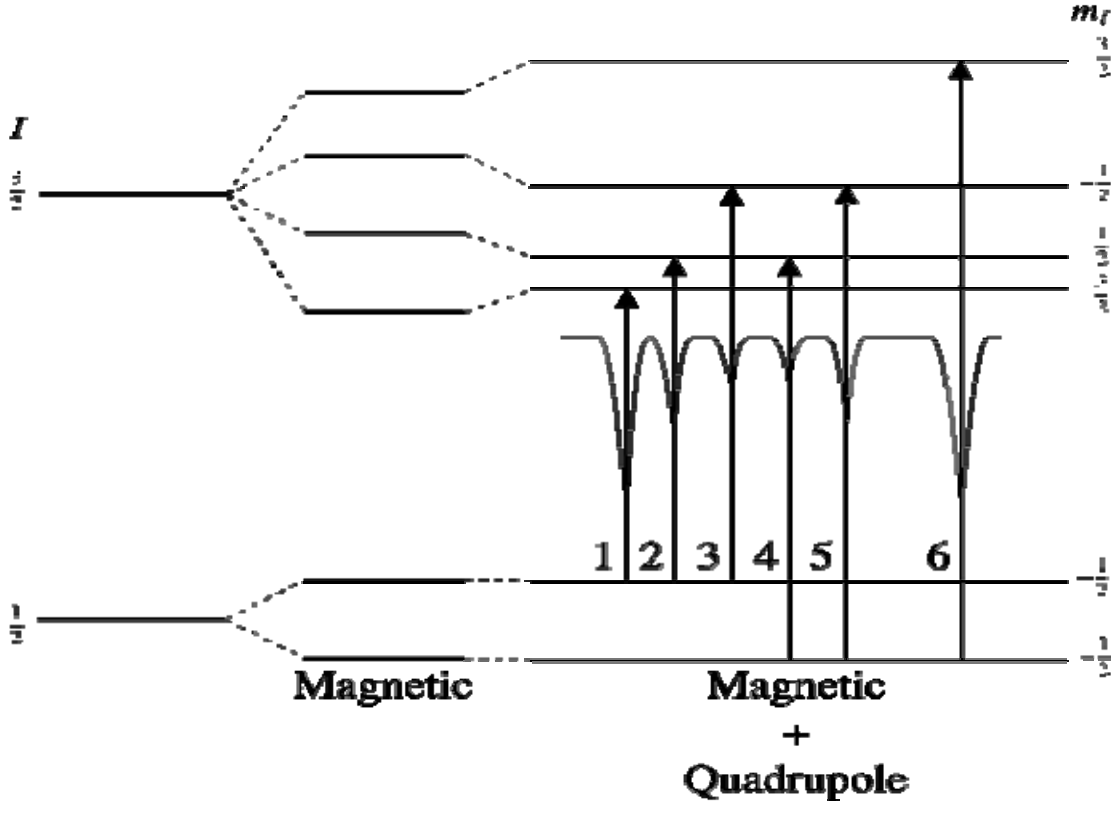

Fig. 4.14 The effect of a first-order quadrupole perturbation on a magnetic hyperfine spectrum for a 3/2→1/2 transition. Lines 2,3,4,5 are shifted relative to lines 1, 6

For most ^{57}Fe spectra the result is a shift in the relative position of lines 1, 6 with lines 2,3,4,5. For a positive quadrupole splitting lines 1,6 are shifted positively relative to lines 2,3,4,5 and vice versa. The line separations are equal when there is no quadrupole effect or when $\cos\theta = 1/\sqrt{3}$.

Spectrum Line Intensities:

The hyperfine interactions thus far have given the relative energies of the various transitions taking place but have not given information on the relative intensities of these transitions in the recorded spectrum. The intensities arise from the coupling of two angular momentum states, which can be expressed as the product of both an angular dependent term and an angular independent term by

$$A(L,\theta) = C^2(J)\Theta(J, \theta)$$

Where $C^2(J)$ is the transition probability of the γ -ray transition between two nuclear sub-levels, and $\Theta(J,\theta)$ is the angular dependence of the radiation probability at an angle θ to the quantisation axis.

The angular independent term is given by the square of the appropriate Clebsch-Gordan coefficient

$$C^2(J) = \langle I_1 J - m_1 m \mid I_2 m_2 \rangle^2$$

where J is the vector sum $J = I_1 + I_2$ and m is the vector sum $m = m_1 - m_2$ [4.16]. J is the multipolarity of the radiation, J = 1 being dipolar and J =2 being quadrupolar. As the multipolarity of the radiation increases the transition probability decreases.

In ^{57}Fe the 14.41keV transition is primarily dipolar and values for this transition are given in Table 4.2.

In a magnetic spectrum the intensities of the outer, middle and inner lines are in a ratio derived from the product $C^2(J)\,\Theta(J,\theta)$. Using the values from Table 4.2 gives

$$3(1+\cos^2\theta) : 4\sin^2\theta : 1+\cos^2\theta$$

from which it can be seen that the outer and inner lines are always in the ratio of 3:1 whilst the middle line varies between $0 \rightarrow 4$ with angle. In polycrystalline samples there is no angular dependence and thus the intensity depends only on $C^2(J)$, giving a sextet of 3:2:1:1:2:3.

Non-magnetic spectra with quadrupole splitting have several degenerate transitions and the intensity of the two lines are in the ratio

$$3(1+\cos^2\theta) : 2+3\sin^2\theta$$

Table 4.2 Relative probabilities for a dipole 3/2→1/2 transition. C^2 and Θ are the angular independent and dependent terms arbitrarily normalised. Relative intensities for θ = 90° and θ = 0^0 are shown with arbitrary normalization.

m_2	$-m_1$	m	C	C^2	Θ	θ = 90°	θ = 0°
$+3/2$	$+1/2$	+1	1	3	$(1+\cos^2\theta)$	3	6
$+1/2$	$+1/2$	0	$\sqrt{2/3}$	2	$2\sin^2\theta$	4	0
$-1/2$	$+1/2$	-1	$\sqrt{1/3}$	1	$(1+\cos^2\theta)$	1	2
$-3/2$	$+1/2$	-2	0	0	0	0	0
$+3/2$	$-1/2$	+2	0	0	0	0	0
$+1/2$	$-1/2$	+1	$\sqrt{1/3}$	1	$(1+\cos^2\theta)$	1	2
$-1/2$	$-1/2$	0	$\sqrt{2/3}$	2	$2\sin^2\theta$	4	0
$-3/2$	$-1/2$	-1	1	3	$(1+\cos^2\theta)$	3	6

Relaxation Phenomena:

There are many contributions to the hyperfine field at the nucleus as seen in Equation, but the major contributor for transition metals such as ^{57}Fe, when in zero applied field, is H_s. This arises from the polarising effect of unpaired electron spins with the direction of the field being related to that of the electron spins. However, this direction is not invariant and can flip after a period of time. This is the relaxation phenomenon. The effects upon the Mössbauer lineshape depend upon the relative time scales of measurement and the relaxation mechanism, there being three time scales to consider: the lifetime of the Mössbauer event, the Larmor precession time and the relaxation time.

The lifetime of the Mössbauer event, τ_m, which is also the limiting time scale of the measurement technique, is determined by the Heisenberg uncertainty relationship as shown in Equation. For ^{57}Fe this is of the order of 10^{-7} s.

The second time scale to consider is the minimum time required for the nucleus to detect the hyperfine field. This is usually assumed to be equal to the Larmor precession time, τ_l, which can be considered as the time taken for a nuclear spin state, I, to split into (2I + 1) substates under the influence of a hyperfine field. τ_l is proportional to the magnitude of the hyperfine field (and hence related to the nuclear energy levels as in Equation) with the following relation

$$\tau_l = \frac{2\pi\hbar}{g\mu_n B}$$

where g is the gyromagnetic constant and μ_n is the nuclear Bohr magneton. In iron oxides the hyperfine field is ~ 400→ 500 kG giving τ_l of the order of 10^{-8} s. This means that $\tau_m >> \tau_l$ and hence the hyperfine fields are detectable by the technique.

The final time scale is the relaxation time, τ_r, associated with the time dependent fluctuations of the electron spin. For the hyperfine field to be observed it must remain constant at the nucleus for at least one Larmor precession period.

There are three regimes which are important when considering the effect of relaxation on the Mössbauer lineshape:

1. If $\tau_r >> \tau_l$ then the hyperfine field is static during a single Larmor precession period. The spectral lines are narrow and Lorentzian in shape.
2. If$\tau_r << \tau_l$ then the nucleus experiences a time averaged hyperfine field. The magnitude is less than the value obtained for a static field as the interaction will have changed many times during a single precession period and tends to zero as τ_r decreases. Narrow Lorentzian lines are still observed.

3. If $\tau_r \approx \tau_l$ then resonance between the relaxation and the precession occurs leading to complex spectra and broadened lineshapes. As τ_l is proportional to the energy difference between the spectral lines τ_l for the outer lines will be less than for the inner lines, causing the inner lines of a sextet to broaden and disappear before the outer ones [4.17].

The two main mechanisms involved in the spin relaxation are Spin-Spin and Spin-Lattice relaxation.

Spin-Spin Relaxation:

This involves energy transfer between interacting spins via dipole and exchange interactions. The relaxation rate depends heavily on the concentration of paramagnetic ions in the sample. This mechanism is largely temperature independent. The relaxation rate can be expressed as

$$R \alpha |\langle i|\mathcal{H}|f\rangle|^2 \phi$$

Where i and f are the initial and final spin states, $\mathcal{H}$ is the Hamiltonian of the mechanism and ϕ is a phase factor

Spin-Lattice Relaxation:

This mechanism involves energy transfer between the electron spin and lattice phonons mostly via the spin-orbit interaction but also weakly through dipolar interactions. The relaxation rate is of the same form as Equation but with ϕ now involving the population of phonon modes. This leads to the spin-lattice contribution to relaxation being strongly temperature dependent.

Mössbauer spectrometer:

The major components are a radioactive source, a Doppler scanning device, the sample, an energy sensitive gamma-ray detector and a pulse handling electronics.

The Mössbauer source is specially prepared using the nuclides appropriate for giving Mössbauer effect. For example, ^{57}Fe nuclide is widely used and its precursor ^{57}Co is embedded in a matrix of crystalline structure of different elements such as Pd, Rh etc.

The points considered during the preparation of source are:

1. The Debye temperature of crystal matrix (It should be much higher).
2. The symmetry of crystal matrix (cubic is favorable).
3. The element used as a matrix (They must be metallic in nature so that there is no effect of electric field of them on source nuclide with their screening effect).
4. The matrix element must not be magnetic

If the transition energy of the source and the absorber nuclides are different as a result of different hyperfine interactions in both, its effect will be to destroy the resonance. To restore the resonance the respective additional energy must be applied to or subtracted from the gamma radiation of the source. Relative motion between the absorber and the source adds Doppler motion energy to the system. The Doppler velocity required to demonstrate the natural width of ^{57}Fe nuclide is $\Delta E/E = \upsilon/c$; υ comes out to be 1.4×10^{-2} cm/sec. The modern commercial equipments operate in a constant-acceleration mode rather where a whole range of velocities is scanned from zero to a preset maximum value. This scanning is accomplished in synchronization with the multi-channel analyzer.

Each channel accumulates the number of transmitted counts for the same given velocity increment during each cycle. The device for this includes constant acceleration cams, electromechanical transducers such as high fidelity loudspeakers.

The Mössbauer detectors are energy sensitive detectors. Different types of detectors are used depending on specifics of the application. Commonly, used detectors are proportional counters and Scintillation detectors.

The hyperfine interaction parameters that can be measured through Mössbauer spectroscopy are discussed in details in previous. The analysis of Mössbauer data is discussed below:

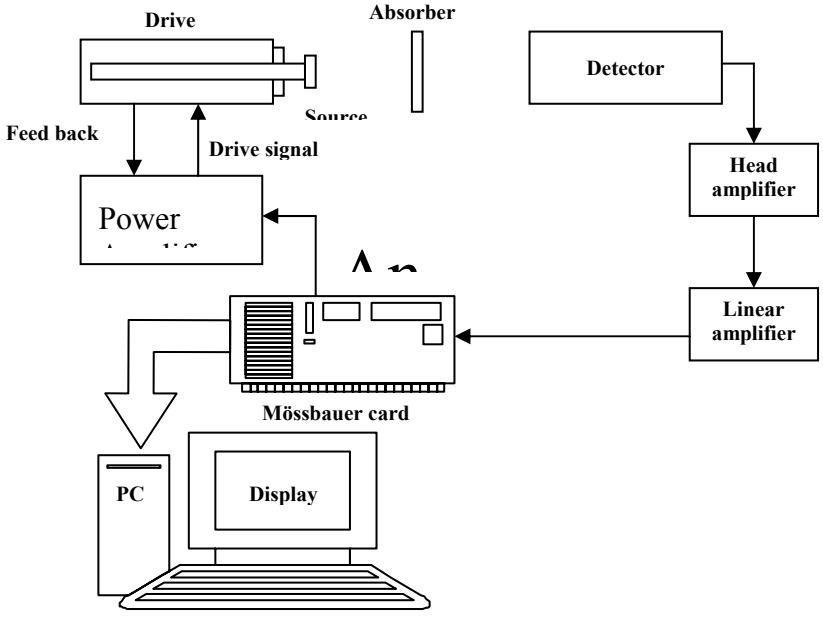

Fig. 4.15 Block diagram of Mössbauer spectrometer

Experimental Set up of Mössbauer spectrometer

Mössbauer line shape and analysis of spectra: The Mössbauer line has the Lorentzian or Breit-Winger shape and can be described by, $I(E) = \dfrac{f_s.f_a.n.\sigma_0.d.(\tau/2)}{(E-E_0)^2 + (\tau/2)}$

where $\Gamma = 2\Gamma_0 = 2\hbar/\tau$ is the measured line width

E_0 = the transition energy

n = the number of resonant nuclides

d = absorber thickness

σ_0 = the resonance absorption cross section

f_s and f_a are the resonance fraction for the source and the absorber .

The analysis of the Mössbauer spectra is done for accurate determination of line positions, line widths and area under the resonant peak. This is done using the standard computational method for curve fitting the Mössbauer spectra according to constrained least square analysis of the different parameters of the theoretical model provided. This is done using computer software [4.16, 4.18-4.19].

The above equation for Lorentzian profile to account for observed spectrum can be given by,

$$Y(x) = b - \frac{Y(0)}{1 + \left(\dfrac{x - x(0)}{\tau_{ex/2}} \right)^2}$$

Here b is the baseline intensity, Y(0) is the amplitude of the peak located at resonance energy (or velocity) x(0) which is nothing but Y(0) = $f_s.f_a.n.\sigma_0.d.(\tau/2)$ and Γ_{ex} is the F.W.H.M. for the line. For n lines, the equations becomes

$$Y(x) = b - \sum_{i=1}^{n} \frac{Y(0)_i}{1 + \left(\frac{x - x(0)_i}{\tau_{ex}/2} \right)^2}$$

The least square fitting of observed and calculated profile is done as follows: goodness of fit is given by χ^2.

$$\chi^2 = \sum_{i=1}^{n} W_r \left[Y_r - Y\left(x_r / q \right) \right]^2$$

where Y_r is observed count at channel r, $Y\left(x_r / q \right)$ is the function above given. W_r is the inverse of variance for channel r. The q is the parameter to be corrected for fitting. The least square fitting is then,

$$d\chi^2 / dq_i = 0$$

This is one iteration the values of q_i are corrected until the change in χ^2 is minimized. The computer software generally does constrained analysis where the theoretical relationship has been established between various q values and so the parameters to be controlled by the users are reduced.

Mössbauer experimental details:

The Mössbauer study was carried out for the following unirradiated and irradiated systems:

- $Li_{0.5(1+x)}Ti_xAl_{0.1}Fe_{2-2x}O_4$ (x = 0.0 to 0.3 with step of 0.1)
- $Li_{0.5(1+x)}Ti_xCr_{0.1}Fe_{2-2x}O_4$ (x = 0.0 to 0.3 with step of 0.1)
- $CuAl_xCr_xFe_{2-2x}O_4$ (x = 0.0 to 0.8 with step of 0.2) (Slow-Cooled & Quenched)
- $MnAl_xCr_xFe_{2-2x}O_4$ (x = 0.0 to 0.8 with step of 0.2)

The Mössbauer spectra for the system $Li_{0.5(1+x)}Ti_xAl_{0.1}Fe_{2-2x}O_4$ at 300K were recorded on the Mössbauer spectrometer at Department of Physics, Bhavnagar University, Bhavnagar. The Mössbauer spectra for the system $Li_{0.5(1+x)}Ti_xCr_{0.1}Fe_{2-2x}O_4$ were carried out on the Mössbauer spectrometer at Department of Physics, Sultan Qaboos University, Muscat OMAN. The Mössbauer spectra at 77K and 295K for all the samples were recorded using a standard absorption method with ^{57}Co-in-Rh source with initial activity of 50mCi placed on a constant acceleration spectrometer using the ferrite powder pressed between two Mylar foils of a sample holder in a LN cryostat.

The spectra for the samples (x = 0.2, 0.4, 0.6) of the system $CuAl_xCr_xFe_{2-2x}O_4$ (Slow-cooled & Quenched) were obtained on the Mössbauer spectrometer at Department of Physics, Calcutta University, Calcutta. All the spectra recorded at room temperature only.

The Mössbauer spectra for the system $MnAl_xCr_xFe_{2-2x}O_4$ were carried out on the Mössbauer spectrometer at IUC-DAEF, Indore. The spectra were obtained using constant acceleration transducer and 512 multi-channel analyzer operating in time mode. A gamma ray source of ^{57}Co in Pd matrix of 25mCi was used. The spectra were obtained in transmission geometry and 14.41 gamma rays were detected by Xenon-Methane filled proportional detector. The spectra were recorded at room temperature and the absorbers were made using the samples in powder form of the thickness around 20-30 mg/cm^2.

The Mössbauer spectra were analyzed using NORMOS computer software. The program is developed by R. A. Brand, Laboratorium fuer Angewandte Physik, Universitaet Duisburg, Lotharstr. 1, D-4100 Duisburg 1. The NORMOS programs are for fitting a wide variety of different Mössbauer spectra. NORMOS/SITE is for fitting spectra composed of a certain number of discrete sub-spectra. The program uses nonlinear least-squares minimization with the Levenberg-Marquardt method. The program gives the final parameters after best fitting the observed spectra with the one theoretical generated by it using the paymasters provided by user and then after refined by it. The goodness of fit can be checked by the χ^2 value. The refined parameters and the stastical errors in them can be obtained along with the observed and fitted in format of plot file, which can be plotted by user. The detailed discussion is given in [4.20-4.22].

References:

4.1 M. F. C. Ladd and R. A. Palmer, "Structure determination by X-ray crystallography", Plenum Press, (1978)

4.2 H. P. Klug and L. E. Alexander, "X-ray diffraction procedures for polycrystalline and amorphous materials", 2nd Ed., Wiley, (1974)

4.3 B. D. Cullity, "Elements of X-ray diffraction", 2nd Ed. Addison Wesley, (1978)

4.4 M. M Woolfson, "An Introduction to X- ray crystallography" Cambridge University Press, (1970)]

4.5 H. P. Klug and L. E. Alexander, "X-ray diffraction procedures for polycrystalline and amorphous materials", 2nd Ed. , Wiley, (1974)

4.6 P. Eugene Bertin, "Principles and practice of X-ray spectrometric Analysis", 2nd Ed. , Plenum press, (1975)

4.7 Energy dispersion X-ray Analysis: X-ray and electron probe analysis, ASTM STP 485, (Philadelphia: American Society for Testing and Materials, 1971

4.8 L. S. Birks. "X-ray Spectrometrial Analysis", 2nd ed. (New York: Interscience, 1969)

4.9 Infrared Spectroscopy, Chapter 15, C. - P. Sherman Hsu, Separations Science, Research and Product Development Mallinckrodt, Inc. Mallinckrodt Baker Division

4.10 Fundamental of Molecular Spectroscopy 4th Edition Colin N. Banwell and Elaine M. McCASH, (Tata McGraw-Hill publishing, New Delhi)]

4.11 Proceeding of National Workshop on Advanced Methods for Materials Characterization (NWMC – 2004), MRSI (Mumbai Chapter), Board of Research in Nuclear Sciences

4.12 S. D. Likhite and C. Radhakrishnamurty, Bulletin Natinal Geophys. Res. Inst., **3** (1965) 1

4.13 S. D. Likhite, C. Radhakrishnamurty and P. W. Sahasrabudhe, Proc. Indian Acas. Sci. **87A** (1978) 245

4.14 A. G. Berndt, X. Chen, H. P. Kunkel, and G. Williams, Phys. Rev. B **52** (1995) 1016

4.15 R. L. Mössbauer, Z. Physik, **151** (1958) 124

4.16 N. N. Greenwood and T. C. Gibb. “Mössbauer Spectroscopy”. Chapman and Hall Ltd, London, (1971)

4.17 H.H. Wickman and I.J. Gruverman, *Mössbauer Effect Methodology*, Plenum Press, New York, (1966)

4.18 A. J. Waston and A. J. Freeman, Phys. Rev. **123** (1961) 2027

4.19 A. J. Stone, Appendix to: G. M. Bancroft., A. G. Maddock., W. K. Ong. R. H. Prince and A. J. Stone, J. Chem. Soc. (A), (1967) 1966

4.20 J. R. Gabriel and S. L. Ruby, Nucl. Instr. Methods, **36** (1965) 23

4.21 B. L. Crisman and T. A. Tumolillo., “Computer Analysis of Mössbauer Spectra”, Dept. of Physics, Univ. of Illinos, Urbana, 111,

4.22 R. A. Brand, User manual for NORMOS software (1992)

CHAPTER: 5

Electrical and Dielectric Properties: Theory and Experiments

5.1 Introduction

In this chapter, the electrical and dielectric properties of ferrites are described in brief, and relevant background and theoretical concepts for the experimental and characterization techniques used for the present work are discussed. The different sections in the chapter describe the various aspects of d. c. resistivity, thermoelectric power, mobility, charge carrier concentration and also give explanation of various models to account for the electrical properties. This chapter provides the relationship between polarization and the electric field in molecules of ferrite materials, types of polarization using dielectric response and impedance spectroscopy.

It is well known that the semiconductor natured polycrystalline spinel ferrites are very important electro-ceramic materials due to their interesting electrical properties of low eddy current and dielectric losses. The spinel ferrites find applications in wide range of frequencies extending from microwave to radio wave. These materials are also applicable in many magnetic devices due to their low electrical conductivity as compared to that of magnetic metals. Hence, the electrical conductivity, which gives valuable information about conduction mechanism, is one of the important properties of ferrites.

5.1.1 Conduction Mechanism

In the case of metal oxides MeO, where Me is the metal ion, activation electrons can be represented as,

$$O^{2-}\, Me^{2+}\, O^{2-}\, Me^{2+} O^{2-} \Leftrightarrow O^{2-}\, Me^{1+}\, O^{2-}\, Me^{3+}\, O^{2-}$$

Due to high activation energy such metal oxides show high resistivity, while small activation energy that results in high conductivity is due to occupation of metal ions with different valency state on crystallographically equivalent sites.

The electron correlation effect, which is responsible for the activation energy, plays a major role in the conduction mechanism of oxides and it depends on,

(1) The difference between the electron affinity and the ionization energy of the free Me^{2+} ion.

(2) The difference in energy of the two configurations (Me^{2+}-Me^{2+}) and (Me^{3+}-Me^{1+})

(3) The difference in stabilizing of crystal field of above configuration and,

(4) The energies of polarization of the surrounding crystal lattice.

The conduction mechanism of transition metal oxides arises on account of the following facts:

(1) The oxides have generally high melting points, often in the range of 2000^{o}C

(2) At elevated temperature it is very difficult to maintain cation to anion ratio

(3) The charge carrier mobility is usually smaller in magnitude compared to many other materials

Therefore, most of the electrical measurements are generally made on sintered polycrystalline materials, as above mentioned factors give rise to unresolved difficulties in the preparation of single crystal specimens.

The relatively good conductivity of ionic compounds with an appreciable concentration of metal ions in two valence states was first investigated, for magnetite, by De Boer and Verwey [5.1]. Magnetite has 1/3 of the metal ions on tetrahedral sites and the remaining 2/3 Fe ions on octahedral sites. The latter contain equal numbers of Fe^{2+} and Fe^{3+} ions which are randomly distributed above a disorder temperature of 119K. Charge transport occurs by the transfer of electron between otherwise trivalent iron ions. The process differs from the one represented by above insofar as the energy terms (1), (2), (3) and (4) are absent. The overlap between the 3*d*-like wave functions of nearest neighbour cations is sufficient to give rise to almost metallic type of conduction. This same mechanism or electron transport does not apply to other simple ferrites where all Fe ions are trivalent. Transport may then be represented by

$$Me^{2+}O^{2-}Fe^{3+} \Leftrightarrow Me^{3+}O^{2-}Fe^{2+}$$

where the activation energy must reflect the difference between the third ionization potentials of Fe^{3+} and Me^{3+} ions in solid [5.2].

In the case of ferrites, the conduction mechanism is quite different from that in semiconductors. In ferrites the temperature dependence of mobility affects the conductivity and the carrier concentration is almost unaffected by temperature variation.

Unlike in semiconductor where in the charge carriers occupy states in wide energy band, the charge carriers in ferrites are localized at the magnetic atoms. In ferrites, the cations are surrounded by close-paced oxygen anion and as a first approximation can well be treated as isolated from each other. There will be little direct overlap of the anion charge clouds or orbitals. Alternatively, the electron associated with particular ion will largely remain isolated and hence a localized

electron model more appropriate in the case of ferrites rather than the collective electron model (Band) model. This accounts for the basically insulating nature of these materials [5.3].

These factors that differentiate the electrical behaviour of ferrites from that of semiconductor, led to *electron hopping* model [5.4, 5.5]. The conduction mechanism in ferrites is explained on the basis of the Verwey de Boer [5.6] mechanism that involves exchange of electrons between the ions of the same elements present in more than one valence sate and distributed randomly over equivalent crystallographic lattice sites. Also, conduction in ferrites is due to exchange of the *3d* electrons, localized at the metal ions, from Fe^{3+} to Fe^{2+} [5.3]. Assuming all the Fe^{2+} ions in the B sites to participate in hopping transport, the number of charge carriers works out to be the order of $10^{22}/cm^3$. Since mobility is very low, the conductivity is low, even though charge carriers are large.

Many models have been suggested to account for the electrical properties.

- Jonker [5.7] derived an expression for mobility from hopping conduction model, based on the localized levels for electrons.
- Band polaron model based on electron transition between localized cell was also suggested [5.8]
- Based on the fact that ferrites are ferrimagnetic materials and their magnetic properties would influence their electrical properties, few models have been evolved [5.9, 5.10]
- Small polaron model has been introduced by Haubenreisser [5.11]
- Lorentz and Ihle [5.12, 5.13] have explained the electrical properties on the basis of thermally activated motion of electrons and
- Srinivasan [5.14] has reported to phonon induced tunneling

The electrical properties of ferrites are affected by the distribution of cations in the sites, by non-magnetic and magnetic substitution, by the amount of Fe^{2+} present, sintering condition, grain size and grain growth effects.

5.1.2 Electron hopping and Polaron

In metallic and covalent solids, electrical conduction is mainly the result of the movement of electrons and/or holes in bands formed due to appreciable overlap of valence electron orbitals. If the interatomic distance is large, however, the orbital overlap decreases, so that the electrons tend to get localized on the parent nuclei. Incidentally, the bonding tends to become ionic. In primarily ionic, stochiometric

compounds, cation-anion interactions lead to low lying bonding levels/bands and high-lying antibonding levels/bands. The energy gap becomes high and electrical conduction via thermal excitation of electrons from the bonding (valence) to antibonding (conduction) band becomes practically impossible. Rather, designation of the antibonding band as the conduction becomes inappropriate and irrelevant. The mechanism of conduction could then be sought, say, in a process in which electrons 'hop' from one site to another within the band gap. That means, after a certain time interval, an electron acquires the necessary activation energy, jumps to an adjacent (Hopping need not necessarily be to adjacent sites only) site, provided it is vacant. Such a thermally activated hopping process becomes feasible at sufficiently high temperatures ($T>>\theta_D$, the Debye temperature). At low temperatures ($T<<\theta_D$), the probability of hopping decreases below that of tunneling, so that the situation corresponds to movement of charge carriers in a narrow conduction band. And, with increasing temperature, transition from band to hopping conduction takes place. Materials, which exhibit hopping electronic conduction, are called 'hopers' or 'electron transfer materials' Some industrially important materials such as ferrites and mixed valence semiconductors fall in to this category.

In non-stochiometric materials hopping conduction is favoured in ionic lattice, in which the same type of cations exists in two oxidation states differing by unity. Pure, stochiometric materials are, however, electrical insulators, since considerable energy needs to be expended in overcoming the repulsive force resulting from transfer of electron from one cation to another of the same oxidation state. It is relatively easier, from energy considerations, to have hopping of charge carriers in non-stochiometric samples. While in broad-band semiconductors the temperature variation of electrical conductivity is mainly due to the exponential change in charge carrier density, the hoppers are characterized by the activated mobility and the carrier density remain practically constant [5.15].

It is well known that the transition metal monoxides such as MnO, CaO, NiO, and ferrites such as Cobalt ferrite, nickel ferrite, magnesium ferrite behave as semiconductor with low mobility of charge carriers and an exponential dependence of electrical conductivity on temperature. The conventional band theory fails to predict the semiconducting properties of these materials. Bloch-type wavefunctions are not appropriate for the description of electrons which are almost wholly localized on

specific cations and appreciable correlation energy opposes the creation of Me^{1+}-Me^{+3} pairs. Another correlation phenomenon may also play a role in determining the mechanism of charge transport.

The electrostatic interaction between a conduction electron (or hole) and nearby ions may result in a displacement of the latter and hence in polarization of the surrounding region, so that the carrier becomes situated at the centre of polarization potential well. If this well is deep enough, the carrier may be trapped at a lattice site and its translation to a neighbouring site may be determined by thermal activation. This has been described as the 'hopping mechanism' and the probability of hopping will contain a term proportional to exp (-q/kT), where q is an activation energy. Heikes and Johnston [5.16] have derived an expression for the mobility of a charge charier subject to the hopping mechanism

$$\mu = \frac{e^2 a^2 \omega_0}{kT} \exp\left(-q/kT\right)$$

where a is the distance between nearest neighbour cations and ω_0 the frequency of vibration of the crystal lattice. With the development of polaron theory it has become evident the above equation is a special case of a much more complicated relationship between μ and the parameters of the ionic lattice [5.17].

The Born-Oppenheimer approximation, assumed in the energy band theory of solids, is no longer tenable when applied to ionic solids. During a longitudinal optical lattice vibration, the positive and negative ions move in opposite directions and this motion set up alternative regions of negative and positive charge densities relative to the equilibrium values. The negatively charged electron can lower its energy by indicating a lattice polarization. In other word, strong electron-optical phonon interactions must exist, which are neglected in he Born-Oppenheimer approximation. The situation is treated by introducing a particle called polaron [5.15].

The conduction electron moving through a primarily ionic solid polarizes and distorts the lattice in its vicinity. A polaron consists of the charge carrier and the distortion of the (ionic) lattice induced by the carrier itself. Further, polarons can be 'large' or 'small'. The large polaron case corresponds to a situation in which the lattice distortion induced around a charge carrier extends over distances larger that the lattice constant. For the small polaron case, the lattice distortion extends over a distance smaller that the lattice constant. Further, for large and small polarons, half

the bandwidth is larger and smaller, respectively, than the maximum polaron binding energy [5.15].

A small polaron is defect created when an electronic carrier becomes trapped at a given site as a consequence of the displacement of adjacent atoms or ions. The entire defect (carrier plus distortion) then migrates by an activated hopping mechanism. Small polaron formation can take place in materials whose conduction electrons belong to incomplete inner (*d or f*) shell which due to small electron overlap, tend to form extremely narrow bands. The possibility for the occurrence of hopping conductivity in certain low mobility semiconductors, especially oxides, has been widely recognized for some time [5.18]. The concept of large polaron is most useful when the carrier mobility is high and the carrier density and temperature both are low [5.19].

Small polaron motion proceeds relatively slowly via a succession of phonon-assisted hopping events. As a result, the small polaron drift mobility increases as a thermal agitation of the solid increases. Above a temperature comparable to the solid's phonon temperature, the diffusivity increases in the Arrhenius manner with reciprocal temperature.

The migration of small polaron requires the hopping of both the electron and the polarized atomic configuration from one site to an adjacent one [5.20]. For drift mobility takes the form

$$\mu = (1-c)ea^{2\Gamma / kT}$$

where e is the electronic charge, a the lattice parameter, c is the fraction of sites which contain an electron (c = n/N), n is the number of electrons and N the number of available site/unit volume. The quantity Γ is the jump rate of polaron from one site to a specific neighbouring site given by

$$\Gamma = P\mu_0 \exp(-E_H / kT)$$

where μ_0 is the appropriate optical mode phonon frequency; E_H is the activation energy; and P is a factor which gives the probability that the electron will transfer after the polarized configuration has moved to the adjacent site. In evaluating P there are two cases to consider depending on the relative value of the electron transfer time t_{el} and the t_{at}, the atomic transfer time which characterizes the transfer of atomic polarization between adjacent sites. Specially, in the adiabatic case $t_{el} << t_{at}$ and P =1.

On other hand, for the non-adiabatic case, for which $t_{el} >> t_{at}$, P<1 and take the form $P \alpha J^2 / (kT)^2$.

For the hopping of polarons in this model we get the expression for the conductivity as [5.18].

$$\sigma = A/T \exp(-E_H/kT)$$

where the factor A is

$$A = Npc(1-c^2) e^2 a^2 \gamma_o / k$$

The small polaron model also explains the low value of mobility, temperature independent Seebeck coefficient and thermally activated hopping. In addition to these properties if the hopping electron becomes localized by virtue of its interaction with phonons, then a small polaron is formed and the electrical conduction is due to hopping motion of small polarons. Some theoretical literature has been developed which consider the small polaron model and its consequences [5.21-5.25]. The particular model developed by Fröhlich [5.26] in order to formulate the interaction Hamiltonian for the 'large Polarons' and introduced the parameter for the discussion of polaron as electron-phonon coupling constant [5.27].

5.2 D. C. Resistivity

Electrical resistivity (also known as specific electrical resistance) is a measure of how strongly a material opposes the flow of electric current. A low resistivity indicates a material that readily allows the movement of electrical charge. The SI unit of electrical resistivity is the ohm meter.

The electrical resistivity ρ (*rho*) of a material is given by

$$\rho = R \frac{A}{\ell}$$

where

ρ is the static resistivity (measured in ohm metres, Ωm);

R is the electrical resistance of a uniform specimen of the material (measured in ohms, Ω);

ℓ is the length of the specimen (measured in metres, m);

A is the cross-sectional area of the specimen.

Electrical resistivity can also be defined as

$$\rho = \frac{E}{J}$$

where

E is the magnitude of the electric field (measured in volts per meter, V/m);
J is the magnitude of the current density (measured in amperes per square metre, A/m²).

Finally, electrical resistivity is also defined as the inverse of the conductivity σ (*sigma*), of the material, or

$$\rho = \frac{1}{\sigma}.$$

In general, electrical resistivity of metals increases with temperature, while the resistivity of semiconductors decreases with increasing temperature. In both cases, electron-phonon interactions can play a key role.

Ferrites are semiconducting in nature and have a very wide range of resistivity from 10^{-4} to 10^{9} Ω.m at room temperature [5.28]. These variations in resistivity of the ferrites are depending upon the nature and their compositions. In ferrite, the high value of resistivity is associated with the simultaneous presence of Ferrous and Ferric ions on equivalent lattice sites (usually the octahedral sites). In nickel-zinc ferrite it was found that the resistivity was about 10 Ω.m when the material contained 0.42 percent by weight of ferrous oxide but this resistivity increased approximately one thousand fold when the specimen was more completely oxidized [5.29]. In polycrystalline ferrites the electrical properties are predominantly governed by heat treatment. Number of parameters like grain size, density, porosity, homogeneity-induced strains etc. and method of preparation, can affect the electrical properties of manufactured components [5.30].

In the case of ferrites, resistivity decreases as temperature increases indicating negative temperature coefficient of resistance. Verwey et al [5.31] in the year of 1950 explained the mechanism of conduction in ferrites. According to this mechanism the extra electron on ferrous ion (Fe^{2+}) require little energy to move to a similarly situated of the ferric ion (Fe^{3+}). The valence states of the two ions are interchanged. Under the

influence of an electric field, these extra electrons can be considered to constitute the conduction current, jumping or hopping from one iron ion to the next.

Since the ferrites belong to a class of semiconductors, their resistivity (ρ) decreases with increase in temperature and thus (ρ) obeys the relation,

$$\rho = \rho_0 \exp(\Delta E/kT)$$

where, ρ_0 = a constant

T = absolute temperature

k = Boltzmann's constant

and ΔE = Activation energy

This relation is indeed often observed and the activation energy ΔE can then be interpreted as the energy required causing the electron jump referred to above. The activation energy varies from several hundredths of eV for Fe^{2+} content to ~0.2 eV to 0.6 eV for stochiometric ferrites. As would be expected with such a conduction mechanism, the high activation energy is associated with a high resistivity at room temperature. It has been found that the pre-exponential factor ρ_0 is almost fully determined by the Fe^{2+} concentration [5.32]. The above mention 'small polaron hopping model' which is believed to be relevant for the conduction mechanism of ferrites, the activation energy ΔE is the sum of the energy needed for removing the electron from and Fe^{2+} (i.e. binding energy of the polaron) and of the mobility activation energy connected with transferring an electron between Fe^{2+} and Fe^{3+} ions. Thus, the higher value of electrical resistivity and activation energy for stochiometric ferrites is due to lack of Fe^{2+} ions. This is because the energy levels of M^{2+} ions in MFe_2O_4 are usually situated below those of Fe^{2+} [5.33]

By addition of small amount of foreign oxides, the conductivity of high resistivity oxides can be increased. If a cation of low valence state is substituted then it gives to p-type of conduction, whereas the substation of cation of high valence state gives rise to n-type of conduction

Apart from the inherent properties of the solid material there are various contributions by which resistivity will also be affected as,

(1) There are some pores in a polycrystalline samples, so that the apparent density is less than that calculated from the lattice dimensions. The air filled pores will have resistivity different from that of a ferrite.

(2) The grain size of the individual crystallites in a polycrystalline samples can affect the number of grain to grain contacts and thus influence the conduction paths and so the resistivity.

(3) Chemical inhomogenity occurs during the preparation, which depends on heat treatment.

The resistivity of ferrites and exponential dependence on temperature and in many cases the slope of the logρ Vs 10^3/T curve changes at the Curie point. The activation energy increases on changing from ferromagnetic to paramagnetic region. This anomaly strongly supports the influence of magnetic ordering upon the conductivity process ferrites.

Experimental Details of D. C. Resistivity:

The compositional and temperature dependence of d. c. electrical resistivity for the unirradiated and irradiated systems $Li_{0.5(1+x)}Ti_xAl_{0.1}Fe_{2-2x}O_4$, $Li_{0.5(1+x)}Ti_xCr_{0.1}Fe_{2-2x}O_4$ $CuAl_xCr_xFe_{2-2x}O_4$ (Slow-Cooled & Quenched), $MnAl_xCr_xFe_{2-2x}O_4$ were carried out at Department of physics, Saurashtra University, Rajkot. All the samples prepared by usual double sintering ceramic technique were in the form of cylindrical pellet of 10 mm diameter with thickness of 2 to 3 mm and 0.5mm in unirradiated and irradiated samples, respectively. In the electrical resistivity measurements a typical sample holder is shown in Fig. 5.1 specially designed and fabricated for the resistivity measurement was used. It consists of two ceramic beads with supporting metal rods. The electrode E_1 and E_2 are also shown in this figure. The spring loaded brass electrode (E_2) is introduced into the ceramic beads and it pressed hard against the surface of the pellets. The brass electrode (E_1) is fixed at the other end.

The resistance of a pellet was measured by two terminal method using meg-ohm meter supplied by Arun electronics. The sample surfaces were rubbed by graphite and thin aluminium foils were placed between the terminals of sample holder with the pellet was placed in a horizontal electric furnace to study the change in resistivity with temperature. The temperature of the furnace was controlled by maintaining the current passing through the heater by means of current controller. The temperature of the sample was measured with Cr-Al thermocouple. Photograph of experimental set-up of d. c. resistivity is given below. The resistance of the each pellet was measured for raising and falling of temperature at the gap of 10^0C. The thickness

and diameter of the pellets were measured by digital vernier calipers. From these observations the resistivity was found us. Logarithm of resistivity (ρ) was plotted against reciprocal of temperature (10^3/T). The activation energies for the ferrimagnetic region (E_f) and paramagnetic region (E_p) in electron volt (eV) were determined from the slopes of these plots.

The activation energy were calculated using the following Arrhenius equation

$$\rho = \rho_0 \exp (\Delta E/kT)$$

where ρ_0 is a constant, T is the absolute temperature, k is Boltzmann's constant, ΔE is the activation energy, which is further simplified to:

$$\rho /\rho_0 = \exp (\Delta E/k\Delta T)$$

$$\ln (\rho /\rho_0) = \Delta E/k\Delta T$$

$$\Delta E = k\Delta T. \ln (\rho /\rho_0)$$

$$= 2.303. k\Delta T. \log_{10} (\rho /\rho_0)$$

$$= 2.303. k\Delta T. [\log_{10} \rho - \log_{10}\rho_0]$$

$$\Delta E = 2.303 \times 8.6 \times 10^{-5} \text{ eV } \{[\log_{10} \rho - \log_{10}\rho_0]/ (1/ \Delta T)\}$$

The bracketed term in above equation is nothing but slope of the particular region.

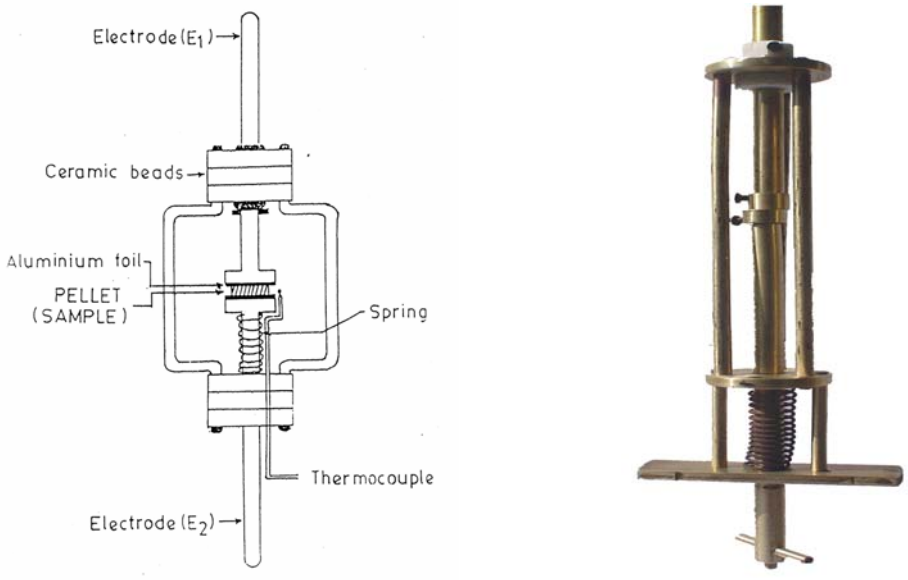

Fig. 5.1 Sample holder

Photograph of and d. c. resistivity set-up

5.3 Thermoelectric Power

The thermopower, or thermoelectric power, or Seebeck coefficient 'α' of a material is a measure of the magnitude of an induced thermoelectric voltage in response to a temperature difference across that material. The thermopower has units of (V / K). The term thermopower is a misnomer since it measures the voltage or electric field (not the electric power) induced in response to a temperature difference. An applied temperature difference causes charged carriers in the material, whether they are electrons or holes, to diffuse from the hot side to the cold side, similar to a classical gas that expands when heated. Mobile charged carriers migrating to the cold side leave behind their oppositely charged and immobile nuclei at the hot side thus giving rise to a thermoelectric voltage (thermoelectric refers to the fact that the voltage is created by a temperature difference). Since a separation of charges also creates an electric field, the buildup of charged carriers onto the cold side eventually ceases at some maximum value since there exists an equal amount of charged carriers drifting back to the hot side as a result of the electric field at equilibrium. Only an increase in the temperature difference can resume a buildup of more charge carriers on the cold side and thus lead to an increase in the thermoelectric voltage.

The thermopower of a material, represented as α, depends on the material's temperature, and crystal structure. Typically metals have small thermopowers because most have half-filled bands. Electrons (negative charges) and holes (positive charges) both contribute to the induced thermoelectric voltage thus canceling each other's contribution to that voltage and making it small. In contrast, semiconductors can be doped with an excess amount of electrons or holes and thus can have large positive or negative values of the thermopower depending on the charge of the excess carriers.

The sign of the thermopower can determine as to which charge carriers dominate the electric transport in both metals and semiconductors.

If the temperature difference ΔT between the two ends of a material is small, then the thermopower of a material is defined as:

$$\alpha = \frac{\Delta V}{\Delta T}$$

and a thermoelectric voltage ΔV is seen at the terminals.

This can also be written in relation to the electric field E and the temperature gradient ΔT, by the equation:

$$\alpha = \frac{E}{\Delta T}$$

Hall effect and thermoelectric properties are widely used in the interpretation of the conduction mechanism in semiconductors. The interpretation of Hall effect is more straightforward, and it also give precise results. However, in the case of low mobility materials such as ferrites, it is sometimes difficult to measure the Hall effect; in such cases thermoelectric power measurements is only alternative. The sign of thermo emf gives vital information about the type of conduction in semiconductors-whether it is p-type or n-type. Another important significance of thermo emf is that it enables one to calculate the values of the Fermi-energy and charge carrier concentration. A knowledge of Fermi-energy helps in the determination of various regions, Viz, impurity conduction, impurity exhaustion, and intrinsic conduction region of a semiconductor.

Theory of Seebeck Coefficient 'α' [5.34]

An expression for the chemical potential may be given as: $\mu = \overline{E} - T\overline{S}$

where $\overline{E}$ and $\overline{S}$ are partial molal internal energy and entropy respectively. If two ends of a samples are held at two different temperatures (T_1, T_2) such that $|T_1\text{-}T_2| << T_1$ or

T_2, then $\overline{E}$ and $\overline{S}$ could be considered as temperature –independent and the Seebeck coefficient (α) is given by,

$$\alpha = \frac{d\left(\theta/e\right)}{dT}$$

$$= \frac{1}{e}.\frac{d\mu}{dT}$$

$$\alpha = -\frac{\overline{S}}{e}$$

The physical meaning of $\overline{S}$, thus is that it is the entropy associated with the mobile charge carrier.

Since electrons remain localized around the lattice sites in between jumps, we could consider a collection of carriers as more or less fixed. Then $\overline{S}$ can be given by

$$\overline{S} = \overline{S}_c + \overline{S}_T$$

where $\overline{S}_c$ and $\overline{S}_T$ are the configuration and thermal entropy terms for the electrons. Now $\overline{S}_c$ is related to the distribution of n carriers (per unit volume) over c'/V sites (per unit volume). For n < c'/V, i.e., s < 1

$$S_c = k_B \ln \frac{\left(\frac{c'}{V}\right)!}{\left(\frac{c'}{V} - n\right)!n!}$$

Using stirling's approximation for large values of c'/V and n, we get

$$\ln\left(\frac{c'}{V}\right)! = \left(\frac{c'}{V}\right)\ln\left(\frac{c'}{V}\right) - \left(\frac{c'}{V}\right);$$

$$\ln\left(\frac{c'}{V} - n\right)! = \left(\frac{c'}{V} - n\right)\ln\left(\frac{c'}{V} - n\right) - \left(\frac{c'}{V} - n\right); \text{ and}$$

ln n! = n ln n-n

Therefore, $S_c = k_B\left\{\left(\frac{c'}{V}\right)\ln\left(\frac{c'}{V}\right) - n\ln n - \left(\frac{c'}{V} - n\right)\ln\left(\frac{c'}{V} - n\right)\right\}$

Then, $\overline{S}_c = \frac{\partial S_c}{\partial n}$

$= k_B\left\{\ln\left(\frac{c'}{V} - n\right) - \ln n\right\}$

$= k_B \ln\frac{\left(\frac{c'}{V} - n\right)}{n}$

Since $n = \frac{c's}{V}$, $\frac{n}{s} = \frac{c'}{V}$

$\overline{S}_c = k_B \ln\frac{\left(\frac{n}{s} - n\right)}{n} = k_B \ln\left(\frac{1-s}{s}\right)$

Therefore, $\overline{S} = k_B \ln\left(\frac{1-s}{s}\right) + \overline{S}_T$ or $\alpha = -\frac{\overline{S}}{e} = -\frac{k_B}{e}\left\{\ln\left(\frac{1-s}{s}\right) + \frac{\overline{S}_T}{k_B}\right\}$

Generally, $\ln\left(\frac{1-s}{s}\right) >> \frac{\overline{S}_T}{k_B}$, so that the Seebeck coefficient (α) is independent of temperature. If the carriers are holes , then

$\alpha = +\frac{k_B}{e}\left\{\ln\left(\frac{1-s}{s}\right) + \frac{\overline{S}_T}{k_B}\right\}$

Thus if

s$\rightarrow$1, $\alpha \rightarrow \infty$ (large positive)

s$\rightarrow$0, $\alpha \rightarrow$ -∞ (large negative)

s$\rightarrow$1/2, $\alpha \rightarrow$ 0 [5.35].

Theory of Fermi energy 'E_F'

Fermi energy (E_F) is one of the most important concepts in solid state science. It originates in the Fermi-Dirac (FD) statistics, which is applicable to indistinguishable particle with half- integral spin and subject to the Pauli Exclusion Principle, such as electron in solids.

The Fermi energy in the case of semiconductor can be obtained from relation

$$QT = (E_G - E_F) + 2KT \text{ , for n-type semiconductor}$$

$$QT = E_F + 2KT \text{ , for p-type semiconductor.}$$

Where, E_G = Energy gap of the ferrite semiconductor,

E_F = Height of the Fermi energy level from the top of the filled valency band and

2KT = the term which accounts for the transfer of kinetic energy of the carriers in moving from the hot region of the ferrite to a cold one.

While discussing the electrical properties of $\propto$ - Fe_2O_3 for which the mobility of the charge carrier is low, Morin [5.36] assumed that the conduction is occurring in exceedingly narrow bands or in localized levels. This assumption leads to the result that the kinetic energy term in the Seebeck effect can be neglected, so that for electrons alone, $QT = E_G - E_F$, while for holes alone $QT = E_F$.

In the region where conduction is due to one kind of charge carriers (electron or holes; not both) the relation between the Seebeck coefficient (α) and Fermi energy (E_F) will be given by [5.37, 5.38]

$$E_F = e\alpha T - AkT$$

Where A is the term connected with the kinetic energy of charge carriers, e, k and T are charge of carrier; Boltzman constant (8.6×10^{-5} eV) and absolute temperature respectively. The value of E_F calculate as a function of temperature for two values of A (A = 0 and 2) and the extrapolated value of E_F to T = 0K, gives the value of E_F (0).

Charge carrier concentration 'n_c'

For a hopping mechanism, the Seebeck coefficient 'α', is independent of temperature and its magnitude primarily depends upon the density of the charge carriers. Its is expressed in the form of the Heike's formula [5.39].

$$\alpha = \frac{k}{e}\left\{\ln\left(\frac{1-s}{s}\right)+\frac{\overline{S}_T}{k}\right\}$$

where $\overline{S}_T$ is the entropy transport by charge carriers, which is temperature independent and $\frac{\overline{S}_T}{k}$ is very small in oxide materials (i.e. ~ 10 μV/k), s is given by n_c/N, where n_c is the carrier concentration and N is the density of states or concentration of the electrical levels involved in the conduction process. Neglecting the term $\frac{\overline{S}_T}{k}$ from the relation and equation can be written as,

$$\alpha = \frac{k}{e}\left\{\ln\left(\frac{1}{s}-1\right)\right\} = \frac{k}{e}\left\{\ln\left(\frac{N}{n_c}-1\right)\right\}$$

$$\frac{\alpha e}{k} = \ln\left(\frac{N}{n_c}-1\right)$$

$$\exp\left(\frac{\alpha e}{k}\right) = \left(\frac{N}{n_c}-1\right)$$

$$\frac{N}{n_c} = 1+\exp\left(\frac{\alpha e}{k}\right)$$

$$n_c = N\left[\frac{1}{1+\exp\left(\frac{\alpha}{k/e}\right)}\right]$$

If V is the volume of the sample under study above equation can be written as:

$$n_c = \frac{N}{V}\left[\frac{1}{1+\exp\left(\frac{\alpha}{k/e}\right)}\right]$$

The values of charge carrier concentration per unit volume have been calculated for all the compositions at each temperature by using the value of the Seebeck coefficient. N is the density of states, in the case of low mobility semiconductors like ferrites having exceedingly narrow bands or localized levels; the density of states N in case of ferrites is $10^{22}/cm^3$ [5.40, 5.41].

Mobility 'μ_D'

The mobility is defined as the magnitude of the average drift velocity per unit electric field and taken as positive for both electron and holes, although their drift velocities are in opposite directions. This is because the electrons and holes are oppositely charged and their currents reinforce one another. The two important factors responsible for the temperature variation mobility are (a) phonons and (b) ionized impurity atoms.

The mobility (μ_D) calculated of the charge carriers can calculate from the experimental values of the electrical resistivity (ρdc) and charge carrier concentration (n_c) using the formula:

$$\mu_D = \frac{1}{\rho_{dc}.n_c.e} = \frac{1}{(ohm.cm)\left(\frac{1}{cm^3}\right)(coulomb)}$$

$$= \frac{cm^2}{ohm.Amp.Sec} \qquad \text{(Coulomb= Amp.Sec)}$$

$$= \frac{cm^2}{Volt.Sec}$$

where e is charge of electron (1.6 x 10-19 coulomb)

Experimental Details of Thermoelectric power:

All the above mention ferrites measured Seebeck coefficient using thermo-emf set up at Department of Physics, Saurashtra University, Rajkot. The experimental set-up to determine thermo-emf of ferrite samples is shown in the Fig. 5.2. It consists of a point contact probe, which acts as a hot junction and a base, which acts as a cold junction. Between the two junctions a ferrite sample is kept. The temperature of the hot probe is raised to a maximum of around 200˚C with the help of an electric heater, which is wound on the hot probe.

A pointed hot probe is used here since ferrite samples are very good thermal conductors; if a pointed probe is not used to upper and the lower surfaces of the samples will attain almost the same temperature and no temperature gradient will be maintained between them. The hot probe and cold base are connected to a digital microvolt meter (model: DMV 001) supplied by Scientific Equipment & Services for measuring the thermo-emf. The ferrite specimens having dimensions of approximately 0.3×0.3 sq.cm and 0.2 to 0.3 cm thickness are used in the present investigation. A photograph of experimental set-up used for thermoelectric power measurements is also displayed below.

In the case of an n-type semiconducting material, the hot surface becomes positively charged, as it loses some of its electrons. The cold surface of the semiconductor becomes negatively charged due to the diffusion of free electrons from the hot portion. Conversely, in a p-type semiconducting material, the hot surface becomes negative, and the cold one positive. Thus the type of conduction in a given semiconducting material can readily be determined from the sign of the thermo-emf.

The values of the thermo-emf have been noted while cooling, because the samples will attain sufficient thermal stability while cooling rather than while heating. The sample is maintained at a given temperature for about 15 to 20 minutes. The temperatures of the two surfaces have been measured with the help of a copper-constantan thermo-couple.

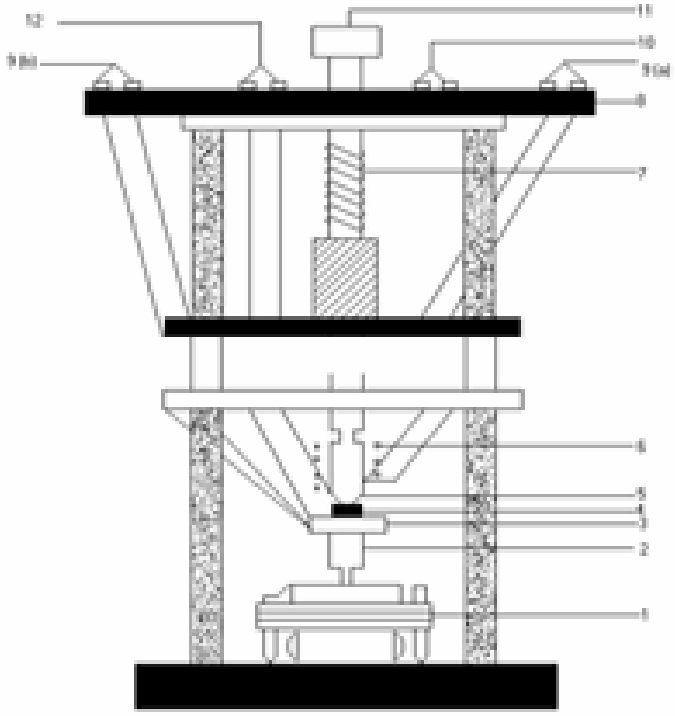

Fig. 5.2 Experimental set-up used for Thermo electric power measurements

1.Base 2.Insulator 3. Electrode 4. Sample 5. Point contact electrode 6. Heater 7.Spring loaded arrangement 8. Insulator 9(a) Hot junction thermocouple 9(b) Cold junction thermocouple 10. Heater supply 11.Knob 12. Microvoltmeter terminals.

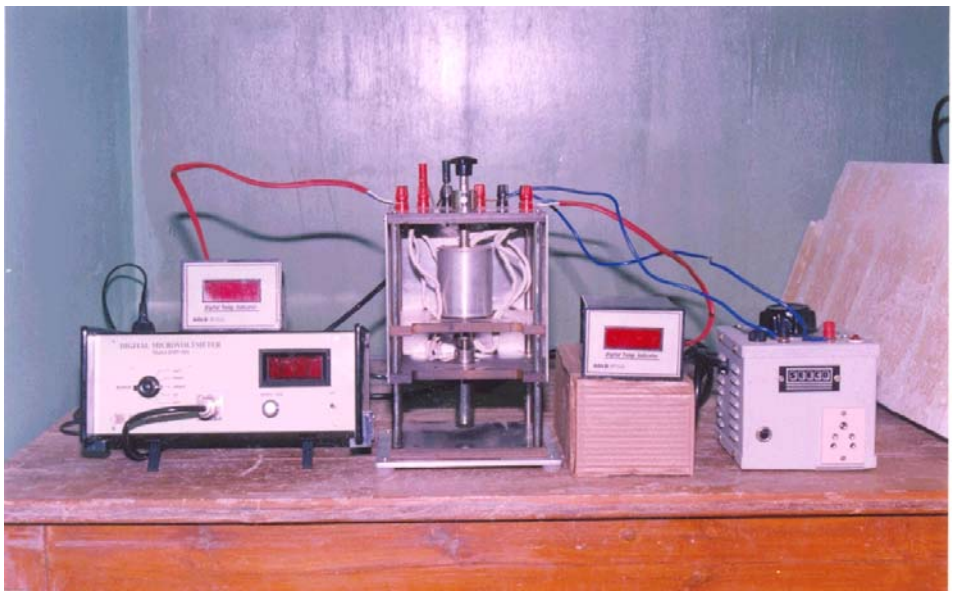

Thermo-electric Power set-up

5.4 Temperature and Frequency dependent Dielectric Properties

Dielectric materials are insulators as they have a large energy gap between the valence and conduction bands. Thus, the electrons in the valence bands cannot jump to the conduction band. Therefore, the resistivity of these materials is very high. Most ceramics are dielectric materials and have a mixture of ionic and covalent bonding. Although these materials do not conduct electric current when an electric field is applied, they are not inert to the electric field. The field may cause a slight shift in the balance of charge within the material to form an electrical dipole. Thus, the material is called a "dielectric" material. The two important applications of dielectric materials are electrical insulators for preventing electricity transfer and capacitors for the storage of electrical charges.

The most important properties of dielectric materials are:

1. Dielectric Constant (Relative permittivity)
2. Complex dielectric constant
3. Tangent of loss angle (tanδ)
4. Dielectric strength

The science of dielectrics is remarkably multi disciplinary- it falls in the field of physics, chemistry, and electrical engineering. The motivation of the various disciplines in pursuing relaxation research was likewise very diverse-electrical engineers were interested primarily in the level of dielectric loss and in the electrical strength of the insulation as well as in its life under operational conditions. Some engineers were interested in the movement of charge on dielectric surfaces which involves predominantly time domain (TD) measurements. Chemists were using dielectric relaxation as a handle on molecular dynamics and were using both the temperature dependence of permittivity at a constant frequency and its frequency dependence at a constant temperature as the principal types of measurement. Such measurements are also being used to monitor the progress of chemical reactions in which dipoles are being created or lost.

5.4.1 Dielectric Constant, Complex Dielectric Constant, Loss tangent and AC resistivity

The capacitance of a parallel plate capacitor (Fig. 5.3), C_0, is proportional to the plate area A, and is inversely proportional to the distance between the two plates, d:

$$C_0 \propto A \text{ and } C_0 \propto 1/d$$

In vacuum, C_0 can be expressed as

$$C_0 = \varepsilon_0 A/d \quad \text{... (5.1)}$$

where ε_0 is the permittivity of vacuum and a constant: $\varepsilon_0 = 8.854 \times 10^{-12}$ F/m.

If a dielectric material is inserted into the plate (Fig. 5.3), Eq. 5.1 should be rewritten as

$$C = \varepsilon A/d \quad \text{… (5.2)}$$

Where ε is defined as the permittivity of the materials. The Permittivity is associated with the ability of the material to polarize and store a charge within the material.

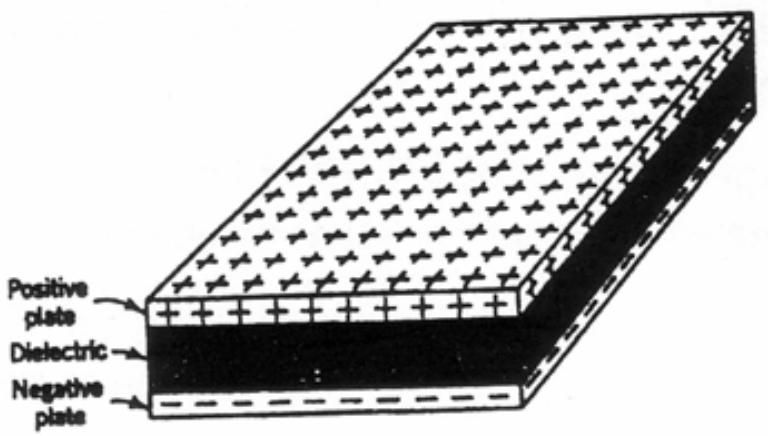

Fig. 5.3 A parallel plate capacitor with dielectric between plate

The dielectric constant (ε') or relative permittivity (ε_r) is the ratio of the permittivity of the dielectric material to the permittivity of vacuum:

$$\varepsilon_r \text{ or } \varepsilon' = \varepsilon/\varepsilon_0 \quad \text{… (5.3)}$$

$$C = \varepsilon'\varepsilon_0 A/d = \varepsilon' C_0 \quad \text{… (5.4)}$$

$$\varepsilon' = C/C_0 \quad \text{… (5.5)}$$

The dielectric constant (ε') is describing the relative ability of a material to polarize and store a charge.

The name "dielectrics", as used here, refers to any material when viewed from the standpoint of electric response. In their reaction to sinusoidal electric fields, dielectrics can be characterized by their complex permittivity,

$$\varepsilon = \varepsilon' - j\varepsilon''$$

These parameters, the real permittivity ε' (dielectric constant), describing the storage of electric energy and the loss factors ε'' (complex dielectric constant) its dissipation, are actually measured in reference to vacuum as a relative complex permittivity. The

absorption of electrical energy by the dielectric material that is subjected to an alternating electric field is termed as dielectric loss. The dielectric loss factor or loss tangent, tanδ is the ratio between the imaginary and the real part of the dielectric constant and is given by the reciprocal of the quality factor Q and that is given by

$\tan\delta = \varepsilon''/\varepsilon' = 1/Q = (\omega C_p R_p)^{-1} = 4\pi\sigma/\omega\varepsilon'$ [5.42]

where $C_p = \varepsilon'\varepsilon_0 A/d$

and $R_p = d/\sigma A$

where σ is the ac conductivity, which is reciprocal of the dc resistivity ($\sigma = 1/\rho$).

The effect of temperature on the dielectric constant of ionic material is generally not high at low temperatures, and if there are no structural changes. It increases with temperature. At elevated temperatures, ion mobility is much higher than at lower temperatures. However, some materials may show large and sudden changes in dielectric constant when the temperature increases.

5.4.2 Dielectric Strength:

Dielectric strength is the maximum voltage gradient that dielectrics can withstand before failure occurs. It is also called breakdown strength.

There are three different mechanisms of dielectric breakdown: intrinsic, thermal and discharge. Intrinsic breakdown begin with the appearance of a number of electrons in the conduction band. These electrons are accelerated rapidly by the high field in the dielectric, thus obtaining high kinetic energy. As a large number of electrons initiate this process, it multiplies itself. The current increases rapidly and finally results in breakdown. Thermal breakdown occurs when dielectric losses cause heating which lowers the breakdown strength. Each dielectric material has a temperature limit over which thermal breakdown may take place. Discharge breakdown takes place when he gas in the dielectric becomes ionized by the field. The gaseous ions are accelerated by the field and impact on the side of the cavity, causing damage and more ionization. Dielectric breakdown may also result in local melting, burning or vaporizing.

5.4.3 Dipoles and Polarization

The dielectric constant of material is an interesting material parameter only if the material is exposed to an electrical field. The effect of the *electrical field* can be twofold:

1. It *induces electrical dipoles* in the material and tries to align them in the field direction. In other words, *with* a field, dipoles come into being that does not exist *without* a field.
2. It tries to *align dipoles* that are already present in the material. In other words, the material *contains electric dipoles even without a field*.

Of course we also may have a combination of both effects: The electrical field may change the distribution of existing dipoles while trying to align them, *and* it may generate new dipoles in addition.

The *total* effect of an electrical field on a dielectric material is called the polarization of the material.

The polarization of charges within the dielectric material in the following ways:

(a) electrons and (positively charged) nuclei will be displaced in such a way that electrons will move in the positive field direction and nuclei in opposite direction

(b) if the bonding were primarily ionic, cations and anions will get displaced with respect to one another; and

(c) if the material contained complex ions or molecules possessing permanent dipole moment, the dipole will tend to align themselves with the filed direction. The net effect will be to induce dipole moment within the material (setting up an internal field).

The term 'polarization' refers to the total induced electric dipole moment per unit volume of the material.

The dipole moment of a pair of charges q separated by a distance r is defined as p = qr. The polarization, P, of a dielectric is the dipole moment per unit volume. The electric displacement, D, and the relative dielectric constant (relative permeability), ε_r are related to the polarization, P, by the following relationship:

$$D = \varepsilon_0 \epsilon + P = \varepsilon_r \varepsilon_0 \epsilon$$

Where ϵ is the electric field and ε_0 is permittivity of free space.

Polarization in dielectric materials has the following distinguishable mechanisms:

(i) Electronic polarization (α_e)

(ii) Ionic polarizationαe (α_i)

(iii) Molecular or orientational polarization (α_o)

(iv) Space charge polarization (α_s)

Electronic polarization: when an electric field is applied to an atom, the electron structure is distorted, with the electrons concentrating on the side of the nucleus near the positive end of the field. The atom acts as a temporarily induced dipole. This effect is small and occurs in all materials.

Ionic polarization: When an ionically bonded material is placed in an electric field, the bonds between the ions are elastically deformed. Consequently, the charge is slightly redistributed within the material. Depending on the direction of the field, cations and anions move either closer together or further apart. The temporarily induced dipoles may also change the overall dimensions of the materials.

Molecular or orientational polarization: Some materials contain natural dipoles. When a field is applied, the dipoles rotate to line up with the applied field. This is also a type of temporarily polarization. In some materials, polarization occurs in the same manner. However, when the filed is removed, the dipoles remain in alignment, thus causing permanent polarization.

Space charge polarization: This type of polarization is caused by the accumulation of charges at phase interfaces in the multiphase dielectrics. When one of the phases has a much higher resistivity than the other, the charge moves on the surface when the material is placed in an electric field. This type of polarization is often found in ferrites and semiconductors at elevated temperatures.

Fig. 5.4 (a), (b), (c), (d) show a schematic drawing of the electronic, Ionic, Molecular and Space charge polarization, respectively. The total polarization of the dielectric can be represented as the sum of the contributions of these mechanism,

$$\alpha = \alpha_e + \alpha_I + \alpha_o + \alpha_s$$

Depending on the detailed nature of the chemical bonding, the magnitudes of the different contributions will vary.

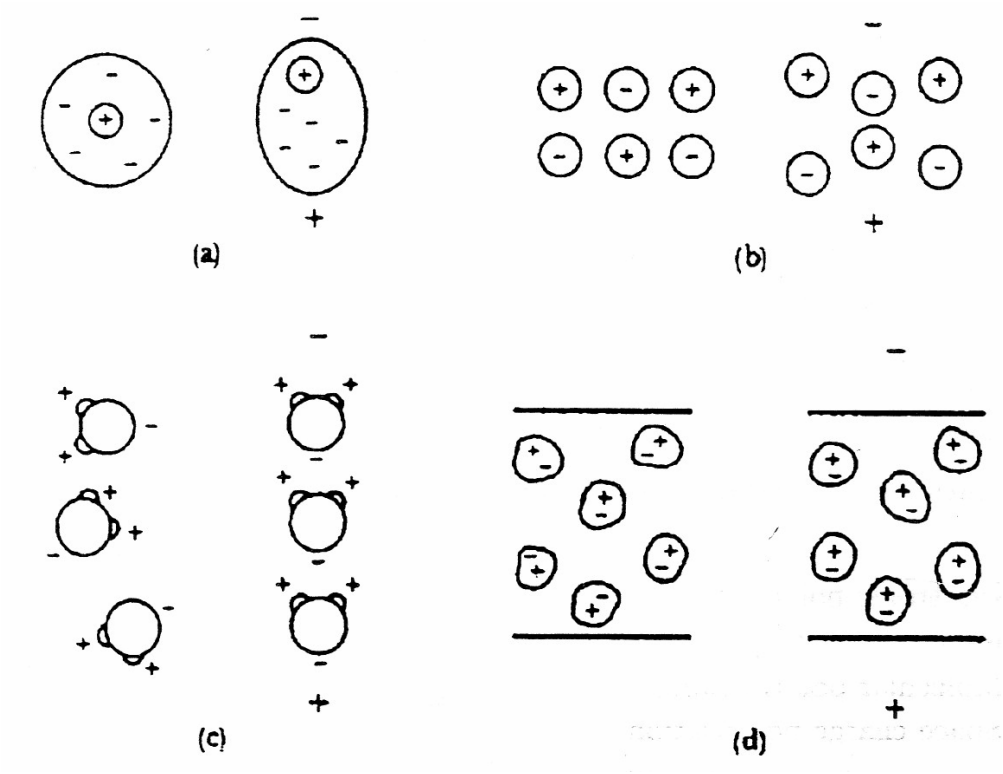

Fig. 5.4 Polarization mechanism in materials: (a) electronic polarization (b) ionic polarization (c) molecular polarization (d) space charges polarization [5.43]

5.4.4 Relaxation Time and Relaxation Frequency

When a parallel plate capacitor works in an AC field, the total polarization, P, and the relative permittivity, ε_r, depend on how easily the dipoles can reverse alignment following the change in the field. Some of the polarization mechanisms do not permit rapid reversal of the dipole alignment. The time required to reach the equilibrium orientation is called the relaxation time and its reciprocal is called relaxation frequency. Fig. 5.5 displays the plots of total polarization and absorption versus the frequency, showing that the different polarization mechanisms have different frequency behaviours. For example, while electronic polarization can be quickly built up in 10^{-14}-10^{-15} sec, ionic polarization may require time period as long as 10^{-11}-10^{-13} sec. As a consequence, while both ionic and electronic polarizabilities respond in the regions from microwave to infrared, only the electronic polarizability contributes to the polarization in the optical to ultraviolet regions. Each contribution to the polarization decays as its characteristic resonant frequency is exceeded.

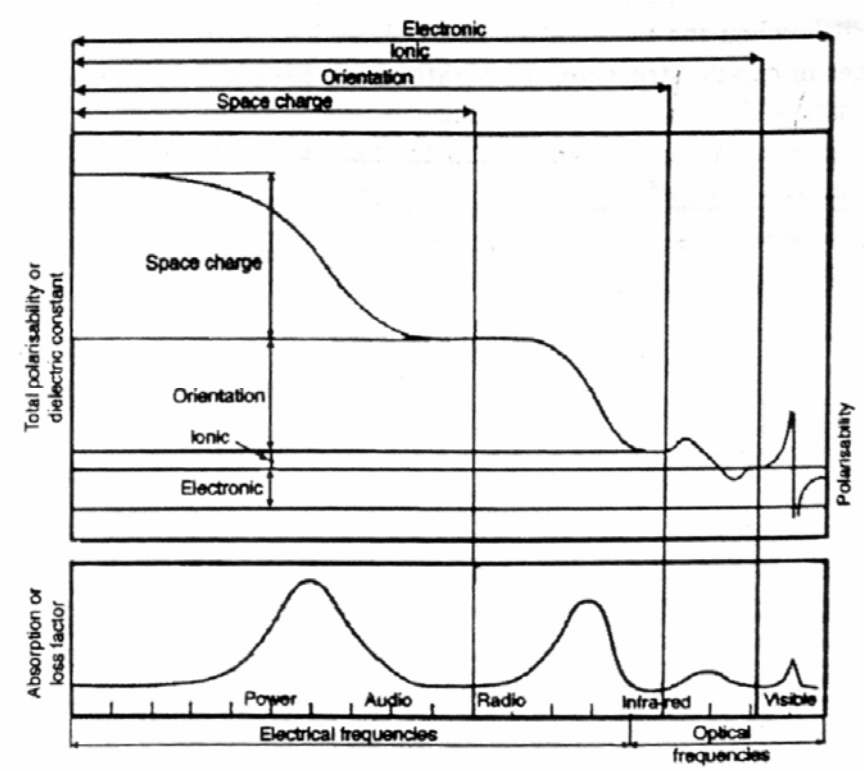

Fig. 5.5 Variation of total polarization and dielectric absorption as a function of frequency

Dielectric spectroscopy in a broad frequency range is widely used to study the electric and dielectric behaviour of various materials. One can obtain important information on the relaxation process occurring in the system from the dielectric frequency response curve at different temperatures. Andrew K. Jonscher [5.44] has given the dielectric relaxation in solids, making use of the existence of a 'universality' of dielectric response regardless of a wide diversity of materials and structures, with dipolar as well as charge-charge polarization. The relaxation on the basis of time-domain (TD) measurements has explained by Feldman et al [5.45] and frequency domain measurements have reported by A. Jonscher [5.46, 5.47].

5.5 Dielectric properties of ferrites

The polycrystalline ferrites are very good dielectric materials. The intrinsic dielectric constant values are found to lie between 8 and 20. The very high dielectric constants often observed at low frequencies have been ascribed to the effect of heterogeneity of the samples i.e. pores and/or surface layers on grains causing poor electrical contact between them. Sometimes some electronic polarization effect is supposed to be connected with the conduction hopping mechanism itself, which also could contribute to the low frequency dispersion of dielectric constant. At higher

frequencies the measured values may be regarded as insensitive to both of these contributions and they are usually taken as actual intrinsic dielectric constants corresponding to normal ionic and electronic polarizations. In the frequency region of the lattice vibrations the ionic polarization becomes slow and damps out (infrared absorption) while the electronic polarization is fast enough to persist to the region of electronic excitations in near infrared and visible part of the spectrum (crystal field and charge transfer transitions). As far as the temperature dependence is concerned, dielectric constant usually increases with increasing temperature together with the electrical resistivity.

The dielectric properties of ferrites are dependent upon several factors including, the method of preparation, chemical composition and grain structure or size. When a ferrite is sintered under slightly reducing condition, the valence state changes, the individual cation formed in the sample leads to high conductivity and when such a material is cooled in an oxygen atmosphere, it is possible to form films of high resistivity over the constituent grains. Such ferrites in which the individual grains are separated by either air gaps or low conducting layers behave as inhomogeneous dielectric materials. Unfortunately, the great volume of work in this area is matched by speculative interpretation and arbitrary conclusions. Among the many workers involved in this type of studies, the prominent ones are Koops [5.42], Moltgen [5.48], Kamiyoshi [5.49], Iwauchi [5.50, 5.51], Rezlescu [5.52, 5.53], Brockman [5.54, 5.55], Avramenko [5.56] and Josyulu [5.57], V. R. K. Murthy [5.58]. The theory and conclusions put forward by Jonscher [5.59] were used to interpret the possible mechanisms in this class of materials. In recent times, the polarization studies were further extended to understand and interpret the earlier theories in a microscopic manner relevant to different materials. These theories were also extended to interpret the low frequency dielectric of ceramic materials including ferrites.

Koops [5.42] gave a phenomenological theory of dispersion based on the Maxwell-Wagner interfacial polarization model [5.60, 5.61] for inhomogeneous dielectric structure. It was assumed that the solid consists of well conducting grains separated by poorly conducting layers. This model explains a strong dispersion in dielectric constant ε' at low frequencies. Thus, it is known that the dielectric constant

of polycrystalline ferrite is related to the average grain size of the specimens of the same compositions.

Experimental details of Dielectric properties:

The dielectric constant for all unirradiated and irradiated bulk samples was calculated by measuring the capacitance of the material. The capacitance and resistance as a function of frequency and temperature was measured using HP 4284 A LCR meter at the frequency range of 20 Hz to 1 MHz and temperature range was 300K to 800K. The test assembly along with furnace and sample holder used is shown in above given Photograph. The temperature of the furnace was controlled by maintaining the current passing through the heater by means of current controller. The temperature of the sample was measured by Cr-Al thermo couple. The following relation was used for the calculation

$$\varepsilon' = C/C_0;$$

where, $C_0 = \varepsilon_0 A/d$, C = Measured Capacitance, ε_0 = Permittivity of free space, A = Area and d = Thickness of the sample.

The dielectric loss factor, tanδ was directly measured from the LCR meter, δ being the dielectric loss angle. Since the loss factor is the ratio of the imaginary and the real parts of the dielectric constant, the imaginary part ε'' can be calculated from the relation

$$\varepsilon'' = \varepsilon' \tan\delta$$

The loss tangent (tanδ) is proportional to the ratio of the power lost in heat to the energy stored per cycle, and therefore is a good measured how 'lossy' a dielectric material is.

The A. C. conductivity was calculated from the relation $\sigma = \frac{2\pi fCDt}{A}$ and the electrical resistivity is reciprocal of conductivity was calculated using the formula $\rho = \frac{1}{\sigma}$. All the parameters measured with the frequency variation at different fixed temperature and the temperature variation at different fixed frequencies. All the measurements were carried out at Department of Physics, Saurashtra University, Rajkot.

Precision LCR meter

5.6 Impedance Spectroscopy

The physical properties of polycrystalline magnetic ceramics like ferrites are influenced by the shape, size, and orientation of grains and grain boundaries, voids, inhomogeneities, surface layers and contacts. Information about the associated physical parameters of the microstructural components is important since the property of the materials is determined by those components. Complex impedance analysis is a well known and powerful tool which has been effectively used for probing into the dielectric materials. These analyses enable one to resolve the contributions of various processes such as the electrode effects, bulk effects and the interface viz the grain boundaries et in the frequency domain.

In general the data in the complex plane could be represented in any of the four basic formalisms, there are Complex impendence $Z^* = Z' - j Z''$, Complex admittance $Y^* = Y' - j Y''$, Complex permittivity $\varepsilon^* = \varepsilon' - j \varepsilon''$, Complex modulus $M^* = M' + I M''$ which are related. When the relaxation times of various processes differ as a consequence of different capacitive component, the complex impedance representation is made use of.

In complex impedance plot (Cole-Cole; Z' vs. –Z'' plotted in a linear scale), depending on the relative value of their relaxation times, they give rise to three semicircular arcs. Generally, the arc at the high frequency end refers to the bulk electrical conduction, the intermediate arc corresponds to conduction by the grain boundaries and the arc at the low frequency end arises from electrode processes. Each

of these semicircles could be represented by a single RC combination. A depressed semicircle whose centre lies below the real axis suggests the departure from the ideal Debye behaviour.

The semicircle passes through a maximum at a frequency f_0 (relaxation frequency) and satisfies the condition.

$$\omega\tau = 1$$

On other hand complex modulus or permittivity plane plots are used to represent the response of dielectric system.

The classical model to describe the impedance behaviour is that of Debye and it is written in the form $Z^* = Z' - j\,Z'' = R/(1 + i\omega\tau)$ where $\tau = RC$. This equation implies a simple RC circuit in parallel which gives rise to a semicircle whose centre lies on the real axis in the complex plane (Z'' vs. Z'; M'' vs. M') a Debye peak in the spectroscopic peak in the imaginary component (Z', M'' vs. log f) where

$$Z' = \frac{R}{1+(\omega RC)^2}$$

$$Z'' = R\left(\frac{\omega RC}{1+(\omega RC)^2}\right)$$

Similarly the real and imaginary parts of modulus functions are expressed by the following

$$M^* = j\omega C_0 Z^*$$

$$M' = \frac{C_0}{C}\left(\frac{(\omega RC)^2}{1+(\omega RC)^2}\right)$$

$$M'' = \frac{C_0}{C}\left(\frac{(\omega RC)}{1+(\omega RC)^2}\right)$$

In the above equations ω is the angular frequency ($=2\pi f$), C_0 is the vacuum capacitance of the measuring cell and electrodes with an air gap of the dimensions of the sample thickness $C_0 = \varepsilon_0 \times A/d$, where ε_0 is the permittivity of free space (8.85×10^{-12} F/m), d is the thickness and A is the area of the specimen. However, in reality, this is most often not he situation, the centre of the semicircle lies off the real axis by an angle θ ($=\beta\pi/2$). It is described by the following equation

$$Z^* = R/(1 + i\omega\tau)^n$$

N = 1-β, where β is the angle of deviation from the ideal semicircle arc. The simple Debye equation for the relaxation is the case for β = 0, i.e., n =1. Complex impedance plane plots of Z' versus Z'' (where Z' and Z'' are the real and imaginary parts of the complex impudence plane, respectively) are useful for determining the dominant resistance of sample but are intensive to the smaller values of resistance.

Similarly, complex modulus plots are useful in determining the smallest capacitance. Sinclair and west [5.62] suggested the combined usage of impedance and modulus spectroscopic plots to rationalize the dielectric properties. The peal heights are proportional to R for the Z'' versus frequency plots and to C^{-1} for the M'' peak. However the power of combined usage of both impedance and modulus spectroscopy is that the Z'' plot highlights the phenomenon of largest resistance whereas M'' pick up those of the smallest capacitance [5.63].

Experimental Details of the Impedance Measurements:

For impedance measurements HP 4284 A LCR meter at the frequency range of 20 Hz to 1 MHz was used. The test assembly along with furnace and sample holder used is shown in above given Photograph. The samples in the form of pellets prepared, by using ceramic technique were used for dielectric measurements. The ohmic contact was ensured by applying silver paint onto both parallel surfaces of the pellet. The real and imaginary parts of the electrical impedance of the unirradiated and irradiated samples were measured as a function of frequency 20 Hz – 1MHz at Room temperature.

In present work absolute value of impedance |Z| and Phase angle ϕ at room temperature were directly measured over a wide range of frequency 20Hz -1MHz range. Using these values of | Z | and ϕ real (Z') and imaginary (Z'') are obtained using the formula:

R or Z' = |Z| cosϕ

X or Z''= |Z| sinϕ

The real part (Z') and imaginary part (Z'') are plotted as parametric functions of frequency to get impedance plot which is a semicircle.

The real (M') and imaginary (M'') parts of the complex electrical modulus were obtainedε'(ω) and ε''(ω) values using the relation

$$M'(\varpi) = \frac{\varepsilon'(\omega)}{\varepsilon'(\omega)^2 + \varepsilon''(\omega)^2} \text{ and } M''(\varpi) = \frac{\varepsilon''(\omega)}{\varepsilon'(\omega)^2 + \varepsilon''(\omega)^2}$$

The form of presentation of the dielectric data have changed from ε'(ω) and ε''(ω) to M'(ω) and M''(ω) based on these equations. Impedance measurements also have been done at department of physics, Saurashtra University, Rajkot.

References

5.1 De Boer, J. H. and E.J.W. Verwey, Proc. Phys. Soc. **49** (1937) extra part, 59

5.2 D. J. Craik, Magnetic Oxides Part I, John Ciley & Sons, New York (1975) 433

5.3 B. Vishwanathan and V. R. K. Murthy, Ferrite Materials Science and Technology (New Delhi: Narosa Publishing House) (1990) 26

5.4 A. A. Samokhvalov and A. G. Rustamov, Sov. Phys. Solid State **6** (1964) 749

5.5 A. A. Samokhvalov and A. G. Rustamov, Sov. Phys. Solid State **7** (1964) 961

5.6 E. J. Verwey and de Boer, Rec. Trav. Chim. Phys. Bas. 55 (1936) 531

5.7 J. H. Jonker, J. Phys. Chem. Solids **9** (1959) 165

5.8 R. R. Dogoadge, A. A. Cherenko and A. Chimadzhev Yu., Sov. Phys. Solid State, **3** (1961) 2698

5.9 R. R. Heiks, Phys. Rev. **99** (1955) 1232

5.10 N. Rezlescu, D. Condurache, P. Petrariu and E. Luca, J. Amer. Ceram. Soc., **57** (1974) 40

5.11 W. Haubenreisser, Phys. Stat. Solidi **21** (1961) 390S

5.12 B. Lorentz and D. Ihle, Phys. Stat. Solidi, **63** (1974) 599

5.13 B. Lorentz and D. Ihle, Phys. Stat. Solidi, **69** (1975) 451

5.14 G. Srinivasan, Phys. Stat. Solidi **57** (1980) K179

5.15 H. V. Keer, Principles of the Solid State (1994) 187

5.16 R. R. Heikes and W. D. Johnston, J. Chem. Phys. **26** (1957) 582

5.17 D. J. Craik, Magnetic Oxides Part I, John Ciley & Sons, New York (1975) 435

5.18 B. Vishwanathan and V. R. K. Murthy, Ferrite materials: Science and Technology, (1990) 30

5.19 S. L. Kakani and C. Hemrajani, Text book of Solid State Physics, Sultan Chand (1997)

5.20 G. Srinivasan and C. M. Srivastava, Phys. Stat. Solidi, **108** (1981) 665

5.21 J. Yamashita and T. Kurosawa, J. Phys. Chem. Solids, **5** (1958) 34

5.22 T. Holstein, Ann. Phys. **8** (1959) 343

5.23 J. Appel, Solid State Phys. **18** (1969) 41

5.24 I. G. Austin and N. F. Mott, Adv. Phys. **18** (1969)

5.25 H. L. Tuller and A. S. Nowick, J. Phys. Chem. Solids **38** (1977) 859

5.26 H. Fröhlich, Adv. Phys. **3** (1954) 325

5.27 D. J. Craik, Magnetic Oxides Part I, John Ciley & Sons, New York (1975) 436

5.28 Van Uitert C. G. Proceeding of I.R.E **44** (1956) 1294

5.29 N. Rezlescu and E. Rezlescu, Phys. Stat. Sol. **23** (1974) 575

5.30 Economous G. "Effect of microstructure on the electrical and magnetic properties of ceramics, W. D. Kingery (Rd.) Ceramic Fabrication Processes, M.I.T. Technology press and John Wiley and Sons. Inc. New York (1958) chap. 21

5.31 Verwey E. J. W., Haayman P. W., Romeijn F. C. and Van Oosterbout G. M., " Controlled Valency semiconductors" Philips Res. Rept. **5** (1950) 173

5.32 N. Miyata, J. Phys. Soc. Japan, **16** (1961) 206

5.33 Krupicka and P. Novak, In "Ferromagnetic Materials" Vol. **3**, Ed. E. P. Wohlfarth, North Holland Publishing Co., (1982) 189

5.34 J. M. Honig, J. chem. Ed., **43** (1966) 76

5.35 H. V. Keer, Principles of the Solid State (1994) 183

5.36 F. J. Morin, Phys. Rev., **93** (1953) 1195

5.37 A. J. Bosman and c. Crevecoeur, J. Phys. Chem. Solids, **30** (1969) 1151

5.38 A. J. Bosman and C. Crevecoeur, Phys. Rev. **144** (1966) 763

5.39 R. R. Heikes, in Thermoelectricity edited by R. R. Heikes and R. W. Ure (Wiley Interscience,, New York) 45

5.40 F. J. Morin and T. H. Gebelle, Phys. Rev., **93** (1955) 467,

5.41 A. A. Samokhavalov and A. G. Rustamov, Sov. Phys-Solid State **6** (1955) 749

5.42 C. G. Koops, Phys. Rev. **83** (1951) 121

5.43 D. R. Askeland, The science and Engineering of Materials, Chapmann & Hall, 1990, P. 683

5.44 Andrew K. Jonscher, J. Phys. D: Appl. Phys. **32** (1999) R57

5.45 Yu Felman, A. Andrianov, E. Polygalov, G. Romanychev, I. Ermolina, Yu Zuev and B. Milgotin, Rev. Sci. Instrum. **67** (1996) 3208

5.46 A. K. Jonscher, Dielectric Relaxation in Solids (London: Chelsea Dielectrics) (1983)

5.47 A. K. Jonscher, Universal Relaxation Law (London: Chelsea Dielectrics) (1996)

5.48 S. Moltgen, Zh. Fur. Ang. Physik. **4** (1952) 216

5.49 K. Kamiyoshi, Sci. Rep. Res. Int. Tohoko Uni. **A3** (1951) 716

5.50 K. Iwauchi, Jpn J. Appl. Phys., **10** (1971) 1520

5.51 K. Iwauchi, S. Yemamato, Y. Bando, Jpn. J. Appl. Phys., **10** (1971) 1513

5.52 N. Rezlescu and E. Rezlescu, Phys. Stat. Sol. (a) **23** (1974) 575

5.53 N. Rezlescu, E. Cucioreanu and V. Petrescu, Rev. Rom.Phys.Tomo. **15** (1970) 965

5.54 F. G. Brockman and K. E. Matterson, J. Amer.Ceram .Soc. **53** (1970) 517

5.55 F. G. Brockman and K. E. Matterson, J. Amer. Ceram. Soc. **54** (1971) 180

5.56 V. P. Avramenko and O. V. Sinyskov, Ukr. Fiz. Zh. (Ukr.Ed.),**13** (1968) 1174

5.57 O. S. Josyulua and J. Sobhanadri, Phys. Stat. Sol. (a), **59** (1980) 323

5.58 V. R. K. Murthy and J. Sobhanadri, Phys. Stat. Sol. (a) **36** (1976) K133

5.59 A. K. Jonscher, Dielectric Relaxation Solids, Chelsea Dielectric Press, London (1983)

5.60 J. C. Maxwell, "Electricity and Magnetism" Oxford Press, London, 1 (1954) 328

5.61 K. W. Wagner, Ann. De. Physik, **40** (1913) 817

5.62 D. C. Sinclair and A. R. West, J. Appl. Phys. **66(8)** (1989) 3850

5.63 Idem., J. Mater. Sci. **29** (1994) 6061

❖ *50 MeV Li^{3+} ions irradiation of $Li_{0.5(1+x)}Ti_xAl_{0.1}Fe_{2.4-1.5x}O_4$*

6A.1 SHI Irradiation effects on Structural and Magnetic Properties

6A.2 SHI Irradiation effects on Structural parameters

6A.3 SHI Irradiation effects on Infrared Spectra

6A.4 SHI Irradiation effects on Elastic properties

6A.5 SHI Irradiation effects on Electrical properties

6A.6 SHI Irradiation effects on Dielectric properties

6A.7 SHI Irradiation effects on Impedance Spectroscopy

Conclusion

References

6A.1 Swift Heavy Ion Irradiation effects on Structural and Magnetic properties of the system $Li_{0.5(1+x)}Ti_xAl_{0.1}Fe_{2.4-1.5x}O_4$

It has been shown through the study of Swift Heavy Ion irradiation of magnetic insulators that irradiation of solids with energetic particle beams leads to the creation of a wide variety of defect states leading to the modifications on their physical properties [6A.1-6A.4]. Generally, the damage produced by swift heavy ion (SHI) irradiation causes large defect clusters or extended defect agglomerates [6A.5]. It has been demonstrated that in the ion energy regime for which the electronic energy loss dominates over the nuclear loss, above a specific energy threshold, the damage created by the high electronic excitation induced by SHI in insulators results in formation of defected region, cylindrical volume of amorphous material extending over the entire ion path [6A.6].

In the spinel structure there are two different types of interstitial sites present, namely, tetrahedral (A) and octahedral (B), which are occupied by different metal ions. In general, the magnetic interactions between these metal ions, limited only to the nearest neighbours, are antiferromagnetic in nature and their magnitudes are given by exchange integrals having relative strengths: $|J_{AB}|>>|J_{BB}|>|J_{AA}|$. One can in principle alter the relative strengths of all these exchange integrals by selective sublattice magnetic dilution of by changing the type of the magnetic ions on A and B sites, and disturbs the long range ferrimagnetic ordering. Similarly, the superexchange interactions between magnetic ions are sensitive to any change in the crystallographic positions leading to change in the magnetic properties. This later point allows modifying the magnetic properties through defect states generated by means of SHI-irradiation. The insufficiency of knowledge is felt when it is attempted to elucidate the SHI-induced modifications in the spinel ferrites owing to the complications caused by the added role of the rearrangement of cations in the interstitial sites and high sensitivity of superexchange interactions to any change in the direction and length of bonds.

In the present study we aim to investigate the influence the Swift Heavy Ion irradiation induced defects on the structural and magnetic properties of the spinel ferrites by means of X-ray diffraction, Magnetization, Low field AC susceptibility and Mössbauer spectroscopy. We have selected the spinel solid solutions of the system $Li_{0.5(1+x)}Ti_xAl_{0.1}Fe_{2.4-1.5x}O_4$ (x = 0.0 to 0.3, step = 0.1) for the SHI irradiation

study by using 50 MeV Li^{3+} ions. The pristine compound $Li_{0.5}\ Fe_{2.5}\ O_4$ is known to have very high Curie temperature (942K) and the magnetic properties of these compounds are sensitive to the distribution of Fe^{3+} ions in the A- and B-sites. Therefore, the magnetic properties of the pre- and post SHI-irradiated specimens can be explained in the light of defect states and rearrangement of cations in the lattice sites.

The polycrystalline samples of the spinel system $Li_{0.5(1+x)}Ti_xAl_{0.1}Fe_{2.4-1.5x}O_4$ (x = 0.0 to 0.3, step = 0.1) were prepared by the double sintering ceramic technique. The chemical stoichiometry of the products was checked by Energy Dispersive X-ray analysis (EDAX) and the EDAX results (Fig. 6A.1) indicated that the oxide ingredients have fully undergone the chemical reaction to form the required ferrite materials. No trace of any impurity was found in the EDAX patterns for these samples. The chemical compositions of the samples were found to be as per the expectations. The formation of mono phase solid solution is equally important to ensure complete substitution of the replacing cations. Therefore, the powder X-ray diffraction (XRD) patterns were recorded at room temperature using CuK_α radiations (λ = 1.5437 Å). No structural phase has been detected in XRD patterns other than the expected face centred cubic spinel phase. Thus, the EDAX and XRD characterizations have ascertained the compositional purity and structural monophasic nature of the specimens. Both of these properties are essential prerequisites for the study of the influence of the swift heavy ion (SHI) irradiation on the structural and magnetic properties of these materials, which is the focus of the present investigations. The targets in the form of thin layer of ferrite material having thickness of about 20 mg/cm^2 for irradiation experiments were prepared by spreading fine ferrite powders in a aluminium ring of 1 cm diameter on a thin aluminium foil, and uniform thickness was achieved by fixing the powder using liquid GE Varnish. The specimens were irradiated in vacuum with 50 MeV Li^{3+} ions with fluence of 5 x 10^{13} ions/cm^2 using 15 UD Pelletron accelerator at Inter University Accelerator Centre (IUAC), New Delhi. The projected range (R_p) and electronic energy loss (S_e) of 50 MeV Li^{3+} ions in these compounds calculated using the SRIM-2003 are around 235μm and 12 eV/Å, respectively. The S_e is less than the S_{eth} = 1.2 KeV/ Å for columnar amorphization suggesting that the SHI-irradiation has generated points/cluster of defects.

The X-ray diffraction patterns of unirradiated and irradiated specimens for the compositions x =0.0, 0.1, 0.2 and 0.3 of the spinel system $Li_{0.5(1+x)}Ti_xAl_{0.1}Fe_{2.4-1.5x}O_4$

are displayed in Fig. 6A.2. It is seen that all the Bragg reflections could be indexed for the *fcc* spinel structure and the peak positions are shifted to lower Bragg angle (2θ) values. This indicates expansion of the unit cell. The value of cell edge parameter (lattice constant, a) for each sample was determined by using the computer program developed on the basis of the Nelson Riley method [6A.7]**.** The lattice constants for unirradiated and irradiated samples are listed in Table 6A.3. The lattice constant is found to increase after SHI irradiation. The compositional increase in lattice parameter for unirradiated and irradiated specimens is due to the larger cationic radius of the replacing cation Ti^{4+} (0.68 Å) than the replaced cation Fe^{3+} (0.64 Å) in the spinel lattice. It is also found that the compositional increase in the cell edge parameter (a) is greater for the irradiated samples than the unirradiated ones.

It is well known that a precise knowledge of the cation distribution in the interstitial voids of the face centered cubic spinel structure is essential to understand the structural changes and magnetic behaviour of these materials. The distribution of the cations in the tetrahedral (A) and octahedral (B) sites of the spinel lattice can be estimated through XRD Bragg reflection intensity analysis. The large difference in the values of the atomic scattering factors of the cations involved in the present system renders good contrast for the accurate determination of the distribution of these cations in the tetrahedral (A) and octahedral (B) voids of the spinel lattice through X-ray diffraction intensity analysis. The XRD intensity analysis was commenced by taking recourse to the information provided by the literature that the Lithium ferrite, $Li_{0.5}\ Fe_{2.5}\ O_4$, x = 0.0, is an inverse spinel with all Li^{1+} ions occupying octahedral sites [6A.8]. It has been found that the Al^{3+} ions distribute themselves almost equally between the A- and B-sites [6A.9, 6A.10]. The Ti^{4+} ions are generally known to have octahedral (B) site preference [6A.11]. Initially they were put on the B-sites in the XRD intensity calculations. However, the calculated values could not be matched with the experimental ones for all the irradiated samples unless Ti^{4+} ions were allowed to occupy the A-sites also. The site occupancies of Ti^{4+}, Fe^{3+} and Al^{3+}ions were varied in a constrained manner such that the stoichiometry of the structure is maintained. The X-ray diffraction intensities of six Bragg reflections (2 2 0), (3 1 1), (4 0 0), (4 2 2), (5 1 1) and (4 4 0) were calculated by using a computer program based on the Buerger's formula: $I_{hkl} = |F_{hkl}|^2 \times P \times L_p$ where, F_{hkl} is structure factor, P is the multiplicity factor and L_p is the Lorentz polarization factor [6A.12]. Since the Bragg planes intensity ratios: $I_{(220)}/ I_{(440)}$ and $I_{(422)} / I_{(440)}$ are considered to be sensitive to the tetrahedral site

occupancy, their calculated and experimentally observed values are listed in Table 6A.2. The greater values of these ratios for irradiated samples are attributable to the greater A-site occupancy of Fe^{3+} or Ti^{4+}. The cation distributions deduced through XRD intensity analysis for the unirradiated and irradiated samples are also given in Table 6A.2; they clearly indicate the redistribution of the cations in the A- and B-sites induced by SHI-irradiation.

The values of the saturation magnetization (σ_s) in emu/gram measured in the peak field of 5kOe are listed Table 6A.3. It is seen that the value of σ_s decreases with Ti concentration (x) for both the sets of samples. According to the Nèel's theory [6A.13], in the ferrimagnetic region below the magnetic transition temperature T_c (Curie Temperature), both the sublattices (A & B) are spontaneously magnetized by the molecular field acting on it with mutually opposite directions and therefore the Neel's moment is :

$$\eta_B^N = M_B - M_A$$

where, the M_A & M_B are the sublattice magnetizations. The values of the Nèel's moments for the present system calculated using the cation distributions deduced through XRD data analysis and the free ion magnetic moment (in Bohr Magneton, μ_B) of the only magnetic cation $Fe^{3+}(5\mu_B)$ are listed in Table 6A.3. The reduction in the observed saturation moment on increasing the Ti-content in both the cases is due to the magnetic dilution of octahedral sites. It is also interesting to note that the observed saturation moment for unirradiated samples agrees well with the Nèel's moment (η_B^N) but at the same time the saturation moment is found to be reduced for all the samples after SHI-irradiation. It is clear from Table 6A.3 that for the irradiated samples the observed saturation moment (η_B^{obs}) is found to be lower compared to the predicted value by the Nèel's theory (η_B^N). This implies that the reduction in the saturation moment after SHI-irradiation cannot be exclusively explained by rearrangement of the cations in the interstitial sites and resultant B-site magnetic dilution. At this juncture, the question arises as to why the observed saturation moment value for SHI irradiated samples is lower than the moment predicted by the Nèel's theory.

The ^{57}Fe Mössbauer spectroscopy is an important microscopic probe for ferrites to study the structural changes, hyperfine interaction parameters, magnetic structure and to deduce unambiguously the distribution of Fe^{3+} ions among two antiferromagnetically coupled sublattices tetrahedral (A) and octahedral (B) of spinel

lattice. The Mössbauer spectra for pre and post SHI irradiated samples were recorded using a standard absorption method with ^{57}Co-in-Pd source placed on a constant acceleration spectrometer. The determination of iron distribution through Mössbauer spectroscopy will unequivocally endorse the cation distribution deduced through X-ray diffraction intensity analysis. The Mössbauer spectra recorded at 300K for the unirradiated and irradiated samples of the system $Li_{0.5(1+x)}Ti_xAl_{0.1}Fe_{2.4-1.5x}O_4$ (x = 0.0, 0.1 and 0.3, are displayed in Fig. 6A.3. The Mössbauer spectra were analyzed and the hyperfine interaction parameters were refined using NORMOS computer software using non-linear least-squares minimization [6A.14]. The Mössbauer spectra exhibit two superimposed asymmetric Zeemann sextets one due to the Fe^{3+} ions at tetrahedral (A) sites and other due to Fe^{3+} ions at octahedral (B) sites and the spectra for irradiated samples exhibit central enhancement or paramagnetic doublet superimposed on the magnetic sextet. The hyperfine interaction parameters deduced through Mössbauer spectra are given in Table 6A.4.

We note that the isomer shifts for both the sites appear to show no significant variation with Ti concentration (x) thus indicating that the s-electron charge distribution of the Fe^{3+} ions is negligibly influenced by Ti substitution. The values of isomer shift for both the sites are well within the range of Fe^{3+} isomer shift values. The isomer shift for tetrahedral Fe^{3+} ions is found less positive than that for the octahedral Fe^{3+} ions. This difference can be attributed to the slight sp^3 covalency, which the tetrahedral ions are known to experience. It is clear from Table 6A.4 that there is no observable quadrupole shift in the magnetic sextets for both the sets of samples in these spinel ferrites. This means that the co-existence of chemical disorder and overall cubic symmetry causes no net observable quadrupole shifts in the magnetic sextets.

The tetrahedral (A-site) hyperfine field shows compositional reduction for unirradiated and irradiated samples due to larger B-site occupancy of diamagnetic cations. It is seen that (Table 6A.4) the nuclear hyperfine field for A-site is lower than that of the B-site for all the samples. This happens because the B-site Fe^{3+} ions experience a stronger average magnetic bonding with A-site Fe^{3+} ions compared to the A-site Fe^{3+} ions for which some of the bonds are with diamagnetic Al^{3+} and Li^{1+} at B-sites. This is corroborated by the observed little increase in the B-site hyperfine field after SHI-irradiation due to B-site magnetic dilution resulting from rearrangement of the cations. The iron distribution parameter $\delta = Fe^{3+}{}_A / Fe^{3+}{}_B$ derived

from Mössbauer Lorentzians area ratio and X-ray diffraction intensity analysis are in good agreement (Table 6A.4). It is seen that all the post-irradiated specimens exhibit central paramagnetic doublet superimposed on the magnetic sextets showing quadropole splitting of the order of 0.25 ± 0.02 mm/sec and the isomer shift 0.35± 0.03 mm/sec. It is known that the electronic energy loss threshold (S_{eth}) required to surmount for producing amorphization is generally of the order of 10^3 eV/ Å, therefore it is difficult to comprehend the creation of columnar amorphization at the value of electronic energy loss (S_e) ~ 12 eV/ Å. The amorphization is not reflected in the X-ray diffraction patterns of the irradiated samples. The generation of point/clusters of defects in these Ti^{4+} – Al^{3+} containing compounds inhibits the long range ferrimagnetic order through redistribution of cation in the localized defected region leadings to the formation of paramagnetic centres. These paramagnetic centres resulted from breaking of magnetic linkages coexist with long range magnetic ordering. The central paramagnetic enhancement in Mössbauer spectra can be explained on the basis of "paramagnetic centres". There are reports [6A.15] on the elucidation of paramagnetic centres through the Mössbauer spectroscopy in Li-Al ferrites in the higher non-magnetic concentration. In the present samples the paramagnetic centres may be thought of created by redistribution of cations induced by SHI-irradiation. The percentage formation of paramagnetic centres deduced from the area under the central paramagnetic doublet for each irradiated samples given in Table 6A.4. The reduction in the saturation magnetic moment after subjected the sample to SHI-irradiation can be understood quantitatively, by considering the rearrangement of the cations and fractional formation of paramagnetic centres by SHI Irradiation. Thus, the central doublet in the Mössbauer spectra of the irradiated samples originates from the SHI-induced paramagnetic centres not due to amorphous phase.

The plots of thermal variation of low field (0.5 Oe) AC susceptibility for both the sets of samples are depicted in Fig. 6A.4 and the Curie temperatures determined through these plots for all the samples are listed in Table 6A.3. It is quite conspicuous that the Curie temperature (T_c) for all the irradiated specimens is lower than their unirradiated counterparts. This confirms the cation distributions determined through XRD intensity analysis and the Mössbauer spectral intensity ratio and further supports the argument of weakening of A-B magnetic linkages due to cumulative effect of the site magnetic dilutions, expansion of the unit cell and fractional creation localized

paramagnetic centres resulting from SHI-irradiation. It is also important to note that the magnetic transition near the Curie temperature for the irradiated samples is sharp, not exhibiting the "tailing" i.e. blur transition, indicating uniform effect of the SHI-irradiation.

6A.2 Swift Heavy Ion Irradiation effects on Structural parameters of the system $Li_{0.5(1+x)}Ti_xAl_{0.1}Fe_{2.4-1.5x}O_4$

The knowledge of cation distribution among the available tetrahedral (A) and octahedral (B) sites in the ferrite structure and other structural and physical parameters like lattice constant, bulk and X-ray density, porosity, ionic radii, oxygen positional parameters etc. are useful in understanding their electrical and magnetic properties. Among some physical properties such as density, porosity etc. is influenced by nature of grains (shape, size and orientation), grain boundaries, voids, inhomogeneities etc. in the ferrites structure. The information about the associated structural and physical parameters of the micro-structural constituent is important since the overall property of the ferrite material is determined by those constituents. Some work has been reported in the literature on structural and physical properties of lithium ferrites. Ravinder studied the effect of porosity and sintering temperature on electrical conductivity and activation energy of lithium ferrite [6A.16, 6A.17]. The structural properties of Mg^{2+} and Al^{3+} co-substituted $Li_{0.5}Fe_{2.5}O_4$ has been studied by K. B. Modi et al [6A.18]. No study of the structural and physical properties are influenced by swift heavy ion irradiation has been reported in the lithium ferrites. Therefore, detailed investigations of structural and physical parameters such as lattice constant, bulk and X-ray density, porosity, ionic radii, bond lengths, site radii, oxygen positional parameter etc. with the effect of 50 MeV Li- ion irradiation of the ferrite $Li_{0.5(1+x)}Ti_xAl_{0.1}Fe_{2.4-1.5x}O_4$ (x = 0.0, 0.1, 0.2 and 0.3) system are presented.

The bulk density (d) was calculated of a specimen in pellet form, from the weight (mass) and bulk dimensions (volume) of the unirradiated and irradiated ferrite samples and the values are given in Table 6A.5. The bulk density is observed to increase with titanium substitution for x = 0.1 and to decrease for the content x = 0.2 and 0.3 as compared to un-substituted (x = 0.0) of unirradiated ferrites. There is no systematic variation in bulk density with the substitution of titanium concentration in present system because the density of the ferrites influenced by preparation conditions such as sintering temperature, atmosphere and pressure. The observed increase in bulk

density for x = 0.1 may be titanium to bring about densification and grain growth but the decrease in bulk density for x = 0.2 and 0.3 may be the number of pores are increased due to the micro-structural changes brought about by the sintering condition. For irradiated ferrites, the bulk density is less for x > 0.0 as compared to the sample x = 0.0. For the comparison of unirradiated and irradiated ferrites, the bulk density of irradiated ferrite is more for x = 0.0 and 0.2 and less for x= 0.1 and 0.3 than the unirradiated ferrites. The increase in bulk density after irradiation for x = 0.0 and 0.2 may be due to the number of pores are reduced by irradiation as a result of which the individual grains come closer to each other and the effective area of grain contact increases and the decrease in bulk density after irradiation for x = 0.1 and 0.3 may be due to the number of pores are increased by irradiation.

The X-ray density (ρ_x) for each composition was calculated using the relation [6A.19].

$$\rho_x = ZM/Na^3$$

where Z is the number of molecules per unit cell (Z = 8) of spinel lattice, M the molecular weight of the ferrite sample, N is Avogadro's number and 'a' the lattice constant of the ferrite. The variation of X-ray density (ρ_x) as a function of Ti concentration of unirradiated and irradiated samples are tabulated in Table 6A.5. The data show the X-ray density decreases with increasing Ti-content (x) for unirradiated and irradiated samples which is due to the increase in lattice constant 'a' with x. After irradiation X-ray density is reduced as compared to unirradiated samples can be attributed to the increase in lattice parameter 'a' due to the expansion of unit cell by generation of paramagnetic centers (point/clusters of defects) after irradiation.

The percentage of porosity (P) was calculated using the relation [6A.19].

$$P = (1 - d/\rho_x) \times 100\%$$

The values of porosity vary between 9.3 – 18.4 % with the change in titanium concentration for unirradiated and irradiated samples (Table 6A.5). There is random variation of porosity with the change in titanium concentration. The variation of porosity (P) with x depends upon the relative values of bulk density (d) and X-ray density (ρ_x). The porosity is lower for the concentration x = 0.0 and 0.2 and is greater for the concentration x = 0.1 and 0.3 of the irradiated samples than the unirradiated ones. The raise of porosity indicates that the presence of Ti hinders the migration of the pore to the grain boundaries and results in high porosity materials. The decrease of

porosity after irradiation in the material can be ascribed to the reduction of the intergranular pores during irradiation.

From the correlation between lattice parameter and ionic radius we can calculate the lattice parameter theoretically from the equation [6A.20].

$$a_{th} = \frac{8}{3\sqrt{3}}\left[(r_A + R_o) + \sqrt{3}(r_B + R_o)\right]$$

where R_o is the radius of the oxygen ions (1.32 Å) and r_A and r_B are the value of the mean ionic radius per formula of the tetrahedral and octahedral sites, respectively. The cation distribution can be suggested as to make conformation between a_{th} and a_{exp}. The proposed cation distribution is specified in Table 6A.2. The theoretical values of the lattice constant (a_{th}) as a function of concentration x for unirradiated and irradiated samples is given in Table 6A.5. The obtained values of a_{th} are somewhat smaller that those of a_{exp}, which confirms the estimated cation distribution (Table 6A.2). The difference observed in a_{th} and a_{exp} which may be the possibility of the effects like "covalency", which could not be considered in the theoretical model.

The value of the mean ionic radius per formula of the tetrahedral (r_A) and octahedral (r_B) sites was determined using the cation distribution for the each composition of unirradiated and irradiated samples, from the relation [6A.21, 6A.22]

$$r_A = [C_{AFe}r(Fe^{3+}) + C_{ATi}r(Ti^{4+}) + C_{AAl}r(Al^{3+})]$$

$$r_B = 1/2[C_{BLi}r(Li^{1+}) + C_{BTi}r(Ti^{4+}) + C_{BAl}r(Al^{3+}) + C_{BFe}r(Fe^{3+})]$$

where $r(Li^{1+})$, $r(Ti^{4+})$, $r(Al^{3+})$, $r(Fe^{3+})$ are the ionic radii of Li^{1+}, Ti^{4+}, Al^{3+} and Fe^{3+} ions respectively, while C_{AFe}, $C_{ATi,}$ C_{AAl} are the concentrations of Fe^{3+}, Ti^{4+} and Al^{3+} ions on A-sites and C_{BLi}, C_{BTi}, C_{BAl} and C_{BFe} are the concentrations of Li^{1+}, Ti^{4+}, Al^{3+} and Fe^{3+} ions on B-sites. The obtained value of r_A and r_B for unirradiated and irradiated samples with the concentration (x) are given in the Table 6A.6. The ionic radii of tetrahedral r_A decreases and the octahedral r_B increases with increasing Ti-content (x) for unirradiated samples. This is because the Ti ions has larger radius (0.68 Å) than that of Fe^{3+} (0.64 Å) and located at octahedral sites and presence smaller radius cation Al^{3+} (0.51 Å) in tetrahedral site. The ionic radii r_A and r_B for irradiated samples are found to increase with increasing Ti-content (x). It can be seen from the table for irradiated samples the ionic radii of tetrahedral site r_A is found to increase and the ionic radii of octahedral site r_B is found to decrease as compared to unirradiated samples. This is due to the change in the distribution of cations among the A-and B-sites by irradiation. According to redistribution of cations, larger cation

Ti migrate to tetrahedral A-site and smaller cation Al^{3+} migrate to octahedral B-site. Therefore the change occurs in the mean ionic radius of the tetrahedral (r_A) and octahedral sites (r_B) after irradiation.

The oxygen positional parameter or anion parameter (u) for each composition of unirradiated and irradiated samples was calculated using the formula [6A.21].

$$u^{\bar{3}m} = \frac{\frac{1}{4}R^2 - \frac{2}{3} + \left[\frac{11}{48}R^2 - \frac{1}{18}\right]^{\frac{1}{2}}}{2R^2 - 2}$$

where R = B-O/A-O; B-O = $\langle r_B + r(O^{-2})\rangle$ and A-O = $\langle r_A + r(O^{-2})\rangle$, where $r(O^{-2})$ is the radius of the oxygen ion and the value of the mean ionic radius per formula of the tetrahedral (r_A) and octahedral (r_B) sites. The calculated values of oxygen positional parameter (u) for unirradiated and irradiated samples are given in Table 6A.6. A value of 'u' depends on the preparation condition, chemical composition and heating procedure. It has ideal value equal to 0.375 Å for unit cell origin at $\bar{4}3m$ and 0.250 Å for unit cell origin at $\bar{3}m$ .For investigated samples, u is of order 0.2614 Å for unit cell origin at $\bar{3}m$ which is greater than the ideal value of spinel ferrite structure. This indicates the presence of some deviation from ideal case. Values of 'u' decrease with increasing Ti-content (x) due to the changes in the inter-bond angles between cations and anions as well as the variation in the ratio of B-O to A-O bond lengths. Additional, indirect evidence for cation disorder or rearrangement of cations in irradiated spinel ferrite is obtained from determination of oxygen positional parameter 'u', in the structure analysis. After irradiation, slight decrease in oxygen positional parameter 'u' as compared to unirradiated samples. The bond length B-O and A-O are average bond lengths, based on the cation distribution are listed in Table 6A.6. The obtained data of bond lengths B-O and A-O for unirradiated and irradiated samples are vary according to ionic radii r_B and r_A of octahedral (B) and tetrahedral (A) sites, respectively.

Further more the X-ray data was used to calculate the tetrahedral and octahedral site radii (R_A and R_B). The site radii R_A and R_B for unirradiated and irradiated samples were calculated using the relations [6A.23, 6A.24]

$$R_A = a\sqrt{3}\left(\delta + 1/8\right)$$

$$R_B = a\left(3\delta^2 + 1/16 - \delta/2\right)^{1/2}$$

where $\delta = u_{system} - u_{ideal}$

u_{system} = oxygen positional parameter of system

u_{ideal} = ideal oxygen parameter = 0.250 Å

It can be seen that from the Table 6A.6, the tetrahedral site radii R_A decreases and the octahedral site radii R_B increases linearly with increasing Ti-content (x) for unirradiated samples. This is attributed to the substitution process and increases of the size of the unit cell and decreases the oxygen positional parameter (u). For irradiated specimen, both R_A and R_B increase linearly with Ti-content (x), which can be attributed to the fact that the lattice parameter increase linearly with x (Table 6A.3) and oxygen positional parameter all most constant for higher substitution after irradiation. The site radii R_A reduces for x = 0.0 and 0.1 while rise for x = 0.2 and 0.3 irradiated samples and the site radii R_B increases for all the compositions of irradiated samples than the unirradiated samples. The change in site radii R_A and R_B can be attributed to enhance of the size of unit cell and the variation of oxygen positional parameter (u) after irradiation due to generation of point/cluster of defects and rearrangement of cations.

The configuration of ion pairs in spinel ferrites with favourable distances and angles for effective magnetic interactions are shown in Fig. 6A.5. The inter-ionic distances between the cations (b, c, d, e and f) (Me-Me) and between the cations and anion (p, q, r and s) (Me-O) were calculated for unirradiated and irradiated samples using experimental values of lattice constant (a) and oxygen positional parameter (u) (Table 6A.3 & 6A.6) by the relations [6A.25, 6A.26] and summarized in Table 6A.7.

Me – O	Me – Me
$p = a\,(1/2 - u)$	$b = (a/4)2^{1/2}$
$q = a\,(u - 1/8)\,3^{1/2}$	$c = (a/8)11^{1/2}$
$r = a\,(u - 1/8)\,11^{1/2}$	$d = (a/4)\,3^{1/2}$
$s = a/3\,(u + 1/2)\,3^{1/2}$	$e = (3a/8))\,3^{1/2}$
	$f = (a/4)\,6^{1/2}$

It can be seen that the inter-ionic distances Me-O and Me-Me of unirradiated and irradiated samples increase with increasing concentration (x), except for Me-O distances ‘q ‘ and ‘r’ of unirradiated samples. The increase in Me-O and Me-Me distances should results in the weakening of the interatomic bonding and as a result one can expect a reduction in the Nèel temperature on Ti substitution. The increase in

Me-O and Me-Me distances after irradiation as compared to unirradiated ones, excluding Me-O distance 'q' and 'r' for x = 0.0 and 0.1 should result in the reduce of strength of magnetic interactions by rearrangement of cations in the system.

The bond angles (θ_1, θ_2, θ_3, θ_4 and θ_5) from the Fig. 6A.5 are determined by simple trigonometry principles using the values of inter-ionic distances for unirradiated and irradiated samples. It can be seen that angles θ_1, θ_2, and θ_5 is found to increase while θ_3, θ_4 decrease with increasing x (Table 6A.7) for both unirradiated and irradiated samples. The increase in θ_1, θ_2, and θ_5, which is related with A-B and A-A interactions suggest weakening of A-B and A-A interactions. The observed decrease in θ_3, θ_4 angles suggest strengthening of B-B interaction. It is found that the angles θ_1, θ_2, and θ_5 increase and θ_3, θ_4 decrease of irradiated samples with corresponding to unirradiated one, may have effect of irradiation on strength of magnetic interactions in the system.

6A.3 Swift Heavy Ion Irradiation effects on Infrared Spectra of the system $Li_{0.5(1+x)}Ti_xAl_{0.1}Fe_{2.4-1.5x}O_4$

It is well known infrared absorption spectroscopy is an important and non-destructive characterizing tool, which provides qualitative information regarding structural details of crystalline and non-crystalline materials [6A.27, 6A.28].The absorption bands in the spinel ferrites mainly arises from lattice vibrations of oxide ions with cations producing various frequencies of the unit cell. The frequencies of vibrations depend on atomic mass, unit cell parameters, cationic radius, cation distributions and cation-anion bonding in complex manner. Infrared spectral analysis have been carried out for several ferrites by Waldron [6A.29] who reported two absorption bands within the wave numbers 200-800 cm^{-1}, which could be respectively attributed to the tetrahedral and octahedral group complexes of the spinel structure. There are several data and publications about the lithium ferrites. In previous work, the IR spectrum of pure Li-ferrite was discussed in more details by Mazen et al [6A.30]. Furthermore, Mössbauer and Infrared studies of Cr^{3+}-substituted Li-ferrites [6A.31], Infrared absorption of Ti^{4+} and Zr^{4+} substituted Li-Zn ferrites [6A.32], IR absorption and dielectric properties of Li-Ti ferrites [6A.33], Infrared studies of some mixed Li-Cd ferrite [6A.34], Far-infrared spectra of lithium-cobalt mixed ferrites [6A.35], Infrared absorption and dielectric properties of Li-Cu ferrites [6A.36], Far-infrared spectral studies of Mg and Al co-substituted lithium ferrites

[6A.24], Infrared absorption and dielectric properties of Li-Ga ferrite [6A.37] have been reported by many investigators. In the present work, the results regarding the effect of swift heavy ion (SHI) irradiation on IR absorption spectroscopy of Ti^{4+} substituted Li-Al ferrites are discussed. The infrared spectra for all the compositions at 300K were recorded in the wave number range of 400-850 cm^{-1}. For the present samples, BRUKER IFS 66v FT-IR spectrometer was used to carry out the infrared spectroscopic studies in KBr medium.

The room temperature infrared spectra for unirradiated and irradiated $Li_{0.5(1+x)}Ti_xAl_{0.1}Fe_{2.4-1.5x}O_4$ ferrite system with x = 0.0, 0.1, 0.2 and 0.3 are revealed in Fig. 6A.6a-6d, exhibited two principal bands ν_1 and ν_2 followed by a shoulders or splittings (ν_{1sh} or ν_{1sp} and ν_{2sh} or ν_{2sp}) to each of the bands. The band positions of all the unirradiated and irradiated Ti-substituted Li-Al mixed ferrites are presented in Table 6A.8. It is clear that the unirradiated and irradiated ferrites, the high frequency band ν_1 and second absorption band ν_2 are found to be in the range of 518-589 cm^{-1} and 408-488 cm^{-1}, respectively depending on Ti-concentration. These bands are common features of all the ferrite [6A.29]. Waldron [6A.29] has classified the vibrations of the unit cell of cubic spinel can be constructed in the tetrahedral (A-) site and octahedral (B-site). Hence, the occurrence of the vibrational frequency bands ν_1 is caused by the stretching vibration of the tetrahedral metal-oxygen bond and the vibrational frequency bands ν_2 is caused by metal-oxygen vibrations in octahedral sites. Thus, it may be assumed that the Fe^{3+}-O^{2-}, Al^{3+}-O^{2-} and Ti^{4+}-O^{2-} complexes present at tetrahedral sites may be responsible for the occurrence of the ν_1 band while the second absorption band ν_2 is due to vibrations of Fe^{3+}-O^{2-}, Al^{3+}-O^{2-}, Ti^{4+}-O^{2-} and Li^{1+}-O^{2-} complexes.

No systematic variation is observed in the principal bands except slight shift in the band positions with concentration (x). The occurrence of shoulders or side bands near ν_1 band for unirradiated samples x = 0.0, 0.1 and 0.2 indicate the presence of small amount of Fe^{2+} ions in tetrahedral sites. Therefore, this band is assigned $\nu_1$sh/sp and can be attributed to Fe^{2+}-O^{2-} tetrahedral complex.

For the unirradiated specimens, after addition of titanium content the intensity of all the principal bands and their shoulders decrease is found to continuously up to x = 0.3, whereas an increase in broadness of the bands was observed. The sample with x = 0.3 exhibits broader bands than other samples. The broadening of bands has been

reported earlier many workers [6A.24, 6A.34, 6A.38-6A.40]. The decrease in intensity and increase in broadness are explained on the basis cation distribution of Li-Al mixed ferrites (Table 6A.2). It can be seen that there is a 1:3 order of cations on the octahedral sites. As the content of Ti^{4+} increase, Ti^{4+} ions consistently replace Fe^{3+} ions at B-sites. At the same time, the content of Li^{1+} ions on the octahedral site increases by 0.5(1+x). This disturbs the 1:3 orders on the octahedral site with increase in Li-Ti content. This gives rise to a type of chemical disorder on octahedral site, i.e. the statistical distribution of Fe^{3+} ions in B-sites. The disorder systems give rise to broad bands in their IR spectrum [6A.41]. Thus, it can be concluded that increase in Ti^{4+} ion leads to more disordered state. The decrease in intensity of the shoulders and their complete disappearance for x = 0.3 suggest that the Fe^{2+} ion formation has been hampered by increase in titanium content and only the ν_1 and ν_2 bands are exhibited.

The decrease in intensity of all the absorption bands with increasing Li-Ti concentration can be ascribed on the basis of the change in dipole moment with the inter-nuclear distances (dμ/dr). It is known that the intensity ratio as a function of change in dipole moment with inter-nuclear distances (dμ/dr)) [6A.42]. So one can conclude that the IR spectra can give an idea about the change of the molecular structure of ferrites due to the perturbation exerted on Fe-O bonds by introducing Li^{1+} and Ti^{4+} ions and this consequently affects the (dμ/dr)) of Fe-O bonds of the A and B - sties.

After irradiation the ν_1 band shifts towards the higher frequency side even though the bond lengths (A-O) increase as compared to unirradiated ones, which can be attributed to the shifting of Fe^{3+} ions towards oxygen ion on occupation of tetrahedral site by Ti^{4+} ions with larger ionic radii decreases the Fe^{3+}-O^{2-} distance [6A.43]. The ν_2 band slight shifts towards higher frequency side which can be anticipated as bond length (B-O) decrease after irradiation. On the other hand, the IR spectra results as irradiation shifts ν_1 and ν_2 to higher frequencies, due to probably the creation of Fe^{2+} induced by irradiation on both octahedral and tetrahedral sites. The accumulation of Fe^{2+} ions, which have a larger ionic radius than the Fe^{3+} ions, on tetrahedral and octahedral sites, causes a shift in the ν_1 and ν_2 bands to higher frequencies. In accordance with the XRD results, the observed shifting of main absorption bands towards higher frequency side after irradiation is attributed to the expansion of unit cell dimensions.

In case of post-irradiated specimens, it is noticed that the irradiation causes the increase in shoulders/splitting of main absorption bands ν_1 and ν_2 for all the samples. It is also important to note that the new subsidiary bands 673.1 and 651.9 observed for only one composition x = 0.1 in the system after irradiation. The increase in shoulders/splitting and growth of new subsidiary bands can be ascribed to the destruction of the Fe^{3+}-O-Fe^{3+} bonds and the corresponding generation of Fe^{2+}-O^{2-} bonds by redistribution of cations under irradiation. The observed $\nu_2$sh/sp band could be due to the lattice vibrations of L^{1+}-O^{2-} complexes on the octahedral site.

6A.4 Swift Heavy Ion Irradiation effects on Elastic properties of the system $Li_{0.5(1+x)}Ti_xAl_{0.1}Fe_{2.4-1.5x}O_4$

In the industry, the elastic data are very much useful to determine the strength of the materials under various strained conditions while basic research, the data are useful in obtaining an insight into the structure of inter-atomic and inter-ionic forces in solids especially of the long-range type forces. A study of the elastic behaviour of ferrites also would enable one to compute the thermodynamic parameter of importance such as Debye characteristic temperature. The information is available on elastic behaviour of Li-Ti [6A.44], Li-Zn [6A.45], Li-Cd [6A.46], Li-Co [6A.47], Li-Cu [6A.48] mixed ferrites in the literature. We have carried out a systematic study of the swift heavy ion irradiation (SHII) effect on elastic properties of Li-Al-Ti mixed ferrites and results of such a study are presented in the work.

The force constant is a second derivative of potential energy with respect to the site radius, the other independent parameters kept constant [6A.24]. The force constant, for tetrahedral site (k_t) and (k_o) have been obtained from the IR absorption data using the standard formulae suggested by Waldron [6A.29]. According to Waldron the force constants, k_t and k_o for respective sites are given by:

$$k_t = 7.62 \times M_1 \times \nu_1^2 \times 10^{-7}$$

$$k_o = 10.62 \times M_2/2 \times \nu_2^2 \times 10^{-7}$$

where M_1 and M_2 are the molecular weights of cations on A-and B-sites, respectively, calculated from cation distribution have determined through X-ray intensity (Table 6A.2); ν_1 and ν_2 are the corresponding centre frequency on tetrahedral and octahedral sites, respectively. Furthermore, the value of average force constant 'k' ($k = (k_t + k_o)/2$) and lattice constant 'a' (Table 6A.3) have been used for calculating bulk modulus (B). The variation of force constants k_t, k_o and k of unirradiated and

irradiated samples are given in Table 6A.9. It is observed that the force constants k_t, k_o and k decrease with increasing Li-Ti content (x) for unirradiated and irradiated samples that suggest weakening of interatomic bonding. It is well known that the increase in site radius normally leads to decrease in force constant. The observed decrease in force constant k_o can be ascribed to the increase in site radius (R_B) with increasing Li-Ti concentration (x). However, the force constant k_t is found to decrease with site radius (R_A) decreases with Li-Ti concentration (x) and this result is rather unexpected. This unexpected result can be attributed to the fact that under favourable conditions, oxygen can form stronger bonds with metal ions even at larger inter-nuclear separations. The decrease in force constants (k_t, k_o) after irradiation with compared to unirradiated samples can be recognized by the increase in site radius due to the rearrangement of cations.

The bulk modulus (B) of solids in term of stiffness constants is defined as $B = 1/3[C_{11}+2C_{12}]$, but according to Waldron et al [6A.29], for isotropic materials with cubic symmetry like spinel ferrites and garnets $C_{11} = C_{12}$, therefore B is simply given by C_{11}. Further, force constant (k) is a product of lattice constant and stiffness constant [6A.49]. The value of longitudinal elastic wave velocity (υ_l) have determined using the formula suggested by Waldron [6A.29] $\upsilon_l = (C_{11}/\rho_x)^{1/2}$ and the value of transverse elastic wave velocity (υ_s) have determined by general approximation $\upsilon_l = \sqrt{3}\upsilon_s$ [6A.50-6A.52]. The value of υ_l and υ_s are further used to work out the elastic moduli, mean elastic wave velocity and Debye temperature of the ferrite specimens using the following formulae:

Rigidity modulus (G) = $\rho_x (\upsilon_s)^2$

Poisson's ratio (σ) = (3B-2G)/(6B+2G)

Young's modulus (E) = $(1+\sigma)2G$

Mean elastic wave velocity (υ_m) = $[3\{(\upsilon_s^3\upsilon_l^3)/(\upsilon_s^3+2\upsilon_l^3)\}]^{1/3}$

Debye temperature (θ_D) = $(h/k_B)(3N_A/4\pi V_A)^{1/3}\upsilon_m$ [6A.53]

where V_A is mean atomic volume given by $(M\rho_x)/q$, M the molecular weight and q is the number of atoms (i.e. 7) in the formula unit, ρ_x is X-ray density, N_A is Avogadro's number, h and k_B are Plank's and Boltzmann's constants respectively.

The values of υ_l, υ_s, υ_m and θ_D for all the compositions of unirradiated and irradiated samples are included in Table 6A.10. It is observed that the values of υ_l, υ_s, υ_m are found to decrease continuously up to x = 0.2 with Li-Ti content (x) then it is

slight increase for x = 0.3. The values of υ_l, υ_s, υ_m of irradiated samples are decreased as compared to unirradiated samples. It is interesting to note that the Debye temperature (θ_D) varies linearly with υ_m. The observed decrease in Debye temperature (θ_D) with content (x), suggested that the lattice vibrations are enhanced due to Li-Ti substitution. This may be due to the fact that strength of inter atomic bonding decreases with replacement of Fe^{3+} by Ti^{4+} in $Li_{0.5(1+x)}Ti_xAl_{0.1}Fe_{2.4-1.5x}O_4$ system., as supported to our results on variation of elastic moduli with concentration (x). After irradiation, the Debye temperature (θ_D) is reduced with corresponding to unirradiated samples which can be attributed to change occur in lattice vibrations due to weakening of interatomic bonding by rearrangement of cations under irradiation.

The calculated values of elastic moduli B, E, G and Poisson's ratio (σ) for all the compositions of unirradiated and irradiated samples are given in Table 6A.11. It can be observed from the table that the values of B, E and G are decreased with increasing Li-Ti content (x) for before and after irradiation. From Table 6A.11, further it can be seen that Poisson's ratio remains constant 0.35 for all the compositions. The values of elastic moduli B, E and G of all irradiated samples are reduced than the unirradiated ones. The variation of B, E and G with increasing Li-Ti concentration (x) may be interpreted in terms of interatomic bonding [6A.54]. Thus, it can be inferred from the decrease of elastic moduli with concentration (x) that the interatomic bonding between various atoms is getting weakened continuously. In the present system weakening of interatomic bonding on titanium (Ti^{4+}) substitution for Fe^{3+} ions can be explained as follows: The Fe^{3+} ions with $3d^5$ outer most orbital configurations are replaced by Ti^{4+} ions with $3p^6$ configuration, that form bond with $2p^6$ orbit of oxygen ion (O^{2-}). It is well known that completely filled orbit is more stable as compared to half filled orbit. In the present case Fe^{3+} ions with half with filled orbit ($3d^5$) are replaced by cations Ti^{4+} having completely filled outermost orbit ($3p^6$), which do not contribute to the bond formation. Thus, on increasing titanium substitution strength of bonding is expected to be weakened. The observed reduction in elastic moduli after irradiation can be accredited to modify in strength of interatomic bonding and inter-atomic forces of material under various strain/stress or defects produced by irradiation.

The elastic moduli of any material depend on the density of the material. The ferrites under study known to be porous, the porosity varying from 9.3 ~ 18.4 % in

present samples, so that the elastic moduli measured on these specimens will be less than those of non-porous ones. Hence, the observed elastic moduli of the specimens have been corrected to zero porosity using Hasselman and Fulrath's formulae [6A.55] given by:

$$\frac{1}{E_0} = \frac{1}{E}\left(1 - \frac{3f(1-\sigma)(9+5f)}{2(7-5f)}\right)$$

$$\frac{1}{G_0} = \frac{1}{G}\left(1 - \frac{15f(1-\sigma)}{(7-5\sigma)}\right)$$

$$B_0 = \frac{E_0 G_0}{3(3G_0 - E_0)}$$

$$\sigma_0 = \frac{E_0}{2G_0} - 1$$

The corrected values of bulk modulus (B_0), Young's modulus (E_0), rigidity modulus (G_0) and Poisson's ratio (σ_0) for different compositions of unirradiated and irradiated samples are specified in Table 6A.12. The values of B_0, E_0 and G_0 show regular variation similar to that of B, E and G, except for unirradiated sample x = 0.2 and irradiated sample x = 0.1. The Poisson's ration (σ_0) is found to be 0.37~0.40 and this values lie in the range from -1 to 0.5 which is in conformity with the theory of isotropic elasticity.

6A.5 Swift Heavy Ion Irradiation effects on Electrical properties of the system $Li_{0.5(1+x)}Ti_xAl_{0.1}Fe_{2.4-1.5x}O_4$

Resistivity is sensitive to the chemical composition and condition under which the sample has been prepared like pressure, heating and cooling rate during sintering, porosity and grain size. The dc resistivity of pellets of each ferrite prepared at pressure (P) ≈ 2 x 10^7 Kg/m^2 and sintering at 1000^{o}C for 24 hours has been measured as a function of temperature (300-900K). The variation of dc resistivity ($\log_{10}\rho_{dc}$) with the substitution of Ti^{4+} content (x) for unirradiated and irradiated $Li_{0.5(1+x)}Ti_xAl_{0.1}Fe_{2.4-1.5x}O_4$ ferrite at room temperature is mentioned in Table 6A.13. It is observed that the dc resistivity, in general increase with increasing substitution of Ti^{4+} for unirradiated as well as irradiated ferrite, except those with x = 0.2 for the irradiated ferrites. This may be happen because the replacement of Fe^{3+} by Ti^{4+} in Li-Al containing system dilutes conduction through the octahedral sites. The incorporation of Li-Ti-Al ions which do not participate in the conduction process, limits the degree of $Fe^{3+} + Fe^{3+}$

$\Leftrightarrow Fe^{4+} + Fe^{2+}$ conduction that occurs. Therefore, the efficient method of restraining the conduction process is the replacement of the effective ion (Fe^{3+}) by less effective ones (Li^{1+}, Al^{3+}, and Ti^{4+}). According to Verwey and De Boer [6A.56] a conduction mechanism in ferrites is involve an exchange of electrons between the ions of the same element present in more than one valence state such as Fe^{2+} and Fe^{3+} and distributed randomly over equivalent crystallographic lattice sites without causing a change in the energy state of the crystal. As a result of the transitions hopping between A-A sites does not exist for the simple reason that any Fe^{2+} ions formed during processing preferentially occupy B-sites only. Thus, the variation in resistivity may be explained either by hopping probability of the cations present in B-sites or by the microstructural modifications brought about by the sintering conditions or the both.

In the present system Fe^{3+} ion are replaced by Ti^{4+}. A tetravalent ion is able to form stable electronic bonds with Fe^{2+} ions. Since Ti ion is tetravalent it localizes Fe^{2+} ions which are formed during the sintering process as suggested by Tailhedes et al [6A.57]. The localization phenomenon hinders the Verwey mechanism [6A.58] $Fe^{3+} \Leftrightarrow Fe^{2+}$, which results in increasing resistivity. Moreover, the increase in resistivity with Ti concentration ($x > 0.0$) may be due to the presence of Ti^{4+} that does not contribute to conduction but act as a scattering centre at B-sites and obstructing the degree of easy conduction $Fe^{3+} \Leftrightarrow Fe^{2+}$ and $Fe^{3+} \Leftrightarrow Fe^{4+}$ ions.

In order to study of irradiation effect on the dc resistivity, after irradiation the value of dc resistivity is reduced as compared to unirradiated ones, except those with $x = 0.0$. It is clear (Table 6A.13) that the dc resistivity for concentration $x = 0.0$ is not much more influenced by irradiation, it is slightly increases after irradiation, whereas the substitution of Ti and Li ($x > 0.0$) the effect of irradiation becomes more pronounced and the dc resistivity is reduced in irradiated samples as compared to unirradiated ones. This means that the role of Ti is much more in the presence of small amount of Al for the formation of points/cluster of defect in the present system during irradiation. The observed reduction in the dc resistivity after irradiation is may be attributed to the increase in the Fe^{3+}/Fe^{2+} and Fe^{3+}/Fe^{4+} ratio on octahedral sites by the irradiation process. This causes an enhance in the rate of electrons or holes exchange between Fe^{3+} -Fe^{2+} and Fe^{3+} - Fe^{4+} by the hopping mechanism, which also causes a decrease in the resistivity.

The distance between the magnetic ions (Jump length) L is given by $L_A = a\sqrt{3}/4$ for the A-sites and by $L_B = a\sqrt{2}/4$ for the B-sites [6A.59-6A.61] where 'a' is the lattice constant (Table 6A.3). The variation of jump length (L) as a function of Ti-content (x) for unirradiated and irradiated Li-Al ferrite is summarized in Table 6A.14.

The compositional increase in jump length (L) for unirradiated and irradiated specimens is due to the larger cationic radius of the replacing cation Ti^{4+} (0.68 Å) than the replaced cation Fe^{3+} (0.64 Å) in the spinel lattice. The observed increase in L with content (x) suggest that charge carrier required more energy to jump from one cationic site to other as result resistivity should increase with increase content (x). Our result on variation of dc resistivity with content (x) indicates that ρ_{dc} increases with increasing content (x) (Table 6A.13) in the unirradiated and irradiated specimen but in the case of irradiated specimen controversy result observed values of dc resistivity decreases as compared to unirradiated ones. Jump length L is increase after irradiation but at the same time dc resistivity is decrease as compared to unirradiated ones. This may be due to the expansion of lattice during irradiation but at same time due to the rearrangement of cations (Table 6A.2) in spinel, which is increase the rate of electrons and hole exchange between Fe^{3+} -Fe^{2+} and Fe^{3+} - Fe^{4+} by the hopping mechanism, that result in decrease in dc resistivity after irradiation. The results co-related jump length (L) of the charge carriers between Fe^{3+} and Fe^{4+} (for p-type conduction) for all the samples on the octahedral site to the electrical resistivity.

The ρ_{dc} values for a series of ferrites lie between 10^5 to $10^9\Omega$.cm near room temperature (Table 6A.13); obviously they are good insulators at room temperature. The variation of ρ_{dc} with temperature for compositions x = 0.0 – 0.3 of unirradiated and irradiated ferrites presented in Fig. 6A.7 as plots of $\log\rho_{dc}$ versus $10^3/T$. It is observed that the resistivity decreases linearly with increasing temperature, reflecting the semiconductor nature of ferrites for before and after irradiation. For all the compositions curves reveal three distinct region and two breaks. Similar type of behaviour has for Li-Cu and Li-Mg-Al mixed ferrites [6A.62, 6A.63]. Accordingly, the observed three different regions in the resistivity plots for mixed ferrites, which have been attributed to different types of conduction mechanism. In the first region in the resistivity plot at low temperature indicates conduction due to impurities, while the second region is due to the phase transition and in the third region is due to

magnetic disorder. The conduction process in the present material may be due to grains, grain structure and porosity in region-I, order of Li-ions, and crystal structure changes in region-II and magnetic disorder in region-III.

In ferrites, the electrons are localized and there is little overlap between the wave functions of ions situated on adjacent sites. In the presence of lattice vibrations, the ions occasionally come so close that the transfer of electrons from one ion to another occurs with high probability. Hence the mobility is temperature dependent and is characterized by activation energy. The activation energy for the ferrimagnetic region (E_f) and the paramagnetic region (E_p) in the present case was obtained by fitting the dc resistivity data with the Arrhenius relation (Table 6A.13)

$$\rho = \rho_0 \exp (\Delta E / kT)$$

where ΔE is the activation energy and k is the Boltzmann constant. The activation energy is changing from ferrimagnetic region (region - II) to paramagnetic region (region-III). A change in slope ferrimagnetic region to paramagnetic region is nearly to the Nèel temperature. The values for activation energy and Nèel temperature deduced for the all unirradiated and irradiated compositions are listed in Table 6A.13. According to the theory of magnetic semiconductor, one expect such a reduction in the activation energy as the system undergoes the transition from the paramagnetic to the ferrimagnetic state is an ordered state while the paramagnetic state is disordered, thus the charge carriers require more energy in the conduction. The high value of the activation energy in the paramagnetic state as compared to ferrimagnetic state is due to the volume expansion of the samples during the magnetic transition [6A.63-6A.65]. In general, the activation energies are found to increase with substitution of Li-Ti content (x) with corresponding un-substituted Li-ferrite for the unirradiated and irradiated samples, however the random variation of activation energy is observed in present system. This can be attributed to the increase in inter-ionic distances and lattice parameter due to replacement of smaller cations Fe^{3+} ions by larger cation Ti^{4+} ions. In addition, the activation energy is also influenced by grain size, grain boundary, and porosity the material. So, random behaviour in activation energy may due to affect of grain size, grain boundary, and porosity. In the present system, the activation energies in ferrimagnetic region are much higher than the ionization energies (Ei = 0.1 eV) of donors or acceptors and hence the possibility of band type conduction is ruled out. It is also much larger than electron-transition energy of 0.2

eV such as $Fe^{2+} \Leftrightarrow Fe^{3+}$, which is suggest that the conduction phenomenon in present system is due to polaron hopping.

The irradiated ferrites showed the same behaviour in the plots of $\log\rho_{dc}$ versus $10^3/T$ for all the compositions as those of unirradiated ones. The results for irradiated samples are summarized and given also in Table 6A.13. From this the following can be shown

- The whole range of temperature the value of ρ_{dc} decreases as compared to unirradiated specimen except those with x = 0.0, which is not much more influenced by irradiation.
- Changes occur in activation energy. The values of activation energy of ferrimagnetic region is increased for the compositions x = 0.0 and 0.2 while for x = 0.1 and 0.3 is found to decrease, further the value of activation energy is found to increase, expect those with x = 0.1 for the paramagnetic region with respect to unirradiated ones.
- T_N moves towards lower temperatures for irradiated ferrites as compared with the values for corresponding unirradiated samples (Table 6A.13).

The observed reduction in the ρ_{dc} after irradiation can be attributed to the irradiation by Li-ion generates some points/clusters of defects at different depths, which act as trapping centres. The generation of charge carriers from the trapping centres needs different energies, which can be accomplished by increasing the temperature. This process will decrease the resistivity of the samples. The activation energy increases in paramagnetic region may be due to more disorder produce in samples by irradiation or change may be occur in volume expansion during magnetic transition by irradiation, thus the charge carriers require more energy in the conduction. Therefore, the activation energy increases after irradiation. This reflection can be occurring in Nèel temperature. Consequently, T_N moves towards lower temperature after irradiation as compared to unirradiated ones.

In ferrites, the charge carriers are not complete free but are strongly localized in the d-shell; this localization may be due to the electron-phonon interaction (or formation of polarons). A small polaron defect is created when an electronic carrier becomes trapped at a given site as a consequence of the displacement of adjacent atoms or ions. The entire defect (carrier plus distortion) then migrates by an activated hopping mechanism. The small polaron model also explains the low value of

mobility, temperature independent Seebeck coefficient and thermally activated hopping. The polaron radius (r_p) has determined for all the unirradiated and irradiated compositions by using relation $r_p = ½ [\pi/6N]^{1/3}$, where N = number of sites per unit volume = $96/a^3$. In spinel ferrites 64A (tetrahedral) 32B (octahedral) sites are available per unit volume [6A.63, 6A.66]. The computed values of r_p for all the compositions of unirradiated and irradiated samples are mentioned in Table 6A.14. It is seen that the values of r_p are smaller than inter ionic distances, which are followed an essential conditions for the formation of a small polaron is that the values of polaron radius (r_p) should be less than inter atomic distances and hence are suitable for small polaron conduction. The small polarons conduct in band like manner up to a certain temperature, the resistivity showing a decrease with frequency. At higher temperature, the conduction is by thermally activated hopping. [6A.63]. It is clear from Fig. 6A.19a-19b that the ρ_{ac} decreases with increasing frequency, giving indirect support for small polaron involving a band like mechanism.

It is found that the polaron radius (r_p) increases with Li-Ti concentration (x) for unirradiated and irradiated samples, which is followed trend of lattice parameter (a). After irradiation polaron radius (r_p) is found to higher than the unirradiated ones, which is attributed to the irradiation creates polarons and increases the lattice vibrations as well as enhancement of unit cell parameters.

The compositional variation of the Seebeck coefficient (α) as a function of temperature of all unirradiated and irradiated samples are shown in Fig. 6A.8. The thermoelectric power 'α' is positive for the samples with x = 0.0 - 0.3, indicating that the conduction is due to hole. The thermo electric voltage (ΔE) developed across each pellet of the ferrite material dose not significantly depend upon heating and cooling cycles and reproducible values (within ±10%) are obtained in successive observations. The Seebeck coefficient (α) = $\Delta E/\Delta V$ (ΔV = the temperature difference across the samples) at different temperature (300-500K) for the samples studied before and after irradiation is revealed in Fig. 6A.8. The striking features of the system studied are that

- α is positive for all the compositions over the whole range of temperature for unirradiated and irradiated samples

- α increases with increasing temperature for x = 0.0 and 0.2, while x = 0.1 and 0.3 which is initially decrease and remain constant up to 420K than slightly increase at higher temperature for unirradiated specimen.
- In the case of irradiated samples, a change occurs in Seebeck coefficient values (α)-they become less positive for x > 0.0, while x = 0.0 at lower temperature it is less positive but at higher temperature becomes more positive (above 360K) as compared to unirradiated ones.

The most probable mechanism for n-type conduction is electron hopping between Fe^{3+} and Fe^{2+} ions [6A.67], such as

$Fe^{2+} \Leftrightarrow Fe^{3+} + e^{-}$ (n-type)

The first observation in the present system, α indicating that the majority charge carrier is hole or p-type conduction dominant. Thus, the conduction mechanism for the p-type semiconductor is due to the hole transfer from Fe^{4+} centres to neighbouring Fe^{3+} ions [6A.68]. The coupling mechanism for hole exchange can be represented as

$Fe^{4+} \Leftrightarrow Fe^{3+} + e^{+}$ (hole)

The second observation leads to the conclusion that on increasing temperature the number of Fe^{4+} increases. The observed reduction in seebeck coefficient suggests hindrance of charge carriers by defect produce due to irradiation.

Bashikirav and Liberman [6A.69] have classified ferrites as degenerate semiconductors, if the thermo emf is independent of temperature and as non-degenerate semiconductors, if the thermo emf depends on temperature. In the present study, samples are non-degenerate semiconductors.

In the region, where the conduction is due to one type of charge carrier (electron or holes; not both), the Fermi energy is given by [6A.70],

$$E_F = e\alpha T - AkT$$

where A is dimensionless constant having values 0 and 2 depending on dominant scattering mechanism, which is connected with the kinetic energy of charge carrier and e, k and T are charge of carrier; Boltzmann constant (8.6×10^{-5} eV) and absolute temperature, respectively. The values of E_F for unirradiated and irradiated specimen were calculated for two values of A (A = 0 and A = 2) and plotted as a function of temperature is shown in Fig. 6A.9. The extrapolated value of E_F to T = 0 K, give up the values of $E_F(0)$ (Table 6A.14).

On comparison the activation energy of the ferrimagnetic region (E_f), from resistivity graph is found to be higher than E_F (0) except for x = 0.3. The difference between the two values can be attributed to the activation energy associated with hopping of charge carriers. Thus, activation energy consistent of two components, one that is associated with generation of charge carriers (hole/electron) and the other associated with the hopping of the carriers between crystallographic equivalent sites. It is also observed that the Fermi energy is increase after irradiation for the compositions x = 0.0 and 0.3, while for x = 0.1 and 0.2 decreases as compared to unirradiated ones.

Drift mobility of the above systems has been calculated using equation $\mu_D = 1/\rho_{dc}.n_c.e$, where n_c is the number of the charge carriers per unit volume and is given by the Heike's relation [6A.71].

$$\alpha = \frac{k}{e}\left(\frac{S_r^*}{k} - \log_e \frac{c}{1-c}\right)$$

where S_r^* is the effective entropy of the lattice which is temperature independent and S_r^*/k is very small. c is given by n_c/N, where N is the total number of available sates. Neglecting the term S_r^*/k from the relation gives

$$\alpha = \frac{k}{e}\log_e\left(\frac{1}{c} - 1\right)$$

If V is the volume of the samples under study above equations can be written as:

$$n_c = \frac{N}{V}\left[\frac{1}{1+\exp\left(\frac{\alpha}{k/e}\right)}\right]$$

The value of charge carrier concentration per unit volume has been calculated for all the unirradiated and irradiated compositions at the each temperature by using the value of the Seebeck coefficient |α|. N is the density states, in the case of low mobility semiconductors like ferrites having exceedingly narrow bands or localized level, the value of N can be taken as 10^{22} /cm^3[6A.63, 6A.72-6A.73] and e is the electronic charge (1.6 x 10^{-19} coulomb). The variation of charge carrier concentration (n_c) with temperature behave inversely propositional to seebeck coefficient (∝). It can be seen

from Fig. 6A.10 that the unirradiated and irradiated samples x = 0.0 and 0.2 the charge carrier concentration (n_c) are found to decrease, while samples x = 0.1 and 0.3 initially increase up to 370K after that slight decrease or remain almost constant with increasing temperature. This is due to the holes which are the majority charge carries are remunerated by thermally generated electrons ($Fe^{2+} \leftrightarrow Fe^{3+}$) on increasing temperature in the system. All irradiated samples show higher values of the charge carrier concentration (n_c) with respect to unirradiated samples. This indicates that the more cation vacancies (defect) produce under irradiation which may be act as a p-type charge carriers or may be more charge carriers generated due to electronic rearrangement by irradiation.

To examine the temperature dependence of mobility (μ_D) and $10^3/T$ is shown in Fig. 6A.11. It is noticed from the graph that by increasing temperature, mobility also increases for the samples x = 0.0 and 0.2 whereas initially it is found decrease and then increase for the samples x = 0.1 and 0.3 before and after irradiation. This is due to the hopping of charge carriers from one site to another as the temperature increases. After irradiation the values of drift mobility is found to be lower than the unirradiated samples in the measured temperature range, except irradiated sample x = 0.1. This suggests that the defects are hindrance thermally activated mobility or charge carriers. It can be seen that samples having higher resistivity have low mobility and vice versa [6A.74]. In the present system, the resistivity as well as mobility both is found to decrease in the measured temperature range for irradiated samples x = 0.0, 0.2 and 0.3 with corresponding to unirradiated samples. These results are support to our prediction that the more charge carriers are produced under irradiation and hence increase hopping rate. The value of the mobility is found in the range of 10^{-7}-10^{-11} cm^2/V.sec. This range is consistent with the mobility suggested in the literature for holes (10^{-8} cm^2/V. sec) [6A.75].

6A.6 Swift Heavy Ion Irradiation effects on Dielectric properties of the system $Li_{0.5(1+x)}Ti_xAl_{0.1}Fe_{2.4-1.5x}O_4$

The dielectric behaviour is one of the most important properties of ferrite which depends in the preparation condition, chemical composition, sintering temperature and doping of additives. The study of dielectric properties produces valuable information on the behaviour of localized electronic charge carriers leading to greater understanding of the mechanism of dielectric polarization in ferrites

studied. The dielectric behaviour was previously studied for Li - ferrites [6A.76-6A.78]. Frequency and composition dependence of dielectric behaviour of mixed Li-Cd ferrites have been investigated by Radha et al [6A.79]. Temperature and frequency-dependent dielectric properties of Zn-substituted Li-Mg ferrites have been inspected by Shaikh et al [6A.80]. High frequency dielectric behaviour of Li-Mg ferrites have been studied by Ravinder et al [6A.81]. However, no reports have been found in literature about irradiation study of Li-ferrites. Therefore, the purpose of this work to study the effect of swift heavy ion (SHI) irradiation on dielectric properties as a function of composition, temperature and frequency of $Li_{0.5(1+x)}Ti_xAl_{0.1}Fe_{2.4-1.5x}O_4$ (x = 0.0, 0.1, 0.2 and 0.3) ferrite system.

The dielectric measurements as a function of composition, temperature and frequency were performed on each unirradiated and irradiated samples. Dielectric constant was calculated by using the formula [6A.82]

$$\varepsilon' = C_p d/\varepsilon_0 A$$

where Cp is the capacitance of parallel plate in pF, 'd' is the thickness of the sample , A is the cross-sectional area of the flat surface of the sample and ε_0 is the permittivity of the free space (~ 8.85 x 10^{-12} F/m). The samples for dielectric measurements were in the pellet form of 10 mm in diameter and 2 mm in thickness for unirradiated specimen. The ferrite pellets were cut and polished to require size (10 mm in diameter and 0.3~0.4 mm in thickness) as determined by using the SRIM-98 software for the SHI irradiation experiment. AC resistivity (ρ_{ac}) is obtained from the data of dielectric constant (ε') and loss tangent ($\tan\delta$) using the relation [6A.82]

$$\rho_{ac} = 1/\varepsilon'\varepsilon_0\omega\tan\delta$$

where $\omega=2\pi f$ is the angular frequency. The dielectric loss tangent ($\tan\delta$) was directly measured from the LCR meter. Since the loss factor is the ratio of the imaginary part (ε'') and the real part of the dielectric constant, the imaginary part of ε'' can be calculated from the relation

$$\varepsilon'' = \varepsilon'\tan\delta$$

The capacitance Cp and the loss tangent ($\tan\delta$) were directly measured as a function of temperature (300 – 850 K) and frequency (20Hz-1MHz) using LCR meter.

The compositional, temperature and frequency dependence of dielectric constant (ε'), loss tangent ($\tan\delta$), complex dielectric constant (ε'') and ac resistivity

(ρ_{ac}) of unirradiated and 50 MeV Li^{3+} ion irradiated Ti^{4+}-substituted Li-Al containing ferrite was measured.

Table 6A.15 correlates the variation of the real part (ε') and imaginary part (ε''= ε'tanδ) of dielectric constant and a. c. resistivity ($\log_{10}\rho_{ac}$) for two different frequencies 1kHz and 10kHz as a function Li-Ti content (x) at room temperature (300K). Table show that the unirradiated and irradiated samples with x = 0.2 has the maximum ε' and ε'' as well as minimum ρ_{ac}; this means that the maximum polarization as well as the maximum valence exchange will take place. Introducing Li^{1+} -Ti^{4+} ions into the unirradiated and irradiated samples decrease both ε', ε'' and increase ρ_{ac} for the compositions x = 0.1 and 0.3 with respect to sample x = 0.0. The results can be explained on the basis of that the conduction mechanism could be expressed in terms of electron hopping between ferrous and ferric ions on octahedral sites for n-type semiconductor ferrites and in terms of hole hopping for p-type ferrites [6A.83]. In view of Li^{1+}, Ti^{4+} and Al^{3+} ions are fixed charge state, it is thought that the number of Fe^{3+} ions at the octahedral (B) sites that governs the polarizability in the present system. Some other researchers [6A.84, 6A.85] have reported that the conduction mechanism in Li-Ti mixed ferrites was attributed to the hopping of charge carriers from $Fe^{2+} \Leftrightarrow Fe^{3+}$ octahedral sites. The hole hopping between Fe^{3+} to Fe^{4+} are responsible for electric conduction and dielectric polarization in our system due to p-type ferrites. The $Fe^{4+} \Leftrightarrow Fe^{3+} + e^{+}$ gives the hole concentration in the octahedral sites which produce the local displacement in the opposite direction of applied fields. These displacements determine the polarization as well as dielectric properties. The valence exchange between iron ions is responsible for the polarization which is maximum in the case of Ti concentration x = 0.2. Therefore, a comparatively high value of the dielectric constant (ε'), dielectric loss (ε'') and low value of resistivity (ρ_{ac}) is expected. For the compositions x = 0.1 and 0.3 show higher value of resistivity and activation energy (Table 6A.13) can be attributed to the impedance caused by Ti^{4+} ions to the hopping of electrons/hole, thereby reducing their contribution to conductivity, further lower value of ε', ε'' agree well with the conclusion that, the higher activation energy for dielectric relaxation is associated with lower ε', ε''whereas lower activation energy is associated with higher values of ε', ε'' [6A.86]. For all the compositions of irradiated ferrites are found high value of ε', ε'' with compared to unirradiated samples. This is attributed to the increase valance exchange

of cations as well as polarization and decrease in ac resistivity (ρ_{ac}) by irradiation process.

The variation of real (ε') and imaginary (ε''= ε'tanδ) part of dielectric constant with temperature in the range from 300K to 850K at different frequencies have been performed for x = 0.0, 0.1, 0.2 and 0.3 compositions of unirradiated and irradiated samples are shown in Figs. 6A.12a-12d & 6A.13a-13d. A careful observation of the spectra suggests the following.

- The dielectric constant (ε') and complex dielectric constant (ε'') increase slowly with the temperature in the beginning up to roughly about 550K (in low temperature region) and above this temperature ε' and ε'' increase rapidly and sharply for all the unirradiated and irradiated samples, except for irradiated sample x = 0.0.
- The dielectric constant (ε') shows anomalous (i.e. peak) behaviour with temperature for the irradiated sample x = 0.0. Initially it increases with temperature, reaches a peak value and then decreases with further increase in the temperature. The occurrence of peak was found to be broad as the frequency increases. The values of ε' show maxima peak at relatively high temperature range and it is found to higher in magnitude at high temperature range (above 550K) as compared to unirradiated sample for the different frequencies of 500Hz, 1kHz, 10kHz and 50kHz. Further the frequency increase up to 500kHz, 800kHz and 1MHz, the magnitude of ε' is found to be lower with maxima broad peak in the measured temperature range.
- The magnitude of ε' for irradiated samples x = 0.1, 0.2 and 0.3 is lower than the unirradiated samples in the measured temperature range.
- The values of ε' and ε'' decreases with increasing frequency.

Fig. 6A.12a-12d indicate that the dielectric constant (ε') increases with increasing the temperature; this is normal character of magnetic semiconductor ferrites. This result is in accordance with those obtained earlier for Li-Ti [6A.85], Li-Mg [6A.80] ferrites and other Mg-Zn [6A.87], Mg-Al [6A.88], Ni-Mg [6A.89], Ni-Zn [6A.90] ferrites. Study of the thermoelectric power of the present samples showed that the majority of the electric charge carriers are holes above room temperature and the fall in the dc and ac resistivity for these samples as temperature increases could be

related to the increase in the drift mobility of the thermally activated holes according to hopping conduction mechanism in the studied samples. The hole hopping (exchange) between Fe^{3+} and Fe^{4+} ions on octahedral sites (which is responsible for electric conduction) is thermally activated by increasing the temperature. This holes hopping causes local displacements in the opposite direction of the external applied field; this includes the dielectric polarization in ferrites. As the temperature increases, the dc and ac conductivities increases due to increase in drift mobility of thermally activated holes. As a result, the dielectric polarization increases causing an increase in ε' and ε''.

Furthermore, the temperature dependent dispersion of real (ε') and imaginary (ε'') part of the dielectric constant is quantitatively expressed by the following equations [6A.91],

$$\varepsilon' = \varepsilon_\infty + \frac{\varepsilon_0 - \varepsilon_\infty}{1 + \omega^2 \tau^2}$$

$$\varepsilon'' = \frac{(\varepsilon_0 - \varepsilon_\infty)\omega\tau}{1 + \omega^2 \tau^2}$$

where ε' is the dielectric constant at frequency ω, ε_0 and ε_∞ are respectively low frequency and high frequency dielectric constants, and τ is the relaxation time. The relaxation time decreases with temperature due to high thermal energy supplied to the sample, and hence the dielectric constant increases with temperature.

On the other hand, the temperature dependent behaviour of dielectric constant can further be explained as follows. Dielectric constant in ferrites is attributed to four types of polarizations [6A.92]: interfacial, dipolar, atomic and electronic. At lower frequencies at which all four types of polarizations contribute, the rapid increase in dielectric constant with temperature is mainly due to interfacial and dipolar polarization, which strongly temperature dependent [6A.93]. In case of the interfacial polarization, this is due to the accumulation of charges at the grain boundary, an increase in polarization results as more and more charges reach the grain boundary with increase in temperature. Beyond a certain temperature the charges acquire adequate thermal energy to overcome the resistive barrier at grain boundary and conduction takes place resulting in decrease in polarization. The observed increase in ε'' with increasing temperature at all frequencies is attributed to the increase in the energy dissipation.

The temperature dependence of dielectric loss tangent (tanδ) for all the studied samples at selected frequency range (10kHz to 1MHz) is shown in the Fig. 6A.14a-14d, respectively. It is seen from the figure that tanδ versus temperature (T) for all the unirradiated samples show normal dielectric behaviour of magnetic semiconductors like tanδ increases as the temperature increases, except for x = 0.3 unirradiated sample. The unirradiated sample with x = 0.3 exhibits a slight broad maxima (broad peak) and which is shifting to higher temperature side as frequency increases. It is interesting to note that all the irradiated samples show sharp and more pronounced broad peak at frequency range 500Hz to 100kHz as compared to unirradiated samples. The position of broad maxima (peak) shifts towards higher temperature side or broad peak disappear as the frequency increases up to 500kHz to 1MHz, except for x = 0.2 irradiated sample. The value of tanδ is found to be higher for all the irradiated samples than the unirradiated ones. The dielectric loss (tanδ) for unirradiated and irradiated samples is decreased with increasing frequency.

The temperature dependent dispersion exhibited by the irradiated samples is consistent with Debye-type of dispersion for loss [6A.94].

$$\tan\delta = \frac{\varepsilon''}{\varepsilon'} = \frac{(\varepsilon_0 - \varepsilon_\infty)\omega\tau}{\varepsilon_0 + \varepsilon_\infty \omega^2 \tau^2}$$

According to this equation, tanδ would increase with decrease relaxation time for a given frequency. Therefore, as the relaxation time decreases with increase in temperature, tanδ increases. However, with further increase in temperature, tanδ shows a decline after a certain maximum values. This behaviour is typical of relaxation losses [6A.91]. The quick increase in the tanδ curve at higher temperatures cause the conduction losses, which increase with temperature due to increased conduction. Furthermore, the change occur in ε', ε'' and tanδ of irradiated samples with respect to unirradiated samples is attributed to modify polarizability by irradiation.

Fig. 6A.15a-15d shows the electrical resistivity (ρ_{ac}) and the reciprocal of absolute temperature (10^3/T) as a function of the applied frequency before and after irradiation. The obtained data obeys the well known Arrhenius relation [6A.95]. Increasing temperature leads to decrease in ρ_{ac} which is the normal behavior of the semi conducting materials and two conduction mechanism are expected here, the first

being the hopping mechanism below the transition temperature, where the resistivity is mainly frequency and temperature dependent. While the second mechanism above the transition temperature which is temperature dependent and frequency independent, is related to the drift mobility of thermally activated electron/holes and not to thermally creation of the charge carriers. The valance exchange between $Fe^{2+} \leftrightarrow Fe^{3+}$ and the hole hopping between $Fe^{3+} \leftrightarrow Fe^{4+}$ at B sites are the main source of hopping in present samples. The a. c. resistivity (ρ_{ac}) values of irradiated samples are inferior than unirradiated ones, apart from x = 0.1 and 0.3 reveal higher values of resistivity at particular frequency range 50kHz to 1MHz in the higher temperature region. This decrease in ρ_{ac} can be attributed to the increase in the ratio of Fe^{2+}/Fe^{3+} and Fe^{3+}/Fe^{4+} on the octahedral sites as a consequence of the hopping process under irradiation or may be irradiation process helps the alignment of charge carriers (hopping electron/holes) which are disturbed due to thermal energy.

The effect of frequency on the ε', ε'' and tanδ at different temperatures (300K to 773K) are represented in Figs. 6A.16a-16b, 6A.17a-17b & 6A.18a-18b, respectively for all studied unirradiated and irradiated samples. The variation of ε', ε'' and tanδ with frequency reveals the dispersion due to Maxwell-Wagner [6A.96, 6A.97] type interfacial polarization in agreement with Koop's phenomenological theory [6A.98]. Initially the values of all the parameters ε', ε'' and tanδ are found to decrease rapidly with increase in the frequency but beyond 10kHz remain fairly constant for unirradiated and irradiated samples in accordance with the normal behaviour of ferrites. The value of dielectric constant (ε') is much higher at lower frequency. It is because of the predominance of species like Fe^{2+} ions, oxygen vacancies, grain boundary defects, interfacial dislocation pile-up, voids etc. The decreasing trend ε' with the increase in the frequency is natural due to the fact that any species contributing to polarizability is found to show lagging behind the applied field at higher frequencies. Also the decrease of ε' with increasing frequency is ascribed to the increase of the jumping of the frequency of the charge carriers, which gives remarkable dispersion. Further, the polarization in ferrites is through a mechanism comparable to the conduction mechanism [6A.99] and the dielectric behaviour for the present samples can be explained on the foundation that the mechanism of polarization process. The swap of holes between (Fe^{4+}) and ferric ion (Fe^{3+}) on octahedral site may lead to local displacement of holes in the direction of the

applied field and these holes determine the polarization. Beyond a certain frequency, the holes exchange does not follow the alternating field and so the dielectric constant reaches a constant and small value.

A comparison of the dispersion curve for all the unirradiated and irradiated samples with Ti ion concentration and at different temperatures show that the change in the values of the ε', ε'' and tanδ at lower frequency is larger than that at higher frequencies of the externally applied field as well as irradiation effects. After SHI irradiation, for the frequency range studied there is a considerable increase in the magnitude of the real (ε') and imaginary (ε'') part of dielectric constant, apart from x = 0.3 at particular temperature 300K, 373K, 473 and 573K but nature remain constant before and after irradiation. This is because the irradiation helps in initiating some defects or vacancies which act as trapping centers for the charge carries. By increasing the temperature and frequency this trapping centers become sources of charge carries for hopping process as well as the formation of cation vacancies (defects) act as a p-type charge carrier and increase in the hopping rate accordingly raise observed in polarization. The observed reduction in the magnitude for the irradiated sample x = 0.3 may be due to the same defects hinder the polarization process taking place. In the other words, exchange holes may be trap in defects. These defects act as a trapping center so that local displacement of holes in the direction of the applied field restricted and decrease polarization.

The dielectric loss tangent (tanδ) of irradiated samples exhibit higher value considerable particularly up to 100kHz after which is coincides with unirradiated curve, expect for x = 0.0. The value of tanδ for irradiated sample x =0.0 is found to be lower as compared to unirradiated sample at lower frequencies while it is matching with unirradiated curve in the higher frequency region. This is due to the formation of defects under irradiation also act as a scattering centers so that holes requires more energy dissipates to transfer between Fe^{3+} and Fe^{4+} ions on octahedral. On the other hand, it is well known that different size of dipoles as well as different level of heterogeneity occur in these materials which interrupt the flow of the charge carriers at the interfaces and leads to the formation of barrier layers. It is assumed that dipoles in dielectrics usually interact with neighbouring dipoles and orientations of the dipoles with applied electric field would be very much dependent on the dipole-dipole interactions. If this interaction is weak, orientation will be easier and orientation will

be difficult if this is strong. The observed variation of tanδ with applied signal frequency can be explained on the basis of the fact that upon irradiation, dipole-dipole interaction gets weakened, so they can be oriented easy in the direction of the applied field. On increasing the frequency the rotation of dipoles lags behind the signal frequency so loss starts decreasing and for the frequency greater than 100kHz it shows variation similar to that of unirradiated samples.

The dielectric constant (ε') shows an anomalous (resonance peak) behaviour with frequency for irradiated samples x = 0.0 (at T = 573 K) and x= 0.2 (at T = 473K & 573K) with corresponding to unirradiated samples, even as tanδ shows same an anomalous behaviour for unirradiated sample x = 0.0 (at T= 773K). The occurrence of anomaly (peak) in the variation of ε' and tanδ with frequency can be observed when the hopping frequency is approximately equal to that of the externally applied electric field; that means 'resonance phenomena'. The condition for observing a maximum in ε' and tanδ of a dielectric material is given by the relaxation [6A.36, 6A.84]: $\omega\tau = 1$, where ω is the $2\pi f_{max}$ and τ is relaxation time. Now the relaxation time τ is related to the jumping probability per unit time p, by the equation $\tau = ½ p$ or $f_{max} \propto p$, f_{max} is proportional to jumping or hopping probability. So, the presence of f_{max} indicates that the hopping or jumping probability per unit time increases in particular samples.

The ac resistivity (ρ_{ac}) of the unirradiated and irradiated samples was measured at different temperature with frequency in the range 100Hz to 1 MHz is presented in Fig. 6A.19a-19b for all the compositions. The values of ac resistivity (ρ_{ac}) are found to decrease with increasing frequency and temperature for both unirradiated and irradiated samples. All irradiated samples show lower values of ac resistivity (ρ_{ac}) as compared to unirradiated samples, excluding x = 0.0 (at T = 773K) and x = 0.3 (at T = 373K & 473K) for the measured frequency range. The dielectric losses in ferrites are generally reflected in the resistivity measurements. Materials with high resistivity exhibit low dielectric losses and vice versa [6A.100]. The increase of loss tangent values in the studied ferrites confirms the decrease of resistivity supporting to the Verway conduction mechanism [6A.101]. Further, the resistivity was observed to decrease with increasing frequency can be explained on the basis of the grains and grain boundaries effect of the materials. At low frequency, where the resistivity has the highest value and the grain boundary effect is dominant,

more energy is required for exchange charge carriers located on the grain boundaries and result dielectric losses are high.

6A.7 Swift Heavy Ion Irradiation effects on Impedance Spectroscopy of the system $Li_{0.5(1+x)}Ti_xAl_{0.1}Fe_{2.4-1.5x}O_4$

The dielectric properties of materials can be expressed in various ways using different representations like the conductivity ($\sigma^* = \sigma' + i\sigma''$), the dielectric permittivity ($\varepsilon^* = \varepsilon' - i\varepsilon''$) or dielectric modulus ($M^* = M' + iM''$), Complex impedance ($Z^* = Z' - iZ''$).

Impedance spectroscopy is important tool to investigate the electrical properties of highly resistive grain boundaries since the grain boundaries frequently cause an additional semicircle in the complex impedance. When the grain boundary resistance is larger than the bulk, two semicircles are often obtained in complex plots. The deviations from ideal semicircles have been attributed to the distribution of relaxation times arising from the microstructural inhomogeneity or disorder in the samples [6A.102]. The complex impedance Z can be represented as $Z^* = Z' - i Z'' = |Z| \cos\theta - i |Z| \sin\theta$, where Z' and Z'' are the real and imaginary part of complex impedance, and |Z| and θ are the modulus and complex angle of the complex impedance, respectively. The complex impedance measurement was done for all the compositions of Li-Ti-Al ferrites with two separate unirradiated (10mm in diameter and 2~3 mm in thickness) and irradiated (10mm in diameter and 0.3~0.4mm in thickness) samples having different dimensions using LCR meter.

The imaginary part (Z'') of impedance versus real (Z') part of impedance is plotted over a wide range of frequency 100Hz to 1MHz at room temperature are shown in Fig. 6A.20. It can bee seen that the impedance data exhibit single semicircular arc only for the unirradiated sample x = 0.0 and 0.2, remaining all other unirradiated and irradiated samples do not acquire a complete shape of arc but rather exist a straight line with a hump at high frequency region. Generally, the two semicircles at high and low frequencies are identified as due to the grain or bulk and grain boundary phenomena, respectively. So, the high frequency semicircles can be attributed to the grain properties of the materials rising due to parallel combination of the grain resistance (R_g) and grain capacitance (C_g) of the materials. The low frequency semicircle is due to the sum of resistance of grain and grain boundary R_{gb} and C_{gb}. It is reported that two semicircle arcs of the impedance spectrum can be

expressed as an equivalent circuit consisting of a parallel combination of low resistance and capacitance connected in series (R-C circuit) [6A.103]. The relation between the electrical parameters for the RC circuit and impedance can be written as [6A.104].

$$z' = \frac{R_g}{1+\omega_g^2 C_g^2 R_g^2} + \frac{R_{gb}}{1+\omega_{gb}^2 C_{gb}^2 R_{gb}^2}$$

$$z'' = \frac{-R_g^2 \omega_g C_g}{1+\omega_g^2 C_g^2 R_g^2} + \frac{-R_{gb}^2 \omega_{gb} C_{gb}}{1+\omega_{gb}^2 C_{gb}^2 R_{gb}^2}$$

where ω_g and ω_{gb} are the frequency at the peaks of the semicircles for grain and grain boundary, respectively. R_g and C_g are the resistance and capacitance of the grain while R_{gb} and C_{gb} are that of grain boundary.

The present samples show single semicircle at room temperature. Consequently, the impedance response from the grain and grain boundary is not resolved, which suggest a predominant contribution from grain and that the contribution from the grain boundary is not well resolved in the present study.

The frequency dependence of the impedance (Z' and Z'') in the range of 100Hz to 1MHz at room temperature for all unirradiated and irradiated samples are illustrated in Fig. 6A.21. The results show that the values of Z' is decreased with increasing the frequency with corresponding to increase in ac conductivity. The curve Z'' versus log f show that Z'' reveals the maximum value for the unirradiated samples x = 0.0 and 0.2 at particular frequency (Z''_{max}) and then decreases with further increase in frequency, whereas unirradiated samples for x = 0.1 and 0.3 are found to decrease continuously with increasing frequency. After irradiation, this peak (Z''_{max}) is disappeared or shifting to lower frequency side with corresponding to unirradiated samples x = 0.0 and 0.2, while irradiated sample x = 0.3 is appeared Z''_{max} with respect to unirradiated sample for the same measured frequency range.

The modulus formalism is widely used to study electrical relaxation in ionically and electronically conducting materials, as it has the advantage of suppressing electrode polarization effect. The complex electric modulus was defined as the electric analogue of the dynamical mechanical modulus is related to the complex permittivity $\varepsilon^*(\omega)$ by $M^* = 1/\varepsilon^*(\omega) = M'(\omega) + iM''(\omega)$ [6A.105]. The real (M') and imaginary (M'') part of the complex electrical modulus were obtained from $\varepsilon'(\omega)$ and $\varepsilon''(\omega)$ values using the relation

$$M'(\omega) = \frac{\varepsilon'(\omega)}{\varepsilon'(\omega)^2 + \varepsilon''(\omega)^2} \text{ and } M''(\omega) = \frac{\varepsilon''(\omega)}{\varepsilon'(\omega)^2 + \varepsilon''(\omega)^2}$$

Using the above equations, the changed form of presentation of the electrical data from ε'(ω) and ε''(ω) to M'(ω) and M''(ω).

The variation of real (M') part and imaginary (M'') part of electric modulus with frequency at different temperatures for unirradiated and irradiated samples are illustrated in Fig. 6A.22a-22b. The obtained modulus spectra M'' versus log F exhibits peak or hump at selected temperatures in both cases that shifts systematically toward higher frequencies with increasing temperature. The frequency at which M'' maximum corresponds to the relaxation frequency. The peak position of the M'' spectra shift towards higher frequencies as the temperature increases, which means an increase in relaxation rate because of the thermal activation of the charge carriers.

The M* Cole-Cole plots for all unirradiated and irradiated samples at different temperature are shown in Fig. 6A.23a-23b. From the spectra of M''(f) $\rightarrow$ M' (f), it can be observed that there is one semicircle (or at least a part of it) in unirradiated specimens x = 0.0 and 0.2 at lower temperature, while for x = 0.1 and 0.3 semicircles are not well resolve at lower temperature. As increase the temperature, the diameter of semicircle is found to decrease for particular unirradiated samples x = 0.0 and 0.2 while single semicircle has appeared at higher temperature for the specimen x = 0.1 and 0.3. Even two semicircles have emerged at particular temperature 473K, 573K and 673K for unirradiated sample x =0.1. For the composition x = 0.1 and 0.3 at high temperature, the grain boundary conductivity is comparable to the bulk conductivity. This may be attributed to a growth of grain boundaries at high temperature.

For irradiated samples x = 0.0 and 0.2, the modulus data do not exhibit semicircle but present a straight line with large slope, whereas specimen x = 0.1 and 0.3 show single semicircle and the diameter of semicircle decreases with increasing temperature. The magnitude of modulus data of irradiated samples are found to higher than the unirradiated samples.

Scaling is an important feature in any data evolution program. The ability to scale different data sets so as to collapse all to one common curve (master curve) indicate that the process can be separated into a common physical mechanism [6A.106, 6A.107]. If the electric modulus M* data gave that master curve, this will show that the solid belongs to a category having a properties that suggest to be called

"electric stiffness" (i.e. how difficult dipoles are created and/or oriented in the solids) is dominating. Whilst, if the permittivity ε* data gave that master curve, this will show that the solid belongs to a category having the reciprocal property dominating and suggested to be called "electric compliance" (i.e. how easy dipoles are created and/or oriented in the solid) [6A.107]. S. A. Saafan et al [6A.107] have tried to apply scaling methods upon all possibly alternative functions σ', ε'', M', σ'', M'' in the available range of temperature and frequency. Furthermore, they have used for scaling purpose the characteristics frequency, f_c and DC conductivity (σ_{DC}) values. Specifically, they have displayed the scaling results of Al-substituted MnZn ferrites and most successful scaling was for ε'', M' and M'' either by using σ_{DC} or f_c, leading to a substantial results. In the present work, we have used for scaling purpose the characteristic frequency, f_c, which is known as the conductivity relaxation frequency [6A.108] and defined as the frequency at which a peak occurs in M"(f) curve. Fig. 6A.24 illustrates our attempt of scaling for the four investigated compositions of unirradiated Ti-substituted Li-Al-ferrites. It can be seen that the successful scaling was found for M" by using f_c in the available range of temperature and frequency.

Conclusion

We conclude that the 50 MeV Li^{3+} ion irradiation produce the point/clusters of defects in the samples of Ti^{4+} substituted $Li_{0.5}Al_{0.1}Fe_{2.4}O_4$. The increase in the cell edge parameter after irradiation is attributed to the rearrangement of the cations in the lattice. The reduction in saturation moments and the Curie temperature and appearance of the paramagnetic doublet in the Mössbauer spectra after SHI irradiation can be understood on the basis of SHI-induced formation of the paramagnetic centres and the redistribution of the cations in the irradiated samples. The central enhancement observed in the Mössbauer spectra of the irradiated samples is not due to amorphization but its origin lies in the formation of localized paramagnetic centers.

The observed change in Me-O and Me-Me distances and bond angles after irradiation suggest modification of strength of magnetic interactions. The IR spectra of the unirradiated and irradiated ferrites show the high frequency band ν_1 and second absorption band ν_2 are found to be in the range of 518-589 cm^{-1} and 408-488 cm^{-1}, respectively depending on Ti-concentration. The occurrence of shoulders or side bands near ν_1 band for unirradiated samples x = 0.0, 0.1 and 0.2 indicate the presence of small amount of Fe^{2+} ions in tetrahedral sites. The decrease in intensity of all the

absorption bands with increasing Li-Ti concentration can be ascribed on the basis of the change in dipole moment with the inter-nuclear distances (dμ/dr) and cation distribution. After irradiation, the ν_1 band shifts towards the higher frequency side and the increase in shoulders/splitting of main absorption bands ν_1 and ν_2 for all the samples. The force constant, elastic moduli and Debye temperature can be determined through IR spectral analysis. The observed decrease of elastic constant and Debye temperature with Ti-substitution suggests weakening of interatomic bonding. The observed reduction in force constant, elastic moduli and Debye temperature after irradiation can be accredited to modify in strength of interatomic bonding and inter-atomic forces of material under various strain/stress or defects produced by irradiation

The compositional increase in jump length (L) suggest that charge carrier required more energy to jump from one cationic site to other as result resistivity should increase with increase content (x). The observed reduction in the dc resistivity after irradiation is attributed to the increase in the Fe^{3+}/Fe^{2+} and Fe^{3+}/Fe^{4+} ratio on octahedral sites by the irradiation process. The controversy result of dc resistivity and jump length (L) after irradiation is due to lattice expansion and the increase the rate of electrons and hole exchange between Fe^{3+} -Fe^{2+} and Fe^{3+} - Fe^{4+} in the conduction process by rearrangement of cations. The resistivity decreases linearly with increasing temperature, reflecting the semiconductor nature of ferrites for before and after irradiation. The value of activation energy suggests that the conduction phenomenon in present system is due to polaron hopping. The thermoelectric power 'α' indicating that the majority charge carrier is hole or p-type conduction dominant in the present system and samples are non-degenerate semiconductors. All irradiated samples show higher values of the charge carrier concentration (n_c) with respect to unirradiated samples indicating more charge carriers generated due to electronic rearrangement by irradiation. The value of the mobility is found in the range of 10^{-7}-10^{-11} $cm^2/V.sec$. This range is consistent with the mobility suggested in the literature for holes (10^{-8} $cm^2/V.$ sec).

The unirradiated and irradiated samples with x = 0.2 has the maximum ε' and ε'' as well as minimum ρ_{ac}; this means that the maximum polarization as well as the maximum valence exchange will take place. The relaxation time decreases with temperature due to high thermal energy supplied to the sample, and hence the increases ε', ε'' and tan δ with temperature. The dielectric constant (ε') shows

anomalous (i.e. peak) behaviour with temperature for the irradiated sample x = 0.0. The change occur in ε', ε'' and tanδ of irradiated samples with respect to unirradiated samples is attributed to modify polarizability by irradiation.

The decreasing trend ε', ε'' and tan δ with the increase in the frequency is natural due to the fact that any species like Fe^{2+} ions, oxygen vacancies, grain boundary defects, interfacial dislocation pile-up, voids etc. contributing to polarizability is found to show lagging behind the applied field at higher frequencies. The occurrence of anomaly (peak) in the variation of ε' and tanδ with frequency can be observed when the hopping frequency is approximately equal to that of the externally applied electric field; that means 'resonance phenomena'. The values of a. c. resistivity (ρ_{ac}) are found to decrease with increasing frequency and temperature for both unirradiated and irradiated samples.

The analysis of data in the complex impedance plane indicates that the capacitive and the resistive properties of the materials are mainly attributed due to the processes, which are associated with the grain and grain boundary. We have picked up the conductivity relaxation frequency, f_c, at the peaks of the M"(f) curves and then have used it to construct master curves.

References

6A.1 J. M. Costantini, F. Studer and J. C. Peuzin,, J. Appl. Phys. **90** (2001) 126,

6A.2 J. M. Costantini, F. Brissrd, J. L. Flament, D. Bourgault, L. Sinopoli and J. L. Uzureau, Nucl. Instr. and Meth. B. **59/60** (1991) 600

6A.3 F. Studer and M. Toulemonde, Nucl. Instr. and Meth B **65** (1992) 560

6A.4 M. Singh, Anjana Dogra and Ravi Kumar, Nucl. Instr. Meth. B**196** (2002) 315

6A.5 F. Thibaudau, J. Cousty, E. Salanzat and S. Bouffard, Phys. Rev. Lett. **67 (12)** (1991) 1582

6A.6 G. Szenes, Phys. Rev. B **51(13)** (1995) 8026

6A.7 B. D. Culity, Elements of X-ray diffraction, II edition, Addison-Wesley, (1978)

6A.8 G. Blasse, Philips Res. Rept. Suppl. **3** (1964) 1

6A.9 U. N. Trivedi, K. B. Modi and H. H. Joshi, Pramana **58** (2002) 1031

6A.10 K. B. Modi, H. H. Joshi and R. G. Kulkarni, J. Mater. Sci. **31** (1996) 1311

6A.11 G. Gavollie and J. Hubsch, J. Mag. Mag. Mat. **36** (1983) 304

6A.12 M. J. Buerger, Crystal Structure Analysis, New York, John Wiley, (1960)

6A.13 L. Neel, Ann. Phys. **3** (1948) 137

6A.14 J. R. Gabriel and S.L.Ruby, Nucl. Insr. and Meth. **36** (1965) 23

6A.15 S. K. Kulshreshtha, J. Mater. Sci. **5** (1986) 638

6A.16 D. Ravinder, Cryst. Technol. **26** (1991) 457

6A.17 D. Ravinder, Mater. Lett. **40** (1999) 198

6A.18 K. B. Modi, J. D. Gajera, M. C. Chhantbar, K. G. Saija, G. J. Baldha and H. H. Joshi, Mater. Lett. **57** (2003) 4049

6A.19 J. Smith and H. P. J. Wijn, 'Ferrites', Philips, Eindhoven, 1959

6A.20 S. A. Mazen, M. H. Abdallah, B. A. Sabrah and H. A. M. Hasham, Phys. Stat. Sol. A **134** (1992) 263

6A.21 K. E. Sickafus and J. M. Wills, J. Am. Ceram. Soc. **82** (1999) 3279

6A.22 A. Globus, H. Pascard and V. Cagan, J. Phys. Suppl. **438** (1977) 439

6A.23 S. S. Bellad, R. B. Pujar and B. K. Chougule, Mater. Chem. Phys. **52** (1998) 166

6A.24 K. B. Modi, J. D. Gajera, M. P. Pandya, H. G. Vora and H. H. Joshi, Pramana -J. Phys. **62(5)** (2004) 1173

6A.25 J. B. Goodenough, J. Phys. Chem. Solids **6** (1959) 287

6A.26 J. Kanamori, J. Phys. Chem.. Solids **10** (1959) 67

6A.27 V. R. K. Murthy, Chitra S. Sonkar, K. V. Reddy and J. Sobhanadri, Ind. J. Pure & Appl. Phys. **16** (1978) 79

6A.28 B. P. Ladgaonkar, C. B. Kolekar and A. S. Vaingankar, Bull. Mater. Sci. **25(4)** (2002) 351

6A.29 R. D. Waldron, Phys. Rev. **99** (1955) 1727

6A.30 S. A. Mazen, M. H. Abdallah, R. I. Nakhla, H. M. Zaki and F. Metawe, J. Mater. Chem. Phys. **34** (1993) 35

6A.31 Navdeep K. Gill and R. K. Puri, Ind. J. of Pure & Appl. Phys. **23** (1985) 71

6A.32 R. S. Patil, S. V. Kakatkar, A. M. Sankpal and S. R. Sawant, Ind. J. of Pure & Appl. Phys. **23** (1994) 193

6A.33 S. A. Mazen, F. Metawe and S. F. Mansour, J. Phys. D: Appl. Phys. **30** (1997) 1799

6A.34 S. S. Bellad, R. B. Pujar and B. K. Chougule, Ind. J. of Pure & Appl. Phys. **36** (1998) 598

6A.35 K. Mohan and Y. C. Venudhar, J. Mater. Sci. Lett. **18** (1999) 13

6A.36 S. A. Mazen, Mater. Chem. and Phys. **62** (2000) 139

6A.37 S. A. Mazen, S. F. Mansour, E. Dhahri, M. H. Zaki and T. A. Elmosalami, J. Alloys and Comp. **470** (2009) 294

6A.38 K. B. Modi, K. H. Jani and H. H. Joshi Acta Ciencia Indica, **25** (1999) 5

6A.39 O. S. Josyula and J. Sobhanadri, Phys. Stat. Sol. A **65** (1981) 479

6A.40 D. Ravinder, Mater. Lett. **40** (1999) 205

6A.41 S. A. Patil, S. M. Otari, V.C. Mahajan and A. B. Patil, Sol. Stat. Commun. **78** (1991) 39

6A.42 J. C. Dwcius, O. G. Maln and A. W. Thomson, Proc. Roy. Soc. (London) A **275** (1963) 295

6A.43 S. C. Watawe, B. D. Sutar, B. D. Sarwade and B. K. Chougule, Inter. J. Inorg. Mater. **3** (2004) 819

6A.44 P. V. Reddy, M. B. Reddy, V. N. Mulay, K. B. Reddy and Y. V. Ramana, J. Mater. Sci. Lett. **7** (1988) 1243

6A.45 D. Ravinder and P. K. Raju, Phys. Stat. Sol. A **136** (1993) 351

6A.46 D. Ravinder, J. Appl. Phys. **75(10)** (1994) 6121

6A.47 Y. C. Venudhar and K. Satya Mohan, Meter. Sci. **55** (2002) 196

6A.48 D. Ravinder and P. V. B. Reddy, Mater. Sci. 57 (2003) 4575

6A.49 S. L. Kakani and C Hemrajani, 'Solid State Physics' Sultan Chand & Sons (1997)

6A.50 D. Ravinder, K. Vijaya Kumar and B. S. Boyanov, Mater. Lett. **38** (1999) 22

6A.51 D. Ravinder and T. A Manga, Mater. Lett. **41** (1999) 254

6A.52 S. R. Murthy, R. S. Narayana and S. Rao, J. Mater. Sci. Lett. **3** (1984) 352

6A.53 O. L. Anderson, in' Physical Acoustics', edited by W. P. Mason **3** (1965) 43 (Academic, New York)

6A.54 W. A. Wooster, Rep. Prog. Phys. **16** (1953) 62

6A.55 D. P. H. Hasselman and R. M. Fulrath, J. Am. Ceram. Soc. **47** (1964) 52

6A.56 E. J. W. Verwey and J. H. de Boer, Rec. Trav, Chim. Phys. Bas. **55** (1936) 531

6A.57 Ph. Tailhedes, Ch. Sarada, P. Millaral and A. Rousset, J. Mag. & Mag. Mater, **104-107** (192) 962

6A.58 E. J. W. Verwey, P. W. Haaijman, F. C. Romeyn and G. W. Can Oosterjout, Philips Res Rep **5** (1950) 173

6A.59 H. Pascard, A. Globus and V. Cabon, J. Physique **38 C1** (1977) 163

6A.60 P. V. Reddy and T. Seshegirirao, J. Less-Common Metals, **75** (1980) 255

6A.61 B. Gillot and F. Jemmali, Phys. Stat. Sol., (a) **76** (1983) 601

6A.62 A. B. Naik, S. A. Patil, and J. I. Pawar, Ind. J. Pure & Appl. Phys. **27** (1989) 149

6A.63 M. P. Pandya, K. B. Modi and H. H. Joshi, J. Mater. Sci. **40** (2005) 5223

6A.64 J. B. Goodenough, Mater. Res. Bull. **8** (1973) 423

6A.65 M. W. Zemansky, "Heat and Thermoynamics", (McGraw Hill, New York) (1968) p. 460

6A.66 A. J. Bosman and H. J. Van Dall, Adv. Phys. **19** (1970) 1

6A.67 E. J. Verwey and J. H. De Boer, Rec. Trav. Chim. Phys. Bas. **55** (1936) 531

6A.68 L. G. Van Uitert, J. Chem. Phys. 23 (1955) 1883

6A.69 S. S. Bashikirav, A. B. Liberman and V. V. Parfenov, Inorg. Mater. **15** (1979) 404

6A.70 A. J. Bosman and C. Crevecoeur, J. Phys. Chem. Sol. **30** (1969) 1151

6A.71 R. R. Heikes, in 'Thermoelectricity', edited by R. R. Heikes and R. W. Ure (Wiley Inter Science, New York 1961) p.45

6A.72 A. A. Samokhavalov and A. G. Rustamov, Sov. Phys. Sol. Stat. **6** (1953) 749

6A.73 F. J. Morin, Phys. Rev. **93** (1953) 1195

6A.74 M. Ajmal and A. Maqsood, Mater. Sci. and Eng. B **139** (2007) 164

6A.75 M. A. Ahmed, M. K. El. Nimr, A. Tawfik and A. M. El.Hasab, Phys. Stat. Sol. (a) **123** (1991)501

6A.76 P. Reddy and T. Rao, J. Less common Met. **105** (1985) 63

6A.77 M. B. Reddy and P. V. Reddy, Appl. Phys. **24** (1991) 41

6A.78 D. Ravinder, J. Mater. Sci. Lett. **11** (1992) 1498

6A.79 K. Radha and D. Ravinder, Ind. J. Pure & Appl. Phys. **33** (1995) 74

6A.80 A. M. Shaikh, S. S. Bellad and B. K. Chougule, J. Mag. & Mag. Mater. **195** (1999) 384

6A.81 D. Ravinder and P. V. B. Reddy, Mater. Lett. **57** (2003) 4344

6A.82 E. C. Snelling, 'Soft ferrites', 2nd Edition, Butterworth, London (1988) p. 34

6A.83 M. A. El. Hiti, J. Mag. & Mag. Mater. **164** (1996) 187

6A.84 M. B. Reddy and P. V. Reddy, J. Phys. D. Appl. Phys. **24** (1991) 975

6A.85 S. A. Mazen, F. Metawe and S. F. Mansour, J. Phys. D: Appl. Phys. **30** (1997) 1799

6A.86 M. A. Hiti, J. Mag. & Mag. Mater. **192** (1999) 305

6A.87 K. Iwauchi, Jpn. J. Appl. Phys. **10** (1971) 1520

6A.88 S. Radhakrishna and K. Badarinath, J. Mater. Sci. Lett. **3** (1984) 867

6A.89 M. El. Hiti and M. Ahmed, Mater. Sci. Technology **14** (1998) 19

6A.90 A. M. Abdeen, J. Mag. & Mag. Mater. **192** (1999) 121

6A.91 A. Verma, O. P. Thakur, C. Prakash, T. C. Goel and R. G. Mendiratta, Mater. Sci. Eng. B **116** (2005)1

6A.92 L. L. Hench and J. K. West, 'Principles of Electronic ceramics', John Wiley and Sons, New York, (1990), p.189

6A.93 L. L. Hench and J. K. West, 'Principles of Electronic ceramics', John Wiley and Sons, New York, (1990), p.205

6A.94 L. L. Hench and J. K. West, 'Principles of Electronic ceramics', John Wiley and Sons, New York, (1990), p.202

6A.95 J. Smit and H. P. Wijn, 'Ferrites' Cleaver-Hume Press London (1959)

6A.96 J. C. Maxwell, 'Electricity and magnetism' (Oxford University Press, London, 1873) Section 328

6A.97 K. W. Wagner, *Ann. Phys.* **40** (1913) 817

6A.98 C. G. Koops, *Phys. Rev.* **83** (1951) 121

6A.99 I. T. Rabinkin and Z. I. Novikova, 'Ferrites' (Minsk: Izv. Acad. Nauk USSR) (1960)146

6A.100 C. B. Kolekar, P. N. Vasambekar, S. G. Kulkarni and A. S. Vaingankar, J. Mater. Sci. **30** (1995) 5784

6A.101 E. J. W. Verway, P. M. Haaijiman, G. M. Romeyn and F. C. Vas Oosterhout, Philips Res. Rep. **9** (1954) 428

6A.102 M. P. Gutièrrez-Amador and R. Valenzuela, Mater. Res. Soc. Symp. Proc. (2002) 699

6A.103 J. E. Bauerle, J. Phys. Chem. Solids **30** (1969) 2657

6A.104 H. Inaba, J. Mater. Sci. **32** (1997) 1867

6A.105 N. Sivakumar, A. Narayanasamy, N. Ponpandian and G. Govindaraj, J. Appl. Phys. **101** (2007) 084116

6A.106 D. L. Sidebottom, Phys. Rev. Lett. **82(18)** (1999) 3653

6A.107 S. A. Saafan, A. S. Seoud and R. E. El Shater, Physica B **365** (2005) 27

6A.108 A. Mansinghand, V. K. Dhawan, Philos. Mag. B **48 (3)** (1983) 215

6A.109 B. Viswanathan and V. R. K. Murthy, Ferrite Materials Science and Technology (Narosa Publishing House, New Delhi (1990) p. no. 9

Table 6A.1: Chemical composition and molecular weight of each specimen of the spinel system: $Li_{0.5(1+x)}Ti_xAl_{0.1}Fe_{2.4-1.5x}O_4$

Content (x)	Chemical composition	Molecular weight (amu)
0.0	$Li_{0.5}Al_{0.1}Fe_{2.4}O_4$	204.19805
0.1	$Li_{0.55}Ti_{0.1}Al_{0.1}Fe_{2.25}O_4$	200.95795
0.2	$Li_{0.6}Ti_{0.2}Al_{0.1}Fe_{2.1}O_4$	197.71785
0.3	$Li_{0.65}Ti_{0.3}Al_{0.1}Fe_{1.95}O_4$	194.47775

Table 6A.2: Results of XRD intensity analysis and Cation distributions for unirradiated and irradiated samples of $Li_{0.5(1+x)}Ti_xAl_{0.1}Fe_{2.4-1.5x}O_4$ system

Content (x)	Sample	I(220)/I(440)		I(422)/I(400)		Cation Distribution
		theo.	obs.	theo.	obs.	
0.0	Unirr	0.781	0.771	0.741	0.732	$(Fe_{0.97}Al_{0.03})\ [Fe_{1.43}Al_{0.07}Li_{0.5}]O_4$
	Irr	0.832	0.829	0.801	0.792	$(Fe_{1.0})[Fe_{1.4}Al_{0.1}Li_{0.5}]O_4$
0.1	Unirr	0.811	0.804	0.753	0.742	$(Fe_{0.95}Al_{0.05})\ [Fe_{1.3}Al_{0.05}Ti_{0.1}Li_{0.55}]O_4$
	Irr	0.845	0.837	0.881	0.871	$(Fe_{0.97}Ti_{0.03})\ [Fe_{1.28}Al_{0.1}Ti_{0.07}Li_{0.55}]O_4$
0.2	Unirr	0.794	0.784	0.725	0.714	$(Fe_{0.9}Al_{0.1})\ [Fe_{1.2}Ti_{0.2}Li_{0.6}]O_4$
	Irr	0.870	0.881	0.862	0.853	$(Fe_{0.92}Ti_{0.08})\ [Fe_{1.18}Ti_{0.12}Al_{0.1}Li_{0.6}]O_4$
0.3	Unirr	0.814	0.819	0.760	0.771	$(Fe_{0.86}Ti_{0.04}Al_{0.1})[Fe_{1.09}Ti_{0.26}Li_{0.65}]O_4$
	Irr	0.892	0.902	0.910	0.921	$(Fe_{0.87}Ti_{0.13})\ [Fe_{1.08}Al_{0.1}Ti_{0.17}Li_{0.65}]O_4$

Table 6A.3: Cell edge parameter (a_{exp}), Saturation magnetization (σ_s), Magneton number (η_B) and Curie Temperature (T_c) for unirradiated and irradiated samples of $Li_{0.5(1+x)}Ti_xAl_{0.1}Fe_{2.4-1.5x}O_4$ system

Content (x)	Sample	a_{exp}(Å) ±0.002 Å	σ_s(emu/gm)	η_B^N (μ_B)	η_B^{obs} (μ_B)	T_c(K) ±5K
0.0	Unirr	8.270	63	2.30	2.30	850
	Irr	8.282	57	2.20	2.10	800
0.1	Unirr	8.281	48	1.75	1.74	855
	Irr	8.317	38	1.55	1.37	820
0.2	Unirr	8.287	41	1.50	1.45	830
	Irr	8.348	34	1.30	1.20	790
0.3	Unirr	8.299	32	1.15	1.11	775
	Irr	8.360	26	1.05	0.91	720

Table 6A.4: Mössbauer parameters: Hyperfine field (H_{nf}), Isomer shift (I.S), Iron distribution parameter ($\delta = Fe^{3+}{}_A/Fe^{3+}{}_B$) and paramagnetic Fraction (I_d) for unirradiated and irradiated samples of $Li_{0.5(1+x)}Ti_xAl_{0.1}Fe_{2.4-1.5x}O_4$ system

Content (x)	Sample	H_{nf} (kOe)± 2 kOe		*I.S (mm/sec)± 0.03(mm/sec)		$\delta = Fe^{3+}{}_A/Fe^{3+}{}_B$		I_d%
		A-site	B-site	A-site	B-site	Möss	XRD	
0.0	Unirr	332	342	0.21	0.31	0.66	0.68	---
	Irr	329	349	0.21	0.28	0.69	0.71	4.5
0.1	Unirr	320	339	0.19	0.29	0.71	0.73	---
	Irr	321	344	0.22	0.32	0.75	0.76	11.6
0.3	Unirr	309	338	0.24	0.35	0.77	0.72	----
	Irr	308	342	0.22	0.32	0.82	0.81	9.1

*Isomer shift with respect to Fe-metal

Table 6A.5: Theoretical lattice constant (a_{th}), Bulk density (d), X-ray density (ρ_x), Pore fraction (f) and Percentage of porosity for unirradiated and irradiated $Li_{0.5(1+x)}Ti_xAl_{0.1}Fe_{2.4-1.5x}O_4$ ferrite system

x	Sample	a_{th} (Å) ± 0.0002	Bulk density (d) $(kg/m^3)x10^3$	X-ray density (ρ_x) $(kg/m^3)x10^3$	Pore fraction (f)	Porosity (%)
0.0	Unirr	8.2529	4.1866	4.7976	0.1274	12.74
	Irr	8.2535	4.2137	4.7768	0.1178	11.78
0.1	Unirr	8.2603	4.2245	4.7027	0.1017	10.17
	Irr	8.2618	3.7789	4.6086	0.1800	18.00
0.2	Unirr	8.2669	3.7683	4.6168	0.1838	18.38
	Irr	8.2702	4.0923	4.5164	0.0939	9.39
0.3	Unirr	8.2752	4.0553	4.5215	0.1031	10.31
	Irr	8.2786	3.8314	4.4233	0.1338	13.38

Table 6A.6: Ionic radii (r_A, r_B), bond lengths (A-O, B-O), oxygen positional parameter (u) and site radii (R_A, R_B) for unirradiated and irradiated $Li_{0.5(1+x)}Ti_xAl_{0.1}Fe_{2.4-1.5x}O_4$ ferrite system

x	Sample	r_A (Å)	r_B (Å)	A – O $(r_A + r_O)$	B – O $(r_B + r_O)$	u (Å)	R_A (Å)	R_B (Å)
0.0	Unirr	0.6361	0.6455	1.9561	1.9655	0.2614	1.9538	1.9777
	Irr	0.6400	0.6435	1.9600	1.9635	0.2608	1.9480	1.9851
0.1	Unirr	0.6335	0.6498	1.9535	1.9698	0.2612	1.9535	1.9819
	Irr	0.6412	0.6459	1.9612	1.9659	0.2602	1.9476	1.9980
0.2	Unirr	0.6270	0.6560	1.9470	1.9760	0.2610	1.9521	1.9848
	Irr	0.6432	0.6479	1.9632	1.9679	0.2602	1.9549	2.0055
0.3	Unirr	0.6286	0.6582	1.9486	1.9782	0.2608	1.9520	1.9892
	Irr	0.6452	0.6499	1.9652	1.9699	0.2602	1.9577	2.0084

Table 6A.7: Inter-ionic distances between cation-anion (Me-O), cation-cation (Me-Me) and bond angles (θ) for unirradiated and irradiated $Li_{0.5(1+x)}Ti_xAl_{0.1}Fe_{2.4-1.5x}O_4$ ferrite system

Me – O (Å)								
x	0.0		0.1		0.2		0.3	
Sample	Unirr	Irr	Unirr	Irr	Unirr	Irr	Unirr	Irr
p	1.9732	1.9811	1.9775	1.9944	1.9806	2.002	1.9851	2.0047
q	1.9539	1.9481	1.9536	1.9477	1.9521	1.9549	1.9520	1.9577
r	3.7412	3.7302	3.7407	3.7294	3.7379	3.7433	3.7378	3.7487
s	3.6356	3.6380	3.6394	3.6504	3.6411	3.6641	3.6454	3.6694
Me – Me (Å)								
x	0.0		0.1		0.2		0.3	
Sample	Unirr	Irr	Unirr	Irr	Unirr	Irr	Unirr	Irr
b	2.9239	2.9281	2.9278	2.9405	2.9299	2.9515	2.9341	2.9557
c	3.4286	3.4335	3.4331	3.4480	3.4356	3.4609	3.4406	3.4659
d	3.5810	3.5862	3.5858	3.6014	3.5884	3.6148	3.5936	3.6199
e	5.3715	5.3793	5.3787	5.4020	5.3826	5.4222	5.3904	5.4299
f	5.0643	5.0717	5.0711	5.0931	5.0747	5.1121	5.0821	5.1194
Bond angles (θ)								
x	0.0		0.1		0.2		0.3	
Sample	Unirr	Irr	Unirr	Irr	Unirr	Irr	Unirr	Irr
θ_1	121.63°	121.81°	121.69°	122.01°	121.76°	122.00°	121.82°	122.01°
θ_2	137.95°	138.67°	138.19°	139.41°	138.43°	139.40°	138.68°	139.40°
θ_3	95.62°	95.29°	95.51°	94.99°	95.40°	94.98°	95.30°	94.99°
θ_4	126.51°	126.44°	126.49°	126.38°	126.46°	126.37°	126.44°	126.37°
θ_5	70.04°	70.51°	70.20°	70.99°	70.36°	70.99°	70.51°	70.98°

Table 6A.8: Positions of IR main absorption bands (ν_1,ν_2) with shoulders/splitting (ν_{sh} or ν_{sp}) and average of main IR absorption bands (ν_{1avg},ν_{2avg}) for unirradiated and irradiated $Li_{0.5(1+x)}Ti_xAl_{0.1}Fe_{2.4-1.5x}O_4$ ferrite system

x	Sample	ν_1 (m^{-1}) x10^2			ν_2(m^{-1}) x10^2		
		ν_1	ν_{1sh} or ν_{1sp}	ν_{1avg}	ν_2	ν_{2sh} or ν_{2sp}	ν_{2avg}
0.0	Unirr	588.5	547.3	567.9	470.4	-	470.4
	Irr	594.0	542.0	568.0	466.7	449.4, 437.8, 426.2	445.0
0.1	Unirr	587.8	549.4	568.6	468.7	-	468.7
	Irr	596.0	540.0, 528.5	554.8	475.5	453.2, 437.8, 424.3, 408.9	439.7
0.2	Unirr	588.8	548.1	568.5	472.3	-	472.3
	Irr	596.0	551.6, 499.5	549.0	476.4	445.5, 412.7	444.9
0.3	Unirr	588.3	-	588.3	473.1	-	473.1
	Irr	599.8	582.5, 538.8, 518.1	559.8	488.0	460.7, 440.4, 430.1, 410.8	446.0

Table 6A.9: Molecular weight (M_1, M_2) of A & B-sites, force constants (k_t, k_o) of A & B- sites respectively and average force constant (k) for unirradiated and irradiated $Li_{0.5(1+x)}Ti_xAl_{0.1}Fe_{2.4-1.5x}O_4$ ferrite system

x	Sample	M_1 (kg) x 10^{-3}	$M_2/2$ (kg) x 10^{-3}	k_t (N/m) x 10^9	k_o(N/m) x 10^9	k (N/m) x 10^9
0.0	Unirr	54.9810	42.6102	1.3512	1.0013	1.1763
	Irr	55.8470	42.1772	1.3729	0.8871	1.1300
0.1	Unirr	54.3956	41.2779	1.3401	0.9630	1.1516
	Irr	55.6080	40.6757	1.3043	0.8353	1.0698
0.2	Unirr	52.9605	40.3785	1.3043	0.9566	1.1305
	Irr	55.2096	39.2539	1.2679	0.8252	1.0466
0.3	Unirr	52.6418	38.9168	1.3883	0.9251	1.1567
	Irr	54.8113	37.8321	0.8308	0.7999	0.8150

Table 6A.10: Longitudinal elastic wave velocity (υ_l), Transverse elastic wave velocity (υ_s), Mean elastic wave velocity (υ_m) and Debye temperature (θ_D) for unirradiated and irradiated $Li_{0.5(1+x)}Ti_xAl_{0.1}Fe_{2.4-1.5x}O_4$ ferrite system

x	Sample	υ_l (m/s)	υ_s (m/s)	υ_m (m/s)	θ_D (K)
0.0	Unirr	6664.27	3847.62	4272.55	588
	Irr	5342.65	3084.58	3424.47	471
0.1	Unirr	5439.61	3140.56	3486.62	479
	Irr	5282.27	3049.72	3385.77	462
0.2	Unirr	5433.98	3137.31	3483.01	479
	Irr	5266.56	3040.65	3375.69	461
0.3	Unirr	5552.84	3205.93	3559.19	488
	Irr	4696.44	2711.49	3010.26	410

Table 6A.11: Bulk modulus (B), Young's modulus (E), rigidity modulus (G) and Poisson's ratio (σ) for unirradiated and irradiated $Li_{0.5(1+x)}Ti_xAl_{0.1}Fe_{2.4-1.5x}O_4$ ferrite system

x	Sample	B (GPa)	E (GPa)	G (GPa)	σ
0.0	Unirr	213.18	191.86	71.06	0.35
	Irr	136.44	122.80	45.48	0.35
0.1	Unirr	139.07	125.17	46.36	0.35
	Irr	128.63	115.78	42.88	0.35
0.2	Unirr	136.42	122.77	45.47	0.35
	Irr	125.37	112.83	41.79	0.35
0.3	Unirr	139.37	125.42	46.45	0.35
	Irr	97.49	87.75	32.50	0.35

Table 6A.12: Corrected to zero porosity of elastic moduli: Bulk modulus (B_0), Young's modulus (E_0), rigidity modulus (G_0) and Poisson's ratio (σ_0) for unirradiated and irradiated $Li_{0.5(1+x)}Ti_xAl_{0.1}Fe_{2.4-1.5x}O_4$ ferrite system

x	Sample	B_0 (GPa)	E_0 (GPa)	G_0 (GPa)	σ_0
0.0	Unirr	363.77	257.30	93.08	0.38
	Irr	221.22	160.58	58.22	0.38
0.1	Unirr	207.71	157.06	57.16	0.37
	Irr	310.22	180.74	64.42	0.40
0.2	Unirr	338.83	193.93	69.03	0.40
	Irr	180.38	138.86	50.62	0.37
0.3	Unirr	209.67	157.93	57.45	0.37
	Irr	171.19	119.67	43.25	0.38

Table 6A.13: dc resistivity ($\log_{10}\rho_{dc}$), Activation energy (E) and Nèel temperature (T_N) for all the compositions of unirradiated and irradiated $Li_{0.5(1+x)}Ti_xAl_{0.1}Fe_{2.4-1.5x}O_4$ ferrite system

x	Sample	$\log_{10}\rho_{dc}$ (Ω.cm) (313K)	Activation energy (eV)		ΔE (eV)	T_N(K) ± 5K	
			E_f	E_p		Resistivity	Susceptibility
0.0	Unirr	4.99	0.186	0.213	0.027	803	850
	Irr	5.01	0.386	0.435	0.049	783	800
0.1	Unirr	8.68	0.726	1.121	0.395	813	855
	Irr	6.31	0.377	0.493	0.116	795	820
0.2	Unirr	5.24	0.149	0.244	0.095	785	830
	Irr	4.67	0.271	0.440	0.169	743	790
0.3	Unirr	8.56	0.618	0.877	0.260	753	775
	Irr	7.41	0.365	1.018	0.653	713	720

Table 6A.14: Jump length (L), Polaron radius (r_P) and Fermi energy ($E_F(0)$) for all the compositions of unirradiated and irradiated $Li_{0.5(1+x)}Ti_xAl_{0.1}Fe_{2.4-1.5x}O_4$ ferrite system

x	Sample	Jump length L (Å)		Polaron radius r_p (Å)	Fermi energy $\| E_f \|$ (eV)
		L_A	L_B		
0.0	Unirr	3.5810	2.9239	0.7278	0.0084
	Irr	3.5862	2.9281	0.7288	0.2954
0.1	Unirr	3.5858	2.9278	0.7287	0.4217
	Irr	3.6014	2.9405	0.7319	0.1308
0.2	Unirr	3.5884	2.9299	0.7293	0.1325
	Irr	3.6148	2.9515	0.7346	0.0372
0.3	Unirr	3.5936	2.9341	0.7303	1.7024
	Irr	3.6200	2.9557	0.7357	2.1933

Table 6A.15: Compositional variation of dielectric constant (ε'), complex dielectric constant (ε'') and a. c. resistivity ($\log_{10}\rho_{ac}$) and for two frequencies (1kHz & 10kHz) at room temperature for all the compositions unirradiated and irradiated $Li_{0.5(1+x)}Ti_xAl_{0.1}Fe_{2.4-1.5x}O_4$ ferrite system

1kHz (300K)						
x	**ε'**		**ε''**		**$\log_{10}\rho_{ac}$**	
	Unirr	**Irr**	**Unirr**	**Irr**	**Unirr**	**Irr**
0.0	154.78	2026.27	1098.17	10961.32	6.2142	5.2150
0.1	75.46	347.53	12.51	752.20	8.1575	6.3786
0.2	193.58	75310.89	1103.73	95993.53	6.2120	4.2727
0.3	100.89	48.63	21.06	149.19	7.9315	7.0812
10kHz (300K)						
0.0	125.98	461.93	124.63	1442.06	6.1593	5.0959
0.1	67.30	101.84	4.39	131.18	7.6125	6.1370
0.2	140.89	16277.12	149.48	27338.37	6.0803	3.8181
0.3	80.85	32.97	9.08	28.41	7.2970	6.8014

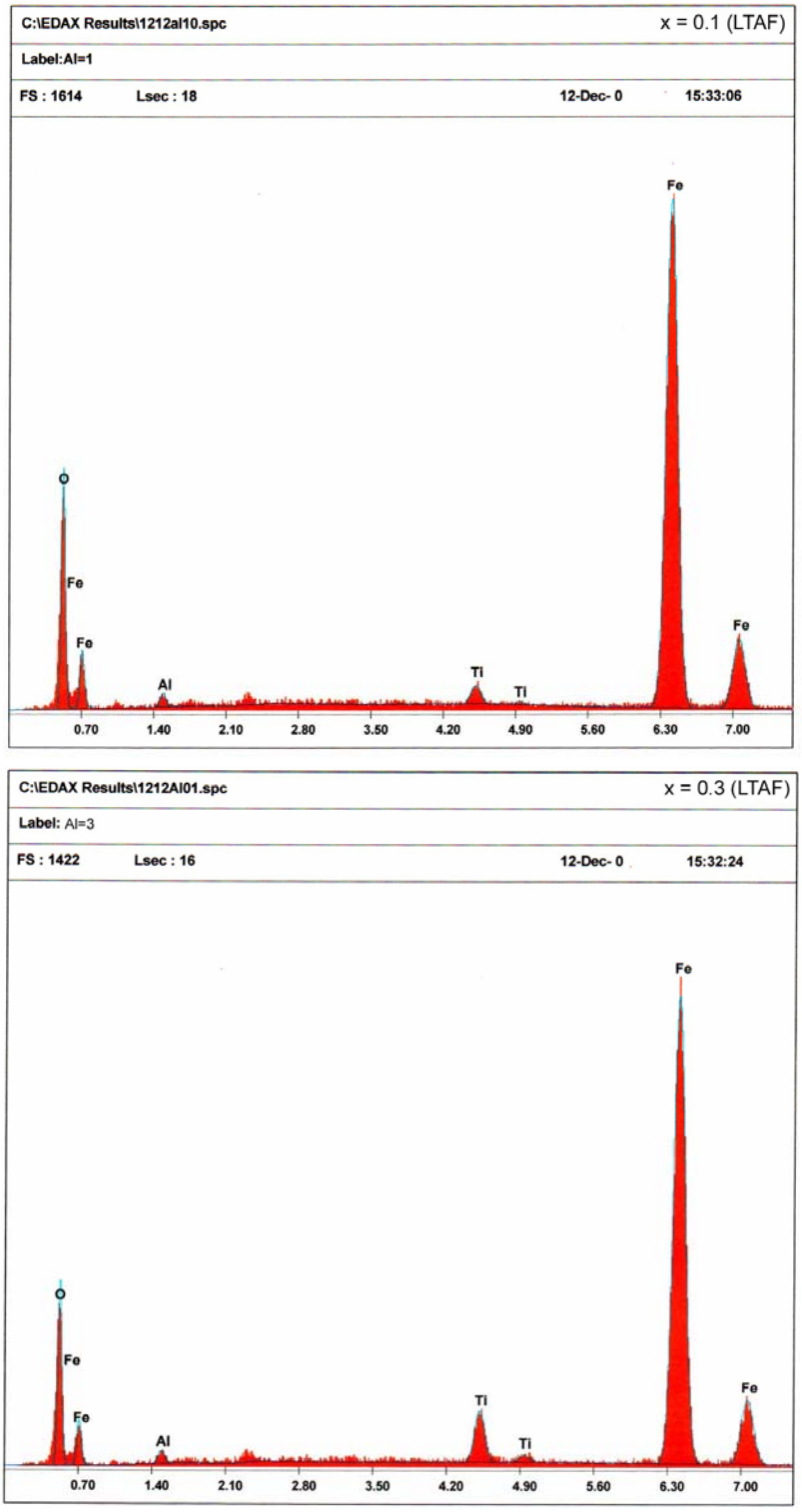

Fig. 6A.1 EDAX patterns for the sample of the compositions: x = 0.1 & 0.3 of the system $Li_{0.5(1+x)}Ti_xAl_{0.1}Fe_{2.4-1.5x}O_4$

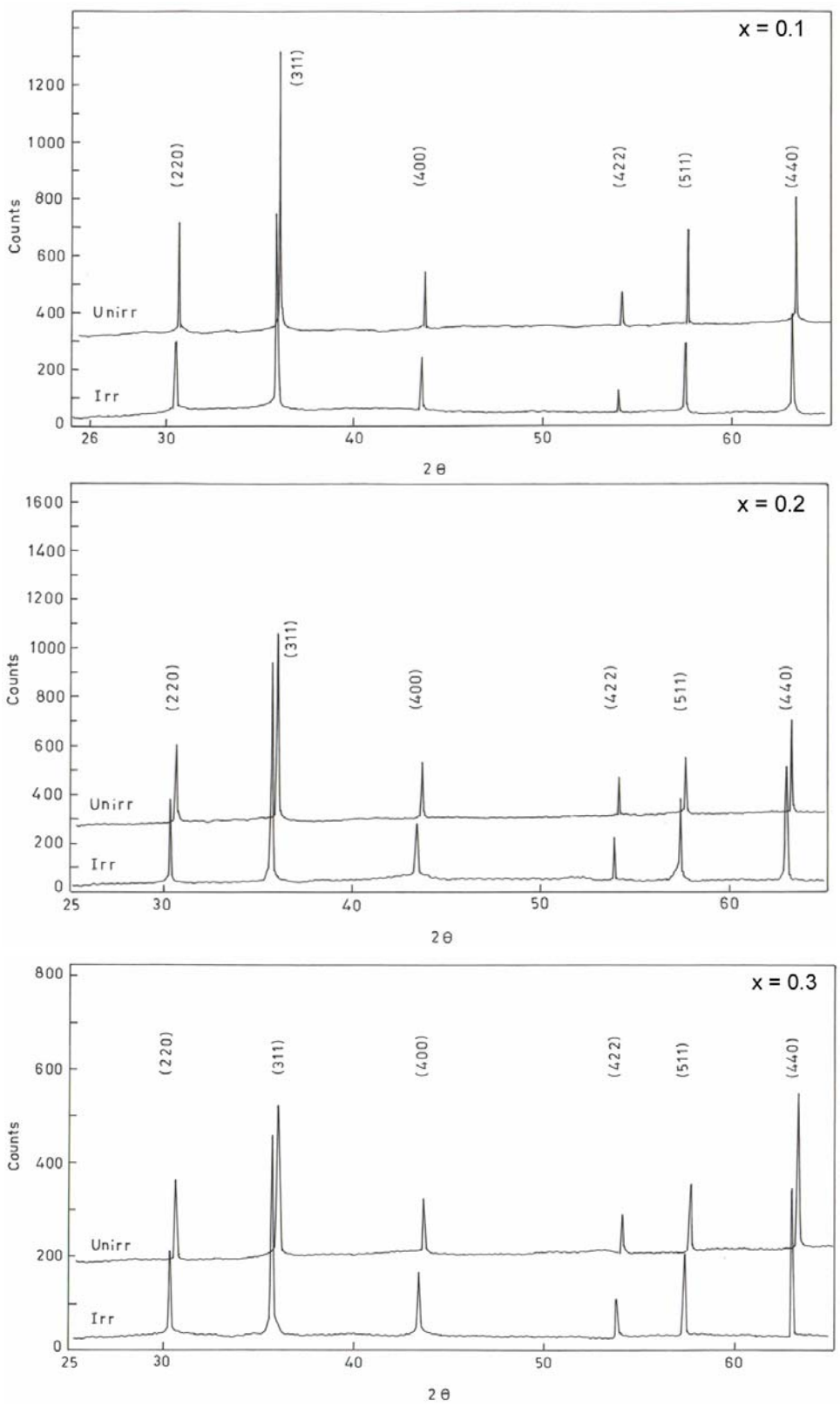

Fig. 6A.2 X-ray Diffraction Patterns of the three representative compositions x = 0.1, 0.2 and 0.3 for Pre and Post SHI Irradiated samples of $Li_{0.5(1+x)}Ti_xAl_{0.1}Fe_{2.4-1.5x}O_4$ system.

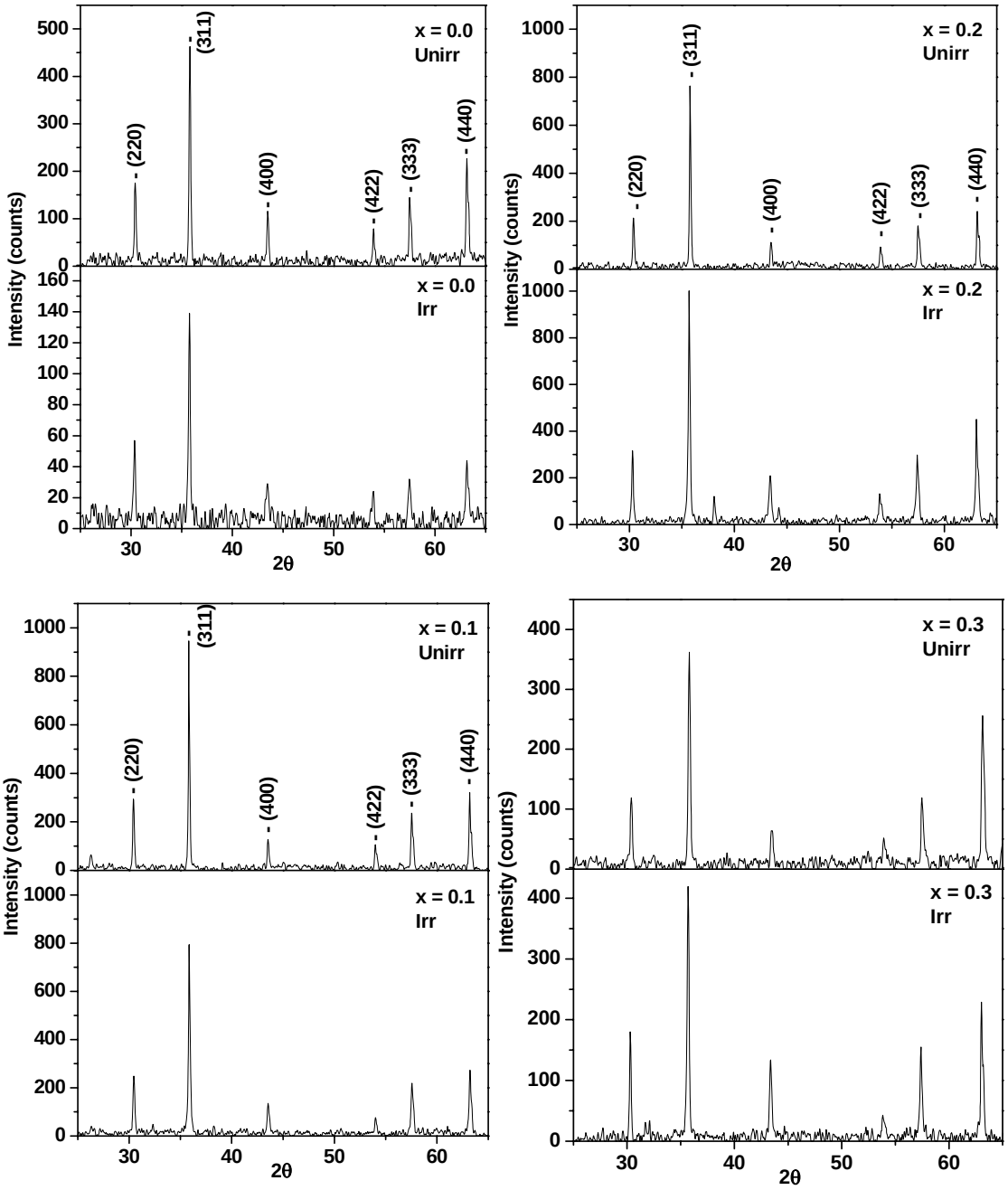

Fig. 6A.2 X-ray Diffraction Patterns of the compositions x = 0.0, 0.1, 0.2 and 0.3 for Pre and Post SHI Irradiated samples of $Li_{0.5(1+x)}Ti_xAl_{0.1}Fe_{2.4-1.5x}O_4$ system

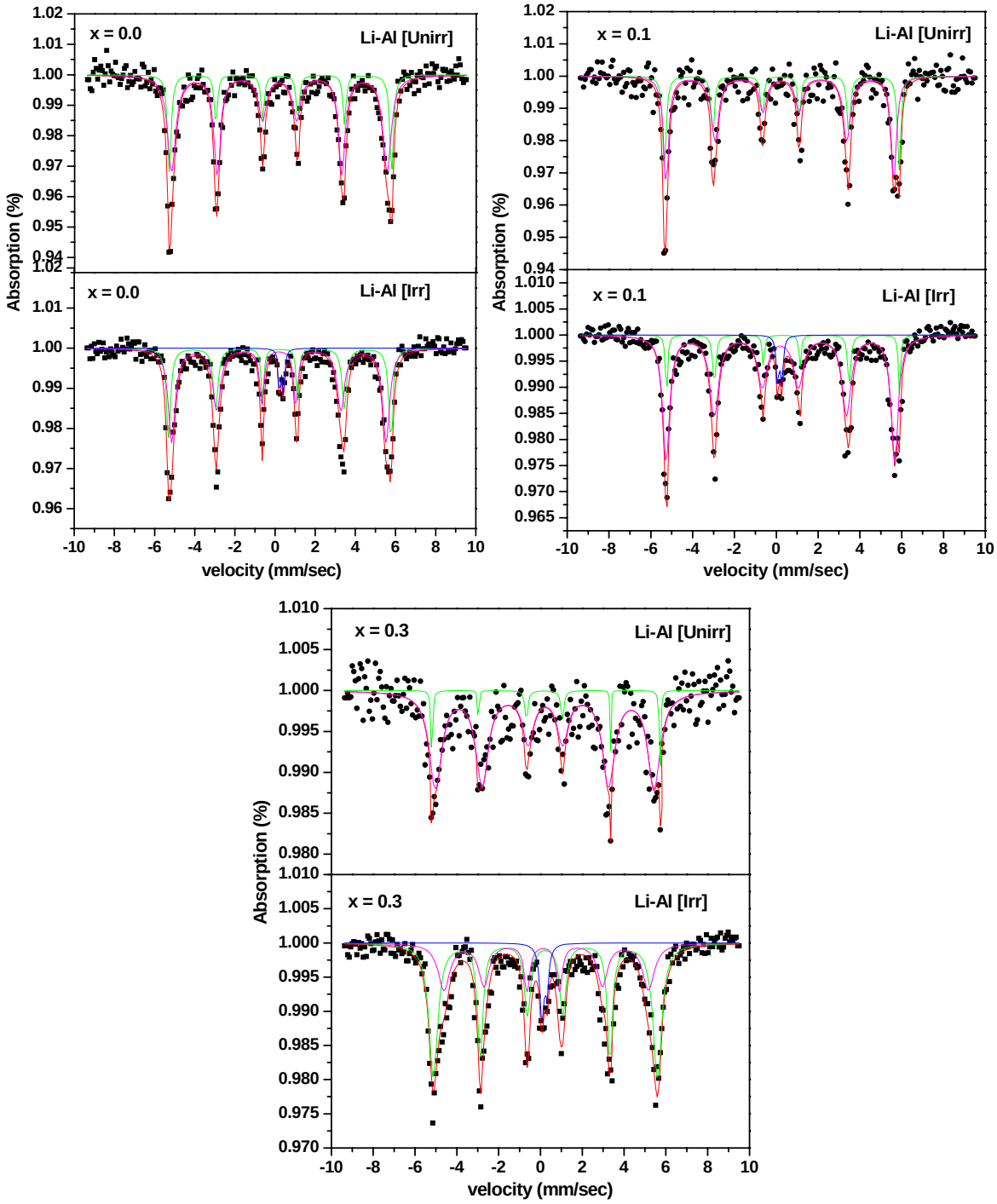

Fig. 6A.3 Mössbauer Spectra at 300K for compositions with x =0.0, 0.1 and 0.3 of the system $Li_{0.5(1+x)}Ti_xAl_{0.1}Fe_{2.4-1.5x}O_4$ before and after SHI irradiation

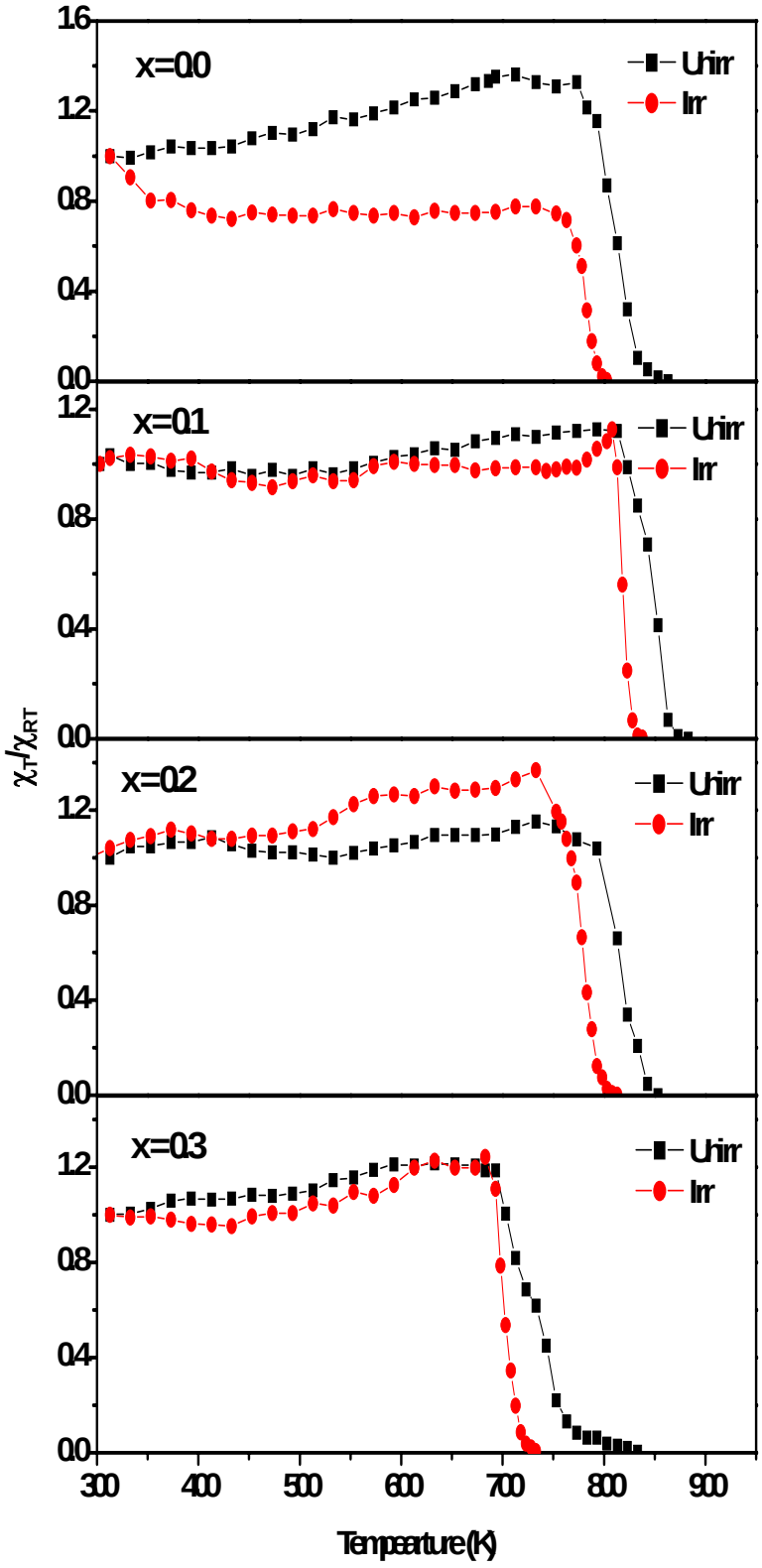

Fig. 6A.4 Thermal variation of low field (0.5 Oe) A. C. Susceptibility of unirradiated and irradiated samples of $Li_{0.5(1+x)}Ti_xAl_{0.1}Fe_{2.4-1.5x}O_4$ system

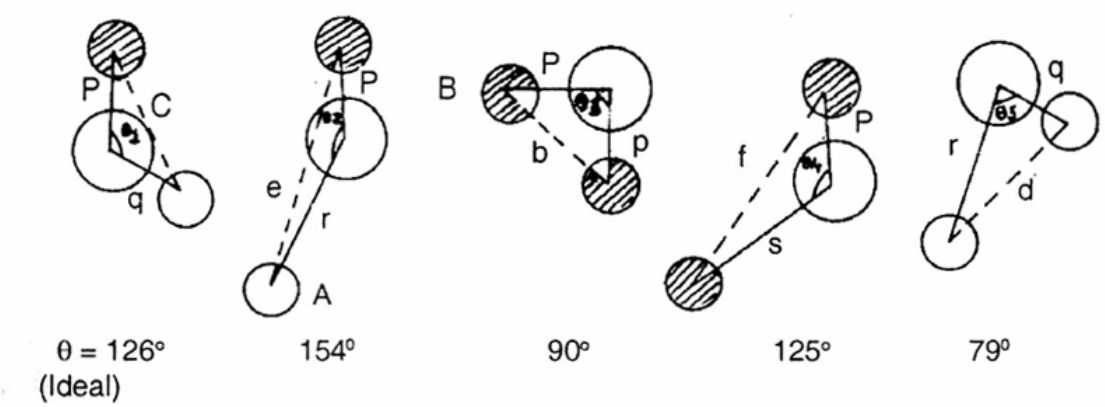

Fig. 6A.5 Configuration of ion pairs in spinel ferrites with favorable distances and angles for effective magnetic interactions. [6A.109]

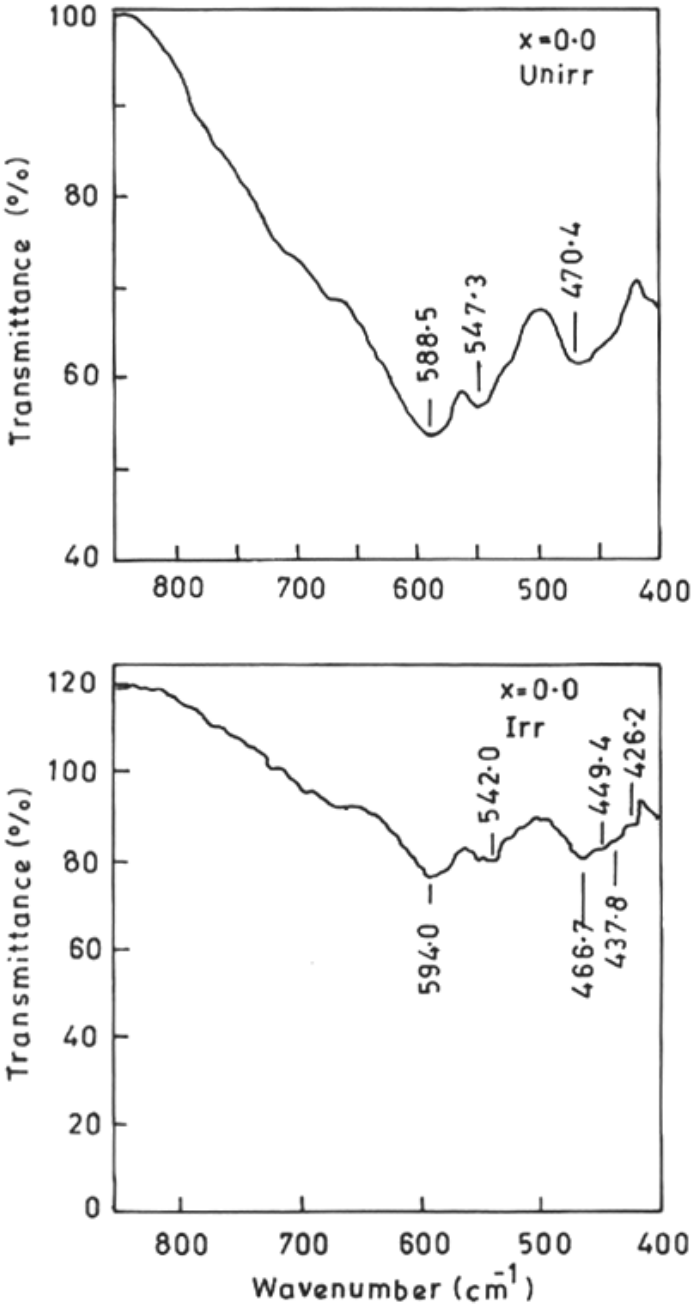

Fig. 6A.6a Infrared spectra of unirradiated and irradiated $Li_{(1+x)0.5}Ti_xAl_{0.1}Fe_{2.4-1.5x}O_4$ system with x = 0.0 sample.

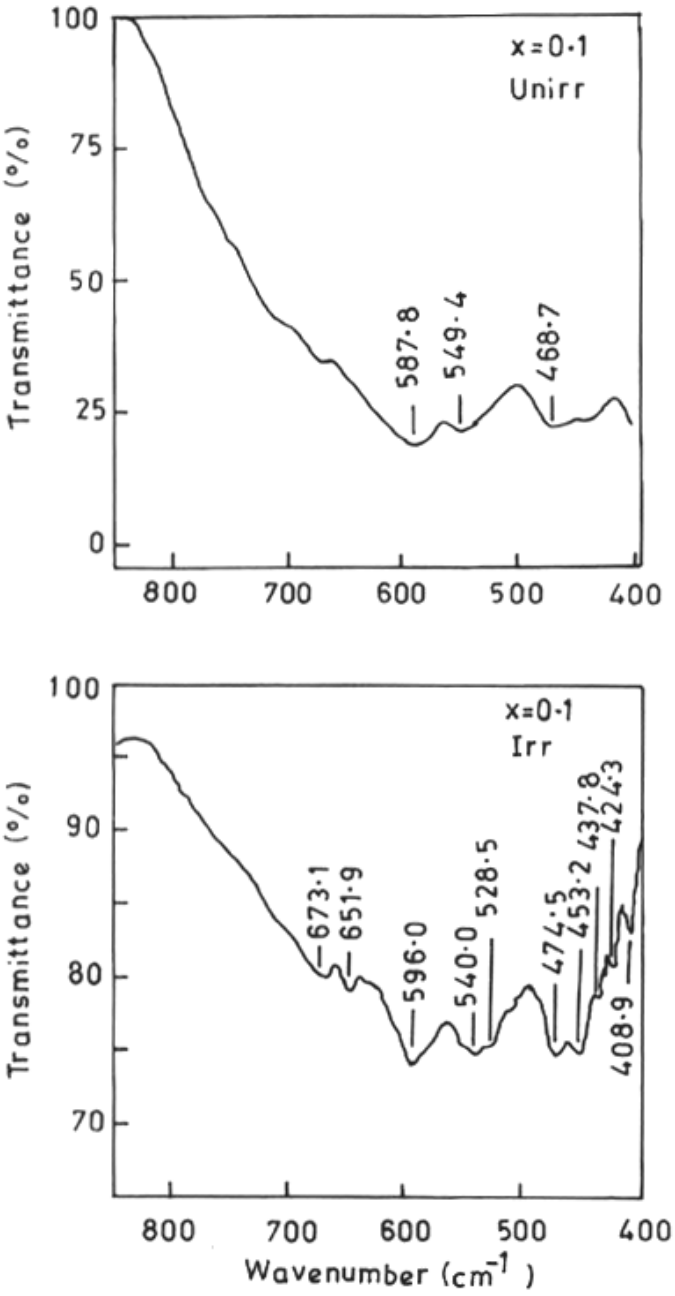

Fig. 6A.6b Infrared spectra of unirradiated and irradiated $Li_{(1+x)0.5}Ti_xAl_{0.1}Fe_{2.4-1.5x}O_4$ system with x = 0.1 sample.

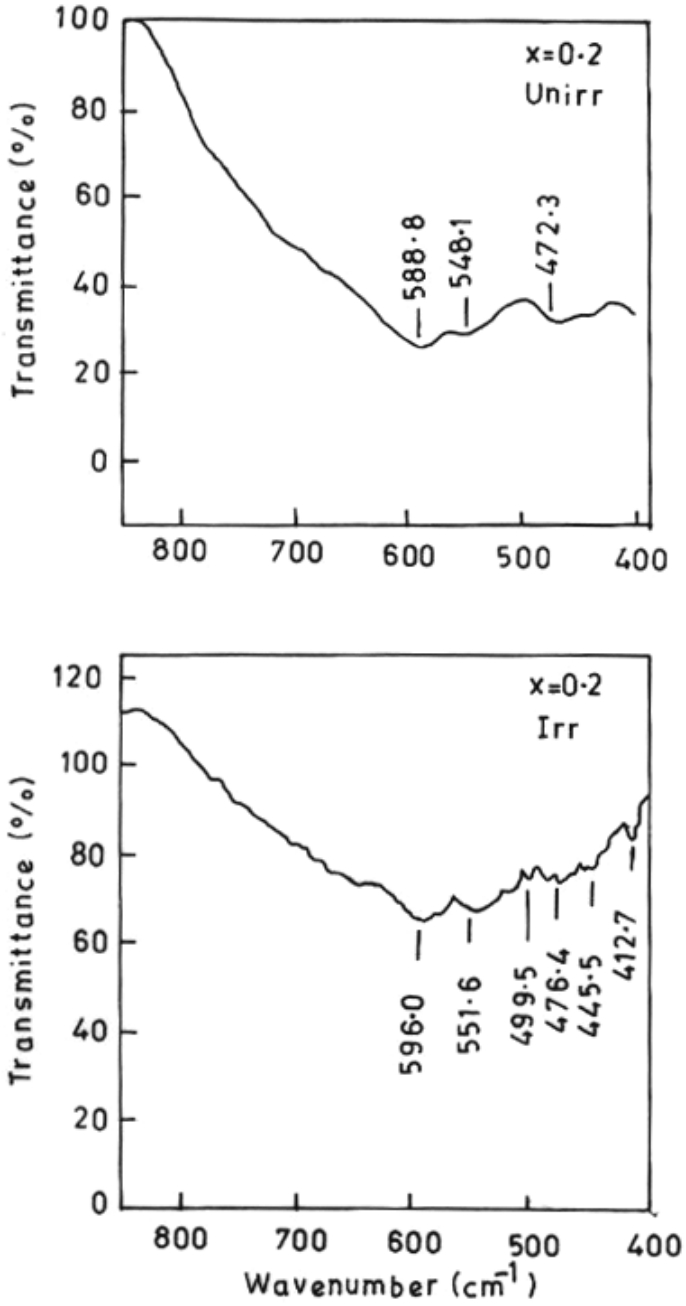

Fig. 6A.6c Infrared spectra of unirradiated and irradiated $Li_{(1+x)0.5}Ti_xAl_{0.1}Fe_{2.4-1.5x}O_4$ system with x = 0.2 sample.

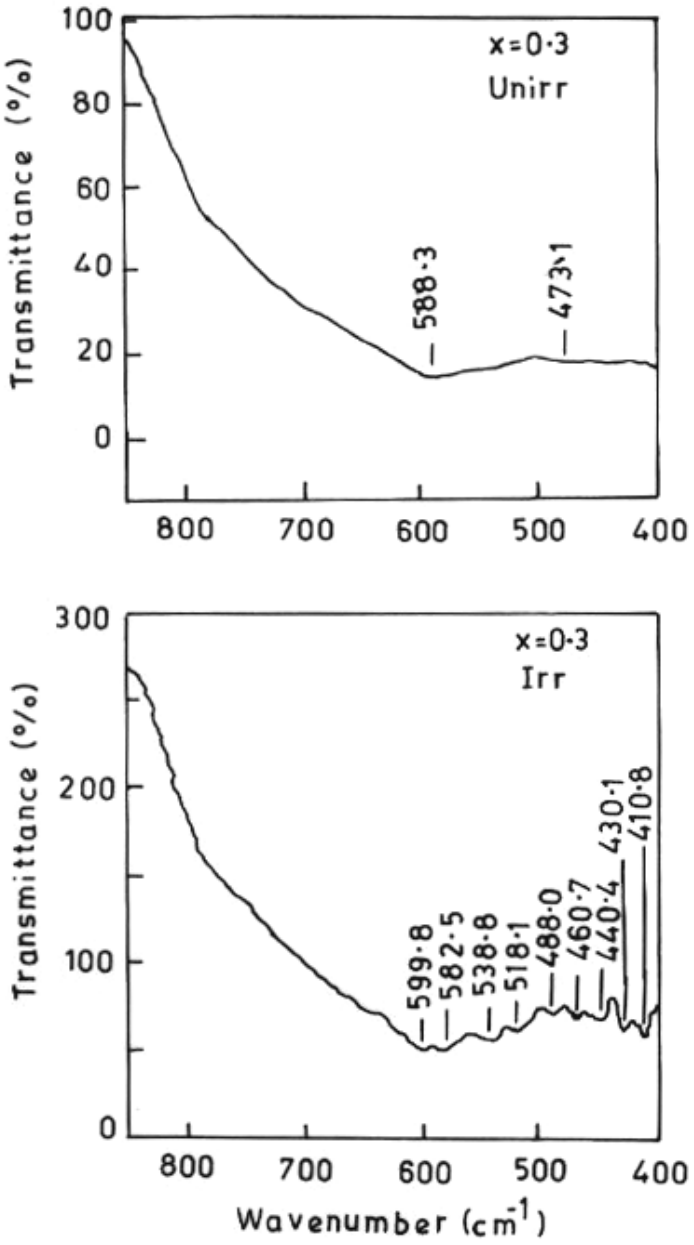

Fig. 6A.6d Infrared spectra of unirradiated and irradiated $Li_{(1+x)0.5}Ti_xAl_{0.1}Fe_{2.4-1.5x}O_4$ system with x = 0.3 sample.

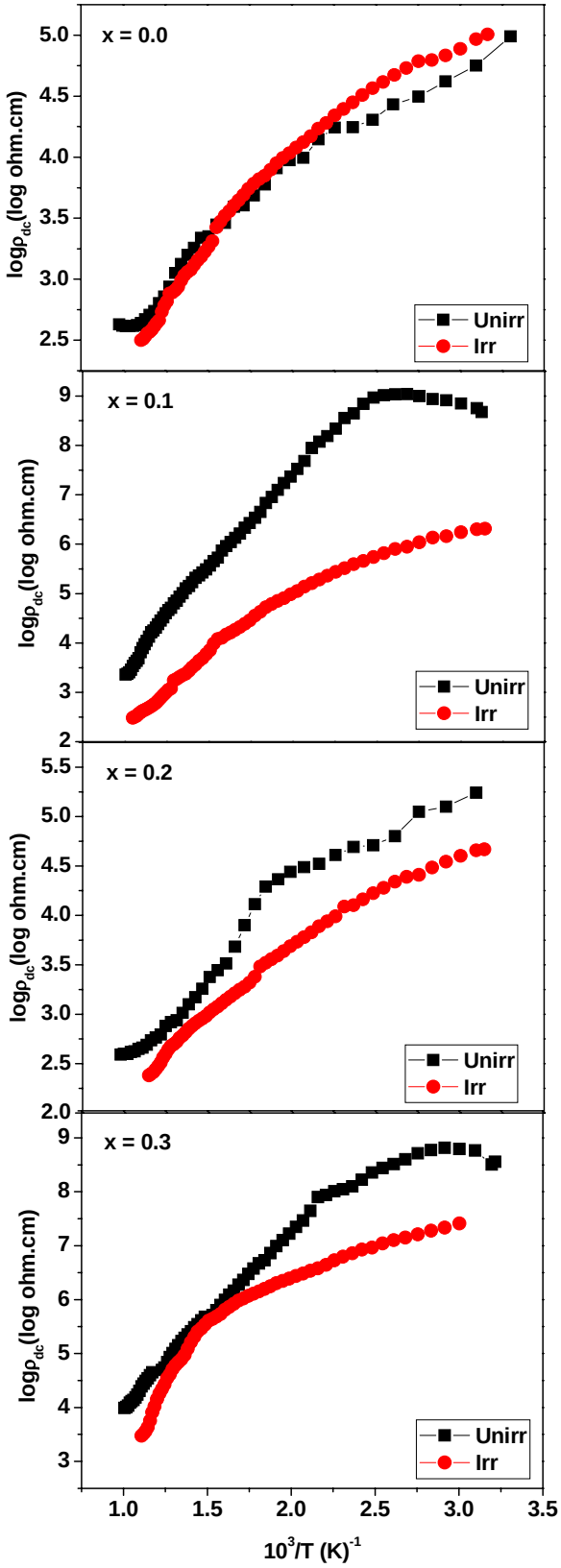

Fig. 6A.7 Thermal variation of d. c. resistivity for the compositions x = 0.0, 0.1, 0.2 and 0.3 of unirradiated and irradiated $Li_{0.5(1+x)}Ti_xAl_{0.1}Fe_{2.4-1.5x}O_4$ system

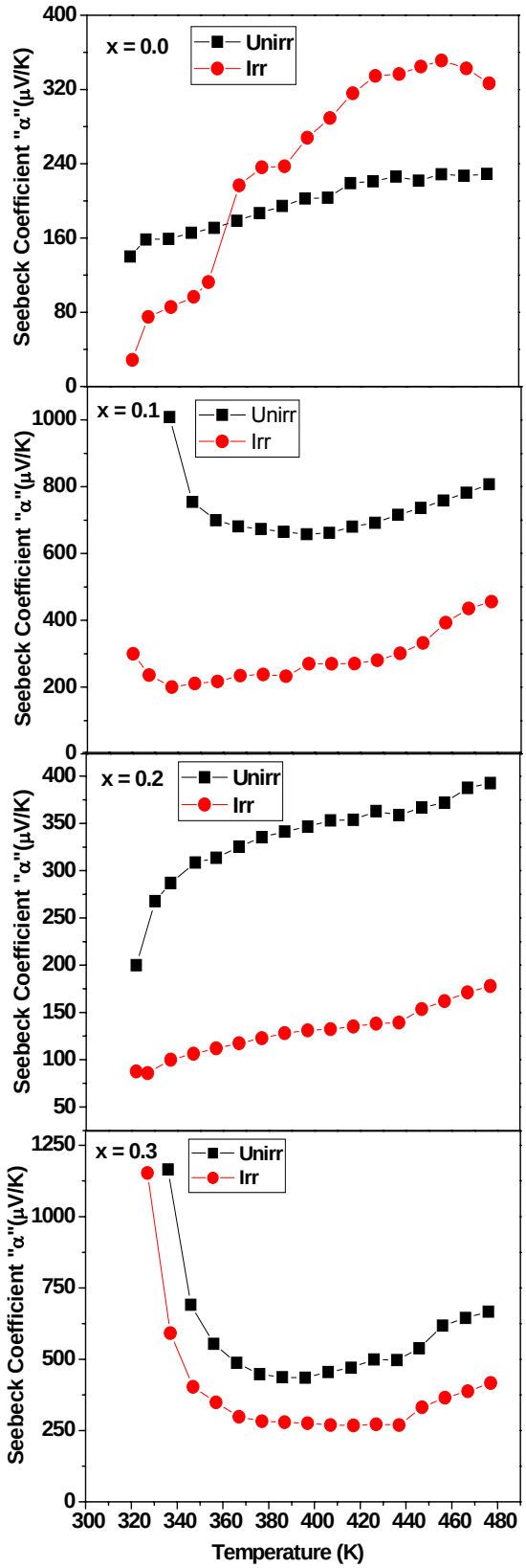

Fig. 6A.8 Thermal variation of Seebeck coefficient for compositions x = 0.0, 0.1, 0.2 and 0.3 of unirradiated and irradiated $Li_{0.5(1+x)}Ti_xAl_{0.1}Fe_{2.4-1.5x}O_4$ system

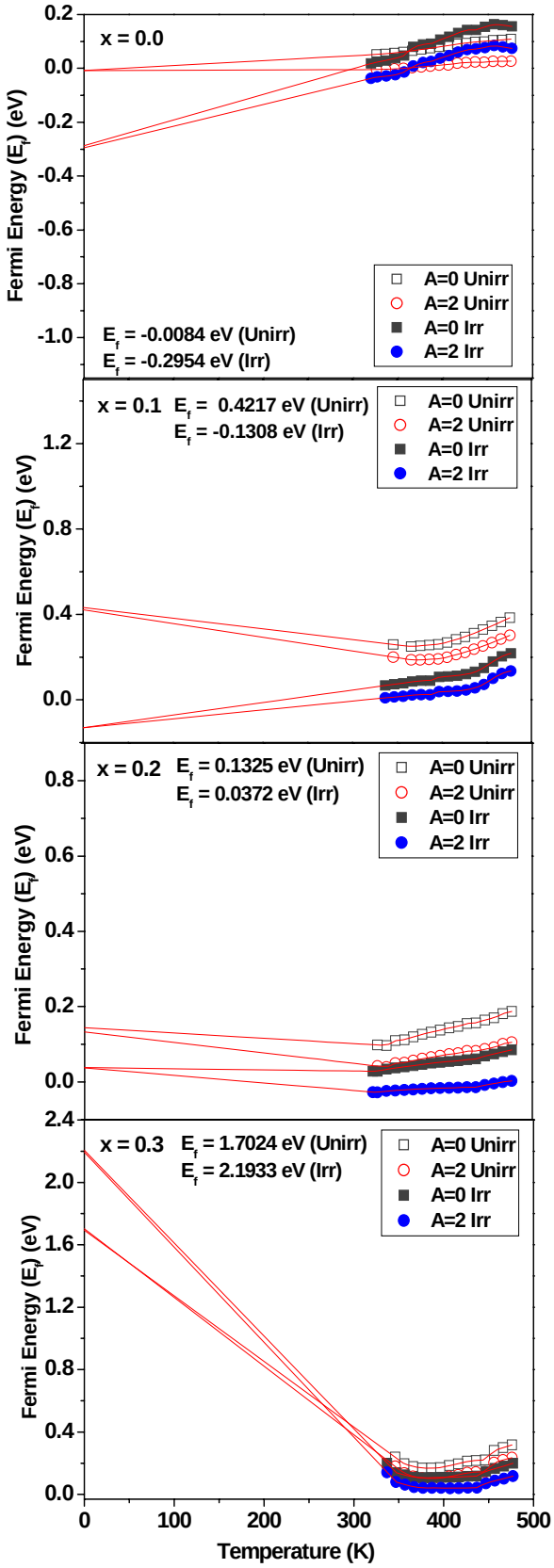

Fig. 6A.9 Temperature dependence of Fermi energy (E_f) for the compositions x = 0.0, 0.1, 0.2 and 0.3 of unirradiated and irradiated $Li_{0.5(1+x)}Ti_xAl_{0.1}Fe_{2.4-1.5x}O_4$ system

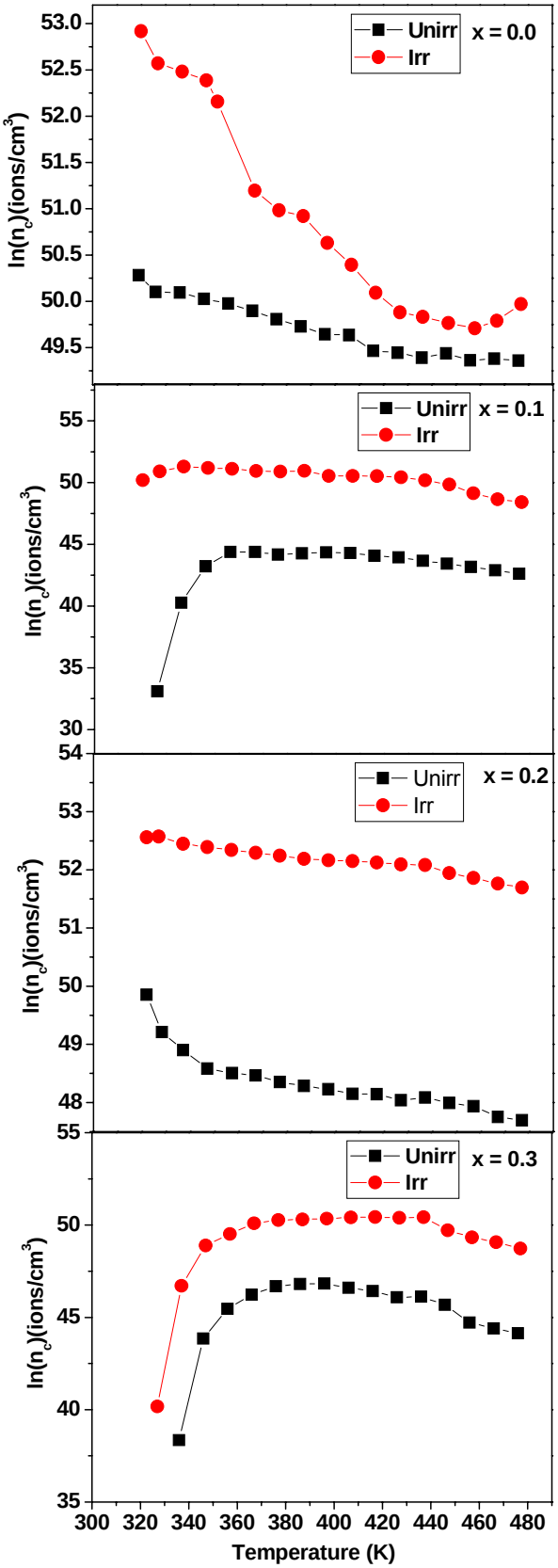

Fig. 6A.10 Variation of charge carrier concentration with temperature for the compositions x = 0.0, 0.1, 0.2 and 0.3 of unirradiated and irradiated $Li_{0.5(1+x)}Ti_xAl_{0.1}Fe_{2.4-1.5x}O_4$ system

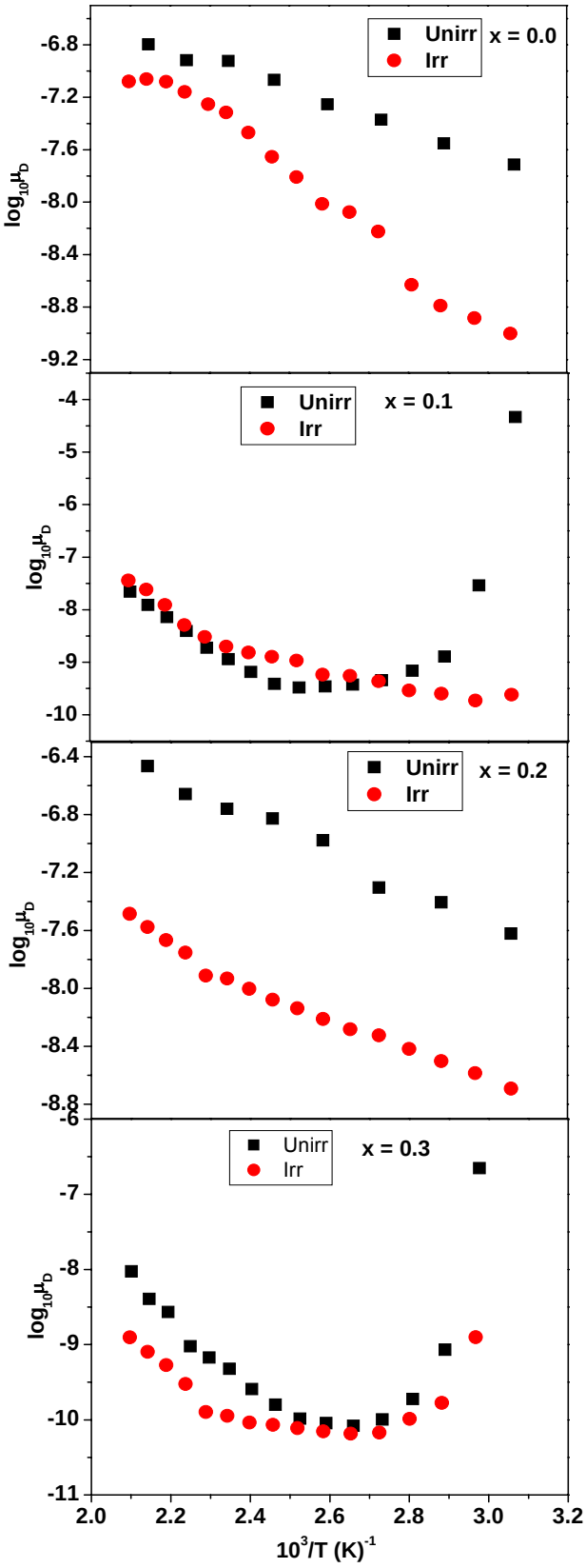

Fig. 6A.11 Thermal variation of mobility for the compositions x = 0.0, 0.1, 0.2 and 0.3 of unirradiated and irradiated $Li_{0.5(1+x)}Ti_xAl_{0.1}Fe_{2.4-1.5x}O_4$ system

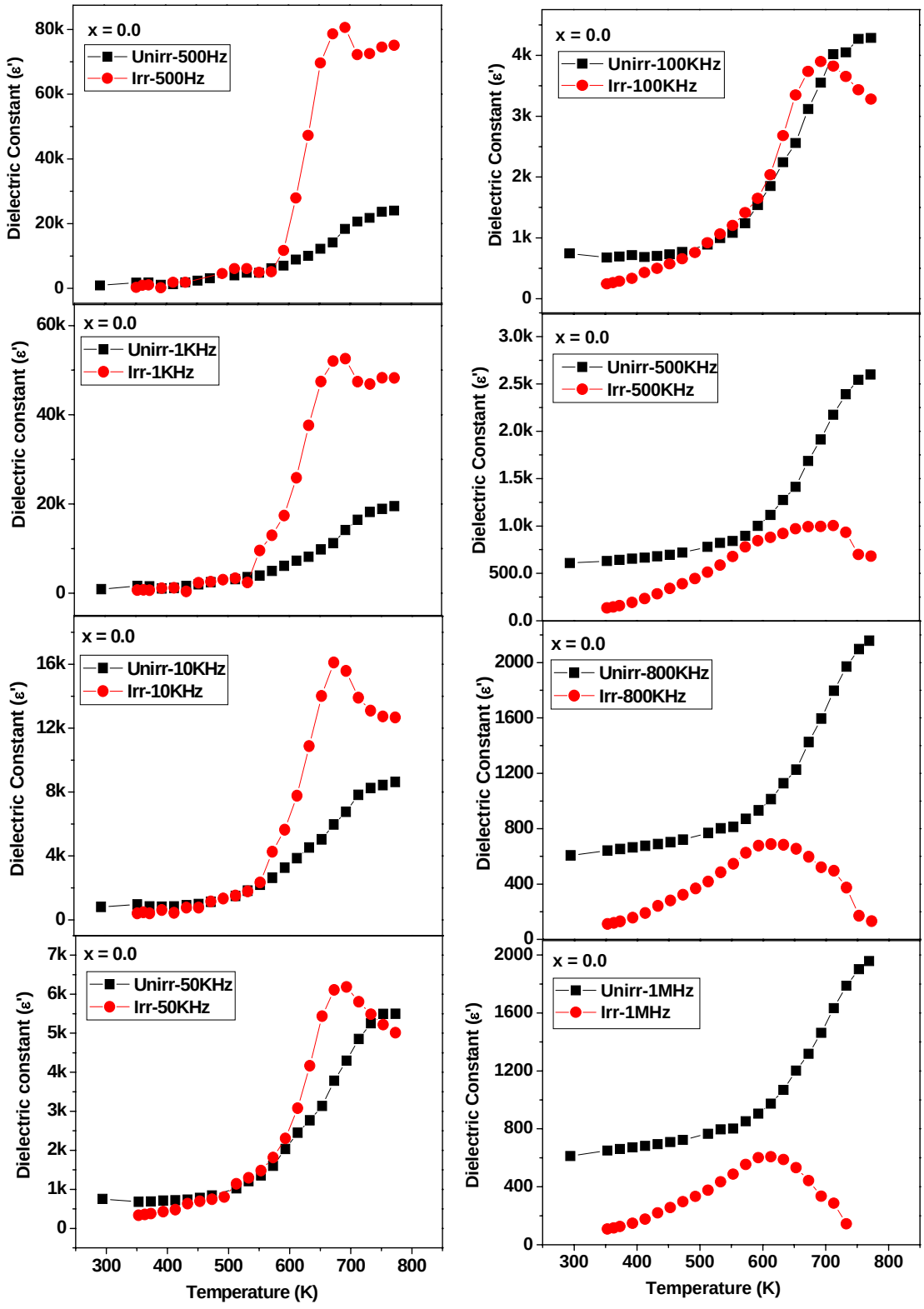

Fig. 6A.12a Thermal variation of dielectric constant at different frequencies for the composition x = 0.0 of unirradiated and irradiated $Li_{0.5(1+x)}Ti_xAl_{0.1}Fe_{2.4-1.5x}O_4$ system

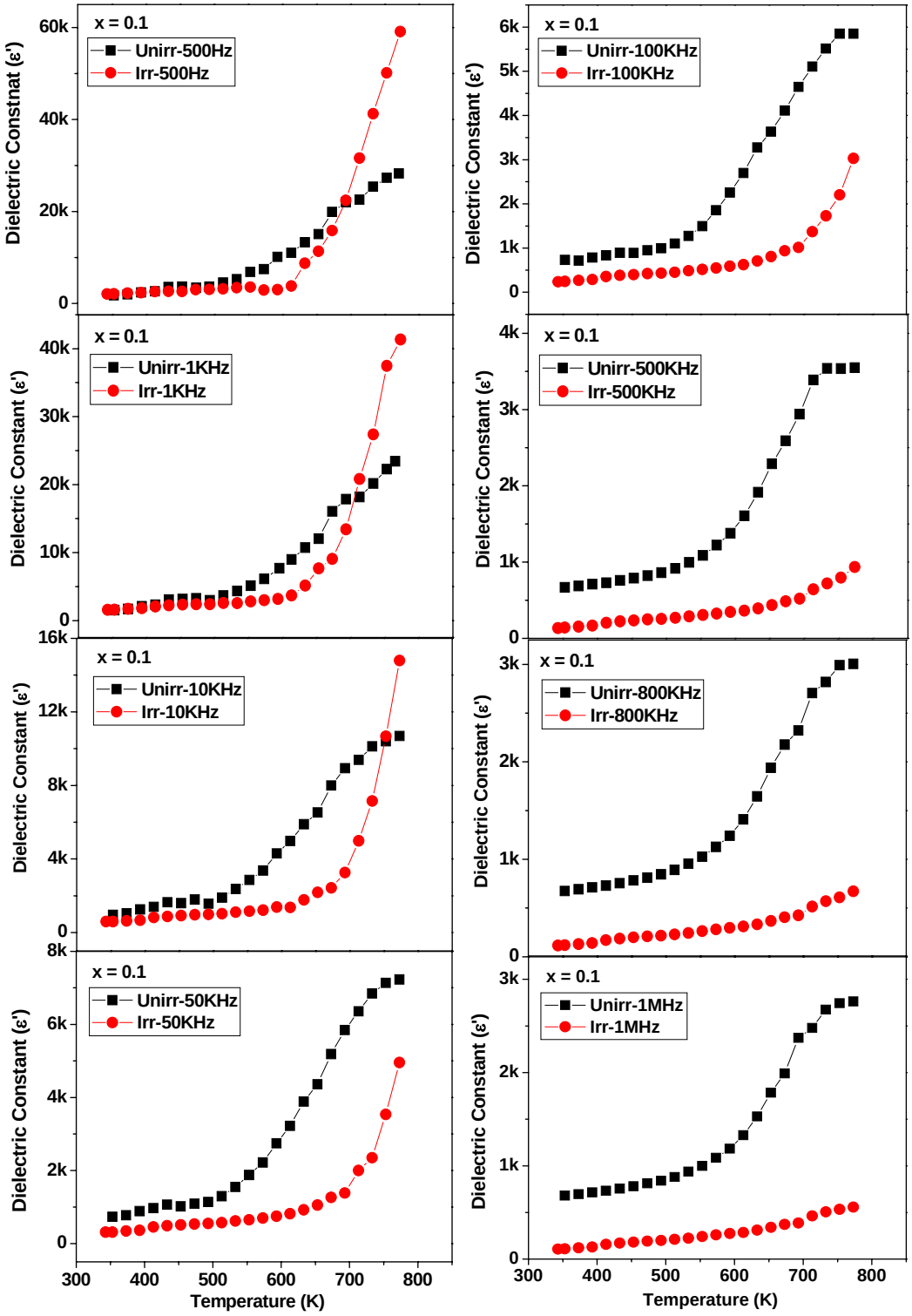

Fig. 6A.12b Thermal variation of dielectric constant at different frequencies for the composition x = 0.1 of unirradiated and irradiated $Li_{0.5(1+x)}Ti_xAl_{0.1}Fe_{2.4-1.5x}O_4$ system

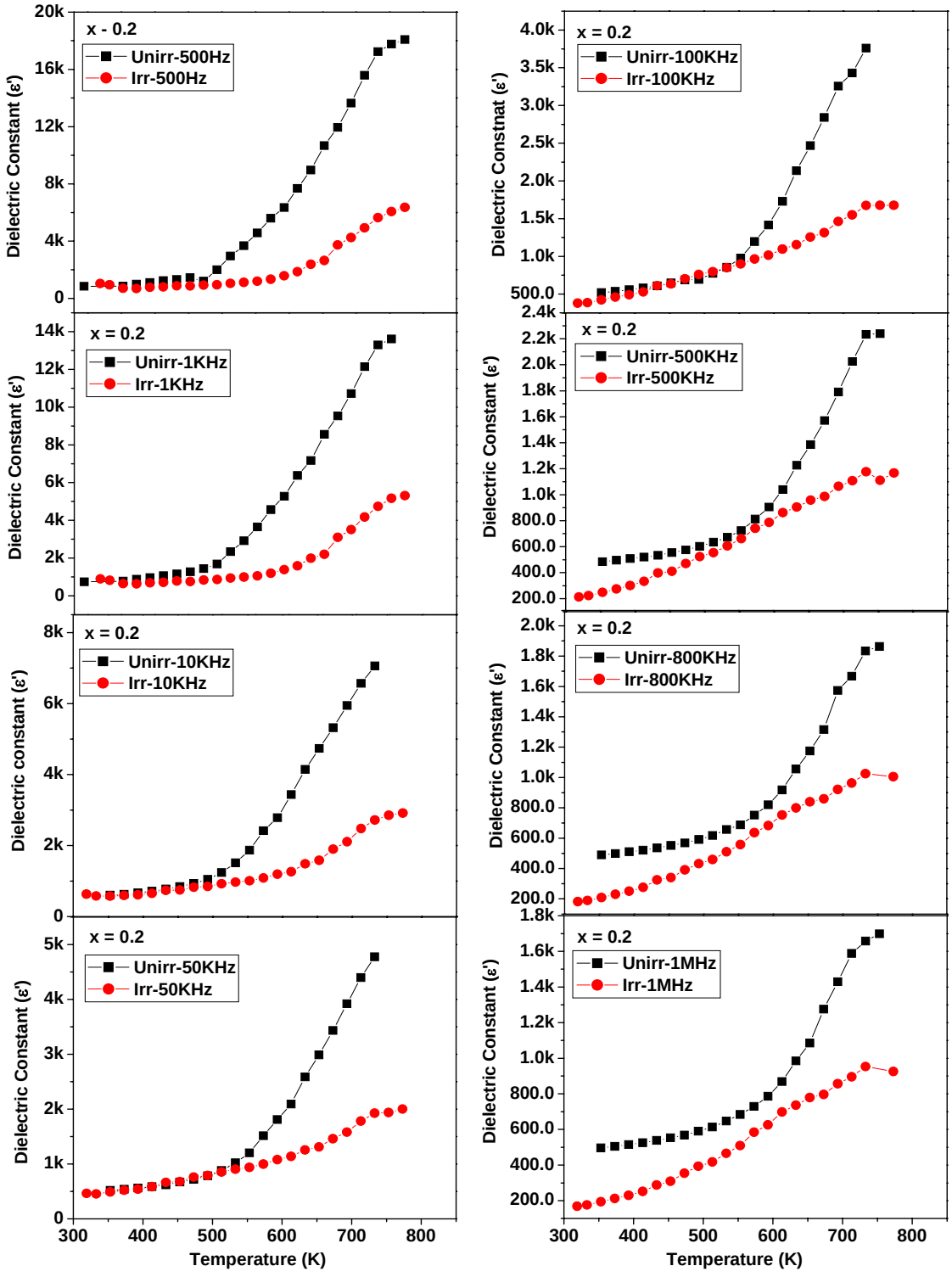

Fig. 6A.12c Thermal variation of dielectric constant at different frequencies for the composition x = 0.2 of unirradiated and irradiated $Li_{0.5(1+x)}Ti_xAl_{0.1}Fe_{2.4-1.5x}O_4$ system

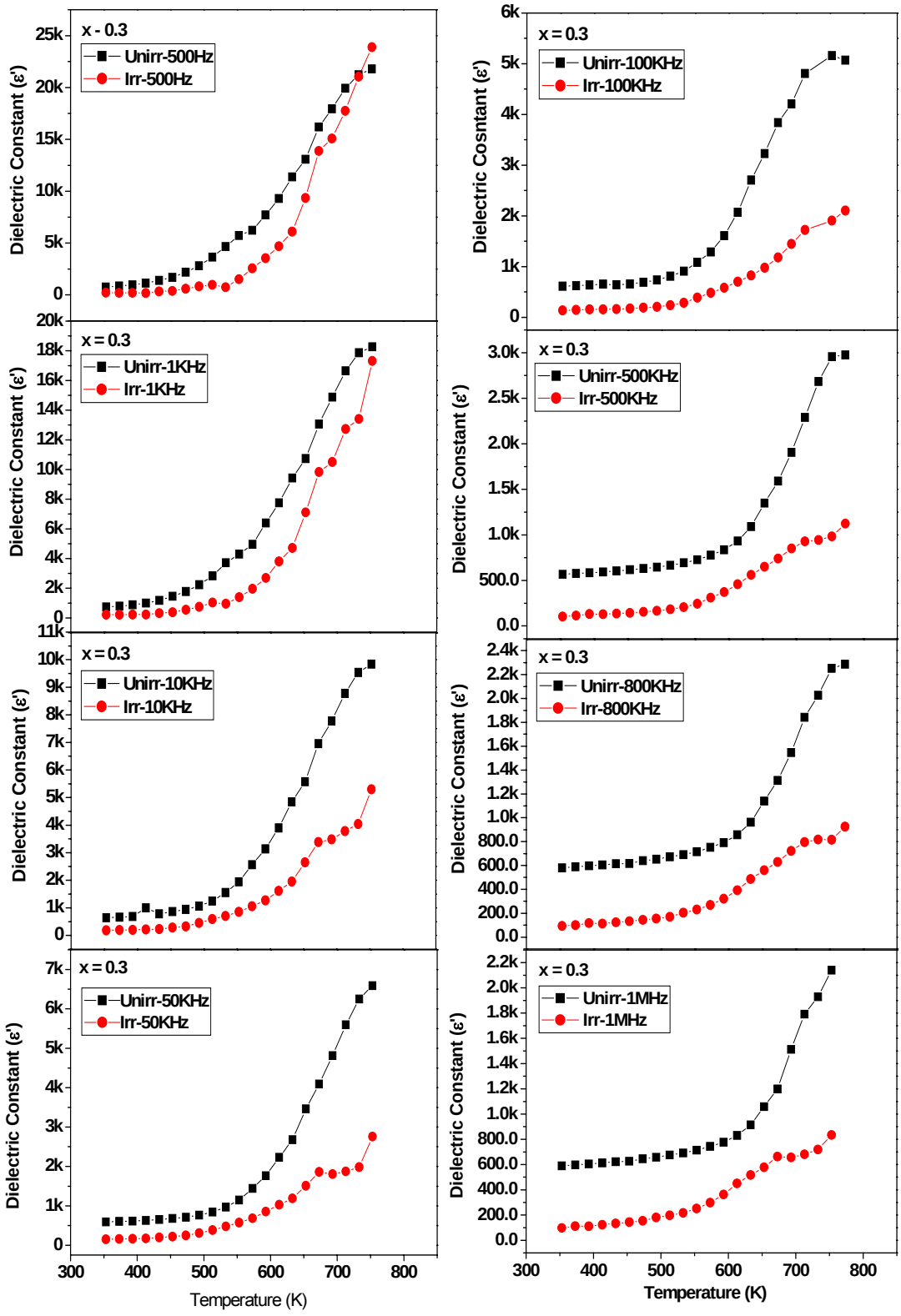

Fig. 6A.12d Thermal variation of dielectric constant at different frequencies for the composition x = 0.3 of unirradiated and irradiated $Li_{0.5(1+x)}Ti_xAl_{0.1}Fe_{2.4-1.5x}O_4$ system

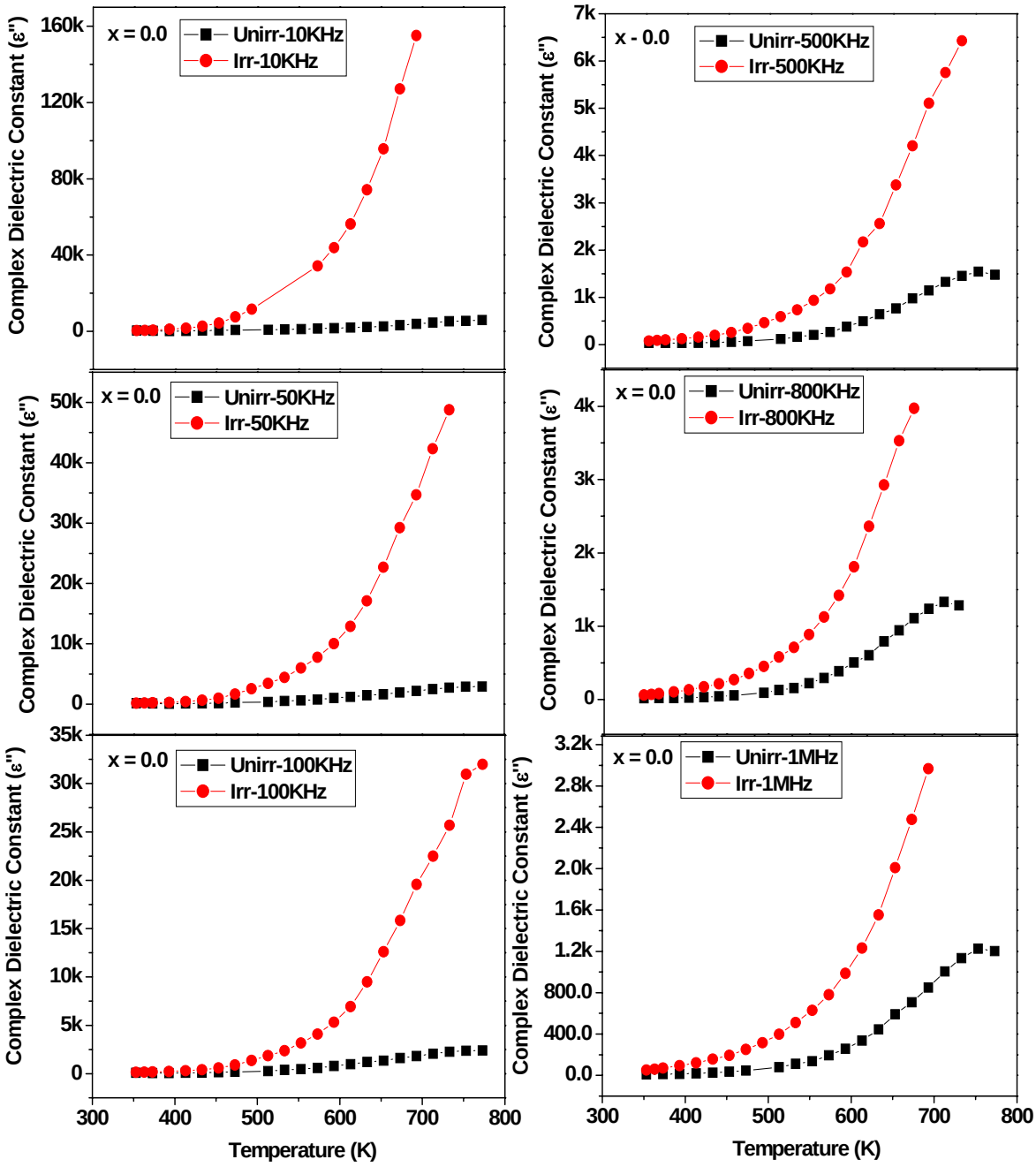

Fig. 6A.13a Thermal variation of Complex Dielectric Constant at different frequencies for the composition x = 0.0 of unirradiated and irradiated $Li_{0.5(1+x)}Ti_xAl_{0.1}Fe_{2.4-1.5x}O_4$ system

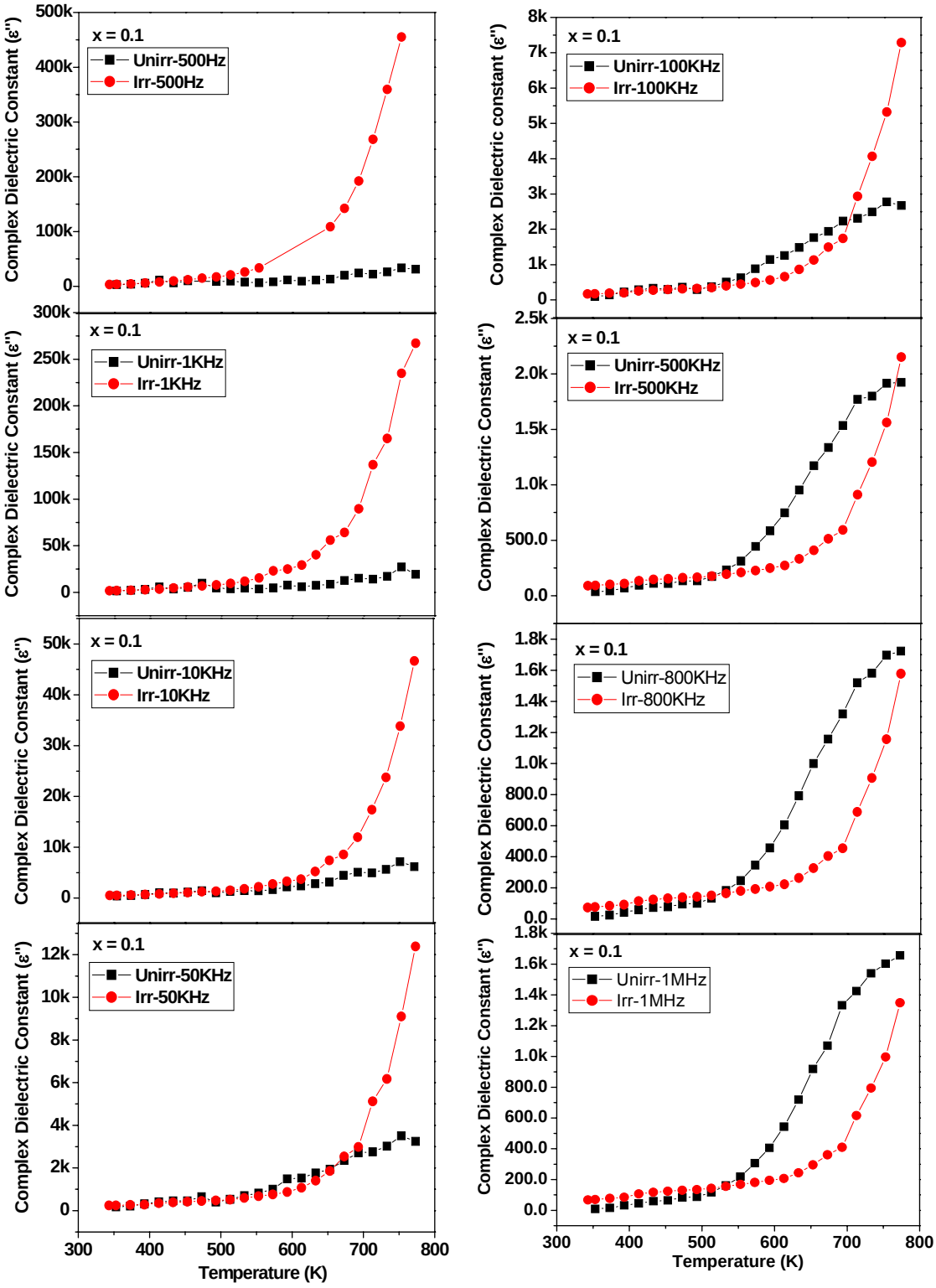

Fig. 6A.13b Thermal variation of Complex Dielectric Constant at different frequencies for the composition x = 0.1of unirradiated and irradiated $Li_{0.5(1+x)}Ti_xAl_{0.1}Fe_{2.4-1.5x}O_4$ system

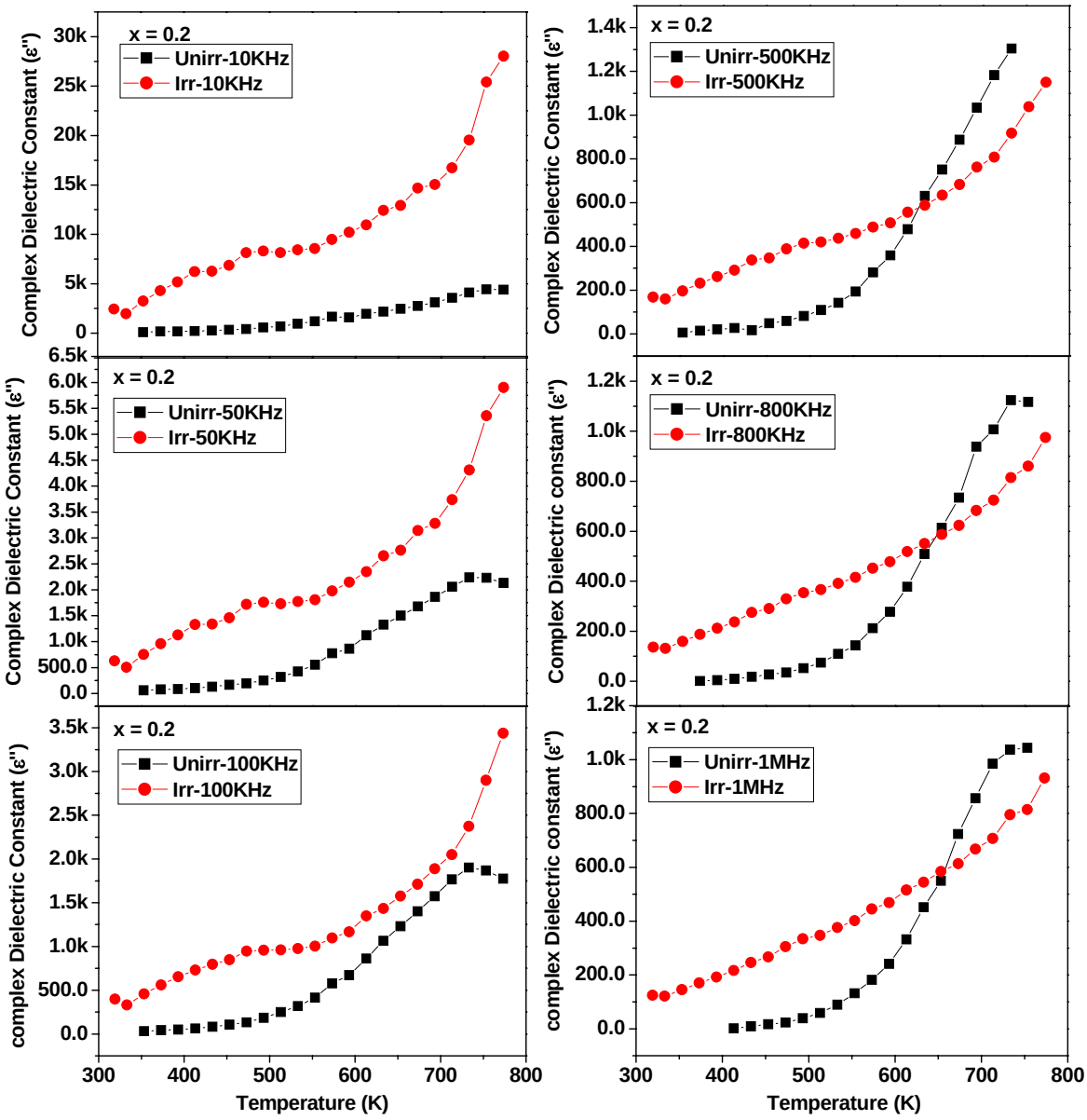

Fig. 6A.13c Thermal variation of Complex Dielectric Constant at different frequencies for the composition x = 0.2 of unirradiated and irradiated $Li_{0.5(1+x)}Ti_xAl_{0.1}Fe_{2.4-1.5x}O_4$ system

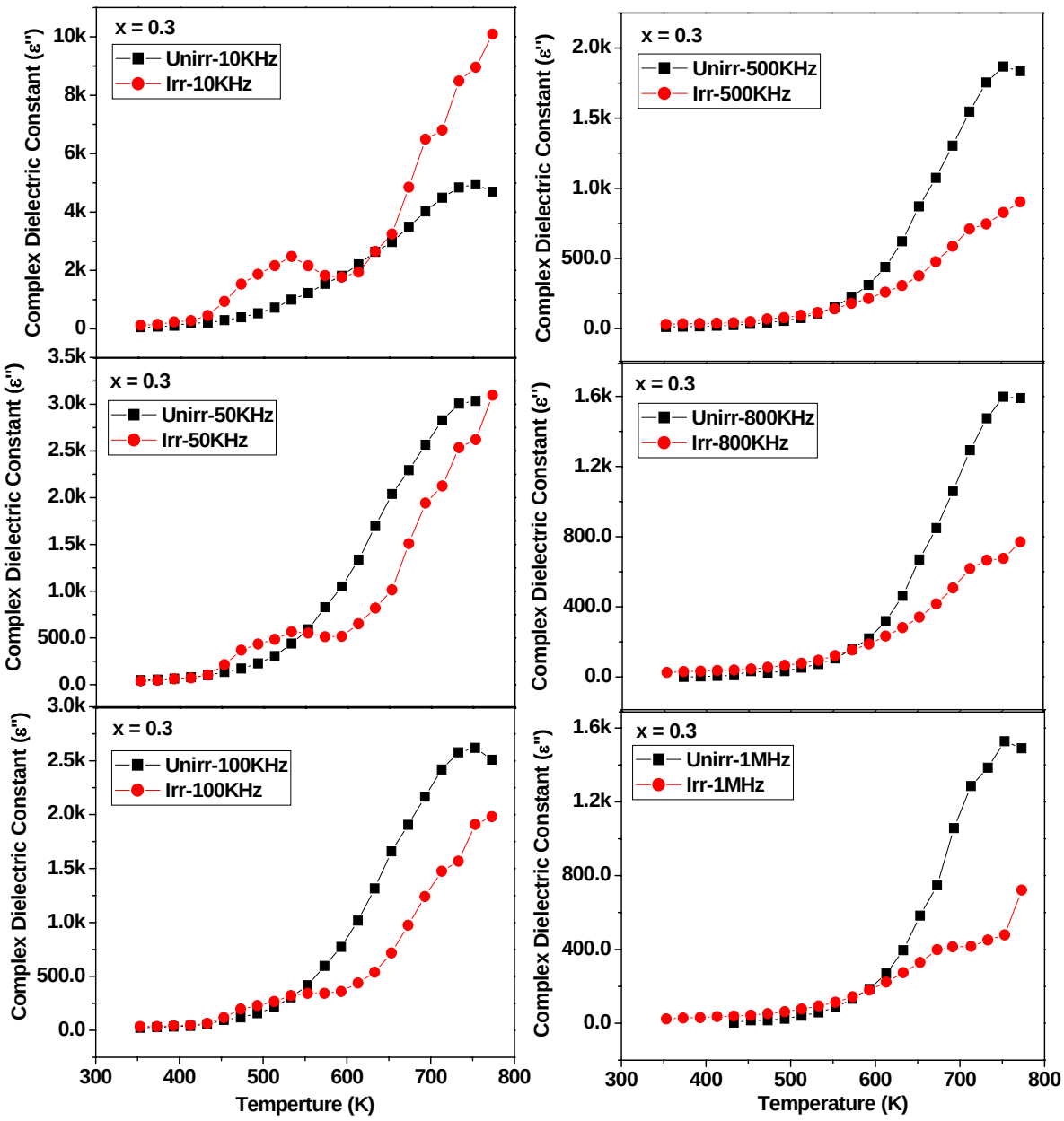

Fig. 6A.13d Thermal variation of Complex Dielectric Constant at different frequencies for the composition x = 0.3 of unirradiated and irradiated $Li_{0.5(1+x)}Ti_xAl_{0.1}Fe_{2.4-1.5x}O_4$ system

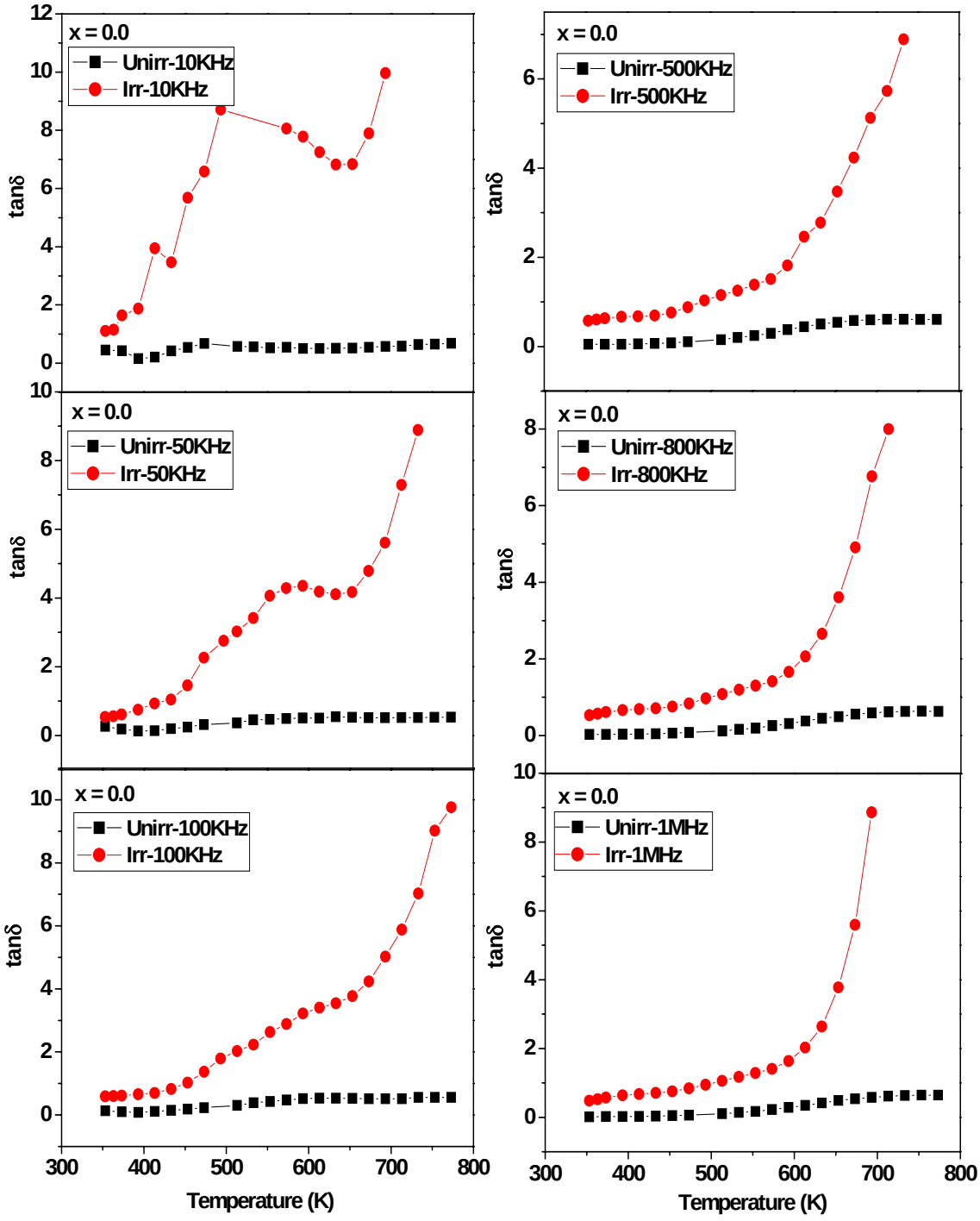

Fig. 6A.14a Thermal variation of Dielectric loss tangent at different frequencies for the composition x = 0.0 of unirradiated and irradiated $Li_{0.5(1+x)}Ti_xAl_{0.1}Fe_{2.4-1.5x}O_4$ system

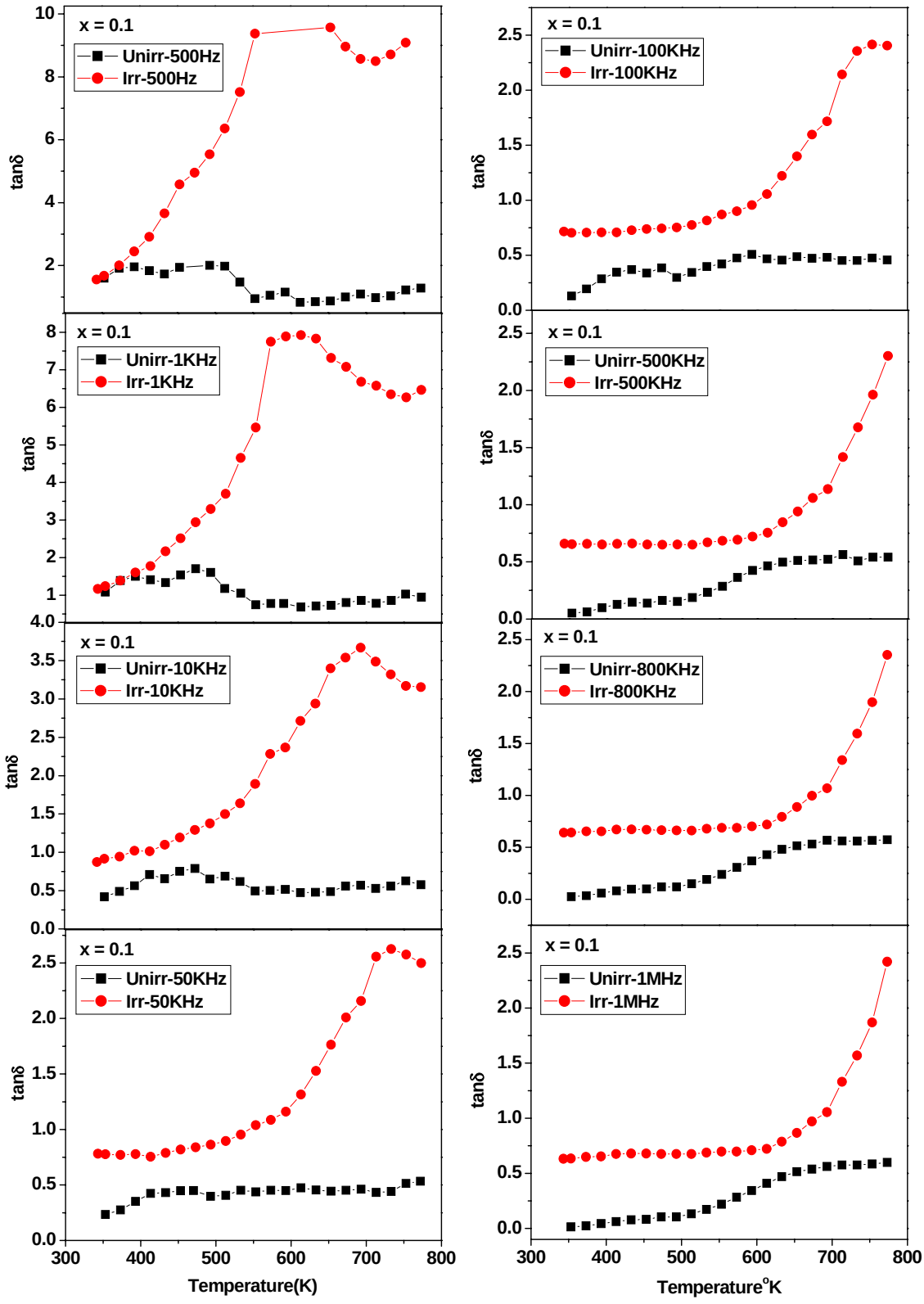

Fig. 6A.14b Thermal variation of Dielectric loss tangent at different frequencies for the composition x = 0.1 of unirradiated and irradiated $Li_{0.5(1+x)}Ti_xAl_{0.1}Fe_{2.4-1.5x}O_4$ system

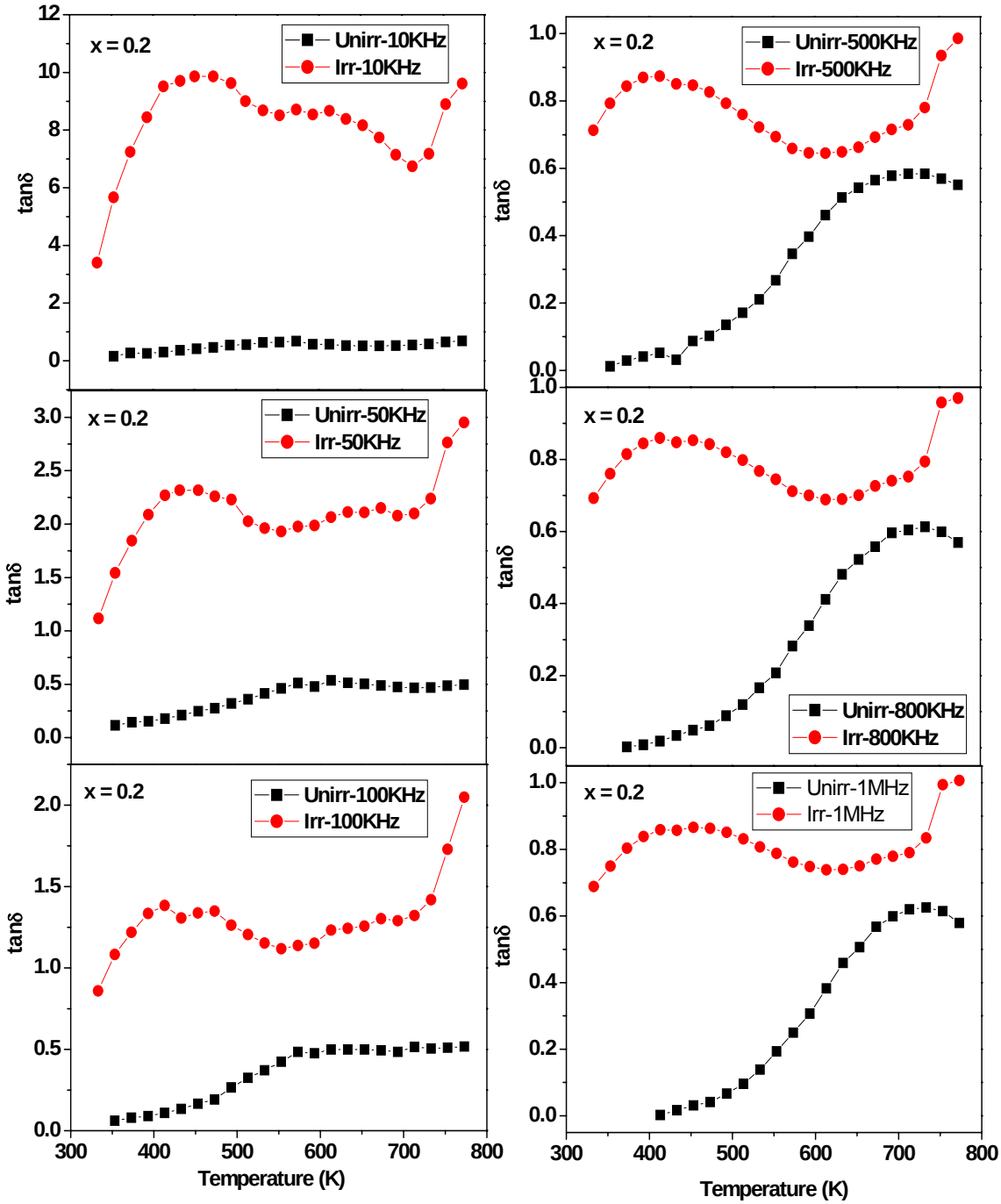

Fig. 6A.14c Thermal variation of Dielectric loss tangent at different frequencies for the composition x = 0.2 of unirradiated and irradiated $Li_{0.5(1+x)}Ti_xAl_{0.1}Fe_{2.4-1.5x}O_4$ system

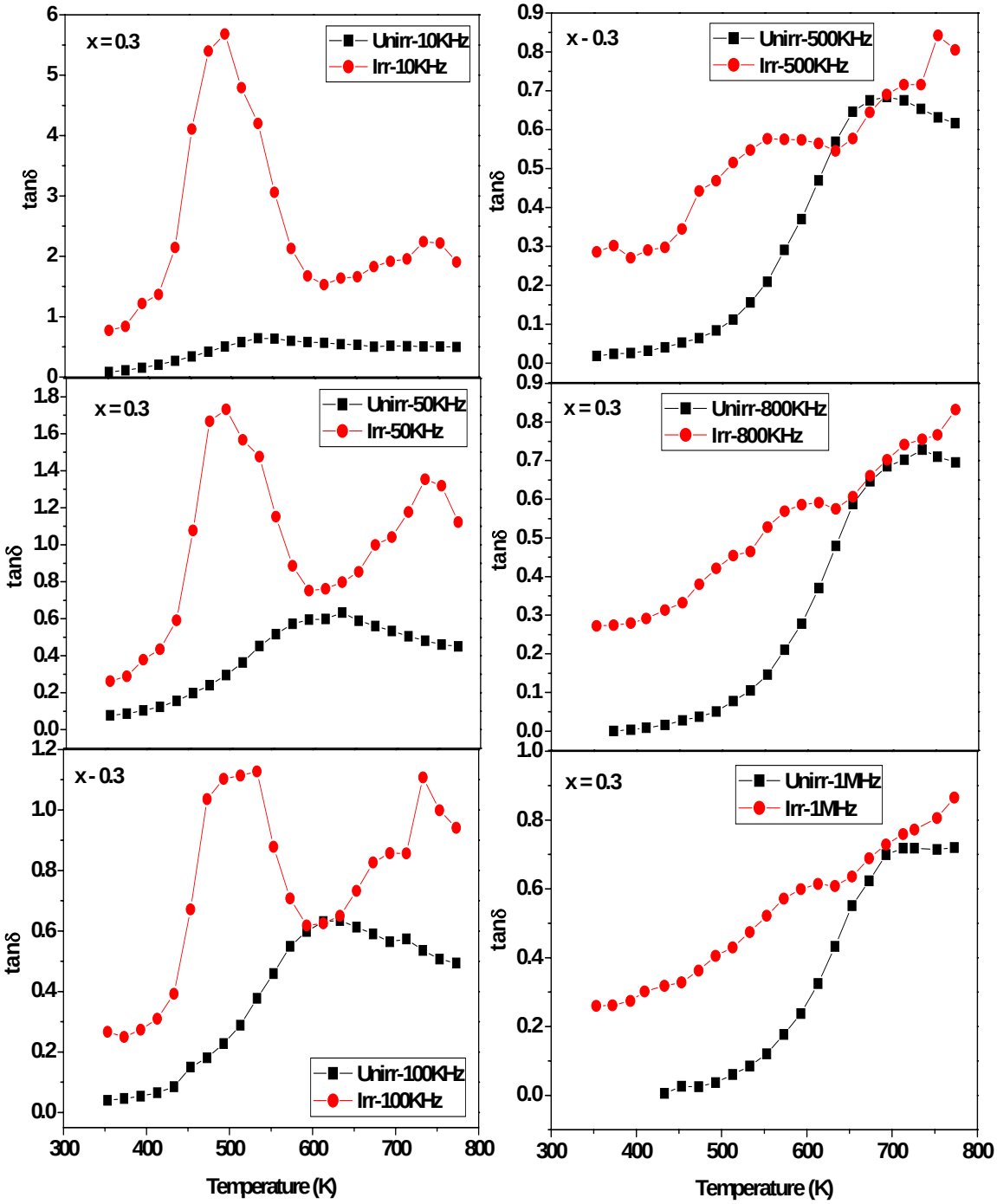

Fig. 6A.14d Thermal variation of Dielectric loss tangent at different frequencies for the composition x = 0.3 of unirradiated and irradiated $Li_{0.5(1+x)}Ti_xAl_{0.1}Fe_{2.4-1.5x}O_4$ system

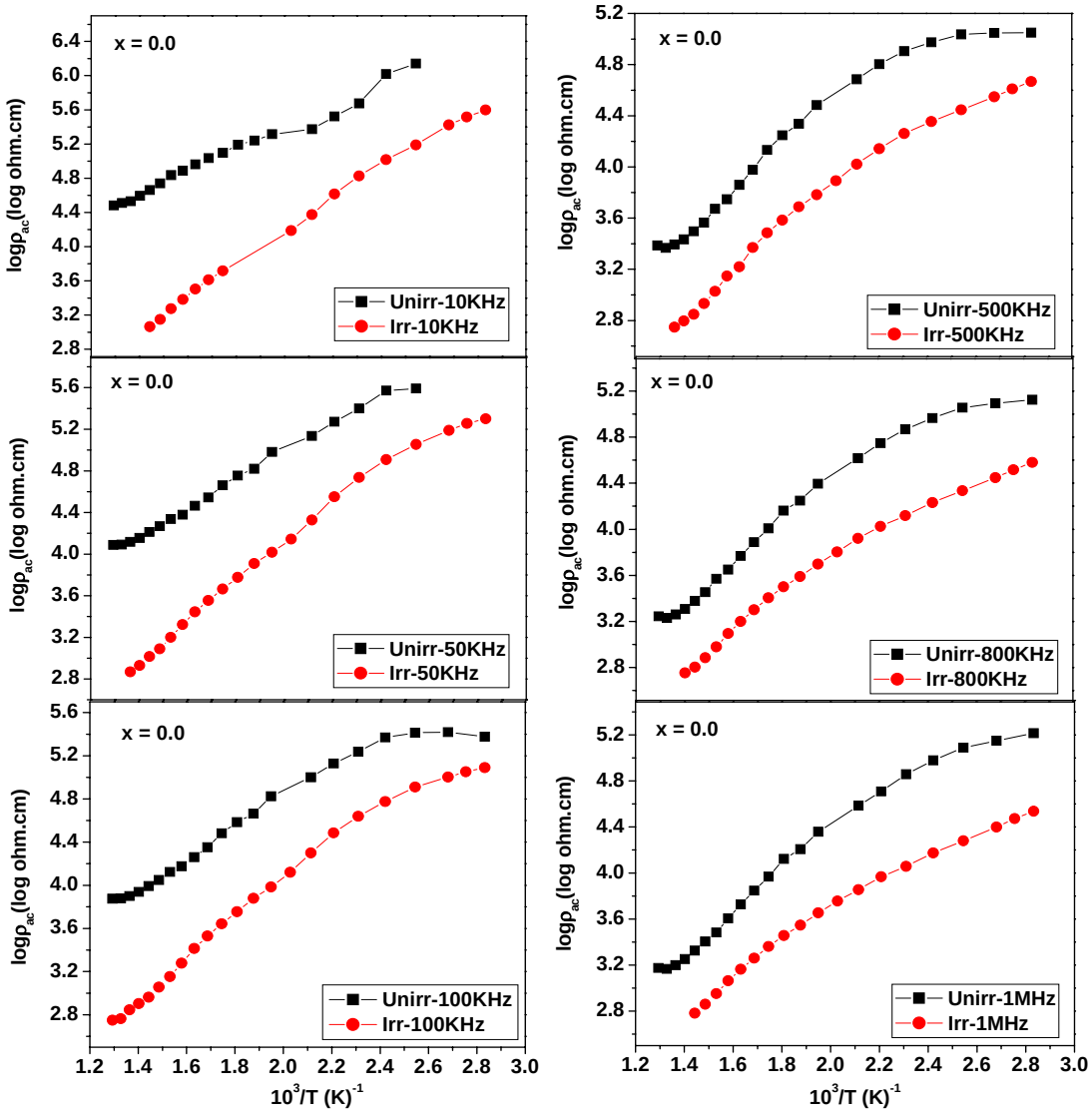

Fig. 6A.15a Thermal variation of a. c. resistivity at different frequencies for the composition x = 0.0 of unirradiated and irradiated $Li_{0.5(1+x)}Ti_xAl_{0.1}Fe_{2.4-1.5x}O_4$ system

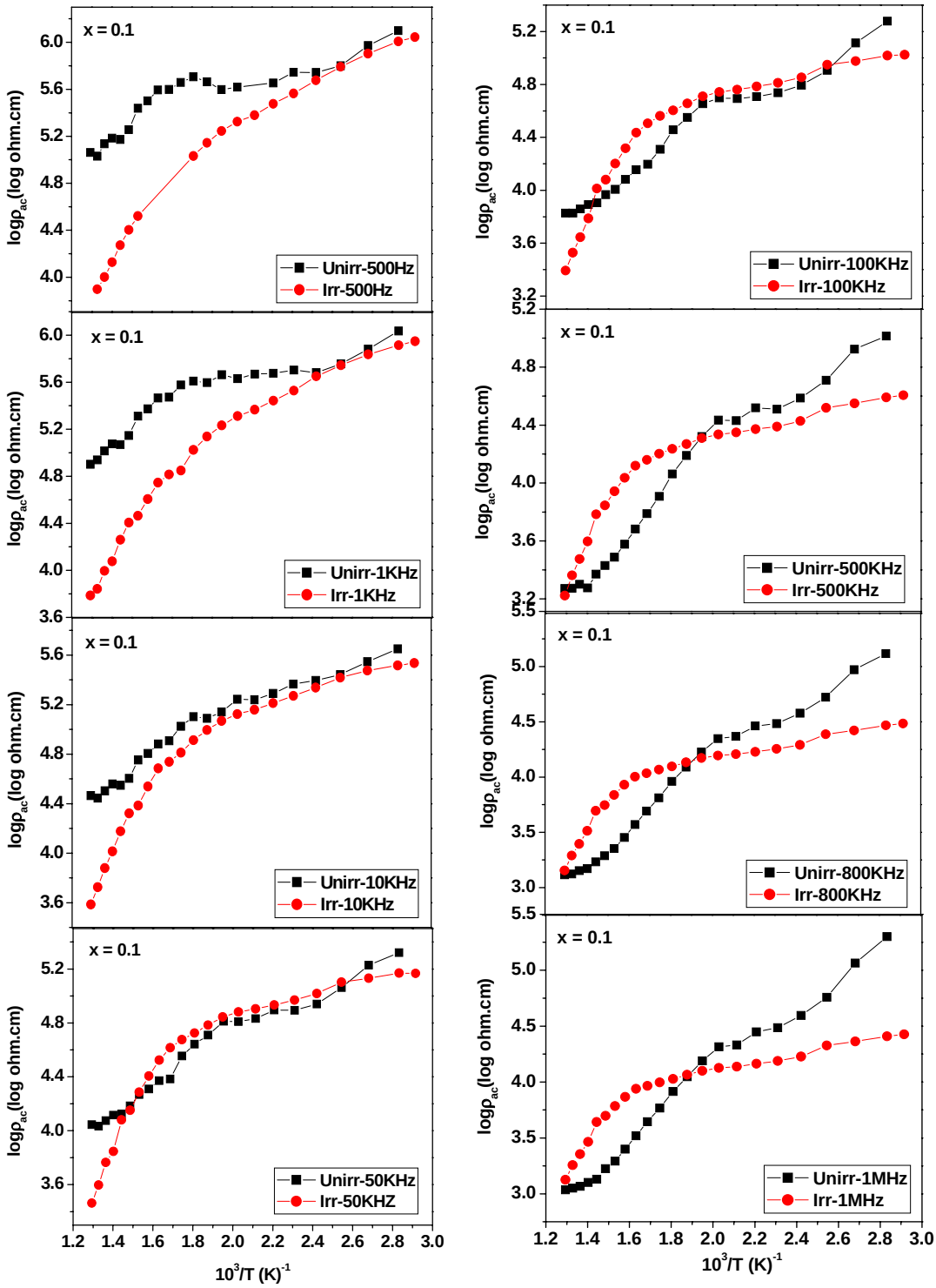

Fig. 6A.15b Thermal variation of a. c. resistivity at different frequencies for the composition x = 0.1 of unirradiated and irradiated $Li_{0.5(1+x)}Ti_xAl_{0.1}Fe_{2.4-1.5x}O_4$ system

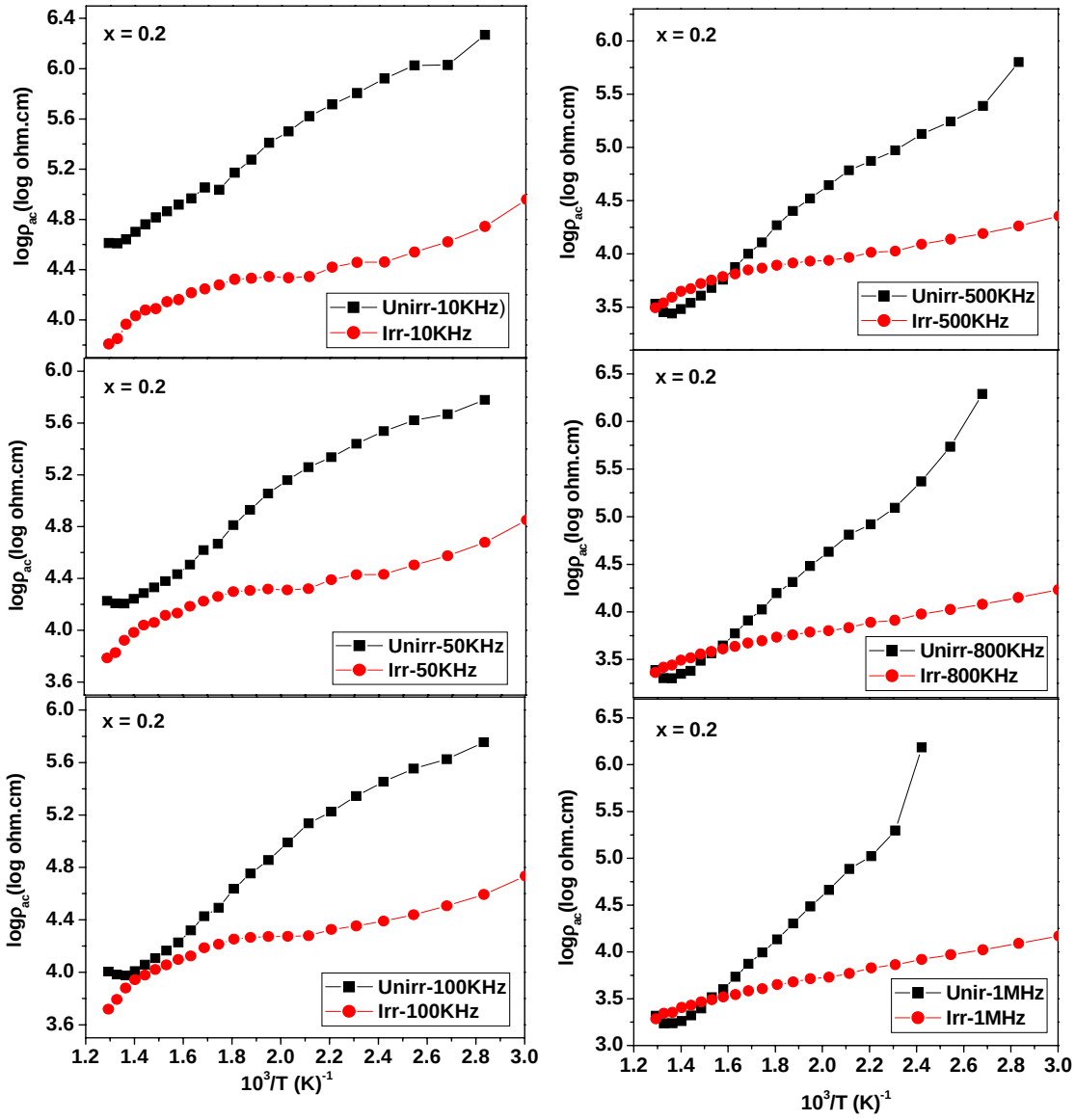

Fig. 6A.15c Thermal variation of a. c. resistivity at different frequencies for the composition x = 0.2 of unirradiated and irradiated $Li_{0.5(1+x)}Ti_xAl_{0.1}Fe_{2.4-1.5x}O_4$ system

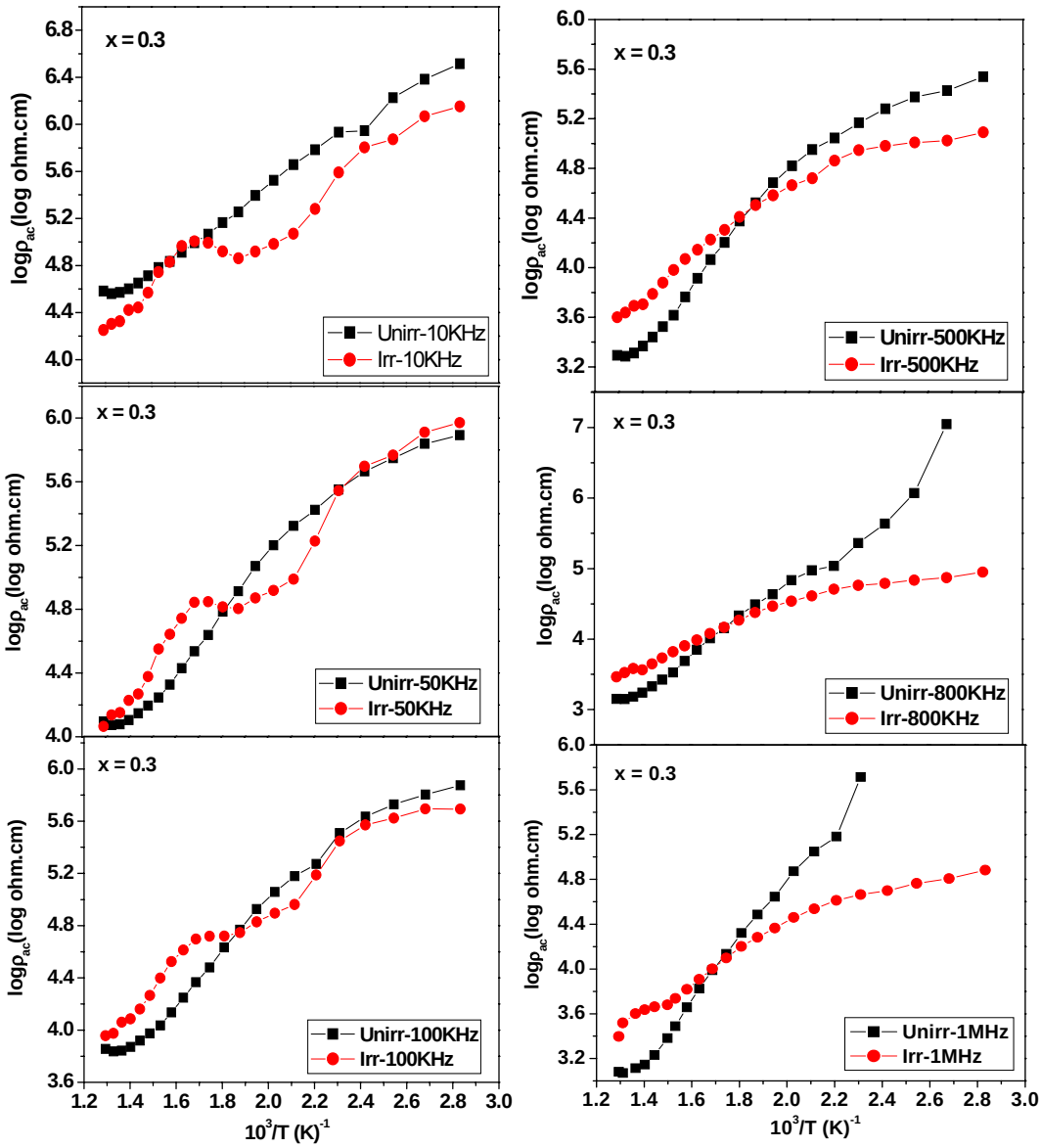

Fig. 6A.15d Thermal variation of a. c. resistivity at different frequencies for the composition x = 0.3 of unirradiated and irradiated $Li_{0.5(1+x)}Ti_xAl_{0.1}Fe_{2.4-1.5x}O_4$ system

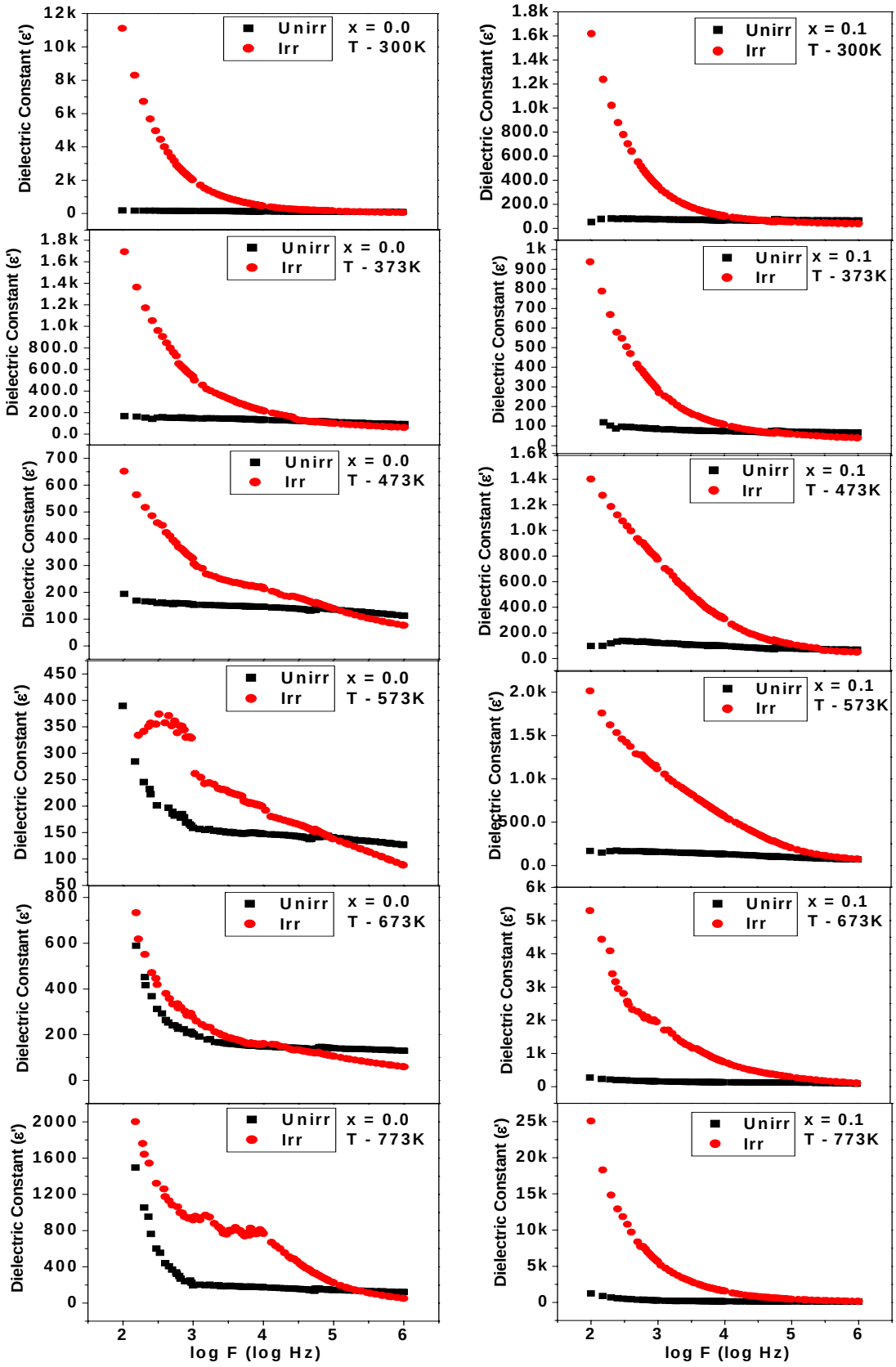

Fig. 6A.16a Dielectric Constant versus frequency at selected temperatures for the compositions x = 0.0 and 0.1 of unirradiated and irradiated $Li_{0.5(1+x)}Ti_xAl_{0.1}Fe_{2.4-1.5x}O_4$ system

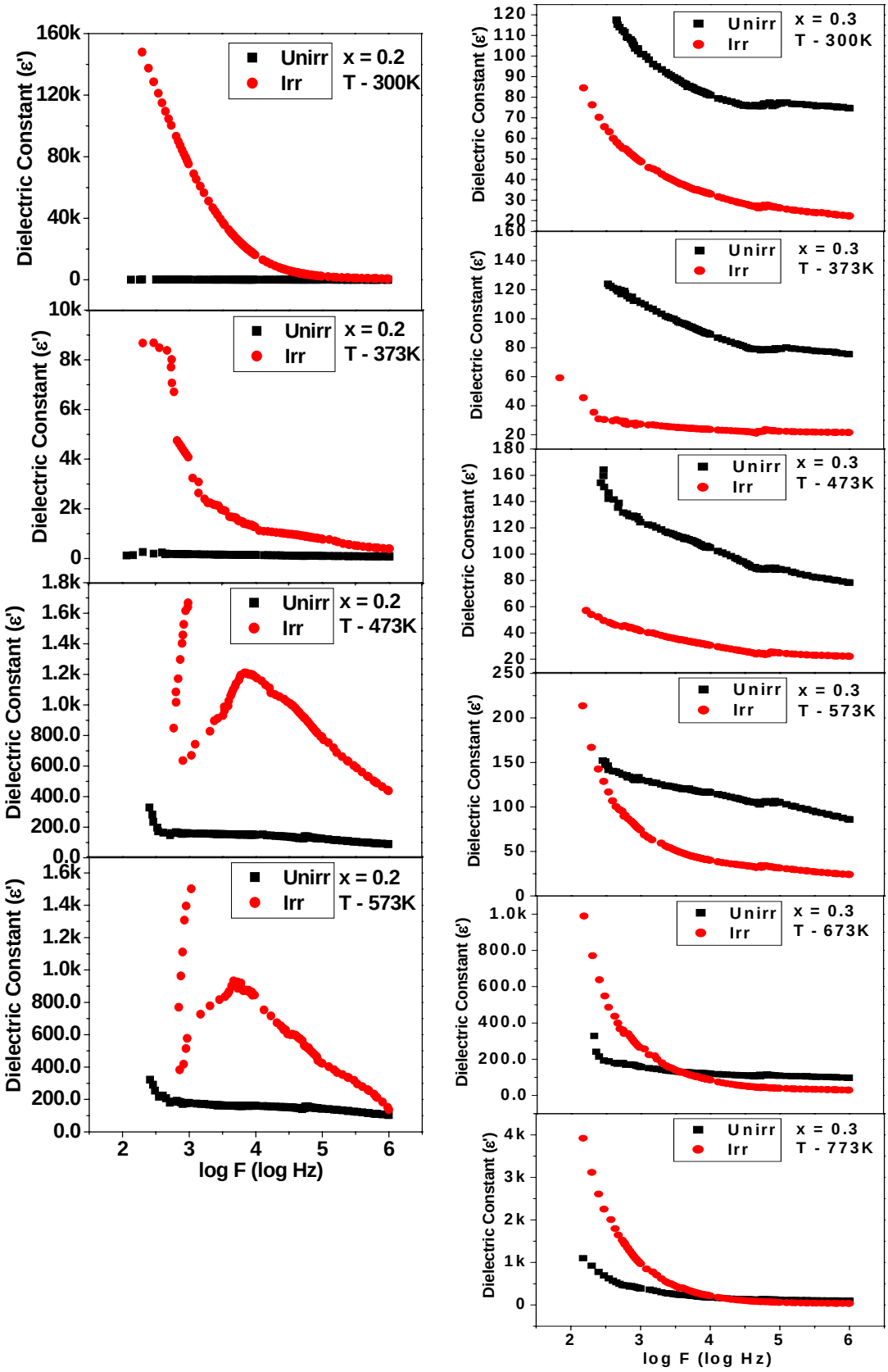

Fig. 6A.16b Dielectric Constant versus frequency at selected temperatures for the compositions x = 0.2 and 0.3 of unirradiated and irradiated $Li_{0.5(1+x)}Ti_xAl_{0.1}Fe_{2.4-1.5x}O_4$ system

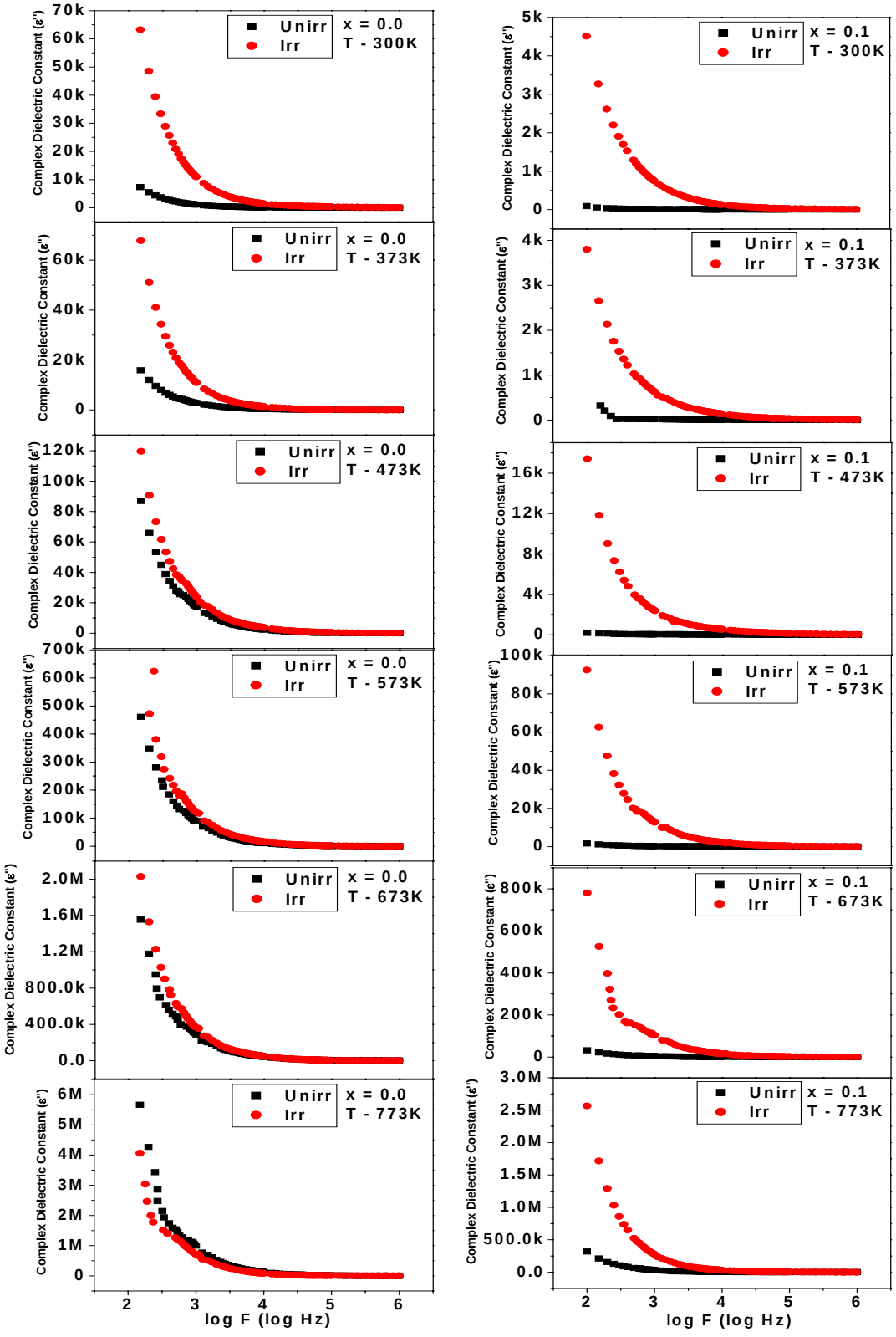

Fig. 6A.17a Complex Dielectric Constant versus frequency at selected temperatures for the compositions x = 0.0 and 0.1 of unirradiated and irradiated $Li_{0.5(1+x)}Ti_xAl_{0.1}Fe_{2.4-1.5x}O_4$ system

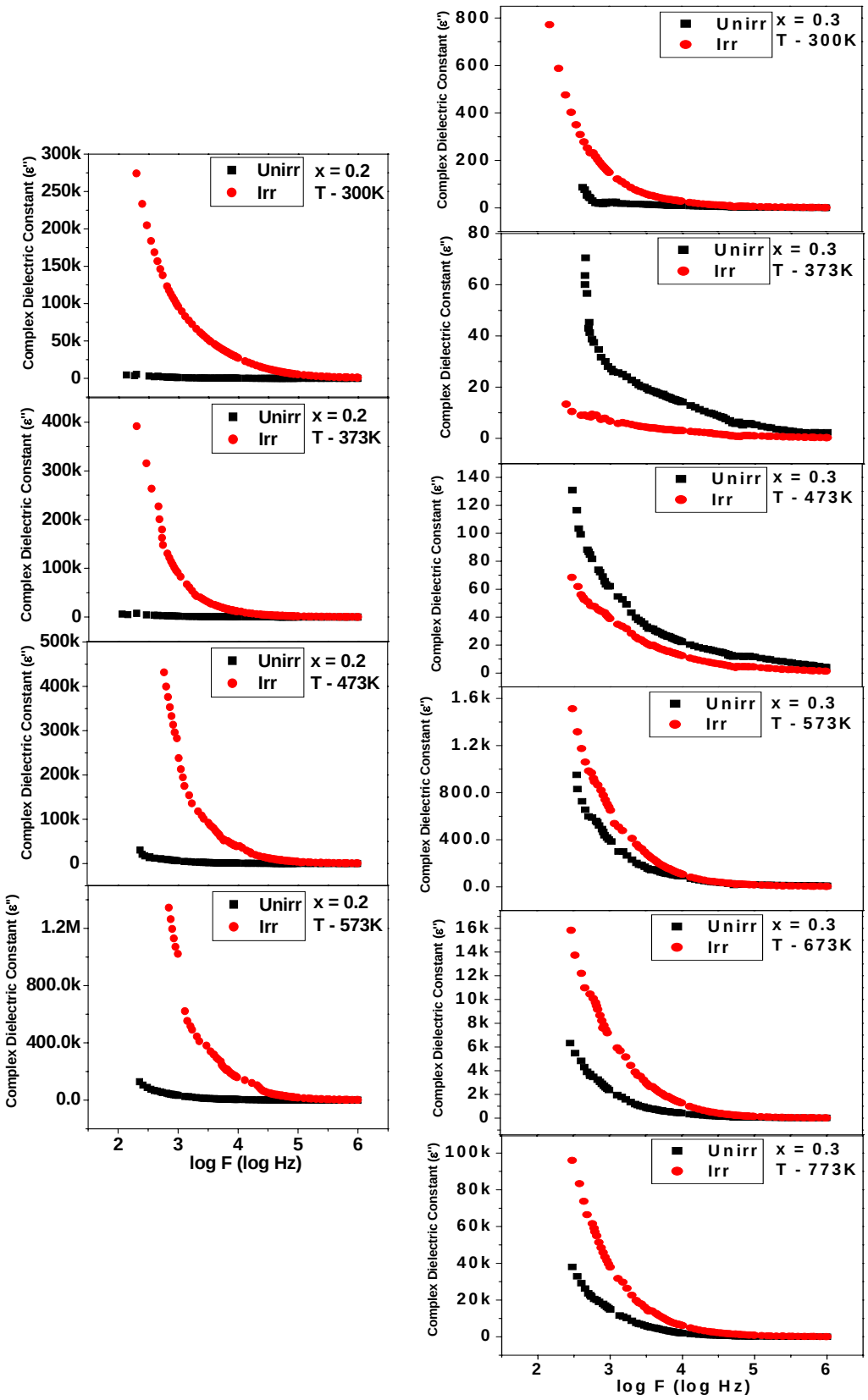

Fig. 6A.17b Complex Dielectric Constant versus frequency at selected temperatures for the compositions x = 0.2 and 0.3 of unirradiated and irradiated $Li_{0.5(1+x)}Ti_xAl_{0.1}Fe_{2.4-1.5x}O_4$ system

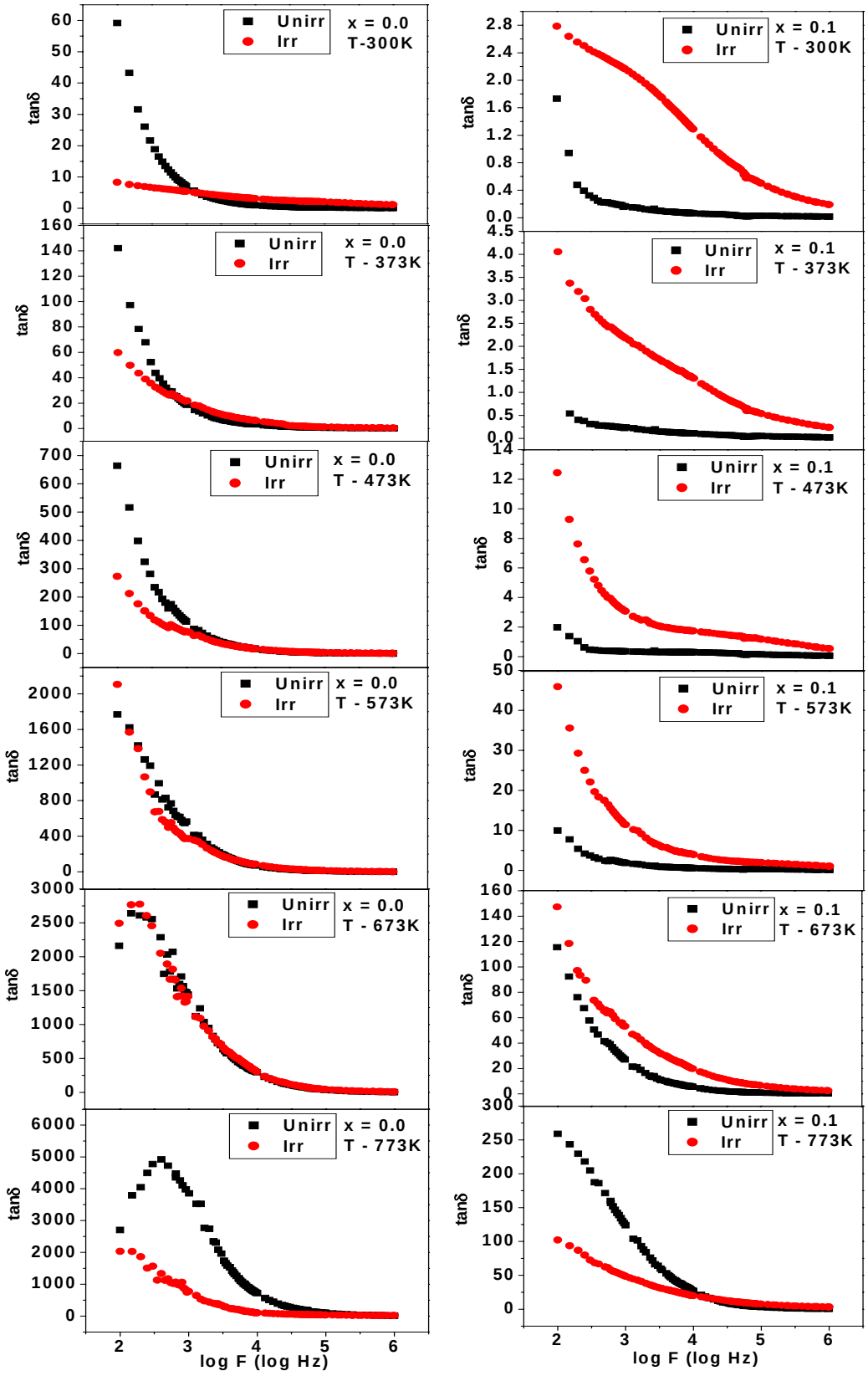

Fig. 6A.18a Dielectric loss tangent versus frequency at selected temperatures for the compositions x = 0.0 and 0.1 of unirradiated and irradiated $Li_{0.5(1+x)}Ti_xAl_{0.1}Fe_{2.4-1.5x}O_4$ system

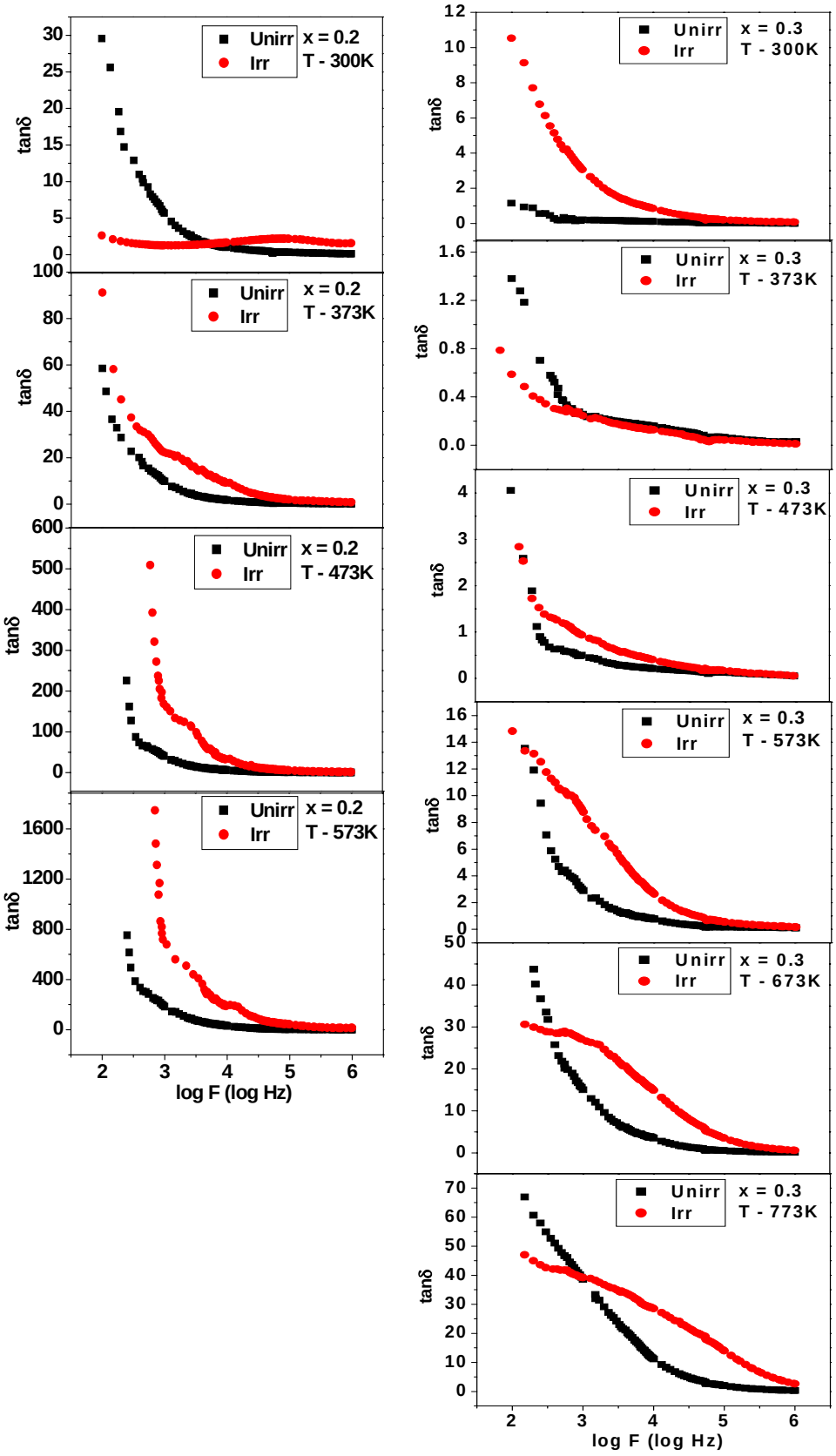

Fig. 6A.18b Dielectric loss tangent versus frequency at selected temperatures for the compositions x = 0.2 and 0.3 of unirradiated and irradiated $Li_{0.5(1+x)}Ti_xAl_{0.1}Fe_{2.4-1.5x}O_4$ system

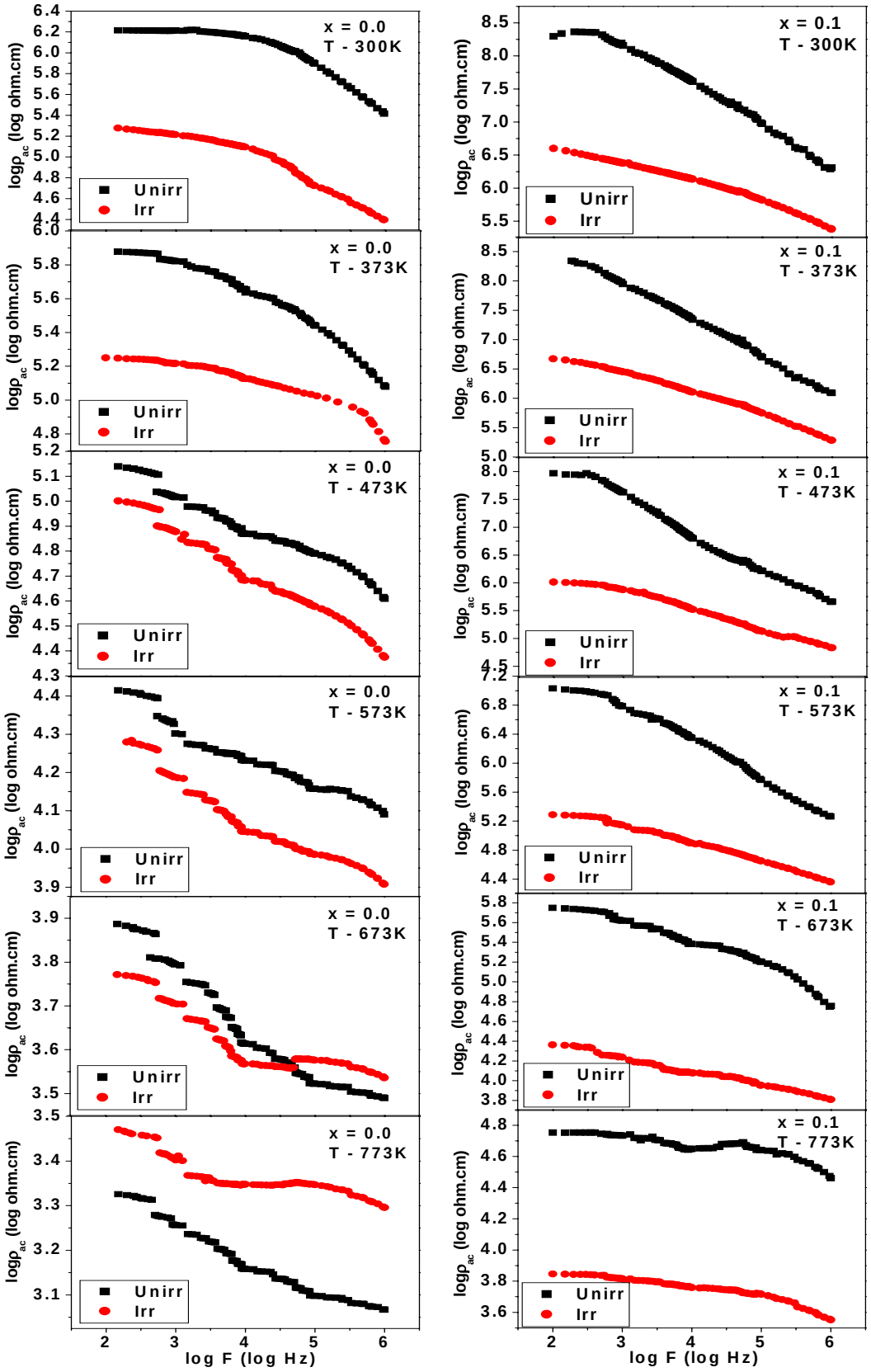

Fig. 6A.19a AC resistivity versus frequency at selected temperatures for the compositions x = 0.0 and 0.1 of unirradiated and irradiated $Li_{0.5(1+x)}Ti_xAl_{0.1}Fe_{2.4-1.5x}O_4$ system

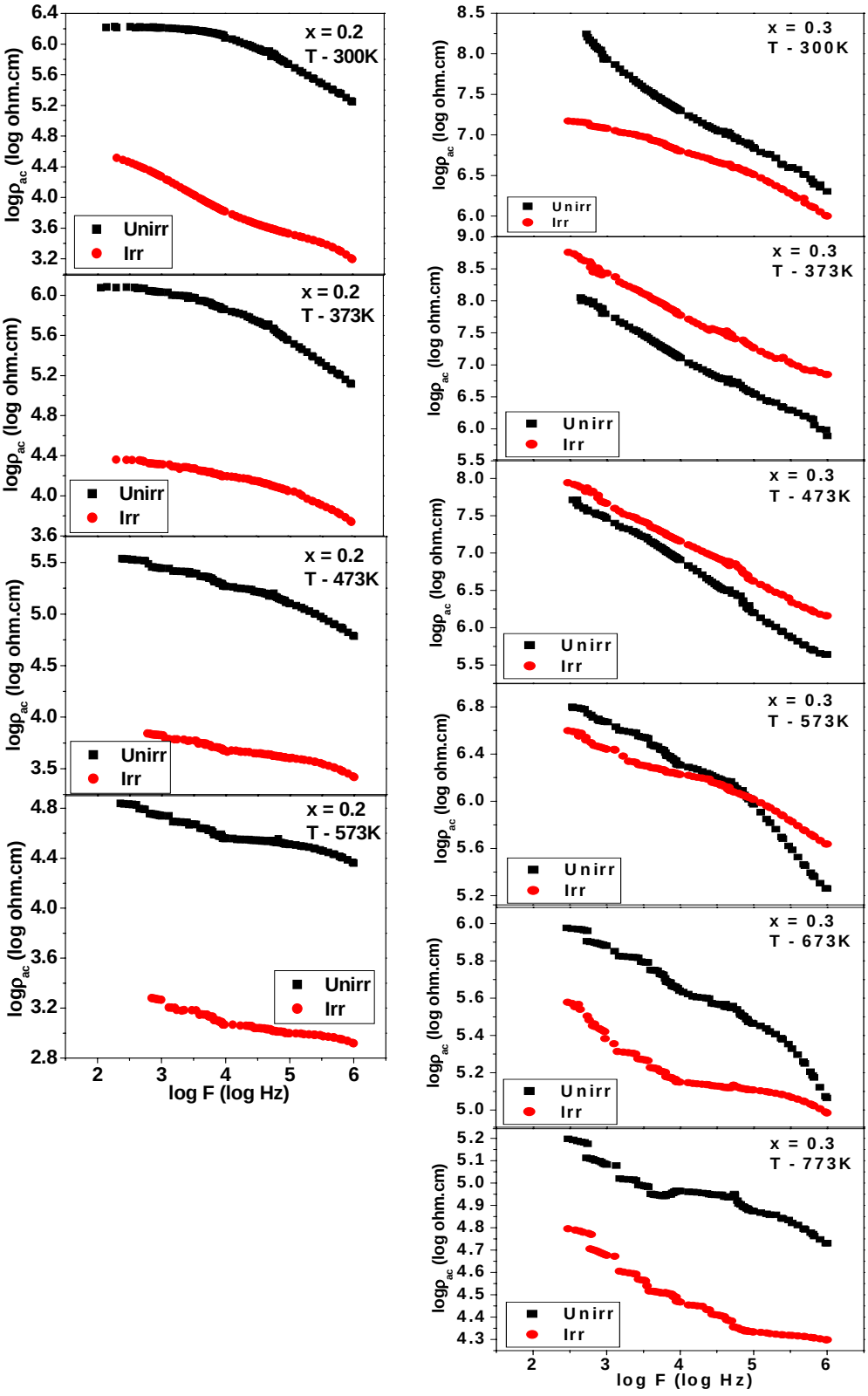

Fig. 6A.19b AC resistivity versus frequency at selected temperatures for the compositions x = 0.2 and 0.3 of unirradiated and irradiated $Li_{0.5(1+x)}Ti_xAl_{0.1}Fe_{2.4-1.5x}O_4$ system

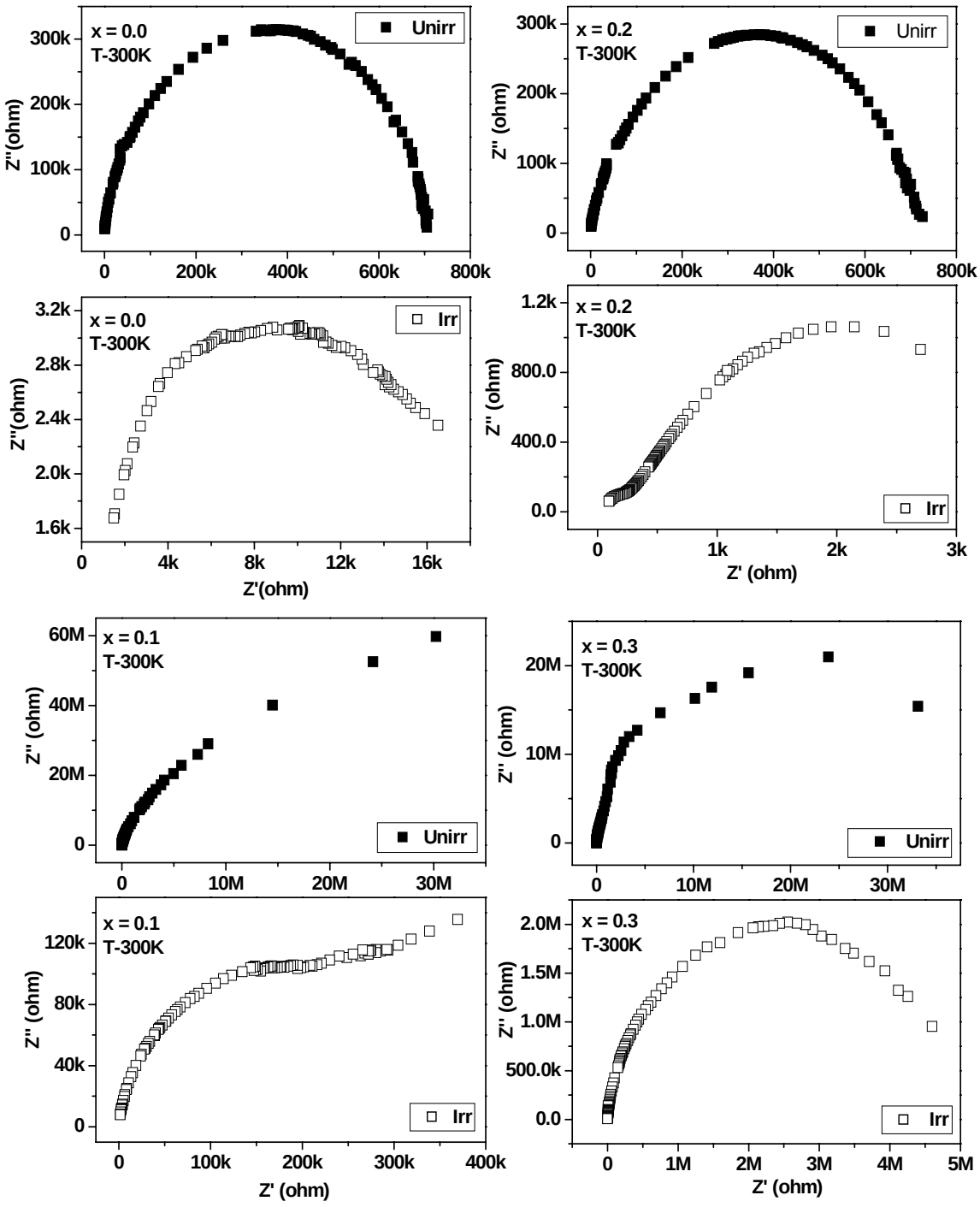

Fig. 6A.20 Real (Z') versus imaginary (Z'') parts of the impedance, Cole-Cole Plots at room temperature for the compositions x = 0.0, 0.1, 0.2 and o.3 of unirradiated and irradiated $Li_{0.5(1+x)}Ti_xAl_{0.1}Fe_{2.4-1.5x}O_4$ system

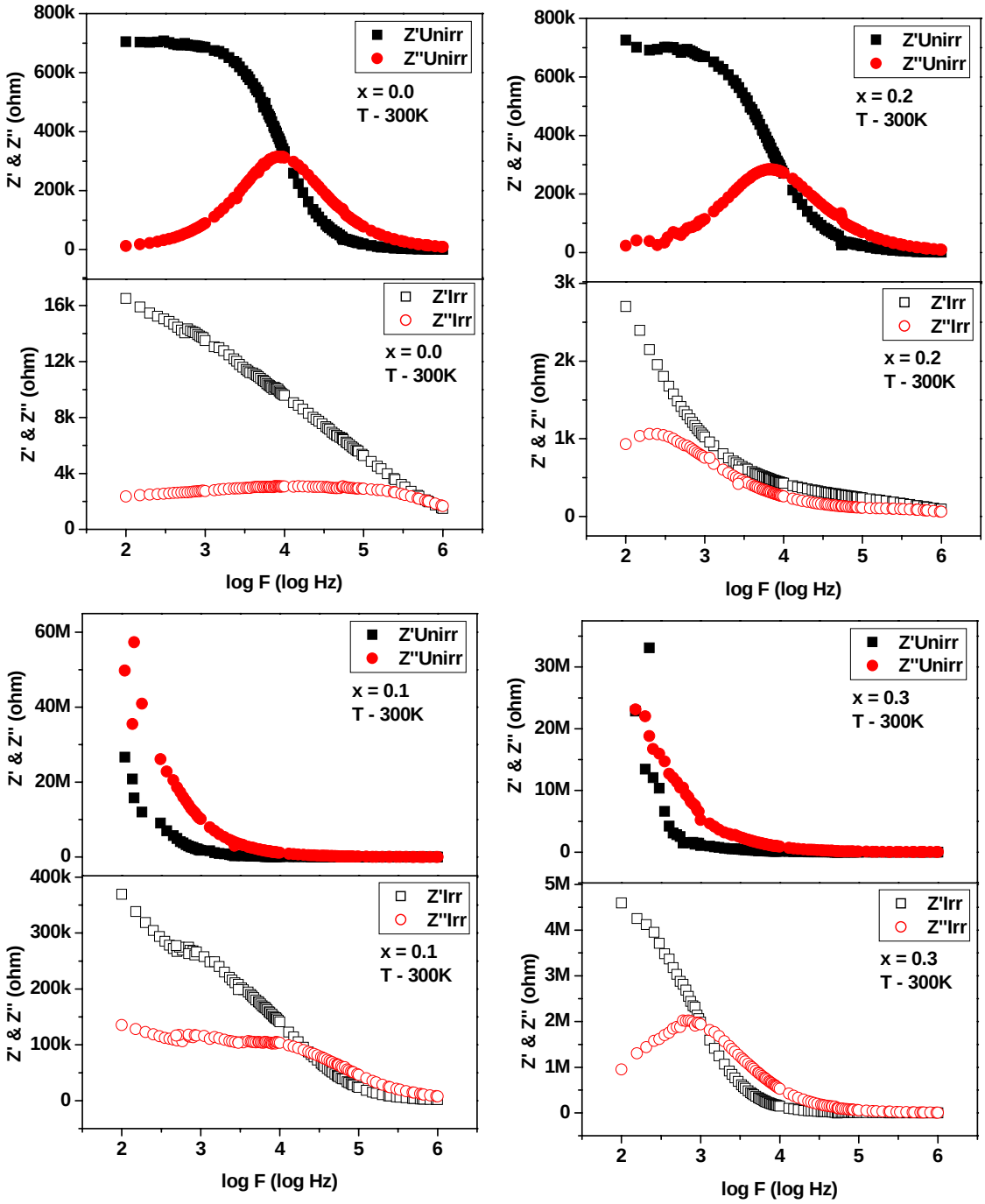

Fig. 6A.21 Variation of real part (Z') and imaginary part (Z'') of the impedance with frequency at room temperature for the compositons x = 0.0, 0.1, 0.2 and 0.3 of unirradiated and irradiated $Li_{0.5(1+x)}Ti_xAl_{0.1}Fe_{2.4-1.5x}O_4$ system

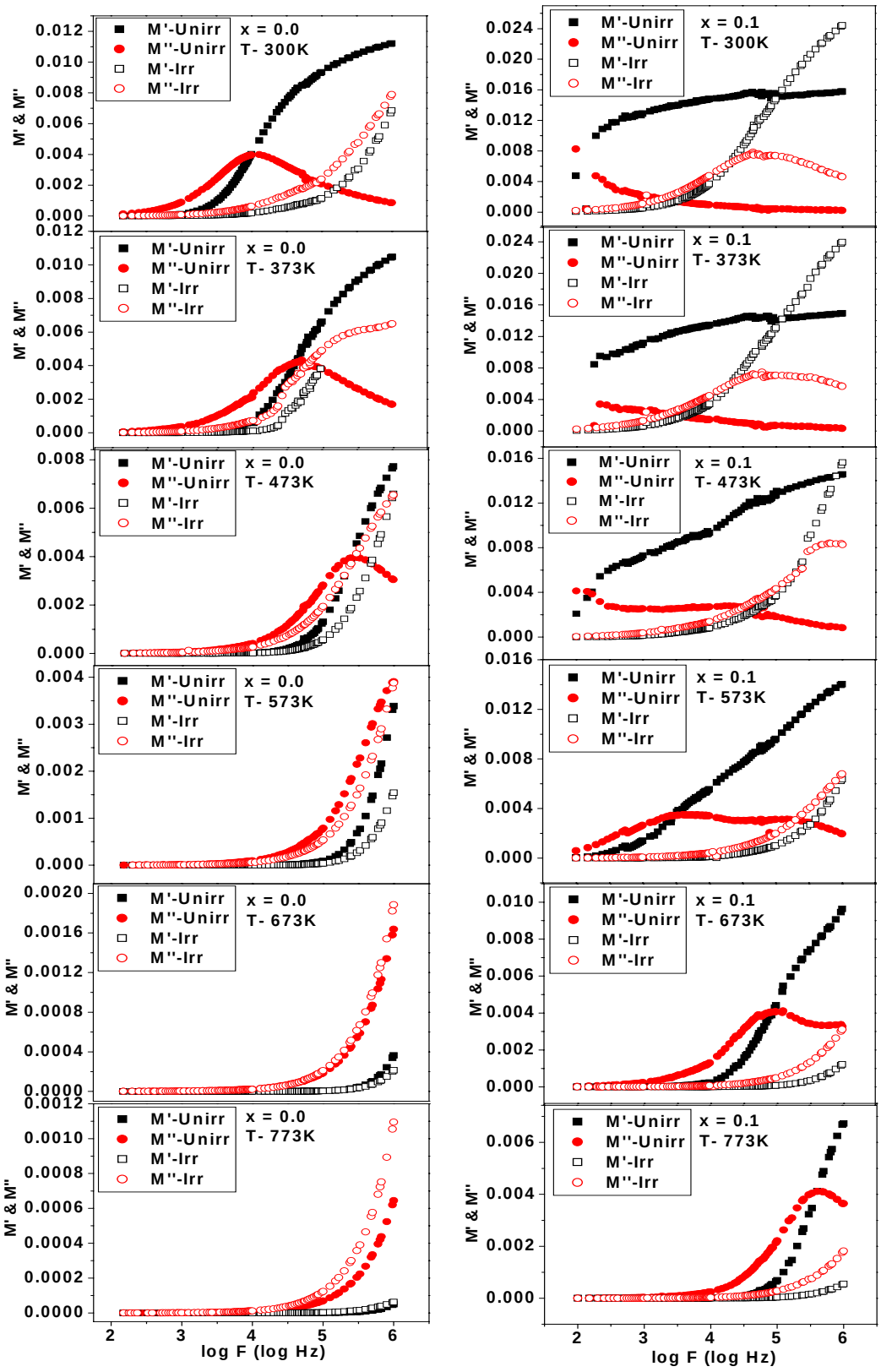

Fig. 6A.22a Real (M') and imaginary (M'') part of the dielectric modulus versus frequency at selected temperatures for the compositions x = 0.0 and 0.1 of unirradiated and irradiated $Li_{0.5(1+x)}Ti_xAl_{0.1}Fe_{2.4-1.5x}O_4$ system

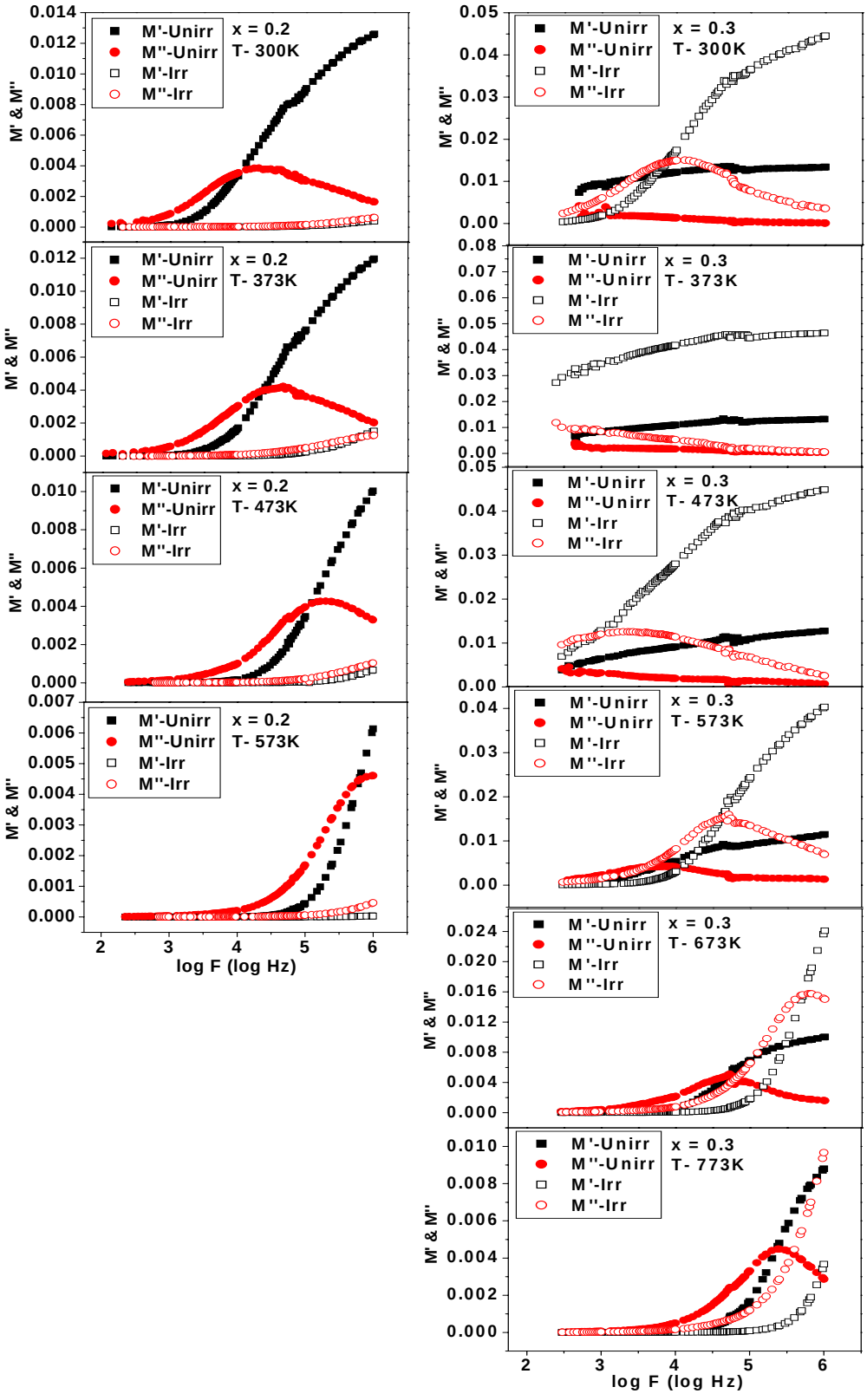

Fig. 6A.22b Real (M') and imaginary (M'') part of the dielectric modulus versus frequency at selected temperatures for the compositions x = 0.2 and 0.3 of unirradiated and irradiated $Li_{0.5(1+x)}Ti_xAl_{0.1}Fe_{2.4-1.5x}O_4$ system

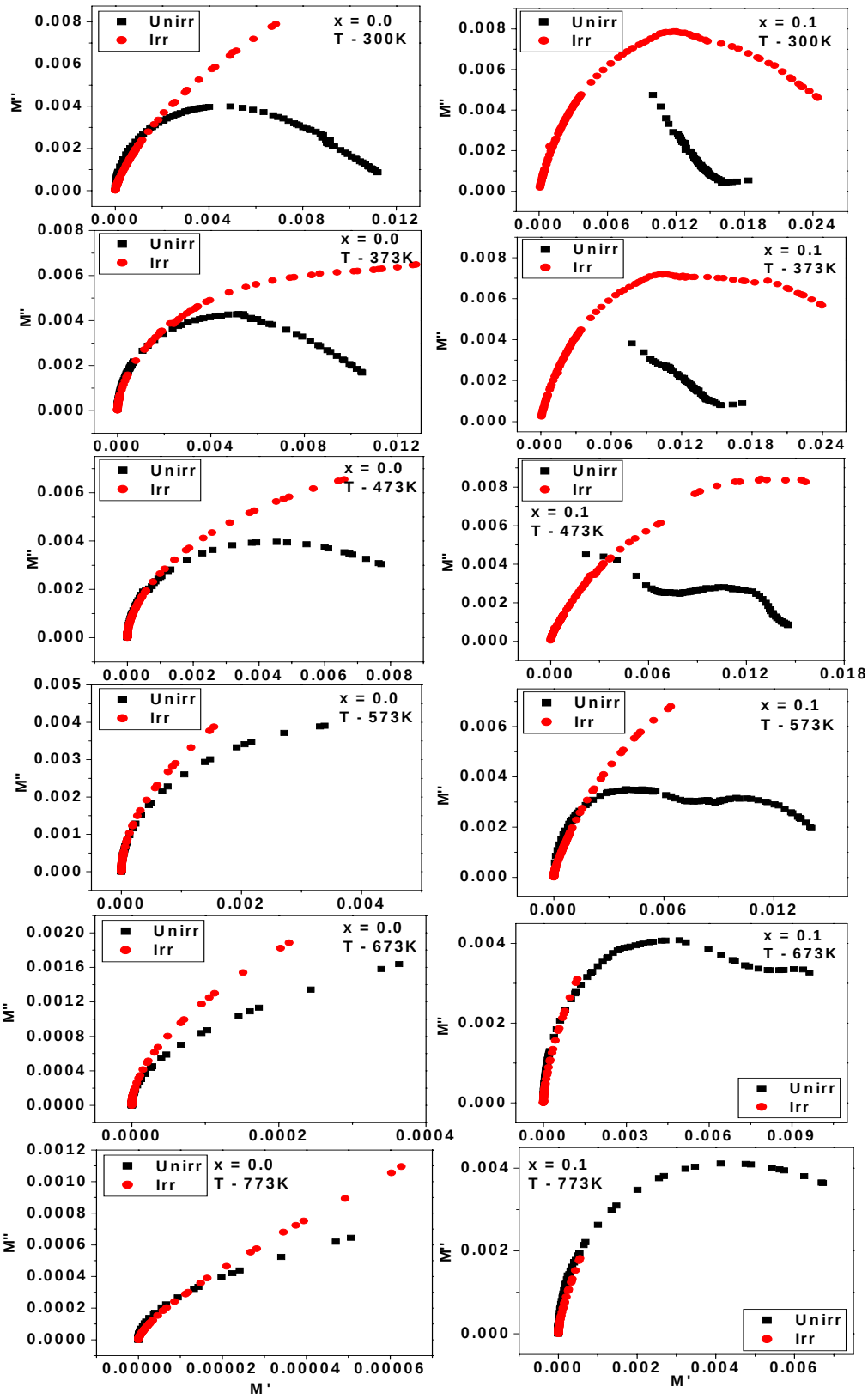

Fig. 6A.23a Real (M') versus imaginary (M'') parts of the dielectric modulus, Cole-Cole Plots of at selected temperatures for the compositions x = 0.0 and 0.1 of unirradiated and irradiated $Li_{0.5(1+x)}Ti_xAl_{0.1}Fe_{2.4-1.5x}O_4$ system

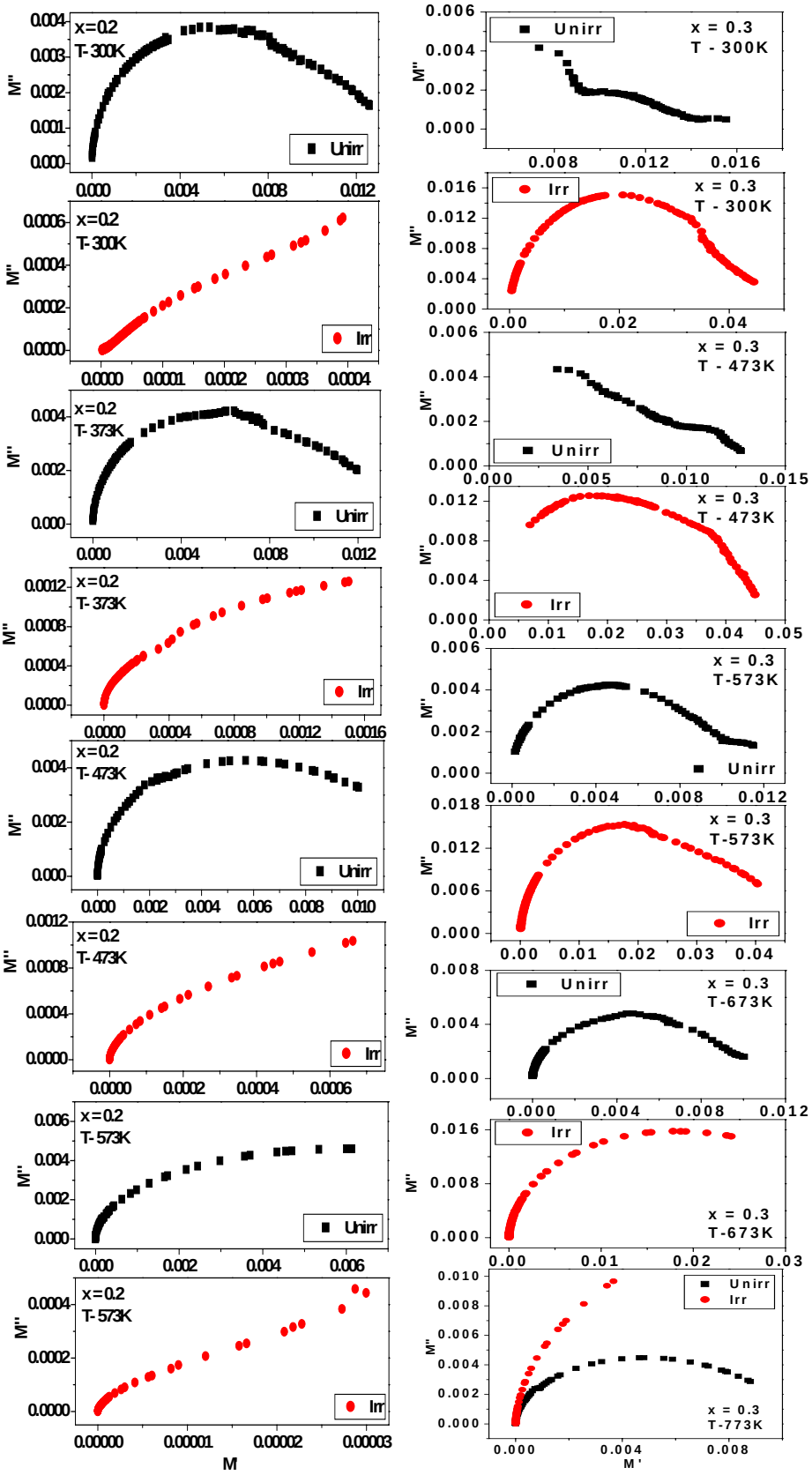

Fig. 6A.23b Real (M') versus imaginary (M'') parts of the dielectric modulus, Cole-Cole Plots of at selected temperatures for the compositions x = 0.2 and 0.3 of unirradiated and irradiated $Li_{0.5(1+x)}Ti_xAl_{0.1}Fe_{2.4-1.5x}O_4$ system

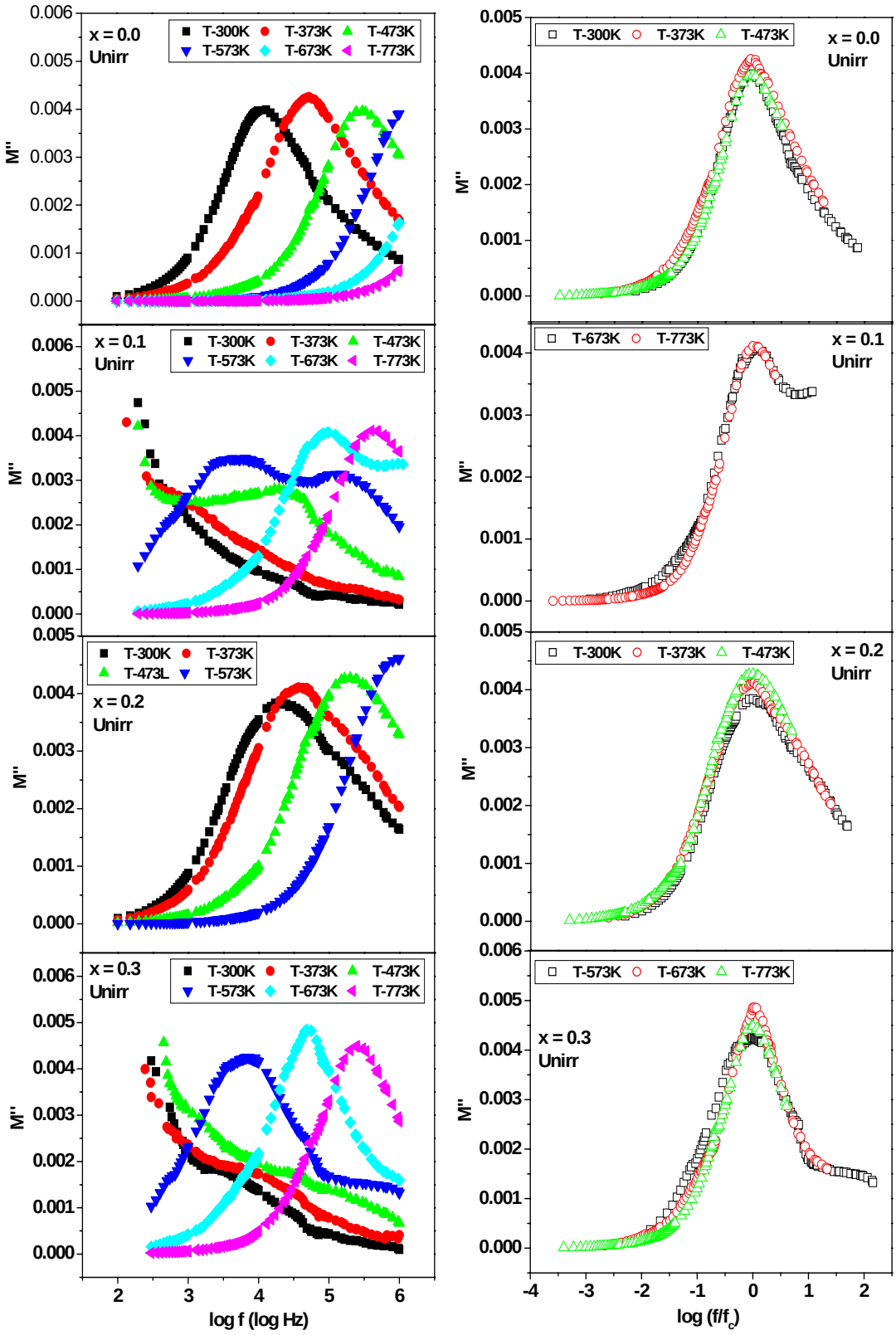

Fig. 6A.24 The variation of the imaginary part (M'') of electric modulus with frequency (f) and normalized frequency (f/f_c) (M'' master curve) at different temperatures for unirradiated samples x = 0.0, 0.1, 0.2 and 0.3 of $Li_{0.5(1+x)}Ti_xAl_{0.1}Fe_{2.4-1.5x}O_4$ system

❖ *50 MeV Li^{3+} ions irradiation of $Li_{0.5(1+x)}Ti_xCr_{0.1}Fe_{2.4-1.5x}O_4$*

6B.1 Swift Heavy Ion Irradiation effects on Structural and Magnetic properties of the system $Li_{0.5(1+x)}Ti_xCr_{0.1}Fe_{2.4-1.5x}O_4$

Commonly in magnetically diluted spinel ferrites the Fe^{3+} ions are distributed among tetrahedral (A) and octahedral (B) positions. The structural and magnetic environments of these two sites are quite different. Knowledge of cation distribution in A- and B- sites is essential in understanding the magnetic behaviour of spinel ferrites. The attraction for the 'spinel' structure undoubtedly rests on its great structural stability allowing selective dilution owing to the site preference of the cations. The introduction of diamagnetic ions is expected to weaken the magnetic coupling, which may affect the magnetic hyperfine field and Curie temperature as a function of diamagnetic substitution. Diamagnetically substituted lithium ferrite has been the subject of a large number of investigations to understand the nature of exchange interactions in spinel lattice, direction of resultant magnetization, spin canting and cation distribution. In the present work, the focus is on the study of the influence of Swift Heavy Ion irradiation (SHI) induced points/clusters of defects on the structural, magnetic, electrical and dielectric properties of the spinel ferrite system $Li_{0.5(1+x)}Ti_xCr_{0.1}Fe_{2.4-1.5x}O_4$ (x = 0.0 -0.3) by means of X-ray diffractometry, Infrared spectroscopy, magnetization , Mössbauer spectroscopy, low field AC susceptibility and dc resistivity, thermoelectric power, dielectric, impendence measurements. The samples were irradiated with 50 MeV Li^{3+} ions beam which can generate only the points/clusters of defects. The pristine compound $Li_{0.5}Fe_{2.5}O_4$ is known to have very high Curie temperature (942 K) and the magnetic properties of these compounds are sensitive to the distribution of Fe^{3+} ions in the A- and B- sites. Therefore, the magnetic properties of the unirradiated and irradiated specimens can be explained in the light of defect states and rearrangements of cations in the lattice sites.

The polycrystalline samples of the spinel system $Li_{0.5(1+x)}Ti_xCr_{0.1}Fe_{2.4-1.5x}O_4$ (x = 0.0 - 0.3, step-0.1) were prepared by double sintering ceramic technique described in chapter-2. The chemical composition and molecular weight for the samples are shown in Table 6B.1. The compositional stoichiometry of the samples was checked by energy dispersive X-ray analysis (EDAX) of some regions of the samples. The EDAX patterns for two representative samples with x = 0.1 and 0.3 are shown in Fig. 6B.1. The results confirm the expected chemical compositions for the samples and no trace of any impurity was detected.

The powder XRD patterns of unirradiated and irradiated specimens for the compositions x = 0.0, 0.1, 0.2 and 0.3 of the spinel system $Li_{0.5(1+x)}Ti_xCr_{0.1}Fe_{2.4-1.5x}O_4$ were recorded using CuKα radiations are depicted in Fig. 6B.2. The X-ray diffraction pattern showed sharp Bragg lines corresponding to face centred cubic spinel structure.

The EDAX and XRD characterizations have ascertained the compositional purity and structural monophasic nature of the specimen. The target in the form of thin layer of ferrite material having thickness of about 20 mg/cm^2 for the irradiation experiments were prepared by spreading fine powders in a aluminium ring of 1 cm diameter on a thin aluminium foil, and uniform thickness was achieved by fixing the powder using liquid GE varnish. The specimens were irradiated in vacuum with 50 MeV Li^{3+} ions with fluence of 5 x 10^{13} ions/cm^2 using 15 UD Pelletron accelerators at IUAC, New Delhi. The projected range and electronic energy loss (S_e) of 50 MeV Li^{3+} ions in these compounds calculated using the SRIM-2003 are around 231μm and 12 eV/Å, respectively. The S_e is less than the S_{eth} = 1.2 keV/ Å for columnar amorphization suggesting that the SHI-irradiation has generated points/clusters of defects [6B.1].

It is seen from XRD pattern (Fig. 6B.2) that all Bragg reflections could be indexed for the *fcc* spinel structure and the peak positions are shifted to lower angle (2θ) values in the case of irradiated samples. This indicates expansion of the unit cell. From the X-ray diffraction pattern the lattice constant 'a' for all the samples were calculated and found that the lattice constant increase continuously from 8.326 Å to 8.331Å as the concentration of Ti^{4+} was increased from 0 to 0.3. The lattice constants for unirradiated and irradiated samples are listed in Table 6B.3. The increase in a lattice parameter is attributed to the replacement of Fe^{3+} ions of radius 0.64 Å by the Ti^{4+} ions of radius 0.68 Å, causing the expansion in the unit cell dimension. It is also found that the compositional increase in the lattice parameter (a) is greater for the irradiated samples than the unirradiated ones. These observations clearly indicate that the 50 MeV Li^{3+} ions irradiation produced the compressive strain (shifting of peak position to lower 2θ values) and also generate some point/clusters of defects in the lattice structure [6B.2, 6B.3]. The lattice parameter is found to increase after SHI-irradiation (Table 6B.3) which is attributable to the rearrangement of the cations and expansion of the unit cell.

The distribution of cations in the spinel system was determined through XRD intensity analysis which commenced by taking recourse to the information provided by the literature that the Li^{1+} and Cr^{3+} ions are known to have marked preference for the B-sites [6B.4-6B.6]. Fortunately good contrast exists in the values of X-ray atomic scattering factors of Ti^{4+} and Fe^{3+} cations. The Ti^{4+} are generally known to have octahedral (B) site preference [6B.7] and inherent tendency of Ti^{4+} ions to induce short range magnetic clusters [6B.8] in ferrite with the higher magnetic dilution. Initially they were put on the B-sites in the XRD intensity calculations. However, the calculated values could not match with experimental ones for all the unirradiated and irradiated samples unless Ti^{4+} ions were allowed to occupy the A-sites also. The site occupancies of Ti^{4+} and Fe^{3+} ions were varied in a constrained manner such that the stoichiometry of the structure is maintained. The cation distributions deduced through XRD intensity analysis for the unirradiated and irradiated samples (Table 6B.2) using the computer simulation based on the Buerger's formula [6B.9] clearly indicated the redistribution of the cations in the A- and B- sites induced by SHI-irradiation. The iron distribution parameter $\delta = {Fe^{3+}}_A/{Fe^{3+}}_B$ deduced through XRD intensity analysis is given in Table 6B.3.

The values of the observed saturation moment (η_B^{obs}) and Neel's moment ($\eta_B^N = M_B - M_A$) [6B.10] (where M_A and M_B are the sublattice magnetization) are listed in Table 6B.3. The values of the Neel's moments for the present system calculated using the cation distribution deduced through XRD data analysis and the free ions magnetic moments of the cation involved. The variation of η_B as a function of x indicates the collinear type of magnetic ordering and supports the cation distribution determined through XRD analysis. The observed reduction in the η_B on increasing the Ti-content in the both cases is due to the magnetic dilution of octahedral sites. This happens because on the B-site Fe^{3+} ($5\mu_B$) is replaced by non-magnetic Ti^{4+} ($0\mu_B$) and Li^{1+} ($0\mu_B$). It is also interesting to note that the values of magneton number at absolute zero derived from the observed saturation magnetization and Brillouin function (J=5/2) for all the unirradiated samples (Table 6B.3) shows good agreement with the Nèel's moment but at the same time the saturation moment is found to be reduced for all the samples after SHI-irradiation for the irradiated samples the observed saturation moment is found to lower compared to the predicted value by the Nèel's theory. This implies that the reduction in the saturation moment after SHI-irradiation cannot be

exclusively explained by rearrangement of the cations in the interstitial sites and resultant B-site magnetic dilution.

The determination of iron distribution through Mössbauer spectroscopy will unequivocally support the cation distribution deduced through X-ray diffraction intensity analysis. The Mössbauer spectra recorded at 295K for the unirradiated and irradiated samples of the system $Li_{0.5(1+x)}Ti_xCr_{0.1}Fe_{2.4-1.5x}O_4$ (x = 0.0, 0.1 and 0.3) are displayed in Fig. 6B.3. The Mössbauer spectra were analyzed and the hyperfine interaction parameters were refined using NORMOS computer software using non-linear least squares minimization [6B.11]. The Mössbauer spectra exhibit two superimposed asymmetric Zeemann sextets one due to the Fe^{3+} ions at tetrahedral and other due to Fe^{3+} ions at octahedral (B) sites. The hyperfine interaction parameters deduced through Mössbauer spectra are given in Table 6B.4.

We note that the isomer shift for both the sites appear to show no significant variation with Ti-concentration (x) thus indicating that the s-electron charge distribution of the Fe^{3+} ions is negligibly influenced by Ti-substitution. The values of isomer shift for both the sites are well within the range of Fe^{3+} isomer shift values. The isomer shift for tetrahedral Fe^{3+} ions is found less positive than that for the octahedral Fe^{3+} ions. This difference can be attributed to the slight sp^3 covalency, which the tetrahedral ions are known to experience. It can be noticed that, there is no effect of SHI- irradiation is observed in the isomer shift. This result indicates that the s-electron charge densities are not influenced by irradiation. No observable quadropole shift in the magnetic sextets for both the sets of samples in these spinel ferrites. This means that the co-existence chemical disorder and overall cubic symmetry causes no net observable shifts in the magnetic sextets.

The nuclear hyperfine field values for the system are almost near to the pure Li-ferrite. The tetrahedral (A-site) hyperfine field shows compositional reduction for unirradiated and irradiated samples due to larger percentage B-site occupancy of diamagnetic cations. The nuclear hyperfine field for A-site is lower than that of the B-site, because the B-site Fe^{3+} ions experience a stronger average magnetic bonding with A-site Fe^{3+} ions compared to the A-site Fe^{3+} ions for which some of the bonds are with diamagnetic Ti^{4+} and Li^{1+} at B-sites. The observed little decrease in the A-site hyperfine field after SHI- irradiation is due to B-site magnetic dilution resulting from rearrangement of the cations. The iron distribution parameter $\delta = Fe^{3+}_A/Fe^{3+}_B$

derived from Mössbauer Lorentzian area ratio and X-ray diffraction intensity analysis are good agreement (Table 6B.3) Most of the hyperfine parameters not much more affected on irradiation. Only an appreciable change is seen in the line width due to the production of defects by SHI irradiation. The A-site sub spectra shows larger line width and the effect being more pronounced after irradiation which is due to more distribution values of A-site hyperfine field arising from non-magnetic Ti^{4+} and Li^{1+} neighbours of A-site Fe^{3+} ions. In the present system, the presence of magnetic ion Cr^{3+} ($3\mu_B$) in the lattice seems to play an important role in keeping the long range order intact in spite of SHI induced defected regions/rearrangement of the cations.

The plots of thermal variation of low filed (0.5 Oe) AC susceptibility are depicted in Fig. 6B.4 and the Curie temperature determined through these plots are listed in Table 6B.3. The variation of Curie temperature (T_c) with Ti content x is given in Table 6B.3 for before and after irradiation. It is evident from the Table that the value of T_c decreases with increase in Ti content x for all the samples. The decrease in T_c is because of non- magnetic substitution of Ti and the substitution of non- magnetic Ti ions reduces the active magnetic linkages per magnetic ion per formula unit, as a result T_c decreases with increase in Ti content x for all the samples. It is quite conspicuous that the Curie temperature (T_c) for the irradiated specimens is lower than their unirradiated counterparts. This confirm the cation distributions determined through XRD intensity analysis and the Mössbauer spectral intensity ratio and further supports the arguments of weakening of A-B magnetic linkages due to cumulative effect of the site magnetic dilutions, expansion of unit cell and fractional creation localized defects resulting from SHI-irradiation.

6B.2 Swift Heavy Ion Irradiation effects on Structural parameters of the system $Li_{0.5(1+x)}Ti_xCr_{0.1}Fe_{2.4-1.5x}O_4$

The density of the ferrite materials is an important parameter from application point of view. Density gives the idea how good was the sintering of the material as it is known that sintering temperature affects the density of the material. There are many reports in the literature on the effect of non-magnetic and magnetic cation substitution on various structural parameters like lattice constant, X-ray density, porosity, site ionic radii, oxygen positional parameter, bond length etc. of lithium ferrites [6B.12-6B.15]. The aim of the present of the work, to study the effect of irradiation on the structural parameter like lattice constant, X-ray density, porosity, site ionic radii,

oxygen positional parameter, bond length etc. of lithium ferrite with the generic formula $Li_{0.5(1+x)}Ti_xCr_{0.1}Fe_{2.4-1.5x}O_4$ (x = 0.0, 0.1, 0.2 and 0.3).

The variation of bulk density (d) as well as the X-ray density (d_x) with chemical composition (x) for unirradiated and irradiated samples of each composition is summarized in Table 6B.5. The bulk density (d) of each specimen was calculated from the precise values of weight and volume of the specimen in the pellet form. The X-ray density (d_x) for each composition was calculated from the molecular weight and the lattice parameter (a) using the relation suggested in the literature [6B.16].

It can be seen from Table 6B.5 that, bulk density (d) and X-ray density (d_x) decreases with increase in Ti content x for unirradiated as well as irradiated samples. This can be ascribed to the atomic weight of Ti^{4+} (47.88) which is lower than those of Fe^{3+} (55.847) and also molecular weight decreases as well as the lattice constant 'a' increases with the increase in the concentration, which thereby increases the volume. This leads to the decrease in the density of the material with the substitution. Further, on irradiation it is evident from table that the X-ray density decreases as compared to unirradiated samples, which is due to the expansion of the unit cell dimensions after irradiation which thereby increases the lattice constant (Table 6B..3). According to the X-ray density calculations the density of the material is directly proportional to the molecular weight and inversely proportional to the third power of the lattice constant 'a' of the material. This leads to the decrease in the X-ray density of the material after irradiation. It is also observed that the bulk density of irradiated samples increase from that of the unirradiated samples, which may be due to shrinkage of the intergranular pores during irradiation. Porosity P of the samples which indicates the presence of minute pores and channels within the samples were calculated from the values of bulk density (d) and X-ray density (d_x) using the standard relation

$P = (1 - d/dx)$

The change of porosity (P) with Ti concentration of unirradiated and irradiated sample for all the compositions are given in Table 6B.5. The addition of Ti increases the porosity of unirradiated and irradiated samples. The increase of porosity may be due to the presence of Ti that hinders the migration of the pore to the grain boundaries and results in high porosity materials. The decrease of porosity after irradiation in the material can be ascribed to the reduction of the intergranular pores during irradiation.

The oxygen positional parameter or anion parameter (u) for each composition of unirradiated and irradiated samples was calculated using the formula [6B.17].

$$u^{3m} = \frac{\frac{1}{4}R^2 - \frac{2}{3} + \left[\frac{11}{48}R^2 - \frac{1}{18}\right]^{\frac{1}{2}}}{2R^2 - 2}$$

where R = B-O/A-O. The bond length B-O and A-O are average bond lengths, based on the cation distribution listed in Table 6B.2; B-O = $\langle r_B + r(O^{-2})\rangle$ and A-O = $\langle r_A + r(O^{-2})\rangle$, where $r(O^{-2})$ is the radius of the oxygen ion and the value of the mean ionic radius per formula of the tetrahedral (r_A) and octahedral (r_B) sites was determined using the cation distribution for the each composition of unirradiated and irradiated samples, from the relation [6B.17, 6B.18]

$$r_A = [C_{AFe}r(Fe^{3+}) + C_{ATi}r(Ti^{4+})]$$

$$r_B = 1/2[C_{BLi}r(Li^{1+}) + C_{BTi}r(Ti^{4+}) + C_{BCr}r(Cr^{3+}) + C_{BFe}r(Fe^{3+})]$$

where $r(Li^{1+})$, $r(Ti^{4+})$, $r(Cr^{3+})$, $r(Fe^{3+})$ are the ionic radii of Li^{1+}, Ti^{4+}, Cr^{3+} and Fe^{3+} ions respectively, while C_{AFe}, C_{ATi} are the concentrations of Fe^{3+} and Ti^{4+} ions on A-sites and C_{BLi}, C_{BTi}, C_{BCr} and C_{BFe} are the concentrations of Li^{1+}, Ti^{4+}, Cr^{3+} and Fe^{3+} ions on B-sites.

Using these formulae, the values of mean tetrahedral (r_A) and octahedral ionic radii (r_B) as well as oxygen positional parameter or anion parameter (u) for each composition of unirradiated and irradiated specimen have been calculated, and they are listed in Table 6B.6. It can be seen that the mean tetrahedral ionic radius and octahedral ionic radius increase continuously with increasing Ti concentration (x) for unirradiated and irradiated samples. The increase in r_A and r_B suggest the replacement of smaller cation Fe^{3+} (0.64 Å) by larger cation Ti^{4+} (0.68 Å) on the A and B-sites, which is revealed in an increase in lattice constant 'a' with x. It is observed that the after irradiation the mean tetrahedral ionic radius (r_A) slightly decrease and the mean octahedral ionic radius (r_B) slightly increase as compared to unirradiated specimen, which can be ascribed to rearrangement of cations and a slight migration of large cation Ti in B-site and small cation Fe in A- site during irradiation process. As such, it can be concluded that in the present system octahedral site substitution plays a dominant role in influencing the value of the lattice constant and which is reflected in an increase in lattice constant 'a' after irradiation (Table 6B.3).

The oxygen positional parameter 'u' is found to be around 0.26. The larger value of 'u' than its ideal value 0.25, indicate anion movements away from the tetrahedrally coordinated A-sites cations along the body diagonals of the cube, which

in term increases the volume of each A-site while the octahedral B-site shrinks. For spinel compounds, the anion sublattice expands or reduces by varying 'u', until the A- and B- site volumes match the radii of the constituent cations. The variation of 'u' as a function of the substitutions factor x is indicated in Table 6B.6 for before and after irradiation. The slightly decrease of 'u' may be due to increasing the content of Ti ions and decreasing the smaller ion Fe^{3+} ions in the A and B-sites but there is no systematic variation observed in oxygen positional parameter with substation Ti ion and no change observed after irradiation in oxygen positional parameters as compared to unirradiated samples.

It is known that there is a correlation between the ionic radius and the lattice constant. The lattice constant can be calculated theoretically for unirradiated and irradiated specimen by the relation suggested by Mazen et al [6B.19]

$$a_{th} = \frac{8}{3\sqrt{3}}\left[\left(r_A + R_o\right) + \sqrt{3}\left(r_B + R_o\right)\right]$$

where R_o is the radius of the oxygen ions (1.32 Å). The agreement between a_{th} and a_{exp} obtained from X-ray data indirectly supports the cation distribution deduced from X-ray intensity calculations. The theoretical values of the lattice constant (a_{th}) as a function of concentration (x) are shown in Table 6B.5. The obtained values of a_{th} are somewhat smaller that those of a_{exp}, which confirms the estimated cation distribution (Table 6B.2). The difference observed in a_{th} and a_{exp} which may be the possibility of the effects like "covalency", which could not be considered in the theoretical model.

The X-ray diffraction data was further used to calculate the tetrahedral and octahedral site radii (R_A and R_B). The site radii, R_A and R_B for unirradiated and irradiated samples were calculated using the relations [6B.20]

$$R_A = a\sqrt{3}\left(\delta + 1/8\right)$$

$$R_B = a\left(3\delta^2 + 1/16 - \delta/2\right)^{1/2}$$

where $\delta = u_{system} - u_{ideal}$

u_{system} = oxygen positional parameter of system

u_{ideal} = ideal oxygen parameter = 0.250 Å

The values of site radii (R_A and R_B) for unirradiated and irradiated specimen calculated from above equations are given in Table 6B.6. It can be seen that the tetrahedral site radii (R_A) decrease and octahedral site radii (R_B) increase linearly with increasing Ti- content (x) for unirradiated as well as irradiated specimen, which can

be attributed to the fact that the lattice parameter increases linearly with x (Table 6B.3). Similar result has been reported for substituted lithium ferrites [6B.21]. The site radius R_B is greater than R_A. After irradiation octahedral site radii (R_B) increase as compared to unirradiated ones, which may be due to the expansion of unit cell volume in irradiated samples.

The various possible configurations of ion pairs in spinel ferrites with favourable distances and angles for an effective magnetic interactions as envisaged by Gorter [6B.22]. The inter ionic distances between the cations (b, c, d, e and f) (Me-Me) and between the cation and anion (p, q, r and s) (Me-O) were calculated for unirradiated and irradiated samples using the experimental values of lattice constant and oxygen positional parameter 'u' (Table 6B.6) by the relations [6B.23].

From the Table 6B.7, it is seen that the inter-ionic distances between cation – anion (Me-O), the distance 'p' increases and the distances q , r and s decrease with increasing Ti-concentration (x) up to x = 0.2 and at higher concentration x = 0.3 the distance 'p' is slight decreases and 'q , r , s' slight increase as compare to lower concentration for unirradiated specimens. After irradiation, there is no systematic variation with the Ti- concentration but in general same behaviour of the unirradiated samples like the distance 'p' increases and 'q, r, s' decrease with increasing concentration (x). The decrease in Me-O distances should results in enhancement of strength of magnetic interactions. It is also observed that the inter-ionic distances between cations (Me – Me) b, c, d, e and f, increase with increasing Ti-content (x) in the unirradiated and irradiated samples. This may be due to the replacement of magnetic Fe^{3+} by non-magnetic Ti^{4+} reduces the strength of magnetic interactions. It can be experiential the inter-ionic distances between cation-anion and between cations for the irradiated samples is increased in general from that of unirradiated samples. This increase in Me-O and Me-Me after irradiation can be explained on the basis of rearrangement of cations or generation of defects by irradiation may be lead to the weakening of the strength of inter-atomic bonding in the system.

The bond angles (θ_1, θ_2, θ_3, θ_4 and θ_5) [6B.24] are calculated by simple trigonometry principle using the values of inter-ionic distances and summarized in the Table 6B.7. It is seen from the Table 6B.7 the general trend of the bond angles θ_1, θ_2 and θ_5 increases while θ_3 and θ_4 decreases with increase in Ti-content (x) as compare to low concentration x = 0.0 for unirradiated and irradiated samples. The increase in

angles θ_1, θ_2 and θ_5, which are related with A-B and A-A interaction, may not have effect on strength of inter atomic bonding and the observed decrease in θ_3 and θ_4 angles suggest strengthening of B-B interactions. There is no systematic variation in bond angles for all the compositions after irradiation as compared to unirradiated samples. For irradiated samples the bond angles θ_1, θ_2 and θ_5 are decreased for the concentration x = 0.0, 0.2 and increased for x = 0.1, 0.3 while θ_3 and θ_4 are increased for the concentration x = 0.0, 0.2 and decreased for x = 0.1, 0.3 from that of the unirradiated samples. This may be due to change observed in the inter-ionic distances after irradiation. This suggest that the after irradiation decrease in angles θ_1, θ_2 and θ_5 strengthen of A-B and A-A interaction in case of x = 0.0 and 0.2 while θ_3 and θ_4 which is related with B-B interactions, may not have effect on strength of inter-atomic bonding for x = 0.0 and 0.2 but contrast behaviour observed for the concentration of x = 0.1 and 0.3.

6B.3 Swift Heavy Ion Irradiation effects on Infrared Spectra of the system $Li_{0.5(1+x)}Ti_xCr_{0.1}Fe_{2.4-1.5x}O_4$

The study of far infrared spectrum is an important tool to get information about the positions of the ions in the crystal through crystal's vibrational modes [6B.25]. It is also used to determine the local symmetry in crystalline solids, non-crystalline solids, ordering phenomenon in spinels, presence/absence of Fe^{2+} ions and also to determine force constant and elastic moduli [6B.26- 6B.29] of ferrite systems. It is known that the normal and inverse cubic spinel ferrites have four IR bands representing the four fundamentals (ν_1, ν_2, ν_3, ν_4) [6B.28]. It has been reported that, the first three IR fundamental bands are due to tetrahedral and octahedral complexes, while the fourth one is due to the lattice vibrations [6B.25].

The room temperature IR spectra for all the investigated compositions of unirradiated and irradiated ferrite system $Li_{0.5(1+x)}Ti_xCr_{0.1}Fe_{2.4-1.5x}O_4$ are obtained from the BRUKER IFS 66V FT-IR Spectrometer in the KBr medium. The typical spectra for the compositions x = 0.0, 0.1 and 0.3 are depicted in Fig. 6B.5a-5c, respectively and the absorption bands are listed in Table 6B.8. The infrared spectra of all the compositions are recorded in the wave number range of 400 – 800 cm^{-1}.

The IR absorption bands of solids in the range 100-1000 cm^{-1} are usually assigned to vibration of ions in the crystal lattice [6B.30]. According to Waldron [6B.27], the ferrites can be considered continuously bonded crystals, meaning that the

atoms are bonded to all nearest neighbours by equivalent forces (ionic, covalent and Van der Waals).The frequency distribution of vibrations is given by a Debye treatment of classical mechanical problem. In the ferrites metal ions are situated in two different sub-lattices designated tetrahedral (A-site) and octahedral (B-site) according to geometrical configuration of the oxygen nearest neighbours. Waldron [6B.27] and Hafner [6B.31] have attributed the band around 600 cm^{-1} to stretching vibrations of the tetrahedral group (ν_1) and that around 400 cm^{-1} to the octahedral group (ν_2).

On inspection of figure, it is found that the spectra consist of two significant absorption bands, the high frequency band ν_1 which is in the range 501-589 cm^{-1} is assigned to intrinsic vibrations of the tetrahedral group and the lower frequency band ν_2 which is in the range 405-489 cm^{-1} is assigned to the intrinsic vibrations of the octahedral cations. In the present system, the IR spectrum of pure Li-Cr ferrite (x = 0.0) indicates new two bands at 710.7 and 675.0 around the first primary band ν_1 and particular this band is disappeared as increase the Ti-content (x) for unirradiated specimen. Similar result has been observed in the IR spectrum of pure Li-ferrite by Mazen et al [6B.32]. It is also observed that the high frequency band ν_1 and lower frequency band ν_2 has a structure consisting subsidiary bands or shoulders, which should be characterized by different splitting bands in the composition x = 0.0 and 0.1, while on increasing the Ti-concentration (x) up to 0.3 the subsidiary, bands or shoulders are disappeared or merged in the main absorption bands for the unirradiated samples. Unirradiated samples x = 0.2 and 0.3 exhibited only two bands ν_1 and ν_2. The band ν_1 is the characteristic of the tetrahedral A-sites and is attributed to complexes of Fe^{3+} - O^{2-} on the A-sites. The band ν_2 is the characteristic of octahedral B-sites and is attributed to complexes of Fe^{3+} - O^{2-}, Cr^{3+}- O^{2-} and L^{1+}- O^{2-} on the B-sites in the present system.

It is seen that no systematic variation is observed in the main principle bands but slightly shifting in the band positions with Ti^{4+} concentration for unirradiated and irradiated samples. It is observed that the centre frequency bands shifting to the higher frequency side with the increasing the Ti-concentration for the unirradiated and irradiated samples are attributed to increase in the unit cell dimension (Table 6B.3) and substitution of cation Ti for the Fe in the system. This may be due to the difference in the micro structure of different ferrites. It is known that decrease in site

radius enhance the fundamental frequency and therefore the centre frequency should shift towards higher frequency side. In present case, the centre frequency bands shifting towards higher frequency side may be due to the decrease in tetrahedral site radius.

It is important to note that on increasing Ti-content (x) in the system, the intensity of all bands and their shoulders decrease whereas bands become broader (Fig. 6B.5a-5c). The sample with x = 0.3 exhibits more broader bands than others. The broadening of bands has been reported earlier by many workers [6B.33, 6B.34]. They have reported that such broadening is commonly observed in normal spinel ferrites and have attributed it to the statistical distribution of Fe^{3+} ions on A- site and B-sites. The decrease in intensity and increase in broadness are explained on the basis of cation distribution of Li-Ti-Cr ferrites (Table 6B.2). In the present case as the content of Ti increases, Ti^{4+} ion consistently replace Fe^{3+} ions from A- and B- sites. At the same time, Li^{1+} ions on octahedral site increase by 0.5(1+x). This disturbs the 1: 3 orders on the octahedral site with increase in Ti-content (x). This gives rise to type of chemical disorder on tetrahedral and octahedral site, i.e., the statistical distribution of Fe^{3+} ions in A- and B-sites. The disordered systems give rise to broad bands in the IR spectrum. Thus, it can be concluded that increase in Ti-ions leads to more disordered state.

The close appraisal of IR spectra revealed the shoulders or splitting of the main absorption bands for the unirradiated samples with x = 0.0 and 0.2 and is ascribed to the Fe^{2+} ion induced Jahn-Teller distortion in the lattice due to non-cubic component of the crystal field potential, unlike Fe^{3+} ions which do not produce any such Jahn-Teller effect [6B.35, 6B.36]. The IR spectrum of pure Li ferrite indicates the presence of splitting in the absorption bands. This spectrum has been studied in detail by Mazen et al [6B.32].

The effect of irradiation on the infrared spectra for three typical compositions x = 0.0, 0.1 and 0.3 of the system is also clarified in Fig. 6B.5a-5c. From the figure, it is noticed that after irradiation the shoulders or splitting increase of the main absorption bands ν_1 and ν_2 for all the samples and also subsidiary band ν^* for sample x = 0.0. It is also important to note that around main absorption band (ν_1) new subsidiary band (ν^*) come into sight with the shoulders or splitting in the range of 601 – 670 cm^{-1} with the compositions x = 0.1, 0.2, and 0.3. It is clear from the Table

6B.8 as well as Fig. 6B.5a-5c that the trend of the main absorption band position shows a shifting towards higher frequency but the centre frequency bands shifting towards lower frequency side after irradiation as compared to unirradiated ones.

The effect of irradiation on the investigated samples gives rise to the production of lattice defects that result in the displacement of atom from their equilibrium positions. Moreover, lattice vacancies generated after irradiation contribute to the structural deformation. Our X-ray studies on the samples reveal that the lattice parameter increases indicating a small distortion of the spinel cubic structure after SHI-irradiation. This lattice defects may leads to the disorder due to the rearrangement of cations as well as destruction of metal-oxygen and metal-metal bonds and generation of new bonds. The observed shifting of centre frequency bands towards lower frequency side after irradiation, which is attributed to the expansion of unit cell dimensions (Table 6B.3). The growing subsidiary band (ν^*) with shoulders which may be assigned to the destruction of the Fe^{3+}- O^{-2}- Fe^{3+} bonds and the corresponding generation of the Fe^{2-} - O^{2-} complexes at the tetrahedral site cause the Ti^{4+} ion migrating to octahedral side under the irradiation. Furthermore, the raise in splitting of the main absorption band ν_1 which is due to the vibration of Fe^{2+}-O^{2-} complexes at the A-sites by the rapid formation of Fe^{2+} and the raise in splitting of the main absorption bands ν_2 may be due to the vibration of Fe^{2+}-O^{2-}, Cr^{4+}-O^{2-} complexes by the generation of Fe^{2+}, Cr^{4+} at the B-sites under the irradiation, which result from the hopping process $Cr^{3+} + Fe^{3+} \leftrightarrow Cr^{4+} + Fe^{2+}$ at the B-site. The presence of Fe^{2+} ions in ferrites can produce splitting of IR absorption bands. This may be because of the local lattice deformation occurs due to the Jahn-Teller effect in Fe^{2+}, which can lead to a non- cubic component in the crystal field potential and to the splitting of the bands.

6B.4 Swift Heavy Ion Irradiation effects on Elastic properties of the system $Li_{0.5(1+x)}Ti_xCr_{0.1}Fe_{2.4-1.5x}O_4$

As discussed earlier, X-ray analysis and IR spectra further used to calculate elastic moduli. In continuation of the present work, the elastic properties of the unirradiated and irradiated spinel ferrite system $Li_{0.5(1+x)}Ti_xCr_{0.1}Fe_{2.4-1.5x}O_4$ with x = 0.0, 0.1, 0.2 and 0.3 are reported and the effect of the cation redistribution, points/clusters of defects on the elastic properties are then discussed. As mentioned earlier, a new method developed by Modi et al [6B.26, 6B.37] to study the elastic

properties of spinel ferrite and garnets systems by infrared spectroscopy. The IR spectral analysis (Table 6B.8) is used to obtain band positions in order to calculate force constant for unirradiated and irradiated samples. Further more, the values of lattice parameter, X-ray density and pore fraction through X-ray diffraction analysis are also used to determine elastic constants of uncorrected and corrected to zero porosity. In this technique, one requires detailed knowledge of cation distribution among available tetrahedral (A-) and octahedral (B-) sites. The details of formula and calculations of force constant, elastic wave velocity and elastic moduli, have been discussed already in the Chapter -6, section- A.

As mentioned earlier, the force constant is a second derivative of potential energy with respect to the site radius, the other independent parameter kept constant. The force constant for tetrahedral and octahedral sites, k_t and k_o respectively were calculated using the standard procedure and formula suggested in the literature [6B. 27]. The compositional dependence, the force constants k_t, k_o and average force constant (k) are listed in Table 6B.9 for unirradiated and irradiated samples. It is seen that the force constant (k) increases with increasing Ti-concentration for unirradiated and irradiated samples, which suggests strengthening of inter-atomic bonding. It is observed that the force constant (k) is decreased after irradiation as compared to unirradiated samples; this can be ascribed to increase in site radii after irradiation. Normally, increase in the site radii leads to the decrease in force constant.

The value of the compressional or longitudinal elastic wave velocity (υ_l) and shear or transverse elastic wave velocity (υ_s) have calculated using the formula suggested by Waldron [6B.27] for different compositions of unirradiated and irradiated Li-Ti-Cr ferrites are given in Table 6B.10. The value of υ_l and υ_s were further used to calculate mean elastic wave velocity (υ_m) is summarized in Table 6B.10. The values of υ_l, υ_s and υ_m increase with increasing Li-Ti content (x) for all the compositions of unirradiated and irradiated samples. The increase in the value of υ_l, υ_s and υ_m can be explained on the basis of the density material. As we have mentioned earlier, the density of the present material is decreased with increasing Li-Ti concentration of unirradiated and irradiated. If there is any distortion of materials from its equilibrium shape the average separation of the atoms within the materials is no longer optimal. Some atoms will be too close to their neighbours, and some too far apart. In either case there will be a restoring force which will act to return the atoms to

their equilibrium separation. The dynamics of the sound wave will be affected by the way the material responds to the restoring force. The two factors most critical in the determining this response is the restoring force per unit displacement (the natural 'springiness' of the substance, and the density of the material. If the density of material is high, i.e. if the mass per unit volume is high, then by the Newton's second law the acceleration due to a given restoring force will be low then it will return to its equilibrium positions only slowly, and the wave disturbance will propagate only slowly [6B.38]. In present case the density of material is decreased with increasing Li-Ti content (x), means the mass per unit volume is low and the acceleration due to a given restoring will be high then it will return to its equilibrium position only quickly and the wave disturbance will propagate only fast. So, the υ_l, υ_s, and υ_m increase with increasing Li-Ti content (x) in the present material. After irradiation, υ_l, υ_s and υ_m is decreased from that of unirradiated samples and that may be due to the density (mass per unit volume) of the material is increased accordingly observed change in elastic wave velocity after irradiation.

In general, the restoring force on a small region of a solid depends on the type of distortion (strain) that has taken place. The parameters that describe the restoring force per unit strain are known as the elastic moduli [6B.38]. The values of elastic moduli like Bulk modulus (B), Young's modulus (E), Rigidity modulus (G) and Poisson's ratio (σ) for different compositions of unirradiated and irradiated Li-Ti-Cr ferrites are given in Table 6B.11. Since ferrites under investigation are porous ($f \approx 0.06$-0.26), the elastic moduli have been corrected to zero porosity using Hosselman and Fulrath's formulae [6B.39]. The corrected values of Bulk modulus (B_0), Young's modulus (E_0), Rigidity modulus (G_0) and Poisson's ratio (σ_0) for different compositions of unirradiated and irradiated Li-Ti-Cr ferrites are given in Table 6B.12. It can be seen from Table 6B.11 that the values of B, E and G of the mixed Li-Ti-Cr ferrites are found to increase with increasing Titanium content (x) for all the unirradiated and irradiated samples, indicates that the corresponding deformation of the solid is difficult and that the solid has a strong tendency to spring (analogous to planes within a solid held together by atomic bond) back to its equilibrium position [6B.40]. The values of B_0, E_0 and G_0 show regular variation similar to that of B, E and G for before and after irradiation. The Poisson's ratio (σ), however remain constant for different composition but the corrected value of Poisson's ratio (σ_0) is found to

increase with increasing Ti-content (x) for unirradiated and irradiated samples. The value to of σ is found to be constant 0.35 and the value of σ_0 lies in the range 0.38-0.46, which is in conformity with the theory of isotropic elasticity. After irradiation it is found that the value of B. E, G and B_0, E_0, G_0, σ_0 are decreased from that of the unirradiated samples. The strain/stress developed in materials due to the creation of defects may be responsible for the modification in their elastic properties after irradiation or on other hand, the disordering in the A and B cation sites, the expansion of the lattice structure (deformation in the lattice structure) of the material may create corresponding structural elastic dipole field and found changes in the elastic properties of the material after irradiation.

The Debye temperature (θ_D) values of all the ferrites have been calculated using the Anderson's formula [6B.41]. The value of Debye temperature (θ_D) for each composition for before and after irradiation is presented in Table 6B.10. It is seen that the Debye temperature (θ_D) increases with increasing Ti-content (x) before and after irradiation. The Debye temperature is the temperature at which maximum lattice vibrations take place. The observed increase in θ_D with content (x) suggested that the lattice vibrations are hindered due to Ti substitution in the material. After irradiation it is decreased from that of the unirradiated samples, indicates that the change the maximum lattice vibration taking place in the sample due to the modification of the strength of the inter-atomic bonding under irradiation and accordingly Debye temperature modified after irradiation.

6B.5 Swift Heavy Ion Irradiation effects on Electrical properties of the system $Li_{0.5(1+x)}Ti_xCr_{0.1}Fe_{2.4-1.5x}O_4$

Compositional variation of dc resistivity ($\log_{10}\rho$) at room temperature of unirradiated and irradiated ferrite system $Li_{0.5(1+x)}Ti_xCr_{0.1}Fe_{2.4-1.5x}O_4$ (x = 0.0, 0.1, 0.2 and 0.3) are given in Table 6B.13. The resistivity has been observed to increase with increase titanium concentration for the unirradiated and irradiated samples, except those with x = 0.2 concentration for the unirradiated specimen.

The ferrites which are affected by substituting can be classified in two different types: excess or oxidation type and deficit or reduction type. For excess type, the resistivity decreases with the addition of higher-valent cations, and increase with addition of lower-valent cations. The inverse relationship occurs in the deficit type, in which resistivity decreases with addition of lower-valent cations and increases with

the higher-valent cations [6B.42]. It can be seen that Li-Ti-Cr ferrites (x = 0.0, 0.1 and 0.3) belong to the deficit type of ferrites, except with x = 0.2 belong to oxidation type of ferrite.

In the present system Fe^{3+} ion are replaced by Ti^{4+}. A tetravalent on is able to form stable electronic bonds with Fe^{2+} ions. Since Ti in is tetravalent it localizes Fe^{2+} ions which are formed during the sintering process. The localization phenomenon hinders the Verwey mechanism $Fe^{3+} \Leftrightarrow Fe^{2+}$, which results in increasing resistivity. Since trivalent valent chromium (Cr^{3+}) ions have a tendency to occupy octahedral sites. The presence of small amount of Cr^{3+} in the present system may be formed number of Fe^{2+} and Cr^{4+} bonds at an octahedral site, which are more stable and has lower energy than the Fe^{2+} ion hence there is an increase in the resistivity. Moreover, Ti^{4+} ions can also act as scattering centres at B-sites [6B.43], obstructing the degree of easy conduction between $Fe^{3+} \Leftrightarrow Fe^{2+}$, $Fe^{3+} \Leftrightarrow Fe^{4+}$ and $Cr^{3+} \Leftrightarrow Cr^{4+}$ions. Therefore, the dc resistivity is found to increase with Li -Ti content. On the other hand, the dc resistivity in general increases with increase in Ti^{4+}- Li^{1+}content (x). This happens because the replacement of Fe^{3+} by Ti^{4+} and Li^{1+} in present system reduces conduction through the octahedral sites. The incorporation of Ti-Li ions which do not participate in the conduction process, limits the degree of $Fe^{3+} + Fe^{3+} \Leftrightarrow Fe^{4+} + Fe^{2+}$ and $Fe^{3+} + Cr^{3+} \Leftrightarrow Cr^{4+} + Fe^{2+}$ conduction that occurs. Thus the efficient method of limiting the conduction process is the replacement of the effective ions (Fe^{3+}) by less effective ones (Ti^{4+} and Li^{1+}). Also, due to the large ionic size of Ti and Li as compared to Fe and Cr, its addition distorts the ferrite lattice and these distortions can affect the motion of charge carrier causing the resistivity of ferrite increase [6B.42]. Further, the ability of Ti^{4+} ions to form locking pairs of Ti^{4+}-Fe^{2+} also contribute to enhance the resistivity. The enormous decrease of dc resistivity of the concentration x = 0.2 for unirradiated sample is attributed to the valence fluctuations of Jahn-Teller ion Cr^{3+} as Cr^{3+} and Cr^{4+} during sintering.

The effect of irradiation on the dc resistivity (at room temperature) of the ferrite samples has been well studied using 50 MeV Li-beam with the fluence of 5×10^{13} ions/cm^2. The results obtained show (Table 6B.13) that the dc resistivity values of irradiated ferrite for the concentration of x = 0.0, 0.1 and 0.3, are less and x = 0.2 is more than the values of the corresponding unirradiated ones. The observed decrease in dc resistivity after irradiation may be result of electronic rearrangements

occur, leading to formation of voids and clusters which help the conduction process and decrease the resistivity of the samples during irradiation. For further concentration of x = 0.2, formation of void and clusters which impede the conduction process and increase the resistivity of the sample. On other hands, the observed reduction in the dc resistivity after irradiation is may be attributed to the increase in the Fe^{3+}/Fe^{2+}, Fe^{3+}/Fe^{4+} and Cr^{3+}/Cr^{4+} ratio on octahedral sites by the irradiation process. This causes an enhance in the rate of electrons or holes exchange between $Fe^{3+} \Leftrightarrow Fe^{2+}$, $Fe^{3+} \Leftrightarrow Fe^{4+}$ and $Cr^{3+} \Leftrightarrow Cr^{4+}$ by the hopping mechanism, which also causes a decrease in the resistivity.

The hopping length or jump length (L) between magnetic ions (the distance between ions) in the tetrahedral A-sites is given $L_A = a\sqrt{3}/4$ and in the octahedral B-sites by $L_B = a\sqrt{2}/4$ [6B.44-6B.46], where 'a' is the lattice parameter (Table 6B.3). The variation of jump length (L) as a function of Ti-content (x) for unirradiated and irradiated Li-Cr ferrite is summarized in Table 6B.14, which shows the dependence of L_A and L_B on the additions of Ti^{4+} and Li^{1+} and they behave similar to the lattice parameter 'a'. Their increase with x is due to increasing the distance between the magnetic ions by the substitution of larger cations Ti^{4+} and Li^{1+} for Fe^{3+} at the A- and B-sites.

We have correlated the jump length (L) of the charge carriers between Fe^{3+} and Fe^{4+} (for p-type conduction) on the octahedral site to the electrical resistivity. For before and after irradiation, the observed increase in jump length (L) with x suggest that charge carriers require more energy to jump from one cationic site to other, which causes an increase in resistivity with increasing x. This is expected, because the replacement of magnetic Fe^{3+} ions by non-magnetic Ti^{4+} and Li^{1+} ions, which do not participate in the conduction process, reduces conduction through the octahedral site; as a result an increase in resistivity value with increasing Ti content may be expected. It is also observed that after irradiation jump length (L) increases as compared to unirradiated samples is attributed to unit cell volume expansion due to formation of void and clusters during irradiation. The increase in jump length (L), enhances the dc resistivity because charge carriers require more energy to jump from one cationic site to other but in present case we have observed defying results. The dc resistivity decreases after irradiation as compared to unirradiated samples except for x = 0.2 concentration. Now this anomaly can be explained on the basis of electronic

rearrangement of cations in the spinel, which increases the rate of electrons and hole exchange between $Fe^{3+} \Leftrightarrow Fe^{2+}$, $Fe^{3+} \Leftrightarrow Fe^{4+}$ and $Cr^{3+} \Leftrightarrow Cr^{4+}$ by the hopping mechanism, that result in decrease in dc resistivity after irradiation.

Ferrites are semiconductors and their resistivity decreases with increasing temperature according to the Arrhenius relation

$$\rho = \rho_0 \exp (\Delta E / kT)$$

where ΔE is the activation energy and k is the Boltzmann constant, ρ is the resistivity at absolute temperature T, and ρ_0 represents the resistivity at 0 K [6B.47]. The temperature variation of resistivity, for both unirradiated and irradiated series, was studied at temperatures ranging from 300 to 1000 K. Temperature variation of dc resistivity has been studied starting from the room temperature to the temperature higher than Curie temperature for before and after irradiation. The plots between $\log_{10}\rho_{dc}$ and $10^3/T$ for the unirradiated and irradiated series are shown in Fig. 6B.6. The dc resistivity is observed to decrease exponentially with raising temperature, exhibit semiconductor behaviour in all the unirradiated and irradiated samples. This may be due to the increase in mobility of the charge carriers with increasing temperature. From the plots represented in this figure three different regions and two breaks with changing slopes have been observed. The change in slope generally occurs at different temperature range approaching to change in the conduction mechanism as discussed earlier. The second break occurs in the neighbourhood to the Curie temperature and this has been attributed to the influence of magnetic ordering over the conduction mechanism.

The irradiated ferrites showed the same behaviour as those of unirradiated ones. It is shown that the value of resistivity of the sample x = 0.0 is slightly higher in the low temperature range, while x = 0.1 and 0.3 decrease in the lower temperature range and x = 0.2 increases in whole range of temperature as those of unirradiated samples. As we know that the generation of points/cluster of defects by the irradiation, which act as trapping centres. The generation of the charge carriers from the trapping centres needs different energies, which can be accomplished by temperature. This process will decrease in the resistivity of the samples after irradiation. The valence exchange between $Fe^{3+} \leftrightarrow Fe^{2+}$ and the hole hopping between $Fe^{3+} \leftrightarrow Fe^{4+}$, $Cr^{3+} \leftrightarrow Cr^{4+}$ at B-sites are the main source of hopping mechanism in our case, the charge carriers are trapped in the trapping centres and trapping centres

hindrance the conduction mechanism and the thermal energy may not sufficient to generate charge carriers from the trapping centres. This process will increase the resistivity of the samples after irradiation.

The activation energy was calculated for ferrimagnetic (E_f) and paramagnetic region (E_p) of all the unirradiated and irradiated samples by using Arrhenius relation (Table 6B.13). The observed values of activation energy for Ti - substituted ferrites in both regions are higher than those for the corresponding to the unsubstituted ferrite (x = 0.0) of the unirradiated and irradiated samples. The substitution of Ti ions instead of Fe ions decreases the Fe^{2+} concentration which increases the activation energy that in term increase the resistivity. The presence of Ti ions in the B-sites impedes the motion of charge carriers. This means that the electron or hole transfer that takes place between Fe^{3+} and Fe^{2+}, Fe^{3+} and Fe^{4+}, Cr^{3+} and Cr^{4+} in the present system is not favored in the case of substituting Fe^{3+} with Ti^{4+}. The observed increase in jump length (L) with x suggest that charge carriers require more energy to jump from one cationic site to the other which causes increase in activation energy with increasing x. one can notice also as the increase in porosity with the Ti-concentration, the activation energy also increases accordingly and this is expected behaviour because the number of scattering centres of charge carriers increases as the porosity increases. It is clear from the table that the activation energy for both ferrimagnetic and paramagnetic region of all the irradiated samples is reduced than the unirradiated ones. As mention above, after irradiation jump length increases as compared to unirradiated samples, so the activation energy should be increase after irradiation because the charge carriers require more energy to jump from one cationic site to the other but in the present case controversy results observed. The observed controversy results can be explained on the basis of the microstructural changes brought about by irradiation. The pore may or may not be filled by air but these pores invariably introduce the insulating or the impeding paths to the electrons. In other words, the pores offer extrinsic contribution to the activation energy. The reduction in the activation energy may be attributed to the reduction in number of grains due to densification by irradiation. Due to reduce number of pores the individual grains come closer and effective area of grain to grain contact increases [6B.48].

The obtained data (Table 6B.13) shows that the activation energy for paramagnetic region (E_p) is higher than that in the ferrimagnetic region (E_f). This could be related to the disordered state in the paramagnetic region with respect to the

ordered one in the ferrimagnetic region in which a charge carrier needs more activation energy to jump between adjacent sites. The higher activation energy values have been found to correspond to samples exhibiting higher resistivity. The activation energy values lies in the range 0.22-1.11 eV. The present values of activation energies suggest that the hopping of small or large polaron is responsible for the conduction in the present samples before and after irradiation.

By comparing, the transition temperature (T_c) of the investigated samples (Table 6B.13), one can find that, the transition temperature (T_c) shifting to lower temperature after irradiation as a result of disordered region.

A polaron consists of the charge carrier and distortion of the (ionic) lattice induced by the carrier itself. For the small polaron case, the lattice distortion extends over a distance smaller than the lattice constant. A small polaron defect is created when an electronic carrier becomes trapped at a given site as a consequence of the displacement of adjacent atoms or ions. An essential condition for the formation of small polaron is that the value of polaron radius (r_p) should be less than the inter-atomic distances. An attempt has been made to calculate the polaron radius for all the compositions studied by the relation [6B.49]. The calculated values of polaron radius (r_p) for all the unirradiated and irradiated samples are summarized in Table 6B.14. It is seen that these values are smaller than inter ionic distances and hence are appropriate for small polaron conduction. It is observed that the polaron radius increase with increasing Ti-concentration for before and after irradiation. It is seen that the value of polaron radius of irradiated samples are enhanced than the unirradiated samples. The increase in polaron radius with increasing Ti-content is attributed to the increase in lattice constant with the substitution of titanium. Some ions are displaced and ionic defects are formed or electronic excitations actually causes some ions and atoms to be displaced from their perfect positions (lattice defects) and expansion of the unit cell dimensions after irradiation this may be responsible to creates polaron or increase in the polaron radius.

Fig. 6B.7 illustrates the variation of thermo electric power with temperature for all the investigated unirradiated and irradiated samples. As shown in the figure the common features of all compositions are the fluctuations of seebeck coefficient 'α' is positive over the whole range of temperature indicating that the charge carriers are holes. Thus the conduction mechanism for the p-type semiconductor is due to the hole

transfer from the Fe^{3+} to Fe^{4+} and Cr^{3+} to Cr^{4+} at octahedral sites. The increase in the seebeck coefficient with temperature for the composition x = 0.0, while seebeck coefficient increase up to 360K and then remains almost constant for the compositions x = 0.1, 0.2 and 0.3 of unirradiated and irradiated samples. The increase in seebeck coefficient is due to the increase in the mobility of charge with the increasing temperature. In the present study, sample x = 0.0 is a completely non-degenerate semiconductor due to the thermo emf depends on temperature, while samples with x = 0.1, 0.2 and 0.3 are non-degenerate semiconductor at lower temperatures (< 360K) and they become degenerate for higher temperatures studied due to the thermo emf independent of temperature [6B.50]. The value of seebeck coefficient become more positive with increasing Ti-content (x), except those with the concentration x = 0.1. In order to study the effect of irradiation on seebeck coefficient, a change occurs in seebeck coefficient value (α) become less positive for the concentration x = 0.0, 0.2 and 0.3, whereas for the concentration x = 0.1 the seebeck coefficient become more positive as compared to unirradiated samples in the temperature range studied. More positive values of Seebeck coefficient after irradiation indicate that the increase in the conductivity values by increase more positive holes, while less positive values of seebeck coefficient after irradiation indicate that the recombination of some holes and electrons since both electrons and holes are responsible for conduction in the samples. This also may be hindrance to the charge carrier movements by the defects produced under irradiation.

The conductivity is due to one type of charge carriers, the Fermi energy can be explained by using the relation between the seebeck coefficient and Fermi energy is given by [6B.51] $E_F = e\alpha T - AkT$, where A is the dimensionless constant having values 0 and 2 depending on dominant scattering mechanism. The values of E_F were calculated and plotted as a function of temperature for all the compositions of unirradiated and irradiated ferrites are shown in Fig. 6B.8, for A = 0 and 2. The extrapolated values, E_F (0), at T = 0 were obtained from respective plots for unirradiated and irradiated samples are given in the Table 6B.14. It can be seen that the value of E_F increases with increasing Ti-content (x) for unirradiated and irradiated samples. It is also observed that the value of E_F for the concentration x = 0.0, 0.1 and 0.3 is increased and decrease for x = 0.2 after irradiation as compared to unirradiated samples. It is known that the Fermi energy lies midway between donor states and

energy of conduction band edge for n-type semiconductor and between acceptor states and energy of valence band edge for p-type semiconductor materials. Thus, the small amount of impurity - either donor or acceptors type can shift E_F from the centre of the band gap. Thus means that, for heavily doped semiconductors, the Fermi energy will move into the conduction and the valence bands, respectively in the cases of n- and p-type materials. As we have seen our thermo emf measurements, the investigated ferrites are p-type semiconductor due to the hole transfer from the cation present in the octahedral site. As increase the titanium in the present ferrites, may be the change in the impurity level as well as the effective density state of holes in the valence band. This may be lead to the increase in the Fermi energy with substitution of titanium. After irradiation, the observed change in the Fermi energy can be ascribed to change in the effective density states of holes in the valence band of the ferrites. On the comparison the activation energy, ΔE, from the resistivity graph is found to be lover than E_F (0). This difference could be attributed to the activation energy associated with hopping of charge carriers. Thus, activation energy consists of two components, one that is associated with generation of charge carriers (hole/electrons) and the other associated with hopping of the carriers between crystallographic equivalent sites [6B.52].

The values of charge carrier concentrations per unit volume have been calculated for all the compositions at each temperature by using the value of the seebeck coefficient. The plots ln (n_c) versus T for various mixed unirradiated and irradiated Li-Ti-Cr ferrites are shown in Fig. 6B.9. It can be seen from the figures that the charge carrier concentration behaves inversely as compared to the variation of seebeck coefficient with temperature. It is observed that for x = 0.0 n_c decreases continuously with temperature, for x = 0.1, 0.2 and 0.3 its decreases up to 350K and than slight increase or almost remains constant of unirradiated and irradiated samples. For irradiated samples it can be seen from the figure for concentration x = 0.0, 0.2 and 0.3 n_c are increase whereas for x = 0.1 it decreases than the unirradiated samples in studied temperature range. The observed variation of charge carrier concentration with temperature may be due to the holes which are majority charge carries are compensated by thermally activated electrons for the x = 0.0 and the concentration of electrons overtakes of hole for temperature than 350K. The increase in charge carrier concentration after irradiation is attributed to the creation of cation vacancies (defects)

in the ferrite lattice by irradiation, which form cation (Fe^{3+} + vacancy) complex, which act as p-type carriers and may be this type of charge carriers increases during irradiation.

The drift mobility (μ_D) of charge carriers was calculated from the experimental values of the electrical resistivity and carrier concentration (n_c). The thermal variation of charge carrier mobility for all the compositions of unirradiated and irradiated samples are shown in Fig. 6B.10 as a plot of $\log_{10}\mu_D$ versus $10^3/T$. It is found that the mobility increases with increasing temperature for all the compositions of unirradiated and irradiated samples. The increase in mobility was caused by the decrease of resistivity with temperature. It can be seen from the figure that the mobility of charge carriers decreases in the whole temperature range for the concentration x = 0.0, 0.2 and 0.3 after irradiation, may be due to the lattice expansion take place by irradiation which hinders the hopping of charge carriers. The magnitude of mobility is found in the range of 10^{-6}-10^{-10} cm^2/V.sec which is consistent with mobility suggested in the literature for holes (10-8 cm^2/V.sec) [6B.53].

6B.6 Swift Heavy Ion Irradiation effects on Dielectric properties of the system $Li_{0.5(1+x)}Ti_xCr_{0.1}Fe_{2.4-1.5x}O_4$

The polycrystalline ferrites are very good dielectric materials. This is possible because in the process of polycrystalline ferrites synthesis, when the powder is sintered under slightly reducing conditions, the divalent iron ions formed in the body leads to high conductivity grains. When such material is cooled in an oxygen atmosphere, it is possible to form layers of very low conductivity over its constituent's grains. Almost all the ferrites in the polycrystalline form have such high conductivity grains separated by low conductivity layers so that behave as inhomogeneous dielectric materials. As such the dielectric properties of ferrites are dependent on several factors including the method of preparation, sintering temperature, sintering atmosphere, chemical composition, and microstructure etc. as a consequence of the inhomogeneous dielectric behaviour, dielectric constants as high as 10^5 are found in the case of ferrites at low frequencies [6B.54]. Study of the effect of composition, temperature and frequency on dielectric behaviour and ac electrical conductivity offers much valuable information on the behaviour of the localized electric charge carriers which can lead to good explanation and understanding of the mechanism of electric conductivity and dielectric polarization in ferrite systems.

Many researchers have studied dielectric properties of Li-Cd [6B.20], Li-Zn [6B.55], Li-Mg [6B.56] and Li-Ni [6B.36] ferrites. The aim of the present work is a study of the SHI irradiation effects of temperature, frequency and Ti ion substitution on the dielectric and ac electrical properties of the $Li_{0.5(1+x)}Ti_xCr_{0.1}Fe_{2.4-1.5x}O_4$ ferrite system prepared by usual double sintering ceramic technique. Considering the effect of irradiation on the dielectric measurements on polycrystalline samples of the stochiometric composition $Li_{0.5(1+x)}Ti_xCr_{0.1}Fe_{2.4-1.5x}O_4$ were carried out. The samples for dielectric measurements were in the form of 10 mm in diameter and 2 mm in thickness for unirradiated specimen. The ferrite pellets were cut and polished to require size (10 mm in diameter and 0.3~0.4 mm in thickness) as determined by using the SRIM-98 software for the SHI irradiation experiment.

We have performed dielectric measurements as a function of frequency in the range 100Hz-1MHz at different temperature and also as a function of temperature in the ranges 300K – 800K for few selected frequencies viz. 100 Hz, 500Hz, 1kHz, 10kHz, 50kHz, 80kHz, 100kHz, 500kHz, 800kHz and 1MHz on unirradiated and 50 MeV Li^{3+} irradiated bulk samples using precision LCR meter and temperature controller (± 1^oC) with two probe method.

The variation of dielectric constant (ε') and a.c. resistivity (ρ_{ac}) at selected temperatures (300K, 373K, 573K, 773K) and frequencies (1kHz, 10kHz, 50kHz, 500kHz, 1MHz) as function of Ti-content of unirradiated and irradiated Li-Cr ferrites are shown in Table 6B.15-16, respectively. It can be seen from the table that the dielectric constant (ε') initially found to decrease with increase in Ti-content up to 0.2 then increase with the further increase in Ti substitution for x = 0.3 of unirradiated samples (Table 6B.15). The a.c. resistivity (ρ_{ac}) initially found to increase with increase in Ti-content up to 0.3 (Table 6B.16) for the unirradiated samples. For the all compositions the dielectric constant (ε') and a. c. resistivity (ρ_{ac}) have inverse trend with each other for the unirradiated samples. These observed variation in both ε' and ρ_{ac} can be explained as follows.

Since both the dielectric constant and electrical conductivity are basically electrical transport properties and the variation with temperature is similar, it may be assumed that the same mechanism is responsible for both the phenomenon. Earlier researchers [6B.57-6B.58, 6B.54] reported a strong correlation between the conduction mechanism and dielectric behaviour of ferrites. These workers have

explained the dielectric behaviour of the ferrites starting with the supposition that the mechanism of the polarization process in ferrites is similar to that of the conduction process [6B.59]. They observed that the electronic exchange between $Fe^{2+} \Leftrightarrow Fe^{3+}$ results in local displacements determine the polarization of the ferrites. A similar explanation is proposed for the present system. In the present system the cation distribution shows (Table 6B.2) the Li^{1+} and Cr^{3+} ions are known to have marked preference for the B-sites while Fe^{3+} and Ti^{4+} occupy A- sites as well as B- sites. As Li^{1+}, Ti^{4+} ions are fixed valence the only source of conduction is from electron $Fe^{2+} \Leftrightarrow Fe^{3+}$ and holes $Fe^{3+} \Leftrightarrow Fe^{4+}$ and $Cr^{3+} \Leftrightarrow Cr^{4+}$. The exchange of electrons $Fe^{2+} \Leftrightarrow Fe^{3+}$ and holes $Fe^{3+} \Leftrightarrow Fe^{4+}$, $Cr^{3+} \Leftrightarrow Cr^{4+}$ may be leads to local displacement of charge carriers in the direction or opposite direction of the applied field, these determine the polarization. As observed in thermo electric power measurements the most probable contribution for the hopping in present system through the exchange of hole $Fe^{3+} \Leftrightarrow Fe^{4+}$, $Cr^{3+} \Leftrightarrow Cr^{4+}$ in the B-sites. The observed variation in dielectric constant may be understood on the basis of space charge polarization which is due to an inhomogeneous dielectric structure governed by the number of space charge carriers and the resistivity of the samples.

The observed decrease in dielectric constant for substituted samples indicates that these cations help to slow down the conduction process between iron and chromium ions. The presence of Fe^{2+} ions in ferrites is known to produce large dielectric constants. On the other hand, if titanium ions in B-sites block the hopping charge carrier, the dielectric constant would decrease. This is in agreement with the observed values of dielectric constant throughout the series. However, the slight increase in dielectric constant with increase in substituents concentration (x = 0.3) may be due to corresponding changes in microstructures brought about by the sintering conditions.

The observed variation in resistivity with the substituents concentration can be explained on the basis of occupation of cations in different lattice sites and hopping between them. Hence the main contribution of resistivity in the present system may be due to the hole hopping. It is obvious that the general trend of the data is the increase of the a. c. resistivity (ρ_{ac}) with increasing Ti-content. The continues increase of the a. c. resistivity is ascribed to the masking effect of the Ti^{4+} ions, which replaces some of the iron ions on the octahedral site. In this case, the polarization decreases with the

result of decreasing the dielectric constant and increasing the a. c. resistivity of the unirradiated samples. On the other words, the increase of the Ti^{4+} -ion concentration decreases the ratio Fe^{3+}/Fe^{2+}, Fe^{3+}/Fe^{4+} and Cr^{3+}/Cr^{4+} as well as electron or hole hopping probably in between different metal ions of different valences on equivalent lattice sites. In the present work the increase in resistivity may be due to the electron hole compensation in the B-sites.

The dielectric loss tangent (tanδ) or simply loss factor measurements have been carried out of unirradiated and irradiated specimen at different temperature and at low and high frequencies, 100Hz to 1MHz. The compositional dependence of dielectric loss tangent (tanδ) at selected temperatures (300K, 373K, 573K, 773K) and frequencies (1kHz, 10kHz, 50kHz, 500kHz, 1MHz) as function of Ti-content of unirradiated and irradiated Li-Cr ferrites are presented in Table 6B.17. It is clear from table that the dielectric loss tangent decreases as the Ti-content increases for unirradiated samples. All the samples containing titanium exhibited lower dielectric losses compared to the basic composition. The results can be explained on the basis of the conduction mechanism i.e. in term of electron hopping between Fe^{2+} and Fe^{3+} in the octahedral sites for n-type ferrites and in terms of hole hopping for p-type ferrites [6B.60, 6B.61]. Hence as the number of Ti^{4+} ions increases instead of Fe^{3+} ions in octahedral site, the number of Fe^{2+} and Fe^{3+}, Fe^{3+} and Fe^{4+}, Cr^{3+} and Cr^{4+} ions between which the hopping conduction mechanism takes place will decrease, and the dielectric loss decreases.

The effect of 50 MeV Li- irradiation on the dielectric properties of the samples has been well studied using a fluence of 5×10^{13} ions/cm^2. The results obtained show that the dielectric constant (ε') initially found to decrease with increase in Ti-content up to 0.2 then increase with the further increase in Ti substitution for x = 0.3 of irradiated samples (Table 6B.15) same as unirradiated samples but as increase the temperature and frequency, there is no systematic variation observed in dielectric constant with the Ti- substitution in irradiated samples. For all the compositions the dielectric constant for irradiated samples is increased in magnitude from that of the unirradiated samples. The effect of irradiation is to increase the polarization with the result of increasing the dielectric constant and decreasing the resistivity of the samples. The effect that the irradiation tends to construct the polarization by initiating some rearrangement of cations, thus increasing the electron or hole exchange between

the different metal ions. It is clear from the table (Table 6B.16) the a.c. resistivity is found to increase with increase in Ti- content up to x = 0.3 of irradiated samples same as unirradiated samples but for the all compositions the a. c. resistivity for irradiated samples is decreased in magnitude from that of all the unirradiated samples. This means more charge carriers are generated by irradiation process and electronic rearrangements occur, which help the conduction process and decreased the a.c. resistivity of the irradiated samples. It is also observed (Table 6B.17) that the dielectric loss tangent decrease with increase in the Ti-content for irradiated samples, except for x = 0.3 same as unirradiated samples but the dielectric loss for the irradiated samples is increased in magnitude from that of all the unirradiated samples. This is obvious because after the irradiation the number of Fe^{2+} and Fe^{3+}, Fe^{3+} and Fe^{4+}, Cr^{3+} and Cr^{4+} ions between which the hopping conduction mechanism takes place will increase, and the dielectric loss increases.

The variation of dielectric constant (ε') with temperature for the compositions x = 0.0, 0.1, 0.2 and 0.3 of unirradiated as well as irradiated specimen at different frequencies are shown in Fig. 6B.11a-11d, respectively. From these experimental results made the following observations:

(a) It is observed from the figure the dielectric constant (ε') gradually increase by increasing temperature at each separate frequency for all unirradiated and irradiated specimens.

(b) As increase the frequency, the magnitude of dielectric constant (ε') is decreases for before and after irradiation for all the samples.

(c) The dielectric constant for the composition x = 0.0 of irradiated sample is increased in magnitude than the values of the corresponding unirradiated ones at the same measuring temperature.

(d) Further the increase in Ti substitution for the composition x = 0.1 the value of dielectric constant for irradiated sample coincide with the value of unirradiated ones in the temperature range 350-600K at selected lower frequencies 100Hz, 500Hz and 1kHz and again increase in magnitude at higher temperature range. Furthermore at particular frequency 10kHz it coincides with the value of the corresponding unirradiated sample in the whole range of temperatures. All over again at selected higher frequencies 50kHz, 100kHz, 500kHz, 800kHz and 1MHz the value of dielectric constant for the irradiated sample is

decreased in magnitude than the value of the corresponding unirradiated ones at the same measuring temperature and peak formed at higher frequencies. The formed peaks are shifted towards lower temperature side on the increasing frequency.

(e) For x = 0.2, the value of dielectric constant for the irradiated sample is overlap with the value of unirradiated sample in the temperature range of 350-550K at selected frequencies 100Hz, 500Hz, 1kHz, 10kHz, 50kHz and 100kHz and as increase frequencies 500kHz, 800kHz, 1MHz the dielectric constant is decreased in magnitude in the temperature range 350-600K however it is rapidly increase in magnitude on increasing the temperature (beyond 550K) and frequency as compared to unirradiated ones. Furthermore at particular frequency 500Hz it is coincide with the value of the corresponding unirradiated sample in the whole range of temperatures and at lower frequency (100Hz) it is observed the dielectric constant is decreased in magnitude at higher temperature range. In this particular composition, the peak formed at higher frequencies 800kHz, 1MHz in the temperature range of 650 - 750K for irradiated sample. The formed peaks are shifted towards lower temperature side on increasing frequency.

(f) On increasing higher Ti concentration for Fe^{3+} in the system, The sample x = 0.3 shows a gradual increase in the dielectric constant with increase temperature without any anomalies but it is observed that the dielectric constant for irradiated sample is decreased in magnitude of ε' from that of the unirradiated sample as the same temperature range. It is also observed that the difference in magnitude between unirradiated and irradiated samples is enhanced as increase in the frequency at the higher concentration.

The dramatic increase in the dielectric constant (ε') for unirradiated as well as irradiated samples with temperature is due to the large thermal energy which is quite sufficient to liberate more dipoles and the field accompanied with the applied frequency aligned them in its direction, though increasing the polarisability as well as the dielectric constant (ε'). The decrease in ε' with increasing frequency is due to the fast alteration of the electric field accompanied with the applied frequency, where the alteration of the dipole increases as well as the friction between them. The quantity of heat dissipated in the entire volume of the sample increases and the aligned dipoles

will be disturbed with the result of decreasing ε' or the decrease of ε' with increasing frequency is ascribed to the increase of the jumping frequency of the charge carriers.

In the lower temperature region up to 600K the value of the dielectric constant (ε') for irradiated samples overlapping with the value of unirradiated samples for particular x = 0.1 and 0.2, may be the thermal energy given to the irradiated samples is not sufficient enough to free the localized dipoles to be oriented in the field direction. For T > 600K ε' increases more clearly but with different rates, which may be due to the large number of dipoles that become free such high thermal energy and the field aligned them in its direction and the value of ε' decreases in magnitude after irradiation at all temperature in the higher frequency region may be due to the formation of point defects, which act as a trapping centres for the charge carriers.

After irradiation, the peak formation at higher temperature region and shifted toward lower temperature side on the increasing frequency (at high frequency region) for the composition x = 0.1 and 0.2 may be attributed to two competitive effects, the first of which is the increase of the mobility of charge carriers with increasing temperature leading to an increase in ε' because the conductivity and polarization of the same origin and the second opposing effect is the hindrance of charge carriers movements due to the thermal agitation as well as trapping centres. The peak position and height were varied depending on both frequency and Ti content. The shift in the peak position toward lower temperature with increasing frequency may be the applied frequency act a pumping force pushing the charge carriers from one conduction state to another or the applied frequency may be due to the strong effect of the field where the dipoles can easily orient themselves in the field direction which is hindrance by trapping centres.

It is observed that the dielectric constant for irradiated sample is decreased in magnitude from that of the unirradiated sample in the same temperature range for the composition x = 0.3 and the difference in magnitude of ε' between unirradiated and irradiated samples is enhanced with increase in the frequency, may be due to the decrease in polarization. This effects is because the irradiation tends to destroy the polarization by initiating some points defects (voids at different depths and clusters), thus decreasing the electron exchange between the different metal ions.

Fig. 6B.12a-12d shows the temperature dependence of the dielectric loss factor, tanδ at different frequencies for the investigated unirradiated and irradiated

samples. It can be seen from the figures that the dielectric loss increases with increasing temperature for all the concentrations. The data clarify that the dielectric loss factor is decreasing with increasing in Ti^{4+} concentration. No dielectric relaxation peak observed in tanδ curves in the concentration $x \leq 0.2$ while x= 0.3 appearance of the relaxation peak (a broad peak) in the low temperature range and this broad relaxation peak shift towards higher temperature with increasing frequency for the unirradiated samples. It is also observed that the sharp decrease in tanδ with increasing frequency for the unirradiated and irradiated samples. On the other hand, for 50 MeV Li^{3+} ion irradiated samples the dielectric loss factor is modified with great extent. For pure Li-Cr ferrite the magnitude of loss factor for irradiated sample is increased in the lower temperature region 300-500K and remains sharply decreased in the higher temperature region up to 800K as compared to unirradiated ones. In the case of irradiated Ti^{4+} substituted Li-Cr ($x > 0.0$) ferrites the magnitude of loss factor (tanδ) is higher than that of the unirradiated samples in the whole temperature range and show relaxation broad peak at low temperature region. As increase the frequency, the intensity of observed relaxation broad peak is abridged and shifts towards higher temperature region after irradiation.

On increasing temperature, both the a.c. [6B.62] and d.c. [6B.63] conductivities were found to increase owing to the increase in the number of charge carriers and their drift mobility which are thermally activated. The mechanism of dielectric polarization in ferrites is similar to that for electric conduction [6B.64, 6B.59]. In the present case, the electron exchange between Fe^{2+} and Fe^{3+} and hole exchange between Fe^{3+} and Fe^{4+}, Cr^{3+} and Cr^{4+} ions on octahedral (B) sites are responsible for electric conduction. These charge carriers are not completely free but are strongly localized. The local displacements of holes and electrons determine dielectric polarization in ferrites. The number and drift mobility of holes and electrons increase as the temperature increases owing to the thermal activation; therefore these local displacement or dielectric polarization as well as dielectric loss increase as the temperature increases as shown in Fig. 6B.12a-12d. As we know that irradiation cause defects in the samples and these structural defects give rise to the trapping centres for the electrons and holes. These defects may also act as scattering centres so that the interaction of charge carriers and thermal fluctuation of the lattice are not identical everywhere and at every time. The energy dissipation due to their friction

will be increased with the result of increasing in dielectric loss after irradiation. The response time for the trapping centres is higher than the time taken for the hopping between the sites of the charged particles. Therefore the peak in the irradiated sample is due to the relaxation in the trapping centres. The decrease in dielectric loss tangent (tanδ) with increasing frequency agrees well with Debye type relaxation process [6B.65]. Furthermore, the shift of peak temperature towards higher temperature side with increasing frequency may due to the increase in p-type carriers after irradiation in the present system.

The dependence of imaginary part of the dielectric constant or complex dielectric constant (ε'') on absolute temperature at different frequencies for the all unirradiated and irradiated samples are shown in Fig. 6B.13a-13d. From the figure, it is clear that the complex dielectric constant (ε'') increases with increasing temperature for all the investigated unirradiated and irradiated samples. This is because the thermal energy given to the system increases the motion of charge carriers and energy dissipation to their friction will be increased with the result of increasing temperature. Actually, the dissipation of charges in ferrites materials is represented as the imaginary part of the relative permittivity or complex dielectric constant. As we know that the loss factor is the ratio of the imaginary (ε'') and real (ε') part of the dielectric constant, ε''=ε'tanδ. So the dielectric loss is directly proportional to the imaginary part of the dielectric constant (ε''). Therefore, we can observe variation in ε'' according to the dielectric loss. The complex dielectric constant (ε'') decreases with increasing frequency due to the fast rotation of the charge carriers under the action of increasing the field variation. Though, the dielectric loss as well as complex dielectric constant (ε'') increases and the energy required to overcome the resistance of the viscous medium will be reduced when the charge carriers rotate thorough a unit angle [6B.66]. For pure Li-Cr ferrite (x =0.0) the complex dielectric constant (ε'') of irradiated sample is higher in magnitude that of the unirradiated samples in the whole range of temperatures, whereas the concentration of Ti^{4+} increases for x = 0.1 and 0.2 the value of ε'' is overlapping with unirradiated samples in the low temperature region and sharply increase in higher temperature region as compare to unirradiated samples but again increase in the concentration of Ti^{4+} for x = 0.3 the value of ε'' is same overlapping with unirradiated sample in the low temperature while sharply decrease in higher temperature region as

compare to unirradiated samples. This is because the irradiation tends to disorder the localized charge carriers, so that the thermal energy dissipation increases due to increasing friction of charge carriers or may be require more energy to hopping process.

Fig. 6B-14a-14d correlates the a. c. resistivity in terms of $\log_{10}\rho_{ac}$ and the reciprocal of the absolute temperature (10^3/T) at different frequencies for unirradiated and irradiated investigated samples. The figure shows the resistivity of the unirradiated and irradiated samples is decreased by increasing both applied frequency and measuring temperature. The decrease of the a. c. resistivity with temperature is attributed to the enhancement of the Verwey hopping mechanism between electron $Fe^{2+} \leftrightarrow Fe^{3+} + e^-$ and holes hopping between $Fe^{3+} + e^- \leftrightarrow Fe^{4+}$, $Cr^{3+} + e^- \leftrightarrow Cr^{4+}$on the B-site, where most of Cr^{3+} ions prefer to occupy B-site together with Fe^{3+} ions. Comparing the resistivity before and after irradiation, it is clear from the figure that the value of a. c. resistivity decreases for the concentration $x \leq 0.2$, and increase for the concentration $x = 0.3$ after irradiation at all frequency and temperature. This decrease in resistivity can be attributed to the more charge carrier generated by irradiation process and the increase the ratio of Fe^{2+}/Fe^{3+}, Fe^{3+}/Fe^{4+} and Cr^{3+}/Cr^{4+} on the octahedral sites as a the consequences of the hopping reactions. This increase in the resistivity due to the trapping of charge carriers in the defects whish is created as a result of irradiation.

The variation of dielectric constant (ε') for Li-Ti-Cr ferrites were studied as a function of an a. c. field in the frequency range from 100Hz to 1MHz at selected different temperatures. Fig. 6B.15a-15b shows the dielectric constant as a function of frequency at different temperatures (298K, 373K, 473K, 573K, 673K and 773K) for various compositions of unirradiated and irradiated Li-Ti-Cr ferrite system. It can be seen from the figure that the value of dielectric constant decreases continuously with increasing frequency reaching a constant value for all the unirradiated samples. The decrease of dielectric constant (ε') with increase in frequency as observed in the case of mixed Li-Ti-Cr ferrites is a normal dielectric behaviour of ferrites. The normal dielectric behaviour was also observed by several other investigators in Li-ferrites [6B.54, 6B.67-6B.68]. The large value of dielectric constant (ε') at lower frequency and the variation of ε' with frequency reveals that the dispersion could be explained on the basis of Koop's [6B.69] model which considered the dielectric structure as an

inhomogeneous of two layers of Maxwell [6B.70] and Wagner [6B.71] type. Ferrite grains which conduct fairly well comprise the first layer which is separated by a second layer of poorly conducting grain boundaries. Dielectric dispersion in ferrite can be explained on the basis of space charge polarization which is a result of the presence of higher conductivity phases (grains) in the insulating matrix (grain boundaries) of a dielectric causing localized accumulation of charge under influence of an electric field. Since an assembly of space charge carriers in a dielectric requires finite time to line up their axes parallel to an alternating electric field, if the frequency of the field reversal increases, a point will be reached when the space charge carriers can not keep up with the field and the alteration of their direction lags behind that of the field; thus resulting in a reduction in the dielectric constant (ε') of the material. As the frequency of the field continue to increase, at some stage of the space charge carriers will barely have started to move before the field reverses and make virtually no contribution to the polarization of the dielectric [6B.72, 6B.73].

The variation of the dielectric constant (ε') with frequency at room temperature for each irradiated samples is same as a unirradiated samples which is normal dielectric behaviour of ferrites but the dielectric constant (ε') for irradiated samples is increased in magnitude from that of the unirradiated samples at all different temperatures. This increase in ε' may be due to the increase in space charge carrier or interfacial polarization after irradiation.

It can be also notice that the dielectric constant of the irradiated samples for the concentrations x = 0.0 and 0.1 increases with increases frequency until reaching a peak after which it decreases with increasing frequency. This peak in ε' is shifted towards higher values of frequencies as the temperature increases which that means there is a dispersion peak above the temperature 298K (room temperature) in the dielectric constant ε'_{max} (abnormal behaviour) in low frequency region and dispersion peak shifted towards higher frequency with increasing temperature. This behaviour was previously reported in other ferrites [6B.64, 6B.74-6B.76] and was interpreted as due to the presence of two types of charge carriers, which sometimes are formed at high temperatures. The anomaly in variation of dielectric constant after irradiation is due to point/clusters of defects creation, which results in collective contribution of p- and n-type of conduction. It is well known that the local displacement of the p-type carriers take part in the polarization in an opposite direction to that of the external

field. Therefore the dielectric constant starts increasing after certain frequency. In addition, since the mobility of p-type carrier is lower than that of n-type carrier, their contribution to polarization decreases more rapidly at lower frequencies in the case of irradiated samples [6B.3]. The position of the maximum of ε' will be dependent on the relative number of the p-type carriers in the material. The higher the number of the p-type carriers, the higher the peak frequency. Therefore, the maximum of ε' is shifted towards higher frequency with increasing temperature due to the increasing hopping frequency of charge carriers after irradiation.

The variation in dielectric loss tangent (tanδ) and complex dielectric constant (ε'') both with frequency at different temperature for unirradiated and irradiated samples for all the compositions are shown in Fig. 6B.16a-16b & 6B.17a-17b, respectively. It can be seen from the figures that the dielectric loss tangent (tanδ) as well as complex dielectric constant (ε'') decrease rapidly with increasing frequency and then reaches a constant value at higher frequency region for both unirradiated and irradiated samples. The decrease in the value of tanδ and ε''with frequency takes place when the jumping frequency of electric charge carriers cannot follow alteration of the electric field applied beyond a certain frequency.

On the other hand, for the irradiated samples the dielectric loss (tanδ) is increased in magnitude as compared to the all unirradiated samples in the whole range of frequency at room temperature. Furthermore as increase the temperature the magnitude of tanδ and ε'' is greater than that of the all unirradiated samples at lower frequency region (up to 100kHz), which is matching with unirradiated samples at higher frequency region. It is also observed that small hump after irradiation in the higher frequency region (at 298K) for the concentration x = 0.2 and 0.3 of irradiated samples. As mention earlier, after irradiation interfacial polarization or space charge increases due to increasing the electric dipole moments and the quantity of heat dissipated in the entire volume of the sample is increased and the aligned dipoles will be disturbed, this causes the dipole orientations difficult. Therefore, the greater value of tanδ and ε''is found for irradiated samples in the low frequency range. On increasing the frequency the rotation of dipoles lags behind the signal frequency so loss starts decreasing and for the frequency greater than 100kHz is shows variation similar to that of unirradiated samples. The presence of small hump in loss factor

may be caused by the difficult orientation of diploes and delayed relaxation of dipoles.

Fig. 6B.18a-18b shows the variation of ac resistivity ($\log_{10}\rho_{ac}$) with the log frequency (logf) at different temperature for all unirradiated and irradiated investigated samples. It is clear from that the figures all the samples show decrease in ρ_{ac} with increase in frequency from 100Hz – 1MHz before and after irradiation, which is the normal behaviour of ferrites. The increase in frequency of the applied field enhances the hopping of charge carriers resulting in an increase in the conduction process there by decreasing the ac resistivity. It is observed that the magnitude of ac resistivity decrease after irradiation with the variation of frequency, which may be due to the more charge carrier generated by electronic rearrangement of cations during irradiation as well as the frequency act as a pumping force that the transfers the charge carriers between the different disordered localized states. As is evident from figure, the ac resistivity has been observed decreasing with the increase in temperature before and after irradiation. This is responsible for pile up of more charge at the layer interface and increases the space charge polarization with increasing temperature.

6B.7 Swift Heavy Ion Irradiation effects on Impedance spectroscopy of the system $Li_{0.5(1+x)}Ti_xCr_{0.1}Fe_{2.4-1.5x}O_4$

Impedance measurements were carried out for all the compositions of unirradiated and irradiated samples at selected temperatures using LCR meter in the frequency range 100Hz-1MHz. The complex impedance measurements were made on all the compositions of Li-Ti-Cr ferrites with two separate unirradiated (10mm in diameter and 2mm in thickness) and irradiated (10cm in diameter and 0.3~0.4 mm in thickness) samples having different dimensions. Typical room-temperature complex impedance spectra Z'' versus Z' for the unirradiated and irradiated ferrites with x = 0.0, 0.1, 0.2 and 0.3 are shown in Fig. 6B.19. It is seen that at the room temperature the impedance data do not take shape of a full one semicircle rather present a straight line with large slope at higher frequency for unirradiated samples, suggesting the insulating behaviour of ferrite composition at room temperature, supported by resistivity measurements. In general, arc on the low-frequency side is due to the grain boundary conduction and that on the high-frequency side is due to the grain conduction. The presence of single half semicircular arc obtained at higher

frequencies corresponds to electrical conduction by the interior of the bulk grain. After irradiation it is observed that the present single half semicircular for x = 0.0 convert into full one semicircular arc and for x = 0.3 large slope straight line convert in two semicircular arc. For the concentration x = 0.1, one semicircular arc convert in straight line with large slope after irradiation. This type of random behaviour in complex impedance at room temperature after irradiation may be due to change in the inter-particle interactions like grain and grain boundary effects by irradiation.

Fig. 6B-20 shows the variation of the real (Z') part and imaginary (Z'') part of the impedance as a function of frequency at room temperature for all the compositions of unirradiated and irradiated samples. The magnitude of the Z' decreases with increasing frequency at room temperature for all the unirradiated and irradiated samples. It is clear from the figure the magnitude of imaginary (Z'') part also decrease with increasing frequency, this may be due to the release of space charges. The observed presence of a single peak after irradiation for x = 0.0 and before irradiation for x = 0.1 in the imaginary spectra of impedance suggest the relaxation and indicate change in conductivity with frequency.

Fig. 6B.21a-21d show the variations in the real (M') and imaginary (M'') part of the complex modulus with frequency at different temperature for all compositions of unirradiated and irradiated Li-Ti-Cr mixed ferrites. The modulus spectra of in figure show the electrical relaxation with peak frequency in the imaginary (M'') part of the modulus spectra of unirradiated samples for all the compositions. After irradiation same electrical relaxation peak disappeared in imaginary part of the modulus spectra in the same studied frequency region. The figure clearly shows that the M'' peak shifts towards higher frequency with increasing temperature. The peak frequency is called relaxation frequency and it increases with temperature because of the thermal activation of localized electric charge carriers which form the electric dipoles [6B.77]. The inverse of the frequency of the maximum peak position can be taken as a convenient measure of the characteristic relaxation time, i.e $\tau = 1/2\pi f_c$. Furthermore, the maximum peak position shifting toward lower frequency side with the increasing Ti content in the system means the relaxation time increases with increasing Ti content in the system at a particular temperature for unirradiated samples. It is observed that the maximum peak position shifting toward higher frequency side with increasing temperature. This suggests that the relaxation time

decreases with the measuring temperature. This may be due to the electric dipoles in ferrites originates from hopping of charge carriers. When the charge carriers are thermally activated, the hopping rate increases and hence the relaxation time decreases with temperature. Electrical relaxation peak disappeared in the imaginary part of modulus spectra in irradiated samples can be ascribed to change the charge carrier hopping rate or change in the dipole-dipole interactions after irradiation in the system. Any change in the spectra of the real (M') part of the modulus is an indication of a change in the stiffness of the material under test and frequency region where this change occurs is emphasized by loss peak in the imaginary part of the modulus [6B.78].

Fig. 6B.22a-22d shows the imaginary (M'') part of electrical modulus versus the real (M') part of the electrical modulus plotted in the frequency range 100Hz – 1MHz at several temperatures for all the compositions of unirradiated and irradiated ferrites. It is seen that at room temperature, the spectrum consists of one semicircular arc for the concentration x = 0.0 and 0.1 at lower frequency side. As the Ti- content increase for x = 0.2 and 0.3, curve towards at higher frequency side corresponds to the electrical conduction by interior of the grains boundaries for unirradiated samples. As increase the temperature for all the compositions of unirradiated samples, the diameter of the semicircular arc decrease and the shape of the semicircular arc towards a straight line with a large slope, indicating a reduction of the grain boundary interior resistance. After irradiation, the electrical modulus data do not take any shape of a semicircular arc but rather present a straight line with large slope, suggesting the change in grain and grain boundary effects in the hopping of charge carries after irradiation.

Conclusion

The effect of irradiation on the structural and magnetic properties of the spinel ferrite system $Li_{0.5+0.5x}Ti_xCr_{0.1}Fe_{2.4-1.5x}O_4$ for the compositions with x = 0.0, 0.1, 0.2 and 0.3 has been investigated by means of XRD, Infrared spectroscopy, high field magnetization, AC susceptibility and Mössbauer spectroscopy. XRD patterns show all Bragg reflections could be indexed for the *fcc* spinel structure and the peak positions are shifted to lower angle (2θ) values in the case of irradiated samples. The 50 MeV Li^{3+} ions irradiation produced the compressive strain (shifting of peak position to lower 2θ values) and also generate some point/clusters of defects in the

lattice structure. It is also found that the compositional increase in the lattice parameter (a) is greater for the irradiated samples than the unirradiated ones, which are attributable to the rearrangement of the cations and expansion of the unit cell. The cation distributions deduced through XRD intensity analysis for the unirradiated and irradiated samples using the computer simulation based on the Buerger's formula is clearly indicated the redistribution of the cations in the A- and B- sites induced by SHI-irradiation.

The compositional variation of saturation moment η_B indicates the collinear type of magnetic ordering and supports the cation distribution determined through XRD analysis. The observed reduction in the η_B on increasing the Ti-content in the both cases is due to the magnetic dilution of octahedral sites because on the B-site Fe^{3+} ($5\mu_B$) is replaced by non-magnetic Ti^{4+} ($0\mu_B$) and Li^{1+} ($0\mu_B$). Most of the Mössbauer hyperfine parameters not much more affected on irradiation. Only an appreciable change is seen in the line width due to the production of defects by SHI irradiation. The A-site sub spectra shows larger line width and the effect being more pronounced after irradiation which is due to more distribution values of A-site hyperfine field arising from non-magnetic Ti^{4+} and Li^{1+} neighbours of A-site Fe^{3+} ions. The presence of magnetic ion Cr^{3+} ($3\mu_B$) in the lattice seems to play an important role in keeping the long range order intact in spite of SHI induced defected regions/rearrangement of the cations. The compositional decrease in T_c is because of the substitution of non- magnetic Ti ions reduces the active magnetic linkages per magnetic ion per formula unit and the Curie temperature (T_c) for the irradiated specimens is lower than their unirradiated counterparts.

The structural parameter like X-ray density, porosity, site ionic radii, oxygen positional parameter, and bond length and bond angels is clearly influenced by SHI irradiation. The IR spectra consist of two significant absorption bands, the high frequency band ν_1 which is in the range 501-589 cm^{-1} is assigned to intrinsic vibrations of the tetrahedral group and the lower frequency band ν_2 which is in the range 405-489 cm^{-1} is assigned to the intrinsic vibrations of the octahedral cations. The intensity of all bands and their shoulders decrease whereas bands become broader on increasing Ti -content (x) in the present system. The shifting of band positions and shoulders/splitting increases is recognized the presence of small amount of Fe^{2+} after irradiation. It is also important to note that around the main absorption band (ν_1) new

subsidiary band (ν*) come into sight with the shoulders or splitting in the range of 601 – 670 cm^{-1} with the compositions x > 0.0 after irradiation. The force constant (k) increases with increasing Ti-concentration for unirradiated and irradiated samples, which suggests strengthening of inter-atomic bonding. The increase in the value of υ_l, υ_s and υ_m can be explained on the basis of the density material. The strain/stress developed in materials due to the creation of defects may be responsible for the modification in their elastic properties after irradiation.

The present system also studied by means of dc resistivity, thermoelectric power, dielectric measurements and impedance spectroscopy before and after irradiation. The compositionally increase in electrical resistivity is due to Ti^{4+} ions act as scattering centres at B-sites, obstructing the degree of easy conduction between $Fe^{3+} \Leftrightarrow Fe^{2+}$, $Fe^{3+} \Leftrightarrow Fe^{4+}$ and $Cr^{3+} \Leftrightarrow Cr^{4+}$ions. The observed increase in jump length (L) with x suggests that charge carriers require more energy to jump from one cationic site to other, which causes an increase in resistivity with increasing x. The activation energy values lies in the range 0.22-1.11 eV which suggests the hopping of small or large polaron is responsible for the conduction in the present samples before and after irradiation. The activation energy for paramagnetic region (E_p) is higher than that in the ferrimagnetic region (E_f). The thermoelectric power explain the conduction mechanism for the p-type semiconductor is due to the hole transfer from the Fe^{3+} to Fe^{4+} and Cr^{3+} to Cr^{4+} at octahedral sites in the present system. The charge carrier concentration and mobility as a function of temperature for unirradiated and irradiated samples have also studied.

The dielectric properties and ac resistivity in studied samples have been explained on the basis of space charge polarization according to Maxwell and Wagner's two layers model and the hopping between adjacent $Fe^{2+} \leftrightarrow Fe^{3+}$ as well as the hole hopping between $Fe^{3+} \leftrightarrow Fe^{4+}$ and $Cr^{3+} \leftrightarrow Cr^{4+}$ ions at B-sites. The complex impedance (Cole-Cole plots) analysis is used to separate the grain and grain boundary effect of the present system. The electrical modulus M''(f) spectra show the electrical relaxation with peak in the measured frequency range at different temperatures of unirradiated samples for all the compositions. After irradiation same electrical relaxation peak is found to disappeared in M''(f) spectra for the same studied frequency region, clearly indicates that the M'' peak shifts towards higher frequency with increasing temperature. The relaxation peak position shifting towards higher

frequency side with increasing temperature suggests that the relaxation time decreases with the measuring temperature due to the electric dipoles in ferrites originates from hopping of charge carriers. The disappearance of electrical relaxation peak in the imaginary part of modulus spectra in irradiated samples can be ascribed to change the charge carrier hopping rate or change in the dipole-dipole interactions after irradiation in the system.

References

6B.1 M. C. Chhantbar, K. B. Modi, G. J. Baldha, H. H. Joshi, R. V. Upadhyay and Ravikumar, Nucl. Instr. and Meth. **B 244** (2006) 124

6B.2 M. Singh, Anjana Dogra and Ravi Kumar, Nucl. Instr. and Meth. **B 196** (2002) 315

6B.3 Anjana Dogra, M. Singh and Ravi Kumar, Nucl. Instr. and Meth. **B 207** (2003) 296

6B.4 G. N. Abelyashev et al, Sov. Phys Solid State, **33 (6)** (1990) 1059

6B.5 G. Blasse, Philips Res. Rept. Suppl. **3** (1964) 1

6B.6 Hua Yang et al, Matt. Letters **57** (2003)2455

6B.7 G. Gavollie and J. Hubsch, J. Mag. Mag. Mat. **36** (183) 304

6B.8 C. R. K. Murty and N. G. Nandikar, Pramana **13** (1979) 413

6B.9 M. J. Buerger, Crystal Structure Analysis, John Wiley, New York, 1960

6B.10 L. Neel, Ann. Phys. **3** (1948) 137

6B.11 J. R. Gabrial and S. L. Ruby, Nucl. Instr. and Meth. **36** (1965) 23

6B.12 D. Ravinder, Cryst. Technol. **26** (1991) 457

6B.13 D. Ravinder, Mater. Lett. **40** (1999) 198

6B.14 K. B. Modi, J. D. Gajera, M. C. Chhantbar, K. G. Saija, G. J. Baldha and H. H. Joshi, Mater. Lett. **57** (2003) 4059

6B.15 Mamata Maisnam, Sumitra Phanjoubam, H. N. K. Sarma, Chnadra Prakasha, L. Radhapiyari and O. P. Thakur, Physica B **370** (2005) 1

6B.16 J. Smith and H. P. J. Wijn, Ferrites, Philips, Eindhoven, (1959)

6B.17 K. E. Sickafus and J. M. Wills, J. Am. Ceram. Soc. **82** (1999) 3279

6B.18 A, Globus, H. Pascard and V. Cagan, J. Phys. Suppl. **438** (1977) 439

6B.19 S. A. Mazen, M. H. Abdallah, B. A. Sabrah and H. A. M. Hasham, Phys. Stat. Sol. a **134** (1992) 263

6B.20 S. S. Bellad, R. B. Pujar, B. K. Chougule, Mater. Chem. Phys. **52** (1998) 166

6B.21 S. S. Bellad, S. C. Watawe and B. K. Chougule, J. Magn. Magn. Mater. **195** (1999) 57

6B.22 E. W. Gorter, Philips Res. Rept. **9** (1954) 321

6B.23 J. Kanamori, J. Phys. Chem.. Solids **67** (1959) 10

6B.24 B. Viswanathan and V. R. K. Murthy, "Ferrite Materials Science and Technology", Narosa Publishing House (1990) Chapter-1, Page No. 9

6B.25 K. Mohan and Venudhar, J. Mater. Sci. Lett. **18** (1999) 13

6B.26 K. B. Modi, J. Mater. Sci. **39** (2004) 2887

6B.27 R. D. Waldron, Phys Rev. **99** (1955) 1727

6B.28 D. Ravinder, J. Mater. Lett. **40** (1999) 205

6B.29 B. P. Ladgaonkar, C. B. Kolekar and A. S. Vaingankar, Bull. Mater. Sci. **25** (2002) 351

6B.30 V. A. M. Brabers, Phys. Stat. sol. **33** (1969) 563

6B.31 S. T. Hafner and Z Kristallogr. **115** (1961) 331

6B.32 S. A. Mazen, M. H. Abdallah, R. I. Nakhla, H. M. Zaki and F. Metawe, Mater. Chem. Phys. **34** (1993) 35

6B.33 S. S. Bellad, R. B. Pujar and B. K. Chougule, Ind. J. Pure & Appl. Phys. **36** (1998) 598

6B.34 K. B. Modi, J. D. Gajera, M. P. Pandya, H. G. Vora and H. H. Joshi, PRAMANA- J. Phys. **62(5)** (2004) 1173

6B.35 V. R. Potakova, N. D. Zevrey and V. P. Romanov , Phys. Stat. Sol. a **12** (1972) 623

6B.36 P. V. Reddy and V. D. Reddy, J. Magn. Magn. Mater. **136** (1994) 279

6B.37 K. B. Modi, M. C. Chhantbar, P. U. Sharma and H. H. Joshi, J. Mater. Sci. **40 (5)** (2005) 1247

6B.38 Michel de Podesta, "Understanding the properties of matter" second edition, Published by Taylor & Francis (2002) chapter 7, page no. 195-196

6B.39 D. P. H. Hosselman and R. M. Fulrath, J. Amer Ceramic Soc., **47** (1964) 52

6B.40 K. B. Modi, M. K. Rangolia, M. C. Chhantbar and H. H. Joshi, J. Mater. Sci. **41** (2006) 7308

6B.41 O. L. Anderson, in "Physical Acoustics" edited by W. P. Mason, vol. **3B** (Academic Press, New York, 1965) P. 45

6B.42 Long Wu, Tien-Shou Wu and Chung-Chuang Wei, J. Phys. D: Appl. Phys. **13** (1980) 259

6B.43 B. V. Bhise, V. C. Mahajan, M. G. Patil, S. D. Lotke and S. A. Patil, Ind. J. Pure & Appl. Phys. **33** (1995) 459

6B.44 B. Gillot and F. Jemmali, Phys. Stat. Sol. a **76** (1983) 601

6B.45 O. M. Hemeda, M. A. Amer, S. Aboul-Enein, M. A. Ahmed, Phys. Stat. Sol. a **156** (1996) 29

6B.46 H. Pascard, A. Globus and V. Cabon. J. Phys. **38** (1977) C1-163

6B.47 F. C. Romeijn, Philips Res. Rep. **8** (1953) 316

6B.48 A. B. Naik and J. I. Powar, Ind. J. Pure & Appl. Phys. **23** (1985) 436

6B.49 A. J. Bosman and H. J. Van Dall, Adv. Phys. 19 (1970) 1

6B.50 S. S. Bashikirav, A. B. Liberman and V. V. Parfenov, Inorg. Mater. **15** (1979) 404

6B.51 A. J. Bosman and C. Crevecoeur, J. Phys. Chem. Solids **30** (1969) 1151

6B.52 B. P. Ladgaonkar, P. N. Vasamber and A. S. Vaingankar, Bull. Mater. Sci. **23(2)** (2000) 87

6B.53 M. A. Ahmed, M. K. El. Nimr, A. Tawfik and A. M. El. Hasab, Phys. Stat. Sol. (a) **123** (1991) 501

6B.54 K. Radha and D. Ravinder, Ind. J. Pure & Appl. Phys. **33** (1995) 74

6B.55 D. Ravinder, J. Mater. Sci. Lett. **11** (1992) 1498

6B.56 Y. Purusotham, M. B. Reddy, P. P. Kishan, D. Sagar and V. Reddy, Mater. Lett. (North Holland) **17** (1993) 341

6B.57 O. S. Josyulu and J. Sobhanadri, Phys. Stat. Sol. (a), **59** (1980) 323

6B.58 Kozo Iwauchi, Jpn J Appl Phys. **10** (1971) 1520

6B.59 L. I. Rabinkin and Z. I. Novikova, Ferrites, Minsk (1960) 146

6B.60 P. V. Reddy, T. S. Rao and S. M. D. Rao, J. Less-Common Met. **79** (1981) 191

6B.61 P. V. Reddy, F. S. Rao and S. M. D. Rao, J. Less-Common Met. **79** (1981)1

6B.62 M. A. Ahmed, M. A. El Hiti , M. K. El-Nimr and M. Amer, J. Magn. Magn. Mater. **152** (1995) 391

6B.63 M. A. El Hiti, M. K. El-Nimr and M. A. Ahmed, Phase Trans. **54** (1995)137

6B.64 N. Rezlescu and E. Rezlescu, Phys. Stat. Sol. (a) **23** (1974) 575

6B.65 P. Debye, "Polar Molecules", chemical catalogue Company, New York (1929)

6B.66 A. M. El-Rifae, Egypt. J. Sol. **23(1)** (2000) 93

6B.67 A. M. Shaikh, S. S. Bellad and B. K. Chougule, J. Magn. Magn. Mater. **195** (1999) 384

6B.68 D. Ravinder and P. Vijaya Bhasker Reddy, Mater. Lett. **57** (2003) 4344

6B.69 C. G. Koops, Phys. Rev. **83** (1951) 121

6B.70 J. C. Maxwell, ''Electricity and magnetism'' (Oxford University Press, London, 1873) Section 328

6B.71 K. W. Wagner, Ann. Phys. **40** (1913) 817

6B.72 Manas Chanda, "Science of engineering materials" **Vol 3** (The Macmillan Company of India Ltd., New Delhi, India, 1989) p. 267

6B.73 B. Parvatheeswara Rao and K. H. Rao, J. Mater. Sci. **32** (1997) 6049

6B.74 V. R. Kulkarni and A. S. Varingankar, J. Mater. Sci. **22** (1987) 4087

6B.75 M. A. Ahemed, M. K. El-Nimr, A. Tawfik and A. M. El-Hasab, J. Magn. Magn. Mater. **98** (1991) 33

6B.76 M. A. Hiti, M. A Ahemed, M. M. Mosaad and S. M. Attia, J. Magn. Magn. Mater. **150** (1995) 399

6B.77 N. Sivkumar, A. Narayanswamy, C. N. Chinnasamy and B. Jeyadevan, J. Phys. Condens. Matt. **19** (2007) 38620

6B.78 N. Ponpandian and A. Narayanasamy, J. Appl. Phys. **92(5)** (2002) 2770

Table 6B.1: Chemical composition and molecular weight of each specimen of the spinel system: $Li_{0.5(1+x)}Ti_xCr_{0.1}Fe_{2.4-1.5x}O_4$

Content (x)	Chemical composition	Molecular weight (amu)
0.0	$Li_{0.5}Cr_{0.1}Fe_{2.4}O_4$	206.6995
0.1	$Li_{0.55}Ti_{0.1}Cr_{0.1}Fe_{2.25}O_4$	203.4594
0.2	$Li_{0.6}Ti_{0.2}Cr_{0.1}Fe_{2.1}O_4$	200.2193
0.3	$Li_{0.65}Ti_{0.3}Cr_{0.1}Fe_{1.95}O_4$	196.9792

Table 6B.2: Results of XRD intensity analysis and Cation distributions for unirradiated and irradiated samples of $Li_{0.5(1+x)}Ti_xCr_{0.1}Fe_{2.4-1.5x}O_4$ system

(x)	Sample	I(220)/I(440)		I(400)/I(422)		Cation Distribution
		theo.	obs.	theo.	obs.	
0.0	Unirr	0.879	0.793	1.131	1.448	(Fe) $[Li_{0.5}Cr_{0.1}Fe_{1.4}]O_4$
	Irr	0.876	0.905	1.132	1.359	(Fe) $[Li_{0.5}Cr_{0.1}Fe_{1.4}]O_4$
0.1	Unirr	0.887	0.737	1.115	1.399	$(Fe_{0.96}Ti_{0.04})$ $[Li_{0.55}Ti_{0.06}Cr_{0.1}Fe_{1.29}]O_4$
	Irr	0.886	0.845	1.102	1.285	$(Fe_{0.962}Ti_{0.038})$ $[Li_{0.55}Ti_{0.062}Cr_{0.1}Fe_{1.288}]O_4$
0.2	Unirr	0.920	0.573	1.045	1.309	$(Fe_{0.93}Ti_{0.07})$ $[Li_{0.6}Ti_{0.13}Cr_{0.1}Fe_{1.17}]O_4$
	Irr	0.924	0.888	1.022	1.236	$(Fe_{0.934}Ti_{0.066})$ $[Li_{0.6}Ti_{0.134}Cr_{0.1}Fe_{1.166}]O_4$
0.3	Unirr	0.851	0.529	1.269	1.445	$(Fe_{0.85}Ti_{0.15})$ $[Li_{0.65}Ti_{0.15}Cr_{0.1}Fe_{1.1}]O_4$
	Irr	0.947	1.021	1.149	1.292	$(Fe_{0.87}Ti_{0.13})$ $[Li_{0.65}Ti_{0.17}Cr_{0.1}Fe_{1.08}]O_4$

Table 6B.3: Lattice constant (a), Magneton number (η_B), Curie temperature (T_c) and iron distribution parameter ($\delta = Fe^{3+}{}_A/Fe^{3+}{}_B$) for unirradiated and irradiated samples of $Li_{0.5(1+x)}Ti_xCr_{0.1}Fe_{2.4-1.5x}O_4$ system

Content (x)	Sample	a_{exp}(Å) ±0.002 Å	$\eta_B{}^{obs}$ (μ_B)	$\eta_B{}^{N}$ (μ_B)	T_c(K) ±5K	$\delta = Fe^{3+}{}_A/Fe^{3+}{}_B$	
						XRD	Moss
0.0	Unirr	8.326	2.29	2.30	865	0.71	0.68
	Irr	8.329	2.29	2.30	856	0.71	0.71
0.1	Unirr	8.328	1.93	1.95	857	0.74	0.72
	Irr	8.331	1.92	1.93	780	0.75	0.77
0.2	Unirr	8.329	1.48	1.50	784	0.79	0.77
	Irr	8.338	1.45	1.46	714	0.80	0.79
0.3	Unirr	8.331	1.51	1.55	755	0.77	0.74
	Irr	8.347	1.29	1.35	677	0.81	0.80

Table 6B.4: Mössbauer parameters: Hyperfine field (H_{nf}), Isomer shift (I.S), Line width ($\Delta\Gamma$), paramagnetic fraction (I_d) for the unirradiated and irradiated samples of $Li_{0.5(1+x)}Ti_xCr_{0.1}Fe_{2.4-1.5x}O_4$ system

Content (x)	Sample	H_{nf} (kOe) ± 2 kOe		I.S (mm/sec) ± 0.03		$\Delta\Gamma$ (mm/s) ± 0.03		I_d%
		A-site	B-site	A-site	B-site	A-site	B-site	
0.0	Unirr	493	506	0.38	0.45	0.50	0.37	Absent
	Irr	494	508	0.40	0.43	0.50	0.51	
0.1	Unirr	490	504	0.40	0.46	0.51	0.25	
	Irr	485	502	0.37	0.42	0.64	0.39	
0.3	Unirr	465	489	0.40	0.43	0.61	0.32	
	Irr	462	487	0.35	0.41	0.75	0.44	

Table 6B.5: Theoretical lattice constant (a_{th}), Bulk density (d), X-ray density (d_x), Pore fraction (f) and Percentage of porosity (P) for unirradiated and irradiated $Li_{0.5(1+x)}Ti_xCr_{0.1}Fe_{2.4-1.5x}O_4$ ferrite system

Content (x)	Sample	a_{th} (Å)± 0.0002(Å)	Bulk density (d) $(kg/m^3)x10^3$	X-ray density (d_x) $(kg/m^3)x10^3$	Pore fraction (f)	Porosity P (%)
0.0	Unirr	8.2829	4.1248	4.7591	0.1332	13.328
	Irr	8.2829	4.4648	4.7539	0.0608	6.081
0.1	Unirr	8.2925	3.9374	4.6811	0.1588	15.887
	Irr	8.2926	4.0395	4.6761	0.1361	13.614
0.2	Unirr	8.3021	3.5170	4.6112	0.2372	23.729
	Irr	8.3020	3.8924	4.5900	0.1519	15.198
0.3	Unirr	8.3121	3.3197	4.5271	0.2667	26.671
	Irr	8.3119	3.5236	4.5011	0.2171	21.710

Table 6B.6: Ionic radii (r_A, r_B), bond lengths (A-O, B-O), oxygen positional parameter (u) and site radii (R_A, R_B) for unirradiated and irradiated $Li_{0.5(1+x)}Ti_xCr_{0.1}Fe_{2.4-1.5x}O_4$ ferrite system

(x)	Sample	r_A (Å)	r_B (Å)	A – O $(r_A + r_O)$	B – O $(r_B + r_O)$	u (Å)	R_A (Å)	R_B (Å)
0.0	Unirr	0.6400	0.6545	1.9600	1.9745	0.2619	1.9742	1.9874
	Irr	0.6400	0.6545	1.9600	1.9745	0.2619	1.9750	1.9881
0.1	Unirr	0.6416	0.6572	1.9616	1.9772	0.2615	1.9689	1.9908
	Irr	0.6415	0.6573	1.9615	1.9773	0.2611	1.9639	1.9946
0.2	Unirr	0.6428	0.6601	1.9628	1.9801	0.2610	1.9620	1.9948
	Irr	0.6426	0.6602	1.9628	1.9802	0.2614	1.9699	1.9940
0.3	Unirr	0.6460	0.6620	1.9660	1.9820	0.2615	1.9697	1.9916
	Irr	0.6452	0.6624	1.9652	1.9824	0.2611	1.9676	1.9983

Table 6B.7: Inter-ionic distances between cation-anion (Me-O), cation-cation (Me-Me) and bond angles (θ) for unirradiated and irradiated $Li_{0.5(1+x)}Ti_xCr_{0.1}Fe_{2.4-1.5x}O_4$ ferrite system

Me – O (Å)								
x	0.0		0.1		0.2		0.3	
Sample	Unirr	Irr	Unirr	Irr	Unirr	Irr	Unirr	Irr
p	1.9824	1.9831	1.9862	1.9903	1.9906	1.9895	1.9869	1.9941
q	1.9742	1.9750	1.9689	1.9639	1.9620	1.9699	1.9697	1.9676
r	3.7804	3.7818	3.7702	3.7606	3.7569	3.7720	3.7716	3.7678
s	3.6624	3.6638	3.6614	3.6608	3.6594	3.6653	3.6627	3.6678
Me – Me (Å)								
x	0.0		0.1		0.2		0.3	
Sample	Unirr	Irr	Unirr	Irr	Unirr	Irr	Unirr	Irr
b	2.9437	2.9448	2.9444	2.9455	2.9448	2.9479	2.9455	2.9511
c	3.4518	3.4530	3.4526	3.4539	3.4530	3.4568	3.4539	3.4605
d	3.6053	3.6066	3.6061	3.6074	3.6066	3.6105	3.6074	3.6144
e	5.4079	5.4098	5.4092	5.4111	5.4098	5.4157	5.4111	5.4215
f	5.0986	5.1005	5.0998	5.1017	5.1005	5.1060	5.1017	5.1115
Bond angles (θ)								
x	0.0		0.1		0.2		0.3	
Sample	Unirr	Irr	Unirr	Irr	Unirr	Irr	Unirr	Irr
θ_1	121.48°	121.48°	121.61°	121.73°	121.76°	121.63°	121.61°	121.73°
θ_2	137.35°	137.35°	137.83°	138.30°	138.43°	137.94°	137.83°	138.30°
θ_3	95.88°	95.89°	95.67°	95.46°	95.41°	95.61°	95.67°	95.46°
θ_4	126.58°	126.58°	126.53°	126.48°	126.48°	126.52°	126.53°	126.49°
θ_5	69.65°	69.65°	69.96°	70.27°	70.36°	70.04°	69.96°	70.28°

Table 6B.8: Positions of IR main absorption bands (ν_1,ν_2), Subsidiary band position (ν^*) and average of main IR absorption bands (ν_{1avg},ν_{2avg}) for unirradiated and irradiated $Li_{0.5(1+x)}Ti_xCr_{0.1}Fe_{2.4-1.5x}O_4$ ferrite system

x	Sample	ν^* (m^{-1}) x 10^2	ν_1 (m^{-1}) x 10^2	ν_{1avg} (m^{-1}) x 10^2	ν_2 (m^{-1}) x 10^2	ν_{2avg} (m^{-1}) x 10^2
0.0	Unirr	710.7, 675.0	584.4, 551.6	568.0	471.6, 452.3, 442.6, 433.0, 415.6, 408.6	437.3
	Irr	705.9, 670.2, 652.9	589.2, 551.6, 540.0, 522.7, 512.7, 501.5	536.3	477.3, 469.6, 461.9, 442.6, 430.1, 419.5, 412.7, 405.0	439.8
0.1	Unirr	-	582.4, 550.3	581.4	469.3, 405.5	437.40
	Irr	670.0	586.3, 559.3, 538.1, 515.0	549.7	480.2, 447.5, 428.2, 415.0	442.7
0.2	Unirr	-	588.2	588.2	475.4	475.4
	Irr	653.8, 634.5, 592.9	587.5, 551.6, 536.2	558.4	489.9, 468.7, 451.3, 416.6	456.6
0.3	Unirr	-	588.8	588.8	469.1	469.1
	Irr	667.3, 646.1, 601.7	586.3, 565.1, 540.0, 515.0	563.8	488.0, 462.9, 447.5, 405.0	466.1

Table 6B.9: Molecular weight (M_1, M_2) of A & B-sites, force constants (k_t, k_o) of A & B- sites respectively and average force constant (k) for unirradiated and irradiated $Li_{0.5(1+x)}Ti_xCr_{0.1}Fe_{2.4-1.5x}O_4$ ferrite system

x	Sample	M_1 (kg) x 10^{-3}	$M_2/2$ (kg) x 10^{-3}	k_t (N/m) x 10^2	k_o(N/m) x 10^2	k (N/m) x 10^2
0.0	Unirr	55.8470	43.4280	1.3729	0.8820	1.1275
	Irr	55.8470	43.4280	1.2240	0.8921	1.0581
0.1	Unirr	55.5283	41.9663	1.4303	0.8528	1.1416
	Irr	55.5443	41.9583	1.2789	0.8733	1.0761
0.2	Unirr	55.2893	40.4648	1.4576	0.9712	1.2144
	Irr	55.3212	40.4489	1.3144	0.8956	1.1050
0.3	Unirr	54.6520	39.1625	1.4438	0.9152	1.1795
	Irr	54.8113	39.0828	1.3276	0.9018	1.1147

Table 6B.10: longitudinal elastic wave velocity (υ_l), transverse elastic wave velocity (υ_s), Mean elastic wave velocity (υ_m) and Debye temperature (θ_D) for unirradiated and irradiated $Li_{0.5(1+x)}Ti_xCr_{0.1}Fe_{2.4-1.5x}O_4$ ferrite system

x	Sample	υ_l (m/s)	υ_s (m/s)	υ_m (m/s)	θ_D (K)
0.0	Unirr	5334.32	3079.77	3419.13	468.1
	Irr	5169.46	2984.59	3313.46	453.4
0.1	Unirr	5411.44	3124.30	3468.57	474.7
	Irr	5255.80	3034.44	3368.80	460.9
0.2	Unirr	5623.05	3246.47	3604.20	493.5
	Irr	5373.42	3102.35	3444.20	470.8
0.3	Unirr	5592.31	3228.72	3584.49	490.5
	Irr	5446.86	3144.75	3491.24	476.8

Table 6B.11: Bulk modulus (B), Young's modulus (E), rigidity modulus (G) and Poisson's ratio (σ) for unirradiated and irradiated $Li_{0.5(1+x)}Ti_xCr_{0.1}Fe_{2.4-1.5x}O_4$ ferrite system

x	Sample	B (GPa)	E (GPa)	G (GPa)	σ
0.0	Unirr	135.42	121.88	45.14	0.35
	Irr	127.04	114.35	42.35	0.35
0.1	Unirr	137.08	123.36	45.69	0.35
	Irr	129.17	116.26	43.06	0.35
0.2	Unirr	145.80	131.22	48.60	0.35
	Irr	132.53	119.29	44.18	0.35
0.3	Unirr	141.58	127.41	47.19	0.35
	Irr	133.54	120.18	44.51	0.35

Table 6B.12: Corrected to zero porosity of elastic moduli: Bulk modulus (B_0), Young's modulus (E_0), rigidity modulus (G_0) and Poisson's ratio (σ_0) for unirradiated and irradiated $Li_{0.5(1+x)}Ti_xCr_{0.1}Fe_{2.4-1.5x}O_4$ ferrite system

x	Sample	B_0 (GPa)	E_0 (GPa)	G_0 (GPa)	σ_0
0.0	Unirr	238.64	166.03	59.98	0.38
	Irr	158.46	130.15	47.74	0.36
0.1	Unirr	283.12	180.62	64.80	0.39
	Irr	231.46	159.64	57.63	0.38
0.2	Unirr	635.92	249.26	86.87	0.43
	Irr	261.90	171.21	61.54	0.39
0.3	Unirr	1062.98	272.51	93.50	0.46
	Irr	453.81	212.12	74.58	0.42

Table 6B.13: dc resistivity ($\log_{10}\rho_{dc}$), Activation energy (E) and Nèel temperature (T_N) for unirradiated and irradiated $Li_{0.5(1+x)}Ti_xCr_{0.1}Fe_{2.4-1.5x}O_4$ ferrite system

x	Sample	$\log_{10}\rho_{dc}$ (Ω.cm) (313K)	Activation energy (eV)		ΔE (eV)	T_N(K) ± 5K	
			E_f	E_p		Resistivity	Susceptibility
0.0	Unirr	5.92	0.285	0.951	0.666	813	865
	Irr	5.05	0.272	0.224	0.048	793	856
0.1	Unirr	6.91	0.460	1.052	0.592	853	857
	Irr	6.02	0.349	0.670	0.321	773	780
0.2	Unirr	5.82	0.344	0.829	0.485	783	784
	Irr	6.72	0.396	0.502	0.106	763	714
0.3	Unirr	7.21	0.417	1.106	0.689	743	755
	Irr	6.65	0.381	0.488	0.107	693	677

Table 6B.14: Jump length (L), Polaron radius (r_P) and Fermi energy ($E_F(0)$) for unirradiated and irradiated $Li_{0.5(1+x)}Ti_xCr_{0.1}Fe_{2.4-1.5x}O_4$ ferrite system

x	Sample	Jump length L (Å)		Polaron radius r_p (Å)	Fermi energy $\|E_f(0)\|$ (eV)
		L_A	L_B		
0.0	Unirr	3.6053	2.9437	0.7327	0.1315
	Irr	3.6066	2.9447	0.7330	0.1957
0.1	Unirr	3.6061	2.9444	0.7329	0.2411
	Irr	3.6074	2.9455	0.7331	0.7877
0.2	Unirr	3.6066	2.9447	0.7330	0.9027
	Irr	3.6105	2.9479	0.7337	0.2214
0.3	Unirr	3.6074	2.9455	0.7331	1.1710
	Irr	3.6144	2.9511	0.7345	2.4821

Table 6B.15: Compositional variation of dielectric constant (ε') at different temperature and frequency for unirradiated and irradiated $Li_{0.5(1+x)}Ti_xCr_{0.1}Fe_{2.4-1.5x}O_4$ ferrite system

x	1kHz (ε')							
	300K		373K		573K		773K	
	Unirr	Irr	Unirr	Irr	Unirr	Irr	Unirr	Irr
0.0	242.76	57219.98	286.61	6231.98	438.16	455.27	5235.86	1572.16
0.1	164.39	985.02	194.26	261.86	278.32	192.17	186.85	275.59
0.2	76.12	437.43	80.17	359.83	108.22	797.16	112.41	5864.88
0.3	89.70	984.77	93.14	747.50	103.50	260.56	106.92	4717.73
10kHz (ε')								
0.0	154.49	20581.82	183.63	4191.11	323.31	378.58	1670.43	516.48
0.1	108.89	326.13	129.22	185.36	237.02	220.80	171.60	337.69
0.2	68.39	172.12	70.92	233.47	98.40	486.59	99.11	2469.42
0.3	85.66	273.89	86.58	240.29	99.08	164.89	102.42	1767.01
50kHz (ε')								
0.0	130.21	6379.20	142.16	2611.61	245.92	254.54	716.73	---
0.1	97.01	147.44	105.70	141.42	188.41	199.00	159.46	254.66
0.2	65.24	79.31	67.81	125.62	82.42	316.23	89.15	1098.95
0.3	84.01	85.41	84.51	112.91	79.14	115.01	85.96	562.12
500kHz (ε')								
0.0	114.73	785.89	120.21	1030.07	160.27	115.83	271.35	---
0.1	89.94	51.86	92.63	72.42	120.64	123.86	142.75	138.29
0.2	60.90	31.77	63.12	39.56	68.89	136.27	77.84	244.97
0.3	78.04	29.17	78.35	38.29	87.68	107.86	95.53	129.27
1MHz (ε')								
0.0	111.57	387.16	116.16	731.24	144.93	93.58	220.88	---
0.1	87.64	38.75	90.61	55.31	108.01	104.35	132.98	106.15
0.2	59.47	27.03	61.51	30.73	66.75	100.98	74.98	132.35
0.3	75.80	26.03	76.12	30.84	85.65	77.66	92.62	79.26

Table 6B.16: Compositional variation of a.c. resistivity ($\log_{10}\rho_{ac}$) at different temperature and frequency for unirradiated and irradiated $Li_{0.5(1+x)}Ti_xCr_{0.1}Fe_{2.4-1.5x}O_4$ ferrite system

x	1kHz ($\log_{10}\rho_{ac}$)							
	300K		373K		573K		773K	
	Unirr	Irr	Unirr	Irr	Unirr	Irr	Unirr	Irr
0.0	4.4577	4.2310	6.2251	4.2970	4.9811	3.9036	3.7964	3.0484
0.1	7.1237	5.9838	6.8718	5.9099	5.2308	4.5593	3.9951	3.5351
0.2	7.9269	6.5311	7.7706	6.4182	6.0726	4.8253	4.7341	3.7199
0.3	8.1789	5.7089	8.0975	5.9498	6.5665	4.8785	5.1754	3.4815
10kHz ($\log_{10}\rho_{ac}$)								
0.0	6.3043	3.7933	6.0379	4.1569	4.9134	3.8691	3.7368	2.8526
0.1	6.8072	5.6493	6.4664	5.7022	5.1562	4.4427	3.9634	3.4968
0.2	7.5450	6.0653	7.3124	5.9244	5.9250	4.6659	4.5838	3.6659
0.3	7.6482	5.4705	7.5478	5.6995	6.3448	4.7163	5.0466	3.4431
50kHz ($\log_{10}\rho_{ac}$)								
0.0	6.0979	3.4953	5.8238	3.9900	4.8716	3.8645	3.6798	---
0.1	6.5175	5.3607	6.1693	5.5156	5.0638	4.4037	3.9882	3.4782
0.2	7.0182	5.6899	6.8946	5.5252	5.8026	4.5443	4.5427	3.6079
0.3	7.0278	5.2810	6.9125	5.4228	6.3425	4.6504	5.0195	3.4259
500kHz ($\log_{10}\rho_{ac}$)								
0.0	5.6161	3.1846	5.4296	3.5392	4.6040	3.8152	3.5813	---
0.1	5.9186	4.9009	5.7124	4.8897	4.7321	4.2504	3.9387	3.4066
0.2	6.1869	5.2738	6.1232	5.0119	5.5417	4.2637	4.4548	3.4369
0.3	5.9908	5.1126	6.0392	5.0175	5.8102	4.1918	4.9456	3.3966
1MHz ($\log_{10}\rho_{ac}$)								
0.0	5.3809	3.0996	5.2493	3.3283	4.4955	3.7803	3.5400	---
0.1	5.6366	4.7642	5.5342	4.6849	4.6261	4.1568	3.9038	3.3775
0.2	5.9182	5.1485	5.8870	4.9104	5.4158	4.1406	4.4248	3.3852
0.3	5.7164	5.0482	5.7923	4.9174	5.6581	4.1072	4.8959	3.3708

Table 6B.17: Compositional variation of loss tangent (tanδ) at different temperature and frequency for unirradiated and irradiated $Li_{0.5(1+x)}Ti_xCr_{0.1}Fe_{2.4-1.5x}O_4$ ferrite system

x	1kHz (tanδ)							
	300K		373K		573K		773K	
	Unirr	Irr	Unirr	Irr	Unirr	Irr	Unirr	Irr
0.0	2.5826	1.8465	3.7366	14.5629	34.0891	328.7816	54.8977	1023.42
0.1	0.8228	1.8950	1.2436	8.4506	32.4801	172.1097	973.5272	1903.35
0.2	0.2796	1.2103	0.3804	1.9082	11.8240	22.4906	295.1485	58.4440
0.3	0.1328	3.5702	0.1543	2.7009	4.0547	60.8672	112.3225	125.7854
10kHz (tanδ)								
0.0	0.5777	1.4063	0.8975	2.9897	6.7909	64.2125	19.7381	488.9364
0.1	0.2574	1.2365	0.4755	1.9260	5.2961	29.3878	114.0190	169.6567
0.2	0.0750	0.8991	0.1235	0.9167	2.1722	7.9772	47.3093	15.7169
0.3	0.0472	2.2224	0.0588	1.4951	0.8205	20.9609	15.7728	36.6906
50kHz (tanδ)								
0.0	0.2205	1.8026	0.3797	1.4093	1.9657	19.3056	10.4902	---
0.1	0.1126	1.0632	0.2305	0.7760	1.6484	7.1355	23.1767	46.9644
0.2	0.0529	0.9262	0.0676	0.8545	0.6875	3.2481	11.5653	8.0725
0.3	0.0402	2.2050	0.0521	1.2032	0.2066	6.9947	4.0006	24.0015
500kHz (tanδ)								
0.0	0.0759	2.9922	0.1113	1.0089	0.5586	4.7520	3.4765	---
0.1	0.0482	0.8714	0.0753	0.6403	0.5525	1.6317	2.9019	10.1974
0.2	0.0384	0.6029	0.0429	0.8847	0.1500	1.4383	1.6213	5.3696
0.3	0.0471	0.9515	0.0419	0.9022	0.0635	2.1441	0.4268	11.1657
1MHz (tanδ)								
0.0	0.0671	3.6929	0.0872	1.1549	0.3965	3.1869	2.3483	---
0.1	0.0474	0.7988	0.0580	0.6717	0.3939	1.2011	1.6879	7.1040
0.2	0.0365	0.4726	0.0379	0.7195	0.1034	1.2883	0.9019	5.5969
0.3	0.0456	0.6182	0.0381	0.7055	0.0461	1.8092	0.2468	9.6609

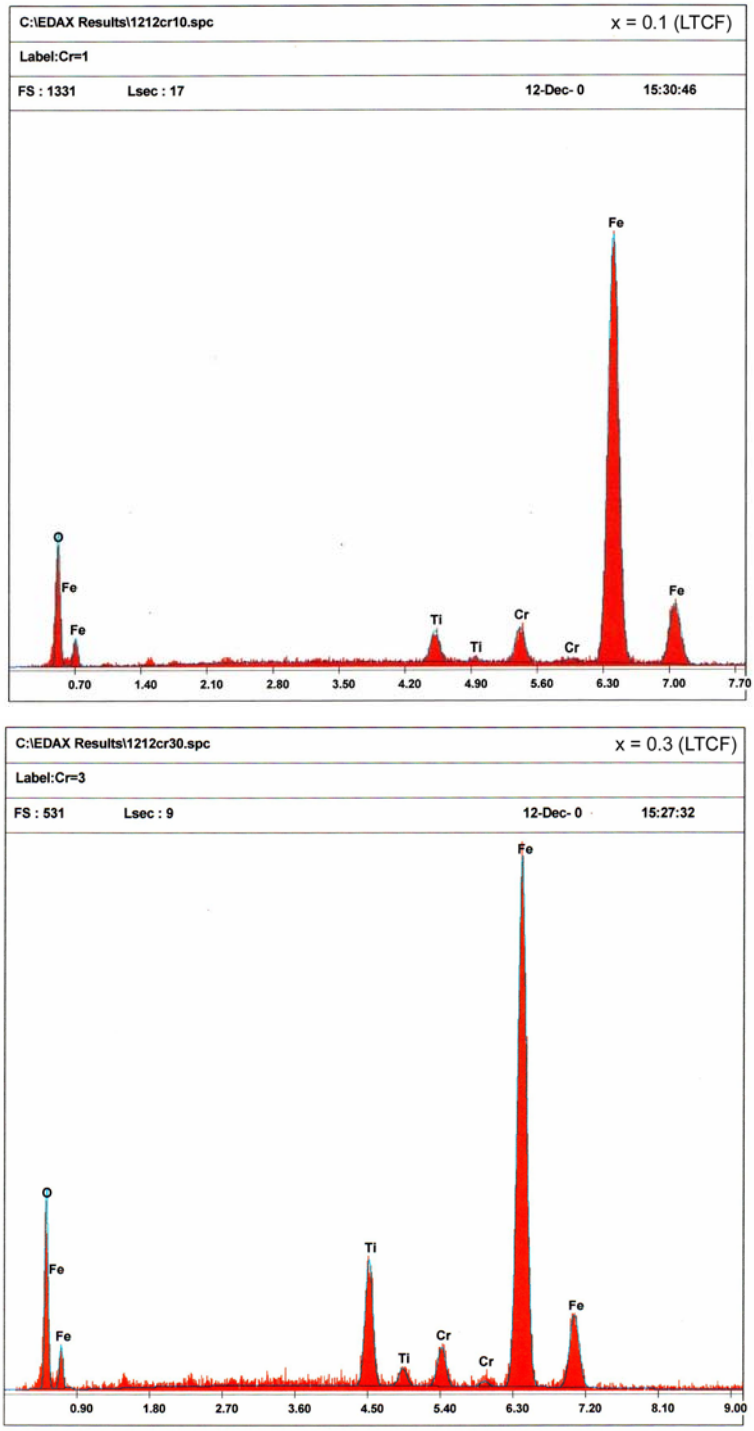

Fig. 6B.1 EDAX patterns for the compositions x = 0.1 & 0.3 of the system $Li_{0.5(1+x)}Ti_xCr_{0.1}Fe_{2.4-1.5x}O_4$

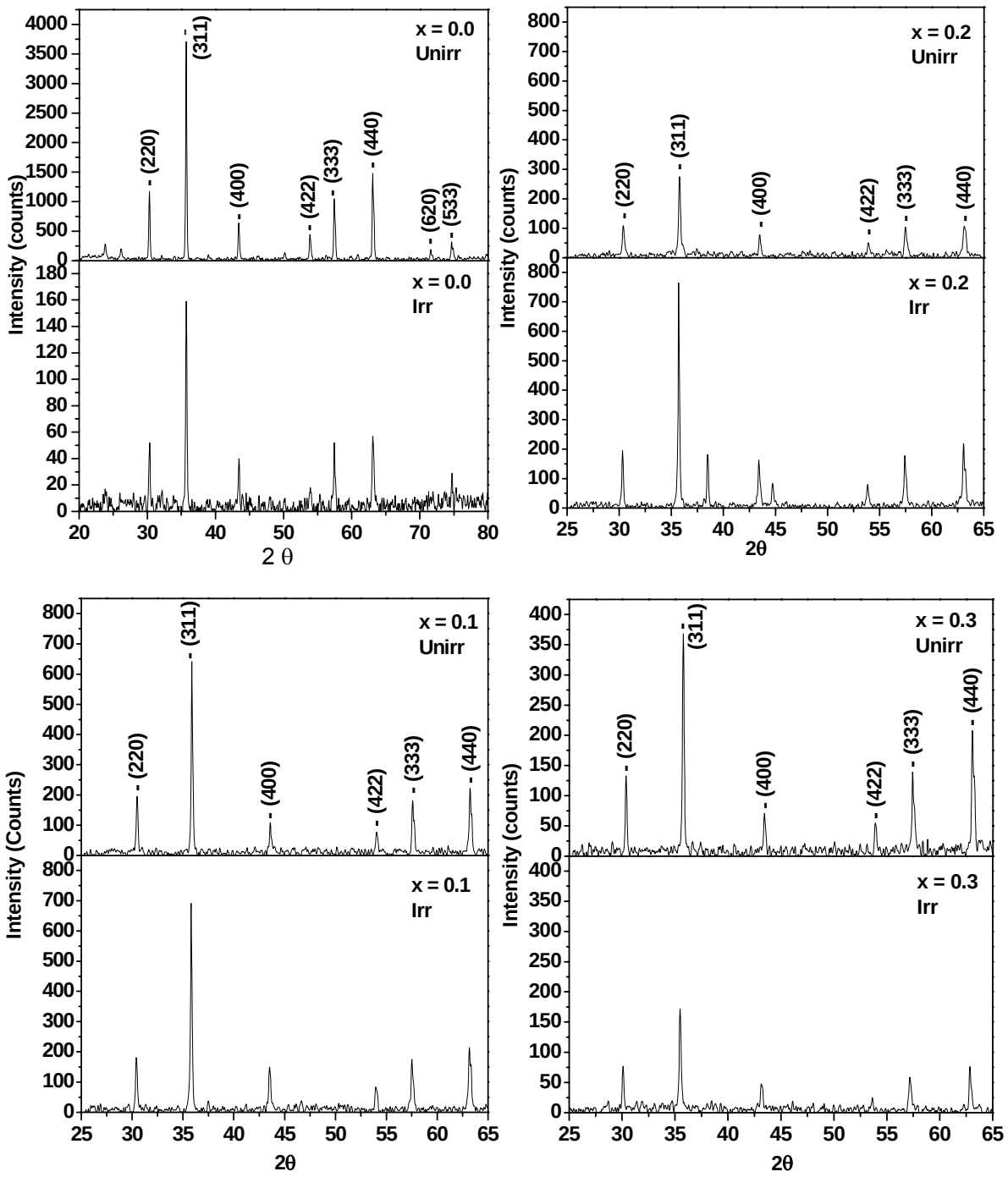

Fig. 6B.2 X-ray diffraction patterns: x = 0.0, 0.1, 0.2 and 0.3 of the unirradiated and irradiated $Li_{0.5(1+x)}Ti_xCr_{0.1}Fe_{2.4-1.5x}O_4$ system, λ = 1.5406 Å

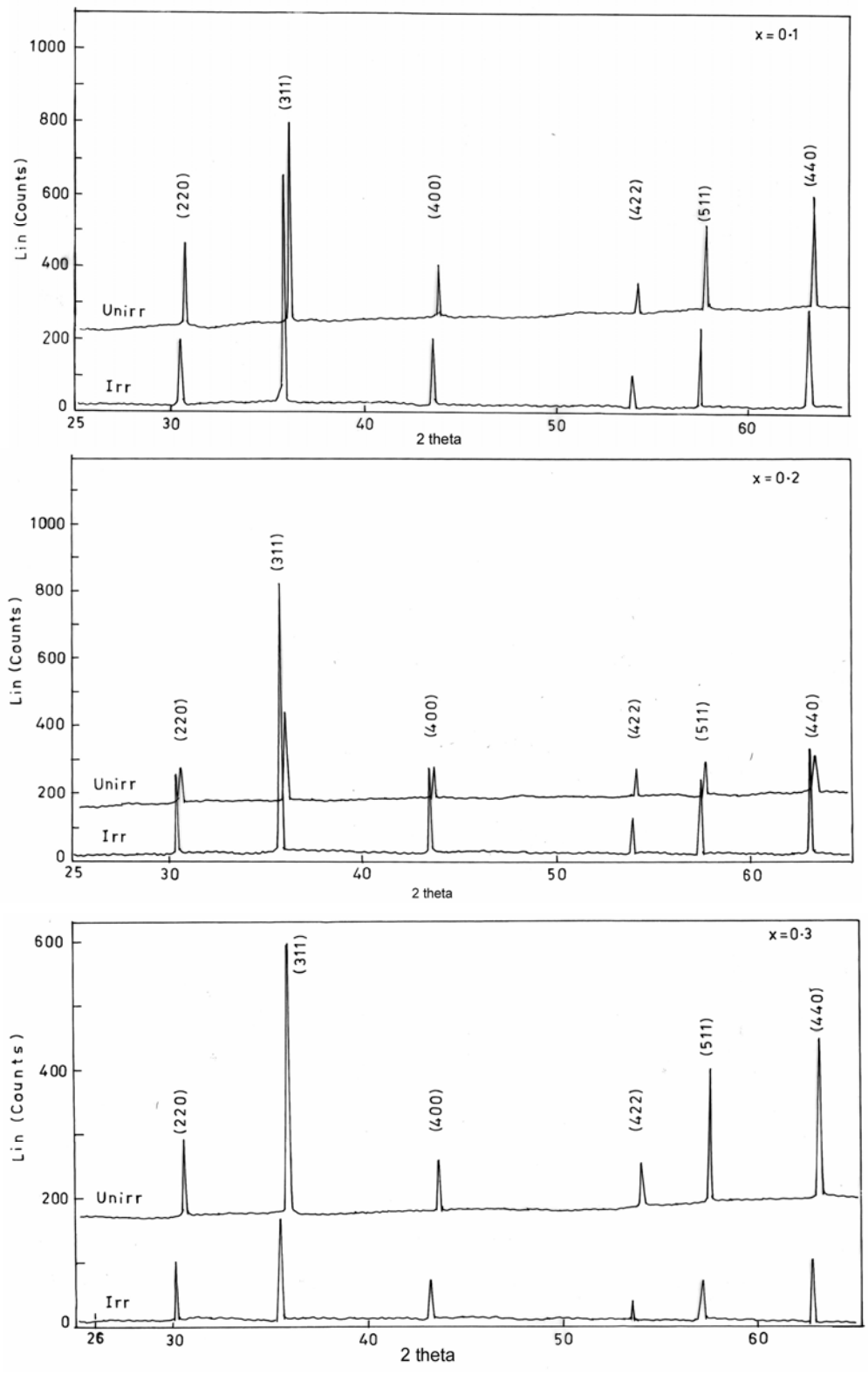

Fig. 6B.2 X-ray diffraction patterns: x = 0.1, 0.2 and 0.3 of the unirradiated and irradiated $Li_{0.5(1+x)}Ti_xCr_{0.1}Fe_{2.4-1.5x}O_4$ system, λ = 1.5406 Å

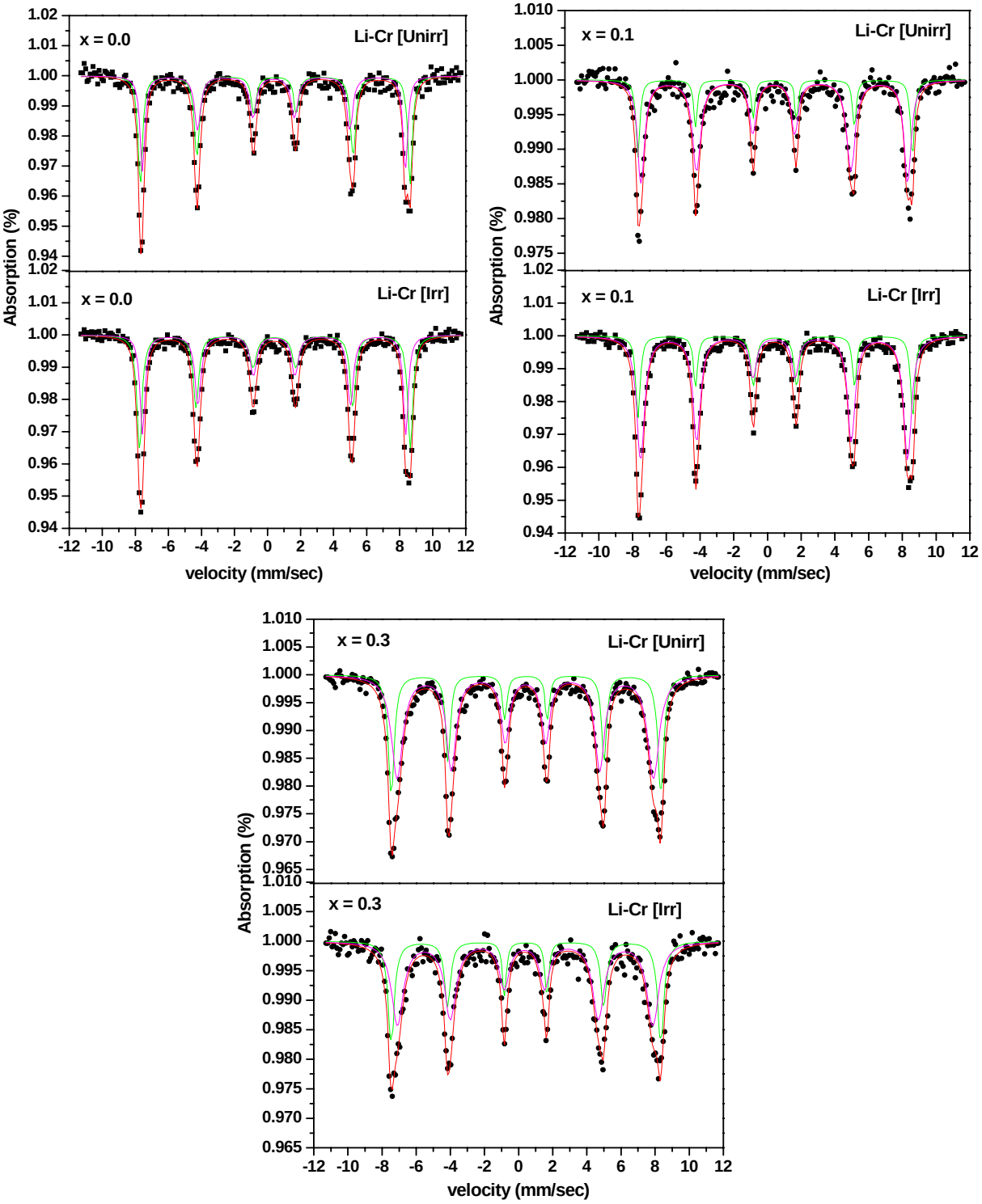

Fig. 6B.3 Mössbauer spectra at 300K for the compositions with x = 0.0, 0.1 and 0.3 of $Li_{0.5(1+x)}Ti_xCr_{0.1}Fe_{2.4-1.5x}O_4$ system before and after irradiation.

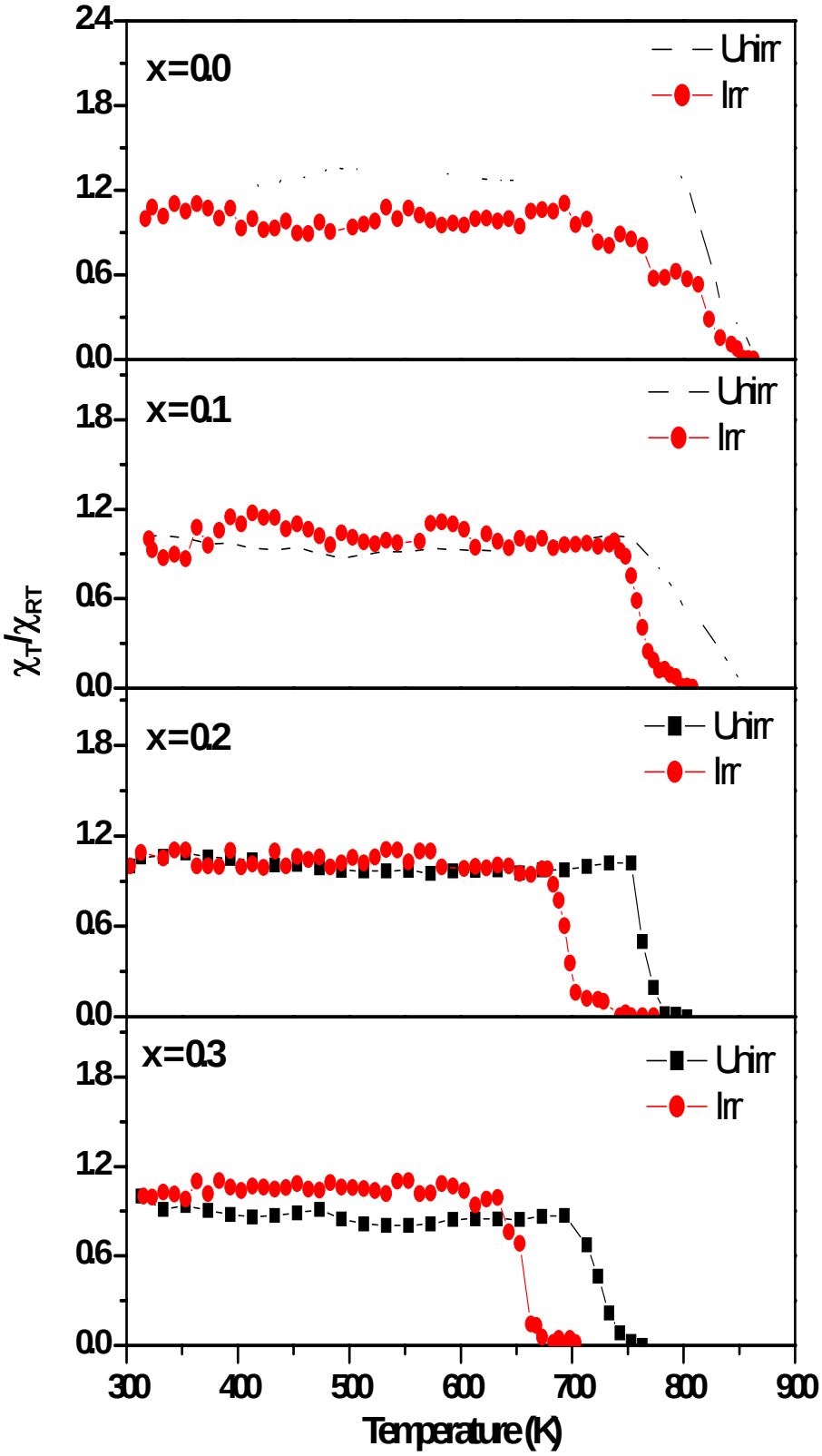

Fig. 6B.4 Thermal variation of low field (0.5 Oe) AC Susceptibility of unirradiated and irradiated samples of $Li_{0.5(1+x)}Ti_xCr_{0.1}Fe_{2.4-1.5x}O_4$ system

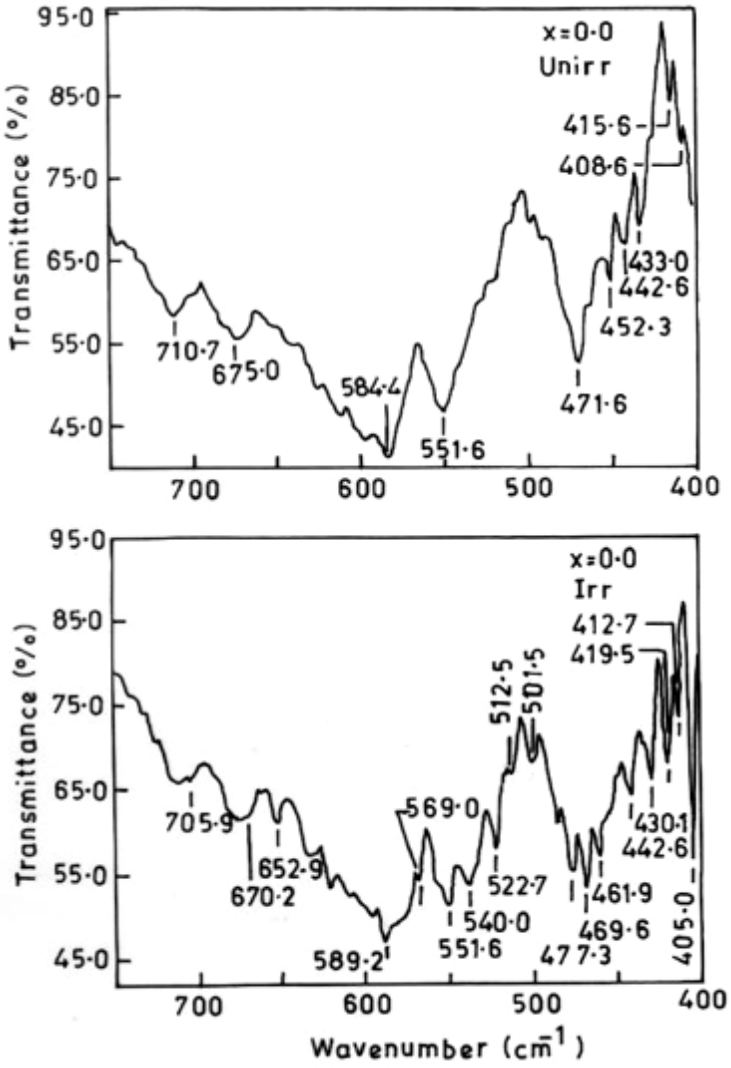

Fig. 6B.5a Infrared spectra of unirradiated and irradiated $Li_{(1+x)0.5}Ti_xCr_{0.1}Fe_{2.4-1.5x}O_4$ system with x = 0.0 sample

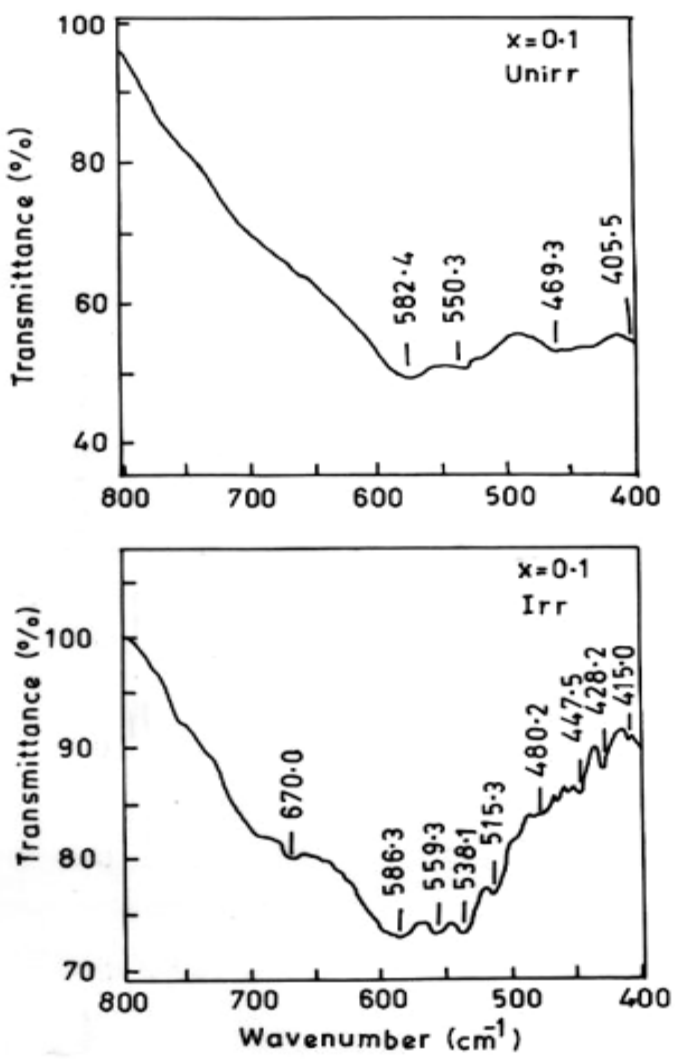

Fig. 6B.5b Infrared spectra of unirradiated and irradiated $Li_{(1+x)0.5}Ti_xCr_{0.1}Fe_{2.4-1.5x}O_4$ system with x = 0.1 sample

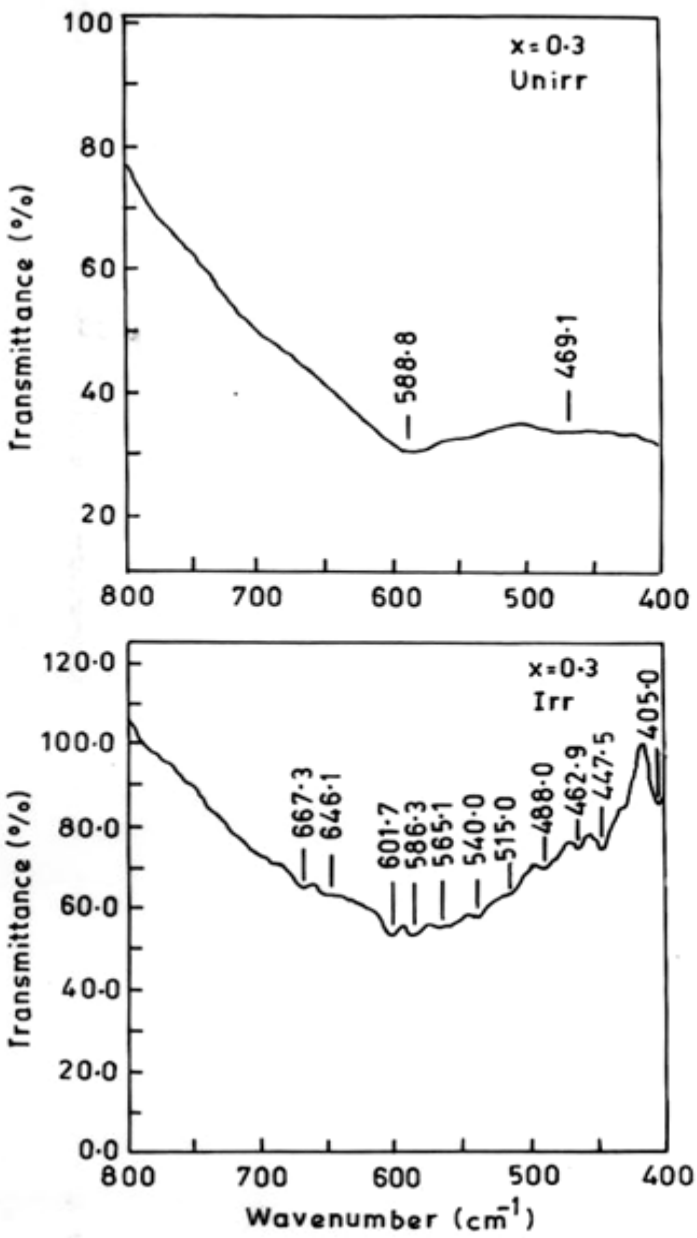

Fig. 6B.5c Infrared spectra of unirradiated and irradiated $Li_{(1+x)0.5}Ti_xCr_{0.1}Fe_{2.4-1.5x}O_4$ system with x = 0.3 sample

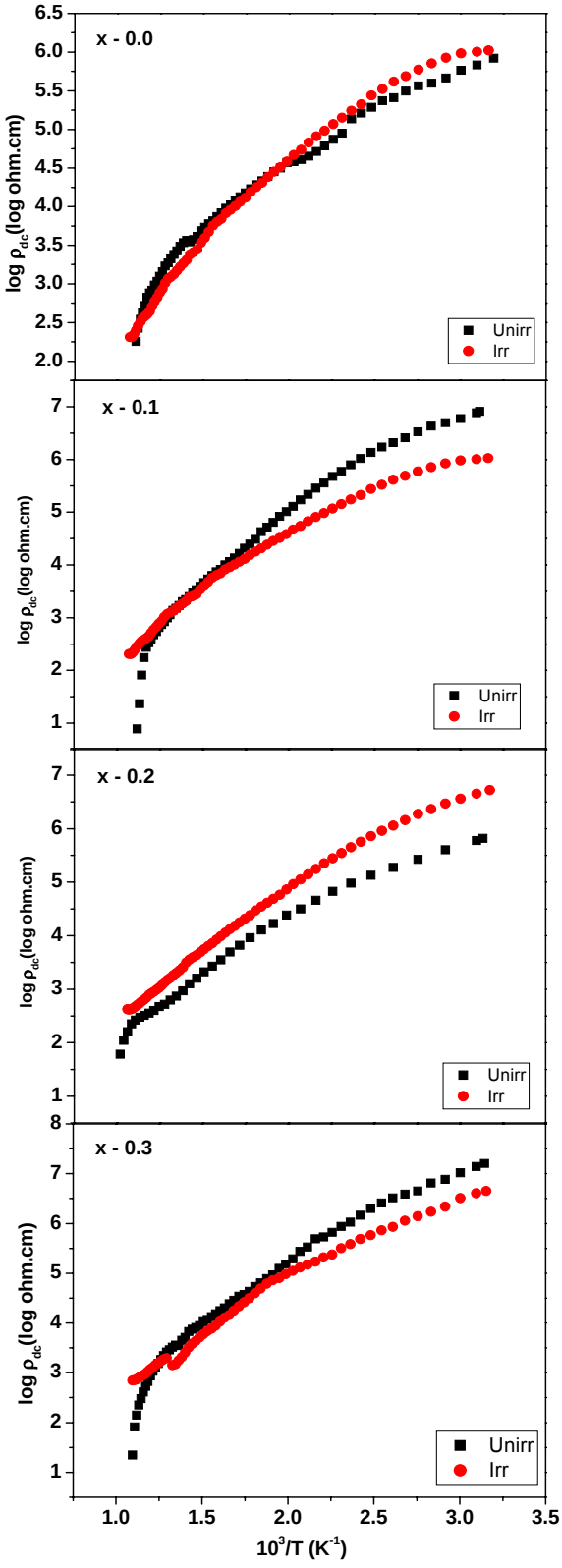

Fig. 6B.6 Electrical resistivity ($\log_{10}\rho_{dc}$) versus temperature ($10^3/T$) for the compositions x = 0.0, 0.1, 0.2 and 0.3 of unirradiated and irradiate $Li_{0.5(1+x)}Ti_xCr_{0.1}Fe_{2.4-1.5x}O_4$ system

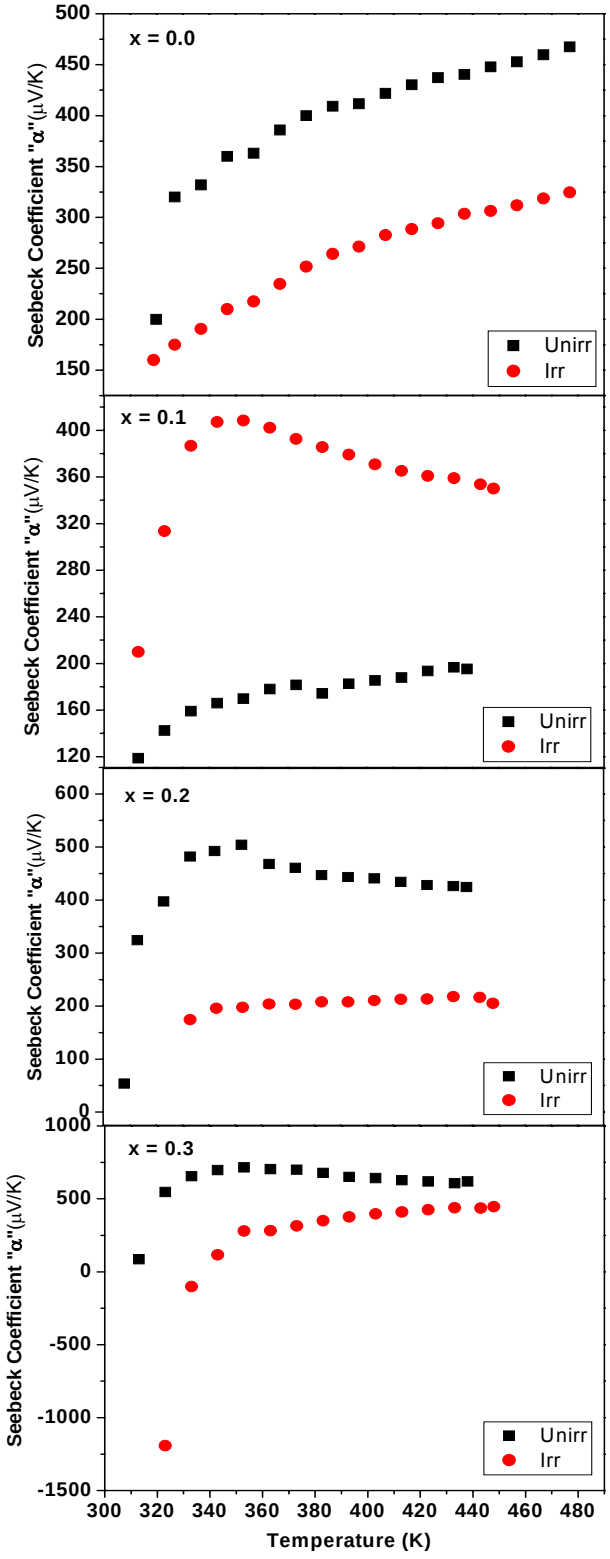

Fig. 6B.7 Thermal variation of Seebeck coefficient for the compositions x = 0.0, 0.1, 0.2 and 0.3 of unirradiated and irradiated $Li_{0.5(1+x)}Ti_xCr_{0.1}Fe_{2.4-1.5x}O_4$ system

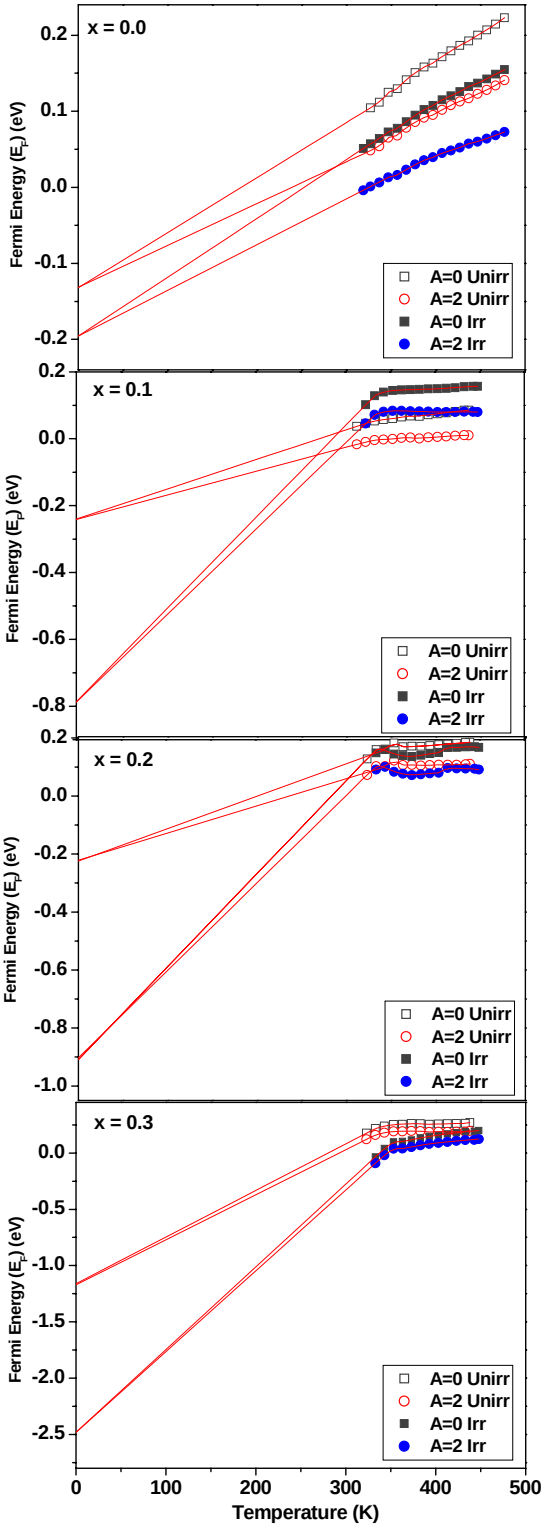

Fig. 6B.8 Temperature dependence of Fermi energy (E_F) for the compositions x = 0.0, 0.1, 0.2 and 0.3 of unirradiated and irradiated $Li_{0.5(1+x)}Ti_xCr_{0.1}Fe_{2.4-1.5x}O_4$ system

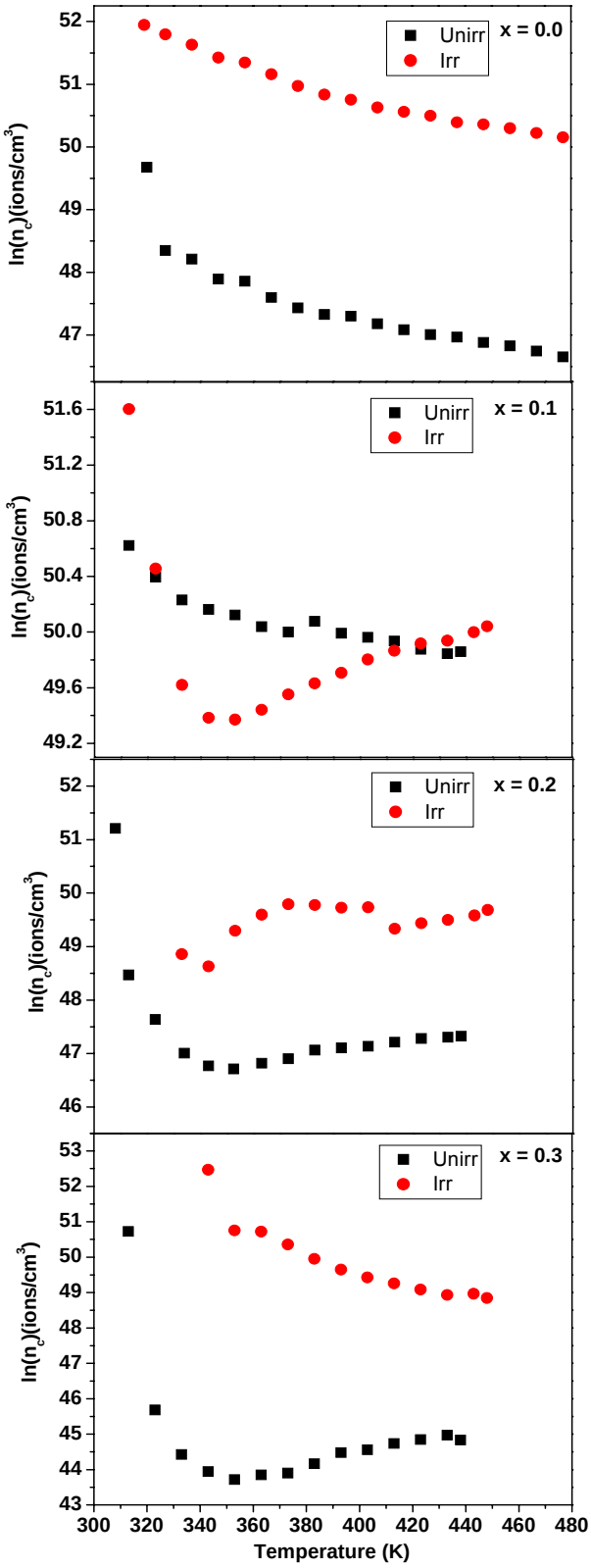

Fig. 6B.9 Variation of charge carrier concentration (n_c) with Temperature for the compositions x = 0.0, 0.1, 0.2 and 0.3 for the unirradiated and irradiated $Li_{0.5(1+x)}Ti_xCr_{0.1}Fe_{2.4-1.5x}O_4$ system

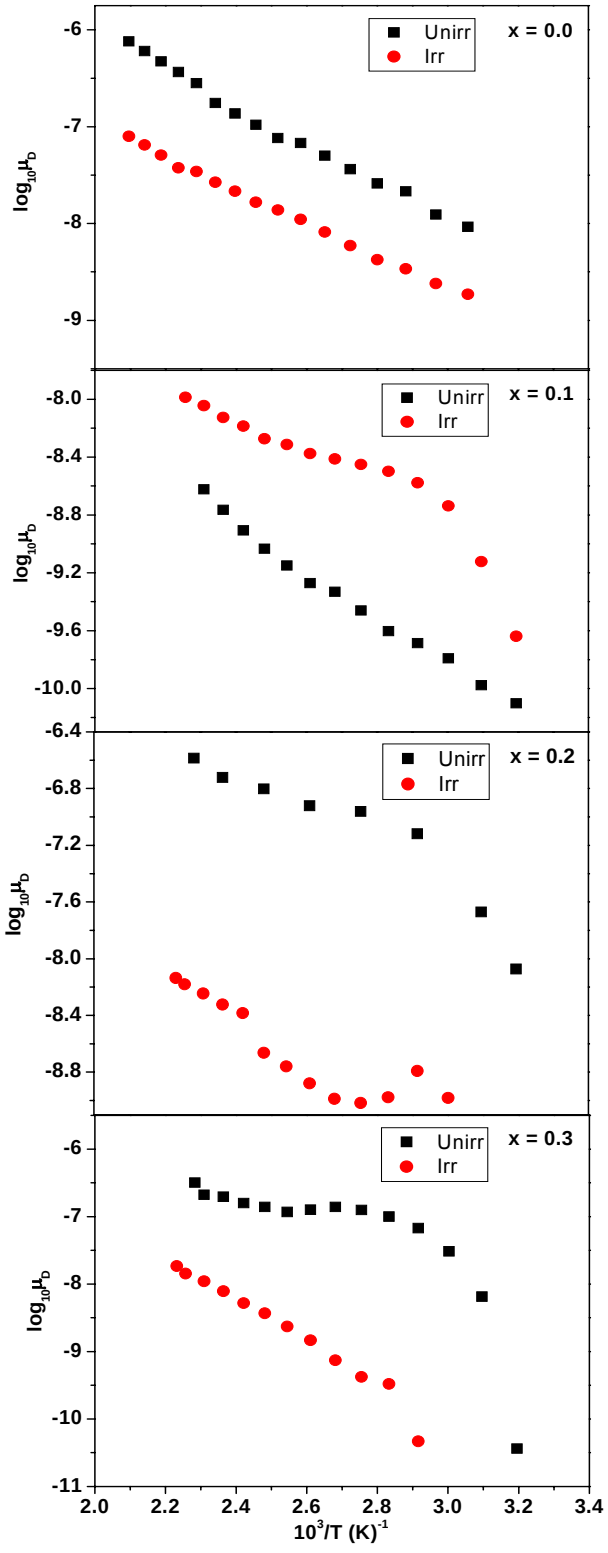

Fig. 6B.10 Thermal variation of mobility (μ_D) for the compositions x = 0.0, 0.1, 0.2 and 0.3 of unirradiated and irradiated $Li_{0.5(1+x)}Ti_xCr_{0.1}Fe_{2.4-1.5x}O_4$ system

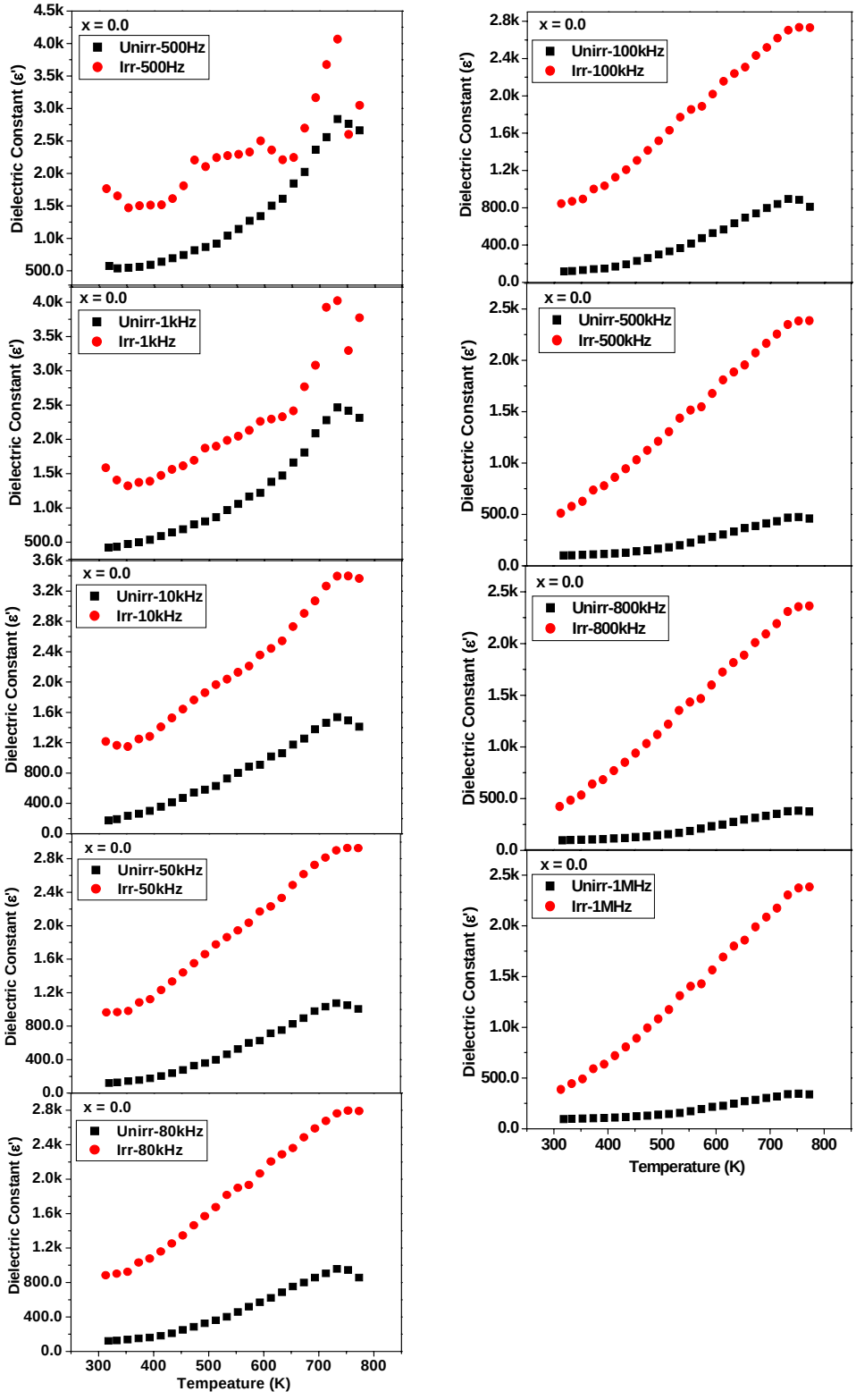

Fig. 6B.11a Thermal variation of dielectric constant (ε') at different frequencies for the composition x = 0.0 of unirradiated and irradiated $Li_{0.5(1+x)}Ti_xCr_{0.1}Fe_{2.4-1.5x}O_4$ system

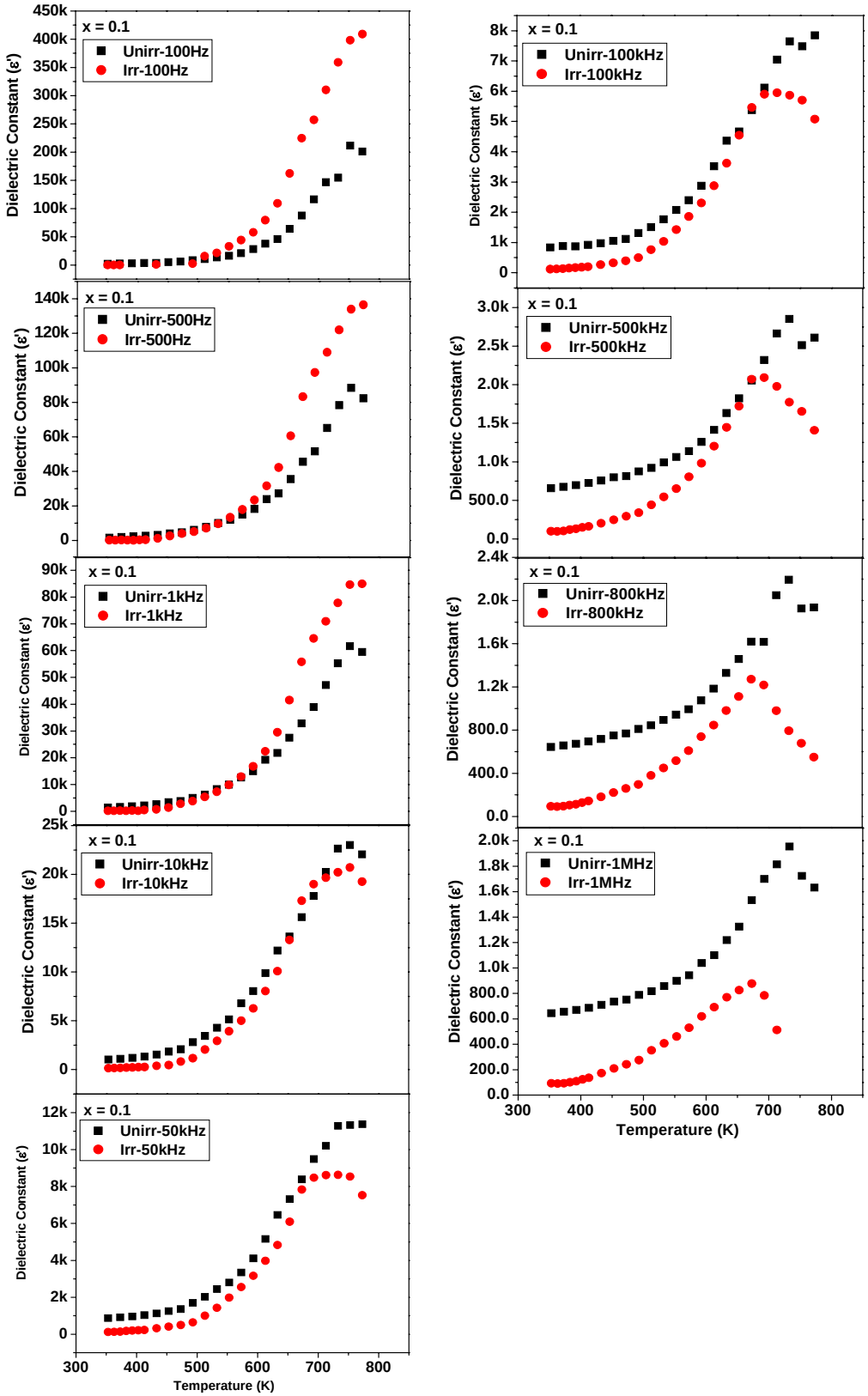

Fig. 6B.11b Thermal variation of dielectric constant (ε') at different frequencies for the composition x = 0.1 of unirradiated and irradiated $Li_{0.5(1+x)}Ti_xCr_{0.1}Fe_{2.4-1.5x}O_4$ system

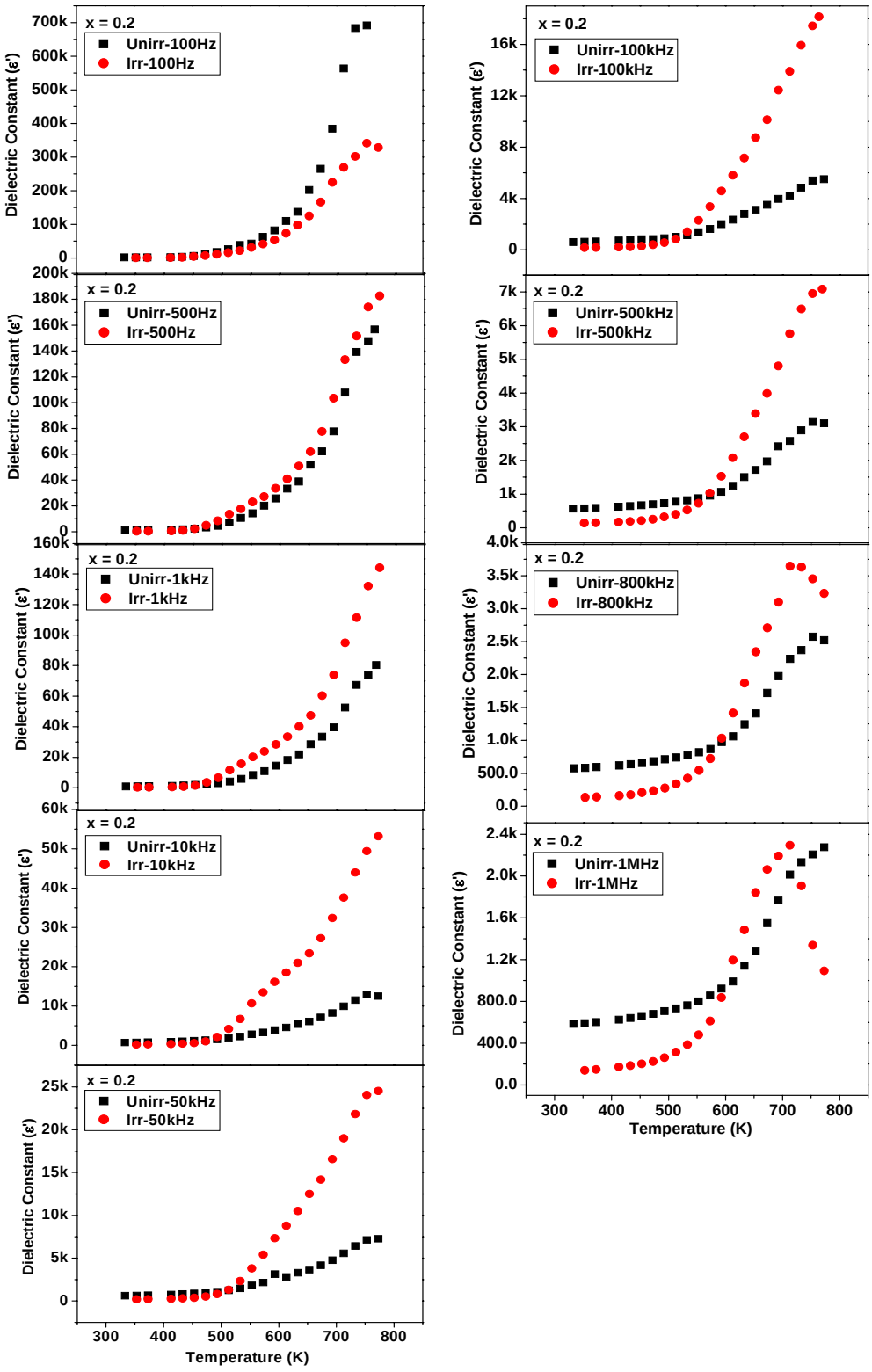

Fig.6B.11c Thermal variation of dielectric constant (ε') at different frequencies for the composition x = 0.2 of unirradiated and irradiated $Li_{0.5(1+x)}Ti_xCr_{0.1}Fe_{2.4-1.5x}O_4$ system

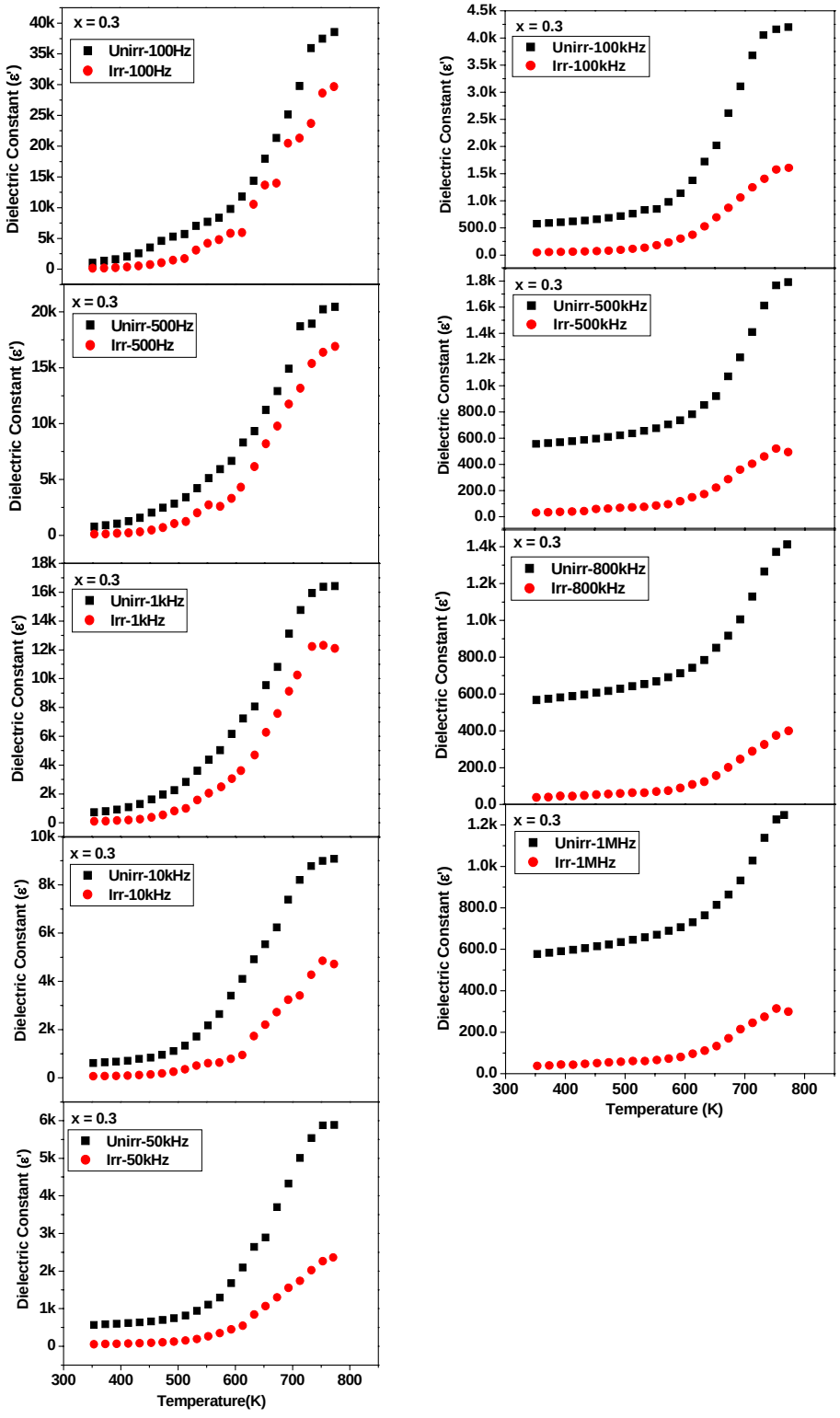

Fig. 6B.11d Thermal variation of dielectric constant (ε') at different frequencies for the composition x = 0.3 of unirradiated and irradiated $Li_{0.5(1+x)}Ti_xCr_{0.1}Fe_{2.4-1.5x}O_4$ system

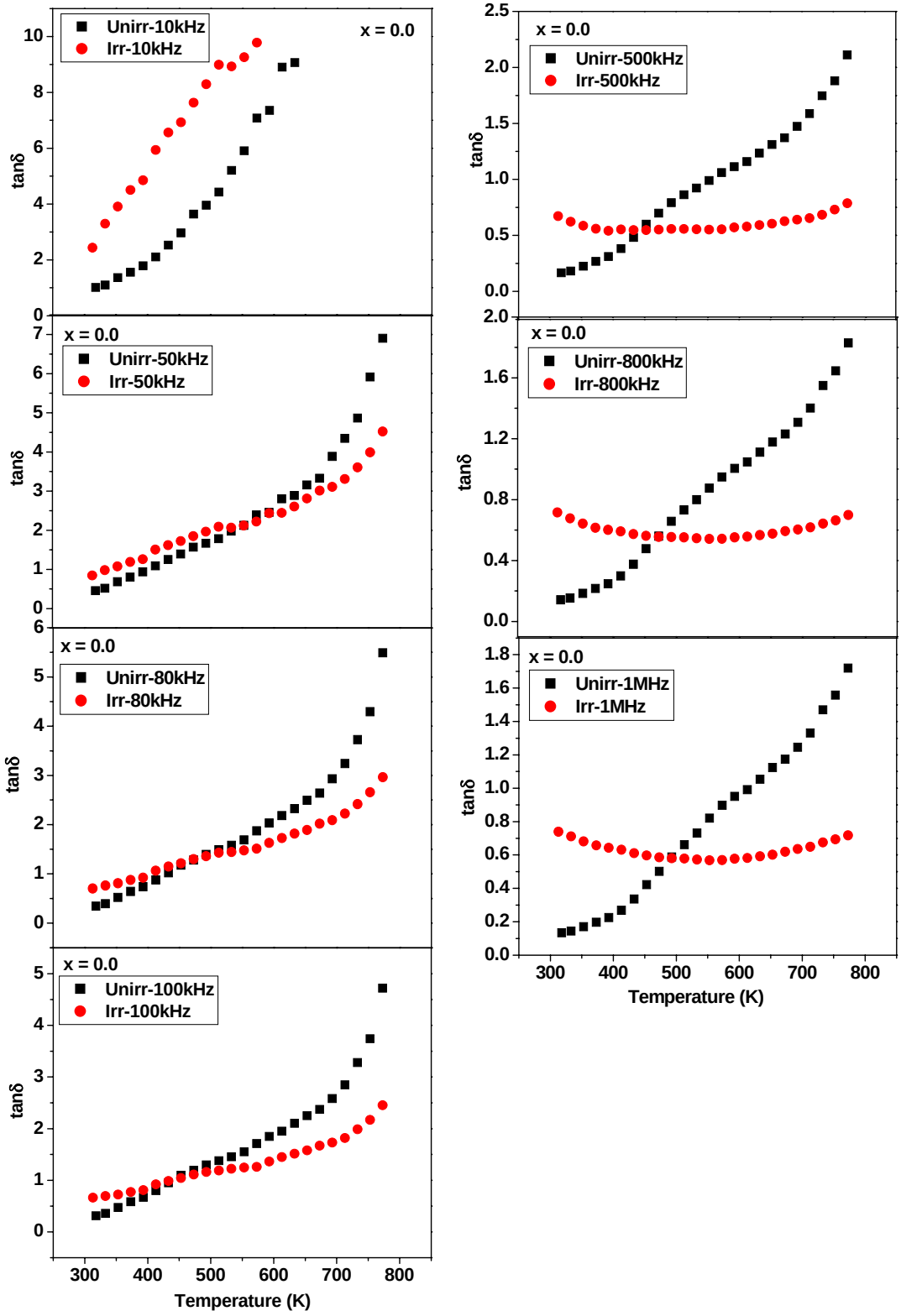

Fig. 6B.12a Thermal variation of dielectric loss tangent (tanδ) at different frequencies for the composition x = 0.0 of unirradiated and irradiated $Li_{0.5(1+x)}Ti_xCr_{0.1}Fe_{2.4-1.5x}O_4$ system

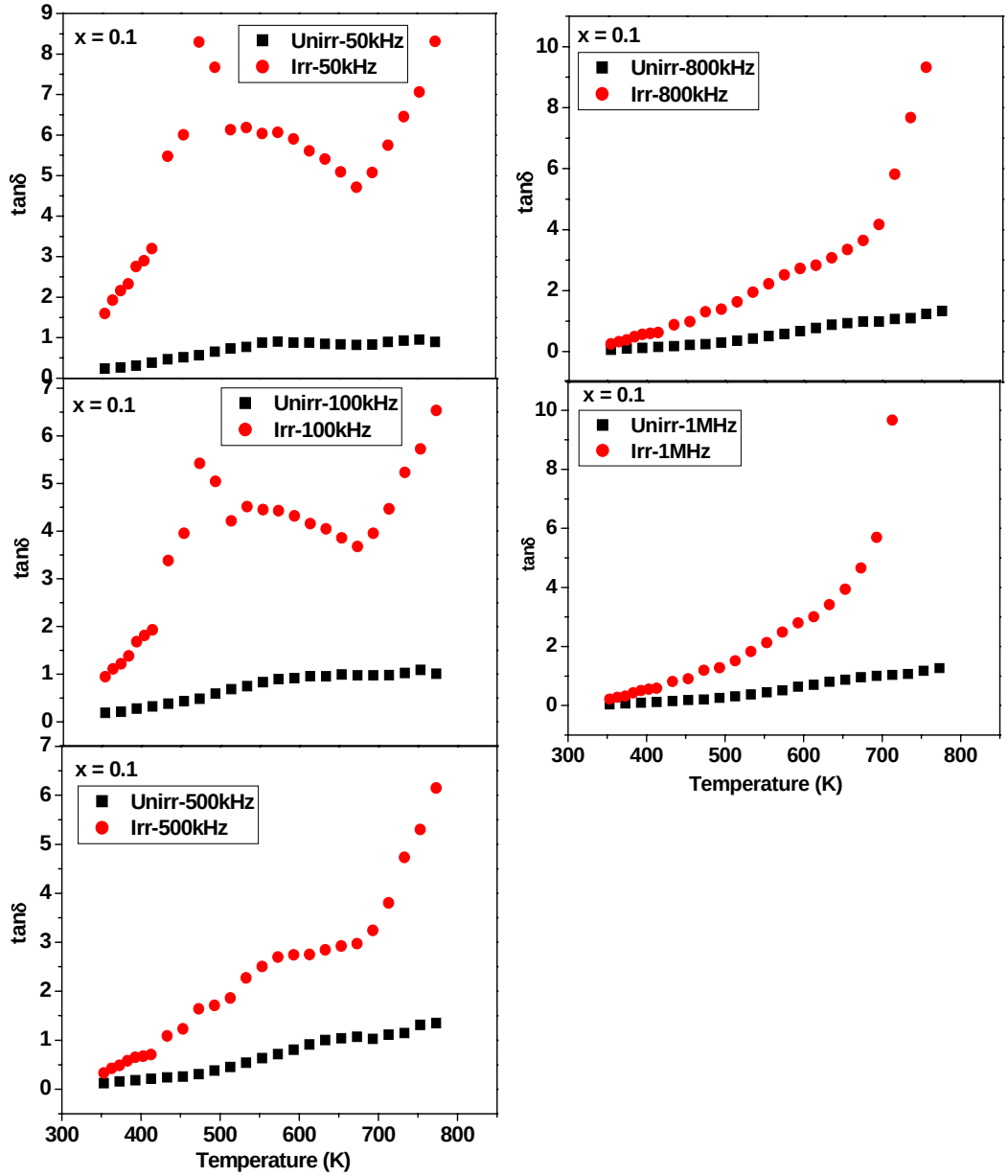

Fig. 6B.12b Thermal variation of dielectric loss tangent (tanδ) at different frequencies for the composition x = 0.1 of unirradiated and irradiated $Li_{0.5(1+x)}Ti_xCr_{0.1}Fe_{2.4-1.5x}O_4$ system

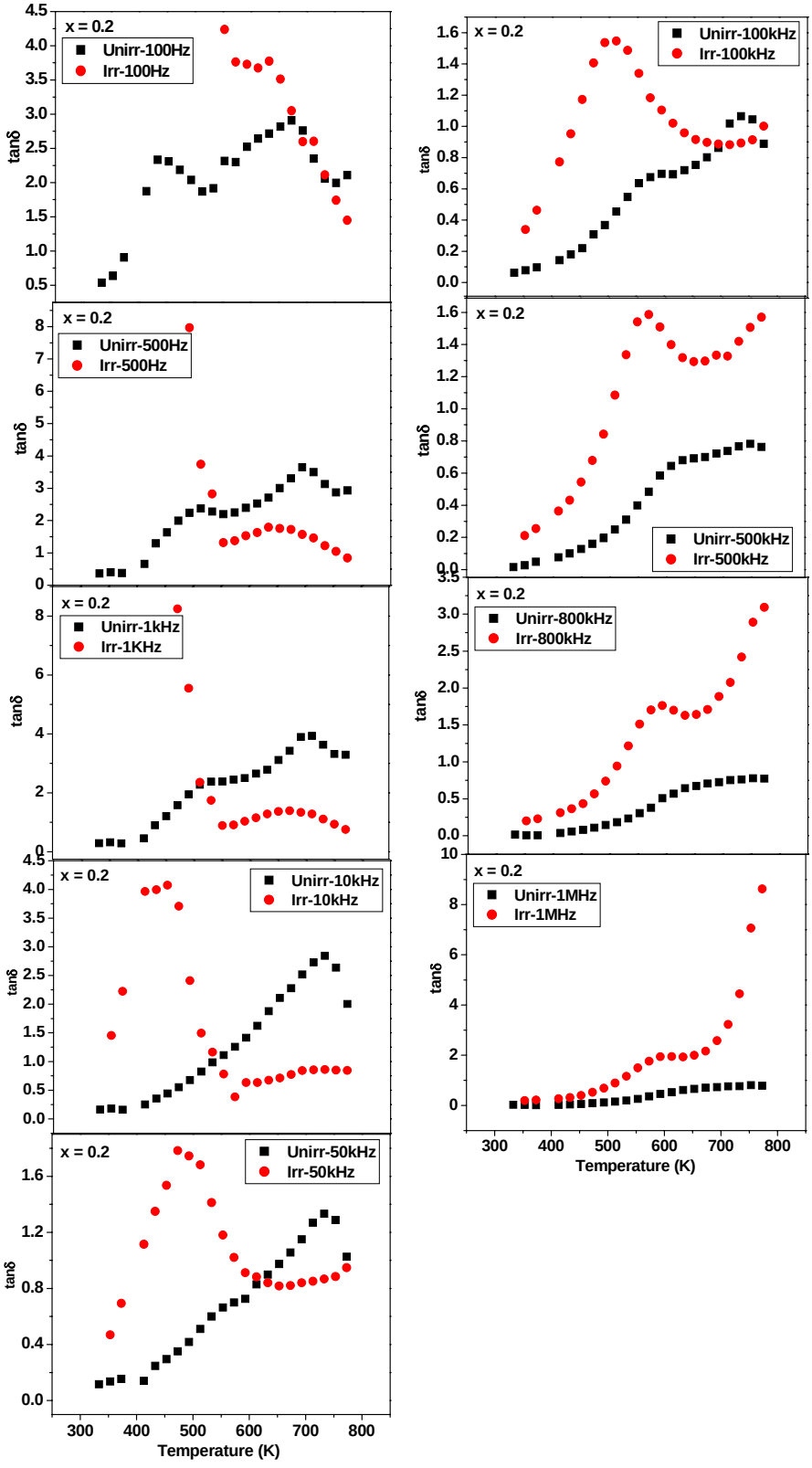

Fig. 6B.12c Thermal variation of dielectric loss tangent (tanδ) at different frequencies for the composition x = 0.2 of unirradiated and irradiated $Li_{0.5(1+x)}Ti_xCr_{0.1}Fe_{2.4-1.5x}O_4$ system

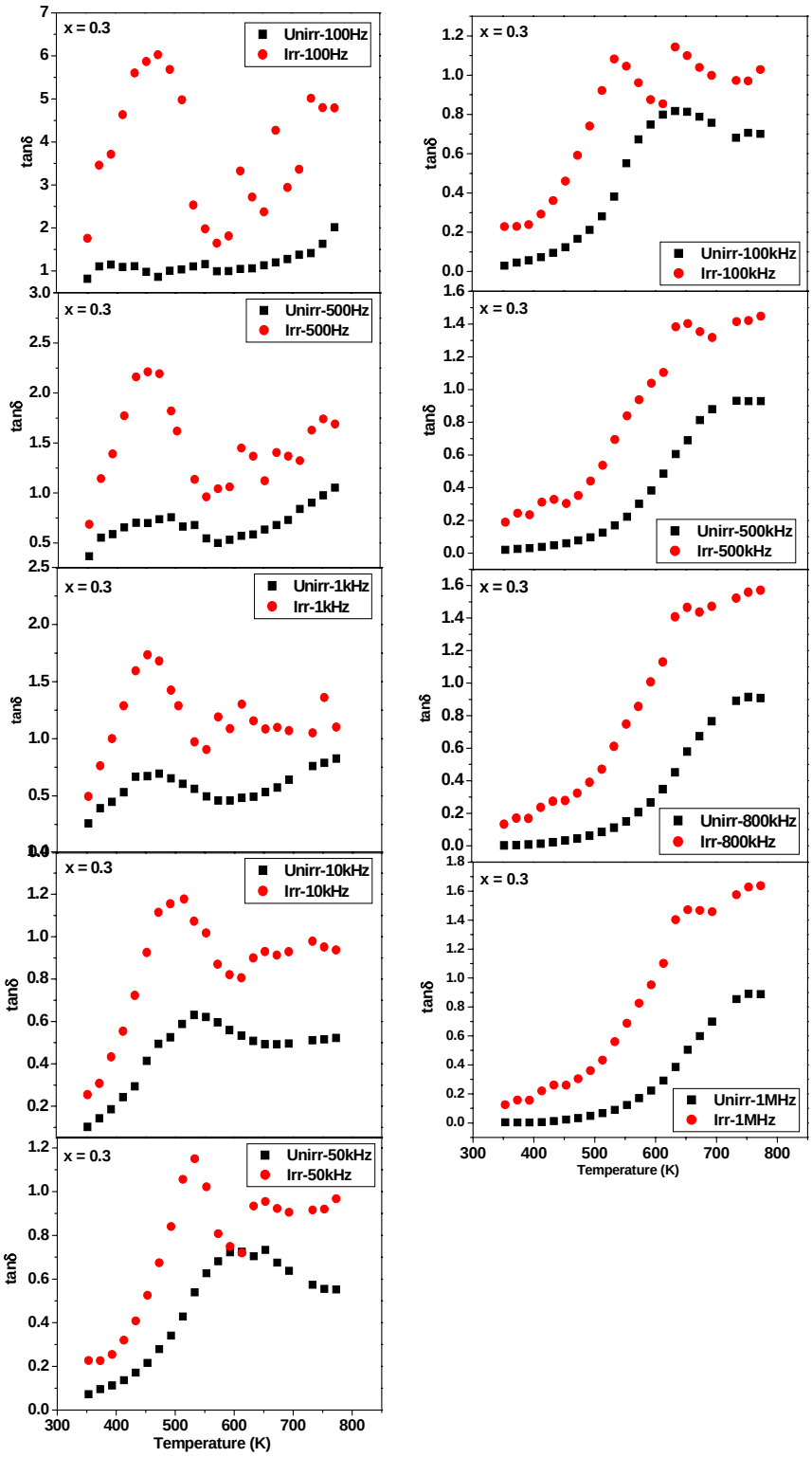

Fig. 6B.12d Thermal variation of dielectric loss tangent (tanδ) at different frequencies for the composition x = 0.3 of unirradiated and irradiated $Li_{0.5(1+x)}Ti_xCr_{0.1}Fe_{2.4-1.5x}O_4$ system

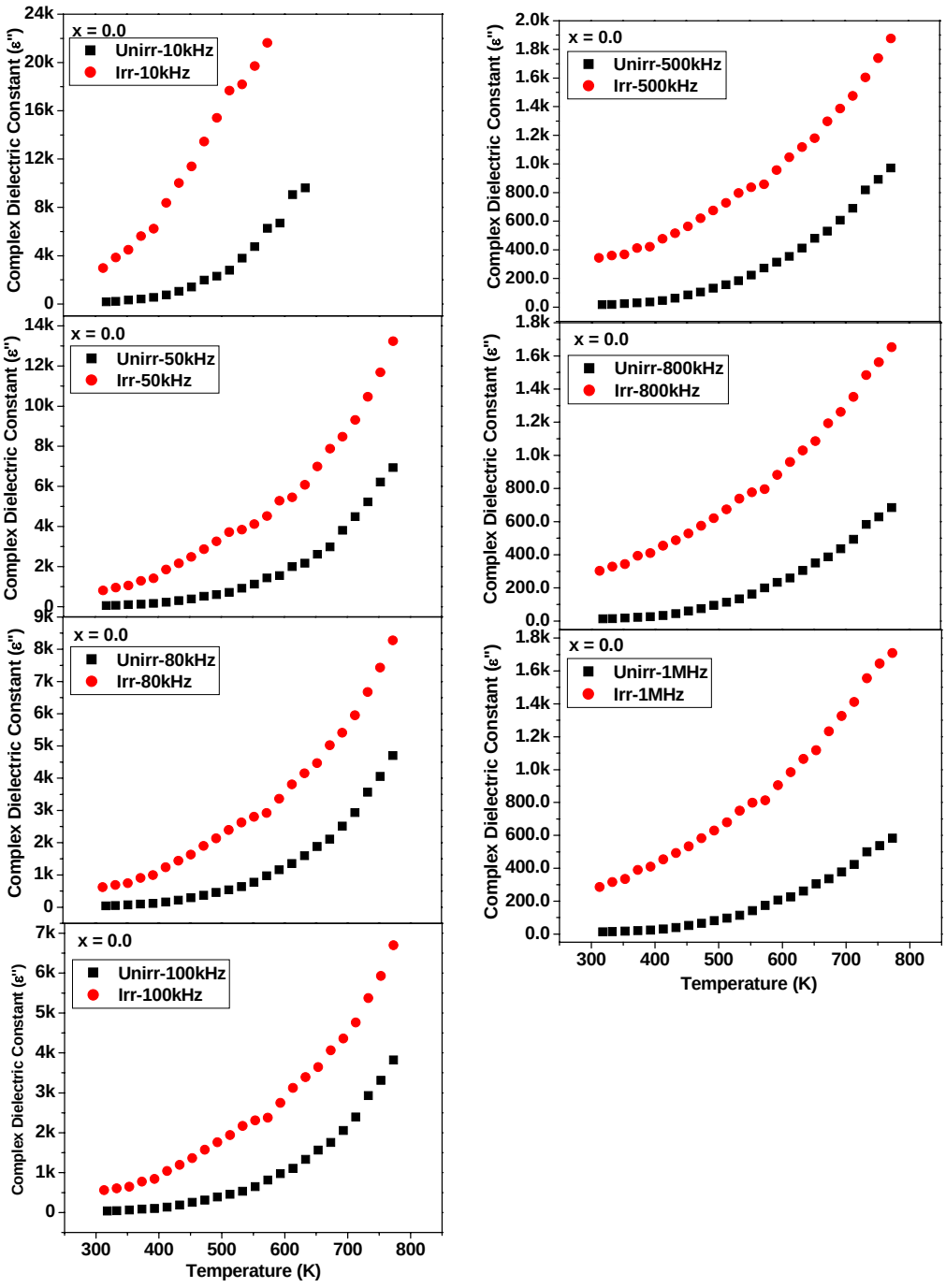

Fig. 6B.13a Thermal variation of Complex Dielectric Constant (ε'') at different frequencies for the composition x = 0.0 of unirradiated and irradiated $Li_{0.5(1+x)}Ti_xCr_{0.1}Fe_{2.4-1.5x}O_4$ system

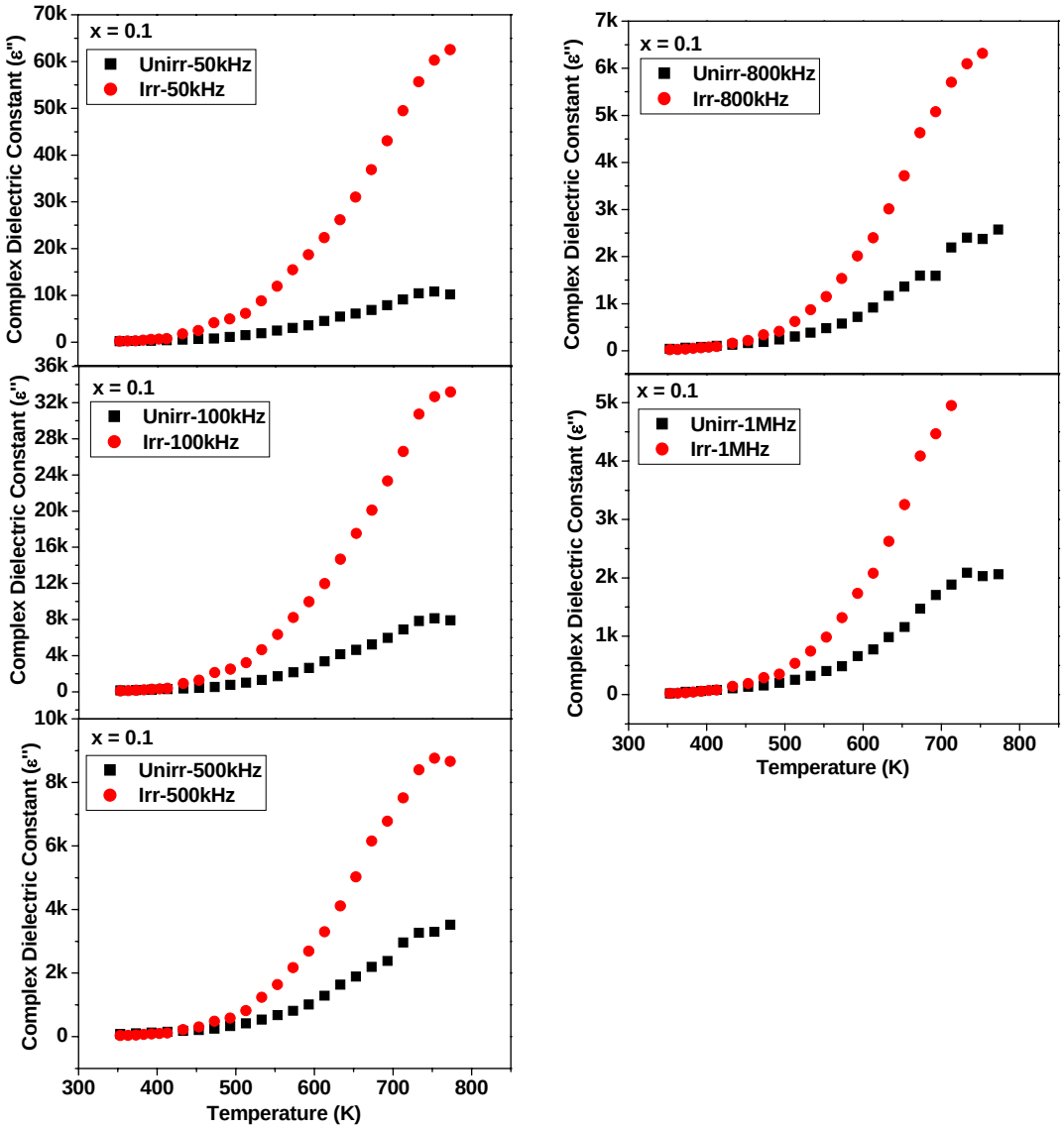

Fig. 6B.13b Thermal variation of Complex Dielectric Constant (ε'') at different frequencies for the composition x = 0.1 of unirradiated and irradiated $Li_{0.5(1+x)}Ti_xCr_{0.1}Fe_{2.4-1.5x}O_4$ system

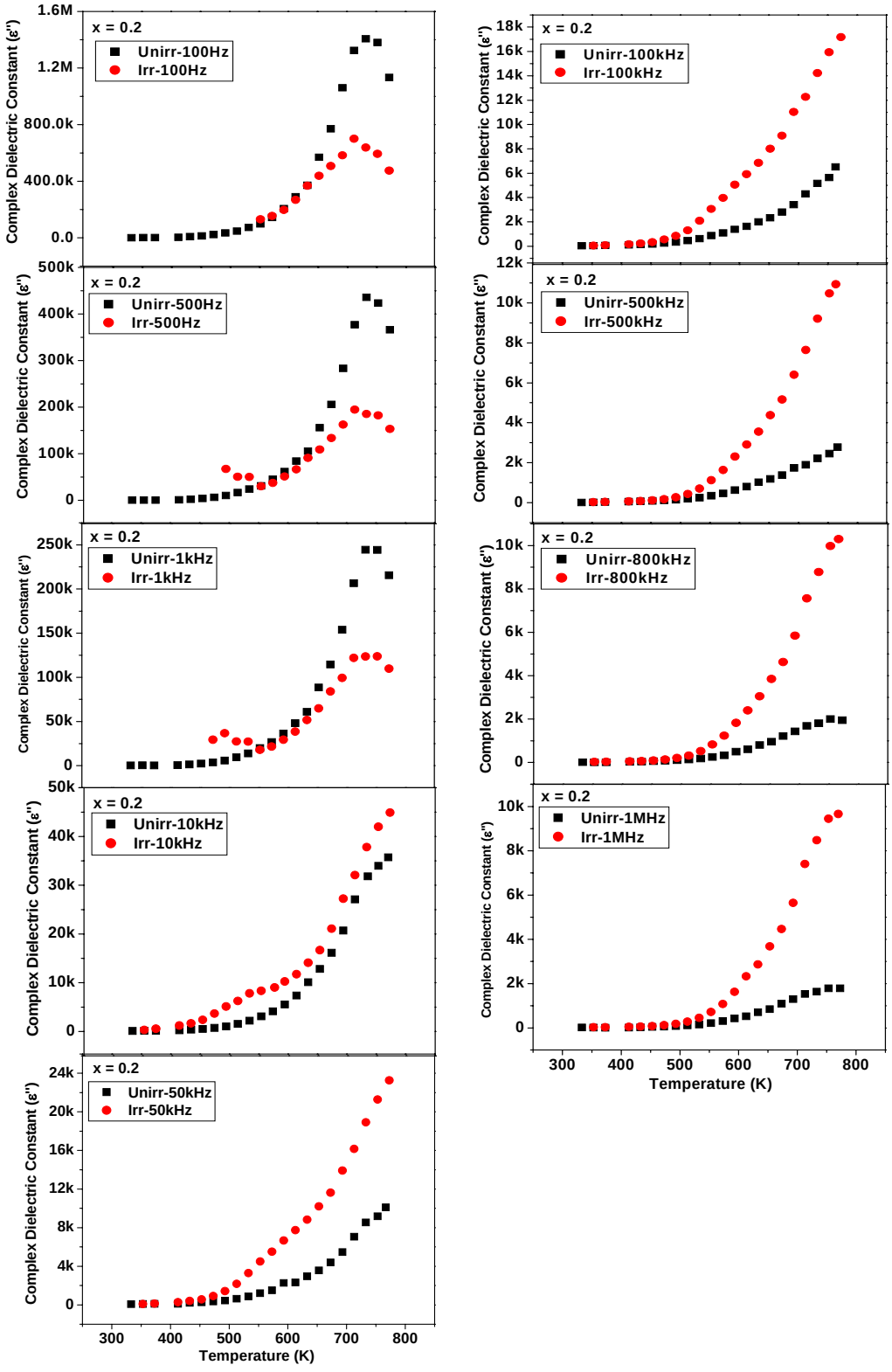

Fig. 6B.13c Thermal variation of Complex Dielectric Constant (ε'') at different frequencies for the composition x = 0.2 of unirradiated and irradiated $Li_{0.5(1+x)}Ti_xCr_{0.1}Fe_{2.4-1.5x}O_4$ system

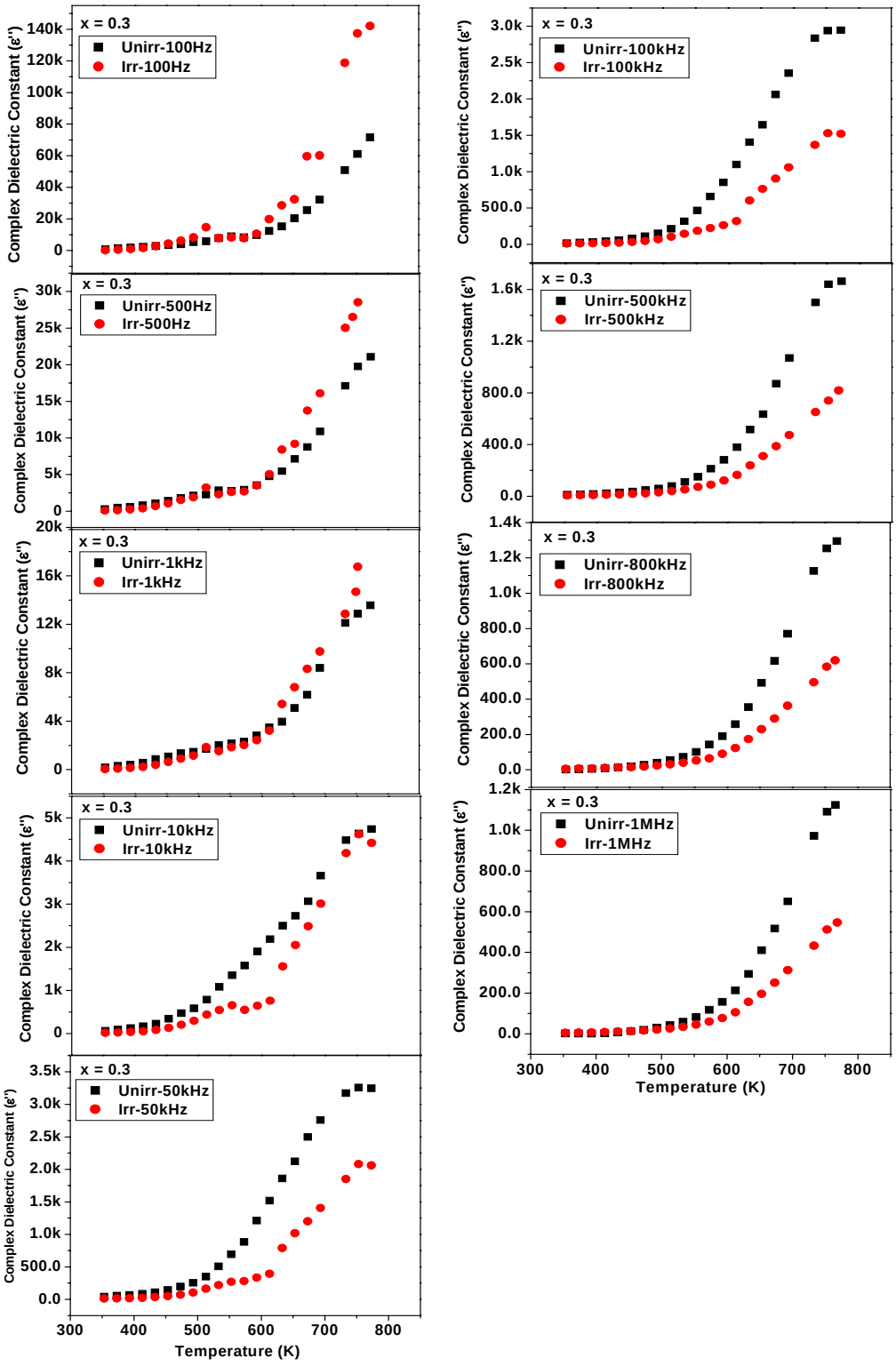

Fig. 6B.13d Thermal variation of Complex Dielectric Constant (ε'') different frequencies for the composition x = 0.3 of unirradiated and irradiated $Li_{0.5(1+x)}Ti_xCr_{0.1}Fe_{2.4-1.5x}O_4$ system

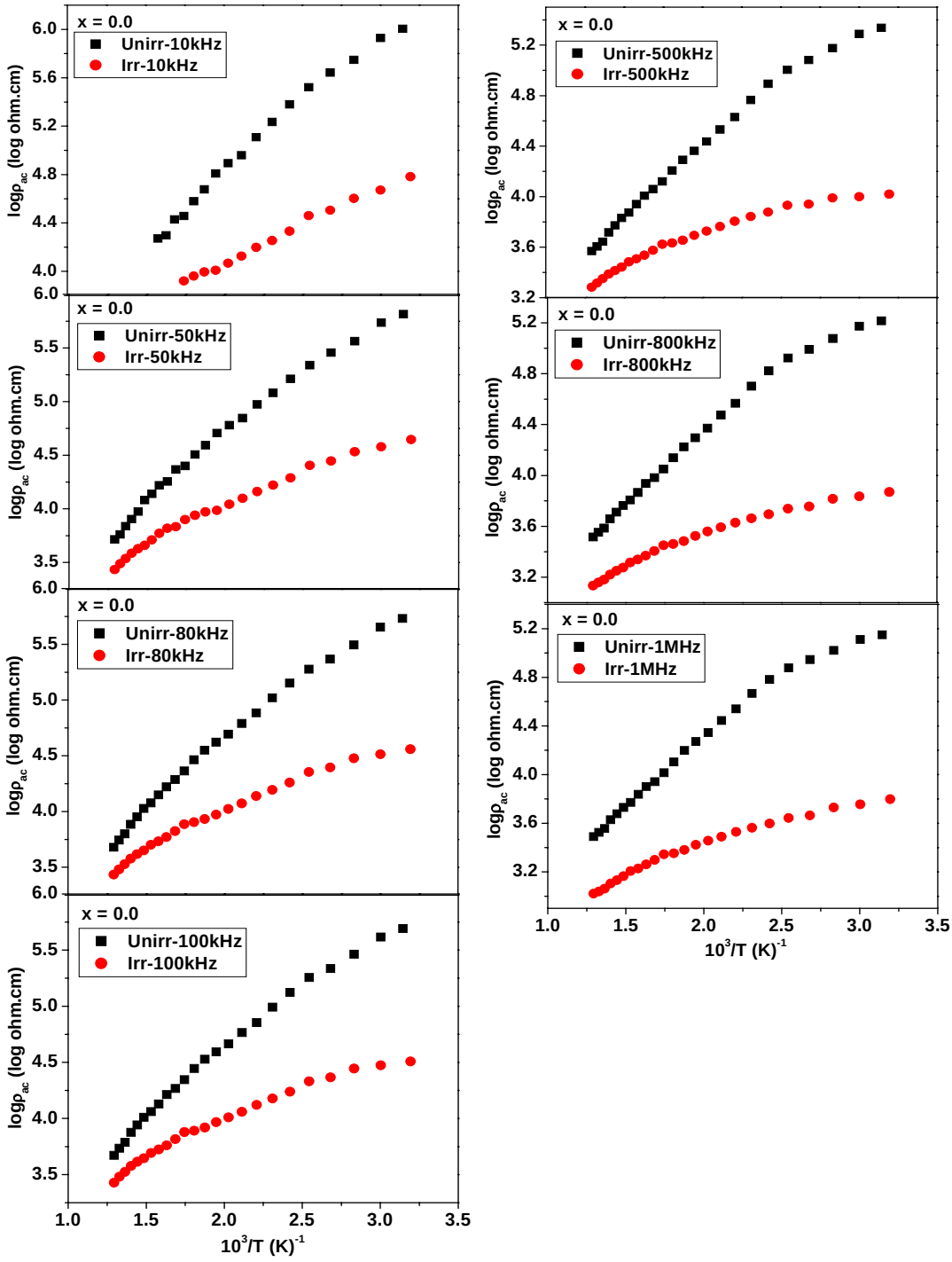

Fig. 6B.14a Thermal variation of a.c. resistivity ($\log\rho_{ac}$) at different frequencies for the composition x = 0.0 of unirradiated and irradiated $Li_{0.5(1+x)}Ti_xCr_{0.1}Fe_{2.4-1.5x}O_4$ system

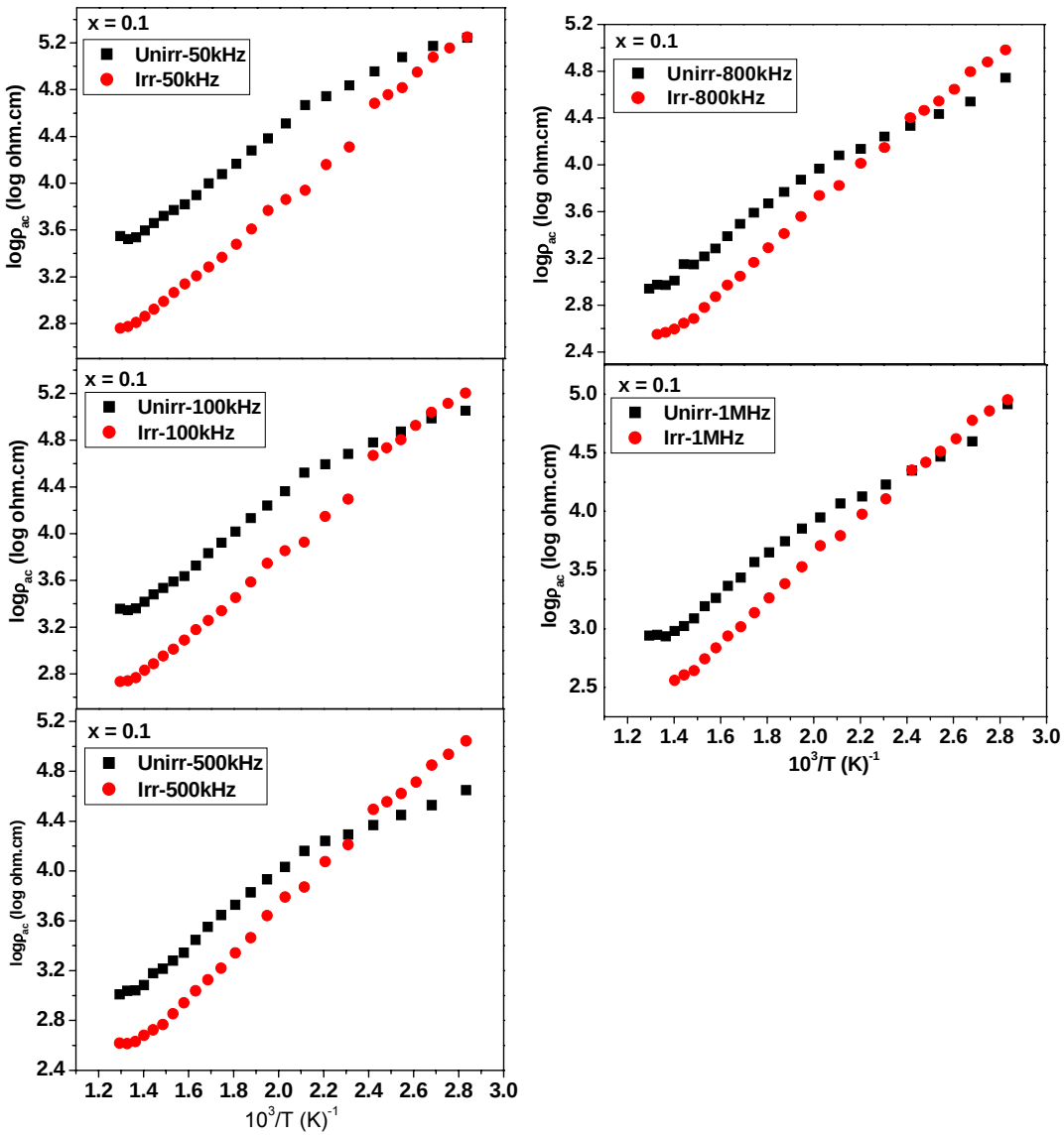

Fig. 6B.14b Thermal variation of a.c. resistivity ($\log\rho_{ac}$) at different frequencies for the composition x = 0.1 of unirradiated and irradiated $Li_{0.5(1+x)}Ti_xCr_{0.1}Fe_{2.4-1.5x}O_4$ system

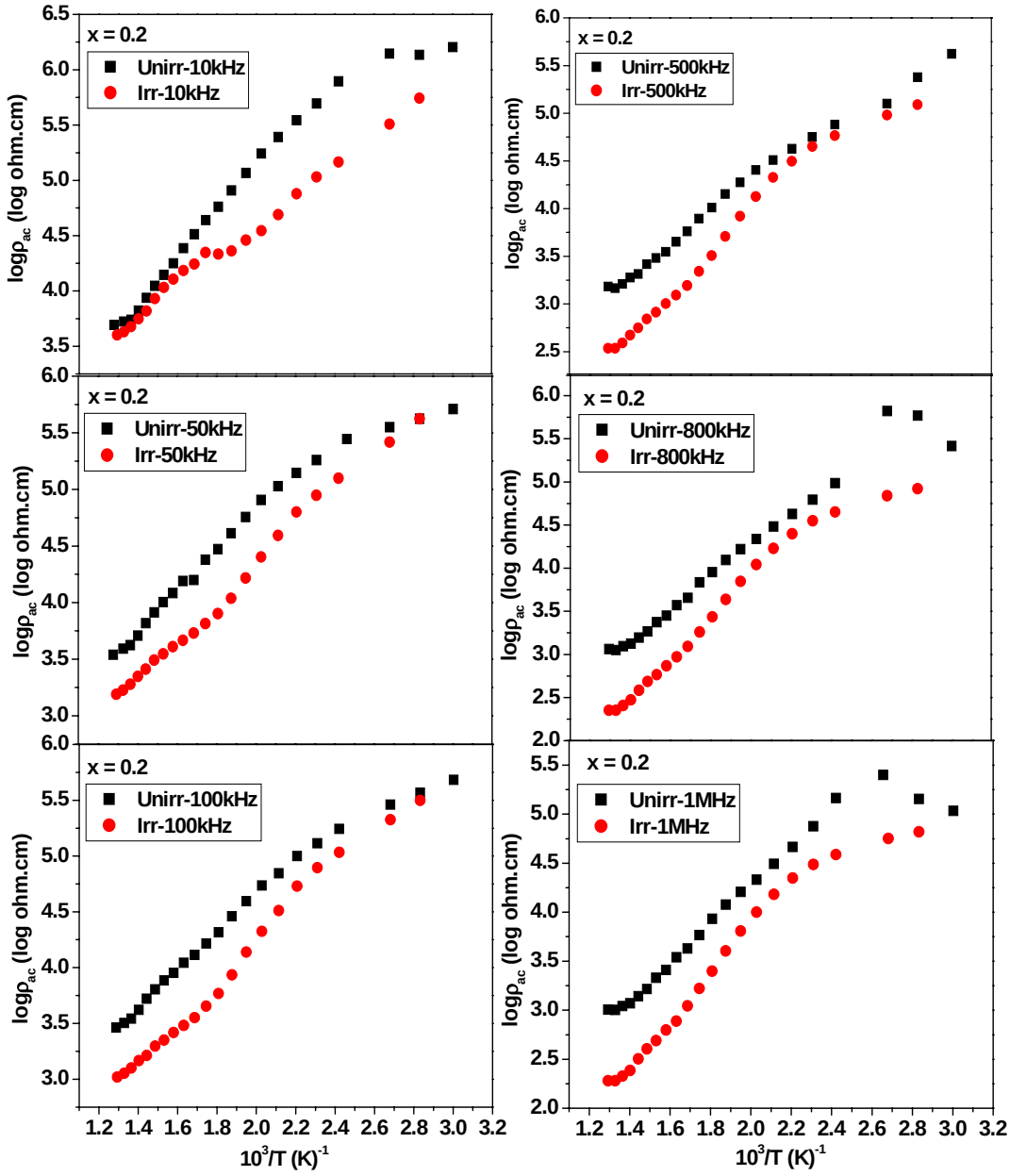

Fig. 6B.14c Thermal variation of a.c. resistivity ($\log\rho_{ac}$) at different frequencies for the composition x = 0.2 of unirradiated and irradiated $Li_{0.5(1+x)}Ti_xCr_{0.1}Fe_{2.4-1.5x}O_4$ system

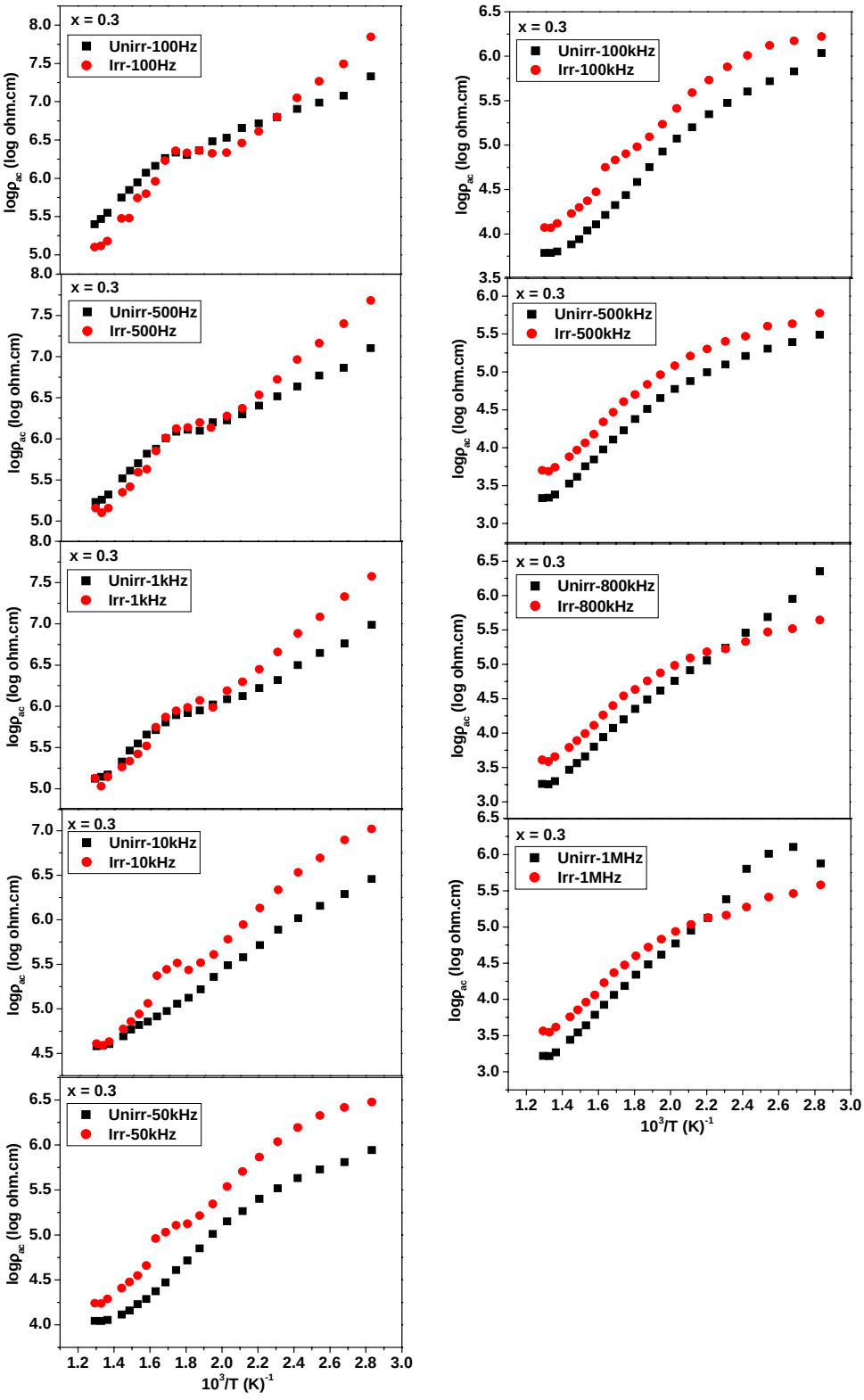

Fig. 6B.14d Thermal variation of a.c. resistivity ($\log\rho_{ac}$) at different frequencies for the composition x = 0.3 of unirradiated and irradiated $Li_{0.5(1+x)}Ti_xCr_{0.1}Fe_{2.4-1.5x}O_4$ system

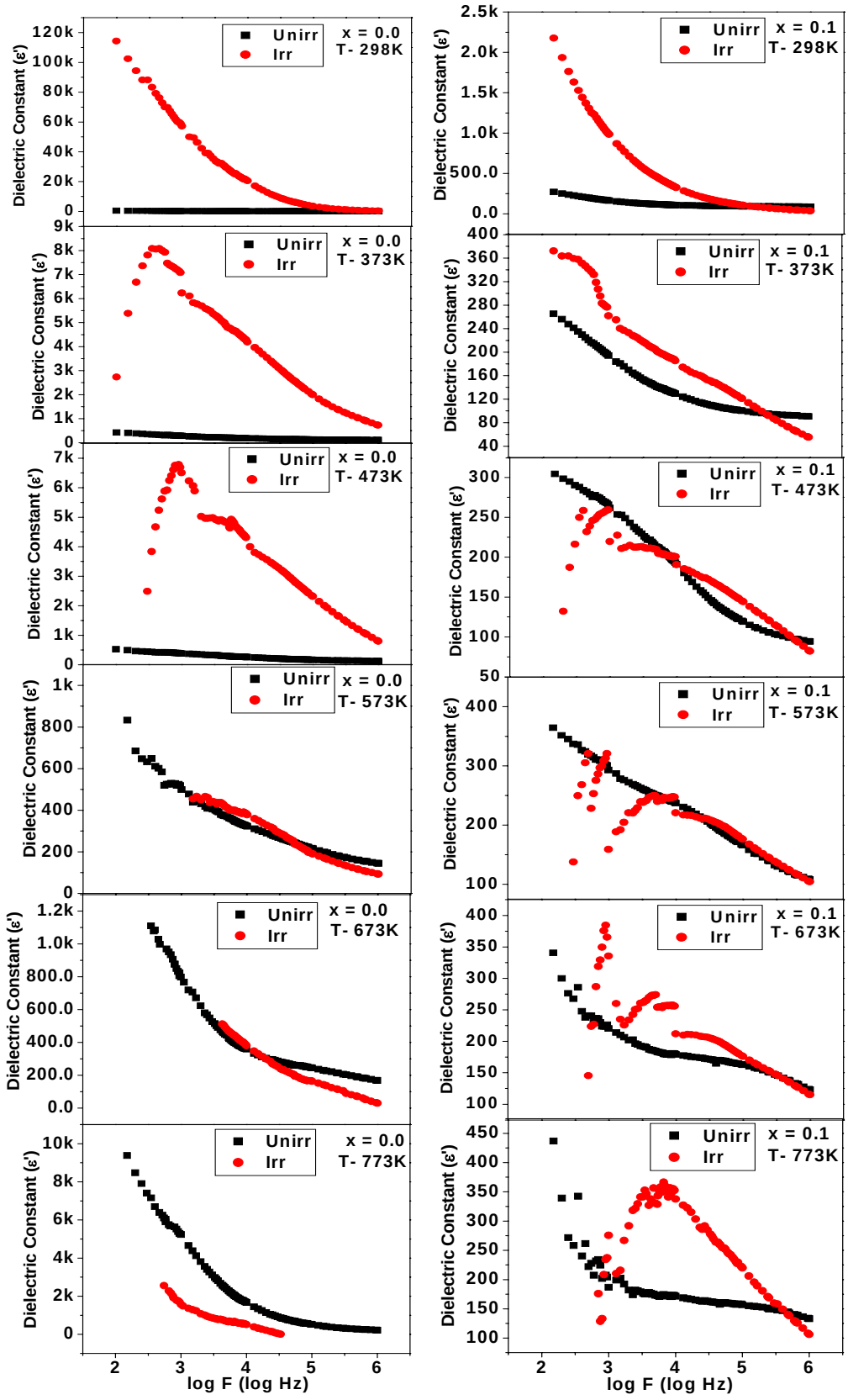

Fig. 6B.15a Dielectric Constant (ε') versus frequency at different temperatures for the compositions x = 0.0 and 0.1 of unirradiated and irradiated $Li_{0.5(1+x)}Ti_xCr_{0.1}Fe_{2.4-1.5x}O_4$ system

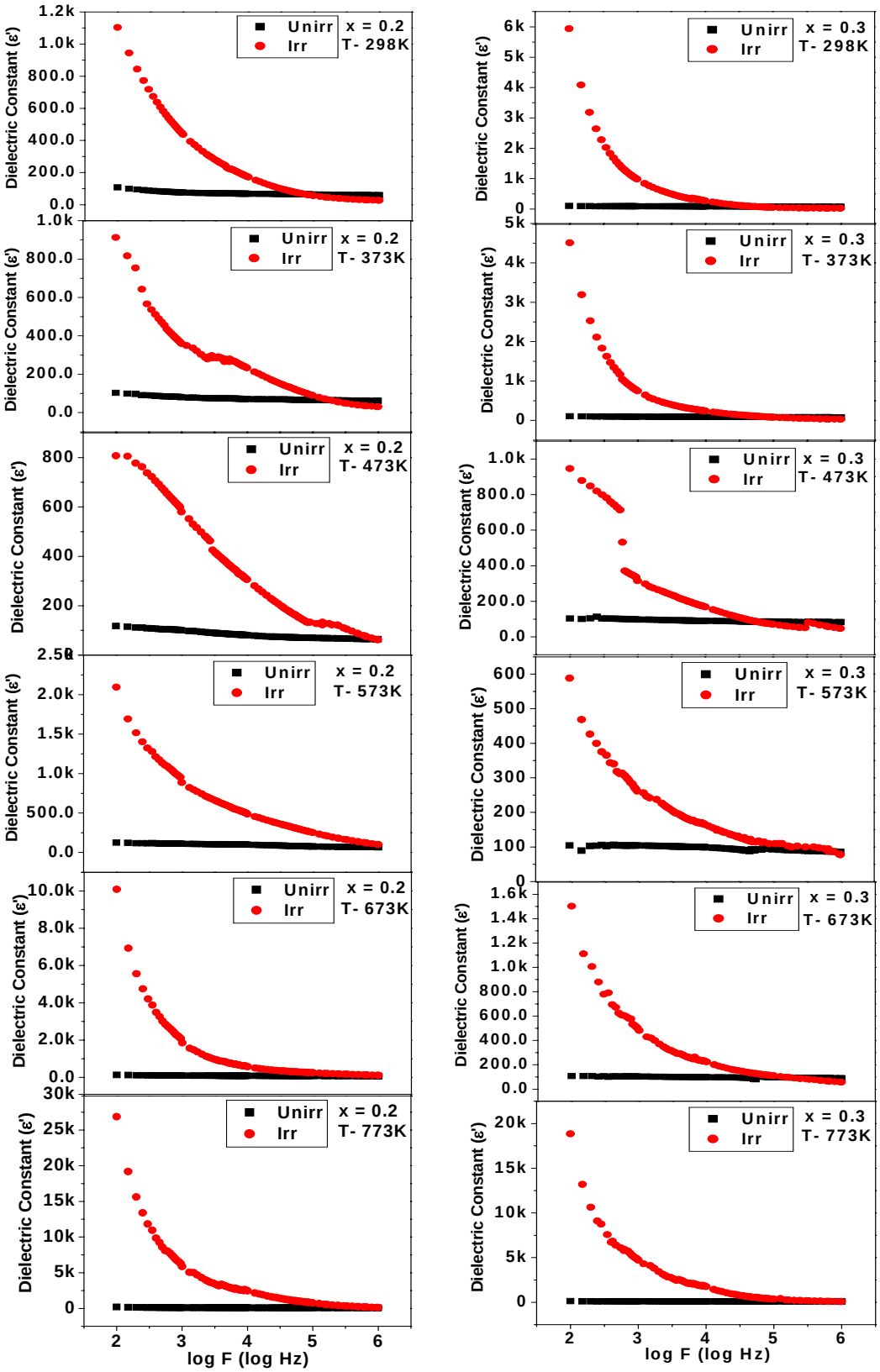

Fig. 6B.15b Dielectric Constant (ε') versus frequency at different temperatures for the compositions x = 0.2 and 0.3 of unirradiated and irradiated $Li_{0.5(1+x)}Ti_xCr_{0.1}Fe_{2.4-1.5x}O_4$ system

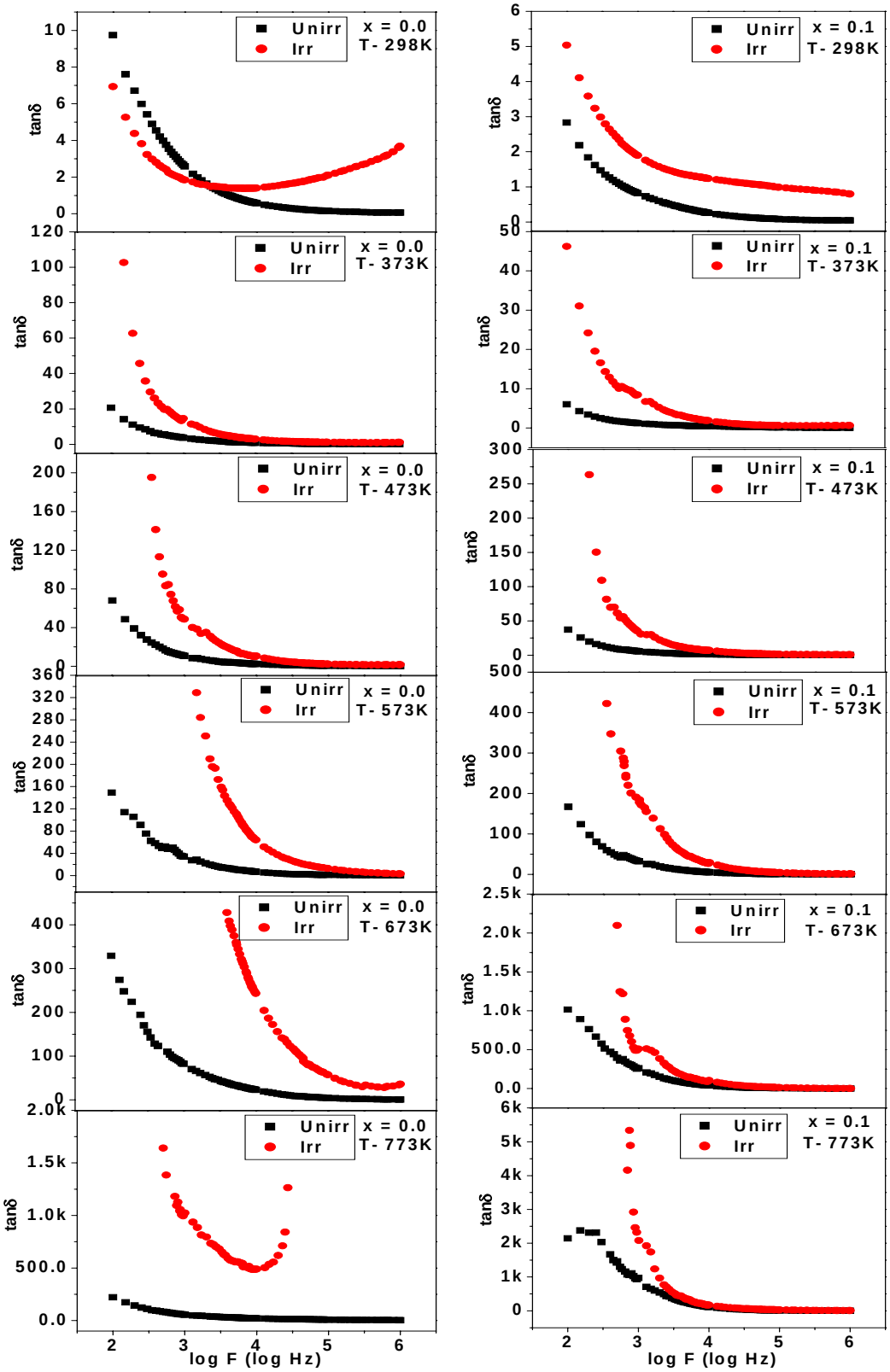

Fig. 6B.16a Dielectric loss tangent (tanδ) versus frequency at different temperatures for the compositions x = 0.0 and 0.1 of unirradiated and irradiated $Li_{0.5(1+x)}Ti_xCr_{0.1}Fe_{2.4-1.5x}O_4$ system

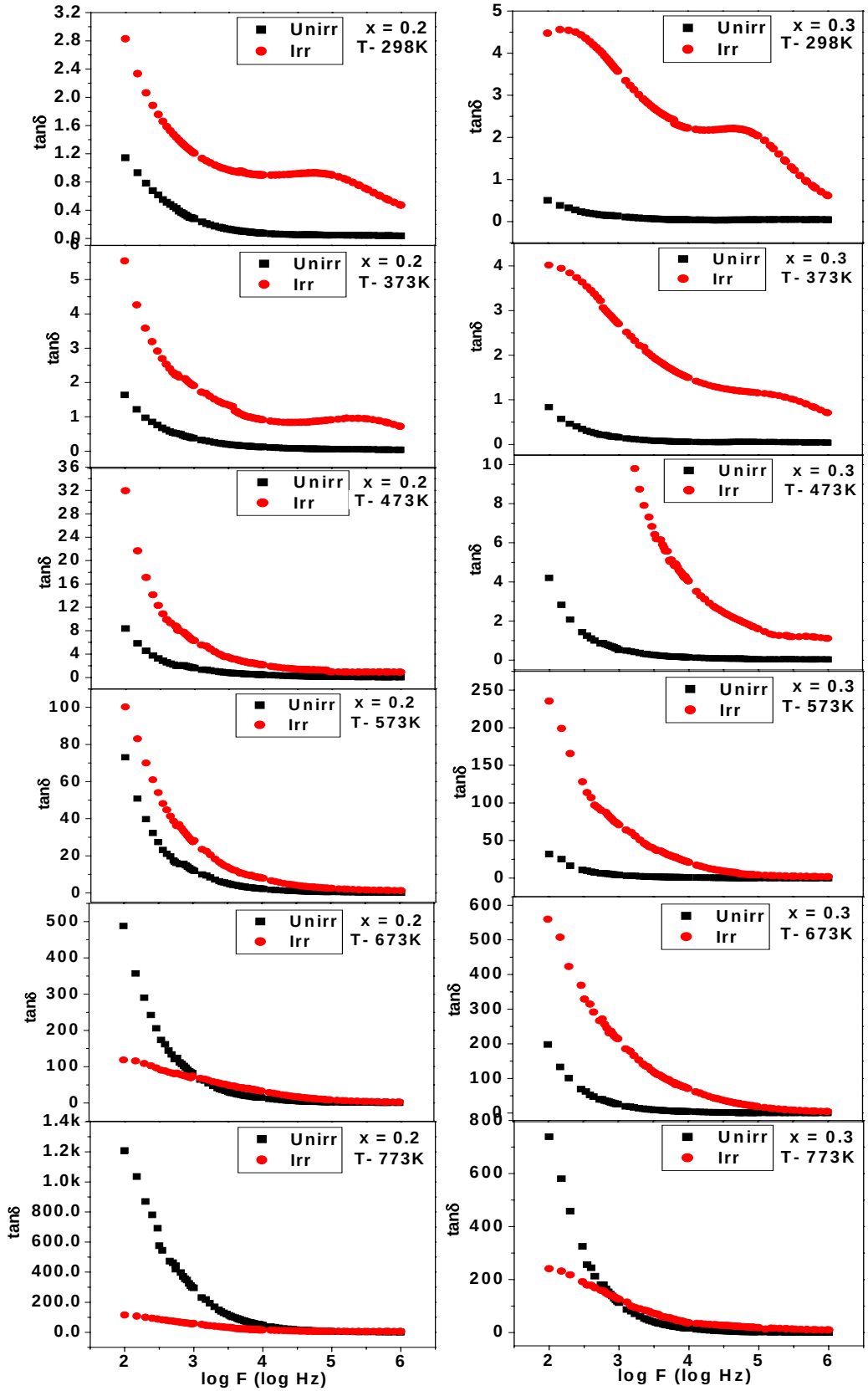

Fig. 6B.16b Dielectric loss tangent (tanδ) versus frequency at different temperatures for the compositions x = 0.2 and 0.3 of unirradiated and irradiated $Li_{0.5(1+x)}Ti_xCr_{0.1}Fe_{2.4-1.5x}O_4$ system

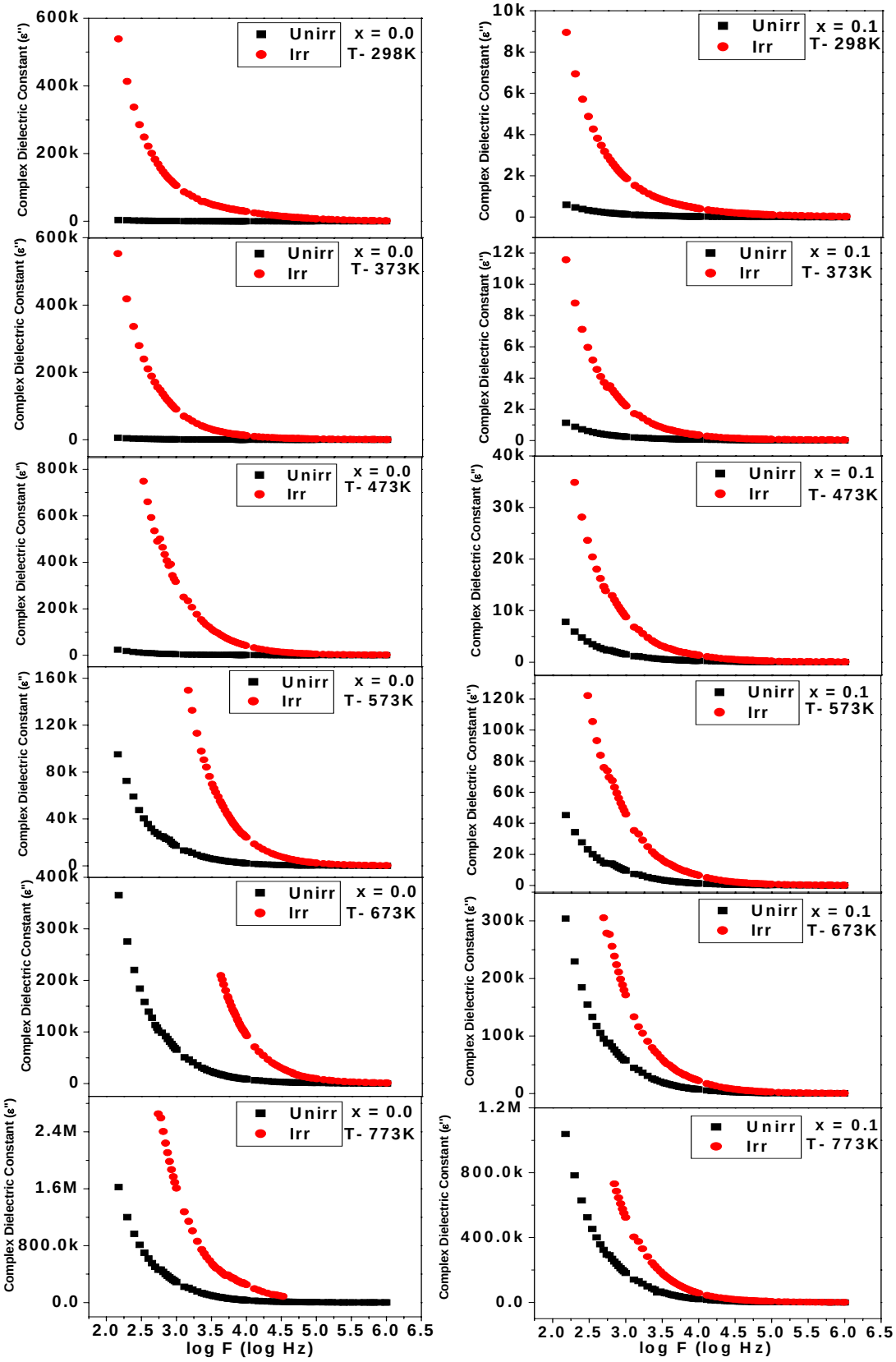

Fig.6B.17a Complex Dielectric Constant (ε'') versus frequency at different temperatures for the compositions x = 0.0 and 0.1 of unirradiated and irradiated $Li_{0.5(1+x)}Ti_xCr_{0.1}Fe_{2.4-1.5x}O_4$ system

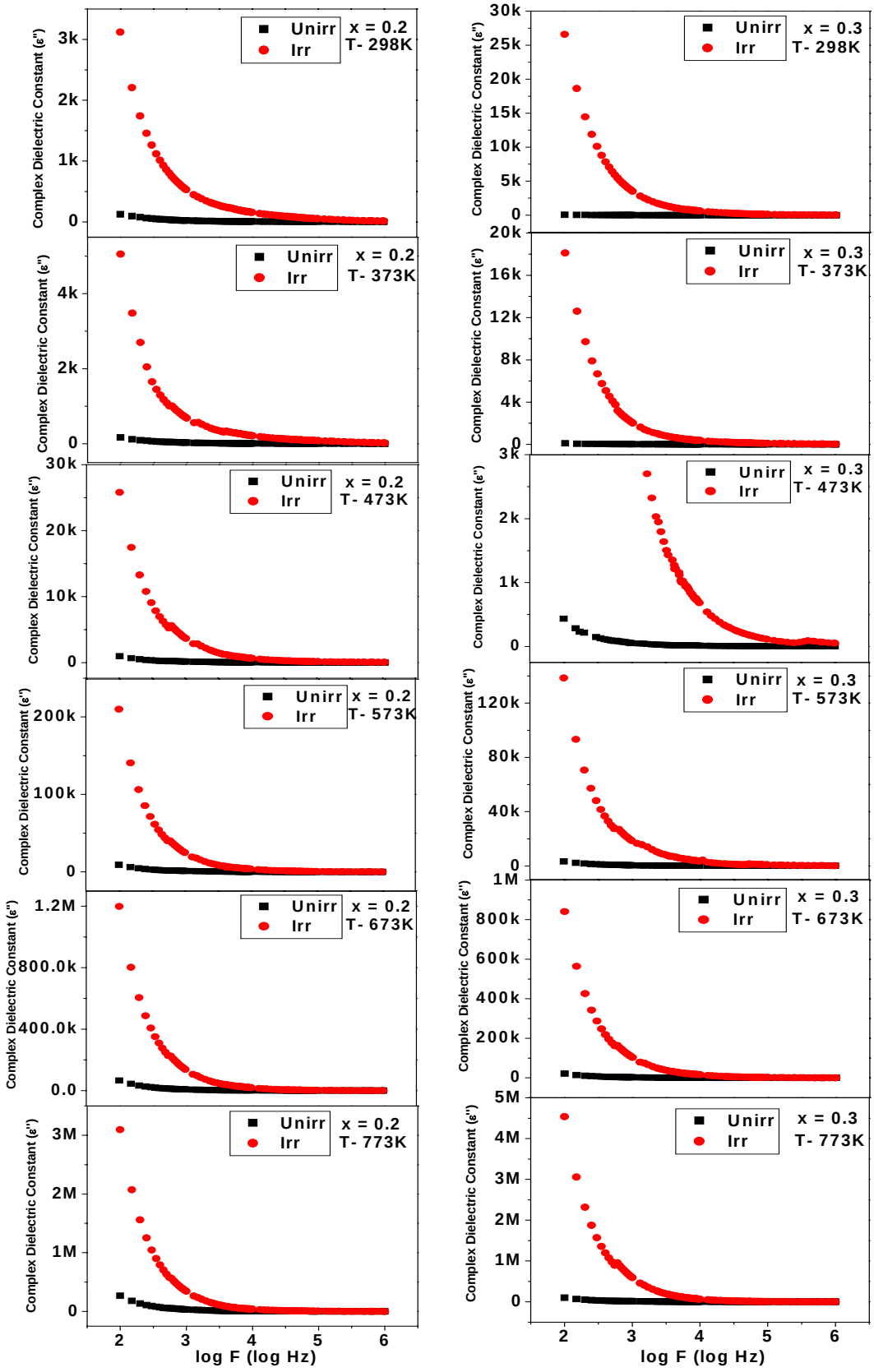

Fig. 6B.17b Complex Dielectric Constant (ε'') versus frequency at different temperatures for the compositions x = 0.2 and 0.3 of unirradiated and irradiated $Li_{0.5(1+x)}Ti_xCr_{0.1}Fe_{2.4-1.5x}O_4$ system

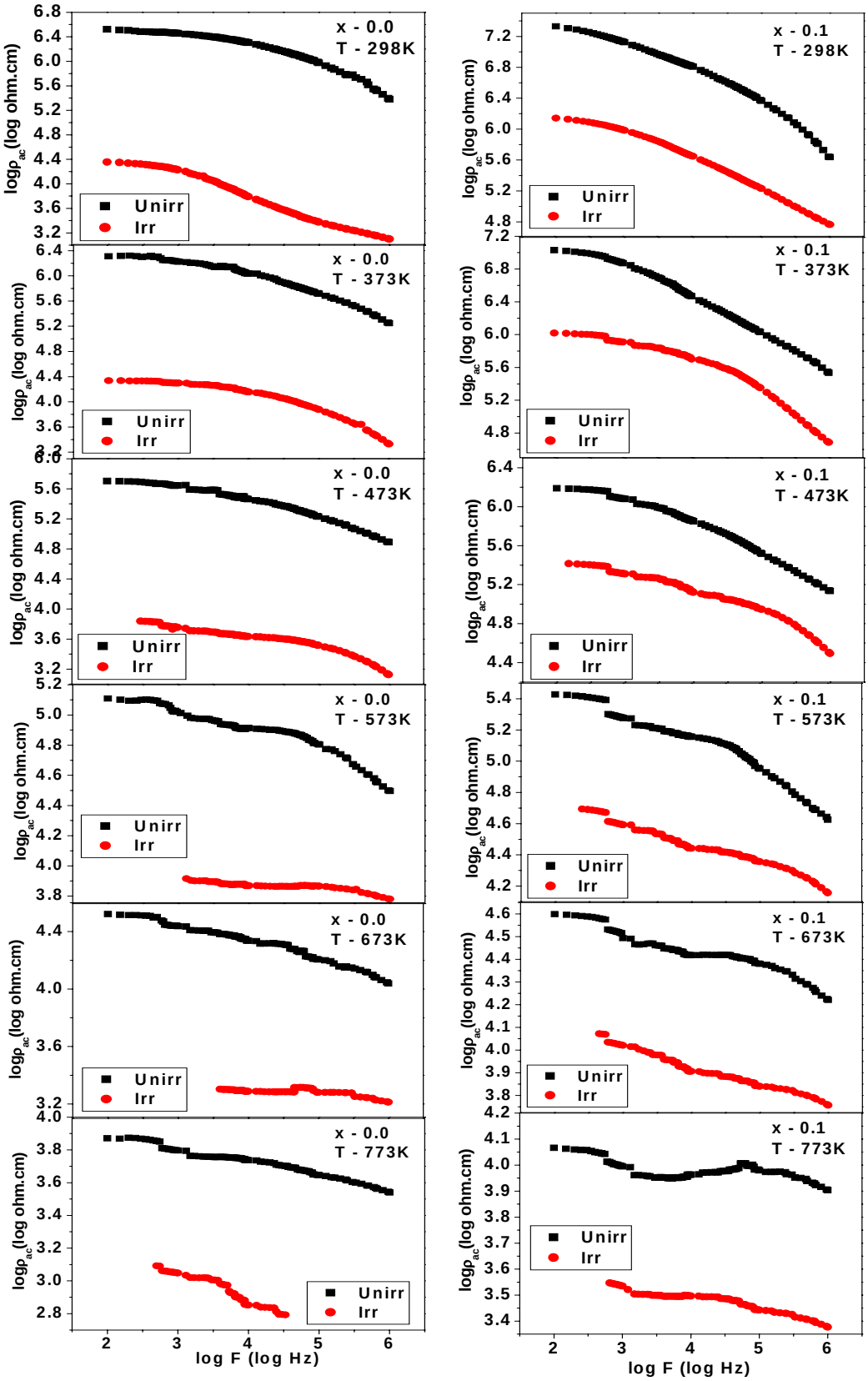

Fig. 6B.18a a.c. resistivity ($\log_{10}\rho_{ac}$) versus frequency ($\log_{10}F$) at different temperatures for the compositions x = 0.0 and 0.1 of unirradiated and irradiated $Li_{0.5(1+x)}Ti_xCr_{0.1}Fe_{2.4-1.5x}O_4$ system

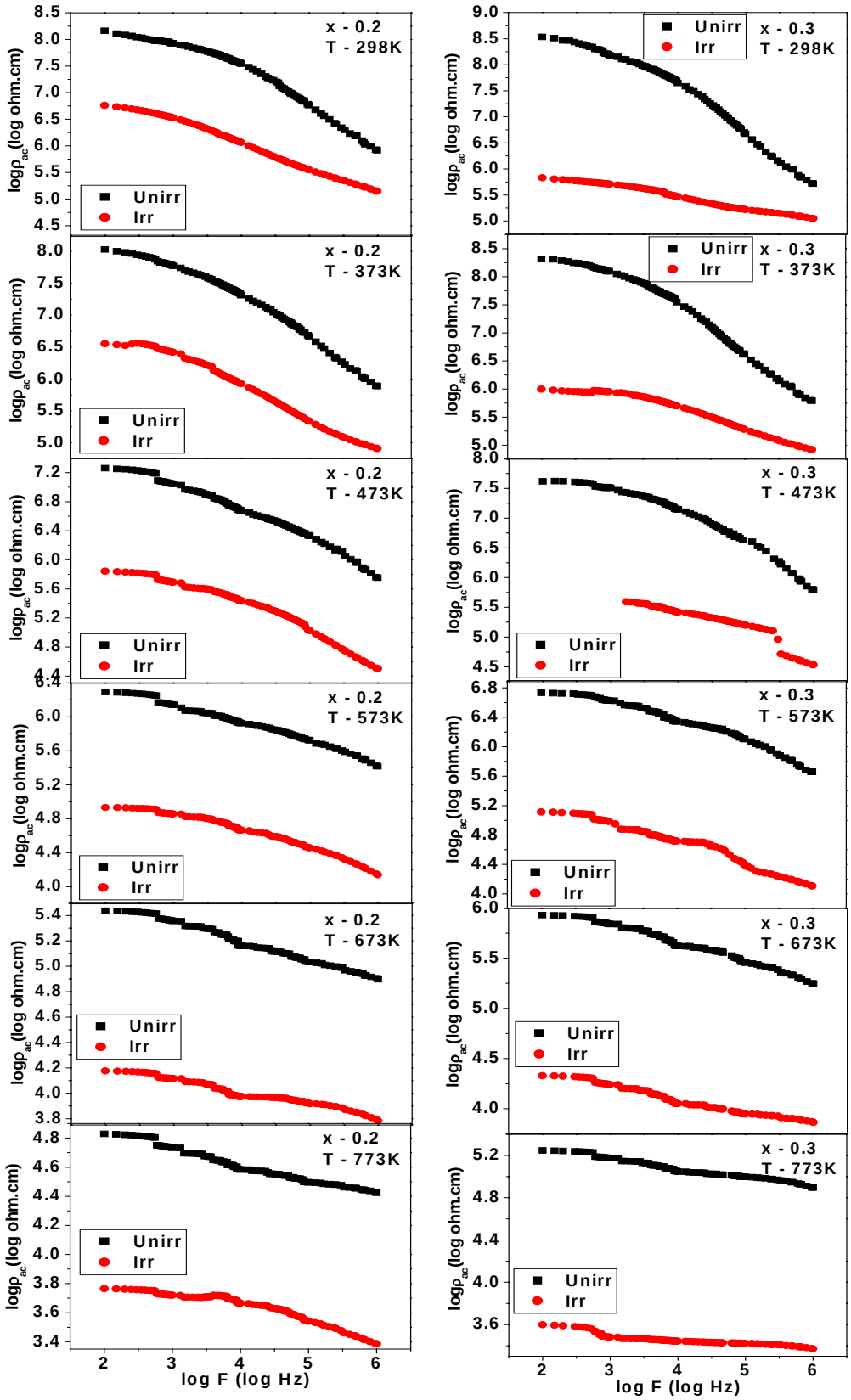

Fig. 6B.18b a.c. resistivity ($\log_{10}\rho_{ac}$) versus frequency ($\log_{10}F$) at different temperatures for the compositions x = 0.2 and 0.3 of unirradiated and irradiated $Li_{0.5(1+x)}Ti_xCr_{0.1}Fe_{2.4-1.5x}O_4$ system

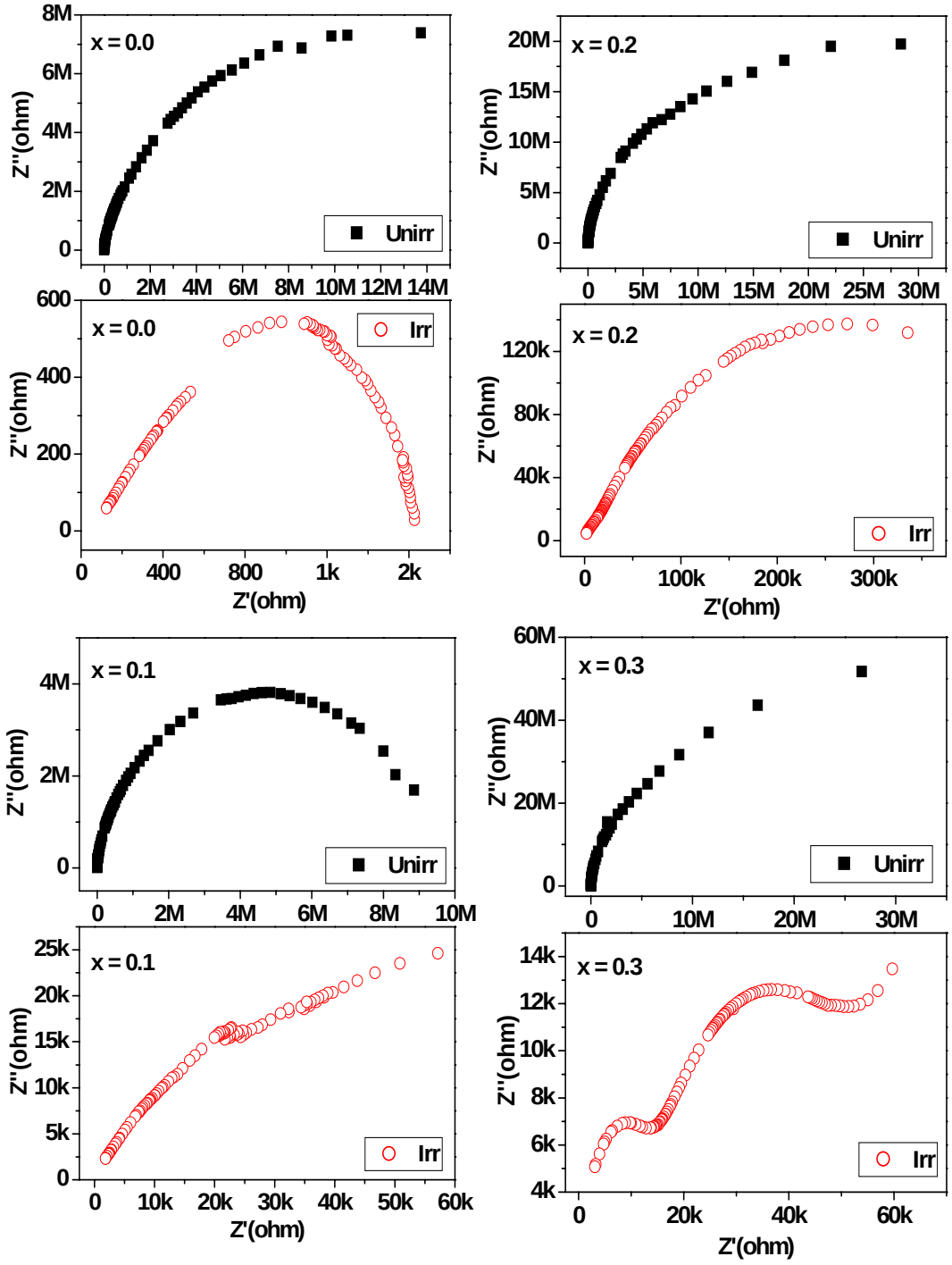

Fig. 6B.19 Real (Z') versus imaginary (Z'') parts of the impedance, Cole-Cole Plots at room temperature for the compositions x = 0.0, 0.1, 0.2 and 0.3 of unirradiated and irradiated $Li_{0.5(1+x)}Ti_xCr_{0.1}Fe_{2.4-1.5x}O_4$ system

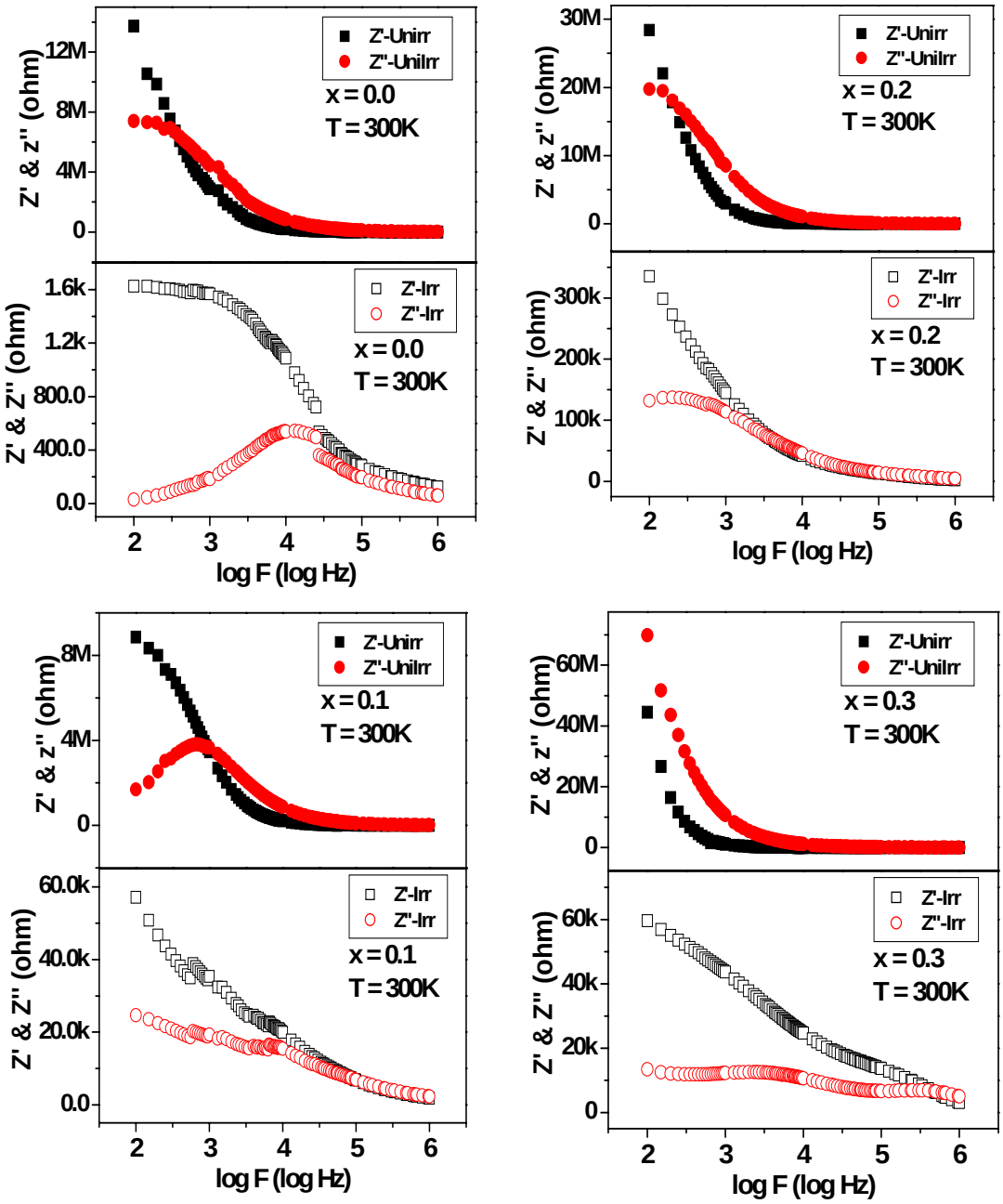

Fig. 6B.20 Variation of real part (Z') and imaginary part (Z'') of the impedance with frequency at room temperature for the compositions x = 0.0, 0.1, 0.2 and 0.3 of unirradiated and irradiated $Li_{0.5(1+x)}Ti_xCr_{0.1}Fe_{2.4-1.5x}O_4$ system

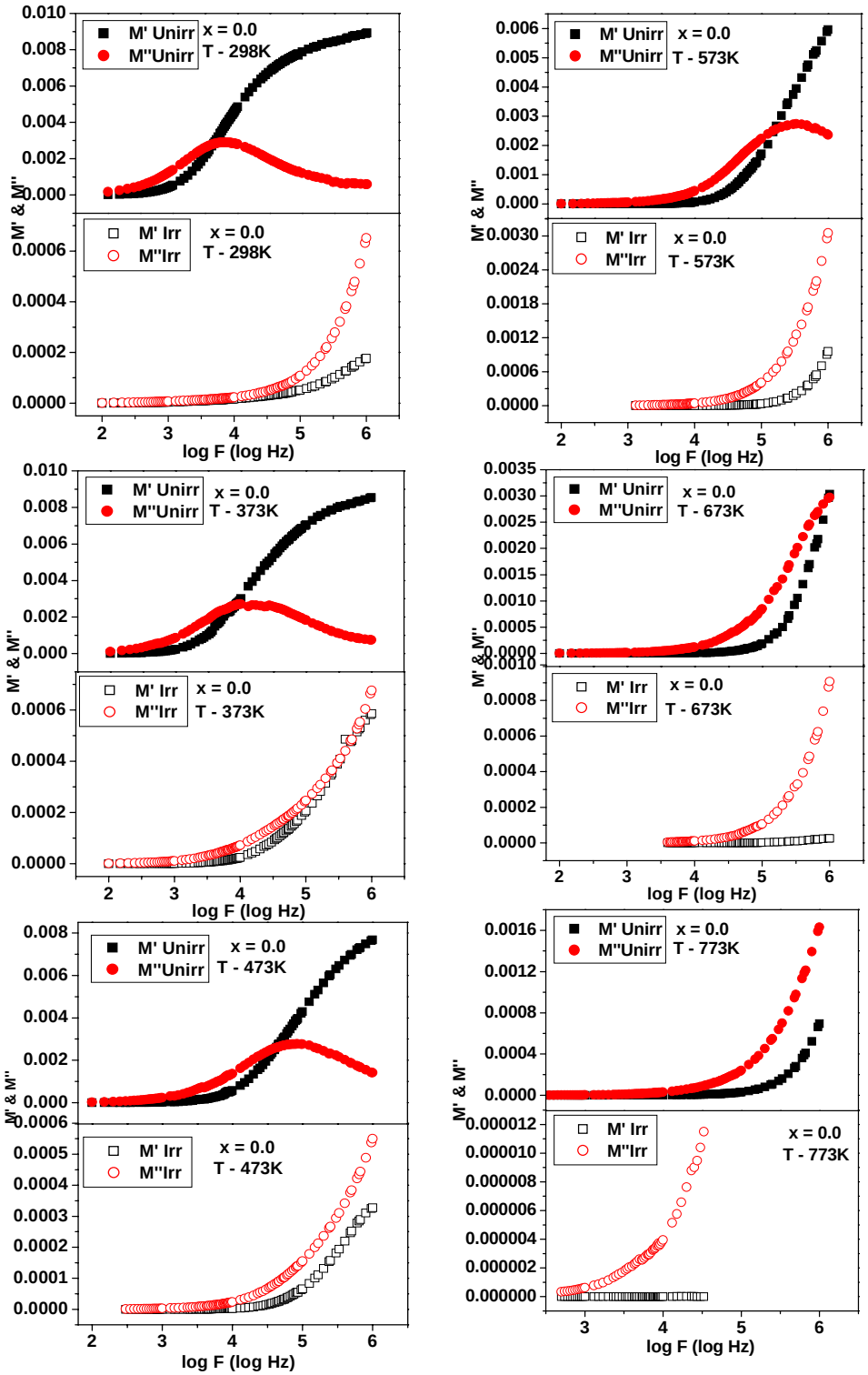

Fig. 6B.21a Real (M') and imaginary (M'') part of the dielectric modulus versus frequency at selected temperatures for the composition x = 0.0 of unirradiated and irradiated $Li_{0.5(1+x)}Ti_xCr_{0.1}Fe_{2.4-1.5x}O_4$ system

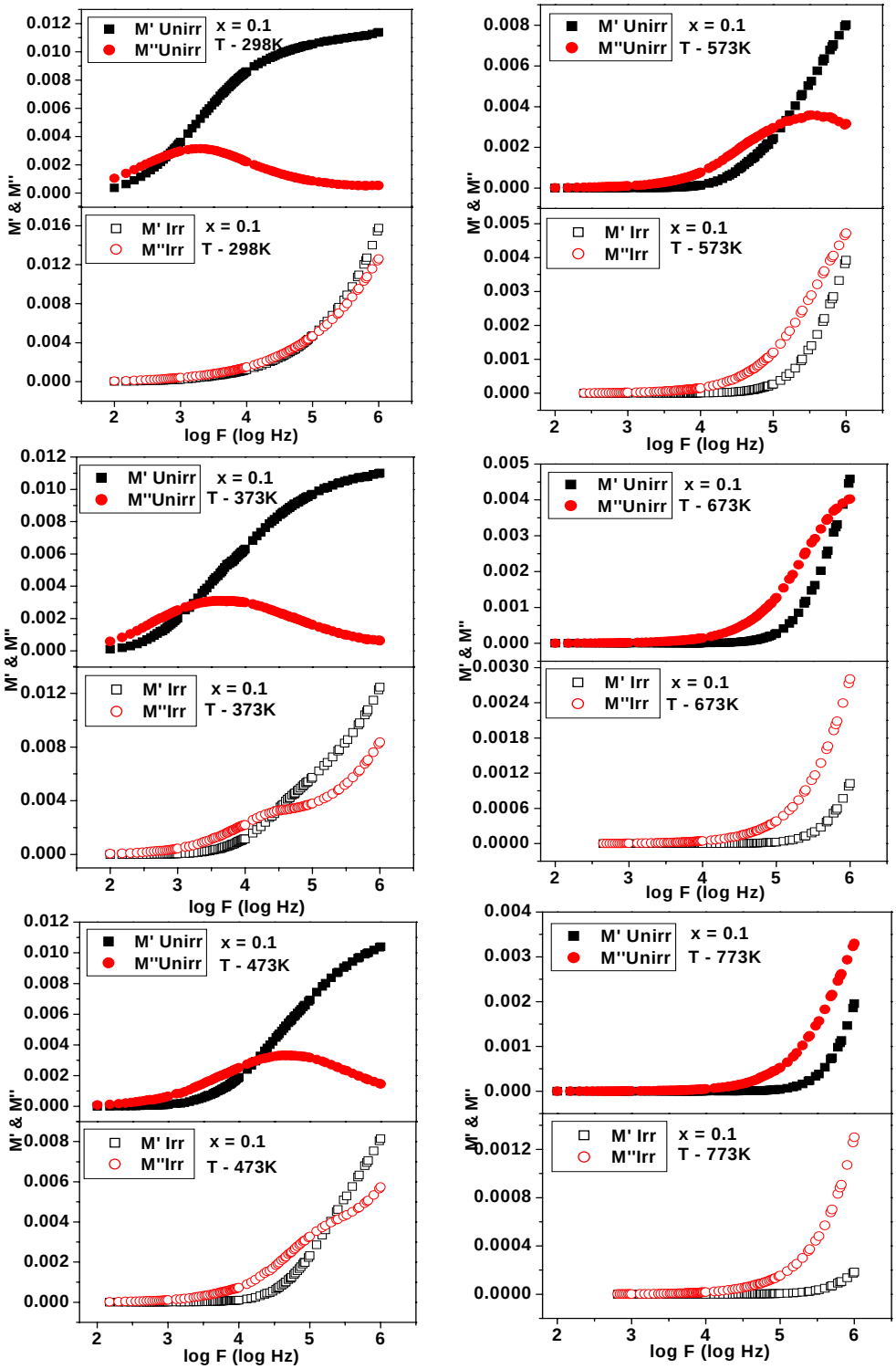

Fig. 6B.21b Real (M') and imaginary (M'') part of the dielectric modulus versus frequency at selected temperatures for the composition x = 0.1 of unirradiated and irradiated $Li_{0.5(1+x)}Ti_xCr_{0.1}Fe_{2.4-1.5x}O_4$ system

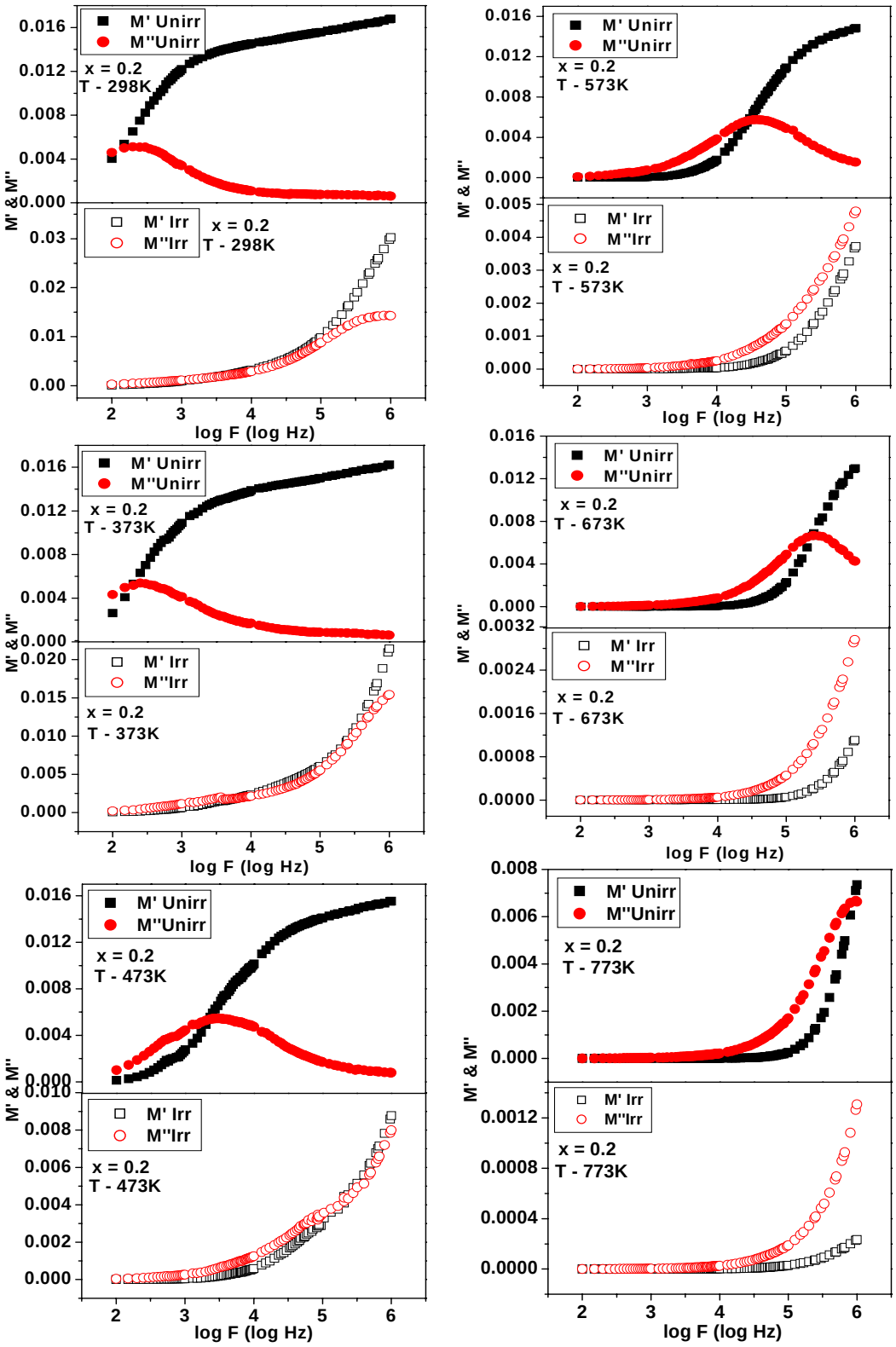

Fig. 6B.21c Real (M') and imaginary (M'') part of the dielectric modulus versus frequency at selected temperatures for the composition x = 0.2 of unirradiated and irradiated $Li_{0.5(1+x)}Ti_xCr_{0.1}Fe_{2.4-1.5x}O_4$ system

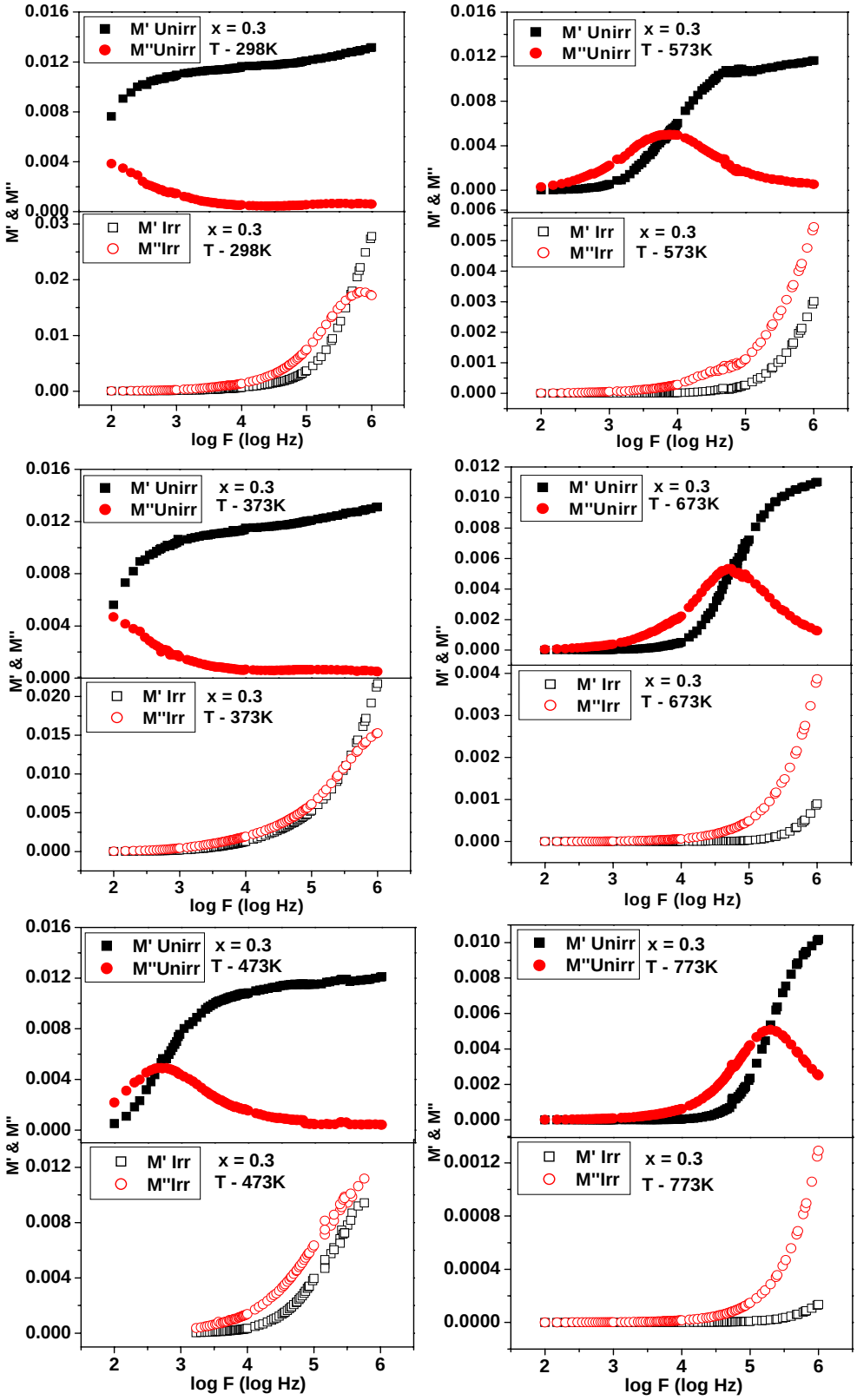

Fig. 6B.21d Real (M') and imaginary (M'') part of the dielectric modulus versus frequency at selected temperatures for the composition x = 0.3 of unirradiated and irradiated $Li_{0.5(1+x)}Ti_xCr_{0.1}Fe_{2.4-1.5x}O_4$ system

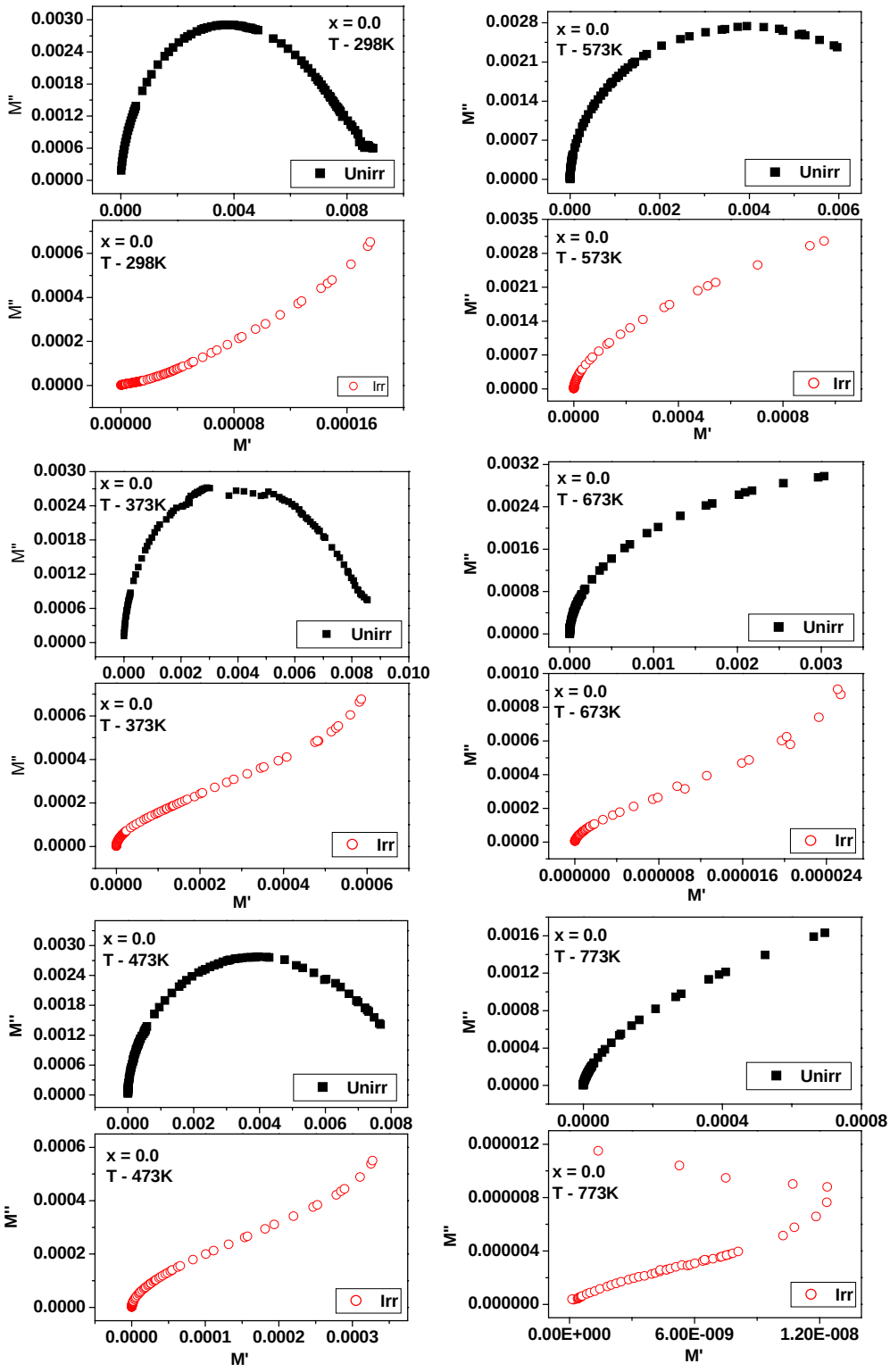

Fig. 6B.22a Real (M') versus imaginary (M'') parts of the dielectric modulus, Cole-Cole Plots at selected temperatures for the composition x = 0.0 of unirradiated and irradiated $Li_{0.5(1+x)}Ti_xCr_{0.1}Fe_{2.4-1.5x}O_4$ system

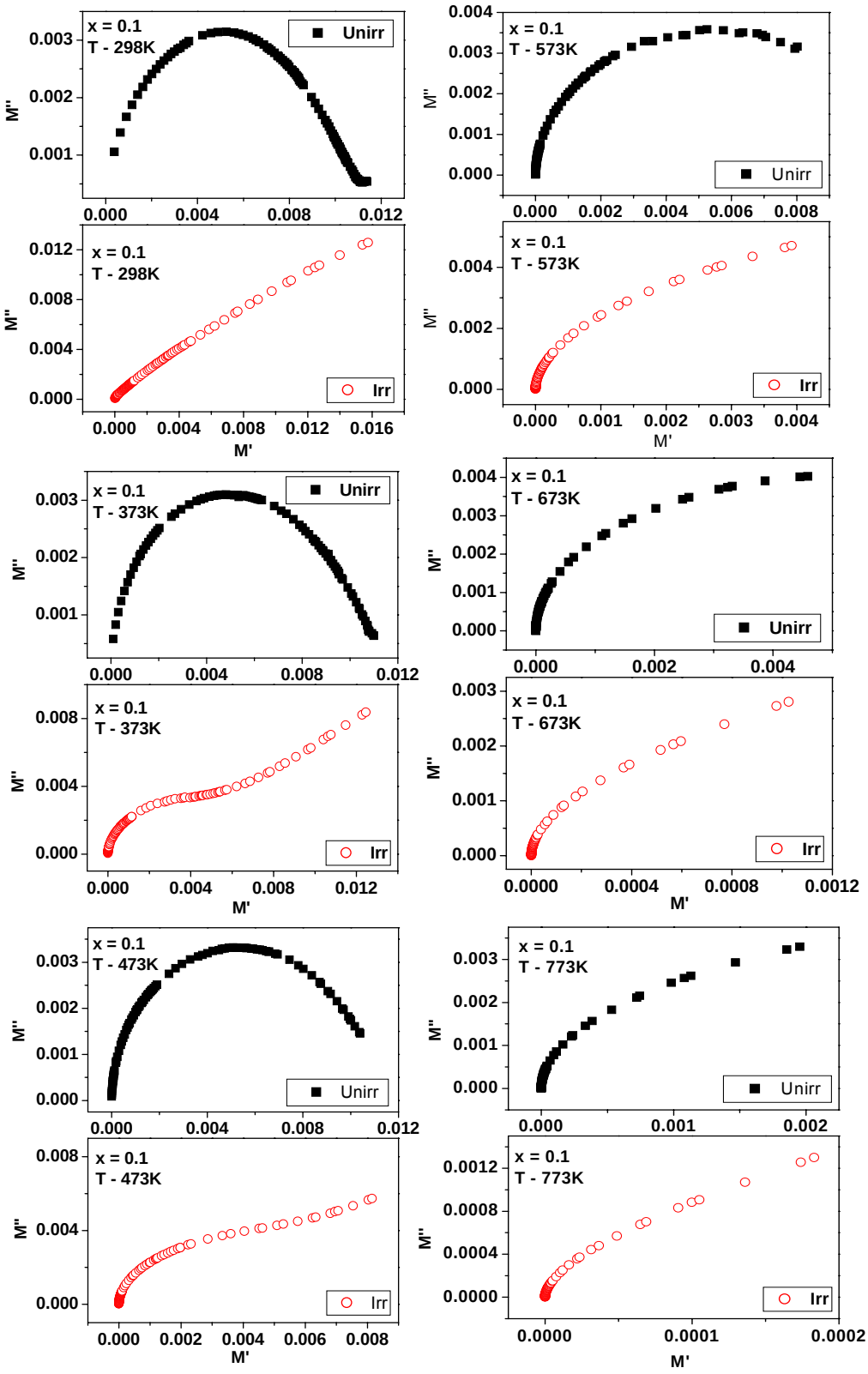

Fig. 6B.22b Real (M') versus imaginary (M'') parts of the dielectric modulus, Cole-Cole Plots at selected temperatures for the composition x = 0.1 of unirradiated and irradiated $Li_{0.5(1+x)}Ti_xCr_{0.1}Fe_{2.4-1.5x}O_4$ system

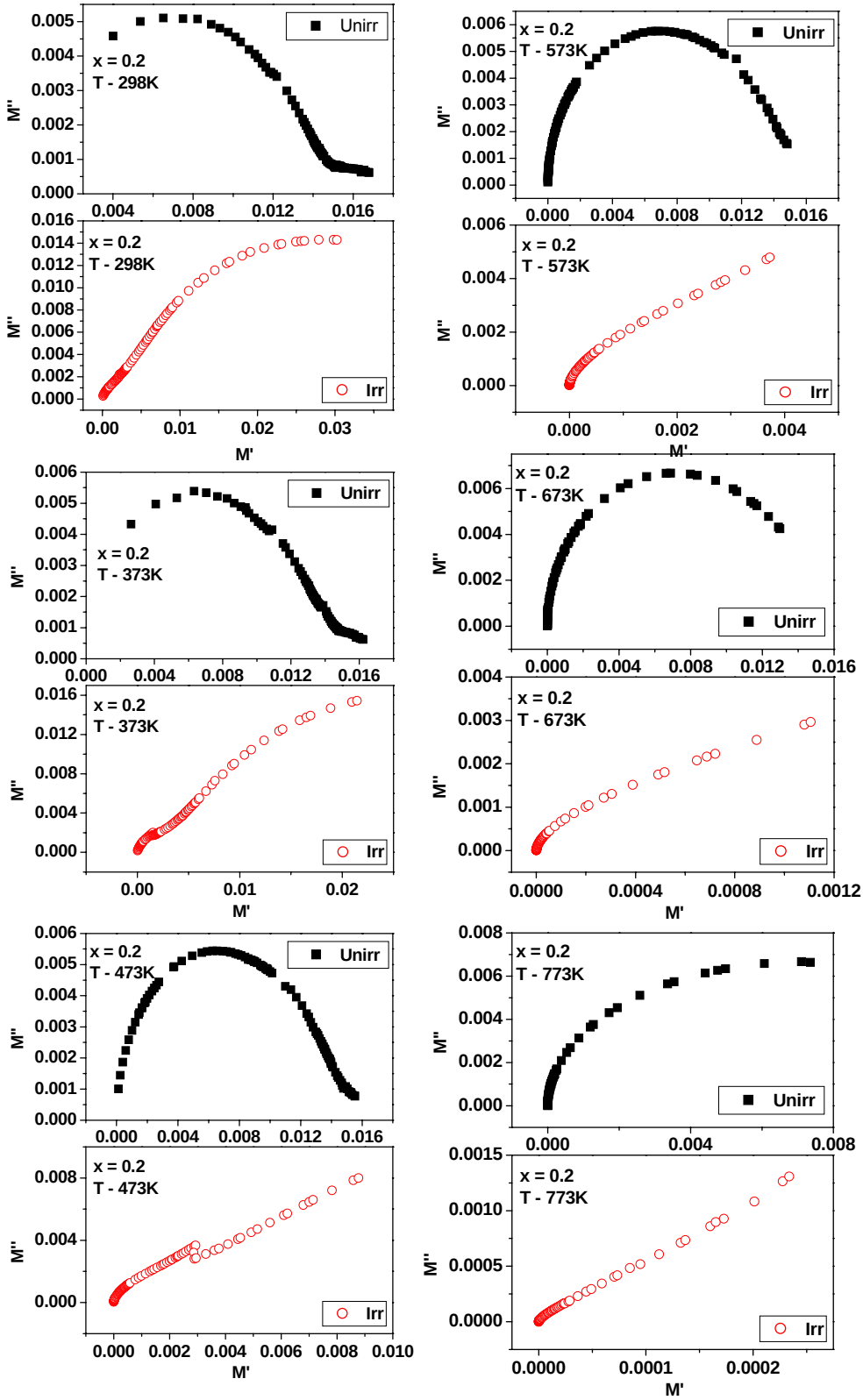

Fig. 6B.22c Real (M') versus imaginary (M'') parts of the dielectric modulus, Cole-Cole Plots at selected temperatures for the composition x = 0.2 of unirradiated and irradiated $Li_{0.5(1+x)}Ti_xCr_{0.1}Fe_{2.4-1.5x}O_4$ system

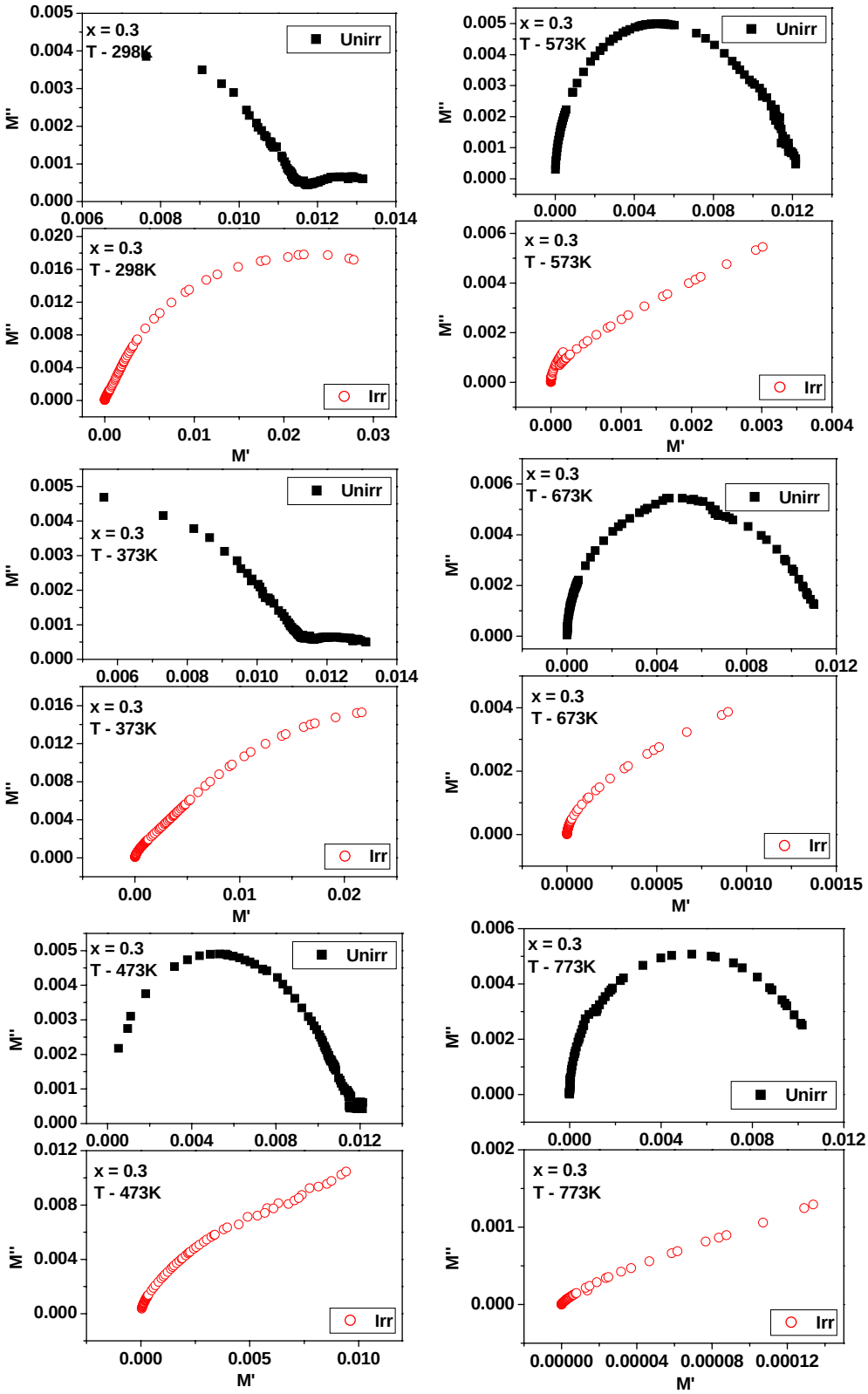

Fig. 6B.22d Real (M') versus imaginary (M'') parts of the dielectric modulus, Cole-Cole Plots at selected temperatures for the composition x = 0.3 of unirradiated and irradiated $Li_{0.5(1+x)}Ti_xCr_{0.1}Fe_{2.4-1.5x}O_4$ system

❖ *50 MeV Li^{3+} ions irradiation of $MnAl_xCr_xFe_{2-2x}O_4$*

6C.1 SHI Irradiation effects on Structural and Magnetic Properties

6C.2 SHI Irradiation effects on Structural parameters

6C.3 SHI Irradiation effects on Infrared Spectra

6C.4 SHI Irradiation effects on Elastic properties

6C.5 SHI Irradiation effects on Electrical properties

6C.6 SHI Irradiation effects on Dielectric properties

6C.7 SHI Irradiation effects on Impedance Spectroscopy

Conclusion

References

6C.1 Swift Heavy Ion Irradiation effects on Structural and Magnetic properties of the system $MnAl_xCr_xFe_{2-2x}O_4$

It was also resolved to study the influence of Swift Heavy Ion (SHI) irradiation on the spinel oxide system $MnAl_xCr_xFe_{2-2x}O_4$ (MAC) since it exhibited very interesting results before subjected to the irradiation. The system is the result of simultaneous substitution of Fe^{3+} with trivalent cations Al^{3+} (non-magnetic) and Cr^{3+} (magnetic: free ion moment:$3\mu_B$). Five compositions x= 0.0 ($MnFe_2O_4$) to 0.8 step 0.2 were synthesized by standard double sintering ceramic technique. The chemical compositions and molecular weights are given in the Table 6C.1.

The chemical stoichiometry of the compositions of $MnAl_xCr_xFe_{2-2x}O_4$ was ascertained by Energy Dispersive X-ray mapping. The EDAX patterns of two representative samples are shown in Fig. 6C.1. All the samples showed impurities of Ca and Si of about less than 1%, which might have crept in to the samples due to contacts of pellet surface and porcelain boat at high temperature sintering. The important point is that the EDAX results showed no loss of ingredients after high temperature sintering and the results matched the expected values within the experimental error. The samples with expected stoichiometry can be used confidently for the SHI experiments to study the SHI induced micro-structural changes. After having ascertained the chemistry of the ferrite samples, they were characterized by X-ray diffraction for the revelation of monophasic nature and structural studies. All the specimen were found single phase spinels without any traces of impurities (detected by EDAX), unreacted ingredients or unwanted secondary structural phases. The indexed X-ray diffraction patterns are displayed in Figs. 6C.2a-2c. All the patterns were analyzed using POWDER-X software [6C.1]. Thus, the samples were ready for the SHII study satisfying the prerequisites for the experiment. The well-characterized samples (in powder as well as in thin pellet form) were irradiated with 50 MeV Li^{3+} ion beam with fluence values 1 x 10^{13} ions/cm^2 using 15UD Pelletron accelerator at Inter University Accelerator Centre, New Delhi. The projected range (R_p), electronic energy loss (S_e) and nuclear energy loss (S_n) of 50 MeV Li^{3+} ions in all the compounds calculated using the SRIM-2003 are as follows 223 μm,13.2 eV/Å and 7.10x 10^{-3} eV/Å for the system.

The lattice parameters found from the X-ray diffraction data analysis are listed in Table 6C.3**.** It is clear that the lattice cell edge parameter decreases with Al-Cr

concentration (x). The lattice parameter for $MnFe_2O_4$ (x=0.0) deduced from XRD data is 8.489Å which is slightly lower than the reported value for Mn-ferrite 8.510 Å [6C.2]. The plot of compositional variation of lattice parameter is linear (Fig. 6C.3**).** The linear decrease in cell edge parameter with concentration (x) follows the Vegard's law [6C.3]. The Vegard's law is based on the change due to the ionic radii of the replacing and replaced ions in the spinel lattice. The law predicts the linear variation of lattice constant with substitution of different ions. In the present case Al^{3+} is smaller ion with radius 0.51 Å compared to the radii of Fe^{3+} (0.64 Å) and Cr^{3+} (0.63 Å). Its substitution with Fe^{3+} results in a linear decrease in cell edge. The X-ray density decreases with increase in the concentration (x).

The distribution of cations in $MnFe_2O_4$ cannot be deduced from its saturation moment by assuming the Nèel's type collinear magnetic structure as both the magnetic ions Mn^{2+} and Fe^{3+} possess the same values of free ion magnetic moment of 5 μ_B . The cation distribution of $MnFe_2O_4$ has been the topic of controversy for many workers. It has been reported by Hastings and Corliss [6C.4] and Harrison [6C.5] that it is 19% inverse spinel ferrite containing Mn^{3+} and Fe^{2+} ions in octahedral sites. The NMR studies of Yasuoka [6C.6] suggested the 54% degree of inversion with the presence of Mn^{2+}, Mn^{3+}, Fe^{2+} and Fe^{3+} ions on octahedral sites. The Mn^{3+} ion has preference for octahedral coordination while Mn^{2+} has no specific preference for tetrahedral or octahedral sites. The neutron diffraction study by Satya Murthy et al [6C.7] showed that the cation distribution in $MnFe_2O_4$ has 8% degree of inversion. Thus, the cation distribution of Mn-ferrite is not completely normal or inverse and the degree of inversion varies depending upon the preparation conditions.

Since there is no difference in X-ray atomic scattering factors for the coexisting cations Fe^{3+} and Mn^{2+}, it is not possible to obtain their distribution in tetrahedral and octahedral sites using X-ray diffraction intensity calculation. In such a situation where the atoms have no contrast in their atomic scattering factors, one should resort to the technique like iron- Mössbauer spectroscopy. The Mössbauer spectrum of Mn-ferrite (unirradiated) is depicted in Fig 6C.4a**.** The spectrum was analyzed using the NORMOS software and the Mössbauer hyperfine parameters are given in Table 6C.4**.** The cation distribution deduced for Mn-ferrite is given in Table 6C.2**.** The degree of inversion found is 40%.

The X-ray atomic scattering factor for Cr^{3+} is also not appreciably different from that of Fe^{3+} , whereas the scattering factor of Al^{3+} is significantly low compared

to those of the other cations. With this contrast, the distribution of Al^{3+} ions can be obtained accurately from X-ray diffraction intensity calculations. The Cr^{3+} ions have been reported to have the strongest B-site preference [6C.8]. The Cr^{3+} ions were fixed on the B-sites through the calculations. The Al^{3+}, Mn^{2+}, Fe^{3+} ions have been found to occupy the A- and B-sites in different proportions. In the X-ray intensity analysis the B-site occupancy of Mn^{2+} i.e. degree of inversion is kept constant through out the calculation and the distribution of Al^{3+} was continuously varied along with the Fe^{3+} ions to maintain the overall stoichiometry of the structure. The cation distributions for both unirradiated and irradiated samples are given in Table 6C.2 along with the plane intensity ratios. Recall the linear decrease of lattice parameter as a function of concentration. The systematic linear decrease of lattice constant indirectly supports the assumption that the degree of inversion remains constant for all the compositions before irradiation. It is clear that the cell edge parameter is sensitive to the migration of Mn^{2+} (0.80 Å) ions in the lattice.

The saturation magnetization (σ_s) in emu/g of all the compositions of the present system was measured at 80K at the peak field of 5kOe using hysteresis loop tracer. The σ_s and magneton number (saturation magnetization per formula unit in Bohr Magneton, μ_B) values are given in Table 6C.3. The values of Nèel moments ($n_B^N = M_B(x) - M_A(x)$) derived assuming Nèel's collinear model using the free ion moments of the magnetic cations and the cation distributions deduced through X-ray diffraction and Mössbauer spectroscopy are also given in the Table 6C.3. The free ion spin only moments for all the constituent magnetic cations are as follows: Fe^{3+} (5 μ_B), Mn^{2+} (5μ_B) and Cr^{3+} (3μ_B). It is clear that the difference between the Nèel's moment and the observed moment decreases monotonically with increase in Al-Cr (x) content. The n_B^N and n_B^{obs} converge at x = 0.6 .

It is seen that the difference between the observed moment (n_B^{obs}) and the Neel's moment (n_B^N) is the largest for $MnFe_2O_4$ (x = 0.0). This lower value of n_B compared to the reported values within the range 4.6 μ_B to 4. 85 μ_B is ascribed to the higher degree of inversion in the present case which also explains the higher value of the Curie temperature [6C.9] observed in the present case compared to the reported values [6C.2]. The origin of the overall reduction of the observed magnetic moment, reported by other workers as well as in the present case, for Mn-ferrite lies in the "dynamical nature of super-exchange interaction" in Mn-ferrite [6C.10]**.** The neutron spectroscopy study has revealed that during the interaction of thermal neutron with an

ion it observes different number of interacting nearest neighbours (magnetic ions). Moreover, the study has also shown that the quadrupole interaction parameter of $3d^5$ electron shell is negative indicating an oblate type deformation. It is also shown that the mixed quadrupole-exchange interactions of Fe^{3+} ions in octahedral sites have been reported to lower the magnetic moment when spin makes non-zero angles with trigonal axis [6C.11]. It is also reported that in Mn-ferrite, ¾ of Fe^{3+} (B) spins make an angle $\theta \sim 70^0$ and lowering the magnetic moments depending upon the number of interacting magnetic ions.

It is seen that the Mössbauer spectra of Mn-ferrite at RT is two Zeeman split sextet due to A-site and B-site Fe^{3+} ions. The significant negative quadrupole shift for B-site and small negative quardupole shift for A-site is conspicuous (Table 6C.4)**,** it is also present for x=0.2 and 0.4 samples. This indicates oblate type of deformation of the $3d^5$ shell which gives rise to dipole field in B-sites resulting in angle with the trigonal axis and lowering of the resultant magnetic moment. Moreover, the earlier studies have ruled out the other causes of moment reduction like the presence of Fe^{2+}, Mn^{3+} or Mn^{4+} on B-sites, non-collinear or spiral type magnetic ordering, and deviation from the spin only moments of Fe^{3+} and Mn^{2+} ions. Thus, the origin of the lower magnetic moment observed for $x < 0.6$ lies in the parent compound $MnFe_2O_4$.

The X-ray diffraction patterns of all the irradiated samples are shown in Fig. 6C.2a-2c**.** All the patterns are seen to shift towards lower Bragg angle indicating expansion of the unit cell. The cell edge parameter of all the compositions are found to increase after subjected to the swift heavy ion irradiation (Table 6C.3). This is due to the migration of Mn^{2+}, largest cation present in the system, to the tetrahedral site after irradiation. The increased A-site occupancy of Mn^{2+} also modifies the site iron distribution ratio. Since the X-ray atomic scattering factors are almost same in case of Mn^{2+} and Fe^{3+}, the combined look at the X-ray diffraction intensity calculation and iron Mössbauer spectroscopy can resolve the cation distribution. The cation distributions after irradiation are given in Table 6C.2. It was not possible to fit the Mössbauer spectra for x=0.6 and x=0.8 for deriving the iron distribution accurately, and X-ray cannot produce adequate contrast in the atomic scattering factors of the ions, therefore 5% increase in the A-site occupancy of Mn^{2+} after the irradiation was assumed for maintaining the trend. This also keeps undisturbed the convergence of Nèel's moment and the observed saturation moment which actually started at x=0.4 after the irradiation.

It is interesting to note that the observed saturation moment of Mn-ferrite is found to increase after SHI-irradiation and attains value almost near to the Nèel's moment. It was explained in the previous paragraphs that the saturation magnetic moment of unirradiated Mn-ferrite is lowered compared to the collinear spin arrangement due to the mixed quadrupole exchange interactions and canting of Fe^{3+} spin depending upon the statistics of the nearest neighbours. The SHI irradiation must be modifying the magnetic micro-structure by reducing the canting favourably and enhancing the observed magnetic moment. The migration of Mn^{2+} and Fe^{3+} does not affect the Nèel's moment as they have equal free ion magnetic moment. This supports the argument that the increase in the magnetic moment is not due to the rearrangement of the cations but due the favourable modification of the magnetic micro-structure that took place in the parent compound Mn-ferrite. It is also clear that the observed magnetic moment matches with the Nèel's moment for all the compositions, in contrast to the unirradiated case where the convergence took place at x=0.6. This again supports the 'origin' of lowering the observed magnetic moment in Mn-ferrite compounds.

It is also inferred that in case of unirradiated samples the deviation from the Nèel's moment is reduced with increase in the Al-Cr concentration(x), due to the increase in disorder with increase in Al-Cr (x) content diluting the effect of mixed-quadrupole exchange interactions i.e. the origin of the lower magnetic moment in Mn-ferrite compounds and causing the convergence of observed magnetic moment and Nèel's moment. This is due to the coexistence of Al^{3+} and Cr^{3+} in the system. The similar disorder must have been introduced after the SHI irradiation causing the enhancement of observed magnetic moment going almost near to the Nèel's moment. Therefore, no central enhancement has been observed in the Mössbauer spectra after the SHI-irradiation but the Mössbauer line widths are found to increase.

The AC susceptibility plots of all the unirradiated and irradiated compositions of present system are displayed in Fig. 6C.5 and the Curie temperatures determined through these plots for all the samples are listed in Table 6C.3. The decrease in T_c is found with increase in Al-Cr Content (x) for both unirradiated and irradiated samples. The shape of the AC susceptibility curves for initial sample x = 0.0 show normal ferrimagneitc behaviour however the compositions x = 0.2 to 0.6 show dominant tailing effect. This tailing effect may be due to the existence of "clusters" in the vicinity of T_c. It is quite conspicuous that the Curie temperature (T_c) for the irradiated

specimens x = 0.0 and 0.4 is lower and for x = 0.2 and 0.6 is higher than their unirradiated counterparts.

6C.2 Swift Heavy Ion Irradiation effects on Structural parameters of the ferrite system $MnAl_xCr_xFe_{2-2x}O_4$

Previous studies have shown that the swift heavy ion irradiation induced modifications in structural and magnetic properties of the ferrite system $MnAl_xCr_xFe_{2-2x}O_4$. The magnetic interactions, especially the superexchange interactions are highly sensitive to any change in bond length, bond angle and cation distribution and the defects present in the materials. Here, the present work reports the study of the effect of swift heavy ion irradiation on structural parameters like bond length, oxygen positional parameter, site ionic radii, bulk density, X-ray density, porosity etc. of studied $MnAl_xCr_xFe_{2-2x}O_4$ ferrite system.

It is well known that the density plays a key role in controlling the properties of polycrystalline ferrites. The effect of Al and Cr ion on the bulk density (d) and porosity (P) are shown in the Table 6C.5. By incorporating Al^{3+} and Cr^{3+} ions into the Mn-ferrites, a significant decrease is observed in the bulk density (d) for unirradiated and irradiated samples. The highest bulk density 4.1932 g/cm^3 and 4.2405 g/cm^3 are obtained for the composition x = 0.0 of unirradiated and irradiated sample, respectively. The decrease in bulk density with Al-Cr substitution in the Mn-ferrites may be attributed to the increase in number of pores at higher sintering temperature which decreases the effective area of the grain contact. This can also be ascribed to the atomic weight and density of Al^{3+} (26.9815, 2.70 g/cm^3) and Cr^{3+} (51.996, 7.19 g/cm^3), which are lower than those of Fe^{3+} (55.847, 7.87 g/cm^3). The X-ray density for each composition was calculated using the relation [6C.12]. The compositional variation of X-ray density for unirradiated and irradiated samples is given in Table 6C.5. It can be seen that the X-ray density decreases with increase of Al-Cr content (x) in spite of decrease in cell-volume (lattice constant) with content (x), which is due to the fact that the decrease in mass overtake the decrease in volume. The percentage of porosity was calculated for unirradiated and irradiated samples using the relation [6C.12, 6C.13]. The porosity of the samples varies within 16.30 % - 47.23% (Table 6C.5), which indicates the existence of more pores in the present samples. The porosity values are found to increase significantly with increasing Al^{3+} and Cr^{3+} ions concentrations.

From the Table 6C.5 it is clear that the bulk density increases after the irradiation for x = 0.0, 0.4 and 0.6. This can be attributed to the strong effect of irradiation on the microstructure of the samples. No systematic trend is observed in the bulk density and porosity after irradiation of the present samples. The X-ray density of the irradiated samples is lower than the unirradiated samples, which can be attributed to the change in the lattice parameter after irradiation. Our X-ray results show that the lattice parameter increases after irradiation due to the expansion of the unit cell dimensions.

The correlation between the ionic radii (r_A, r_B, R_o) and the theoretical lattice constant (a_{th}) is calculated [6C.14, 6C.15] for unirradiated and irradiated samples. The r_A and r_B have been calculated by the cation distribution (Table 6C.2) using the following equations:

$r_A = C_{AMn}r(Mn^{2+}) + C_{AAl}r(Al^{3+})\ C_{AFe}r(Fe^{3+})$

$r_B = (1/2)\ [C_{BMn}r(Mn^{2+})+C_{BAl}r(Al^{3+})+C_{BCr}r(Cr^{3+})+C_{BFe}r(Fe^{3+})$

where $r(Mn^{2+})$, $r(Al^{3+})$, $r(Cr^{3+})$, $r(Fe^{3+})$ are the ionic radii of Mn^{2+}, Al^{3+},Cr^{3+} and Fe^{3+} ions respectively while C_{AMn}, C_{AAl} and C_{AFe} are the concentration of Mn^{2+}, Al^{3+} and Fe^{3+} ions on A-sites and C_{BMn},C_{BAl}, C_{BCr} and C_{BFe} are the concentration of Mn^{2+}, Al^{3+}, Cr^{3+} and Fe^{3+} ions on B-sites. The calculated theoretical lattice constant 'a_{th}' of all investigated samples are tabulated in Table 6C.5. The difference between a_{exp} and a_{th} may be related to the lattice defects for polycrystalline material and ignoring the presence of Fe^{2+} ions on A or B sites [6C.15].

The results of ionic radii r_A and r_B show (Table 6C.6) that the ionic radii of tetrahedral site r_A is constant up to x = 0.6 then it decreases for x =0.8 while the ionic radii of octahedral site r_B linearly decreases with increasing Al-Cr content (x) for unirradiated samples, this happens because of the replacement of (2x) of Fe^{3+} (0.64 Å) by (x) of Al^{3+} (0.51 Å) and (x) of Cr^{3+} (0.63 Å) with increasing (x).. For irradiated samples, r_A initially decrease up to x = 0.2 after that it is increases while r_B is linearly decreases with increasing Al-Cr content (x). For irradiated samples, the ionic radii r_A is higher and r_B is lower than the unirradiated samples. The post irradiation trend of ionic radii is due to the variation in the cation distribution where Mn^{2+} (0.80 Å) has played the major role. The bond lengths A-O and B-O are average bond lengths (Table 6C.6); A-O = $r_A + R_o$ and B-O = $r_B + R_o$, where R_o is the radius of the oxygen ion (1.32 Å). The variation of bond lengths can be understood in accordance with ionic radii.

Depending on the cation distribution estimated using the X-ray intensity and Mössbauer spectroscopy, the value of oxygen positional parameter 'u' were calculated using formula suggested in literature [6C.16] for each composition of unirradiated and irradiated samples and summarized in Table 6C.6 . It is seen all the compounds of present system show larger values of 'u' parameter (~0.26) denoting the shift of O^{2-} ions towards trigonal axis. The observed negative quadrupole shift combined with the large value of 'u' parameter (Table 6C.4) indicates the oblate type of deformation of $3d^5$ shell.

The radii of the tetrahedral (R_A) and octahedral (R_B) sites and inter-ionic distances (Me-O , Me-Me) were also calculated using experimental values of lattice constant and oxygen positional parameter for unirradiated and irradiated samples using equations from [6C.17, 6C.18]. The results can be explained on the basis of higher oxygen parameter.

From the Table 6C.7 it can be seen that the inter-ionic distances between cation-anion (Me-O) 'p', 's' decrease and 'q', 'r' increase with increasing Al-Cr concentration (x), whereas inter-ionic distances between cations (Me-Me) (b, c, d, e, f) is found to decrease with increasing Al-Cr content (x) for unirradiated and irradiated samples. The decreases in Me-O and Me-Me distances may be due to smaller Al^{3+} and Cr^{3+} are replaced by larger Fe^{3+} ions. The increase in Me-O (q and r) cannot explain on the basis of difference of ionic radius of substituent cations. The increase in Me-O (q and r) should result in the weakening of interatomic bonding. The inter-ionic distances Me-O and Me-Me of irradiated samples are found to increase with respect to unirradiated samples. This indicates the weakening of interatomic bonding. The compositional and after irradiation the change in the bond angle favours the strengthening of inter-sublattice (A-B) interaction.

6C.3 Swift Heavy Ion Irradiation effects on Infrared Spectra of the system $MnAl_xCr_xFe_{2-2x}O_4$

The room temperature infrared spectra (800-400 cm^{-1}) for $MnAl_xCr_xFe_{2-2x}O_4$ system with x = 0.0, 0.2, 0.4, 0.6 and 0.8 of unirradiated and irradiated samples are shown in Fig. 6C.6a-6e and the band positions are given in Table 6C.8. For ferrites, two assigned absorption bands appeared around 600 cm^{-1}: ν_1, which was attributed to stretching vibrations of tetrahedral groups Fe^{3+}-O^{2-} and that around 400 cm^{-1}, and ν_2, which was attributed to the octahedral group complexes Fe^{3+}-O^{2-}. In the present

system for all the samples, band ν_1 appears in the range 565-615 cm^{-1} and ν_2 appears in the range 470-503 cm^{-1}. The difference in band positions is expected because of the difference in the Fe^{3+}-O^{2-} for the octahedral (0.199 nm) and tetrahedral (0.189 nm) complexes. The change in band position and intensity is observed as a function of Al-Cr content (x).

Around 400 cm^{-1}, a small band with low intensity appeared for $MnFe_2O_4$ and the band is not seen clearly but the shape of the spectrum suggest the possibility of its presence. Furthermore, the intensity of band ν_2 is found to increase with the increase in Al-Cr concentration. This may be attributed to changes in the Fe^{3+}-O^{2-} complexes by Cr^{3+}- O^{2-} and Mn^{3+}-O^{2-} complexes in the octahedral sites on the substitution of Al-Cr ions in the system. An increase in the intensity of the ν_2 band is expected and is conformed by the results. The change in band positions is due to the change in the Fe^{3+}-O^{2-} internuclear distances for the A- and B-sites. Fig. 6C.6a-6e and Table 6C.8 show clearly that the bands ν_1 and ν_2 shift towards the higher frequency side with increasing Al^{3+} and Cr^{3+} substitution for Fe^{3+} ions for unirradiated and irradiated samples. This may be explained on the basis of decreasing the concentration of Fe^{3+} ions amongst the A- and B-sites, which cause increasing the metal-oxygen stretching vibrational energies and cause decreasing the B-site ionic radius and reducing the size of the unit cell i.e. the lattice parameter 'a' (Table 6C.3).

It is also important to note that on increasing Al-Cr content (x) in the system, band ν_1 become narrower and decrease in intensity while band ν_2 become broader and increase in intensity for unirradiated samples whereas after irradiation both bands ν_1 andν_2 become more broad as compared to unirradiated samples. In the present system, the broadening of bands dependent on the statically distributed of the cations amongst the A- and B-sites, as the content of Al-Cr increases, Al^{3+} and Cr^{3+} ions consistently replace Fe^{3+} ions from B-sites and this may be gives rise to chemical disorder on octahedral site, i.e. the statistical distribution of Fe^{3+} ions in B-sites. The disordered systems give rise to broad bands in their IR spectrum. Thus, it can be concluded that increase in Al-Cr ions leads to more disordered state. By irradiation induced change in statistical distribution of cations and this may be also gives rise disordered in systems and broad bands in IR spectrum of irradiated samples.

The IR spectra for pure $MnFe_2O_4$ show the shoulders/splitting (ν_{sh}) of the main absorption band ν_1 for the unirradiated sample (x = 0.0). This shoulders also

revealed up to the concentration with $x \leq 0.4$ but as increase the Al and Cr content the intensity of shoulders of the main absorption band (ν_{sh}) is reduced and their complete disappearance or amalgamate with main absorption band ν_1 for $x > 0.4$. The presence of divalent Mn^{2+} ions on tetrahedral sites would be responsible for shoulders due to the vibrations of Mn^{2+}-O^{2-} in tetrahedral complexes. The decrease in intensity of shoulders and their complete disappearance for $x > 0.4$, suggest that the Fe^{2+} ion formation has been hampered by increase Al-Cr content and only the ν_1 and ν_2 bands are exhibited.

The IR spectra of irradiated ferrites show more splitting of main absorption bands ν_1, ν_2 as well as ν_{sh} for the samples with $x \geq 0.4$, while at higher concentrations $x = 0.6$ and 0.8 no shoulders/splittings are observed. This may be due to the generation of small fraction of Jahn-Teller effect of the ions (Fe^{2+}, Cr^{4+}, Mn^{3+}) at A- and B-sites, where the Jahn Teller effect can cause a local distortion of the cubic spinel lattice. The shifting of main absorption bands ν_1 and ν_2 after irradiation towards high frequency is also due to the irradiation induced mixed valence of Fe-ions.

6C.4 Swift Heavy Ion Irradiation effects on Elastic properties of the ferrite system $MnAl_xCr_xFe_{2-2x}O_4$

The force constant k_t (tetrahedral sites) and k_o (octahedral sites) have been found from the IR spectra [6C.19] (Table 6C.9). The compositional dependence shows that the force constant of tetrahedral site (k_t) is found to increase with site radii R_A and the force constant of octahedral site (k_o) is found to decrease with site radii R_B for the unirradiated and irradiated samples. This suggests strengthening and weakening of A-site & B-site interatomic bonding, respectively. Normally, increase in site radius leads to decrease in force constants. This can be attributed to the fact that under favourable conditions, oxygen can form stronger bonds with metal ions even at lager inter-nuclear separations [6C.20-6C.22]. The force constant values are found smaller for irradiated samples for $x = 0.0$ and 0.2 and larger for $x > 0.2$ as compared to unirradiated samples. This suggests that the change in inter-ionic distances as well as bond length and bond angles due to rearrangement of cations by irradiation.

The values of lattice constant and average force constant ($k = (k_t + k_o)/2$) for unirradiated and irradiated have been used for calculating bulk modulus (B) and are given in Table 6C.11 respectively. The value of longitudinal elastic wave velocity (υ_l)

and transverse elastic wave velocity (υ_s) have been determined for unirradiated and irradiated samples by using the formula suggested in literature [6C.19, 6C.23-6C.24] and listed in Table 6C.10. The value of υ_l and υ_s are further used to calculate the other elastic moduli (G) and Debye temperature of the unirradiated and irradiated ferrite specimens using the formulae suggested in literature [6C.24] and are given in Table 6C.10 and 6C.11.

It can be seen from the table the B, E and G are found to increase initially up to $x \leq 0.4$ and thereafter, they decrease for unirradiated and irradiated samples. The Poisson's ratio, however, remain constant as a function of composition. The value of σ is found 0.35 for all the compositions. This values lies in the range from -1 to 0.5 which is in conformity with theory of isotropic elasticity. Following the Wooster's work [6C.25], the variation of B, E and G with increasing Al-Cr concentrations may be interpreted in terms of the binding forces between various atoms of the spinel lattice. Thus, it can be inferred from initial the increase of elastic moduli with concentration (x) that the interatomic bonding between various atoms is getting strengthened and the decrease may be due to the weakening of interatomic bonding on higher Al-Cr concentration (x). On other hand, initially the increase in elastic moduli with increasing Al-Cr content (x), indicate that the deformation of the solid is difficult and the solid has a strong tendency to "spring" back to its equilibrium position. The elastic moduli values of irradiated ferrites for x = 0.0 and 0.2 is found to be lower and higher for x > 0.2 as compared to unirradiated ferrites. This is attributed to induced deformation of the irradiated ferrites by strain/stress produce during irradiation process.

The values of υ_l, υ_s, υ_m and θ_D for all unirradiated and irradiated compositions are included in Table 6C.10. It can be seen that the room temperature velocities υ_l, υ_s and υ_m of unirradiated samples increase from 5586 m/s to 5900 m/s, 3225 m/s to 3406 m/s and 3580 m/s to 3782 m/s, while velocities υ_l, υ_s and υ_m of irradiated samples increase from 5562 m/s to 5968 m/s, 3211m/s to 3446 m/s and 3565 m/s to 3825 m/s with increasing Al-Cr concentration (x), respectively. This variation can be explained on the basis of material X-ray density. In the present samples, the density of the ferrites is found to decrease with increasing Al-Cr content (x), causing faster propagation of the disturbance. It is also observed that the υ_l, υ_s and υ_m of irradiated samples are decreased for $x \leq 0.2$ and increased for $x > 0.2$ as compared to

unirradiated samples. This can be ascribed to change in density after irradiation. The Debye temperature (θ_D) is found to increase with increasing Al-Cr content (x) for unirradiated and irradiated samples. It is observed that the Debye temperature (θ_D) of irradiated samples is lower for $x \leq 0.2$ and higher for $x > 0.2$ than the unirradiated samples. It is interesting to note that the Debye temperature (θ_D) varies with υ_m. As mentioned earlier, the Debye temperature is the temperature at which maximum lattice vibrations take place. The observed increased in θ_D with content (x) suggested that lattice vibrations are hindered due to Al-Cr substitution. This is due to the increases in strength of inter atomic bonding with the replacement of Fe^{3+} by Al^{3+} and Cr^{3+} in $MnAl_xCr_xFe_{2-2x}O_4$ system. However, observed change in θ_D for irradiated samples may be due to the change in strength of inter-atomic bonding and hindrance to the lattice vibrations caused by irradiation.

6C.5 Swift Heavy Ion Irradiation effects on Electrical properties of the system $MnAl_xCr_xFe_{2-2x}O_4$

Table 6C.12 shows the variation of dc resistivity ($\log_{10}\rho_{dc}$) at room temperature as a function of Al and Cr concentration for the unirradiated and irradiated samples. The resistivity decreases initially with the increases of Al-Cr content for x = 0.2 and 0.4 and then increases for the concentration x = 0.6 and 0.8 with respect to x = 0.0 of unirradiated samples. The resistivity is found to increase monotonically with increasing Al-Cr content of irradiated samples. Simsa [6C.26] has proposed a model for interpretation of most of the results for $MnFe_2O_4$ considering the hopping process $Mn^{2+} + Fe^{3+} \Leftrightarrow Fe^{2+} + Mn^{3+}$. The pair of ions $Fe^{2+} + Mn^{3+}$ is more stable in octahedral sites and has lower energy than the untrapped Fe^{2+}. The processes in the conduction mechanism like $2Fe^{3+} \rightarrow Fe^{4+} + Fe^{2+}$ and $Mn^{3+} + Fe^{3+} \rightarrow Mn^{4+} + Fe^{2+}$ have been neglected by Simsa [6C.26]. Goodenough [6C.27] and Rogers et al [6C.28] proposed the formation of Mn^{3+} clusters. The formation of clusters of Mn^{3+} actually lowers the concentration of stable pairs of $Fe^{2+} + Mn^{3+}$ and all Mn^{3+} ions occupy octahedral positions as the nearest neighbours. In the present system, $2Fe^{3+}$ ions are replaced by Al^{3+} and Cr^{3+} ions. Initially, the decrease in resistivity for the unirradiated samples can be explained on the basis of clusters of Mn^{3+} ions. This clusters effectively reduces the concentration of stable bonds of $Fe^{2+} + Mn^{3+}$ and conduction may be due to the more number of Mn ions at octahedral sites [6C.29]. As an increase Al and Cr content, more number of Fe^{2+} and Mn^{3+}, Fe^{2+} and Fe^{4+}, Fe^{2+} and

Cr^{4+} bonds are formed at octahedral sites, which are more stable and has lower energy than the Fe^{2+} ion hence there is an increase in the resistivity. Resistivity is also influenced by the microstructural factors such as grain size, porosity and gain boundary area. The increase in dc resistivity with increasing Al-Cr content for the irradiated samples can be attributed to the simultaneously influence of change in porosity, grain size and conduction mechanism by irradiation.

The change in resistivity after irradiation can be related to the variation in the porosity and microstructure due to irradiation. Smaller the grain size more would be the grain boundaries. The ferrites grains being conducting, the bulk of the resistivity is contributed by insulating grain boundaries [6C.30, 6C.3]. The irradiation causes greater density and grain growth resulting in a corresponding decrease in porosity and the number of grain boundaries leading to decrease in resistivity for the irradiated samples x = 0.0, 0.4 and 0.6. Higher porosity in irradiated samples x = 0.2 and 0.8 may be obstructing hopping process between the ions co-existing at the A and B-sites in the spinel lattice. Thus, the porosity is directly influenced by irradiation process and induces change in resistivity after irradiation.

The electrical resistivity as a function of temperature for the unirradiated and irradiated system $MnAl_xCr_xFe_{2-2x}O_4$ in the form of $\log_{10}\rho_{dc}$ versus $10^3/T$ are shown in Fig. 6C.7 for the compositions x = 0.0 to 0.8 with step of 0.2. The electrical resistivity-temperature behaviour obeys the well known Arrhenius relation [6C.12], indicating the semiconductor nature of the compositions $x \leq 0.4$ under investigations. For the compositions with x = 0.6 and 0.8, the dc resistivity slightly increases with increasing temperature in the lower temperature range; thereafter it follows the conventional behaviour of decreasing dc resistivity with increase in temperature. They show metal to insulator type transition at temperature 405K and 310K, respectively. Earlier such type of transition has been observed by Modi et al [6C.32] in $MgAl_xFe_{2-2x}O_4$ and by Chhaya et al [6C.33] for $NiAl_xCr_xFe_{2-2x}O_4$ systems. It is known that the conduction mechanism in ferrites is controlled generally by the band conduction or the hopping model or polaron model. According to the band theory, the temperature dependence of conductivity is mainly due to the variation in the charge carrier concentration with temperature, while in the hopping model, the change in charge mobility with temperature is considered to lead to the conduction by jumping or hopping from one iron to the next. Thus, the conduction in ferrites increases with

temperature and consequently, the resistivity falls with increasing temperature. The temperature dependence of dc resistivity curve for x = 0.0 – 0.6 consist three different regions and two breaks for unirradiated and irradiated samples. The change in the slope in different regions generally occurs at a temperature approaching the Curie temperature (T_c) of the sample. This is attributed to the changes in the conduction mechanism at magnetic phase transition as discussed earlier. No magnetic transition observed for the x = 0.8, suggesting that this sample is paramagnetic at room temperature. The values of T_c are in good agreement to those found experimentally from susceptibility v/s temperature measurements. The Curie temperature (T_c) is found to decrease with increasing Al-Cr concentration (x) for unirradiated and irradiated samples.

Temperature dependence of electrical resistivity for irradiated samples shows the same behavior as those of unirradiated ones. It can be seen from the Fig. 6C.7 the value of dc resistivity is diminished in the un-substituted Mn-ferrite (x = 0.0) and slightly change occur substituted with Al-Cr content for the concentration x = 0.2 and 0.4 as compared to unirradiated samples within the measuring temperature range. As increase Al-Cr substitution for x = 0.6, the value of dc resistivity is enhanced in the ferromagnetic region (lower temperature region) and decreased in higher temperature region as corresponding to unirradiated ones. It is noticed that at higher Al-Cr concentration x =0.8, the dc resistivity of irradiated sample is higher than the unirradiated ones in the measuring temperature range. It is also observed that the Curie temperature (T_c) slightly shifts towards lower temperature for irradiated ferrites of x = 0.0 and 0.4 whereas T_c is shifts towards higher temperature for x = 0.2 and 0.6 compared with that of corresponding unirradiated samples. In the present system, the conductivity takes place via Mn^{2+} and Fe^{3+} neighbours as $Mn^{2+} + Fe^{3+} \Leftrightarrow Fe^{2+} + Mn^{3+}$ or Fe^{3+} and Fe^{2+} in the parent $MnFe_2O_4$. The formation of Fe^{2+} ions gives rise to conduction in the ferrite due to electron hopping between the Fe^{3+} and Fe^{2+} ions co-existing at the closer spaced B-sties in the spinel lattice. The Fe ions at the A- sites contribute little to conduction due to larger distance between them. Besides, partial oxidation of Mn^{2+} to Mn^{3+} may also add to conductivity due to hopping between the two different oxidation states of Mn [6C.31]. The decrease in resistivity of irradiated $MnFe_2O_4$ ferrite compared to unirradiated ferrite can be assigned to the formation of point/clusters of defects and redistribution cations over the tetrahedral and octahedral

sites in the spinel lattice by irradiation to generate excess amount of Fe^{2+} and Mn^{3+} or charge carriers whereas the temperature accomplished to enhancement of verwey hopping between Fe^{3+} to Fe^{2+} or Fe^{2+} to Mn^{3+} in the irradiated Mn-ferrite. Thus, a more contribution toward conductivity by generation of Fe^{2+} and Fe^{3+} and Fe^{2+} and Mn^{3+} takes place. At higher concentration for x= 0.8 of irradiated samples, more number of Fe^{2+} and Mn^{3+}, Fe^{2+} and Fe^{4+}, Fe^{2+} and Cr^{4+} bonds are formed at octahedral sites and present defect in sample act as a trapping centre of charge carriers and may be charge carriers are trapped in defects, which is hindrance of hopping process consequently dc resistivity is increased of irradiated sample. The shifting in transition temperature in irradiated samples may be due to the change in magnetic ordering by irradiation.

The activation energy of the unirradiated and irradiated samples in the measured temperature range was determined from the slope of plots of dc resistivity using Arrhenius relation and tabulated in Table 6C.12 along with other parameters. The value of activation energy is decreased for ferromagnetic region E_f (lower temperature region) from 0.504 to 0.089 eV and paramagnetic region E_P (higher temperature region) from 0.558 to 0.229 eV of unirradiated samples as the Al-Cr concentration increased from 0.0 to 0.8. The value of activation energy is systematical decreased for the ferromagnetic region from 0.509 to 0.229 eV of irradiated samples with the increasing Al-Cr concentration but random variation observed in activation energy for the paramagnetic region from the range 0. 639 to 0.431 eV with increasing Al-Cr content for irradiated samples. Moreover, it is observed that the value activation energy of all the investigated irradiated samples is raised as those of unirradiated ones.

The hopping of probability depends open the activation energy, which is associated with the electrical energy barrier experienced by the charge carriers during hopping. One of the explanations for the observed decrease in activation energy with increasing Al-Cr content (x) is based on the changes in ionic distances in the ferrites crystal structure. The lattice cell edge parameter 'a' is found to decrease with increasing Al-Cr content (x) (Table 6C.3). The decrease in the value of 'a' manifests itself as decrease in the inter-ionic distances in the ferrite and consequently in a decrease in the barrier height encountered by the hopping charge carries. The activation energy is therefore, expected to decrease with increasing value of Al-Cr constant (x) for unirradiated and irradiated samples. Our XRD results are indicating

expansion of the unit cell and lattice cell parameter is found to increase after irradiation may be due to the activation energy is increased as compared to unirradiated samples.

From the table it is clear that the activation energy for unirradiated and irradiated samples is higher than in the ferromagnetic one. The calculated activation energies in the paramagnetic region are higher than the ionization energy 0.1 eV of donors or acceptors and hence possibility of band type conduction is ruled out. It is also much larger than the electron-transition energy of 0.2 eV such as $Fe^{2+} \Leftrightarrow Fe^{3+}$ and thus indicates that polaron hopping mechanism is favoured [6C.34].

The calculated value of polaron radius (r_p) for all the compositions of unirradiated and irradiated samples are given in Table 6C.13. It is seen that these values are smaller than the interionic distances, and hence are appropriate for small polaron conduction. From the table, it can be seen that the polaron radius (r_p) decreases with increasing Al-Cr content (x) for unirradiated and irradiated samples. Furthermore, polaron radius (r_p) of all irradiated specimens is higher than the unirradiated samples. This variation can be explained on the basis of cell edge parameter is decreased with Al-Cr concentration (x), as well as cell edge parameter is increased after irradiation and according to polaron radius (r_p) is increased with compared to unirradiated specimens. On the other hand, the multiple valence state of Mn^{2+} and Cr^{3+} in the system point towards possible Jahn-Teller distortion occurring in the system resulting in the creation of defects which can facilitate polaron formation. The change in valence state and enhances the electronic defects due to irradiation may be occur change in polaron radius after irradiation.

The values of jump lengths L_A and L_B for unirradiated and irradiated samples are listed in Table 6C.13. It is clear that both L_A and L_B decrease with increasing Al-Cr content (x) for unirradiated and irradiated samples. This is ascribed to the substitution process and the reduction of the size of the unit cell. The decrease in jump length with Al-Cr content (x) suggest that the require less energy to jump charge carriers from one site to other and which causes a decrease in resistivity with increasing x. But in present system d. c. resistivity is found to initially decrease up to x = 0.2 and 0.4, further it is increase with increasing (x) for unirradiated samples while continuously increase with increasing (x) for irradiated samples. In the present system, due to substitution of Al^{3+} and Cr^{3+} (smaller ionic radius) and therefore, jump

length decreases but at the same time Fe^{3+} ion concentration and its B-site occupancy is also decrease. This may be reduce the Fe^{3+}/Fe^{2+}, Fe^{3+}/Fe^{4+}, Mn^{2+}/Mn^{3+}, Cr^{3+}/Cr^{4+} ratios responsible for the conduction process in ferrites. Thus, the resistivity increases with increasing (x). After irradiation, the jump length is found to increase than the unirradiated samples. This is attributed to increase in lattice parameter after irradiation.

Based on the observed Seebeck coefficients in Fig 6C.8, the mixed Mn-Al-Cr ferrites studied in this investigation can be divided in to two groups. The unirradiated specimens x = 0.0 to 0.6 have negative Seebeck coefficients, indicating that they are n-type semiconductors; the unirradiated specimen x = 0.8 is a p-type semiconductor as its Seebeck coefficient is positive whereas irradiated specimen x = 0.0 to 0.4 have negative Seebeck coefficient and x = 0.6 and 0.8 have positive Seebeck coefficient. From the observation it follows that the conduction mechanism in the n-type specimens is predominately due to hopping of electrons from Fe^{3+} to Fe^{2+}, Mn^{2+} to Mn^{3+} and Fe^{2+} to Mn^{3+} ions, whereas the conduction mechanism in p-type specimens is hole transfer from, Fe^{3+} to Fe^{4+} and Cr^{3+} to Cr^{4+} ions. The results of thermoelectric power of irradiated samples are noticed that the value of Seebeck coefficient are more negative for the concentration x = 0.0 to 0.4 and for x = 0.6 is almost similar but sample shows n to p type transition, whereas it is less positive for the concentration of x = 0.8 compared with the corresponding unirradiated samples. This indicates that the conduction mechanism and hopping rate is changed in the investigated samples by electronic rearrangement of cations after irradiation.

The variation of Seebeck coefficient $|\propto|$ with temperature of all unirradiated and irradiated mixed Mn-Al-Cr ferrites is revealed that the Seebeck coefficient $|\propto|$ decreases with increasing temperature, except those with x = 0.0 and 0.2 for irradiated specimens, which is belong to non-degenerate type of semiconductor. The change in $|\propto|$ values for all the compositions with temperature variation may be due to the recombination of some hole and electrons by temperature. Since both electrons and holes are responsible for conduction in these samples. On substitution Al^{3+} and Cr^{3+}, as depicted in Fig. 6C.8, the value of $|\propto|$ is lower for x = 0.2 and 0.4 and higher for x = 0.6 and 0.8 corresponding to x = 0.0 of unirradiated samples, which perhaps could be due to Al^{3+} and Cr^{3+} ions residing at the B-site, which results in the decrease of Fe^{3+} ions at the B-site. Thus, perhaps it is decrease in the population of Fe^{3+} ions at B-

sites which is responsible for decrease of Seebeck coefficient |∝| initially for x = 0.2 and 0.4, although for x = 0.6 and 0.8 small amount of Al^{3+} could be located in A-site and Cr^{3+} with Fe^{3+} at B-site also responsible to increase of Seebeck coefficient |∝| at higher concentration. The change in values of Seebeck coefficient |∝| for irradiated samples with Al-Cr content (x), indicate alteration in cation distribution after irradiation.

The calculated values of Fermi energy (E_F) as a function of temperature for two values of A (A = 0 and 2) [6C.35, 6C.36] for all the compositions of unirradiated and irradiated samples are shown in Fig. 6C.9. The extrapolated value of E_F to T = 0 K, yields the values E_F (0) (Table 6C.13). It is found that the value of Fermi energy (E_F) of Al-Cr substituted ferrites is lower for x = 0.2 to 0.6 and higher for x = 0.8 with compared to un-substituted ferrite x = 0.0 of unirradiated sample, while in case of irradiated samples it is found to lower for x = 0.2, 0.4 and higher x = 0.6, 0.8 with respect to x = 0.0 specimen. As per our TEP measurements, Al - Cr substituted ferrites $x \leq 0.6$ are n-type semiconductor due to electrons transfer and x = 0.8 is p-type semiconductor due to holes transfer from cation present in octahedral site. Initially substitution of Al-Cr may be lead to the alteration in effective density state of electrons in conduction band and further it is modify in density state of holes in valence band, therefore Fermi energy (E_F) initially decreases up to x = 0.6 and further it is found to increase for x = 0.8 of unirradiated samples. The value of Fermi energy (E_F) is found increase for irradiated samples with x = 0.0 and 0.8 and decrease for irradiated samples with x = 0.2, 0.4 and 0.6 than the unirradiated samples.

The charge carrier concentration (n_c) for all the compositions of unirradiated and irradiated samples have been evaluated at different temperatures using value of Seebeck coefficient |∝|. The plots of ln (n_c) versus T for all the compositions are presented in Fig. 6C.10. The values of charge carrier concentration (n_c) are on the order of $10^{22}/cm^3$. From the figure, it clear that the charge carrier concentration (n_c) is nearly constant for the unirradiated samples with x = 0.0 and 0.2, while it is found to increase up to 380 K and then almost constant for the unirradiated samples of x>0.2 with increasing temperature. The decrease in charge carriers concentration (n_c) with increasing temperature for the irradiated samples with x = 0.0, 0.2 and the magnitude of n_c is found to reduce for x = 0.0 and enhance for x = 0.2 as compared to unirradiated samples in same temperature range. Same behaviour is observed of n_c in

the irradiated samples with x >0.2 nevertheless the magnitude of n_c is increased with corresponding to unirradiated samples. The observed increase in n_c may be due to the generation of charge carriers with increasing temperature as well as by irradiation process and decrease in n_c with temperature due to the compensate of electron which are the majority charge carriers with thermally generated holes. The observed decrease n_c for irradiated sample x = 0.0 may be due to the trapping of charge carriers at trapping centers created by irradiation.

The values of charge carrier mobility (μ_D) can be calculated using experimental values of electrical resistivity (ρ_{dc}) and carrier concentration (n_c) obtained from thermoelectric data. The variations of the charge carrier mobility for the different compositions of unirradiated and irradiated samples are shown in Fig. 6C.11, as a plot of $\log_{10}\mu_D$ versus $10^3/T$. It is observed that the mobility of unirradiated and irradiated pure Mn- ferrite (x = 0.0) sample is found to increase continuously with increase in temperature, while Al-Cr substituted samples are revealed initially decrease and subsequently increase with increasing temperature. The increase in mobility with temperature suggests that conductivity of samples is due to thermally activated mobility and not to thermally created charge carriers. For pure irradiated Mn-ferrite show higher value of mobility than the unirradiated ones. This may be due to the increase in hopping of charge carriers after irradiation. But Al-Cr substituted ferrites show lower value of mobility than the unirradiated samples. This can be attributed to the hindrance of charge carriers for hopping due to trapping centers (defects) created by irradiation. It is observed that the mobility is found to increase with increase Al-Cr concentration (x) for unirradiated and irradiated samples. The magnitude of the mobility is found in the range of 10^{-6} to 10^{-12} cm^2/V.Sec. This range is consistent with mobility suggested in the literature [6C.37] for electron (10^{-4} cm^2/V.Sec) and holes (10^{-8} cm^2/V.Sec).

6C.6 Swift Heavy Ion Irradiation effects on Dielectric properties of the system $MnAl_xCr_xFe_{2-2x}O_4$

Dielectric properties in ferrites are contributed by several structural and micro-structural characteristics. Table 6C.14 correlates the variation of the dielectric constant (ε'), a.c. resistivity ($\log_{10}\rho_{ac}$) and dielectric loss tangent (tanδ) for two different applied frequencies 1kHz and 10kHz as a function of Al-Cr content (x) of unirradiated and irradiated samples at room temperature. Introducing Al^{3+} and Cr^{3+}

ions into the samples decreases the dielectric constant (ε') and increases ac resistivity ($\log_{10}\rho_{ac}$) up to x = 0.2, thereafter an increase in dielectric constant and decrease in ac resistivity occurred for unirradiated samples. Of course the values of ε' for x = 0.2 and 0.4 is lower and x = 0.6 and 0.8 is higher than the concentration x = 0.0 for unirradiated samples. The electrical resistivity behave in an opposite manner to that of the dielectric constant (ε') giving an impression that both the dielectric constant (ε') and electrical conductivity, 1/ρ behave more or less in a similar way. The observed compositional variation of dielectric constant (ε') can be interpreted on the basis of space charge polarization which is due to an inhomogeneous dielectric structure discussed by Maxwell -Wagner and which is governed by the number of space charge carriers and the resistivity of the samples. In present system, manganese and iron ions exist at both tetrahedral and octahedral sites. In Al-Cr substituted ferrites, the Al^{3+} and Cr^{3+} are known to replaces Fe^{3+} ion at B-sites and limit the degree of $Fe^{2+} \Leftrightarrow Fe^{3+}$, $Fe^{2+} \Leftrightarrow Mn^{3+}$ electron hopping conduction by blocking up $Fe^{2+} \Leftrightarrow Fe^{3+}$, $Fe^{2+} \Leftrightarrow Mn^{3+}$ patterns causes initially the increases in the resistivity of the unirradiated samples. This increased resistivity obstructs the flow of space charge carriers and therefore impedes the build up of space charge polarization. The dielectric constant is therefore expected to decrease with increasing Al-Cr concentration initially. Further increase dielectric constant at higher concentration may be due the decrease in resistivity by introduction of Mn^{3+} ions in the B sub-lattice, additional conductivity results of due to electron hopping between Mn^{2+} and Mn^{3+} ions and the some of Fe^{3+} ion converted to Fe^{2+} ions to maintain charge neutrality. The electron hopping is increased due to Fe^{2+} in B sub-lattice by hopping of Fe^{2+} and Cr^{4+}, Fe^{2+} and Fe^{4+}. However, holes hopping between Cr^{3+} and Cr^{4+}, Fe^{3+} and Fe^{4+} may be possible to contribute in net polarization therefore the dielectric constant increases at higher concentration for unirradiated samples. The variation of dielectric constant (ε') and a.c. resistivity ($\log_{10}\rho_{ac}$) of substituted irradiated ferrites are observed random behaviour with increasing Al-Cr content (x). Initially, the value of ε' is found to decrease up to x = 0.4 after that it is higher value observed for x = 0.6 and again it is decrease for x = 0.8 with respect to concentration x = 0.0. It is obvious that the dielectric constant of all irradiated samples is found to lower than the all unirradiated samples. The formation of insulating intergranular layers reduces the oxidation rate of Fe^{2+} ions inside the grains during irradiation of the samples and it is possible to increase electrical resistivity by

irradiation owing to the structural heterogeneity generated through the insulating intergranular layers which is the main reason to for decreasing dielectric constant (ε'). It can be seen the electrical resistivity increases with increasing Al-Cr content up to x = 0.4 and than it is lower for x= 0.6 and again it is increase for x = 0.8. In general the change in ε' and ρ_{ac} with Al-Cr content in irradiated samples can be attributed to the simultaneous influence of changes in micro-structural parameters like density, grain and grain boundaries, Fe^{2+} concentration and change occur in the conduction mechanism due to redistribution of cations by irradiation which are mainly contributed in net polarization.

The dielectric loss tangent (tanδ) is obtained maximum at x = 0.6 for unirradiated and irradiated samples. It is observed that the dielectric loss tangent increases at the higher Al-Cr concentration x = 0.4, 0.6 and 0.8 while it is decreases for x = 0.2 with respect to x =0.0 of unirradiated sample. Whereas irradiated samples dielectric loss is found to lower for x = 0.2, 0.4 and 0.8 and higher for x = 0.6 as compared to un-substituted ferrite x = 0.0. It can be seen that the all irradiated samples are found to enhance dielectric loss to corresponding unirradiated samples, except those with x = 0.4.

Fig. 6C.12a-12e shows the variation of dielectric constant (ε') with absolute temperature for all the unirradiated and irradiated investigated samples at different selected frequencies from 100 Hz to 1MHz. It can be seen that all unirradiated and irradiated samples show the dielectric constant (ε') decreases with increasing frequency. This is a normal behaviour observed in most of the ferromagnetic materials, which may be due to the interfacial polarization. It is evident that by increasing temperature, the dielectric constant increases gradually up to the particular temperature about 600K, further than increases quickly into higher temperature range for all the unirradiated and irradiated samples. The behaviour of ε' with the temperature can be explained as follows: at relatively low temperature the charge carriers on most cases cannot orient themselves with respect to the direction of the applied field, therefore they posses a week contribution to the polarization and dielectric constant. As the temperature increases, the bound charge carriers get enough excitation thermal energy to be able to obey the change in the external field more easily. This in turn enhances their contribution to the polarization leading to an increase of the dielectric constant (ε') of all the samples.

The effect of irradiation on temperature dependent dielectric constant (ε') is also shown in Fig. 6C.12a-12e. It is observed that the value of dielectric constant (ε') of irradiated samples are concurred or slightly reduced those of the unirradiated ones in the lower temperature range 300K-600K at low frequencies 100Hz, 500Hz, 1KHz and 10kHz, further increase the temperature the value of ε' is increased corresponding to unirradiated samples in this particular frequencies. This type of behaviour is also observed up to frequencies 10kHz, 50kHz, 80kHz and 100kHz particular irradiated sample x = 0.2. At higher frequencies from 50kHz to 1MHz, it is observed that the values of dielectric constant of all the irradiated samples are lower than the unirradiated samples in the measuring temperature range 300K-800K. It is known that the local displacement of electronic charge carriers cause (or determine) the dielectric polarization in ferrites. The dielectric behaviour of ferrites may be explained on the basis of dielectric polarization process which is similar to that of the conduction mechanism is mainly by the hopping conduction mechanism [6C.38]. The irradiation tends to destroy the polarization by initiating some point/cluster of defects. One can expect that the irradiation may fall upon bound electrons, providing that the electrons do not receive sufficient energy to be ejected from the atoms in lower temperature region, and tend to the disorder the localized dipoles. By increasing temperature, the thermal energy enables these electrons to be ejected from their atoms. These electrons will fluctuate randomly due to the ac electric field accompanied with the applied frequency tending to decrease the polarization as a result decrease in dielectric constant in irradiated samples.

The variation of the loss angle tangent (tanδ) and complex dielectric constant (ε'') as a function of temperature at different frequencies for unirradiated and irradiated samples are depicted in Fig. 6C.13a-13e & 14a-14e. Two distinct region may be observed, the first region from 300 to 600K, in which tanδ and ε'' are frequency and temperature independent and a second region (above 600K) which are frequency and temperature dependent. From the figure it is clear that the tanδ and ε'' is faintly increases up to 600K after which it rapidly increases with increasing temperature for both unirradiated and irradiated samples, except samples with x = 0.8. For particular unirradiated and irradiated sample x = 0.8, the tanδ loses initially decrease up to 500K afterward increase with increasing temperature at lower frequencies 100Hz, 500Hz and 1kHz. The variation of tanδ and ε'' with temperature

can be attributed to the thermal energy given to the system increase the motion of charge carriers and the energy dissipation of their frication will be increased with the result of increasing tanδ and ε''. On the other hand, the rapid rise in the tanδ and ε'' curve at higher temperature is attributed to the conduction losses, which increase with temperature due to increased conduction. A careful examination of the irradiated spectra of tanδ and ε'' suggest following.

- The tanδ losses in case of irradiated samples x = 0.0 and 0.2 are quite low above temperature 600K at frequencies of 1kHz to 100kHz, respectively. Further increase frequency tanδ losses gradually increase in same temperature range (above 600K) with corresponding to unirradiated ones.
- For irradiated sample with x = 0.4 the magnitude of tanδ is found to decrease at measured temperature and frequency range with respect to unirradiated sample.
- The tanδ losses in case of irradiated samples with x =0.6 and 0.8 is observed to high above temperature 600K at frequencies 1kHz to 1MHz respectively, with compared to unirradiated samples.
- For irradiated samples x = 0.2 and 0.4 can be show small hump (loss peak or relaxation peak) at particular frequency 1kHz and it was shifted towards higher temperature with increasing frequency. No strong loss peak or hump was found in the case of unirradiated samples.
- The values of ε'' (ε''= ε'tanδ) are decreased with corresponding to unirradiated samples, except with x = 0.8 for same measured temperature and frequency.

The higher magnitude of tanδ losses and show small hump after irradiation may be due to the disturbance of ordered charge carriers or dipoles by irradiation process.

Fig. 6C.15a-15e illustrates the variation of a.c. resistivity ($\log_{10}\rho_{ac}$) with the reciprocal of the absolute temperature ($10^3/T$) for the all investigated unirradiated and irradiated samples at different frequencies. Generally, the electrical resistivity of ferrites decreases with increase in temperature and follow the well-known Arrhenius relation. This type of behaviour is observed for the compositions with $x \leq 0.4$. For the compositions with x = 0.6 and 0.8, the ac resistivity initially increases with increasing temperature within the temperature range 300-500K: thereafter it follows the conventional behaviour of decreasing resistivity with increase in temperature for unirradiated and irradiated samples. The anomalous electrical behaviour of resistivity

as a function of temperature for Al^{3+} substituted $MgFe_2O_4$ has been explained on the basis to decrease in the Fe-Fe separation distance arising from alminium substitution [6C.32]. Along same lines, it may be assumed that the sufficient (x = 0.6 and 0.8) replacement of larger Fe^{3+} (0.64 Å) ions by smaller Al^{3+} (0.51 Å) and Cr^{3+} (0.63 Å) ions in $MnAl_xCr_xFe_{2-2x}O_4$, decreases the B-site Fe-Fe separation distance below a certain critical value where, besides electron/hole hopping, a nearly band-like conductivity may occur. This is characterized by the metallic conductivity in the temperature range 300-500K. When sample temperature is raised above a certain value, the B-site Fe-Fe separation increases above the critical value due to thermal expansion of the unit cell. This hampers the band-like conduction mechanism and again major conduction mechanism through electron/hole or polaron hopping between two adjacent B-sites becomes dominant. Thus, the conventional thermal behaviour observed for a sample temperature greater than 500K is ascribed to electron/hole and polaron hopping mechanism. With Al^{3+} and Cr^{3+} substitution there is no significant variation in the temperature at which maximum resistivity is obtained. The reduction in the lattice constant, a, due to Al-Cr substitution for the samples with x = 0.6 and 0.8 is 0.024 Å indicate that an almost equal amount of thermal energy may be required to increase the B-site Fe-Fe ion separation distance above a certain critical value.

Comparing the a.c. resistivity before and after irradiation, it is clear that the irradiated samples having the same behaviour as unirradiated samples but the values of a.c. resistivity is higher than the unirradiated ones. It is more pronounced in lower temperature and higher frequency region, though in higher temperature region the value of a.c. resistivity is overlapping with the unirradiated samples for particular samples of x =0.0, 0.2 and 0.6 while it is reduced for the concentration x = 0.8. It is also observed that the a.c. resistivity value of irradiated sample x = 0.4 is higher than the unirradiated ones in the measured temperature at all the frequencies. The increase in the value of a.c. resistivity in lower temperature region is attributed to the hindrance of an increase in drift mobility of the thermally activated charge carriers according to the hopping conduction mechanism cause defect created by irradiation. As the temperature increases, due to more thermal energy the trapped charge carriers in defects may be participated in hopping process and increase drift mobility of charge carriers therefore the ac resistivity is decreased at higher temperature region for particular irradiated samples. The a.c. resistivity decreases with the increases in frequency at all temperature is an acceptable results because the frequency acts as a

pumping force pushing the charge carriers from one conduction state to another, especially at low frequency.

The real (ε') and imaginary (ε'') parts of the dielectric constant and dielectric loss tangent (tanδ) as a function of frequency (100Hz-1MHz) at different temperature (298K, 373K, 473K, 573K, 673K and 773K) for the above mentioned unirradiated and irradiated samples are shown in Fig. 6C.16a-16b, 6C.17a-17b & 6C.18a-18b, respectively. The general trend for all the unirradiated and irradiated compositions are that ε', ε'' and tanδ initially decrease rapidly with increasing frequency and then reaches a constant value beyond a certain frequency. This behaviour may be explained qualitatively by the supposition that the mechanism of the polarization process in ferrite is similar to that the conduction process [6C.38]. In present sample, the decrease in dielectric constant (ε') with increasing frequency is due to the fact that the polarization decreases with increasing frequency and then reaches constant value. By electron/hole exchange between $Fe^{2+} \leftrightarrow Fe^{3+}$, $Mn^{2+} \leftrightarrow Mn^{3+}$, $Mn^{3+} \leftrightarrow Fe^{2+}$, $Fe^{3+} \leftrightarrow Fe^{4+}$ and $Cr^{3+} \leftrightarrow Cr^{4+}$ the local displacement of electrons/holes in the direction of the applied field occurs and these electrons/holes determine the polarization. The polarization decreases with increasing frequency and then reaches a constant value due to fact that beyond a certain frequency of external field, the electrons/holes exchange cannot follow the alternating field.

For the case of pure $MnFe_2O_4$ irradiated ferrite, the value of dielectric constant (ε') is found to high in the low frequency region (~10kHz) and low in the high frequency region with respect to unirradiated sample at room temperature (298K). Furthermore ε' frequently increases as the temperature increases and it is found to higher in magnitude from that of unirradiated sample at higher temperature in the entire measured frequency. However, the dielectric constant (ε') for Al-Cr substituted irradiated samples of x >0.0 show decrease in magnitude from that of the unirradiated samples in measured frequency at all different temperatures. This increase in ε' is due to the large number of dipoles that become free such high thermal energy and the field aligned them in its direction. The higher value of dielectric constant (ε') is obtained for pure irradiated Mn-ferrite may be due to the increase in hopping rate caused from depressing the jump length with the results of more interaction between $Fe^{2+} \leftrightarrow Fe^{3+}$, $Mn^{2+} \leftrightarrow Mn^{3+}$, $Mn^{3+} \leftrightarrow Fe^{2+}$ ions. The jumping electrons oriented in the field direction and, consequently giving rise to ε'. The value

of ε' is decreases after irradiation at all temperatures for the Al-Cr substituted Mn-ferrites (x > 0.0) in measured frequency range. This behaviour may be due to formation of point/clusters of defects, which act as trapping centers for charge carriers. Accordingly, the conductivity as well as ε' decreased because they are of the same origin.

The variation of loss tangent (tanδ) and complex dielectric constant (ε'') of irradiated samples with frequency at different temperature is found to decrease with increasing frequency. After irradiation, the magnitude of tanδ is increased for the samples x = 0.0 to 0.8, except those with x =0.4 with corresponding unirradiated ones. However, tanδ at x = 0.0 and 0.6 show loss peak (relaxation peak) in the lower frequency region at temperature 298K. Initially temperature increases, the peak height reduce and peak is shifted to higher frequency value as further temperature increases (at higher temperature) peak is disappeared in the measured frequency range for irradiated sample x = 0.0. This peak appears when jumping frequency of localized electron approximately become to that of the externally applied ac electric field. The shifting of this peak towards higher frequencies is often attributed to the increase of the hopping frequency of charge carriers. The higher value of tanδ after irradiation may be due to the lag of polarization behind the applied alternating electric field and caused by defects in the crystal lattice. The value of ε'' is higher for irradiated samples with x = 0.0 and 0.2, while lower for x = 0.4, 0.6 and 0.8 with respect to unirradiated samples. The observed change after irradiation in ε'' and tanδ with frequency and temperature, which implies that the complex dielectric constant (ε'') increase or decrease on irradiation of the samples.

Fig. 6C.19a-19b shows the variation of a.c. resistivity as $\log_{10}\rho_{ac}$ versus frequency as $\log_{10}f$ of the studied unirradiated and irradiated samples at different temperatures. All the samples show significant dispersion with frequency, which is the normal ferromagnetic behaviour. The increase in frequency enhances the hopping of charge carriers, resulting in an increase in the conduction process, thereby decreasing the resistivity. The value of a.c. resistivity is reduced after irradiation for the composition x = 0.0 and 0.2 and enhanced after irradiation for the compositions x = 0.4, 0.6 and 0.8. The decreasing in ρ_{ac} with applied frequency and can be explained on basis that the pumping force of applied frequency that helps in transferring the charge carriers between different localized states as well as liberating the trapped

charges from the different trapping centers created by irradiation. These charge carriers participate in the conduction process simultaneously with electron produced from the valence exchange between the different metal ions. At higher concentration x = 0.4, 0.6 and 0.8 the value of a.c. resistivity is increased after irradiation at all frequency and temperature may be due to trapping of charge carriers in the vacancies (defect) which were created as a irradiation.

6C.7 Swift Heavy Ion Irradiation effects on Impedance Spectroscopy of the system $MnAl_xCr_xFe_{2-2x}O_4$

The variation of real (Z') and imaginary part (Z'') of impedance as a function of applied frequency at different compositions of unirradiated and irradiated samples at room temperature are presented in Fig. 6C.20. It can be seen that the value of Z' decreased with increasing the frequency indicating an increase in ac conductivity with frequency. It can be observed that the values of real impedance (Z') are found to decrease up to x = 0.6, thereafter Z' increases with a further substitution of Al-Cr for unirradiated samples, while no systematic variation is observed in real impedance (Z') with Al-Cr content (x) of irradiated samples. For irradiated samples the magnitude of Z' is found lower for the concentration x = 0.0, 0.2 and 0.8 and higher for the compositions x = 0.4 and 0.6 compared to the unirradiated samples.

Compositional dependence imaginary part (Z'') of impedance show higher value for x = 0.2 and 0.8 and lower value for x = 0.4 and 0.6 with respect to x = 0.0 of unirradiated samples. It is clear that Z'' values are found to increase and approach to a maximum peak (Z''_{max}), thereafter it starts decreasing with further increase in frequency for the unirradiated samples x = 0.0, 0.4 and 0.6 but it is found to decrease in magnitude with increasing frequency for the unirradiated samples of x = 0.2 and 0.8. However, Z''_{max} peaks are found to shift towards higher frequency with increase Al-Cr content (x). It is observed after irradiation, the maxima peak Z'' almost convert in small hump and shifting to higher frequency for irradiated samples of x = 0.0 and 0.6, while the maxima peak (Z''_{max}) is appeared for irradiated samples x = 0.2, 0.8 and it is disappeared or shifting to lower frequency for irradiated sample x = 0.4 with respect to unirradiated samples for the same measured frequency. This behaviour suggests change in hopping and relaxation process of charge carriers due to micro-structural defects such as grain, grain boundaries and pores by irradiation.

Fig. 6C.21 shows impedance complex plane plots (Z*- plots) obtained by plotting the imaginary part (Z'') with corresponding real part (Z') of different compositions for unirradiated and irradiated samples at room temperature. It can be seen that each unirradiated plot shows one partially loops or semicircles covering the major part of higher frequency of the studied frequency range 100 Hz to 1MHz, which suggests predominance of contribution from bulk grains in electrical conduction. In terms of impedance plots, the lower frequency dispersion correspond to the presence in grain boundary and the higher frequency dispersion corresponds to the process in the grain [6C.39]. It is evident that irradiated samples x = 0.0 and 0.6 show two semicircles, which is due to the contribution of grain and grain boundary, although the diameter of semicircles increases for irradiated samples of x = 0.2, 0.4 and 0.8, indicating a enhancement of the grain interior resistance after irradiation.

Fig. 6C.22a-22e show the variations in the real (M') and imaginary (M'') part of electrical modulus with frequency at different temperature for unirradiated and irradiated samples. The modulus spectra show the electrical relaxation with peak frequency in the imaginary part of the modulus spectra, M'', giving the relaxation frequency, ω_p. In both cases the magnitude of relaxation peak increases and the peaks shift systematically towards higher frequencies with increasing temperature because the thermal activation of the localized electric charges carriers which form electric dipole. For irradiated samples x = 0.0, 0.2 and 0.6, the relaxation peak position shift towards higher frequencies and x = 0.4 and 0.8 it is shift toward lower frequencies with corresponding to unirradiated samples. This recommends that the change in relaxation rate by irradiation process.

The imaginary (M'') part of modulus versus real part (M') of modulus is plotted over a wide frequency range and different temperature of unirradiated and irradiated samples, for all the compositions are shown in Fig. 6C.23a-23e. From the plots it is seen that in general there are two semicircles at 298K for all the unirradiated specimens, whereas temperature increases, the second semicircle (in high frequency region) slowly disappeared and the diameter of the first semicircle decreases for the unirradiated samples of x = 0.0, 0.2 and 0.4. For the unirradiated samples of x = 0.6 and 0.8, it is seen that at 373K, 473K and 473K, 573K respectively, the modulus data do not take the semicircles but rather present a straight line with large slope in higher frequency region and at higher temperature a semicircle could be traced in lower

frequency region, indicating a decrease in resistivity of samples. This behaviour is directly supported by resistivity measurements. For irradiated samples, it is observed one semicircle at 298K and the diameters of semicircle decreases and curve towards in straight line with large slope with increasing temperature, referring to change in resistivity after irradiation.

Conclusion

The interesting Physics was revealed for the spinel oxide system $MnAl_xCr_xFe_{2-2x}O_4$ with the following results prior to the commencement of the SHII study:

The system maintains the Nèel's type collinear spin structure in spite of increasing Cr^{3+} and Al^{3+} ions in B-sites at the cost of Fe^{3+} ions, which indirectly supports the theory of "exchange disorder" of Fe^{3+} ions in B-sites as the cause of the reduction of magnetic moment for $MnFe_2O_4$ from Nèel's moment. The oblate type of deformation of $3d^5$ shell is reflected in the X-ray diffraction and Mössbauer spectroscopy. The long range ordering of spins is not broken to an appreciable extent even at higher dilution limit as can be inferred from the increase in magnetization at 80K due to magnetic dilution of A-sites compared to B-sites with inclusion of Al^{3+} ions in A-sites for $x > 0.7$. There is the emergence of "spin cluster" in the long range net work of spin as indicated in the AC susceptibility and Mössbauer results at room temperature in $x > 0.7$ compounds.

The post irradiation study has shown that the lattice parameter of all the compositions increases after the SHII. The saturation moment of Mn-ferrite also increase after the SHII suggesting the modification of magnetic micro structure due to SHII. The observed saturation moments of all the compositions becomes almost equal to the Nèel's moments after the SHII in contrast to the unirradiated counterpart where the saturation moment were found less compared to the Nèel's moments due to exchange disorder. This has supported the origin of reduction of magnetic moment in $MnFe_2O_4$ and its compounds. The SHII appears to be modifying the magnetic micro-structure favourably and increases the saturation moments.

The shifting of main absorption bands in IR spectra to higher frequency is due to the irradiation induced mixed valence of Fe ions. The change in the structural parameters after the SHII has also affected the elastic constants of the system. The charge transport in the system has greatly affected by the SHII due to the SHII-

induced modifications in the grain microstructure, density and porosity as revealed by resistivity, dielectric and impedance spectroscopic study.

References

6C.1 Cheng Dong, J. Appl. crystallographic **32** (1999) 838

6C.2 V.A.M. Brabers, "Progress in spinel ferrites", **vol.8**, (Elsevier Science B.V. 1995) 212

6C.3 C. G. Whinfrey, D. W. Eckart, A. Tauber, J. Am. Chem. Soc. **82** (1960) 2695

6C.4 J. M. Hastings and L. M. Corliss, Phy. Rev. **104** (1956) 328

6C.5 S. E. Harrison, C. J. Krissmen and S. R. Pollack, Phys. Rev. **110** (1958) 844

6C.6 H. Yasuoka, J. Phys. Soc. Japan **21** (1966) 393

6C.7 N. S. Satya Murthy, L. Madhav Rao, R. J. Begum, M. G. Natera and S. I. Yussuf, J. de. Phys. **32** (1971) C1-318

6C.8 F. C. Romeijn, Philips Res. Rep. **8** (1953) 304

6C.9 A. R. Corradi, L. Benzoni, N. Burriesci, C. A. Nannetti, M. Petrera and L. Pizzini, J. Phys. (Paris) **38** (1977) C1-291

6C.10 S. Ligenza, Phys. Stat. Sol. (b) **86** (1978) 635

6C.11 S. Ligenza, Phys. Stat. Sol. (b) **105** (1981) 353

6C.12 J. Smith, H. P. J. Wijn, Ferrites, Philips, Eindhoven, (1959)

6C.13 K. J. Standly, Oxide Magnetic Materials (Clarenden Press, Oxford), (1972)

6C.14 S. A. Mazen, M. H. Abdallah, B. A. Sabrah, H. A. M. Hasham, Phys. Stat. Sol. A **134** (1992) 263

6C.15 M. A. Ahmed, Eateia and F. M. Salem, J. Mater. Sci. **42** (2007) 3651

6C.16 K. E. Sickafus and J. M. Wills, J. Amer. Cera. Sco. **82** (1999) 3279

6C.17 J. B. Goodenough, J. Phys. Chem. Solids **6** (1959) 287

6C.18 J. Kanamori, J. Phys. Chem. Solids **10** (1959) 67

6C.19 R. D. Waldron, Phys. Rev. **99** (1955) 1727

6C.20 C. M. Srivastawa and T. T. Srinivasan, J. Appl. Phys. **53** (1982) 8184

6C.21 S. A. Patil, V. C. Mahajan, A. K. Ghatage and S. D. Lotke, Mater. Chem Phys. **57** (1998) 86

6C.22 M. C. Chhantbar, U. N. Trivedi, P. V. Tanna, H. J. Shah, R. P. Vara, H. H. Joshi and K. B. Modi, Ind. J. Phys. **78A(3)** (2004) 321

6C.23 D. Ravinder and T. Manga, Mater. Lett. **14** (1999) 254

6C.24 B. Raj, V. Rajendram and P. Palanichamy, "Science and Technology of Ultrasonics", Narosa Pub. House, New Delhi (2004) 250

6C.25 W. A. Wooster, Rep. Prog. Phys. **16** (1953) 62

6C.26 Z. Simsa, Czech J. Phys. B **16** (1966) 919

6C.27 J. B. Goodenough, J. Appl. Phys., **36** (1965) 1198

6C.28 D. B. Rogers, R. W. Germann and R. J. Arnott, J. Appl. Phys., **36** (1965) 2338

6C.29 B. V. Bhise, A. K. ghatage, B. M. Kulkarni, S. D. Lotke and S. A Patil, Bull Mater. Sci. **19** (1996) 527

6C.30 V. T. Zaspalls, E. Antoniadis, E. Papazoglou, V. Tsakaloudi, L. Nalbandian, and C. A. Sikalidis, J. Magn. Magn. Mater. **250** (2002) 98

6C.31 Anjili Verma, Ratnamala Chatterjee, J. Magn. Magn. Mater. **306** (2006) 313

6C.32 K. B. Modi, H. H. Joshi and R. G. Kulkarni, J. Mater. Sci. **31** (1996) 3111

6C.33 U. V. Chhaya and R. G. Kulkarni, Mater. Letters **39** (1999) 91

6C.34 B. V. Bhise, V. C. Mahajan, M. G. Patil, S. D. Lotke and S. A. Patil, Ind. J. Pure & Appl. Phys. **33** (1995) 459

6C.35 A. J. Bosman, and C. Crevecoeur, Phys. Rev. **144** (1966) 763

6C.36 A. J. Bosman and C. Crevecoeur, J. Phys. Chem. Solid **30** (1969) 15

6C.37 M. A. Ahmed, M. K. El. Nimr, A. Tawfik and A. M. El. Hasab, Phys. Stat. Sol. (a) **123** (1991) 501

6C.38 I. T. Rabinkin and Z. I. Novikova, Ferrites (Minsk: Izv. Acad. Nauk USSR) (1960)146

6C.39 R. S. Devan, Y. D. Kolekar and B. K. Chougule, J. Phys. D: Cond. Matter **18** (2006) 9809

Table 6C.1: The compositions and molecular weights for various compounds of $MnAl_xCr_xFe_{2-2x}O_4$ system

Concentration (x)	Composition	Molecular weights (amu)
0.0	$MnFe_2O_4$	230.6296
0.2	$MnAl_{0.2}Cr_{0.2}Fe_{1.6}O_4$	224.0863
0.4	$MnAl_{0.4}Cr_{0.4}Fe_{1.2}O_4$	217.5440
0.6	$MnAl_{0.6}Cr_{0.6}Fe_{0.8}O_4$	210.9997
0.8	$MnAl_{0.8}Cr_{0.8}Fe_{0.4}O_4$	204.4564

Table 6C.2: Cation distribution and results of XRD Intensity analysis for all the compositions of unirradiated and irradiated $MnAl_xCr_xFe_{2-2x}O_4$ system

x	sample	Cation Distribution	Intensity ratio			
		A-site - B-site	I(220)/I(440)		I(400)/I(422)	
			Cal	Obs	Cal	Obs
0.0	Unirr	$(Mn_{0.60}Fe_{0.40})[Mn_{0.40}Fe_{1.6}]O_4$	0.974	1.023	1.515	1.720
	Irr	$(Mn_{0.63}Fe_{0.37})[Mn_{0.37}Fe_{1.63}]\ O_4$	1.011	0.957	2.006	2.243
0.2	Unirr	$(Mn_{0.60}\ Fe_{0.4})[Mn_{0.40}Al_{0.2}Cr_{0.2}Fe_{1.2}]\ O_4$	0.946	1.074	1.707	1.883
	Irr	$(Mn_{0.68}Al_{0.1}Fe_{0.22})[Mn_{0.32}Al_{0.1}Cr_{0.2}Fe_{1.38}]\ O_4$	1.043	0.943	1.901	2.106
0.4	Unirr	$(Mn_{0.60}Fe_{0.40})[Mn_{0.40}Al_{0.4}Cr_{0.4}Fe_{0.8}]\ O_4$	0.971	1.004	1.709	1.889
	Irr	$(Mn_{0.72}Fe_{0.28.})[Mn_{0.28}Al_{0.4}Cr_{0.4}Fe_{0.92}]\ O_4$	0.924	0.922	1.921	2.027
0.6	Unirr	$(Mn_{0.60}Fe_{0.40})[Mn_{0.40}Al_{0.6}Cr_{0.6}Fe_{0.4}]\ O_4$	0.974	1.089	1.896	2.071
	Irr	$(Mn_{0.77}Fe_{0.23})[Mn_{0.23}Al_{0.6}Cr_{0.6}Fe_{0.57}]\ O_4$	0.957	0.921	1.906	2.041
0.8	Unirr	$(Mn_{0.60}\,Al_{0.1}\,Fe_{0.3})[Mn_{0.4}Al_{0.7}Cr_{0.8}Fe_{0.1}]\ O_4$	1.102	1.191	1.896	2.160
	Irr	$(Mn_{0.82}Fe_{0.18})[Mn_{0.18}\,Al_{0.8}Cr_{0.8}Fe_{0.22}]\ O_4$	0.990	0.942	1.930	2.081

Table 6C.3: Lattice parameter (a), Saturation magnetization σ_s, Nèel moment (n_B) and Curie temperature (T_c) for all the compositions of unirradiated and irradiated $MnAl_xCr_xFe_{2-2x}O_4$ system

Content (x)	Sample	Lattice parameter 'a' (Å) ±.002 (Å)	Magnetization (80K)			Curie Temperature T_c(K) ± 5K
			σ_s (emu/gm)	n_B^N (μ_B)	n_B^{obs} (μ_B)	
0.0	Unirr	8.489	83.3	5.00	3.44	598
	Irr	8.507	119.9	5.00	4.95	587
0.2	Unirr	8.462	56.9	3.60	2.28	526
	Irr	8.473	89.5	3.60	3.59	551
0.4	Unirr	8.430	36.5	2.20	1.42	460
	Irr	8.446	59.7	2.20	2.2	446
0.6	Unirr	8.405	20.3	0.80	0.77	380
	Irr	8.415	21.2	0.81	0.80	408
0.8	Unirr	8.381	12.2	0.40	0.43	---
	Irr	8.406	16.7	0.61	0.59	---

Table 6C.4: Mössbauer hyperfine parameters for all the compositions of unirradiated and irradiated $MnAl_xCr_xFe_{2-2x}O_4$ system

x	Sample	Hyperfine field ± 5 (kGauss)		Isomer shift ± 0.01 (mm/sec)		Quadrupole splitting ± 0.002 (mm/sec)		Line width (ΔΓ) ± 0.02 (mm/sec)	
		A-site	B-site	A-site	B-site	A-site	B-site	A-site	B-site
0.0	Unirr	431	476	0.41	0.29	-0.033	-0.129	0.55	0.41
	Irr	433	478	0.35	0.30	0.009	0.005	0.63	0.57
0.2	Unirr	437	474	0.30	0.32	-0.025	-0.145	0.54	0.42
	Irr	428	466	0.31	0.31	0.001	0.007	0.62	0.69
0.4	Unirr	379	435	0.32	0.29	-0.034	-0.150	0.59	0.47
	Irr	410	421	0.33	0.49	0.671	0.710	1.43	0.75
0.6	Unirr	Relaxation		Relaxation		Relaxation		Relaxation	
	Irr	Relaxation		Relaxation		Relaxation		Relaxation	
0.8	Unirr	---	---	0.36	0.50	-0.674	-0.722	0.40	0.31
	Irr	---	---	0.23	0.39	0.515	0.623	0.33	0.41

Table 6C.5: Theoretical X-ray Lattice Parameters (a_{th}), Bulk density (d), X-ray density (d_x), Pore fraction (f) and Porosity (P) for all the compositions of unirradiated and irradiated $MnAl_xCr_xFe_{2-2x}O_4$ system

(x)	Samples	'a_{th}' (Å) ± 0.0002 (Å)	Bulk density (d) $(kg/m^3)x10^3$	X-ray density (d_x) $(kg/m^3)x10^3$	Pore fraction (f)	Porosity P (%)
0.0	Unirr	8.4773	4.1932	5.0100	0.1630	16.30
	Irr	8.4783	4.2405	4.9783	0.1482	14.82
0.2	Unirr	8.4400	3.2062	4.9146	0.3476	34.76
	Irr	8.4399	2.8971	4.8955	0.4082	40.82
0.4	Unirr	8.4027	3.0643	4.8257	0.3650	36.50
	Irr	8.4066	3.1530	4.7983	0.3429	34.29
0.6	Unirr	8.3653	2.6088	4.7224	0.4476	44.76
	Irr	8.3709	2.6159	4.7056	0.4441	44.41
0.8	Unirr	8.3253	2.6552	4.6154	0.4247	42.47
	Irr	8.3353	2.4138	4.5743	0.4723	47.23

Table 6C.6: Ionic radii (r_A, r_B), bond lengths (A-O, B-O), oxygen positional parameter (u) and site radii (R_A, R_B) for all the compositions of unirradiated and irradiated $MnAl_xCr_xFe_{2-2x}O_4$ system

(x)	Sample	r_A (Å)	r_B (Å)	A – O ($r_A + r_O$)	B – O ($r_B + r_O$)	u (Å)	R_A (Å)	R_B (Å)
0.0	Unirr	0.7360	0.6720	2.0560	1.9920	0.2655	2.0658	1.9994
	Irr	0.7408	0.6696	2.0608	1.9896	0.2659	2.0761	2.0007
0.2	Unirr	0.7360	0.6580	2.0560	1.9780	0.2661	2.0680	1.9886
	Irr	0.7358	0.6581	2.0558	1.9781	0.2660	2.0693	1.9919
0.4	Unirr	0.7360	0.6440	2.0560	1.9640	0.2667	2.0689	1.9768
	Irr	0.7552	0.6344	2.0752	1.9544	0.2681	2.0934	1.9705
0.6	Unirr	0.7360	0.6300	2.0560	1.9500	0.2675	2.0745	1.9652
	Irr	0.7632	0.6164	2.0832	1.9364	0.2693	2.1032	1.9549
0.8	Unirr	0.7230	0.6225	2.0430	1.9425	0.2672	2.0642	1.9617
	Irr	0.7712	0.5984	2.0912	1.9184	0.2706	2.1199	1.9438

Table 6C.7: Inter-ionic distances between cation-anion (Me-O), cation-cation (Me-Me) and bond angles (θ) for all the compositions of unirradiated and irradiated $MnAl_xCr_xFe_{2-2x}O_4$ system

x	Sample	Me – O (Å)			
		p	q	r	s
0.0	Unirr	1.9907	2.0658	3.9557	3.7509
	Irr	1.9915	2.0761	3.9754	3.7618
0.2	Unirr	1.9793	2.0681	3.9600	3.7429
	Irr	1.9827	2.0693	3.9623	3.7471
0.4	Unirr	1.9667	2.0689	3.9618	3.7416
	Irr	1.9586	2.0934	4.0085	3.7454
0.6	Unirr	1.9542	2.0745	3.9724	3.7244
	Irr	1.9413	2.1032	4.0273	3.7376
0.8	Unirr	1.9511	2.0642	3.9527	3.7123
	Irr	1.9283	2.1199	4.0593	3.7399

Me – Me (Å)						
x	Sample	b	c	d	e	f
0.0	Unirr	3.0013	3.5194	3.6758	5.5138	5.1984
	Irr	3.0077	3.5268	3.6836	5.5255	5.2095
0.2	Unirr	2.9918	3.5082	3.6642	5.4962	5.1818
	Irr	2.9957	3.5127	3.6689	5.5034	5.1886
0.4	Unirr	2.9805	3.4949	3.6503	5.4755	5.1623
	Irr	2.9861	3.5015	3.6572	5.4858	5.1721
0.6	Unirr	2.9716	3.4845	3.6395	5.4592	5.1469
	Irr	2.9752	3.4887	3.6438	5.4657	5.1531
0.8	Unirr	2.9631	3.4746	3.6291	5.4436	5.1323
	Irr	2.9719	3.4849	3.6399	5.4599	5.1476

Bond angles (θ)						
x	Sample	θ_1	θ_2	θ_3	θ_4	θ_5
0.0	Unirr	120.3497	133.2516	97.8479	127.0183	66.9325
	Irr	120.2199	132.8154	98.0742	127.0224	66.6397
0.2	Unirr	120.1577	132.5912	98.1864	127.0249	66.4965
	Irr	120.1872	132.7369	98.1309	127.0365	66.5679
0.4	Unirr	119.9707	131.9507	98.5313	126.5341	66.0623
	Irr	119.5328	130.4624	99.3359	127.2791	65.0656
0.6	Unirr	119.7185	131.0902	99.3829	127.2065	65.4892
	Irr	119.1605	129.2162	100.0445	127.3762	64.2285
0.8	Unirr	119.8166	131.4099	100.3380	127.1713	65.7035
	Irr	118.7494	127.8888	100.8165	127.5619	63.3482

Table 6C.8: Positions of IR main absorption bands (ν_1,ν_2) with sholulders/spllitings bands ($\nu_{sh/sp}$) for all the compositions of unirradiated and irradiated $MnAl_xCr_xFe_{2-2x}O_4$ system

x	Sample	ν_{1sh} (m^{-1}) x 10^2	ν_1(m^{-1}) x 10^2	ν_{1sh} (m^{-1}) x 10^2	ν_{2sh} (m^{-1})x10^2	ν_2 (m^{-1}) x 10^2	ν_{2sh} (m^{-1})x10^2
0.0	Unirr	732.97,639.68	565.73	---	---	470	---
	Irr	722.08,656.93, 645.36,632.62,	562.35	552.24, 541.61	484.20	466.83	456.69
0.2	Unirr	738.00, 642.96	584.03	---	---	478.06	---
	Irr	737.03,650.12, 636.04,596.69	587.77	---	---	471.17	463.74
0.4	Unirr	643.61	602.41			487.68	
	Irr	651.64	606.33	598.89		489.21	478.29, 470.67
0.6	Unirr	---	608.07	---	---	487.06	---
	Irr	---	609.35	---	---	491.34	---
0.8	Unirr	---	615.13	---	---	502.92	---
	Irr	---	615.75	---	---	503.18	---

Table 6C.9: Molecular weight (M_1, M_2) of A & B-sites, force constants (k_t, k_o) of A & B- sites respectively and average force constant (k) for all the compositions of unirradiated and irradiated $MnAl_xCr_xFe_{2-2x}O_4$ system

x	Sample	M_1 (kg) x 10^{-3}	$M_2/2$ (kg) x 10^{-3}	k_t (N/m) x 10^2	k_o(N/m) x 10^2	k (N/m) x 10^2
0.0	Unirr	55.3016	55.6652	1.3487	1.3059	1.3273
	Irr	55.2743	55.6788	1.3320	1.2886	1.3103
0.2	Unirr	55.3016	52.3936	1.4374	1.2717	1.3546
	Irr	52.3423	53.8732	1.3779	1.2701	1.3240
0.4	Unirr	55.3016	49.1219	1.5293	1.2407	1.3850
	Irr	55.1925	49.1765	1.5462	1.2499	1.3981
0.6	Unirr	55.3016	45.8503	1.5581	1.1551	1.3566
	Irr	55.1471	45.9276	1.5603	1.1775	1.3689
0.8	Unirr	52.4151	44.0219	1.5113	1.1825	1.3469
	Irr	55.1016	42.6786	1.5919	1.1476	1.3698

Table 6C.10 Longitudinal elastic wave velocity (υ_l), transverse elastic wave velocity (υ_s), Mean elastic wave velocity (υ_m) and Debye temperature (θ) for all the compositions of unirradiated and irradiated $MnAl_xC\ r_xFe_{2-2x}O_4$ system

x	Sample	υ_l (m/s)	υ_s (m/s)	υ_m (m/s)	θ (K)
0.0	Unirr	5586.55	3225.39	3580.79	480.79
	Irr	5562.39	3211.45	3565.32	477.71
0.2	Unirr	5707.22	3295.07	3658.15	492.72
	Irr	5649.69	3261.85	3621.27	487.12
0.4	Unirr	5834.79	3368.72	3739.92	505.26
	Irr	5873.47	3391.05	3764.71	508.08
0.6	Unirr	5846.16	3375.28	3747.20	508.23
	Irr	5879.58	3394.58	3768.63	510.53
0.8	Unirr	5900.88	3406.87	3782.27	514.42
	Irr	5968.68	3446.02	3825.74	518.78

Table 6C. 11: Bulk modulus (B), Young's modulus (E), rigidity modulus (G) and Poisson's ratio (σ) for all the compositions of unirradiated and irradiated $MnAl_xCr_xFe_{2-2x}O_4$ system

x	Sample	B (GPa)	E (GPa)	G (GPa)	σ
0.0	Unirr	156.36	140.72	52.12	0.35
	Irr	154.03	138.62	51.34	0.35
0.2	Unirr	160.08	144.07	53.36	0.35
	Irr	156.26	140.64	52.09	0.35
0.4	Unirr	164.29	147.85	54.76	0.35
	Irr	165.53	148.99	55.18	0.35
0.6	Unirr	161.40	145.26	53.80	0.35
	Irr	162.67	146.39	54.22	0.35
0.8	Unirr	160.71	144.64	53.57	0.35
	Irr	162.96	146.66	54.32	0.35

Table 6C.12: dc resistivity ($\log_{10}\rho_{dc}$), Activation energy (E) and Nèel temperature (T_N) for all the compositions of unirradiated and irradiated $MnAl_xCr_xFe_{2-2x}O_4$ system

x	Sample	$\log_{10}\rho_{dc}$ (Ω.cm) (313K)	Activation energy (eV)		ΔE (eV)	T_N(K) ± 5K	
			E_f	E_p		Resistivity	Susceptibility
0.0	Unirr	7.948	0.504	0.558	0.054	623	598
	Irr	6.766	0.509	0.566	0.057	603	587
0.2	Unirr	7.411	0.440	0.453	0.013	533	526
	Irr	7.597	0.473	0.639	0.166	563	551
0.4	Unirr	7.839	0.370	0.373	0.003	483	460
	Irr	7.633	0.385	0.431	0.046	473	446
0.6	Unirr	8.805	0.089	0.247	0.158	383	380
	Irr	8.576	0.229	0.451	0.222	433	408
0.8	Unirr	8.980	---	0.229	---	---	---
	Irr	11.208	---	0.457	---	---	---

Table: 6C.13: Jump length (L), Polaron radius (r_P) and Fermi energy ($E_F(0)$) for all the compositions of unirradiated and irradiated $MnAl_xCr_xFe_{2-2x}O_4$ ystem

x	Sample	Jump length L (Å)		Polaron radius r_p (Å)	Fermi energy $\lvert E_f \rvert$ (eV)
		L_A	L_B		
0.0	Unirr	3.6758	3.0013	0.7470	0.713
	Irr	3.6836	3.0077	0.7486	0.610
0.2	Unirr	3.6642	2.9918	0.7447	0.075
	Irr	3.6689	2.9957	0.7456	0.189
0.4	Unirr	3.6503	2.9805	0.7418	0.067
	Irr	3.6572	2.9861	0.7432	0.075
0.6	Unirr	3.6395	2.9716	0.7396	0.442
	Irr	3.6438	2.9752	0.7405	1.105
0.8	Unirr	3.6291	2.9631	0.7375	0.904
	Irr	3.6399	2.9720	0.7397	0.719

Table 6C.14: Compositional variation of dielectric constant (ε'), a.c. resistivity ($\log_{10}\rho_{ac}$) and dielectric loss tangent (tanδ) for two frequencies (1kHz & 10kHz) at room temperature for all the compositions of unirradiated and irradiated $MnAl_xCr_xFe_{2-2x}O_4$ system

1kHz - 298K						
x	ε'		$\log_{10}\rho_{ac}$		tanδ	
	Unirr	Irr	Unirr	Irr	Unirr	Irr
0.0	145.77	114.09	7.3615	6.8003	0.5368	2.4968
0.2	120.00	55.72	7.6021	7.1771	0.3746	2.1468
0.4	124.41	36.72	7.1686	8.0102	0.9806	0.4784
0.6	212.75	180.74	6.3158	5.7770	4.0850	16.6275
0.8	269.97	52.99	6.8254	7.5034	0.9959	1.0648
10kHz -298K						
0.0	113.34	38.35	6.8845	6.6218	0.2070	1.1203
0.2	93.98	40.19	7.0628	7.0024	0.1656	0.4451
0.4	94.20	30.73	6.7997	7.5830	0.3028	0.1529
0.6	120.19	53.48	6.2798	5.8242	0.7856	5.0408
0.8	165.50	36.84	6.3951	7.1883	0.4375	0.3164

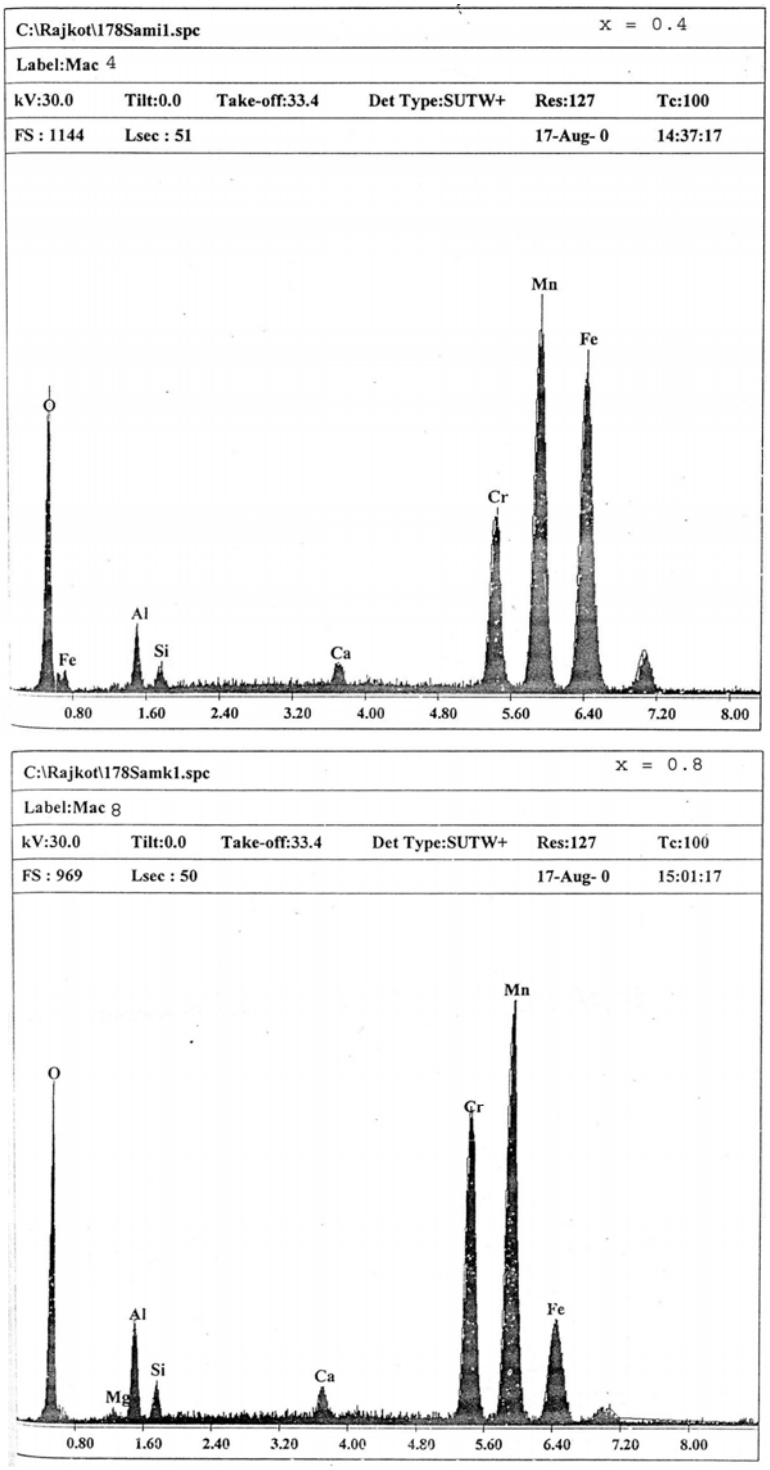

Fig. 6C.1 EDAX measurement spectrum for the compositions x = 0.4 and 0.8 of $MnAl_xCr_xFe_{2-2x}O_4$ system

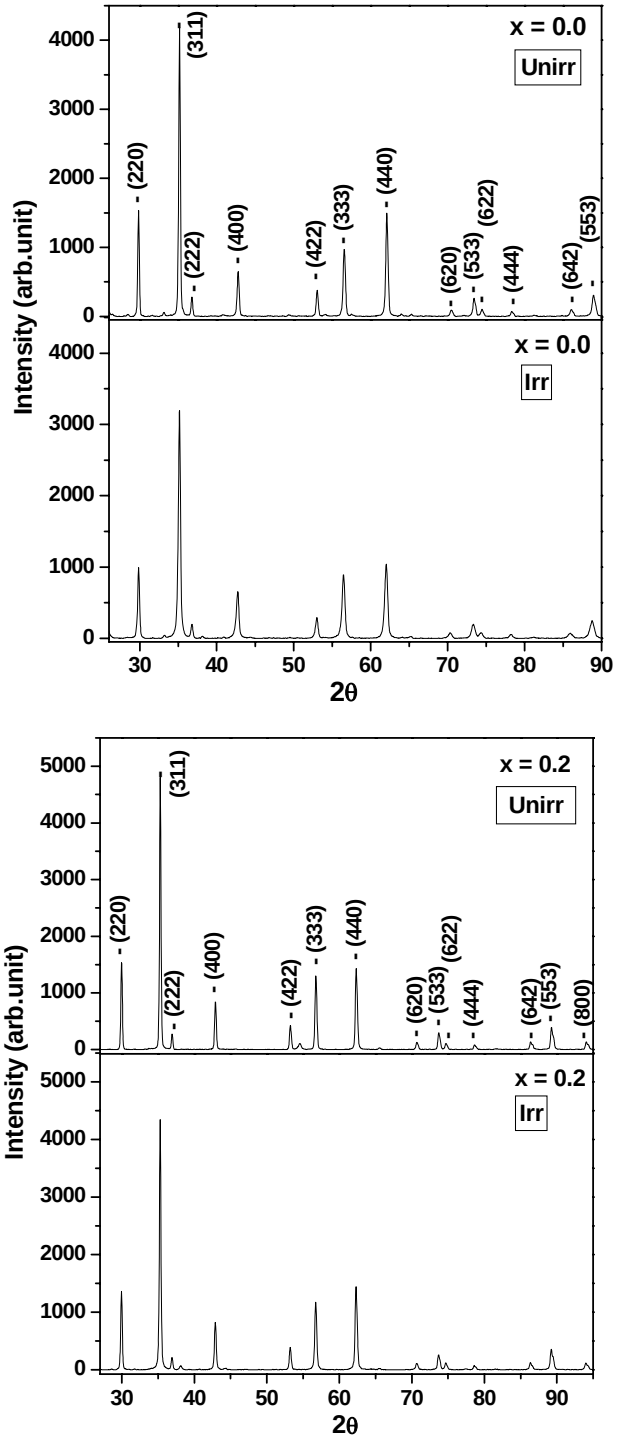

Fig. 6C.2a The X-ray diffraction pattern for the compositions x = 0.0 and 0.2 of unirradiated and irradiated $MnAl_xCr_xFe_{2-2x}O_4$ system

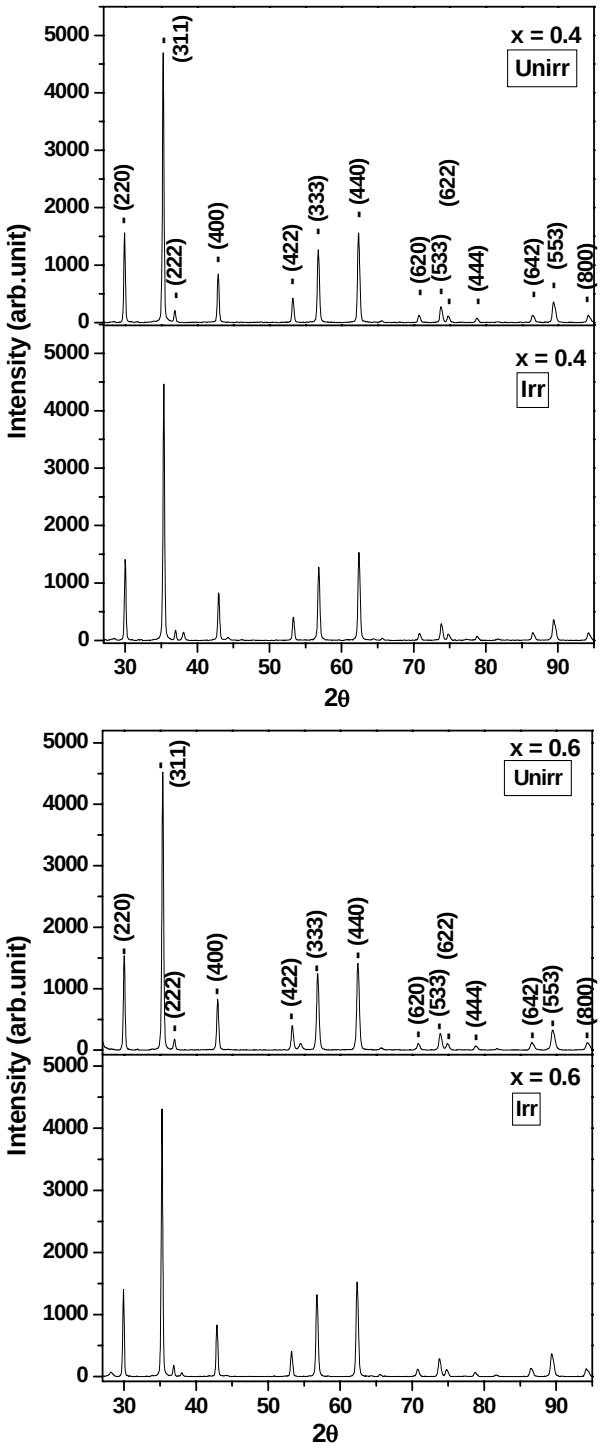

Fig. 6C.2b The X-ray diffraction pattern for the compositions x = 0.4 and 0.6 of unirradiated and irradiated $MnAl_xCr_xFe_{2-2x}O_4$ system

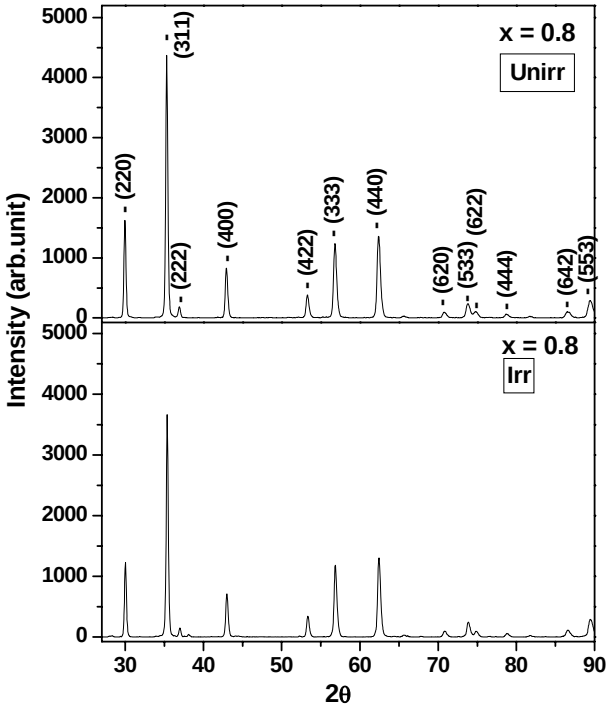

Fig. 6C.2c The X-ray diffraction pattern for the composition x = 0.8 of unirradiated and irradiated MAC system

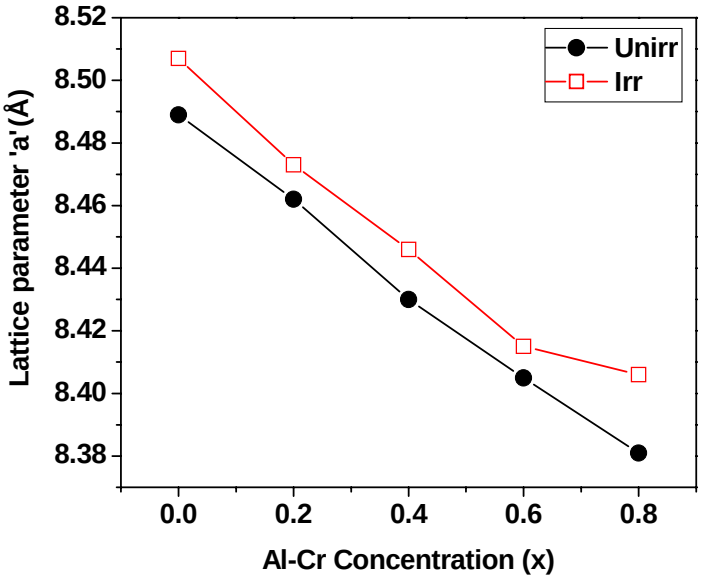

Fig. 6C.3 Compositional variation of lattice parameter (a) of unirradiated and irradiated $MnAl_xCr_xFe_{2-2x}O_4$ system

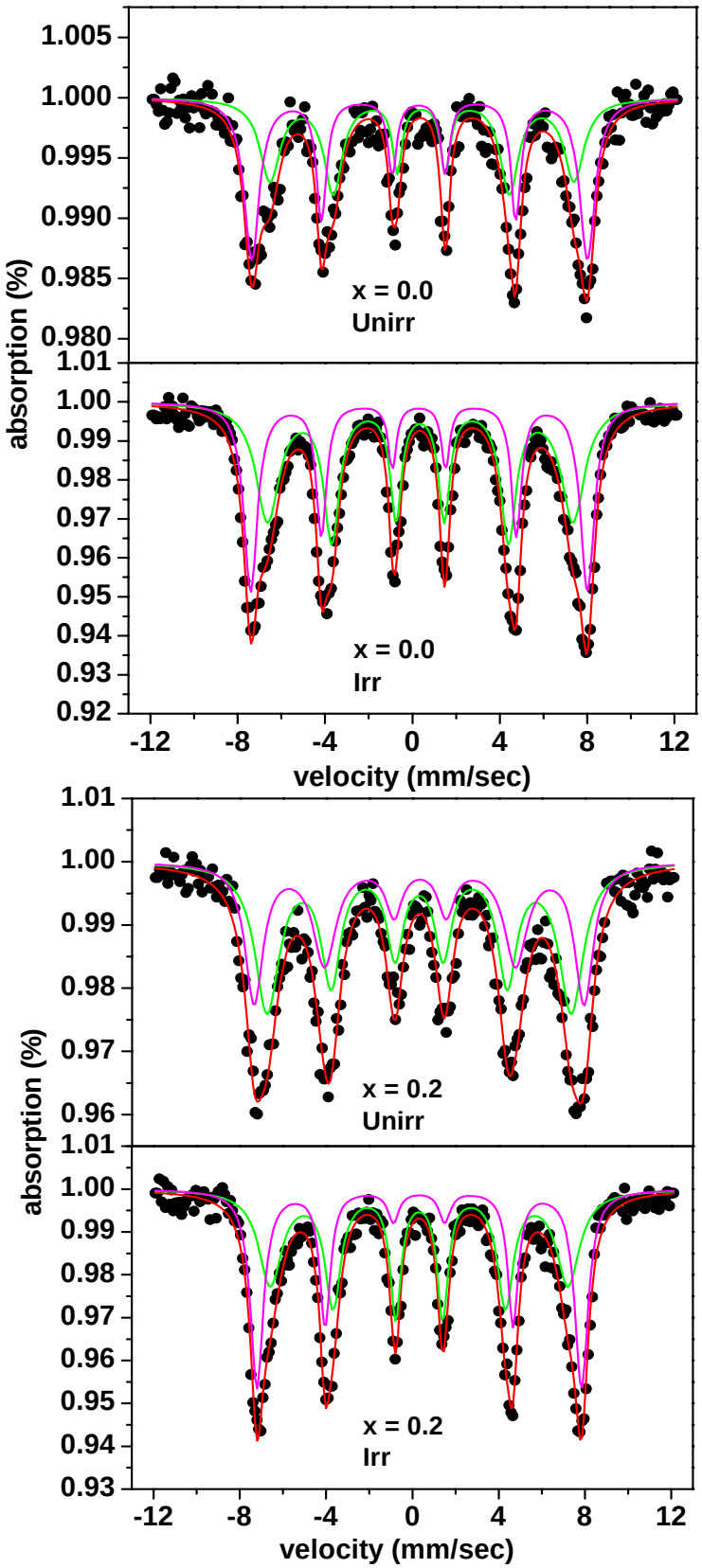

Fig. 6C.4a The refined Mössbauer spectra for the compositions x = 0.0 and 0.2 of unirradiated and irradiated $MnAl_xCr_xFe_{2-2x}O_4$ system

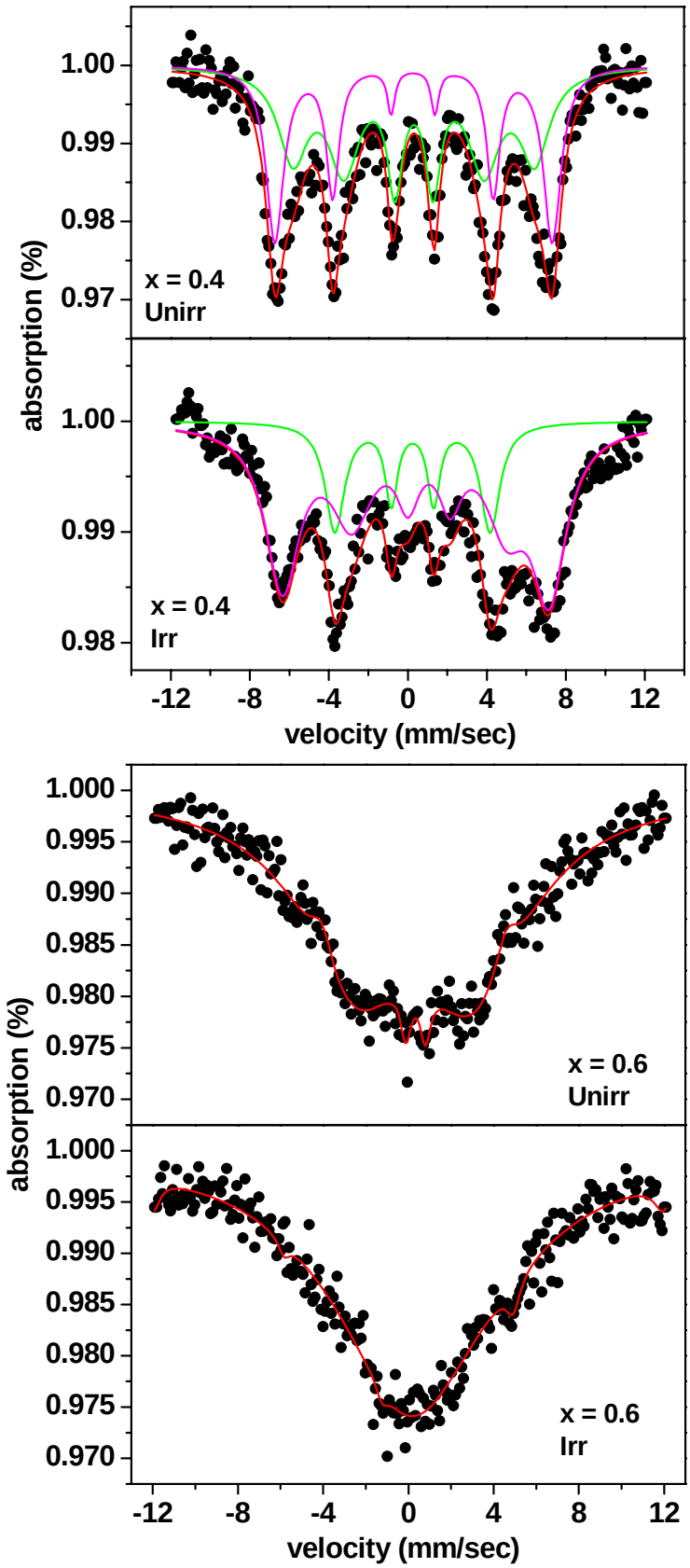

Fig. 6C.4b The refined Mössbauer spectra for the compositions x = 0.4 and 0.6 of unirradiated and irradiated $MnAl_xCr_xFe_{2-2x}O_4$ system

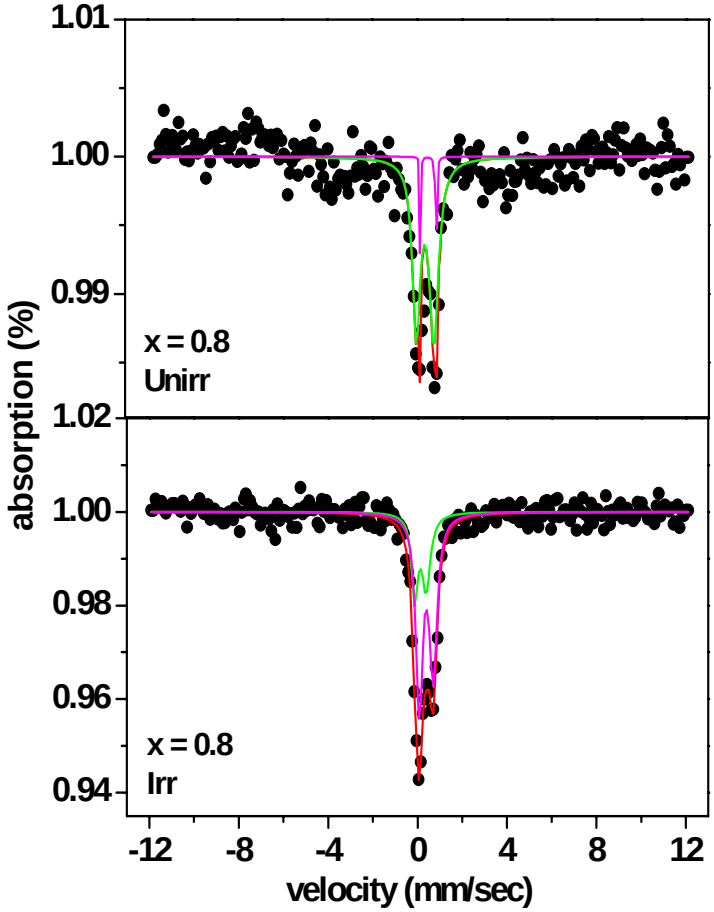

Fig. 6C.4c The refined Mössbauer spectra for the composition x = 0.8 of unirradiated and irradiated $MnAl_xCr_xFe_{2-2x}O_4$ system

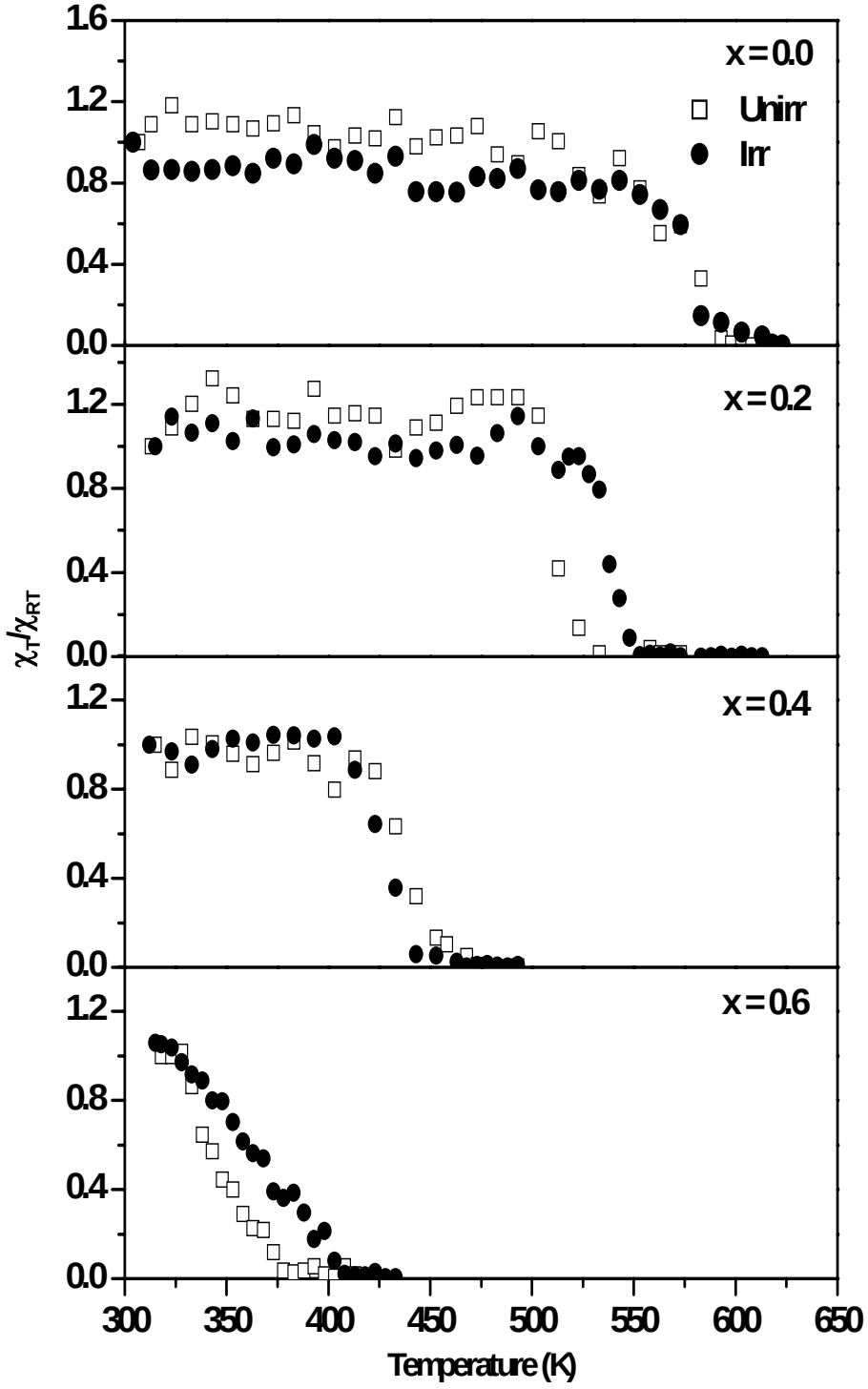

Fig. 6C.5 Thermal variation of AC susceptibility for the compounds x = 0.0, 0.2, 0.4 and 0.6 of unirradiated and irradiated $MnAl_xCr_xFe_{2-2x}O_4$ system

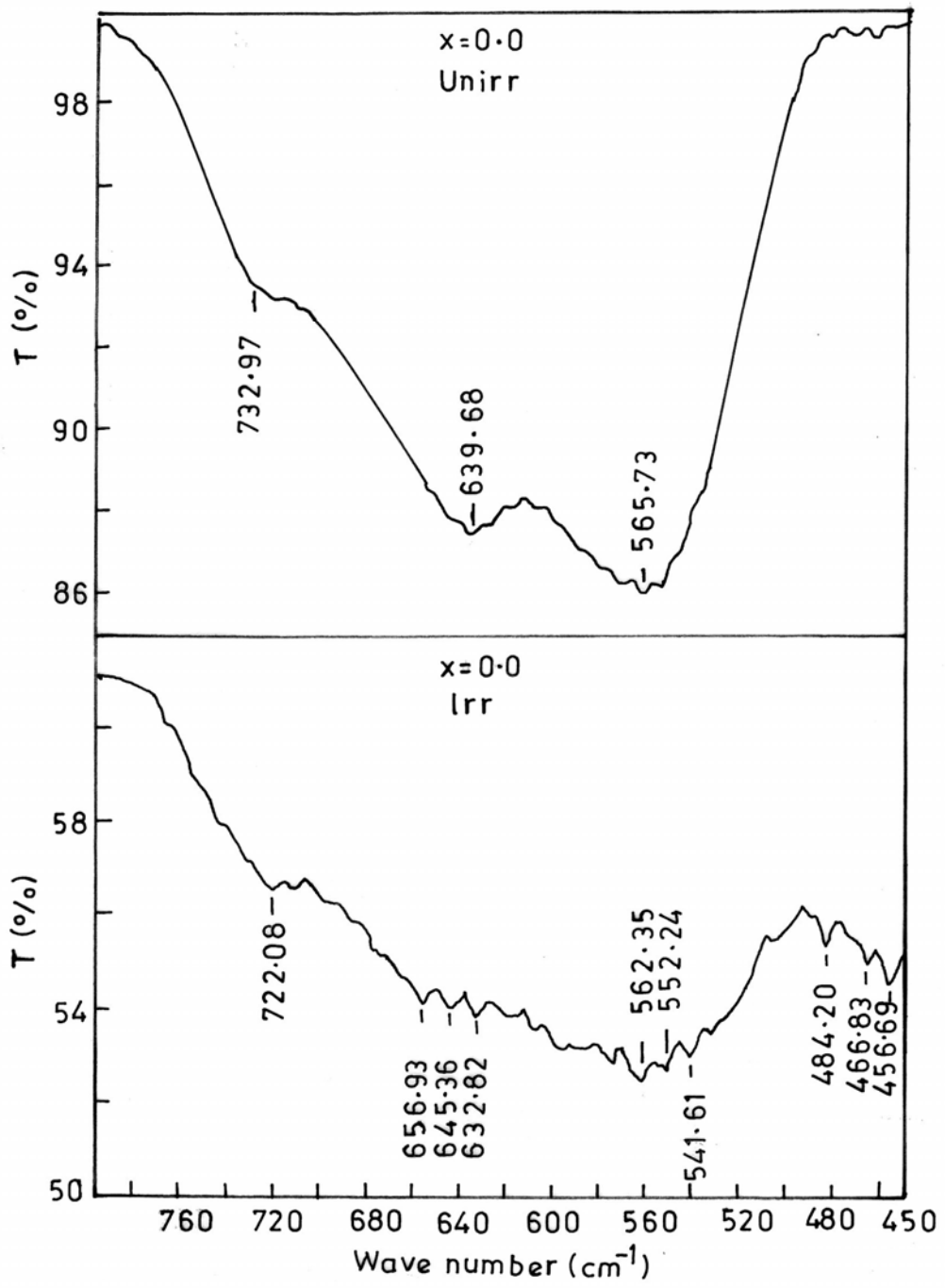

Fig. 6C.6a Infrared spectra of unirradiated and irradiated $MnAl_xCr_xFe_{2-2x}O_4$ system with x = 0.0 sample

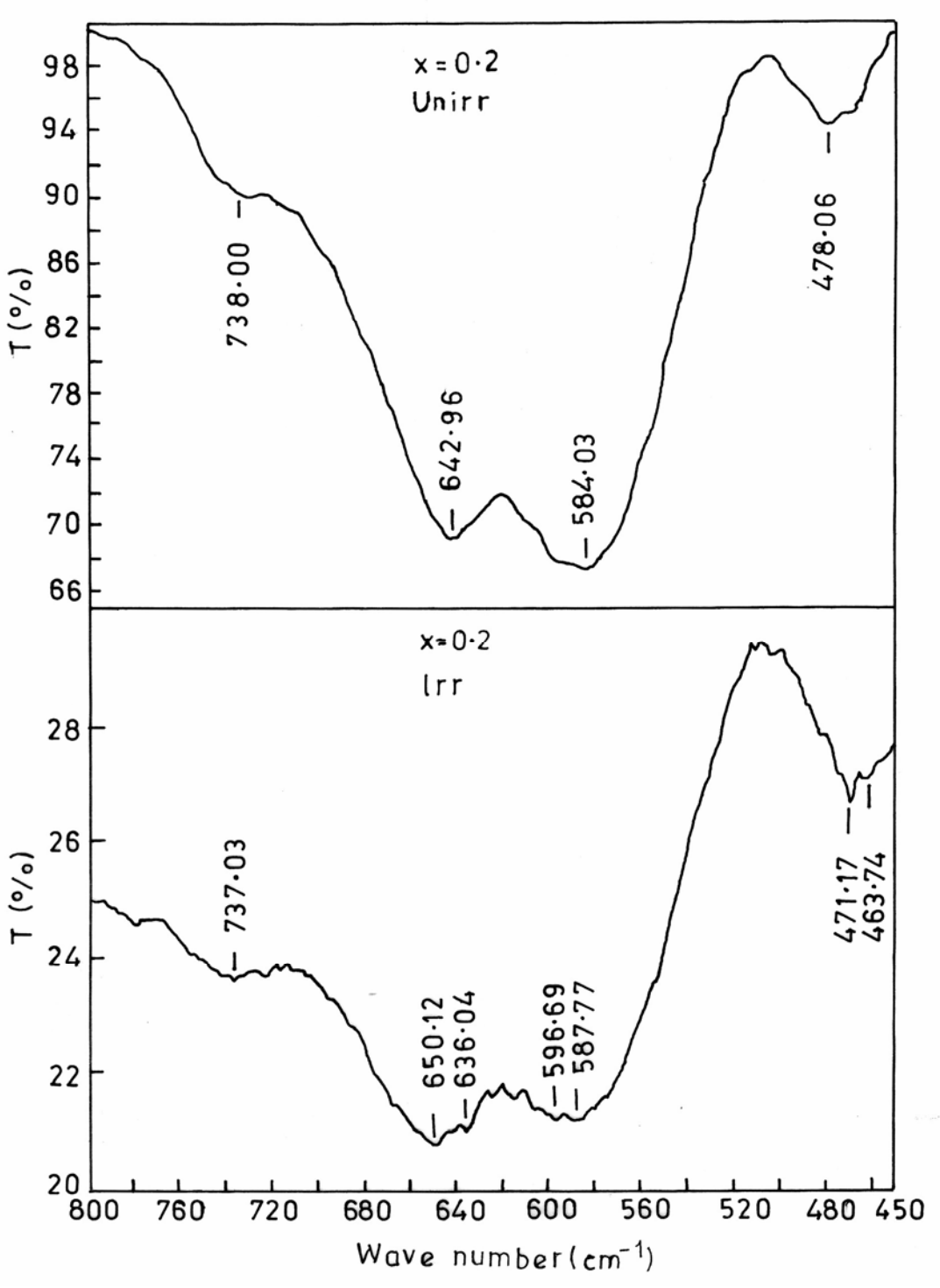

Fig. 6C.6b Infrared spectra of unirradiated and irradiated $MnAl_xCr_xFe_{2-2x}O_4$ system with x = 0.2 sample.

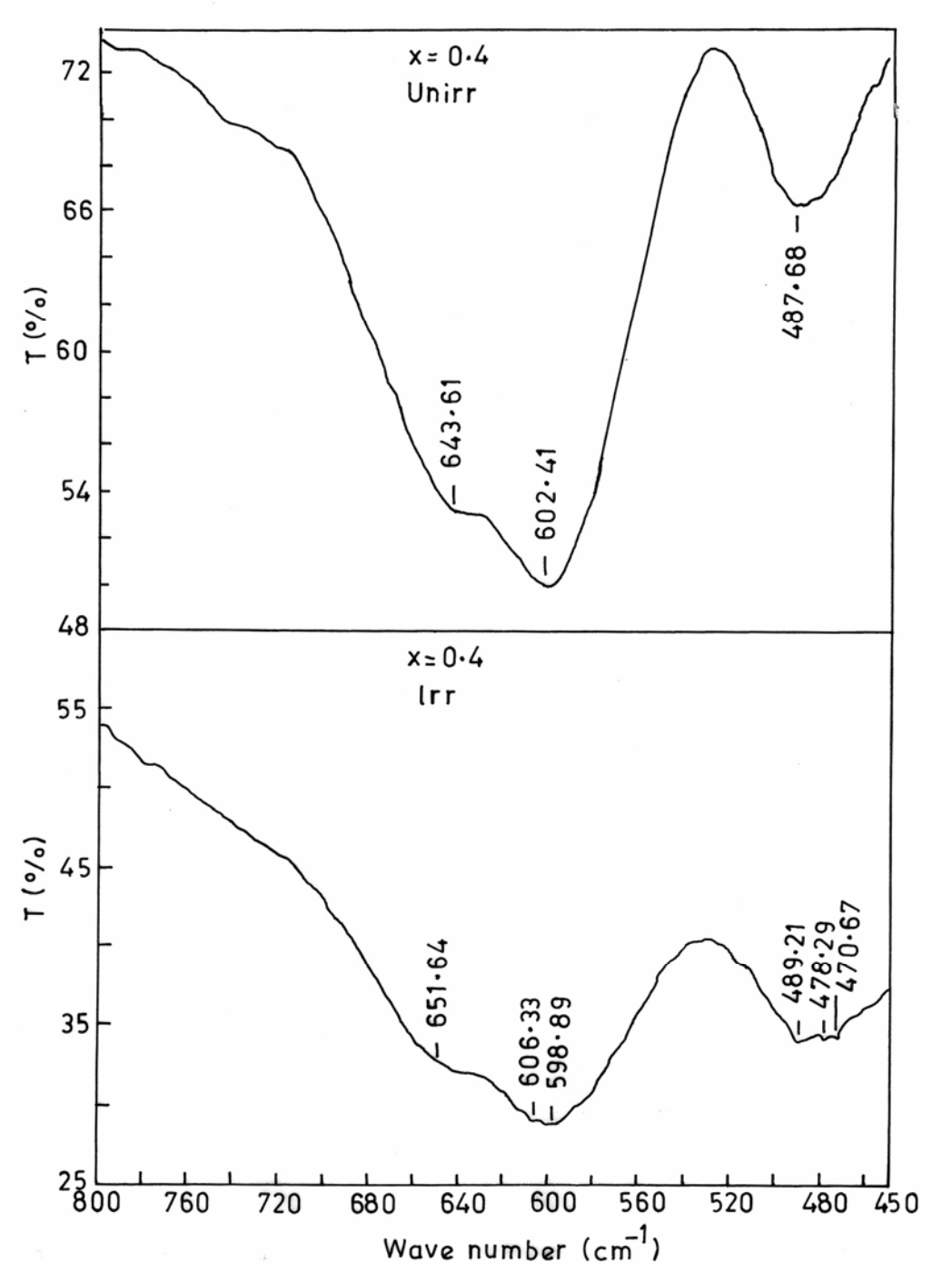

Fig. 6C.6c Infrared spectra of unirradiated and irradiated $MnAl_xCr_xFe_{2-2x}O_4$ system with x = 0.4 sample.

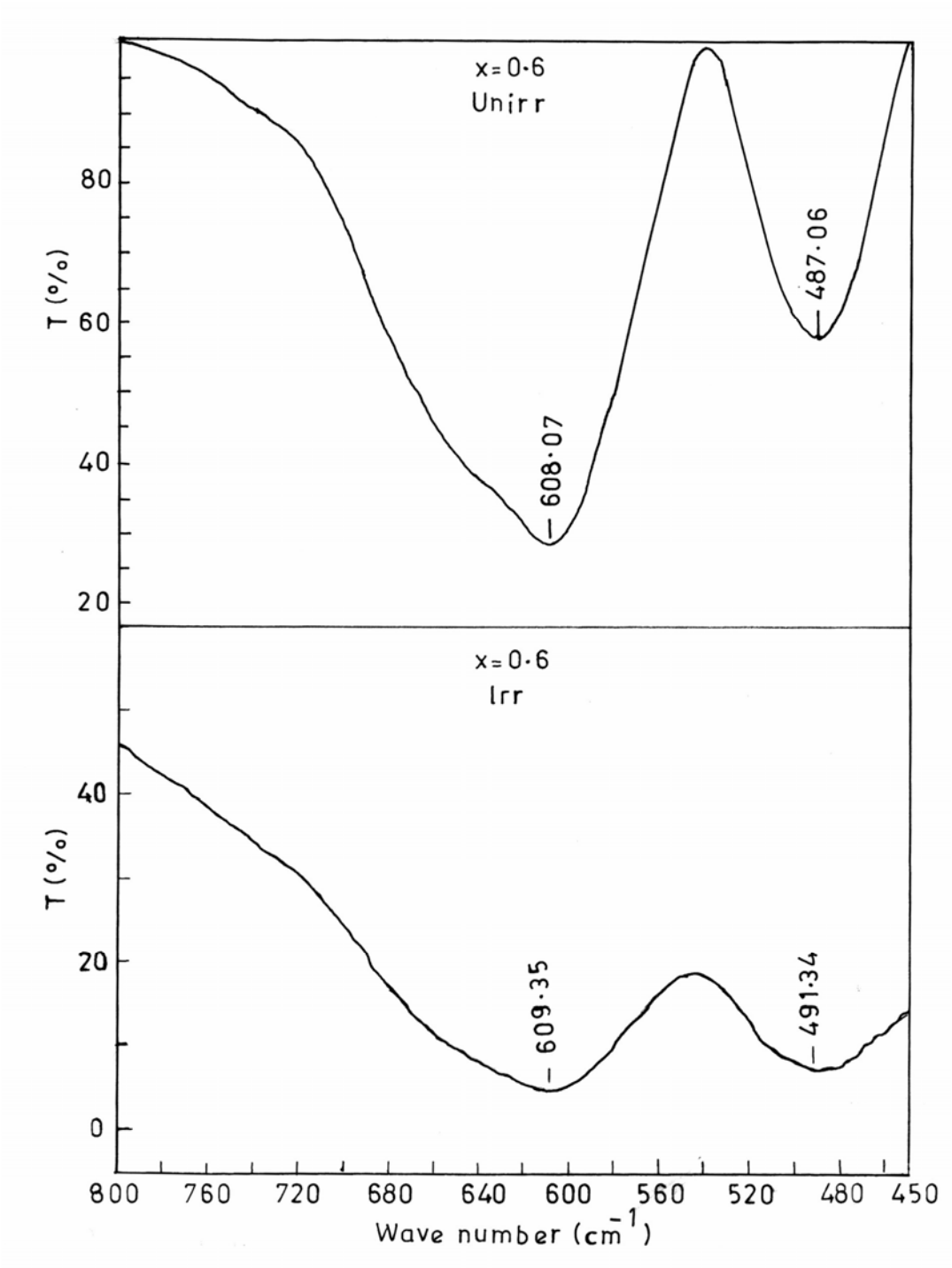

Fig. 6C.6d Infrared spectra of unirradiated and irradiated $MnAl_xCr_xFe_{2-2x}O_4$ system with x = 0.6 sample

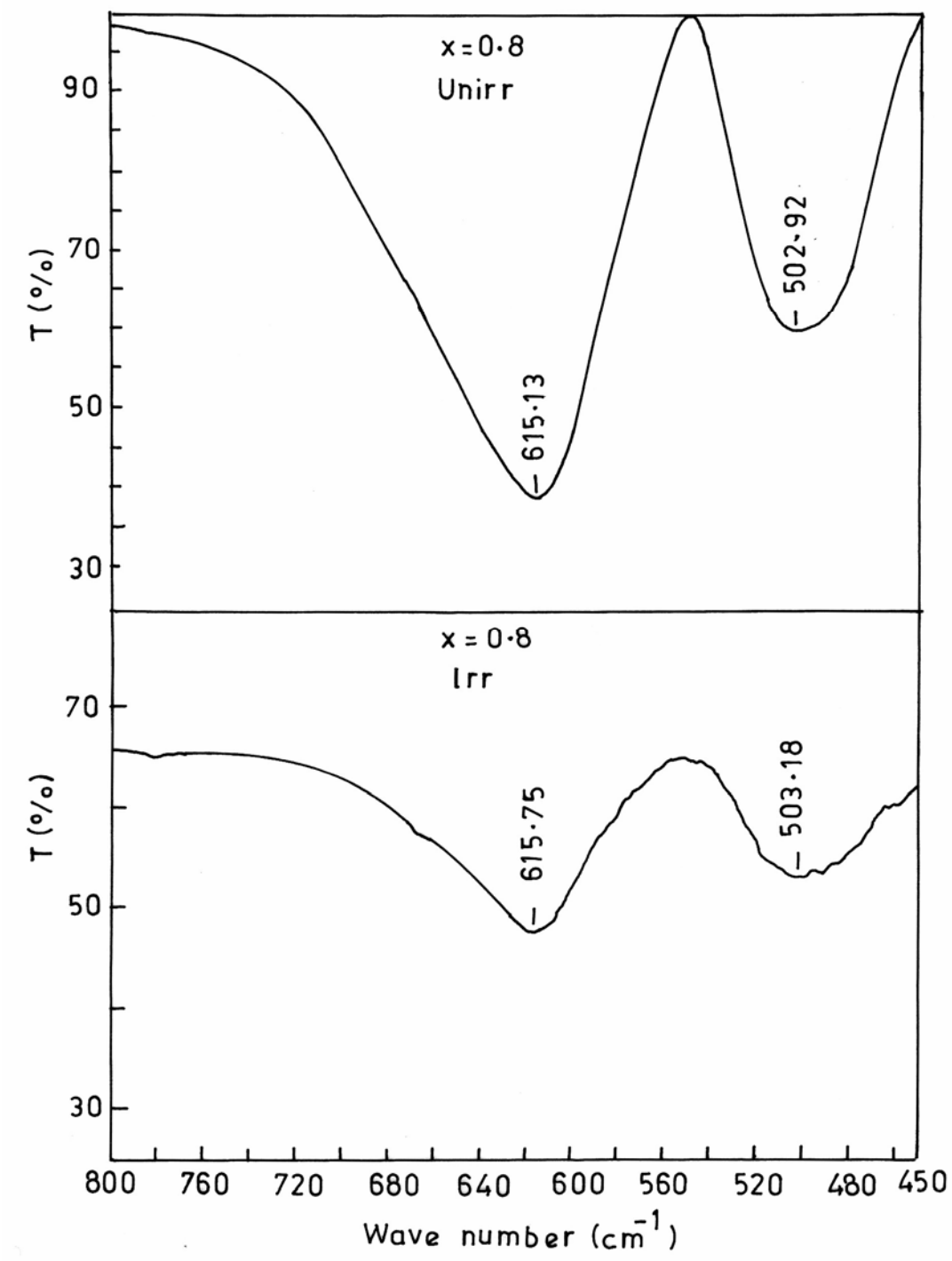

Fig. 6C.6e Infrared spectra of unirradiated and irradiated $MnAl_xCr_xFe_{2-2x}O_4$ system with x = 0.8 sample

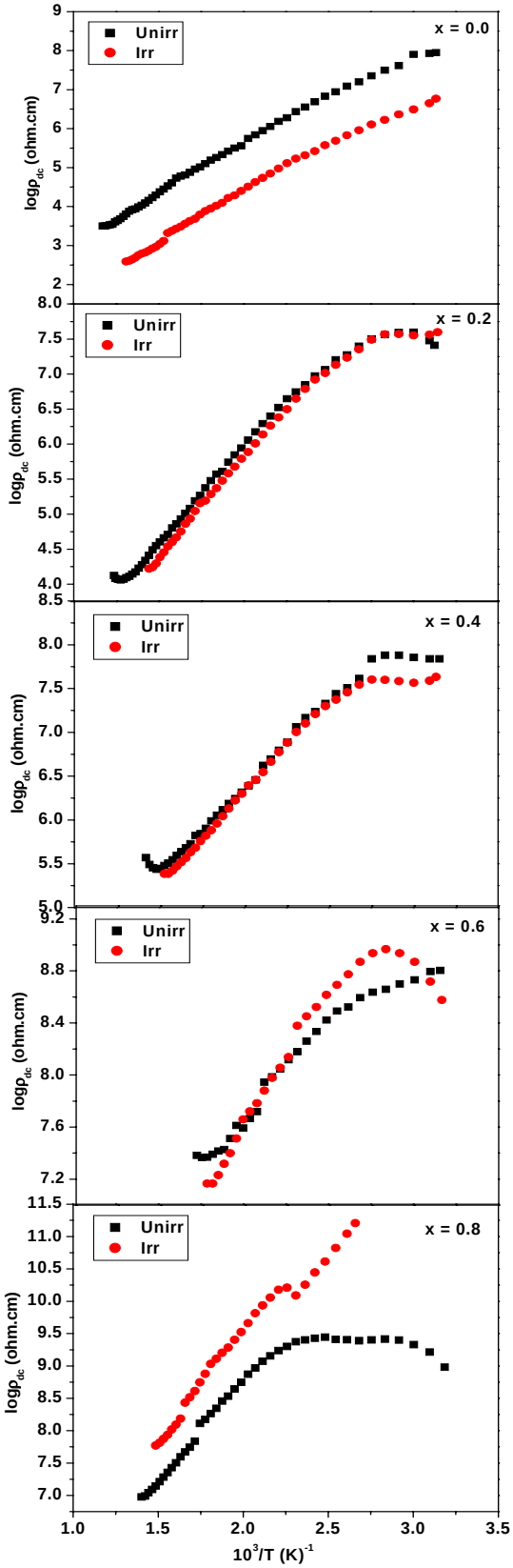

Fig. 6C.7 Electrical resistivity (ρ_{dc}) versus temperature for the compositions x = 0.0, 0.2, 0.4, 0.6 and 0.8 of unirradiated and irradiated $MnAl_xCr_xFe_{2-2x}O_4$ system

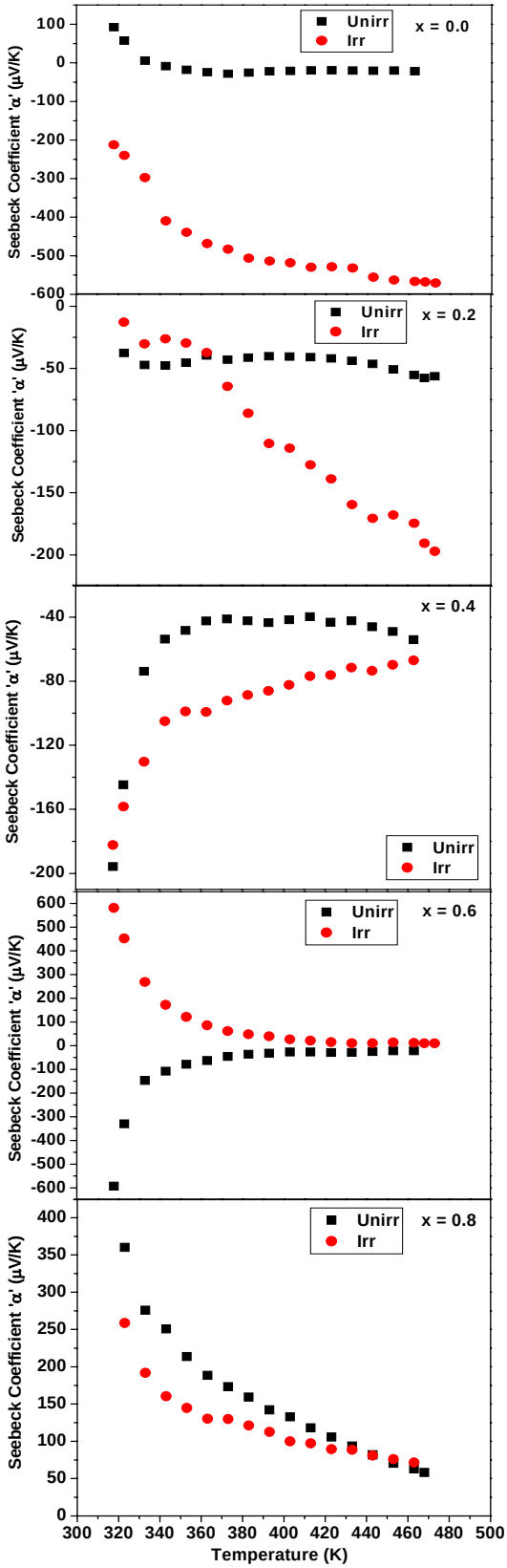

Fig. 6C.8 Thermal variation of Seebeck coefficient for the compositions x = 0.0, 0.2, 0.4, 0.6 and 0.8 of unirradiated and irradiated $MnAl_xCr_xFe_{2-2x}O_4$ system

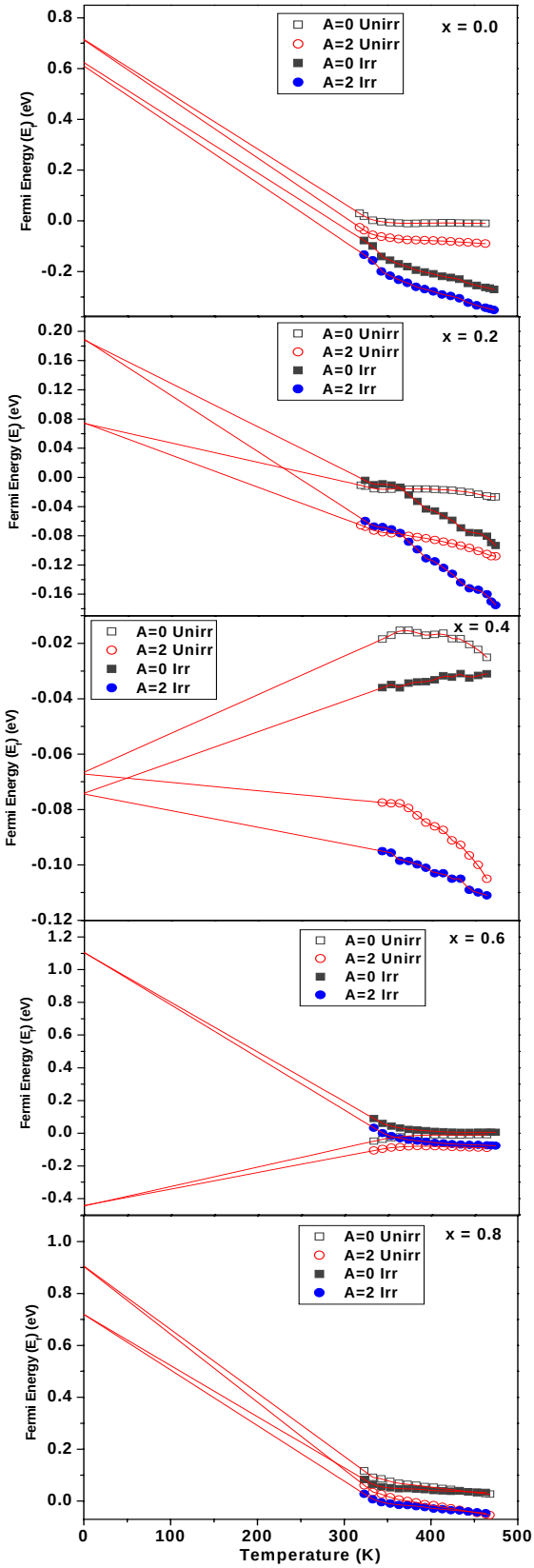

Fig. 6C.9 Temperature dependence of Fermi energy for the compositions x = 0.0, 0.2, 0.4, 0.6 and 0.8 of unirradiated and irradiated $MnAl_xCr_xFe_{2-2x}O_4$ system

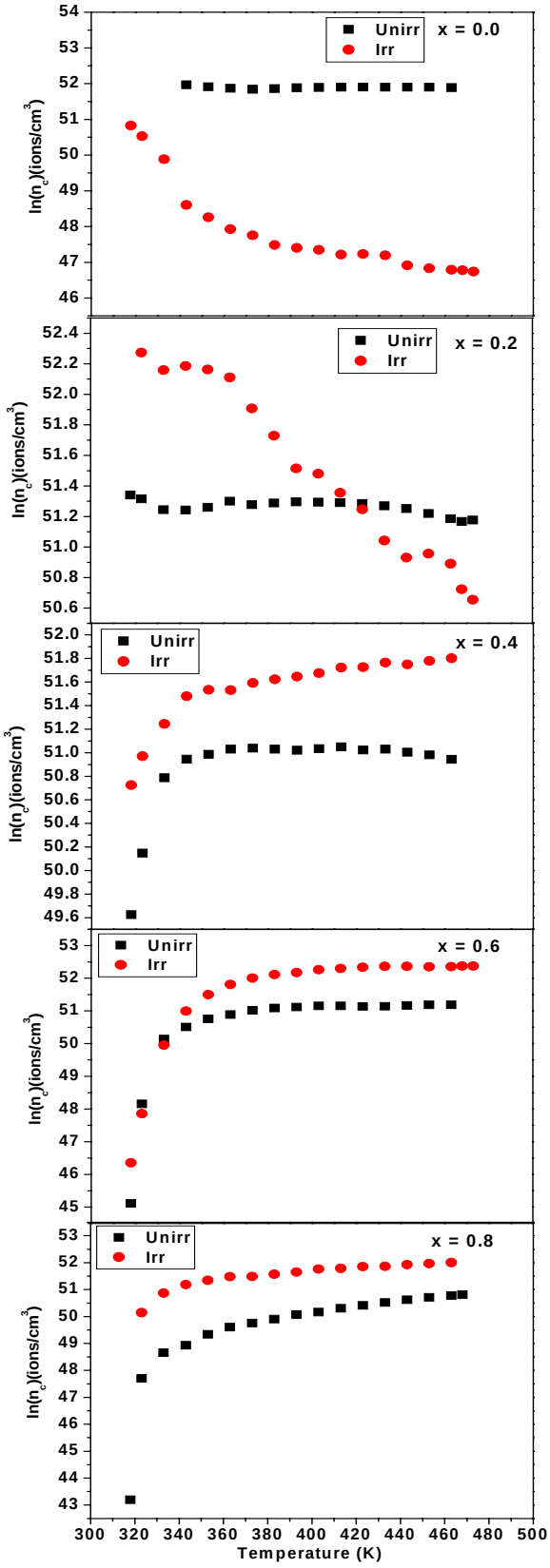

Fig. 6C.10 Variation of charge carrier concentration with temperature for the compositons x = 0.0, 0.2, 0.4, 0.6 and 0.8 of unirradiated and irradiated $MnAl_xCr_xFe_{2-2x}O_4$ system

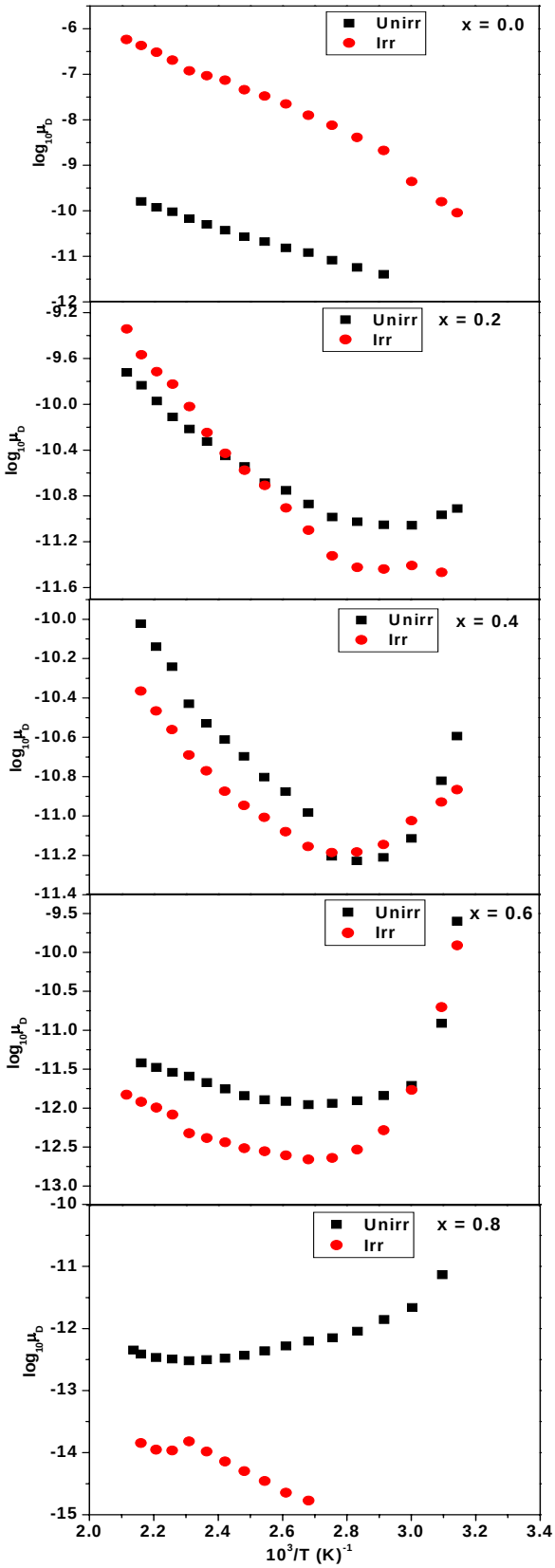

Fig. 6C.11 Thermal variation of mobility for the compositions x = 0.0, 0.2, 0.4, 0.6 and 0.8 of unirradiated and irradiated $MnAl_xCr_xFe_{2-2x}O_4$ system

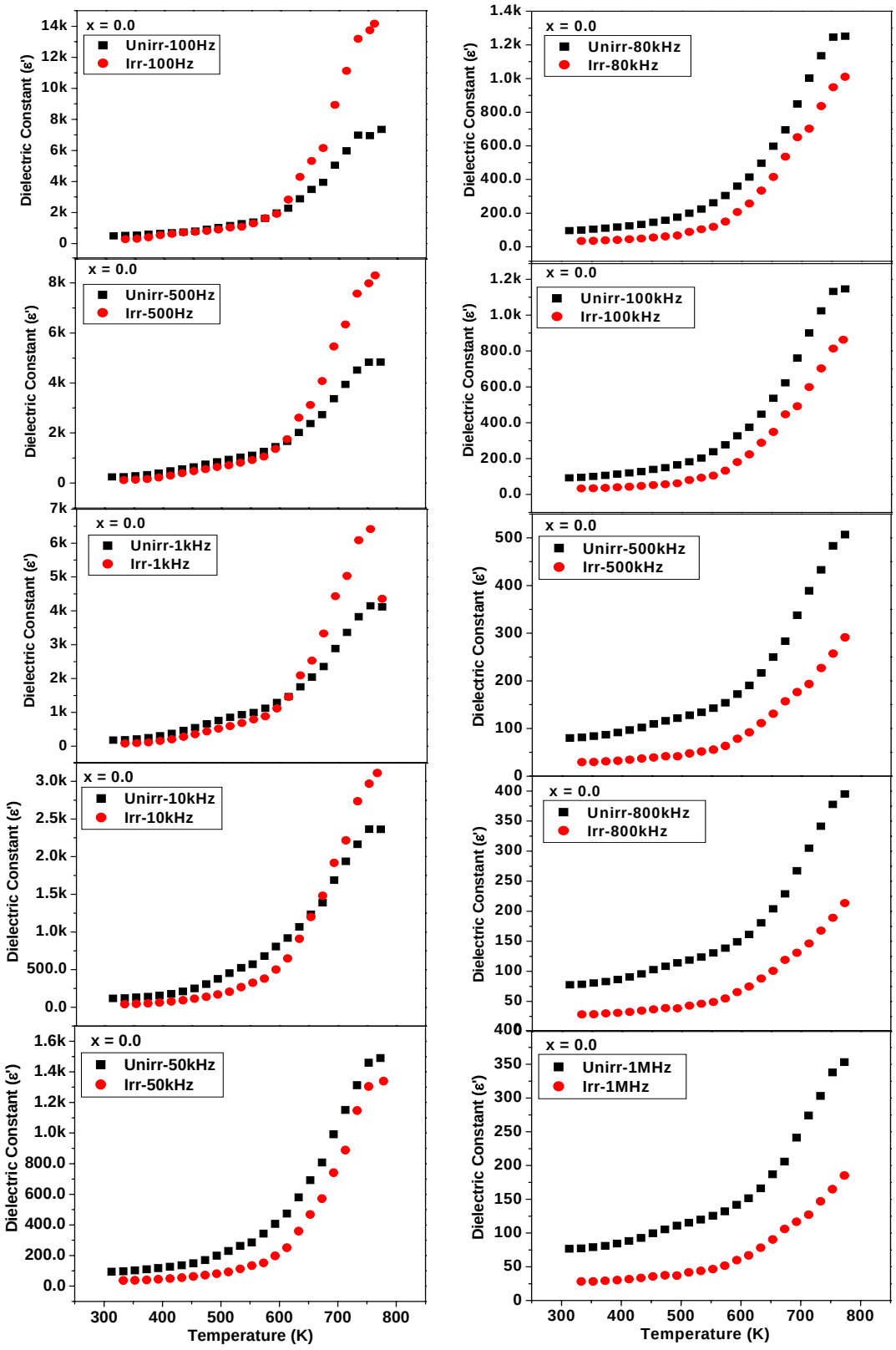

Fig. 6C.12a Thermal variation of dielectric constant (ε') at different frequencies for the composition x = 0.0 of unirradiated and irradiated $MnAl_xCr_xFe_{2-2x}O_4$ system

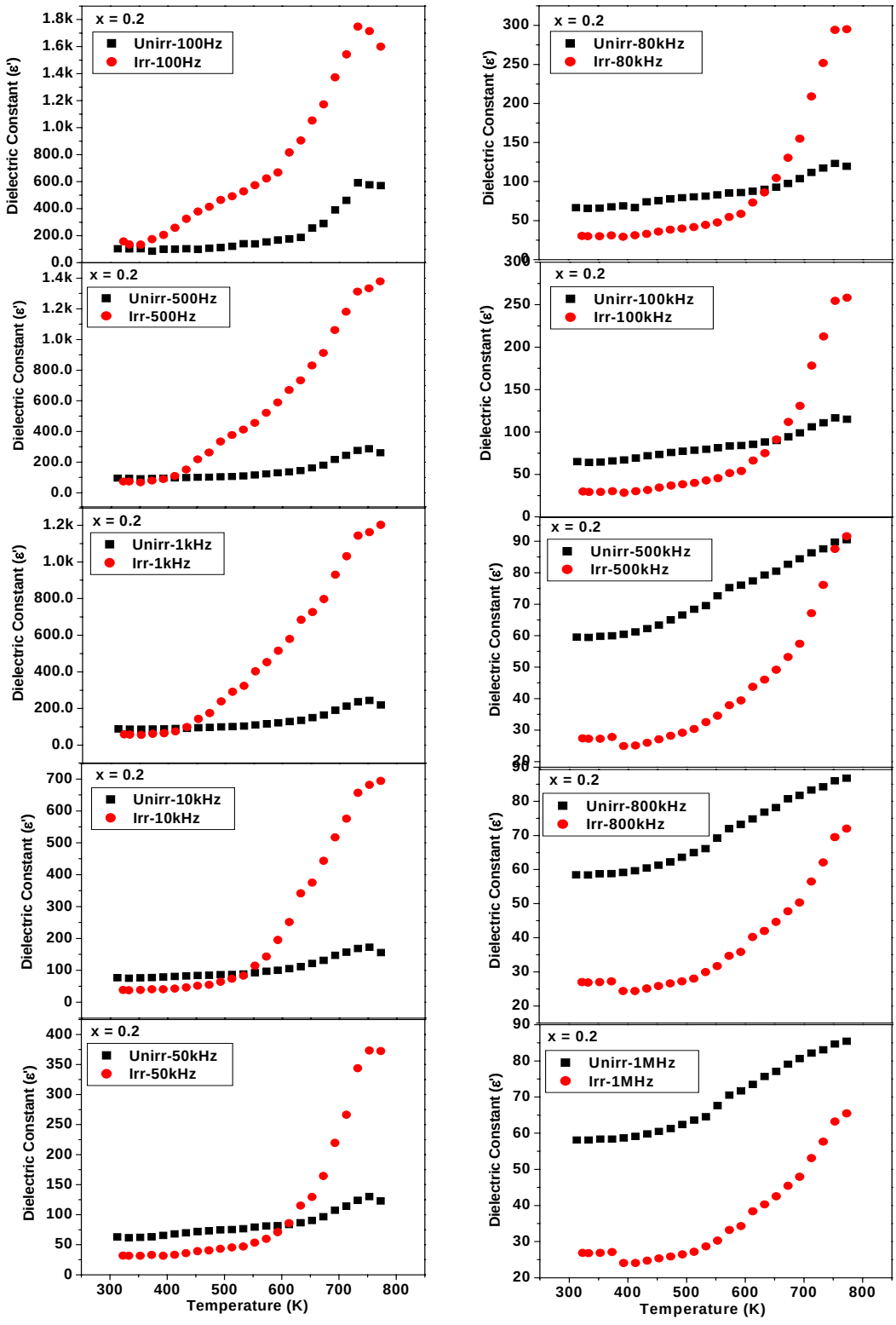

Fig. 6C.12b Thermal variation of dielectric constant (ε') at different frequencies for the composition x = 0.2 of unirradiated and irradiated $MnAl_xCr_xFe_{2-2x}O_4$ system

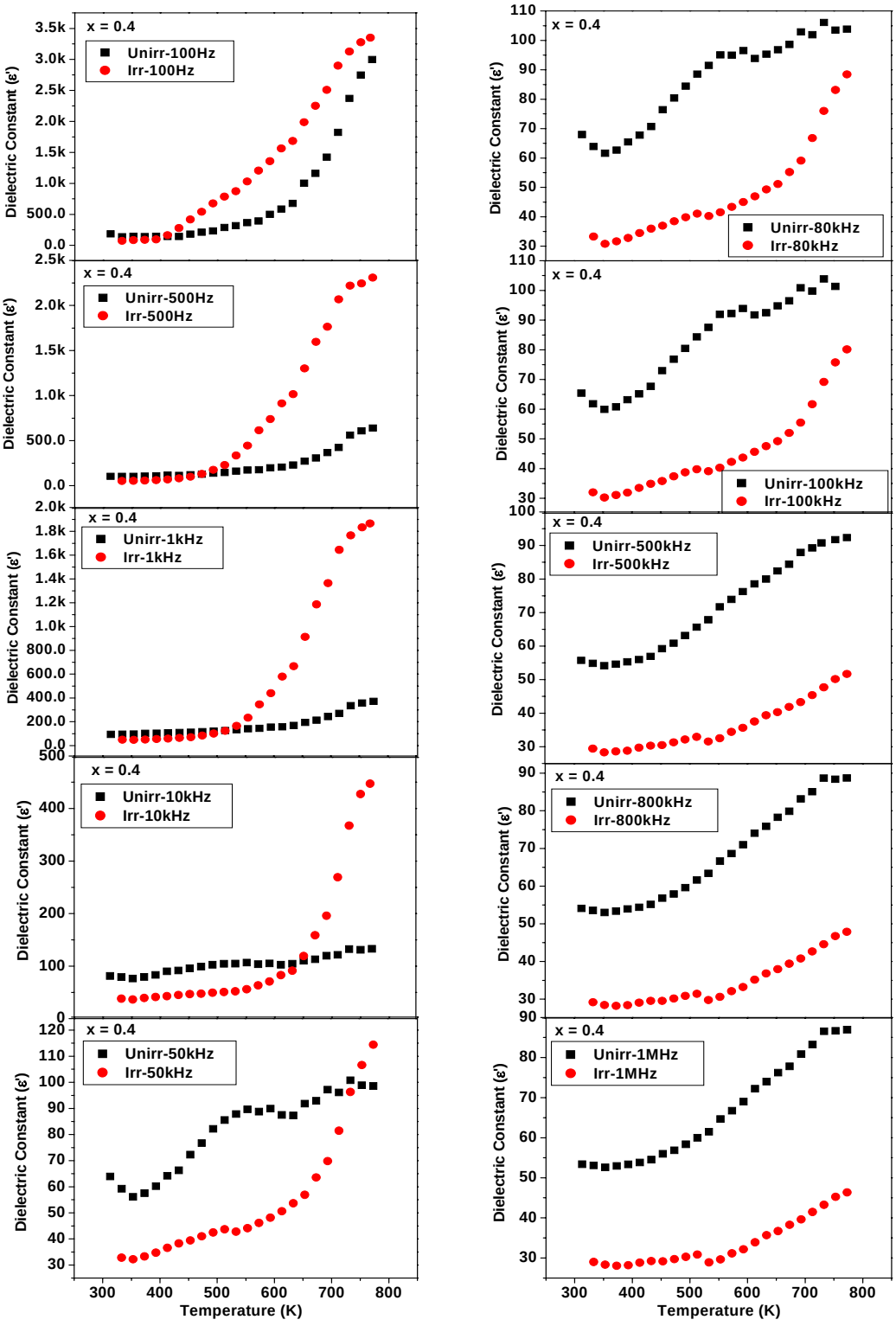

Fig. 6C.12c Thermal variation of dielectric constant (ε') at different frequencies for the composition x = 0.4 of unirradiated and irradiated $MnAl_xCr_xFe_{2-2x}O_4$ system

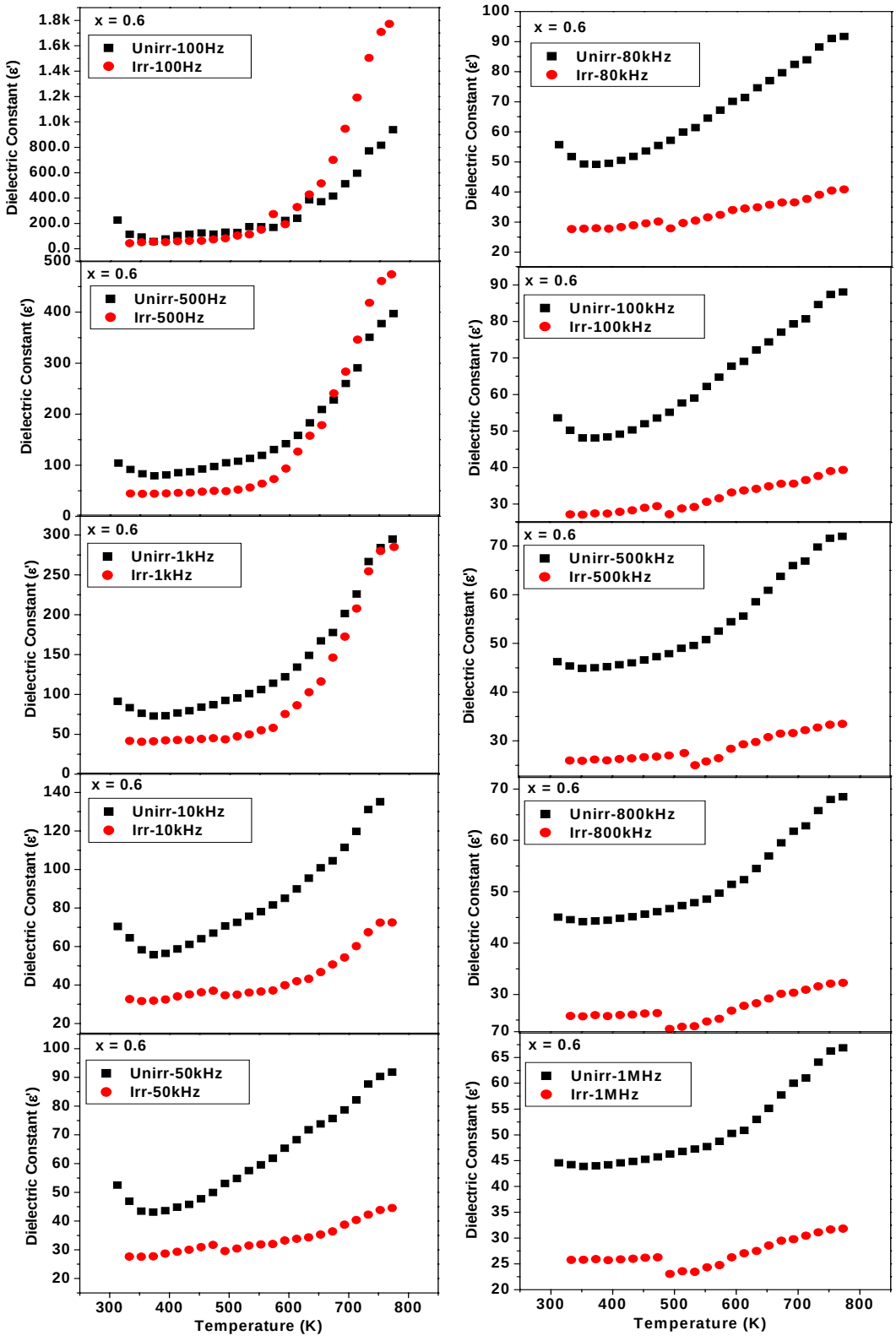

Fig. 6C.12d Thermal variation of dielectric constant (ε') at different frequencies for the composition x = 0.6 of unirradiated and irradiated $MnAl_xCr_xFe_{2-2x}O_4$ system

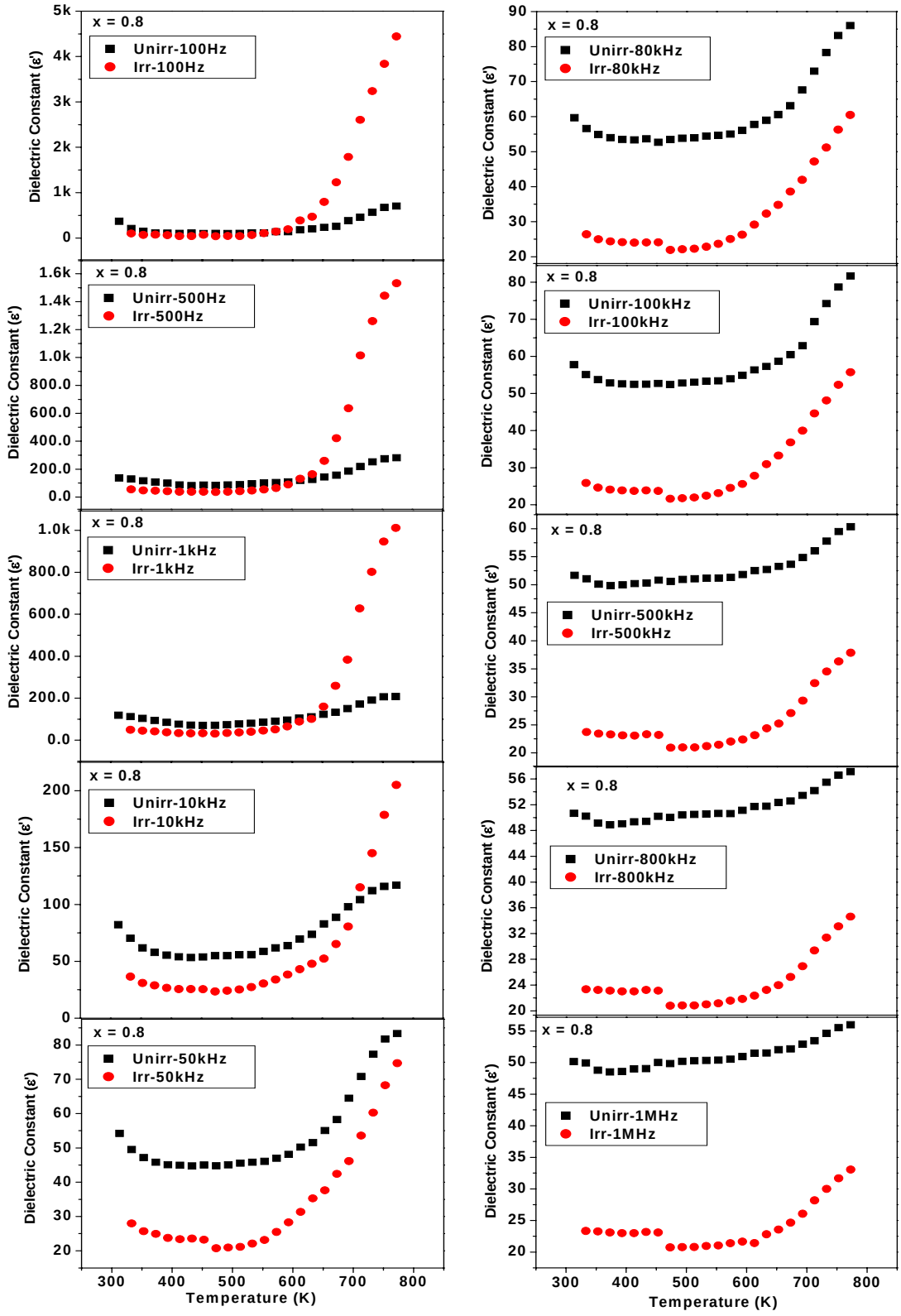

Fig.6C.12e Thermal variation of dielectric constant (ε') at different frequencies for the composition x = 0.8 of unirradiated and irradiated $MnAl_xCr_xFe_{2-2x}O_4$ system

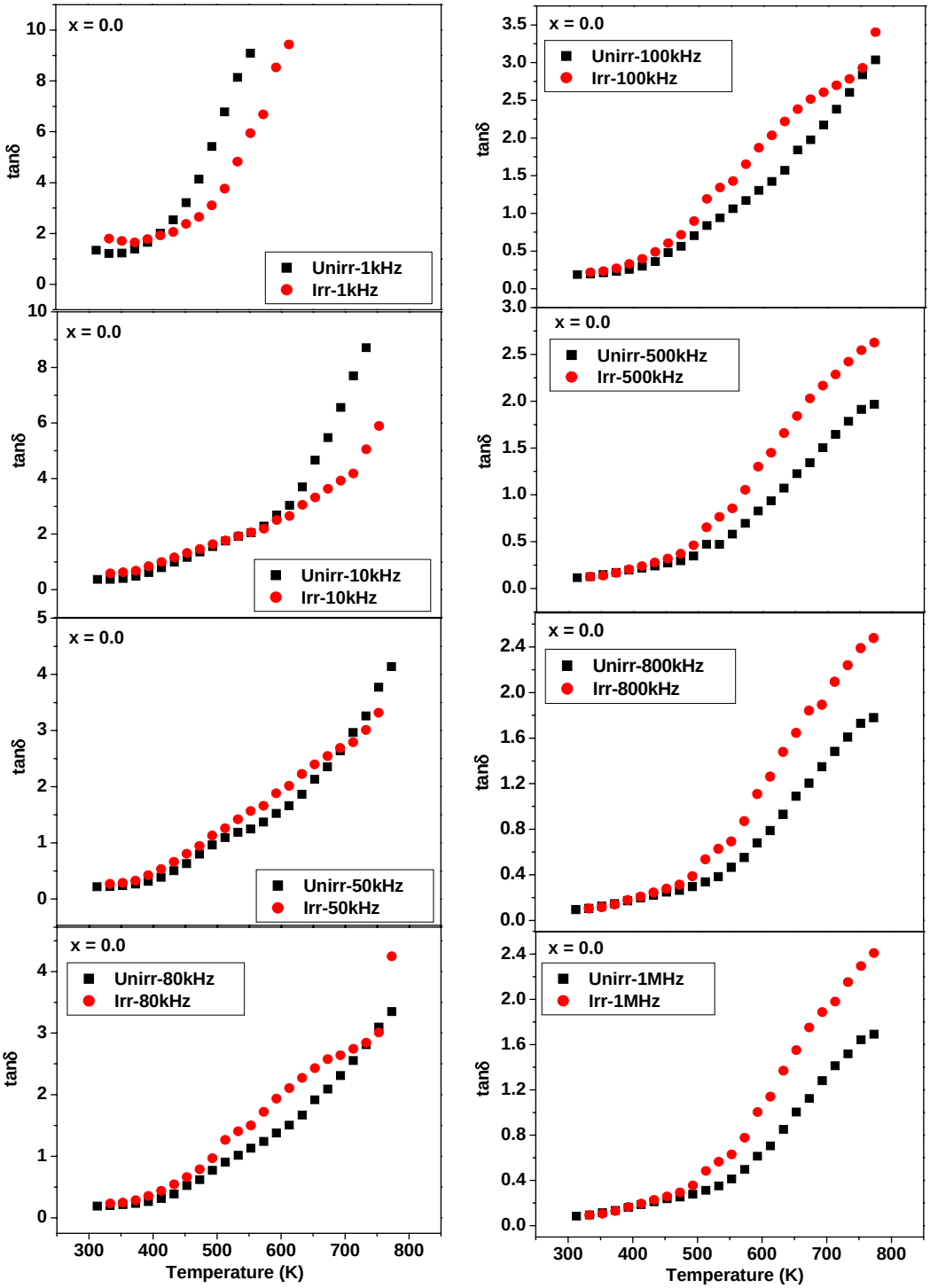

Fig. 6C.13a Thermal variation of dielectric loss tangent (tanδ) at different frequencies for the composition x = 0.0 of unirradiated and irradiated $MnAl_xCr_xFe_{2-2x}O_4$ system

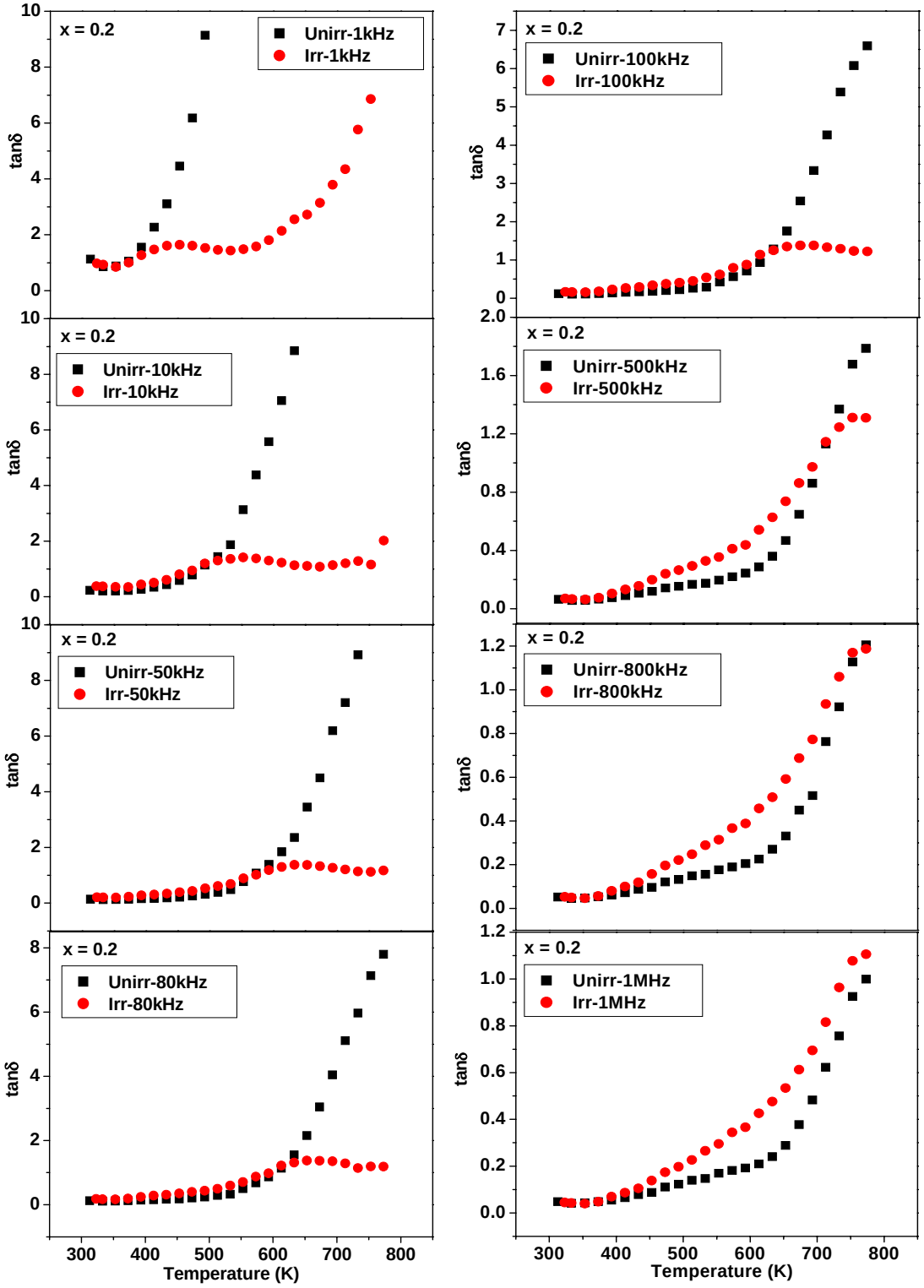

Fig. 6C.13b Thermal variation of dielectric loss tangent (tanδ) at different frequencies for the composition x = 0.2 of unirradiated and irradiated $MnAl_xCr_xFe_{2-2x}O_4$ system

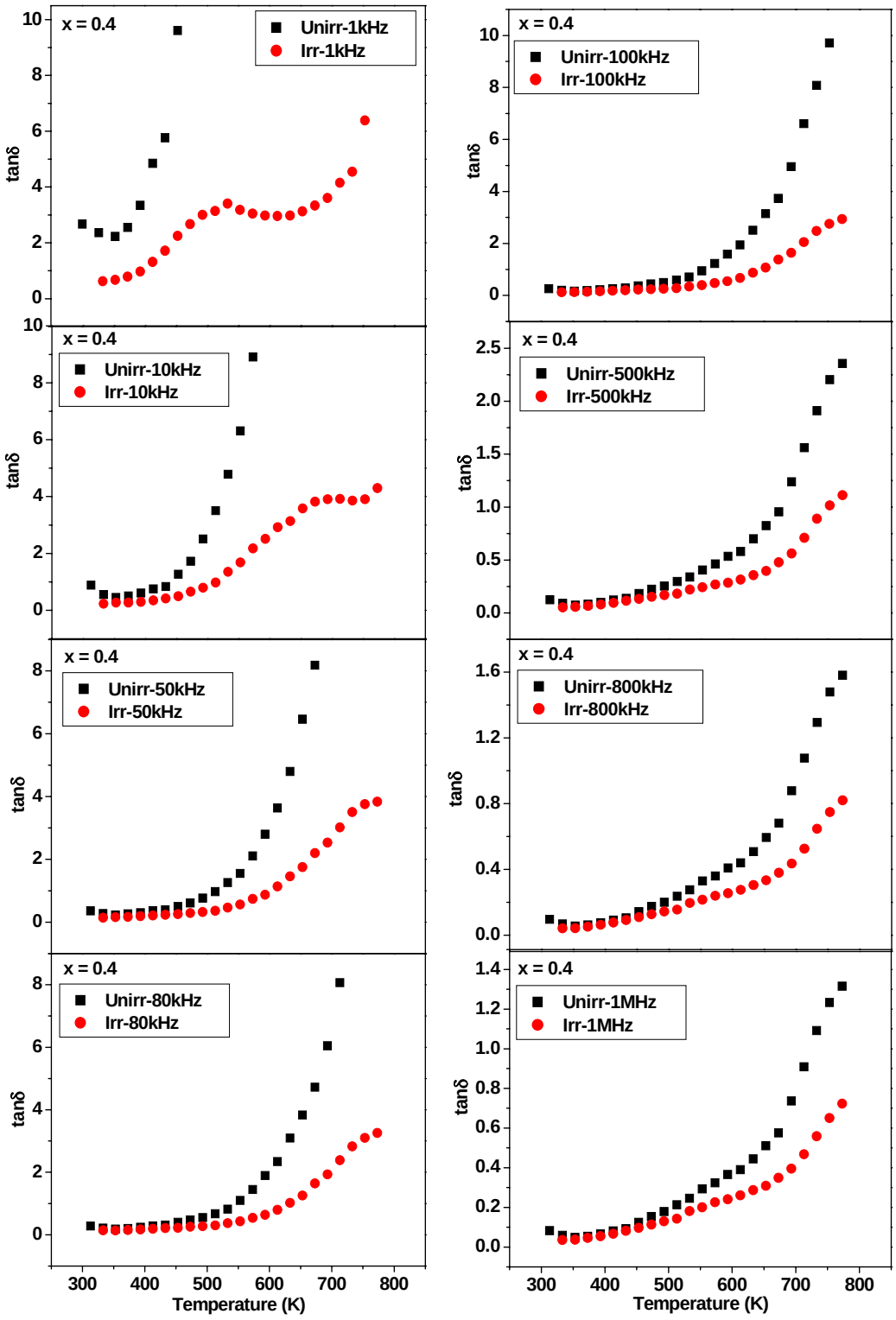

Fig. 6C.13c Thermal variation of dielectric loss tangent (tanδ) at different frequencies for the composition x = 0.4 of unirradiated and irradiated $MnAl_xCr_xFe_{2-2x}O_4$ system

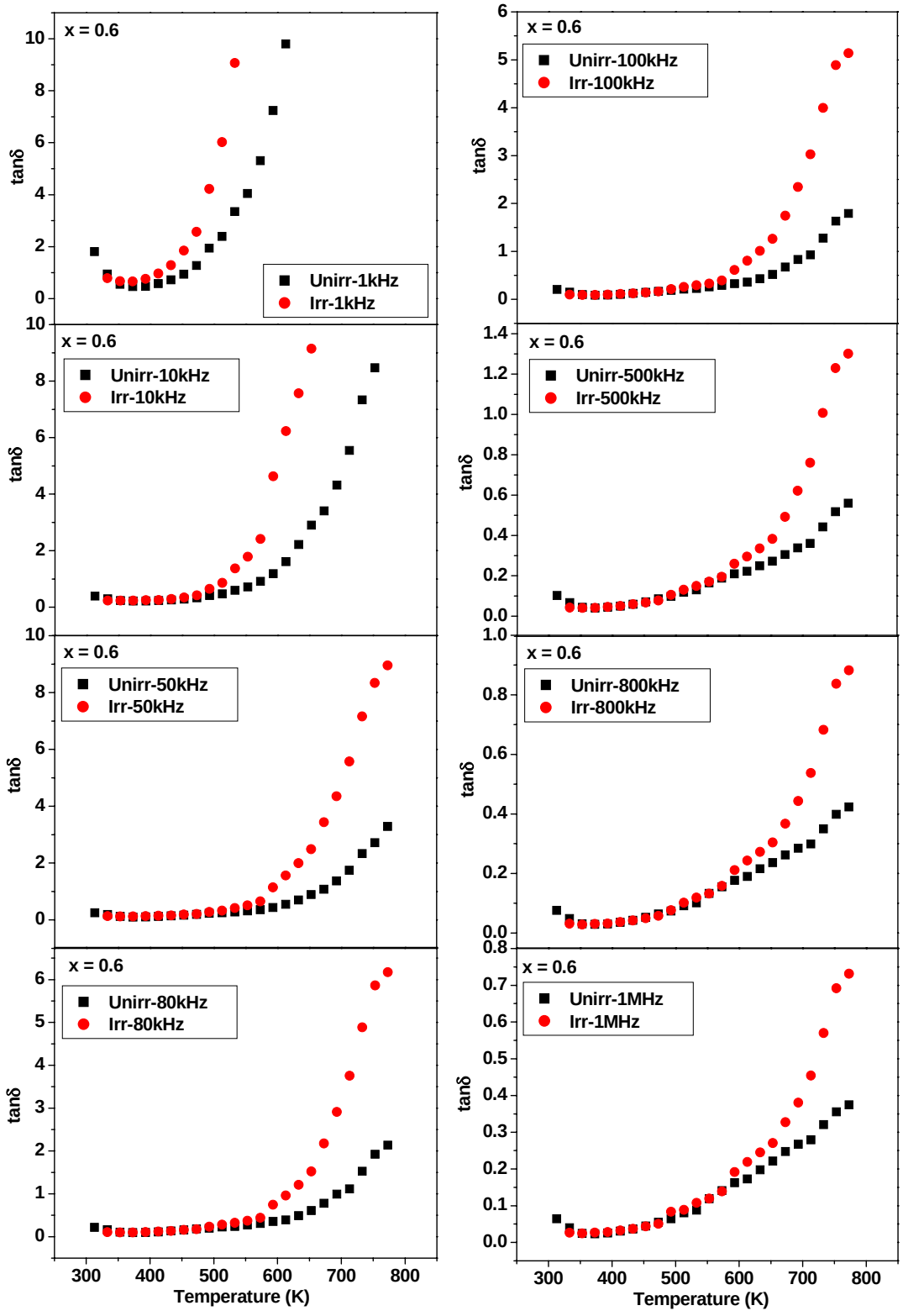

Fig. 6C.13d Thermal variation of dielectric loss tangent (tanδ) at different frequencies for the composition x = 0.6 of unirradiated and irradiated $MnAl_xCr_xFe_{2-2x}O_4$ system

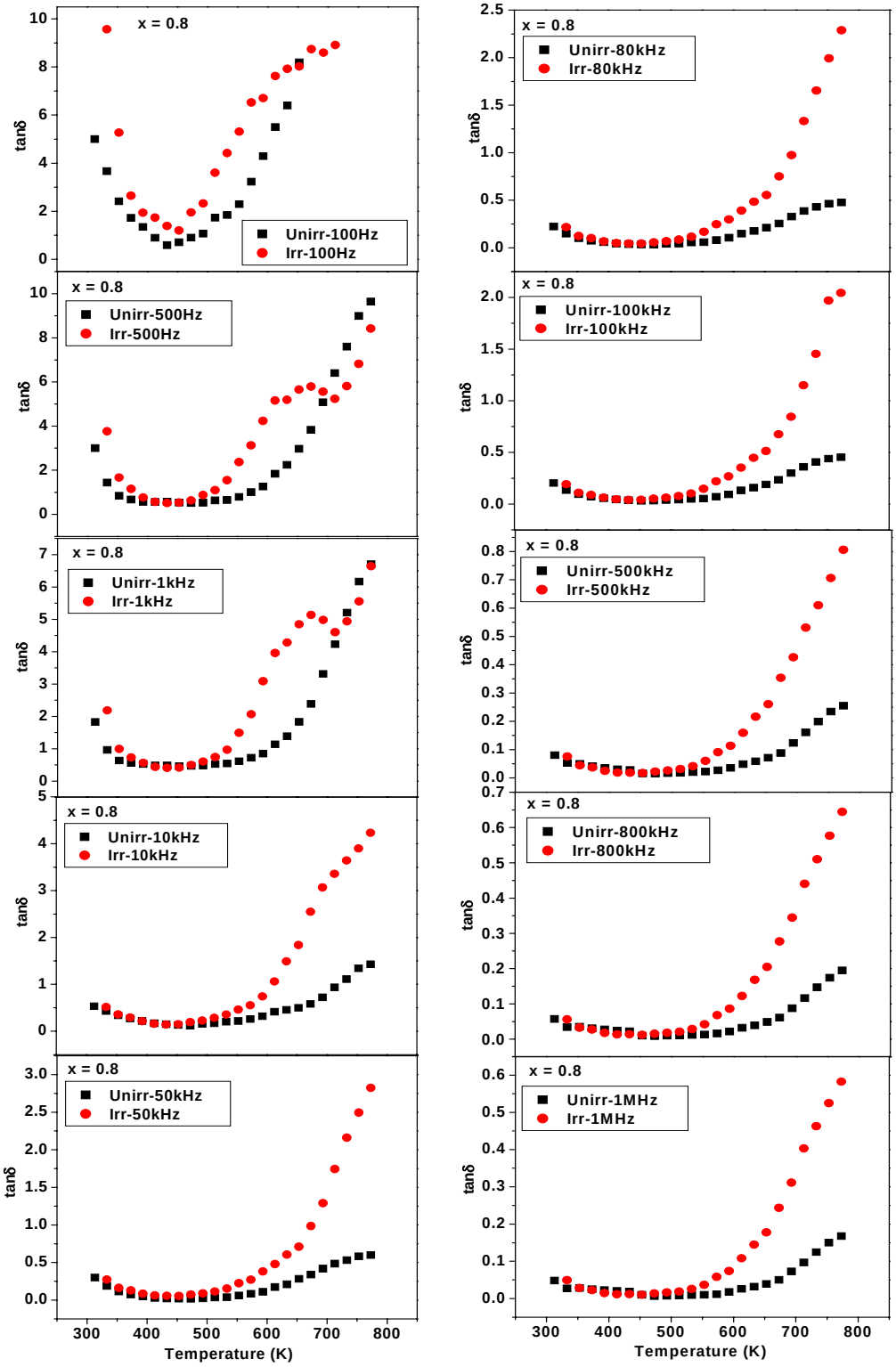

Fig. 6C.13e Thermal variation of dielectric loss tangent (tanδ) at different frequencies for the composition x = 0.8 of unirradiated and irradiated $MnAl_xCr_xFe_{2-2x}O_4$ system

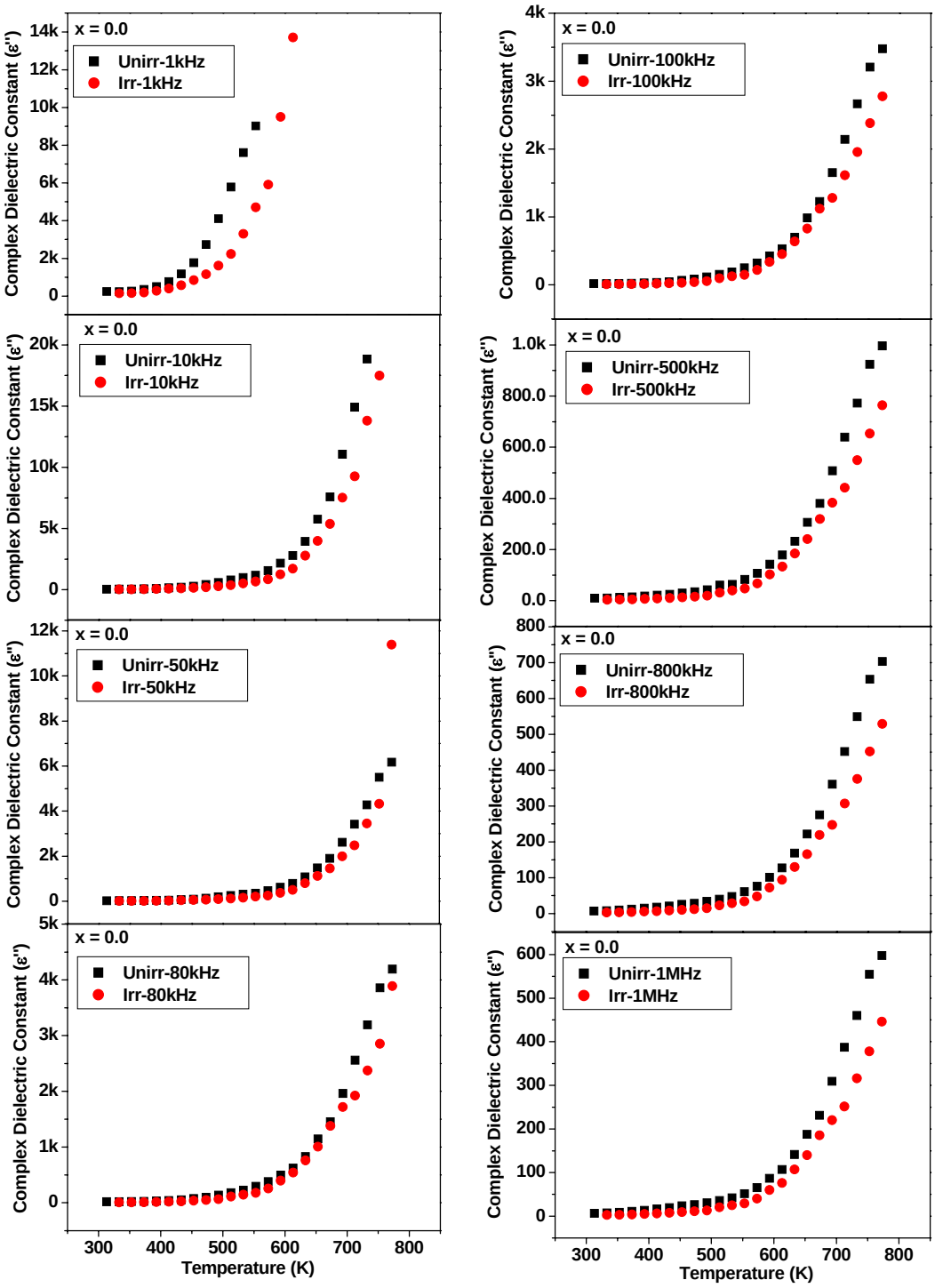

Fig. 6C.14a Thermal variation of Complex Dielectric Constant (ε'') at different frequencies for the composition x = 0.0 of unirradiated and irradiated $MnAl_xCr_xFe_{2-2x}O_4$ system

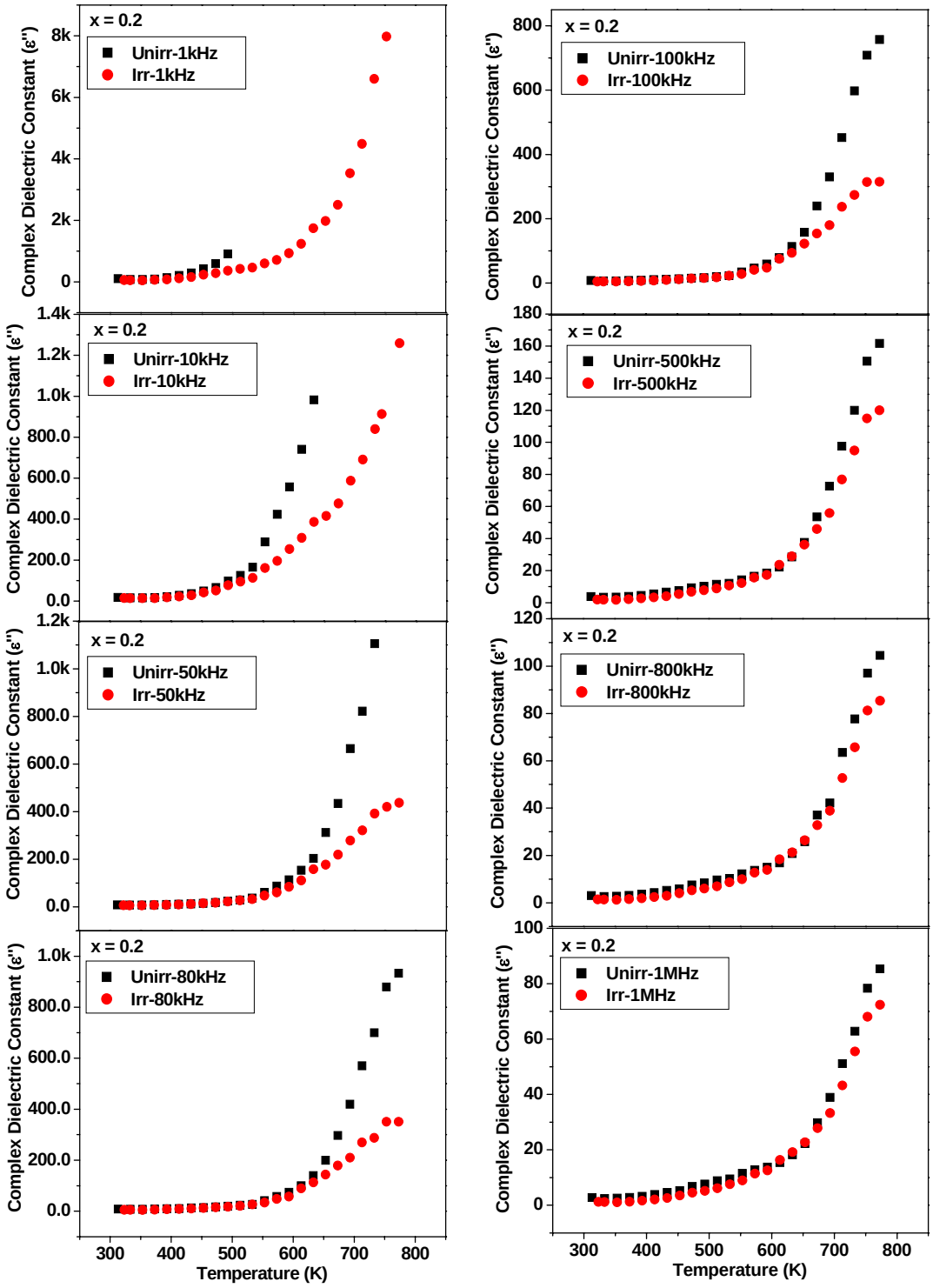

Fig. 6C.14b Thermal variation of Complex Dielectric Constant (ε'') at different frequencies for the composition x = 0.2 of unirradiated and irradiated $MnAl_xCr_xFe_{2-2x}O_4$ system

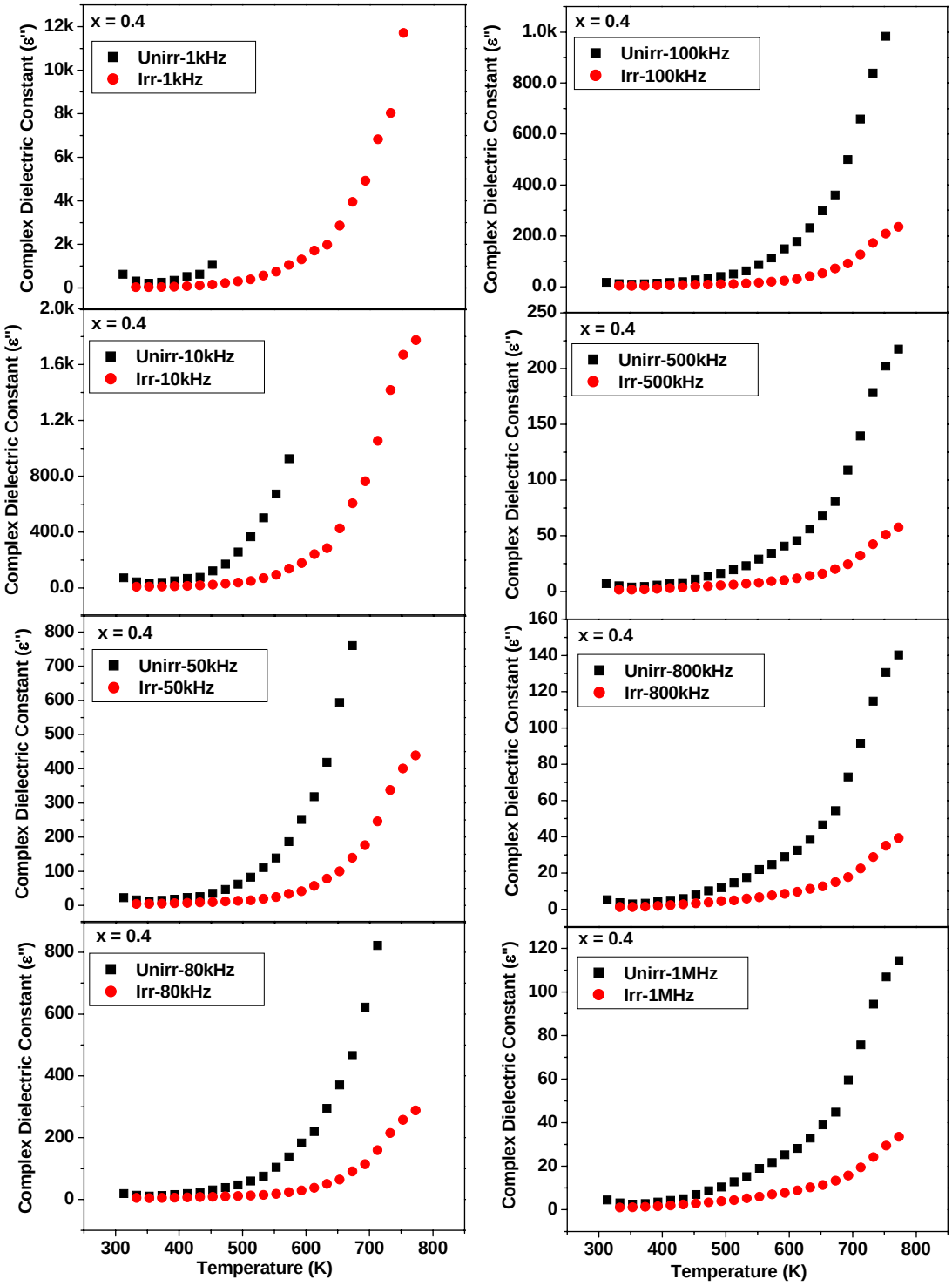

Fig. 6C.14c Thermal variation of Complex Dielectric Constant (ε'') at different frequencies for the composition x = 0.4 of unirradiated and irradiated $MnAl_xCr_xFe_{2-2x}O_4$ system

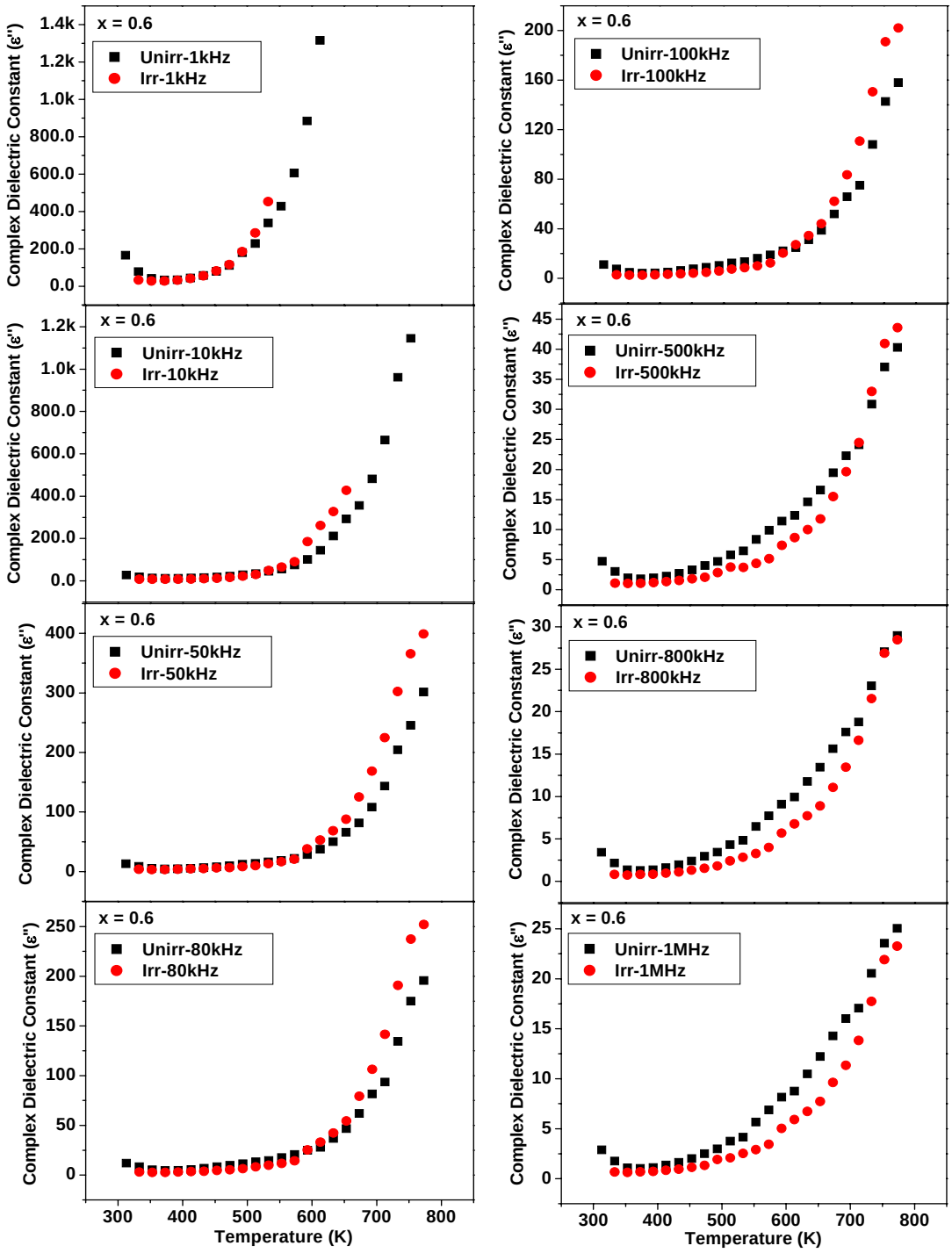

Fig. 6C.14d Thermal variation of Complex Dielectric Constant (ε'') at different frequencies for the composition x = 0.6 of unirradiated and irradiated $MnAl_xCr_xFe_{2-2x}O_4$ system

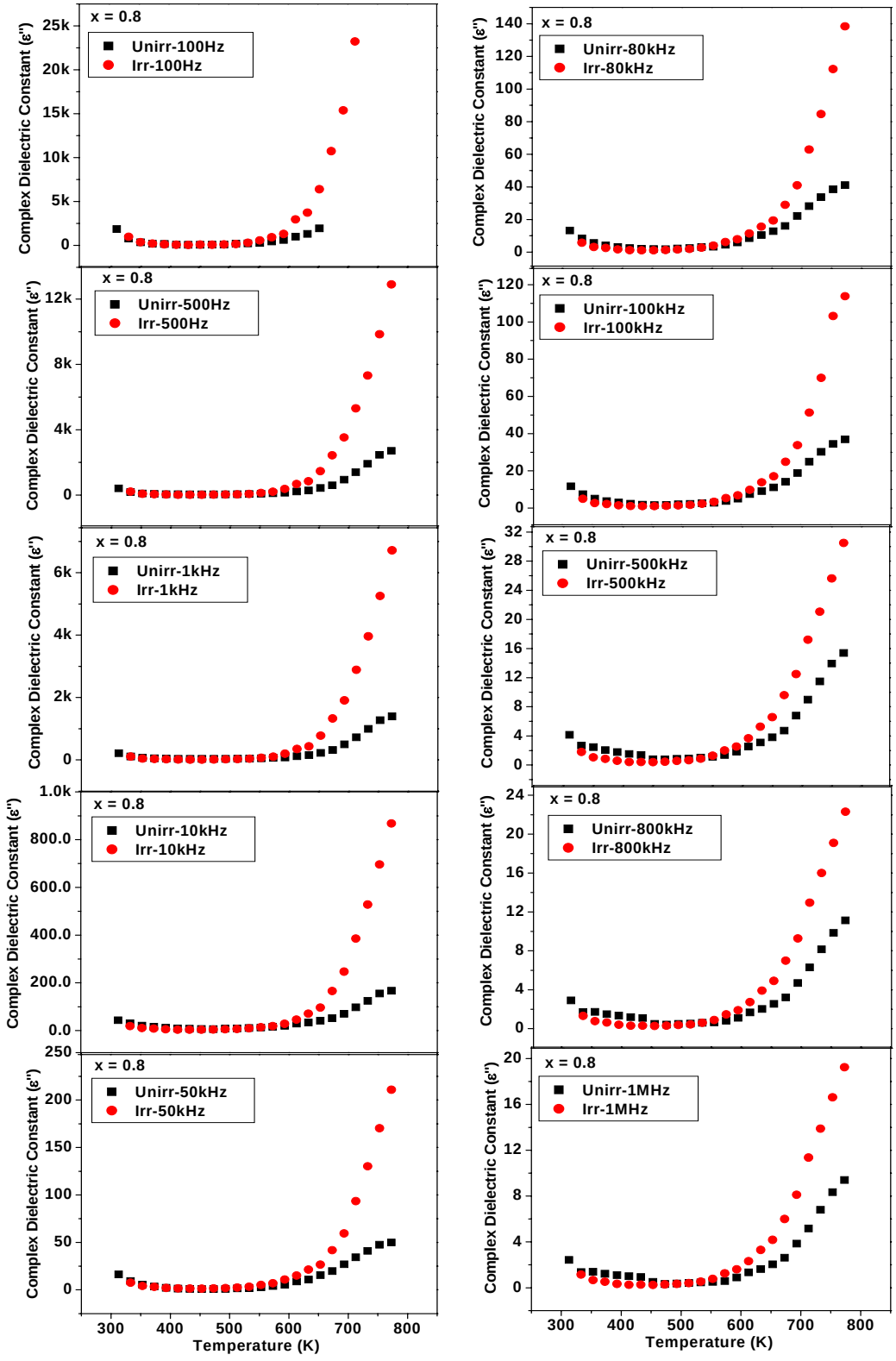

Fig. 6C.14e Thermal variation of Complex Dielectric Constant (ε'') at different frequencies for the composition x = 0.8 of unirradiated and irradiated $MnAl_xCr_xFe_{2-2x}O_4$ system

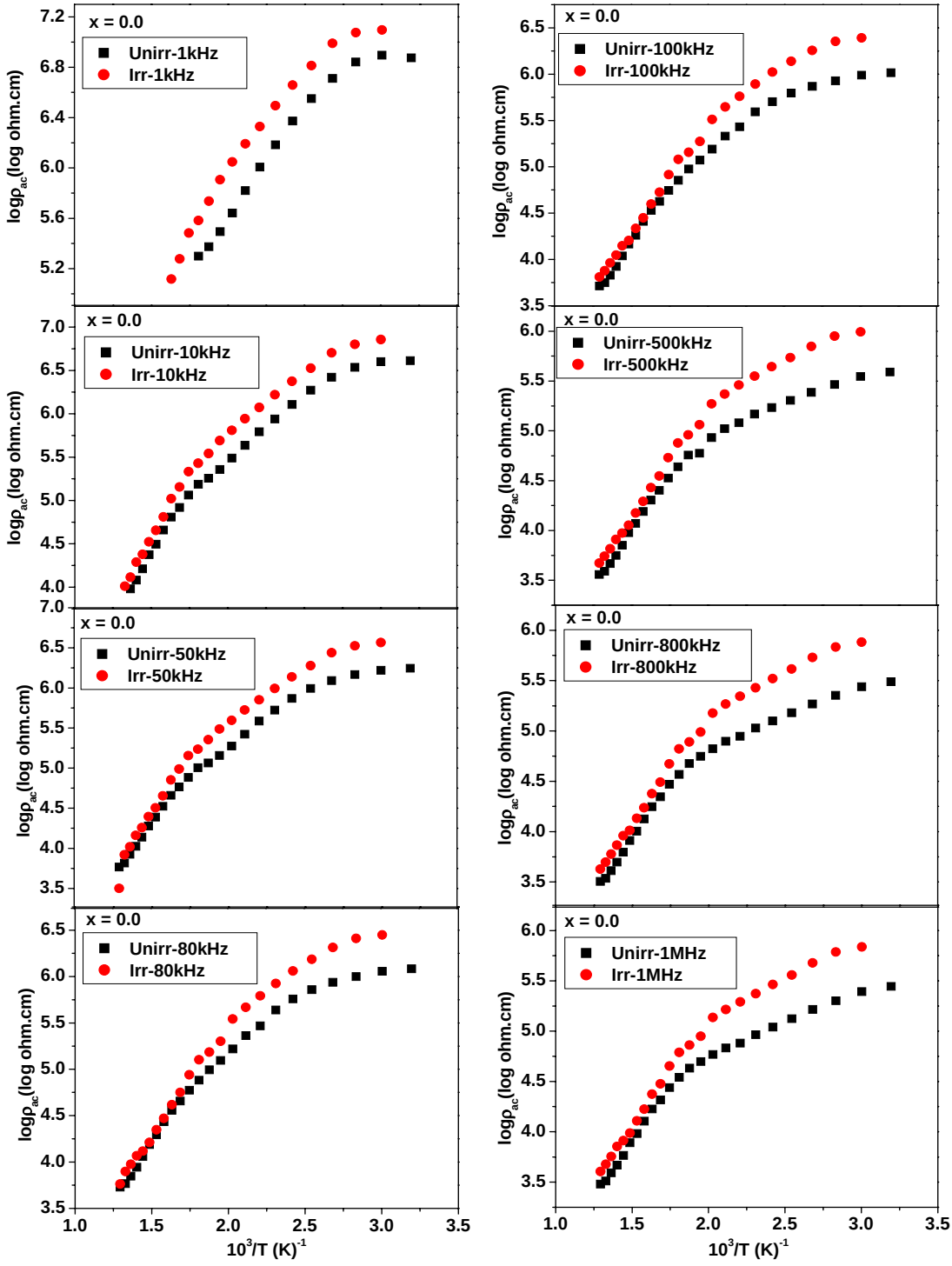

Fig. 6C.15a Thermal variation of a.c. resistivity (ρ_{ac}) at different frequencies for the composition x = 0.0 of unirradiated and irradiated $MnAl_xCr_xFe_{2-2x}O_4$ system

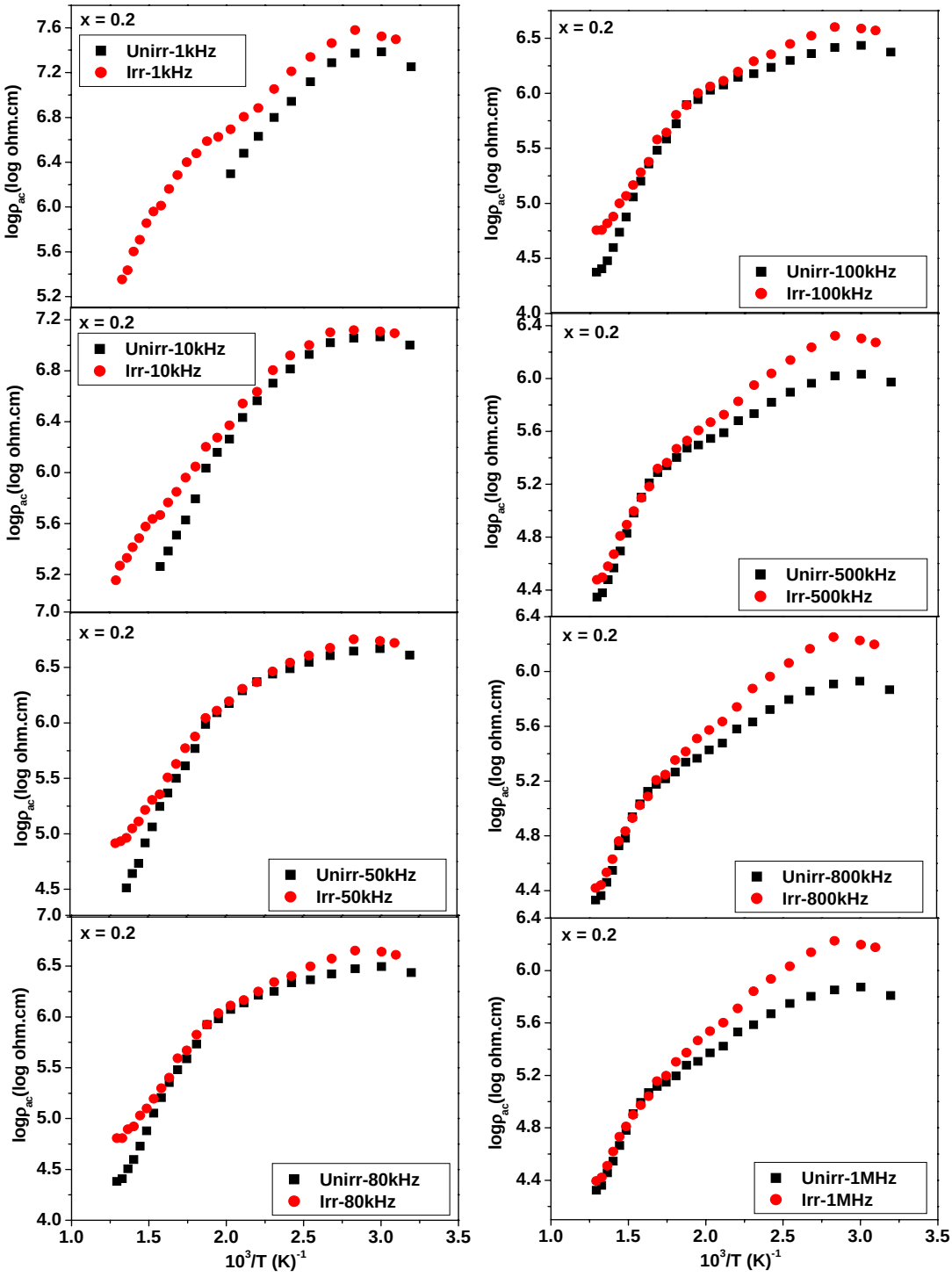

Fig. 6C.15b Thermal variation of a.c. resistivity (ρ_{ac}) at different frequencies for the composition x = 0.2 of unirradiated and irradiated $MnAl_xCr_xFe_{2-2x}O_4$ system

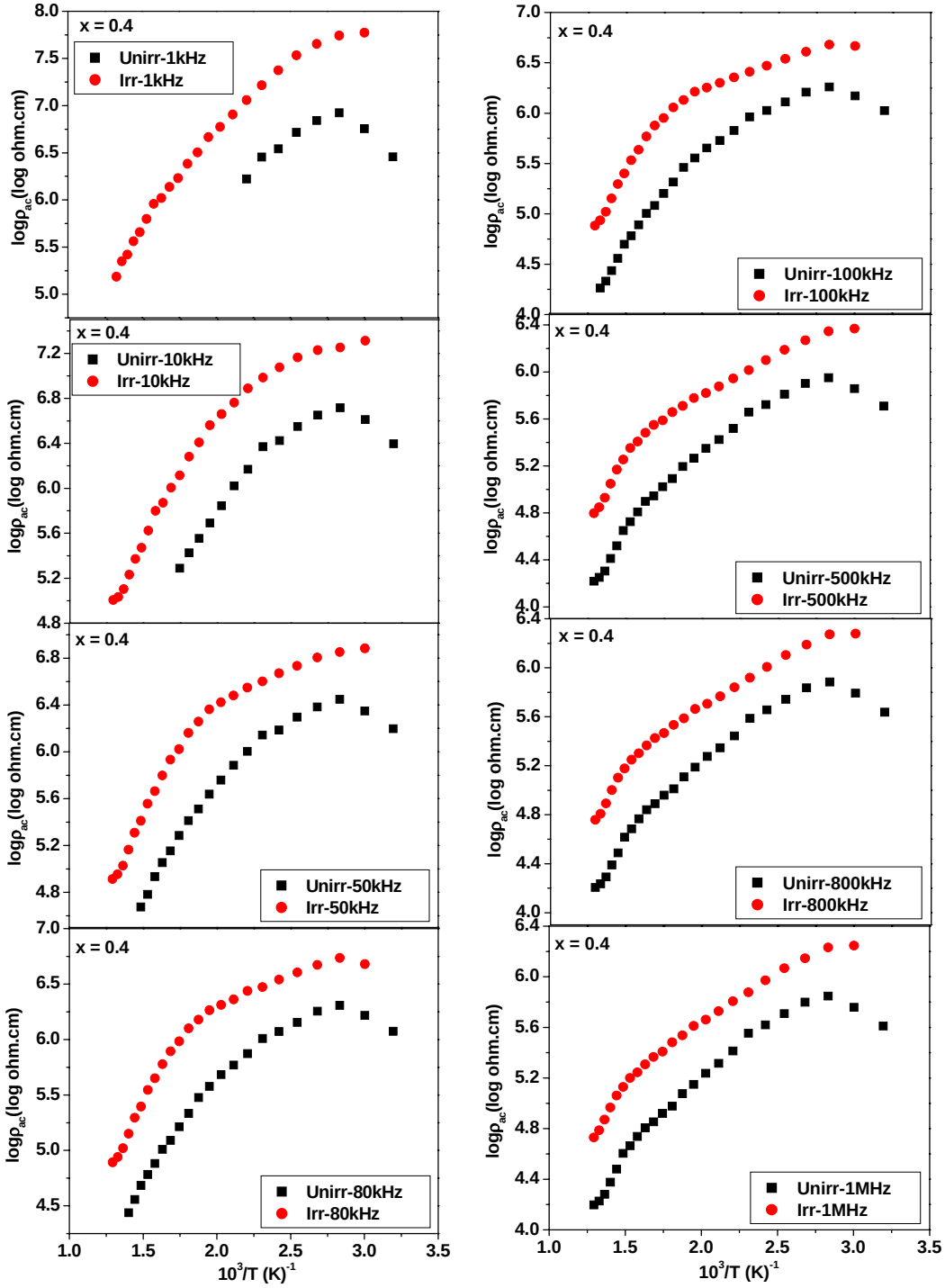

Fig. 6C.15c Thermal variation of a.c. resistivity (ρ_{ac}) at different frequencies for the composition x = 0.4 of unirradiated and irradiated $MnAl_xCr_xFe_{2-2x}O_4$ system

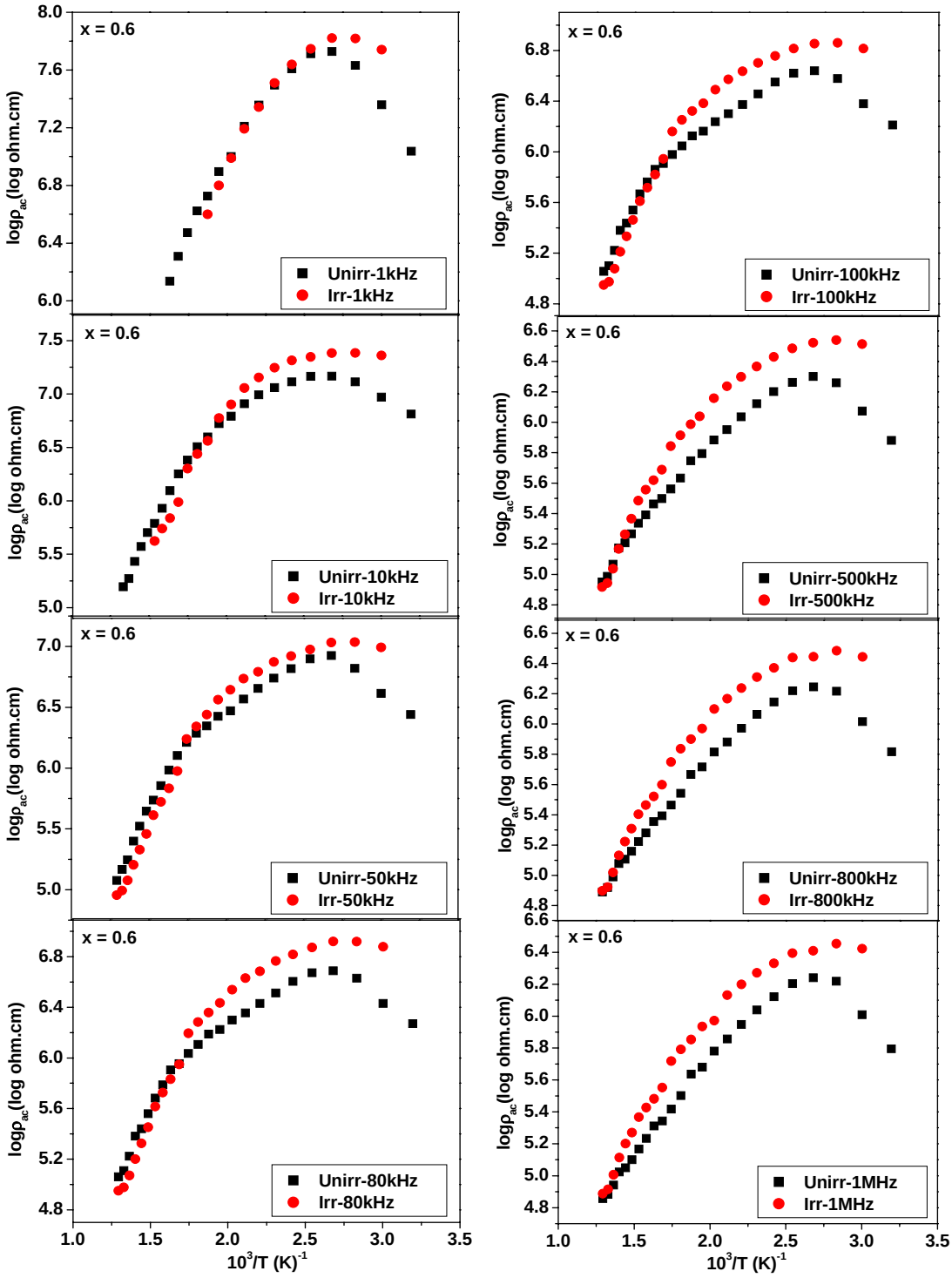

Fig. 6C.15d Thermal variation of a.c. resistivity (ρ_{ac}) at different frequencies for the composition x = 0.6 of unirradiated and irradiated $MnAl_xCr_xFe_{2-2x}O_4$ system

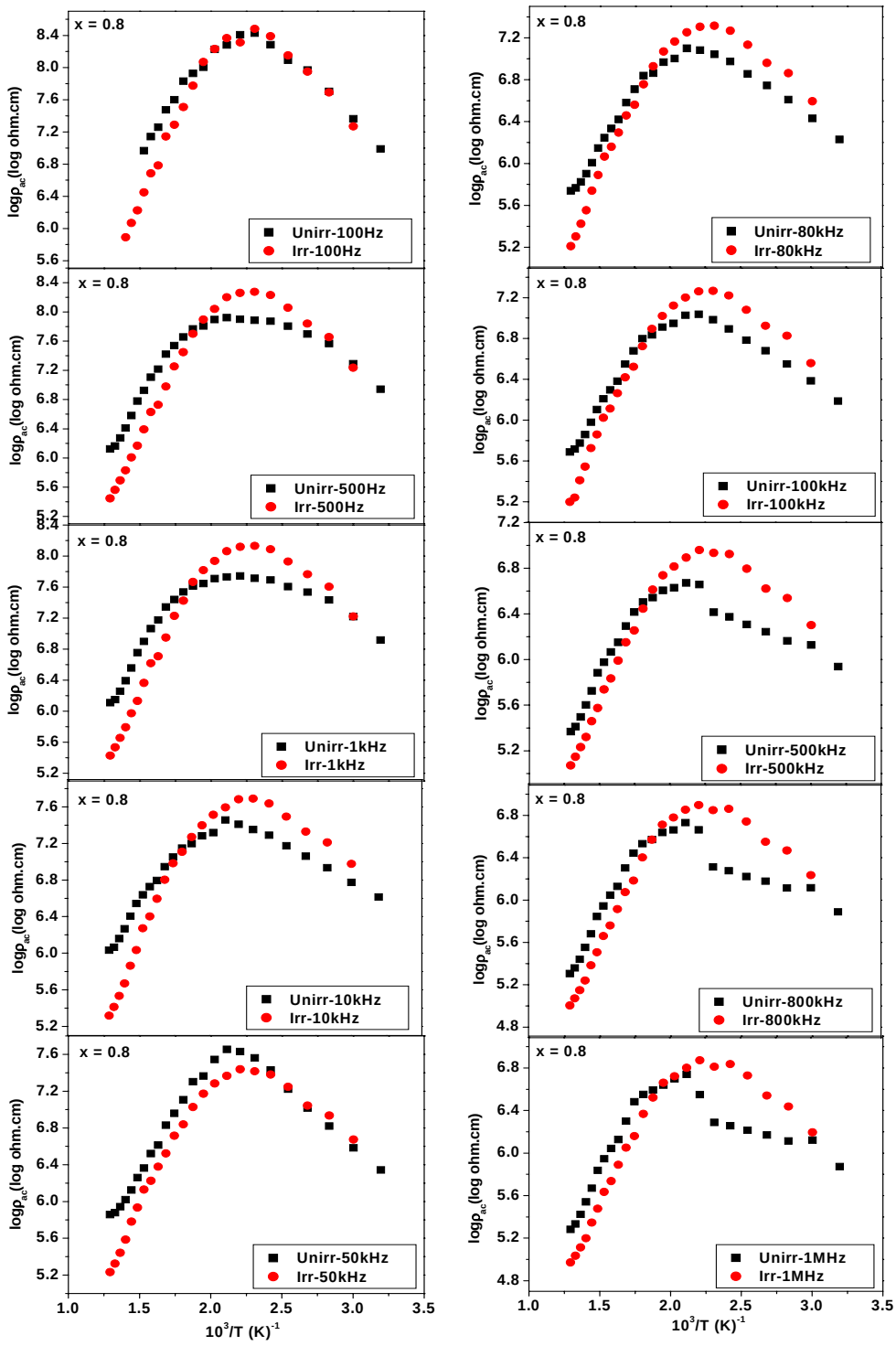

Fig. 6C.15e Thermal variation of a.c. resistivity (ρ_{ac}) at different frequencies for the composition x = 0.8 of unirradiated and irradiated $MnAl_xCr_xFe_{2-2x}O_4$ system

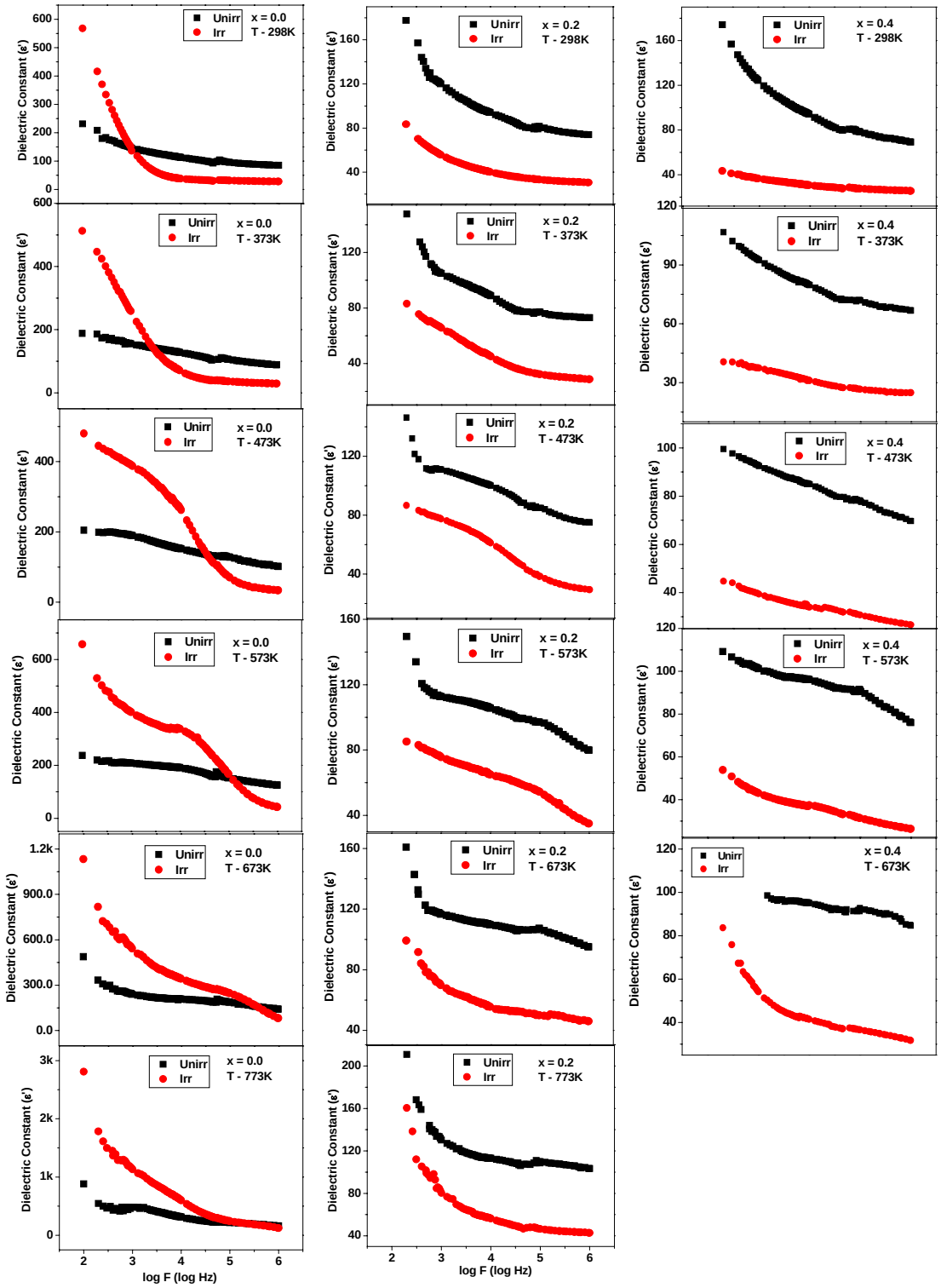

Fig. 6C.16a Dielectric Constant (ε') versus frequency at selected temperatures for the compositions x = 0.0, 0.2 and 0.4 of unirradiated and irradiated $MnAl_xCr_xFe_{2-2x}O_4$ system

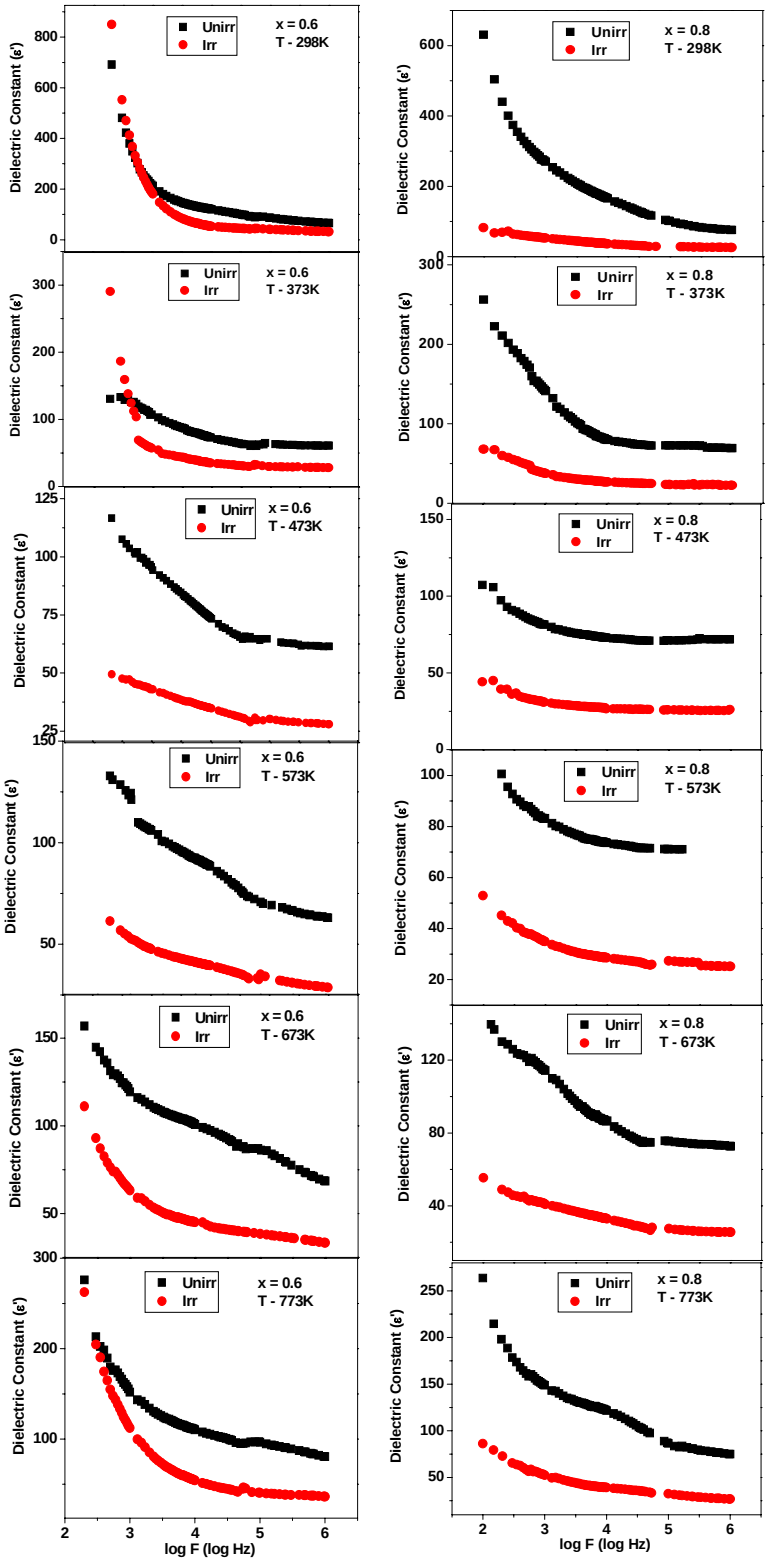

Fig. 6C.16b Dielectric Constant (ε') versus frequency at selected temperatures for the compositions x = 0.6 and 0.8 of unirradiated and irradiated $MnAl_xCr_xFe_{2-2x}O_4$ system

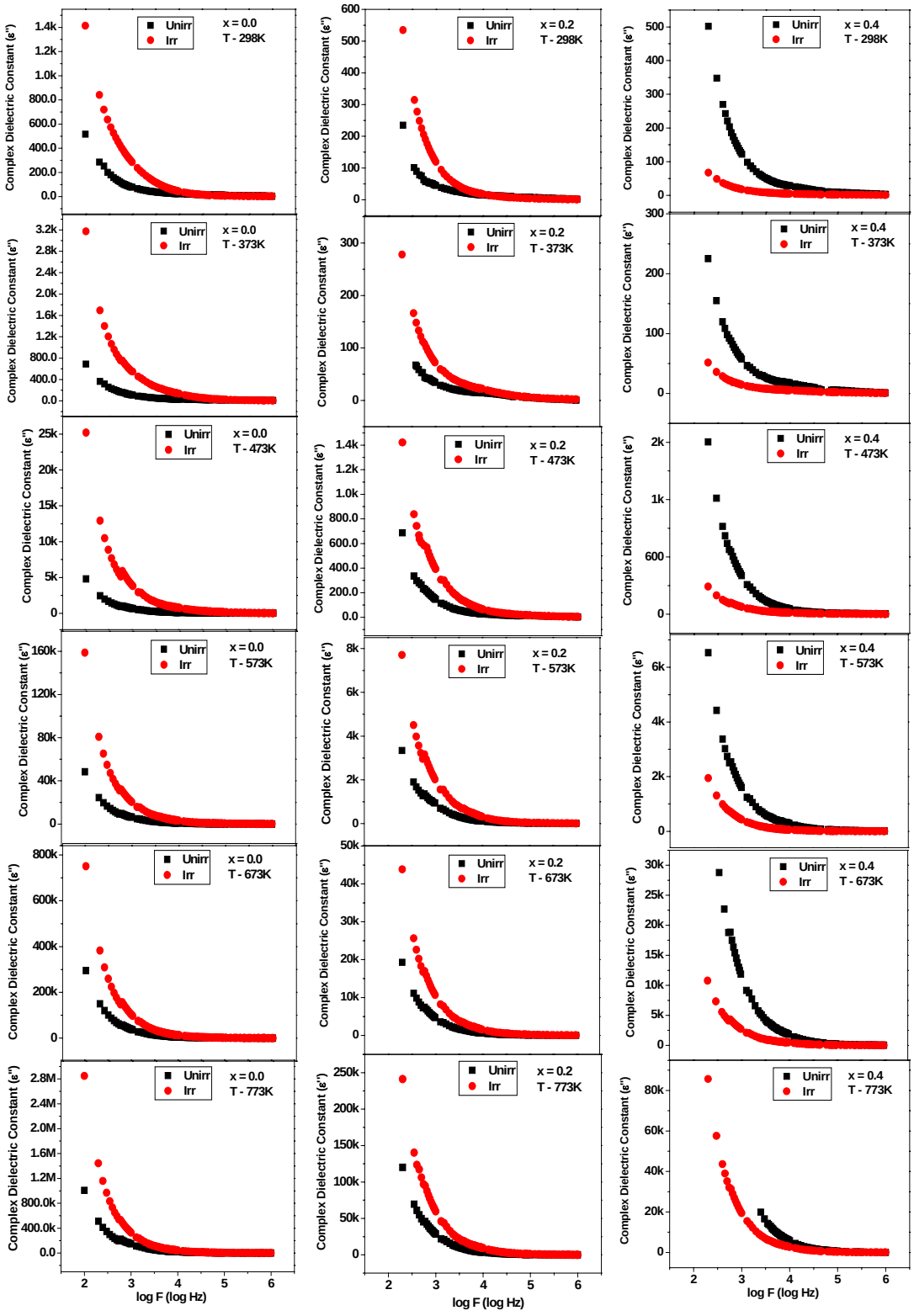

Fig. 6C.17a Complex Dielectric Constant (ε") versus frequency at selected temperatures for the compositions x = 0.0, 0.2 and 0.4 of unirradiated and irradiated $MnAl_xCr_xFe_{2-2x}O_4$ system

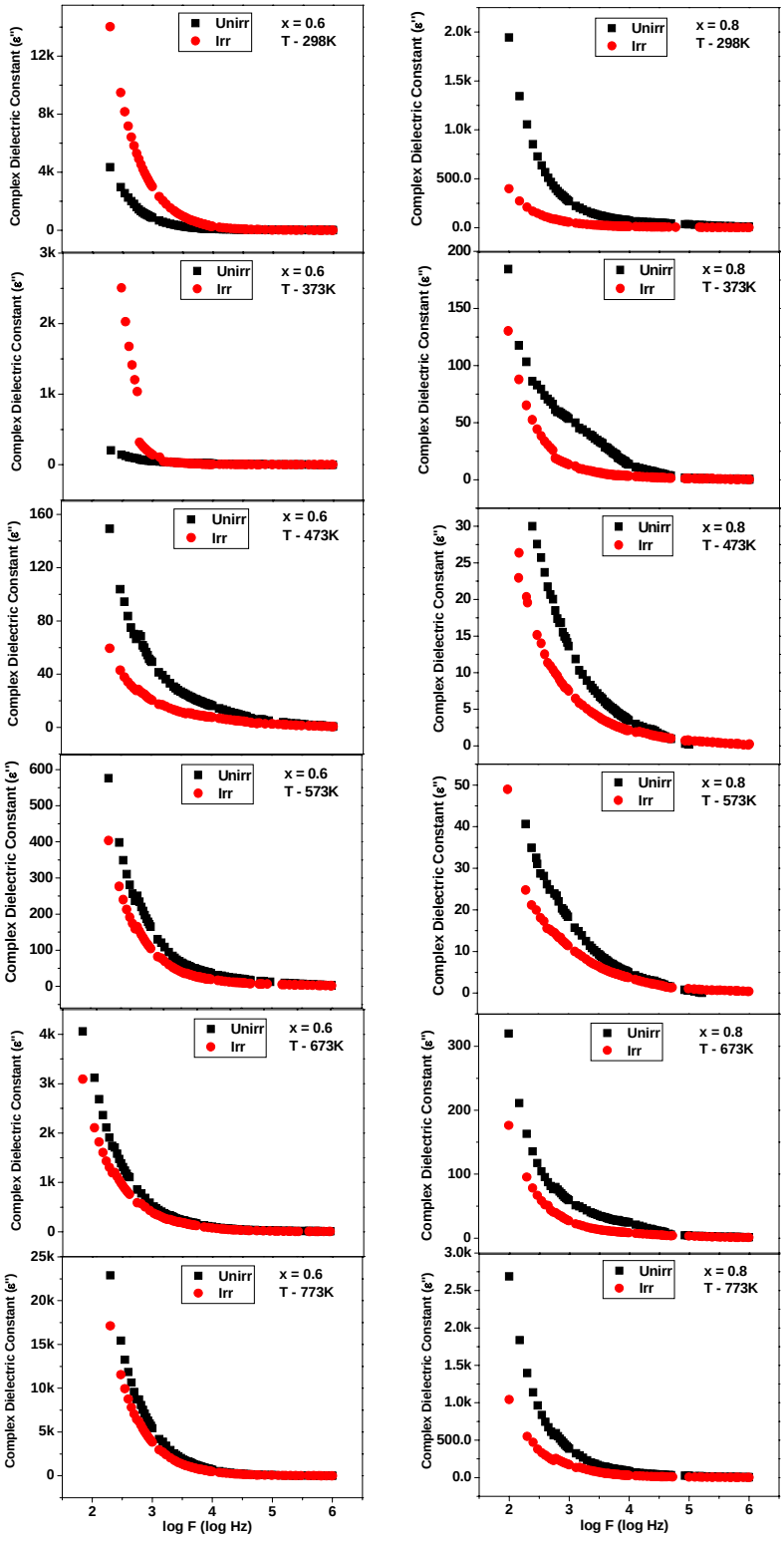

Fig. 6C.17b Complex Dielectric Constant (ε") versus frequency at selected temperatures for the compositions x = 0.6 and 0.8 of unirradiated and irradiated $MnAl_xCr_xFe_{2-2x}O_4$ system

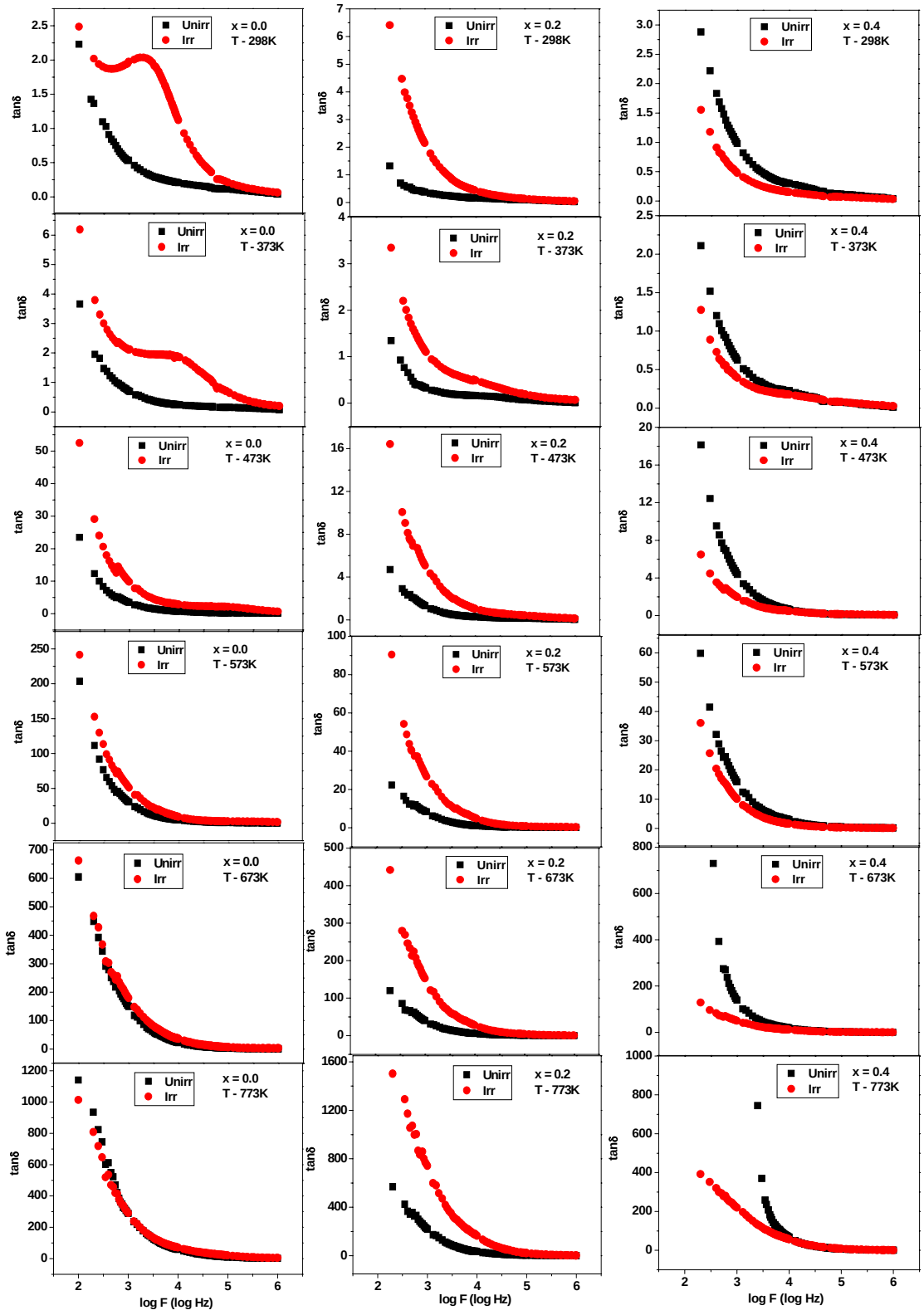

Fig. 6C.18a Dielectric loss tangent (tanδ) versus frequency at selected temperatures for the compositions x = 0.0, 0.2 and 0.4 of unirradiated and irradiated $MnAl_xCr_xFe_{2-2x}O_4$ system

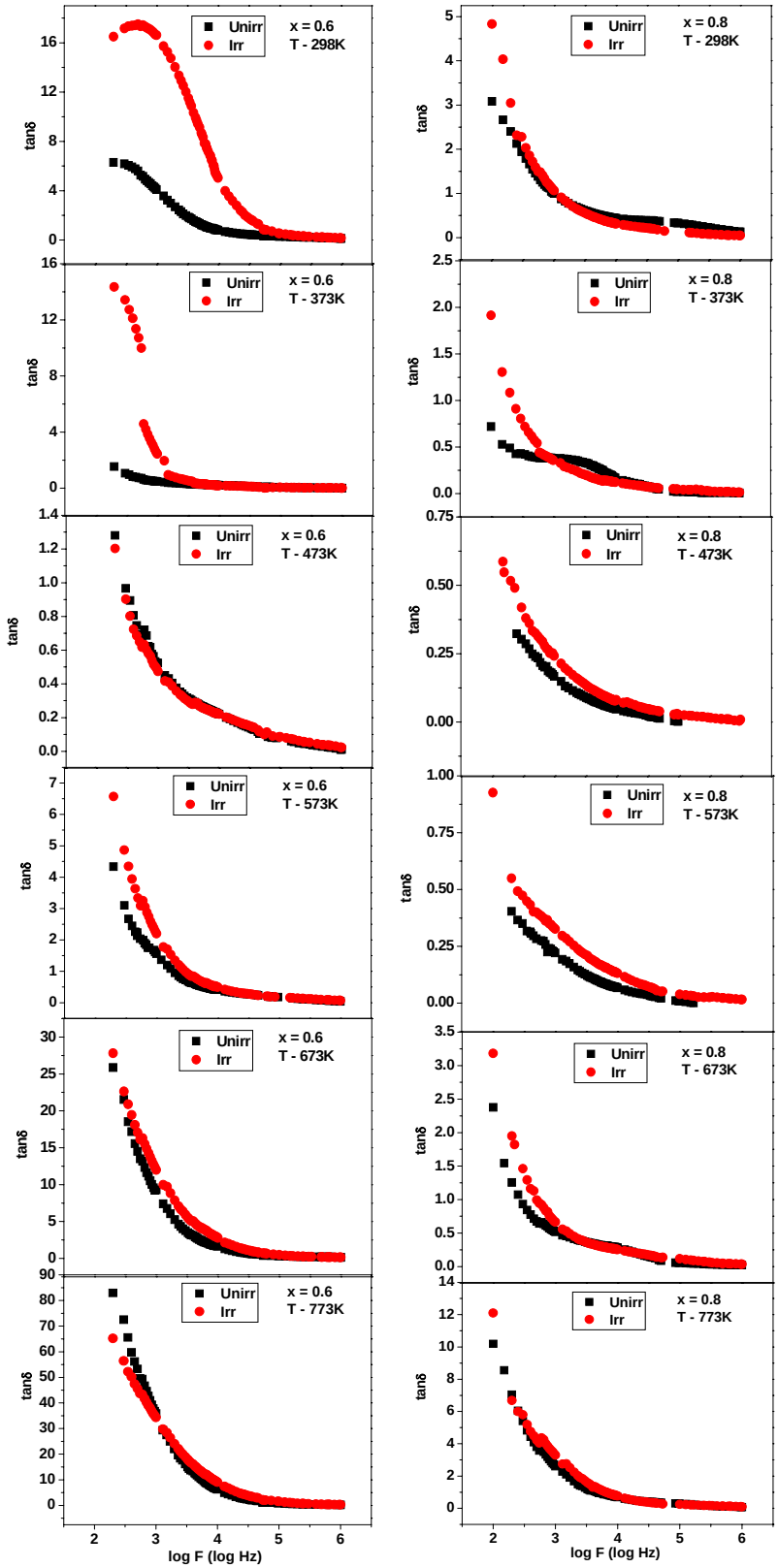

Fig. 6C.18b Dielectric loss tangent (tanδ) versus frequency at selected temperatures for the compositions x = 0.6 and 0.8 of unirradiated and irradiated $MnAl_xCr_xFe_{2-2x}O_4$ system

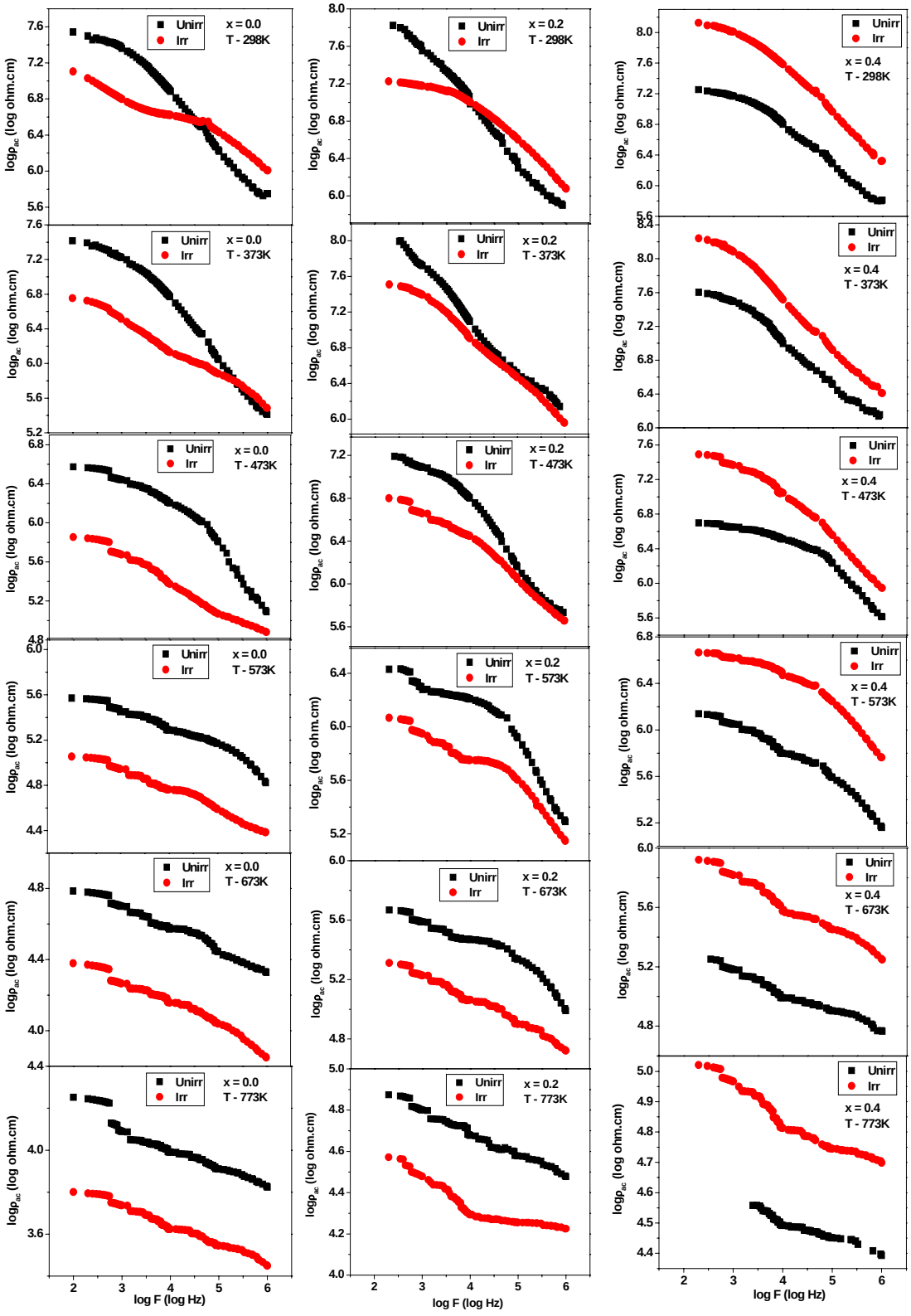

Fig. 6C.19a AC Resistivity (ρ_{ac}) versus frequency at selected temperatures for the compositions x = 0..0, 0.2 and 0.4 of unirradiated and irradiated $MnAl_xCr_xFe_{2-2x}O_4$ system

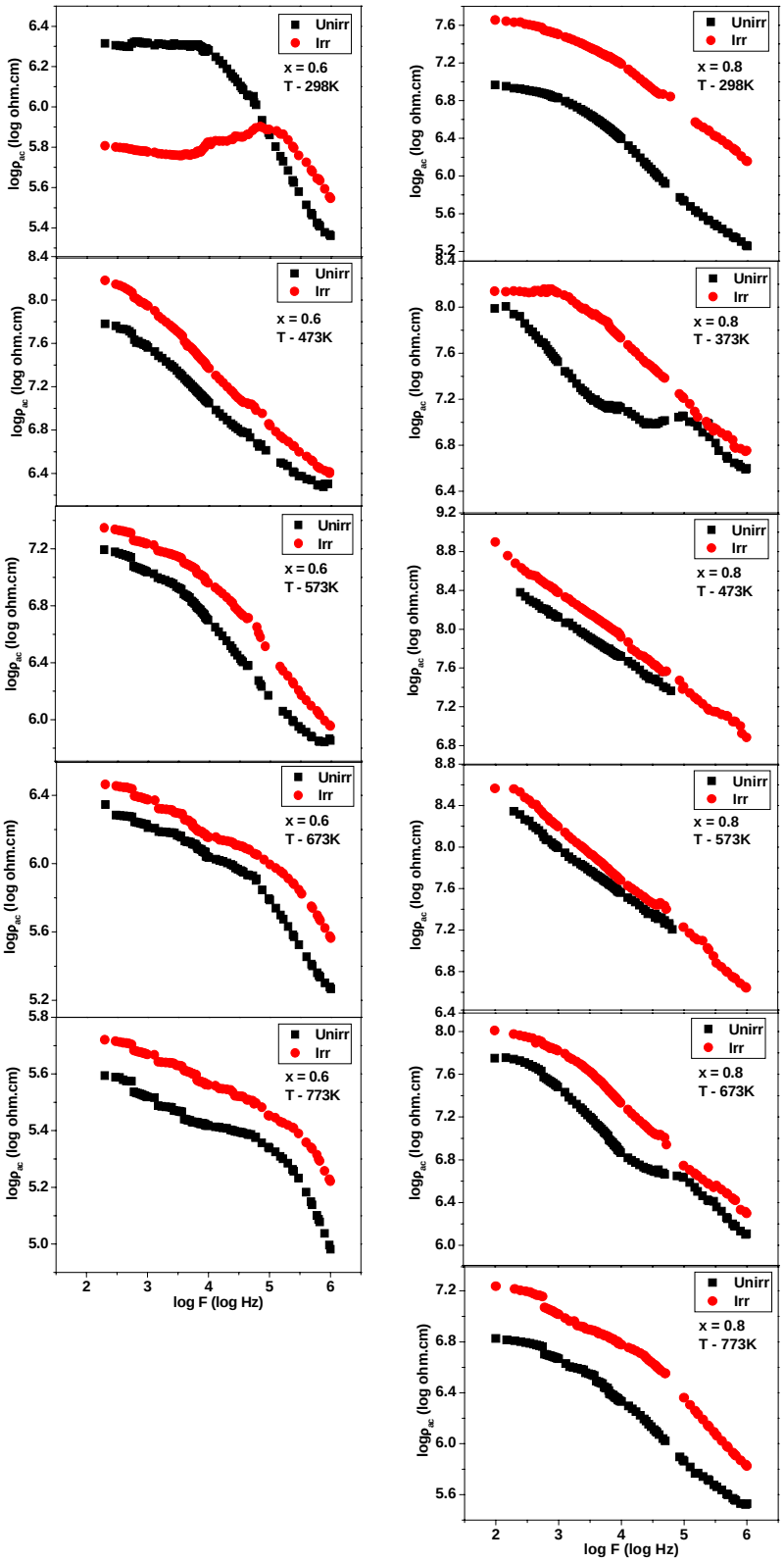

Fig. 6C.19b AC Resistivity (ρ_{ac}) versus frequency at selected temperatures for the compositions x = 0.6 and 0.8 of unirradiated and irradiated $MnAl_xCr_xFe_{2-2x}O_4$ system

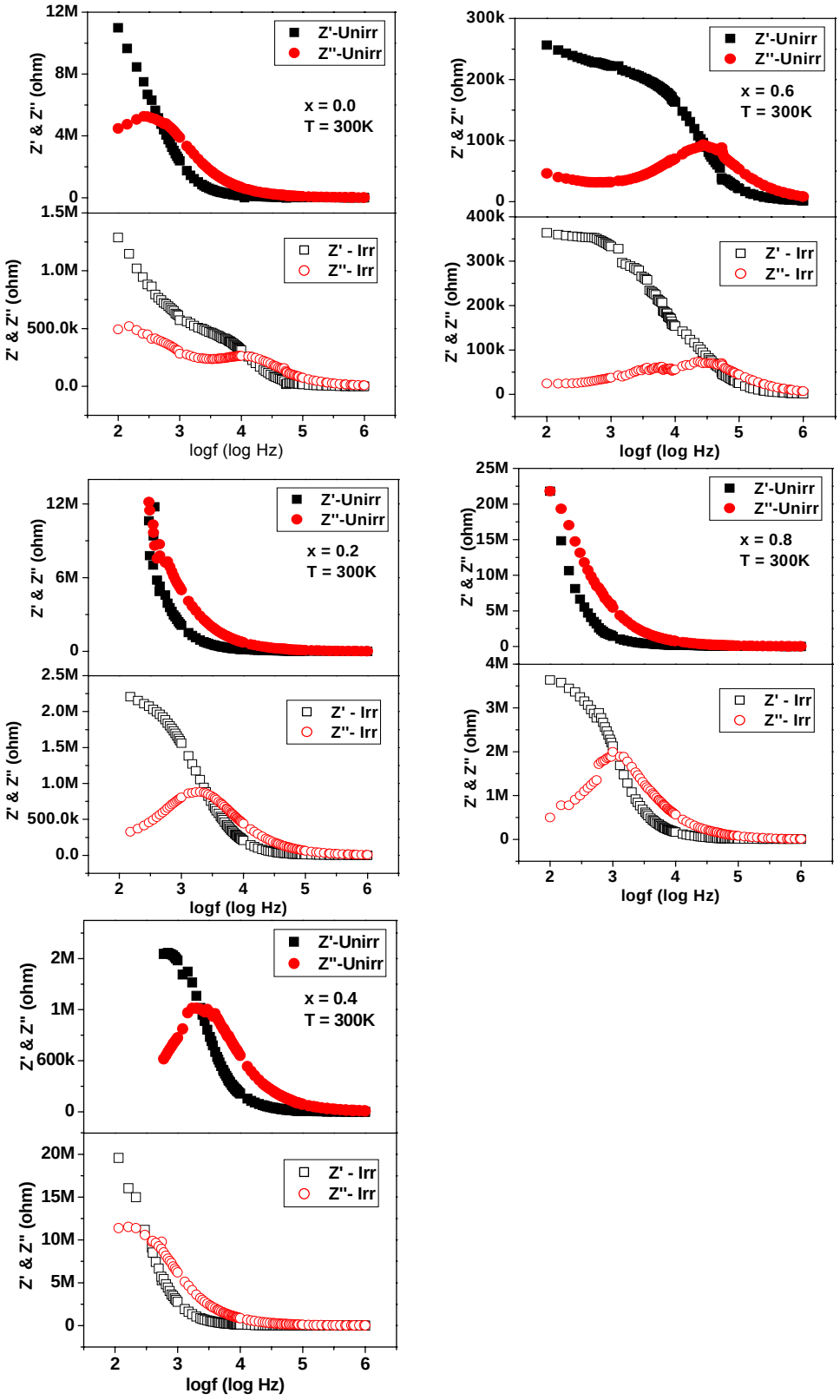

Fig. 6C.20 Variation of real part (Z') and imaginary part (Z'') of the impedance with frequency at room temperature for the compositions x = 0.0, 0.2, 0.4, 0.6 and 0.8 of unirradiated and irradiated $MnAl_xCr_xFe_{2-2x}O_4$ system

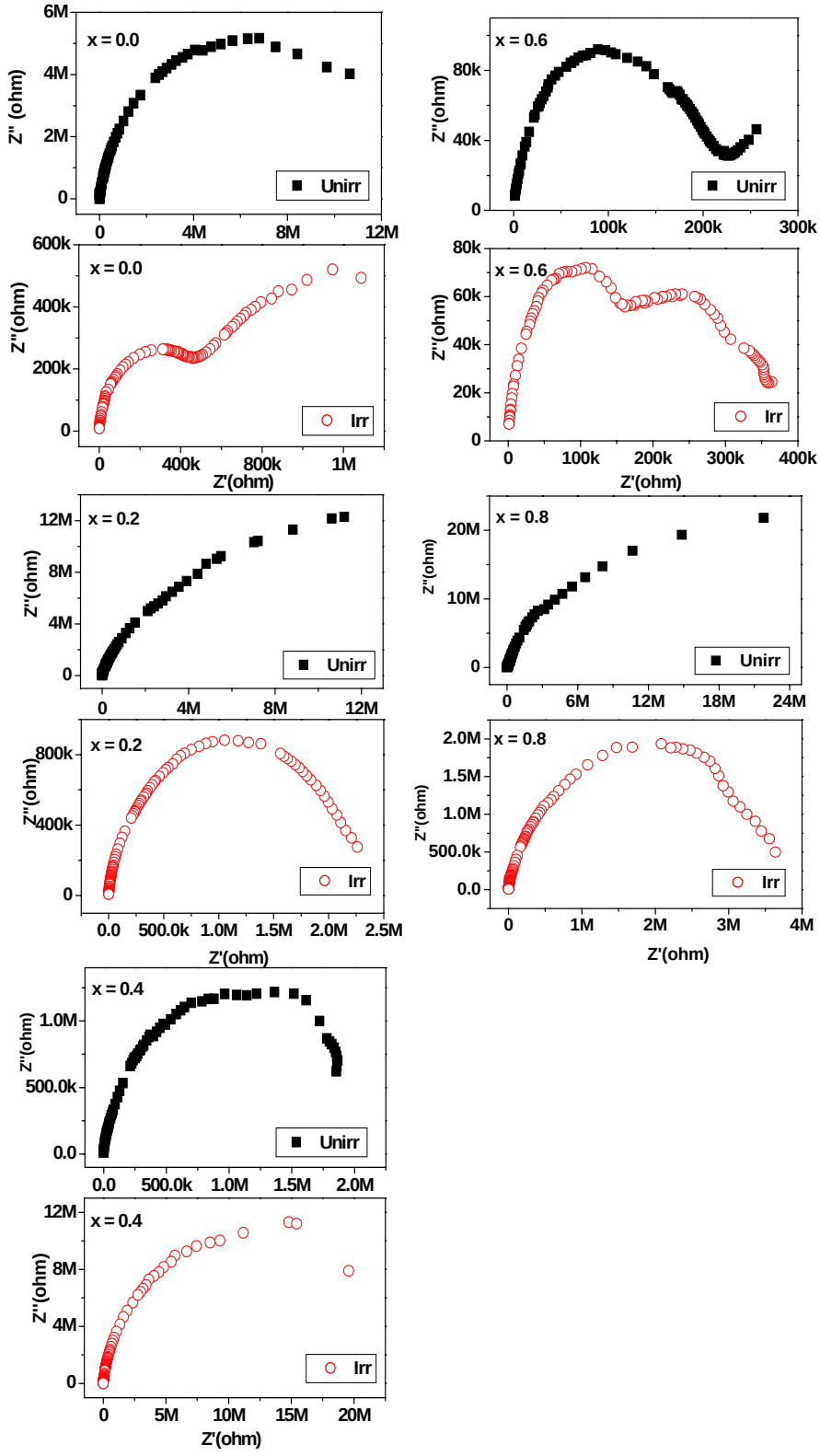

Fig. 6C.21 Real (Z') versus imaginary (Z'') parts of the impedance, Cole-Cole Plots at room temperature for the compositions x = 0.0, 0.2, 0.4, 0.6 and 0.8 of unirradiated and irradiated $MnAl_xCr_xFe_{2-2x}O_4$ system

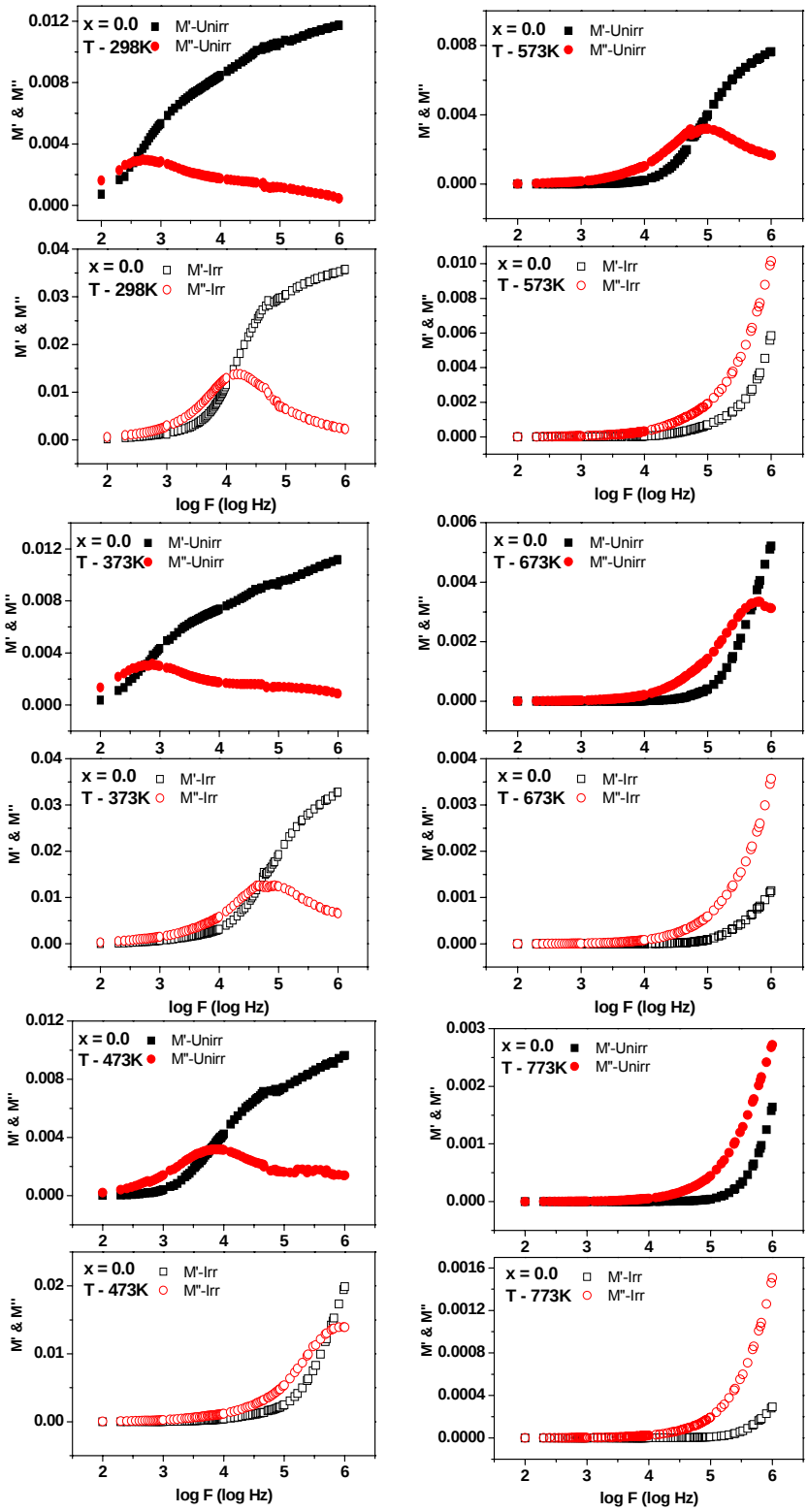

Fig. 6C.22a Real (M') and imaginary (M'') part of the dielectric modulus versus frequency at selected temperatures for the composition x = 0.0 of unirradiated and irradiated $MnAl_xCr_xFe_{2-2x}O_4$system

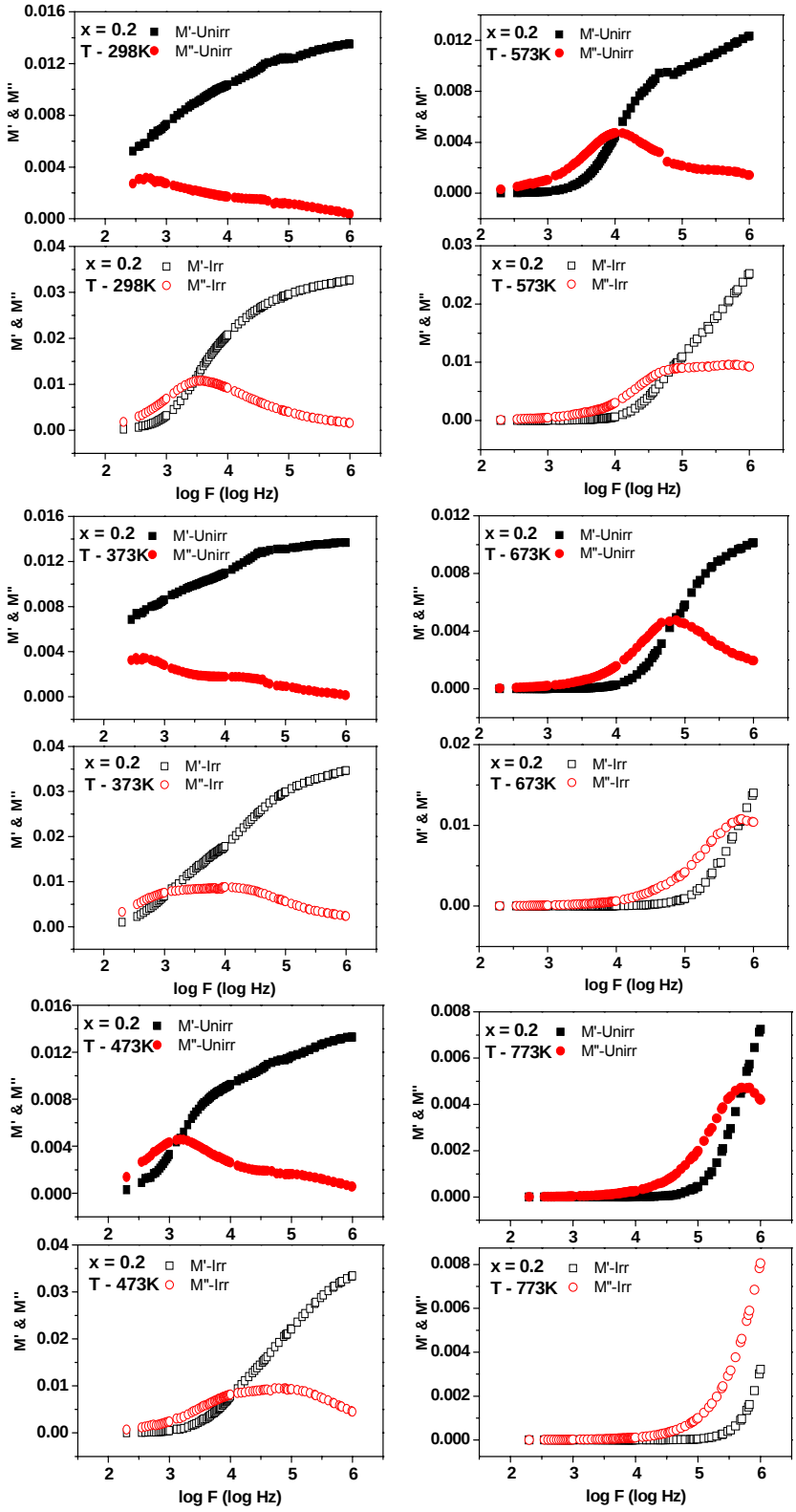

Fig. 6C.22b Real (M') and imaginary (M'') part of the dielectric modulus versus frequency at selected temperatures for the composition x = 0.2 of unirradiated and irradiated $MnAl_xCr_xFe_{2-2x}O_4$system

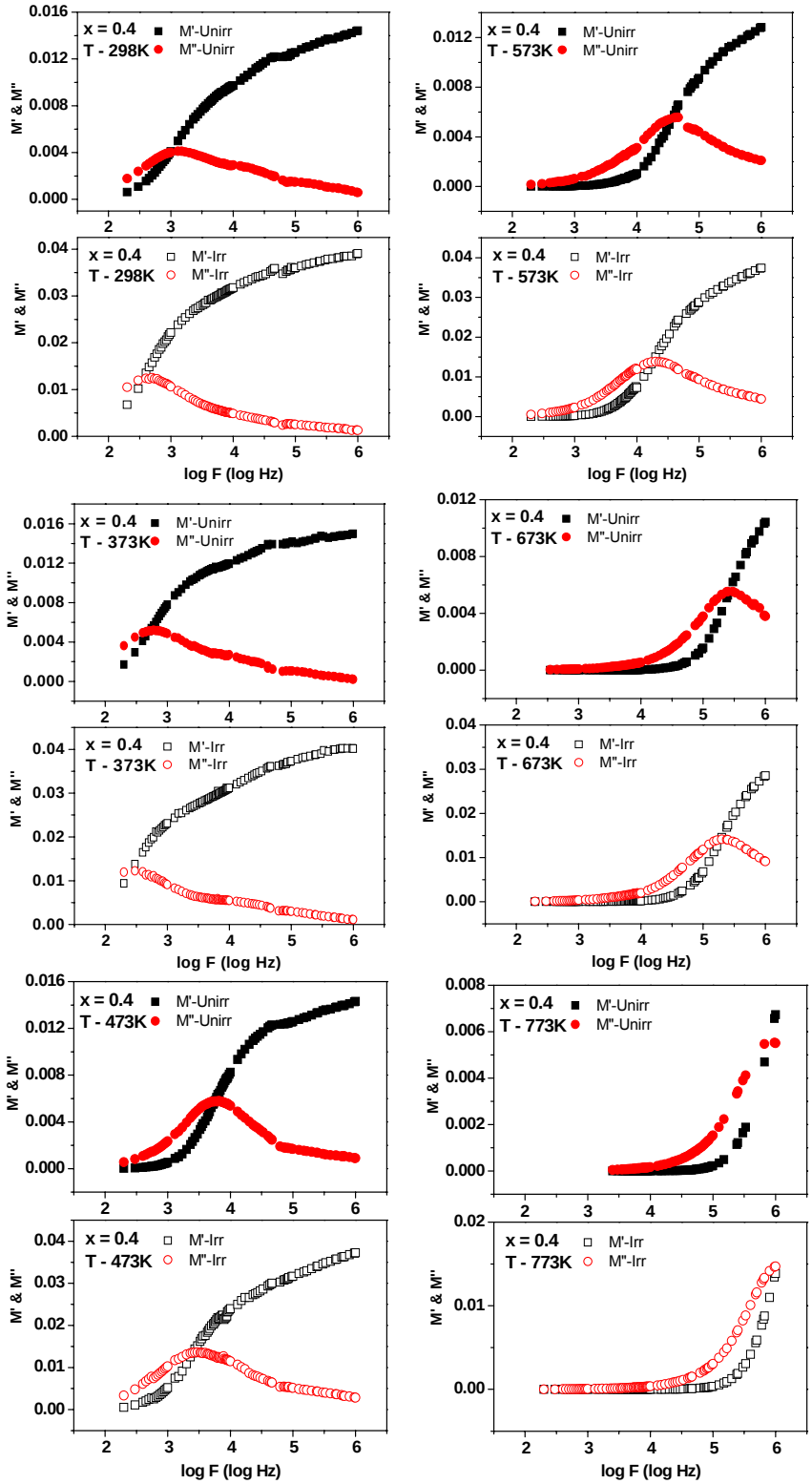

Fig. 6C.22c Real (M') and imaginary (M'') part of the dielectric modulus versus frequency at selected temperatures for the composition x = 0.4 of unirradiated and irradiated $MnAl_xCr_xFe_{2-2x}O_4$system

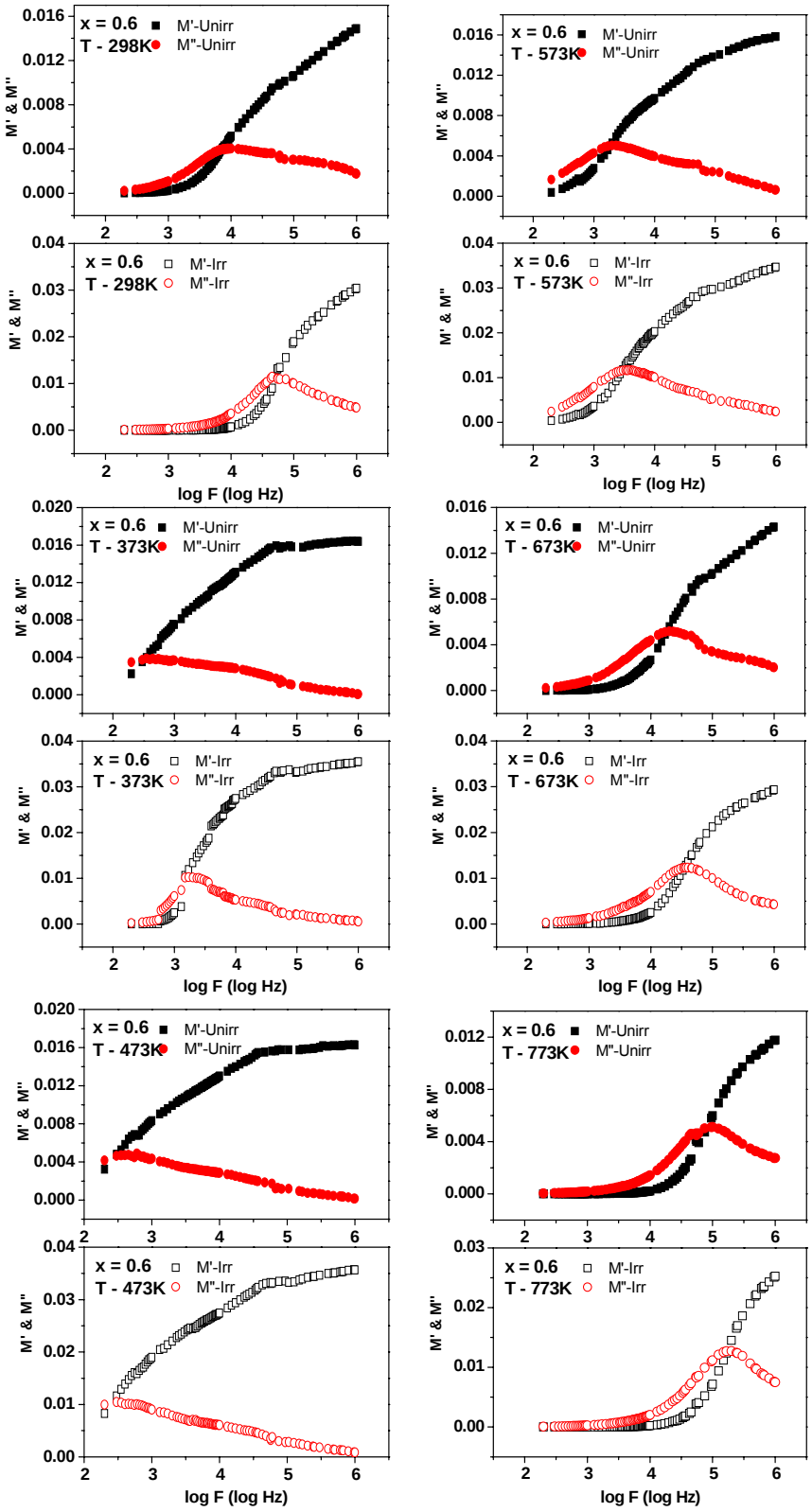

Fig. 6C.22d Real (M') and imaginary (M'') part of the dielectric modulus versus frequency at selected temperatures for the composition x = 0.6 of unirradiated and irradiated $MnAl_xCr_xFe_{2-2x}O_4$system

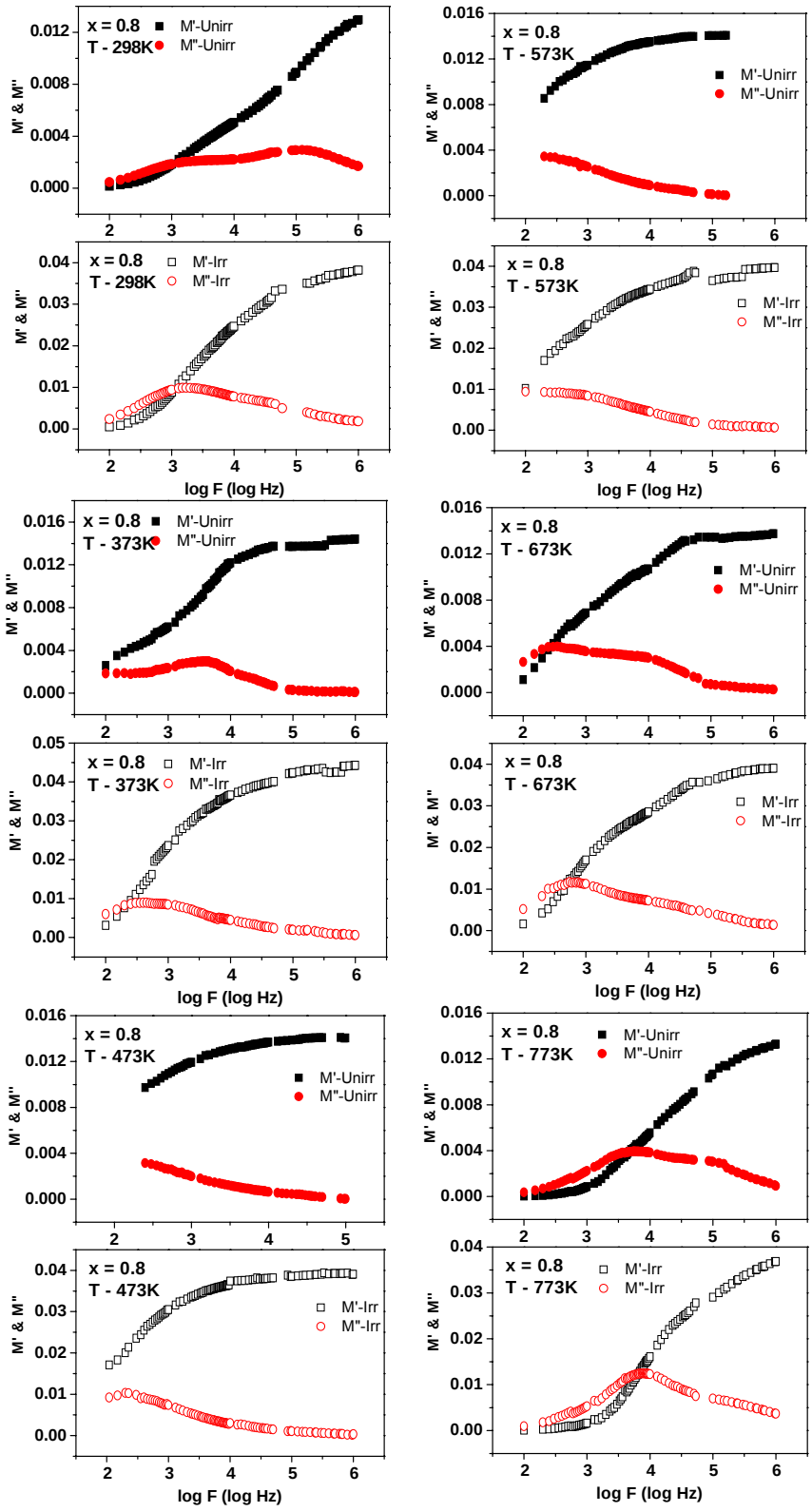

Fig. 6C.22e Real (M') and imaginary (M'') part of the dielectric modulus versus frequency at selected temperatures for the composition x = 0.8 of unirradiated and irradiated $MnAl_xCr_xFe_{2-2x}O_4$system

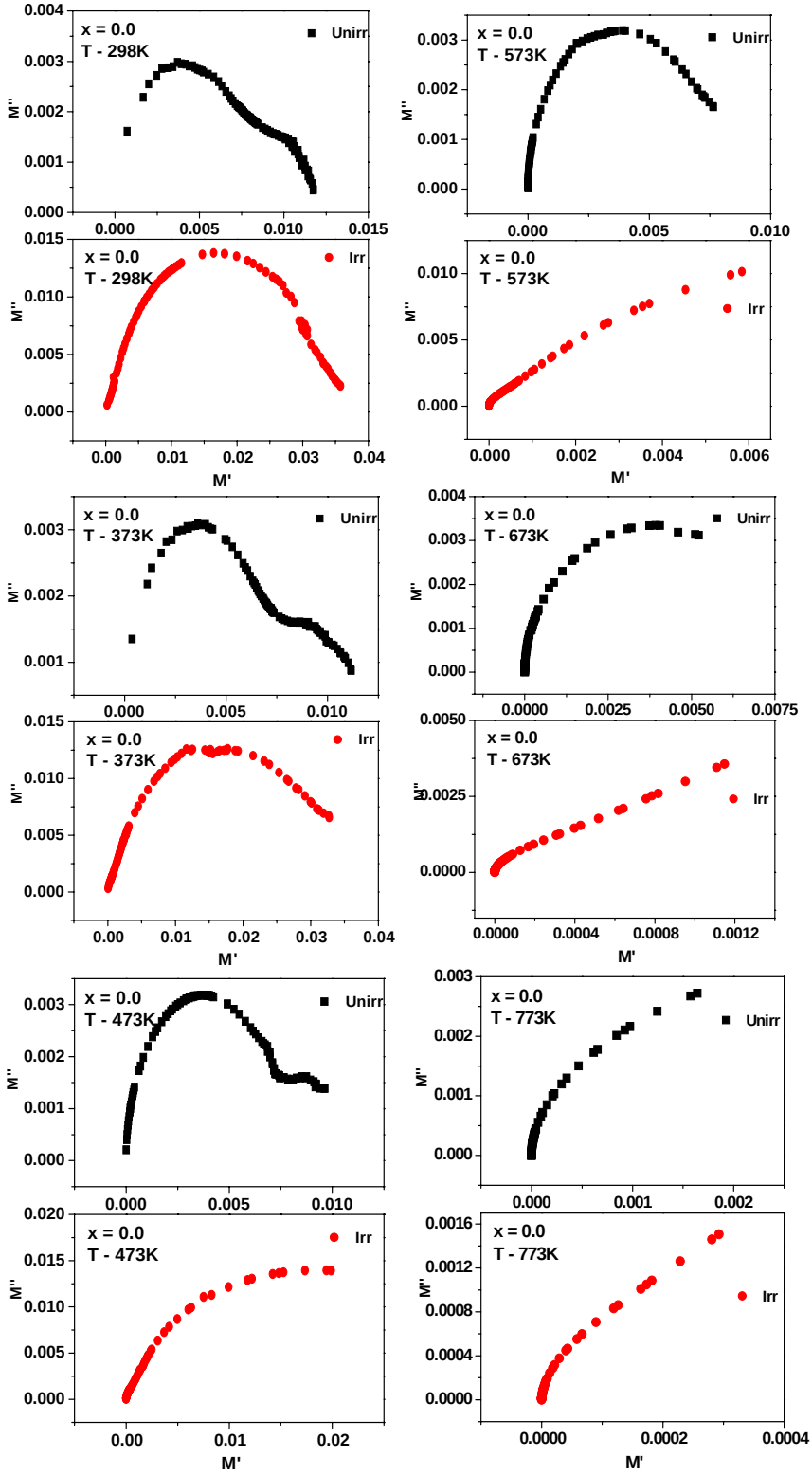

Fig. 6C.23a Real (M') versus imaginary (M'') parts of the dielectric modulus, Cole-Cole plots at selected temperatures for the composition x = 0.0 of unirradiated and irradiated $MnAl_xCr_xFe_{2-2x}O_4$ system

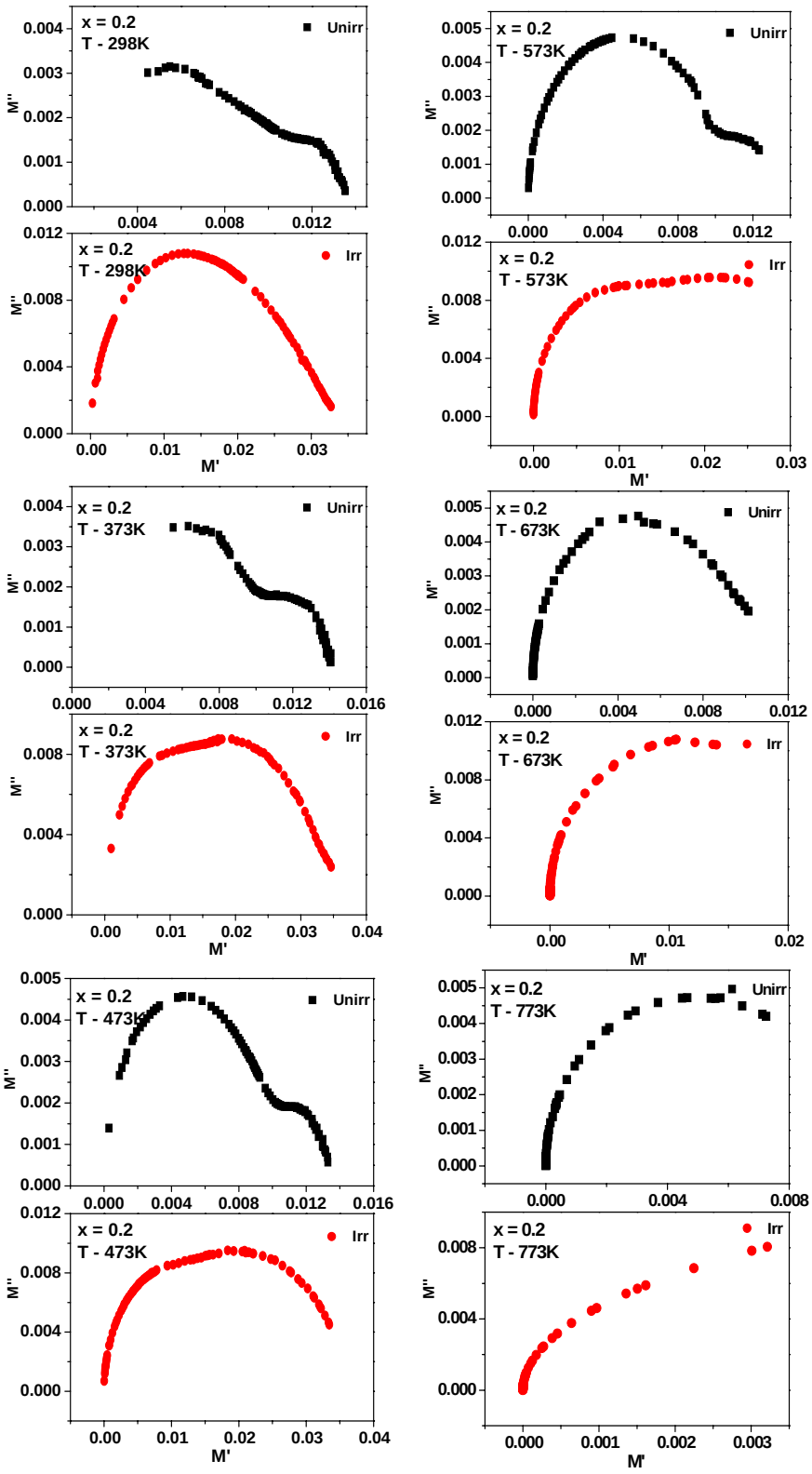

Fig. 6C 23b Real (M') versus imaginary (M'') parts of the dielectric modulus, Cole-Cole plots at selected temperatures for the composition x = 0.2 of unirradiated and irradiated $MnAl_xCr_xFe_{2-2x}O_4$ system

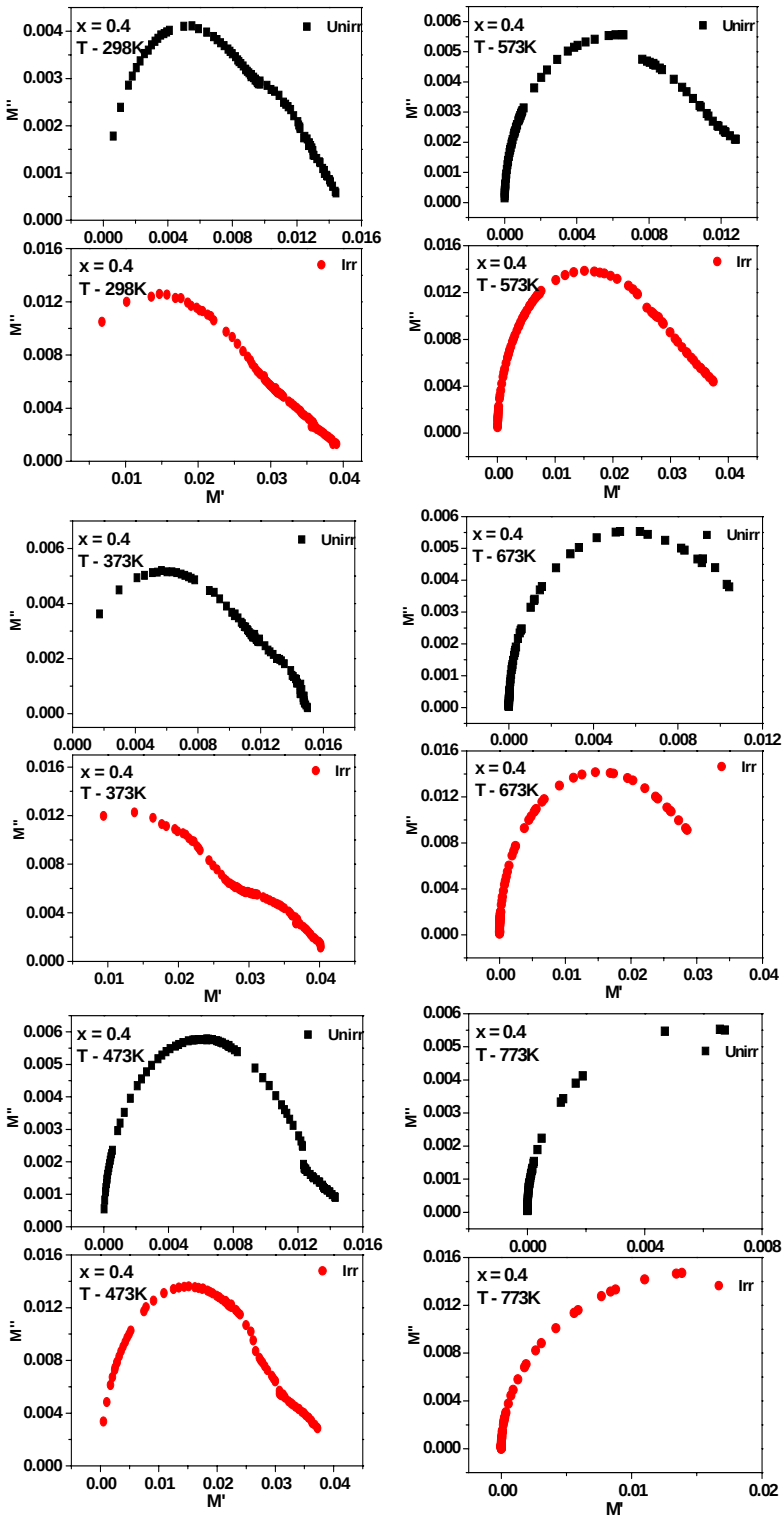

Fig. 6C.23c Real (M') versus imaginary (M'') parts of the dielectric modulus, Cole-Cole plots at selected temperatures for the composition x = 0.4 of unirradiated and irradiated $MnAl_xCr_xFe_{2-2x}O_4$ system

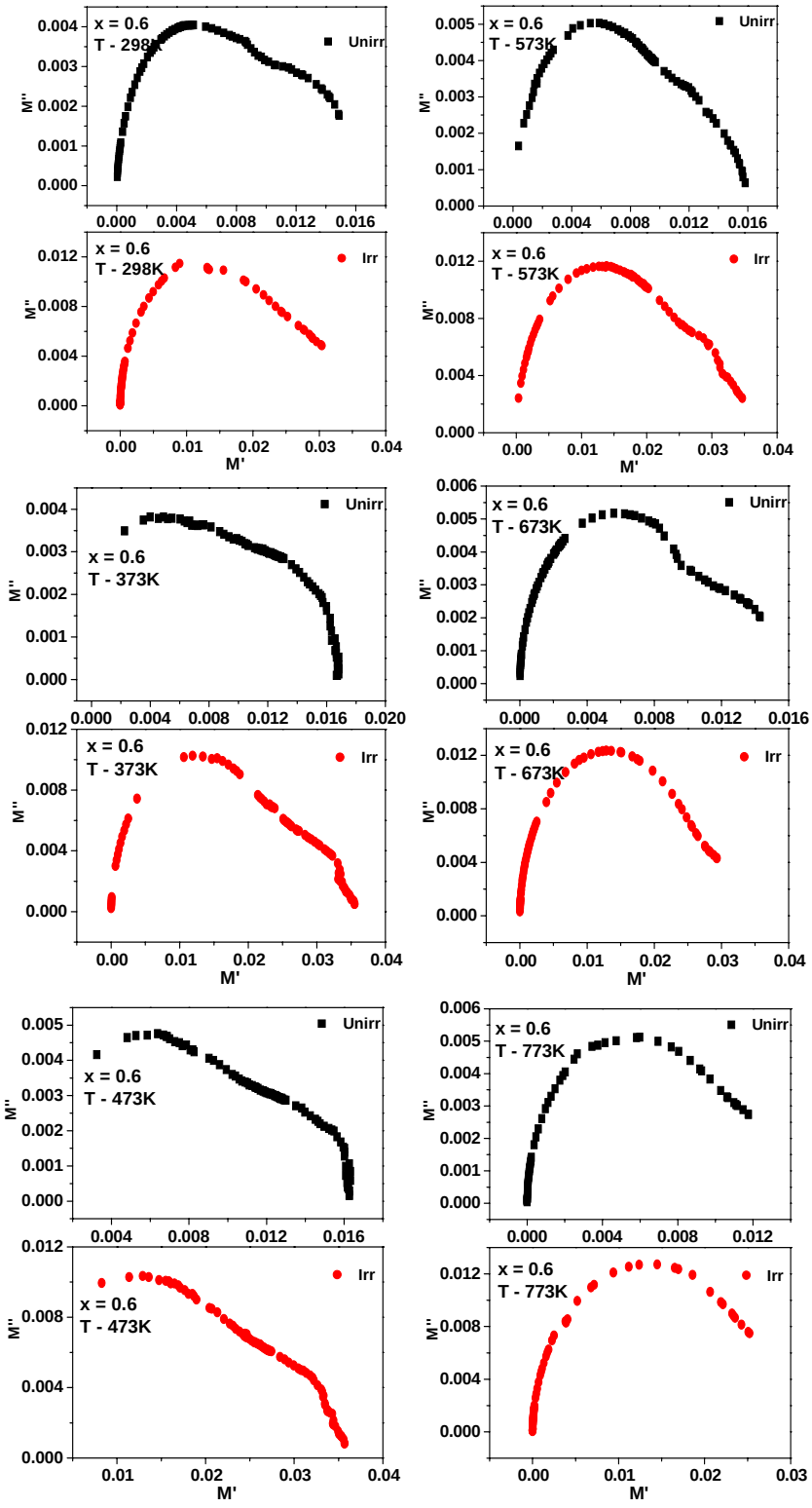

Fig. 6C.23d Real (M') versus imaginary (M'') parts of the dielectric modulus, Cole-Cole plots at selected temperatures for the composition x = 0.6 of unirradiated and irradiated $MnAl_xCr_xFe_{2-2x}O_4$ system

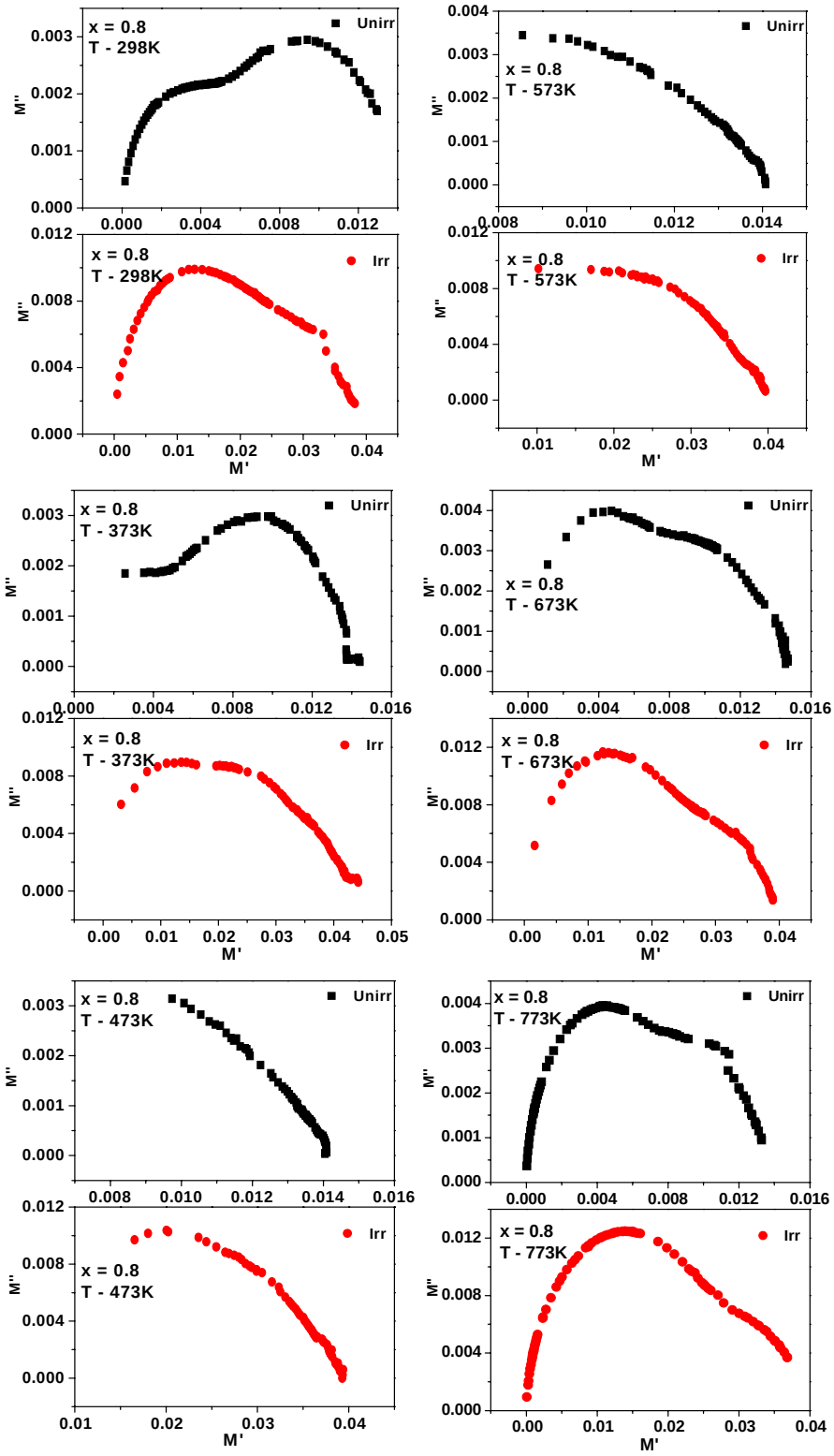

Fig. 6C.23e Real (M') versus imaginary (M'') parts of the dielectric modulus, Cole-Cole plots at selected temperatures for the composition x = 0.8 of unirradiated and irradiated $MnAl_xCr_xFe_{2-2x}O_4$ system

❖ *50 MeV Li^{3+} ions irradiation of $CuAl_xCr_xFe_{2-2x}O_4$*

6D.1 SHI Irradiation effects on Structural and Magnetic Properties

6D.2 SHI Irradiation effects on Physical parameters and Infrared Spectra

6D.3 SHI Irradiation effects on Electrical, Dielectric and Impedance properties

Conclusion

References

6D.1 Swift Heavy Ion Irradiation effects on Structural and Magnetic properties of the system $CuAl_xCr_xFe_{2-2x}O_4$

It is known that the magnetically diluted ferro-spinels or ferrites possess ferric (Fe^{3+}) ions distributed among the octahedral (B) and tetrahedral (A) sites of the *fcc* lattice. In this type of substituted spinels the structural and magnetic environments of these two voids are different; therefore the magnetic and electrical properties of the spinel ferrites become sensitive to the distribution of ferric ions (being main species having the largest magnetic moment among the available cations and causing electrical conduction) in the available sites. The simultaneous substitution of trivalent non-magnetic like Al^{3+} and magnetic like Cr^{3+} in place of Fe^{3+} in the spinel lattice can cause interesting magnetic and electrical properties. It was resolved to choose Copper ferrite, $CuFe_2O_4$ for the substitution because its structural behaviour is sensitive to thermal history or preparation condition in terms of distribution of cations in the sites and degree of tetragonality originating due to Jahn-Teller ion Cu^{2+} .

The simultaneous introduction of magnetic and non-magnetic cations in $CuFe_2O_4$ may alter the degree of inversion, exchange interaction, spin canting, nuclear hyper interactions and Curie temperature. The selective magnetic dilution of the either site leads to non-collinear spin structure. It has been reported that the presence of Cr^{3+} ions gives rise to strong B-B interactions [6D.1]. There are reports on the magnetic properties of Al^{3+} and Cr^{3+} substituted for Fe^{3+} in $NiFe_2O_4$, $Li_{0.5}Fe_{2.5}O_4$ and Garnets [6D.2-6D.6]. The structural study on the Al^{3+} substituted Cu- ferrite [6D.7] has shown the absence of tetragonal distortion for lower Al-content and higher B-site occupancy of Al^{3+} ions. The aim of the present work is two fold: **(i)** To synthesize the spinel system $CuFe_{2-2x}Al_xCr_xO_4$ by standard ceramic route with two different thermal histories- Slow-cooled (programmed cooling with rate 2 ^oC per minute) from final sintering temperature and Quenched to the Liquid Nitrogen temperature (77K) from the final sintering temperature (1100^oC) **(ii)** To study the influence of Swift Heavy Ion irradiation on these specimens on their structural, magnetic, electrical and dielectric properties. With this idea Four compositions: x = 0.0, 0.2, 0.4, 0.6 and 0.8 were prepared. Just after the preparation of the samples, the compositional stoichiometry of the compounds was ascertained by EDAX and the typical EDAX patterns are displayed in the Fig. 6D.1a-1b. The specimens in powered as well as thin pellet form were irradiated in vacuum with 50 MeV Li^{3+} ions with fluence of 5 x 10^{13}

ions/cm^2 using 15 UD Pelletron accelerator at Inter University Accelerator Centre, New Delhi. All the pre and post irradiated samples were characterized by X-ray diffraction to find out structural parameters such as lattice constant, tetragonality i.e. c/a ratio if exists, cation distribution through XRD Bragg reflection intensity analysis. The XRD patterns for all the samples are shown in Fig. 6D.2a-2c. All the samples show tetragonal deformation. The value of lattice parameters ('a' and 'c') is listed in Table 6D.2**.** It is clear that after the SHI-irradiation, the tetragonality almost vanishes and the structure is nearly cubic. All the lattice parameters are found to decrease after the SHII (Table 6D.2).

Let us first concentrate on $CuFe_2O_4$ i.e. x = 0.0 composition of the system. The degree of inversion (fraction of divalent metal ion present on octahedral (B) site is more in case of slow-cooled (SC) sample than that for the quenched (QC) one. The slow-cooled sample of $CuFe_2O_4$ exhibits tetragonal deformation. Several combinations of cation distributions were checked and for the best matched values of the calculated and observed XRD intensity ratios-keeping in mind the saturation moment value since Cu-ferrite is a collinear one. The SHII reduces the tetragonal deformation in SC sample. Thus, the ratio of the Bragg planes intensities calculated and observed values matching better after the specimen subjected to SHII, may be due to removal of tetragonality. The cation distribution is also slightly modified after the SHII. The observed and calculated saturation magnetic moments are found nearly equal for both pre and post irradiated samples.

The quenched sample of $CuFe_2O_4$ shows different cation distribution, the XRD intensity calculation for quenched-unirradiated sample becomes more authentic because the quenched sample does not exhibit tetragonal deformation. But after the irradiation, the cation distribution concluded from XRD intensity calculation does not give the Nèel's moment matching with the observed saturation moment. This happens because the distribution of XRD intensity is greatly affected by SHII causing mismatch of n_B (obs) and n_B (cal).

The SHII reduces the tetragonal distortion in both the cases and significantly modifies the cation distribution in case of quenched sample. It is seen that the absolute XRD intensity of the Bragg planes is affected after the SHII. The calculated and observed values of saturation magnetic moment (n_B) are in good agreement for the slow-cooled sample while in case of quenched samples no agreement is found after the SHII. It is inferred that the presence of tetragonality before the SHII and

"defects" after the SHII cause the mismatch of calculated and observed XRD intensity ratios. The cation distributions for all the samples are given in Table 6D.3. The lattice constants "a" and "c" are found to decrease after the SHII in both the specimens indicated overall unit cell contraction after the SHII. The lattice constants are found to decrease with the Al-Cr concentration(x) which is the expected result due to the smaller cations (Al^{3+}, Cr^{3+}) substitution in $CuFe_2O_4$.

The values of saturation magnetization σ_s (emu/g) measured at the peak field of 1.2 Tesla and at specimen temperature 77K is given in Table 6D.4**.** The plots of field dependence of σ_s for pre and post irradiated SC and QC-samples are depicted in Fig 6D.3**.** Since the T/T_N ratio becomes poor at higher magnetic dilution, these measurements obtained at the high field of 1.2 T and lowest possible temperature (77K) become reliable. The values of magneton number n_B (Bohr magneton) derived from σ_s (emu/g) values and calculated by assuming Nèel's collinear spin arrangement are given in Table 6D.4**.** It is seen that the quenched samples show higher values of σ_s compared to the slow-cooled ones. This is ascribed to the effect of thermal history on the cation distribution. No remarkable change has been observed in the magnetization after the specimens subjected to the SHII. The observed lower values of n_B (observed) compared to the n_B (Nèel) is due to the evolution of canted spin arrangement on account of magnetic dilution caused by substitution of Fe^{3+} (5 μ_B) by Al^{3+} (non-magnetic) and Cr^{3+} (3 μ_B). The presence of Al^{3+} may lead to collapse of long range order (magnetic linkages) and Cr^{3+} is known for enhancing the disorder in the system. This situation does not allow the use of uniform canting approach like Yafet-Kittel model rather one should treat the system with random canting of spin (RCS) or localized canting of spins (LCS) models. The variation of magnetization with magnetic dilution for $CuFe_{2-2x}Al_xCr_xO_4$ system has been explained earlier by using RCS model [6D.8]. Since the aim of the present work is to study the effect of SHII on the bulk magnetization and no remarkable change has been observed due to SHII, no attempt has been made to analyze the magnetic data using any of the statistical models.

The Mössbauer spectra for the slow cooled and quenched samples of compositions x =0.2 and x = 0.6 for pre and post irradiation are depicted in Fig. 6D.4. The spectra were analyzed using NORMOS computer software using non-linear least square minimization method. It is very clear that the SHII by means of producing defects gives rise to distribution values in nuclear hyperfine fields of both the sites.

The Mössbauer spectra of x = 0.2 (SC) sample gives very 'hazy' signature with increased linewidths after the SHII. The quenched sample of this composition seems to be greatly affected by SHII as there are two disorder producing agencies: quenching and SHII. This specimen shows almost "relaxation type" of signature. It is interesting that the x = 0.6 specimen is influenced by high magnetic dilution, heat treatment and SHII. The SC-sample exhibits the magnetic dilution and therefore the increased line widths and the quenching history still further introduces the disorder and line widths are increased. The Mössbauer spectra of irradiated sample of x = 0.6 shows an intense doublet superimposed on large distribution of hyperfine field values.

The Mössbauer parameters deduced are given in Table 6D.5. The isomer shift values are influenced by both heat treatment and irradiation. The slight enhancement in the IS value is due to cation rearrangement as this parameter is sensitive to the chemical environment which may cause fluctuations in s-electron charge density. The hyperfine field values for irradiated samples are just average values due to large disorder effects. The SHII introduces quadrupole interactions through disturbing the symmetry of the charge distribution. It is clear from the table that the SHII affects the micro-magnetic properties like "hyperfine interactions" significantly compared to the bulk properties like saturation magnetization.

Thermal variation of low field AC susceptibility for both the sets before and after SHII is shown in Fig. 6D.5. The Q-sample of $CuFe_2O_4$ shows larger tailing effects near T_c originated from increased cluster effects and larger value of T_c after the SHII. The SC-sample looks almost conventional ferrimagnetic. The fluctuation in T_c value after the SHII in case of both the SC and QC samples are due to variation in cation distributions and disorder. The x = 0.2 QC-sample shows 'hump' type signature which is not observed in SC sample after the SHII confirms the conjecture of SHII-induced micro-structure disorder as evidenced by Mössbauer spectroscopy.

6D.2 Swift Heavy Ion Irradiation effects on Physical parameters and Infrared Spectra of the system $CuAl_xCr_xFe_{2-2x}O_4$

The values of the bulk density (d), X-ray density (ρ_x) and percentage porosity (P %) for the present unirradiated and irradiated ferrites is given in Table 6D.2. From these values, it can be seen that X-ray density decreases linearly with Al-Cr content (x) in spite of the decrease in unit cell volume suggesting that the decrease in mass overtakes the decrease in unit cell volume. Table 6D.2 shows also that the Al-Cr

substitution for Fe ions enhanced the bulk density for the concentration x = 0.2 in SC and x = 0.4 in QC, while reduced for x = 0.4, 0.6 and 0.8 in SC and for x = 0.2, 0.6 and 0.8 in QC specimens of unirradiated and irradiated samples with respect to pure $CuFe_2O_4$.

In this work, we report a detailed analysis of the infrared spectra of slow-cooled and quenched $CuAl_xCr_xFe_{2-2x}O_4$ spinel ferrite systems before and after irradiation, which is a part of our work on structural, magnetic and electrical properties of the system.

The room temperature IR spectra of the above mentioned compositions for unirradiated and irradiated samples are shown in Fig. 6D.6a-6e and band positions are given in Table 6D.6a-6b. The spectra are recorded in the range from 300-800 cm^{-1}. The spectra show two main absorption bands below 750 cm^{-1} as a common feature of all the ferrites and which are found to be in expected range. Earlier, Amer et al [6D.9] have carried out the infrared absorption spectrum along with Mössbauer spectral studies for $CuCr_xFe_{2-x}O_4$ ferrite system. Fourier transform spectral studies in the range of 200-1200 cm^{-1} at room temperature was done by Mazen et al [6D.10] along with some physical properties of Ti^{4+}-subsstituted $CuFe_2O_4$. Infrared spectral studies of Zn-substituted CuFeCrO4 spinel ferrite system has been reported by M. C. Chhantbar et al [6D.11].

The high frequency band ν_1 lies in the range of 559-608 cm^{-1} for SC and 566-661 cm^{-1} for QC specimens of unirradiated and irradiated samples while the low frequency band ν_2 is varying in the range of 398-513 cm^{-1} for SC and 380-517 cm^{-1} for QC specimens of unirradiated and irradiated samples. The difference in the band positions is expected because the difference in Fe^{3+}-O^{-2} distances for octahedral and tetrahedral complexes. From the IR spectra it is noticed the frequency bands ν_1 and ν_2 are shifted to higher frequencies with an increasing Al-Cr concentration for both SC and QC systems before and after irradiation. The band ν_1 is attributed to the stretching vibrations of Fe^{3+}- O^{2-}, Cu^{2+}- O^{2-} in the tetrahedral complexes and the ν_2 band to that of Fe^{3+}- O^{2-}, Cu^{2+}- O^{2-}, Cr^{3+}- O^{2-} in the octahedral complexes. The shifts occur in the frequency bands ν_1 and ν_2 for each tetrahedral and octahedral site are due to the perturbation occurring in the Fe^{3+}-O^{2-} band by introducing Al and Cr ions.

The IR spectra of SC and QC $CuFe_2O_4$ indicates shoulders/splitting around the main absorption band ν_2 and it can be seen up to Al-Cr content x = 0.2 and 0.4 while

it is disappeared completely for x = 0.6 and 0.8 of unirradiated samples. The shoulders/splitting bands $\nu_{sh/sp}$ around ν_2 become more pronounced in QC unirradiated samples as compared to SC unirradiated ones. One can also obtain information about the presence/absence of Fe^{2+} ions in the sample from IR spectra in addition to the valency and the band position. The presence of Cu^{2+} and Fe^{2+} ions in ferrite can cause a shoulder or splitting of the absorption band. Local deformation can occur due to Jahn Teller effect [6D.12] in Cu^{2+} and Fe^{2+} ions which leads to a non-cubic component of the crystal field potential and hence to splitting of the bands. Since, such effect is observed in present case, around ν_2 bands, conforming presence of Fe^{2+} ions. Furthermore, the Cu^{2+} ions mainly the octahedral sites and some fraction go into tetrahedral sites. According, this shoulder/splitting can be attributed to the vibration of Cu^{2+}- O^{2-} in tetrahedral complexes.

The irradiation of the SC-$CuFe_2O_4$ sample causes a shift in the absorption bands ν_1 and ν_2 slightly towards lower frequencies. However, for QC-$CuFe_2O_4$ sample the shift in the ν_1 band to lower frequency and ν_2 bands to higher frequency is observed. Moreover, the IR spectra of irradiated $CuFe_2O_4$ with substitution of Al and Cr showed shifting in the absorption bands ν_1 and ν_2 to higher frequencies as well as an increase in shoulders/splitting with respect to unirradiated samples in both systems. The IR spectra results as irradiation shifts ν_1 and ν_2 to higher frequencies, due to the creation of a large ionic radius of Fe^{2+} induced by irradiation on both octahedral and tetrahedral sites.

6D.3 Swift Heavy Ion Irradiation effects on Electrical, Dielectric and Impedance properties of the system $CuAl_xCr_xFe_{2-2x}O_4$

Among different spinel ferrites, the Cu-containing spinel ferrite is very special due to the characteristics of Jahn-Teller (JT) distortion. The Jahn-Teller (JT) distortion in copper ferrospinel has established that the critical number of octahedral site Cu^{2+} ions per formula unit for a cooperative distortion to tetragonal symmetry at room temperature is 0.8 [6D.13]. The number of research articles related to the electrical and dielectric properties is available in literature covering various aspects of pure and substituted Cu-containing spinel ferrites. The information on the electrical conductivity of Cr-substituted $CuFe_2O_4$ [6D.14] and thermoelectric power studies of Zn-substituted $CuFe_2O_4$ [6D.15] are available in the literature. However, the information is obtainable on the electrical conductivity and cation distribution on Cu-

substituted $CdFe_2O_4$ [6D.16], $NiFe_2O_4$ [6D.17] and $CoFe_2O_4$ [6D.18] in the literature. The interesting results were obtained for the dependence of dielectric parameters (ε',ε" and tanδ) on frequency and temperature in Cu-Zn, Cu-Ni and Cu-Mn ferrites [6D.19-6D.21],where the Cu ions showed a large influence upon the dielectric properties. The dielectric behaviour of Cr-substituted $CuFe_2O_4$ as a function of frequency and temperature has explained in the light of the fact that the dielectric polarization process is similar to that of conduction and the appearance of the dispersion peak of two types charge carriers [6D.22]. The dielectric properties of Cu-Cd ferrites were investigated by Vaingankar et al [6D.23, 6D.24]. Detail study on compositional and temperature dependent electrical properties of $Zn_xCu_{1-x}FeCrO_4$ [6D.25] and the compositional, temperature and frequency dependence of dielectric behaviour of the same system [6D.26] have been carried out.

To our knowledge no work has been reported on compositional, temperature and frequency dependent electrical and dielectric behaviour of Al-Cr substituted $CuFe_2O_4$ with the effect of thermal history and irradiation. Therefore, aim of the present work is to study the mechanism of dielectric polarization and conduction, which is part of our work to study the effect of thermal history and irradiation on structural and magnetic properties of $CuAl_xCr_xFe_{2-2x}O_4$ system.

The variation in dc resistivity (ρ_{dc}) of slow-cooled (SC) and quenched (QC) $CuAl_xCr_xFe_{2-2x}O_4$ as a function of concentration of Al and Cr is not monotonic at room temperature (Table 6D.7). A maximum resistivity is observed at x = 0.0 for the SC unirradiated sample, while it is maximum at x = 0.6 for the QC unirradiated sample. It is interesting to note that the dc resistivity (ρ_{dc}) for SC unirradiated sample is found sudden drop at x = 0.2 and further increase in Al-Cr concentration enhance the resistivity, but the value of ρ_{dc} for all Al-Cr substituted samples (x >0.0) is lower with corresponding to x = 0.0. Whereas the ρ_{dc} increases gradually from x = 0.0 to 0.6 for QC unirradiated samples and at x = 0.8 is slightly reduced.

For irradiated samples, the ρ_{dc} is found to increase with increasing Al-Cr concentration (x), except those with x = 0.6 for SC irradiated sample and x = 0.8 for QC irradiated sample. The increase in ρ_{dc} at higher Al-Cr concentration may be due to the replacement of Fe^{3+} by Al^{3+} and Cr^{3+} in $CuAl_xCr_xFe_{2-2x}O_4$ system reduces conduction through the octahedral sites and presence of Al^{3+} and Cr^{3+} that dose not contributes to conduction but acts as a scattering centre at B-sites. Also, the dc

resistivity of ferrites are determined by several mutually related factors, such as density, porosity, grain size, crystal structure perfection, microstructural homogeneity and impurity level. It is know that the polycrystalline ferrite are usually characterized by conductive grains surrounded by less conductive grain boundaries, among which pores of various size and shapes are distributed. The presence of porosity usually increases the dc resistivity of ferrites, as air/vacuum is a good insulator, and if the pores are closely trapped and uniformly distributed. Otherwise, porosity can reduce the resistivity of ferrites. In the present samples, the porosity of the SC and QC samples are found to increase with Al-Cr concentration (x) for before and after irradiation (Table 6D.2), apart from x = 0.2 (SC) and x = 0.4 (QC) samples accordingly the change observed in ρ_{dc} with Al-Cr concentration before and after irradiation.

All irradiated samples show higher value of ρ_{dc} as compared to unirradiated ones, excluding the SC irradiated samples x = 0.0 and 0.6. For particular SC irradiated sample x = 0.6 the porosity is higher than the unirradiated sample however the value of ρ_{dc} is found lower. This may be due to the pores were large in size and located at grain boundaries, so that electric current would flow around porosity and therefore the porosity did not affect the resistivity. Another factor that greatly reduces the ρ_{dc} of the present SC irradiated samples (x = 0.0 and 0.6) is the formation of Fe^{2+} ions after irradiation. It is also noticed that the porosity of irradiated samples x = 0.2, 0.4 (SC) and x = 0.0 (QC) is found lower than the unirradiated samples but at the same time ρ_{dc} is increased. The increased bulk density values after irradiation also help in explaining the higher ρ_{dc} value obtained for irradiated samples x = 0.2, 0.4 (SC) and x = 0.0 (QC) (Table 6D.2). The high density ferrite containing Cu^{2+} ions is expected to resist the oxidation of Cu^{2+} to Cu^{1+} and Fe^{3+} to Fe^{2+} and helps in decreasing the hopping conduction of electrons/holes from Fe^{3+} to Fe^{2+}, Cu^{2+} to Cu^{1+} and Fe^{3+} to Fe^{4+}, Cr^{3+} to Cr^{4+} thereby increasing its resistivity.

In Fig. 6D.7 the variation of $\log_{10}\rho_{dc}$ with $10^3/T$ has been studied for the unirradiated and irradiated ferrites $CuAl_xCr_xFe_{2-2x}O_4$ (SC and QC) where x = 0.0 to 0.8, step-0.2 in the temperature range 300K to 800K. The dependence of the dc resistivity of the material on the temperature is given by the Arrhenius relationship [6D.27]. The Arrhenius plot (Fig. 6D.7) gives the different region indicative of different types of electrical behaviour. It is interesting to note that the nature of curve

for compositions x = 0.0 and 0.2 is different from that for x $\geq$ 0.4 samples. For the former ferrites $\log_{10}\rho_{dc}$ versus reciprocal of temperature curve consist of three distinct regions and two breaks, while for the x = 0.4 and 0.6 have two slopes with single transition temperature. Similar type of behaviour has been observed for $Cu_xNi_{1-x}Fe_2O_4$ system [6D.17]. They have been ascribed that the region-I extending from room temperature to first break is characterized by partly compensated Cu-ferrites. There is a formation of accepter and donor centres in the ferrite lattice during the sintering process due to loss of oxygen evidenced by chemical analysis of samples, which leads to the type of conduction observed. In the region-II, the explained on the basis of phase transition from tetragonal to cubic form and cation transfer and the change in the conduction mechanism in the region –III is due to the transition of the crystal from ferrimagnetic to paramagnetic state. S. A. Patil et al [6D.28] have discussed electrical resistivity and thermoelectric measurements on the system $Cu_{1+x}Zr_xFe_{2-2x}O_4$ and explained the nature of charge carriers and the possible conduction in this system. They have been observed three regions and two breaks are associated with a change in activation energy. In the low temperature range, the conduction is extrinsic while it is intrinsic at high temperatures. The activation energy in high temperature region consist of two part associated with the generation of electrons and the other part associated with the hopping of polarons between equivalent sites. Furthermore, Ghani et al [6D.29] observed three regions in the temperature variation of resistivity for Cu-Ni ferrites. They attributed the conduction mechanism in the first region to the presence of impurity, in the second region to the phase transition and in the third region to magnetic disorder. Similar results have been reported for Li-Cu [6D.30] and Cu-Co [6D.18] mixed ferrites. The conduction process in the present material may be due to the grains, grain structure and porosity in region-I, crystal structure changes in region –II and magnetic disorder in region-II.

The effect of Li-ions irradiation on the electrical resistivity of the ferrites has studied using a dose of 5 x 10^{13} ions/cm^3 with 50 MeV energy. The plots of $\log_{10}\rho_{dc}$ against $10^3/T$ for the irradiated samples showed the same behaviour as those of unirradiated ones. The resistivity data of the irradiated samples are summarized and also given with unirradiated ones in Table 6D.7. The following points can be shown.

(i) A change occurs in the dc resistivity ρ_{dc} values of SC and QC $CuAl_xCr_xFe_{2-2x}O_4$ (x = 0.0 to 0.8 step – 0.2) ferrites after irradiation. It is found that the dc

resistivity ρ_{dc} values are enhanced for all the compositions of both SC and QC systems, except those with x = 0.0 and 0.6 (SC) in the same measured temperature range with corresponding to unirradiated ones.

(ii) The Nèel temperature (T_N) shifts towards higher temperature for irradiated ferrites with x = 0.0, 0.4, 0.6 (SC-QC) samples, whereas contrast x = 0.2 (SC-QC) T_N is found to shift towards lower temperature as compared to the unirradiated ones.

(iii) It is interesting to note that, in the case of QC unirradiated and irradiated pure $CuFe_2O_4$, electrical resistivity (ρ_{dc}) values found to abruptly increase and again decrease in order to Nèel temperature and for the composition x = 0.4 (QC) irradiated ferrite, ρ_{dc} values are found to rapidly drop in order to Nèel temperature (T_N).

As seen in the plots, the electrical resistivity (ρ_{dc}) decreases with increase in the temperature till the highest temperature of these measurements is reached. There is a remarkable raise in the ρ_{dc} at T = 483K (unirradiated) and T = 603K (irradiated) then again start to drop in case of QC-$CuFe_2O_4$. There is remarkable drop in ρ_{dc} also found after irradiation for particular QC irradiated sample x = 0.4 with respect to unirradiated ones. The electrical behaviour of QC-$CuFe_2O_4$ and QC irradiated sample x = 0.4 at high temperature is due to the change in the electronic states of Cu^{2+} increasing the degeneracy of the orbitals. It is known that five d orbitals on the octahedral ligand field are split into a lower triplet t_{2g} and upper doublet e_g. The electronic configuration of the d^9 orbital of Cu^{2+} is $(t^6_{2g})(e^2_g)e^1_{g,}$ where the parenthesis denote paired electron spins. When Cu^{2+} is subjected to the tetrahedral ligand field, its configuration will be given by $(e^4)(t^4_2)(t^1_2)$. Orbitally degenerate electron configurations of d states with unpaired spins are unstable in the ligand field. Therefore, under the quenching and irradiation the change in the electronic state result in a structural phase transition reflected in temperature dependence of electrical resistivity. Thus it is quite possible that tetragonal $CuFe_2O_4$ undergoes phase transition at quenching while no such phase transition is detected in case of SC-$CuFe_2O_4$ in the same temperature range. This reveals the role of John-Teller cation Cu^{2+} making the crystal structure quenching and irradiation sensitive compared to SC-$Cu^{2+}Fe_2{}^{3+}O_4$. This can be distinguished also by our XRD results (Fig. 6D.2a-2c, Table

6D.2), the unirradiated and irradiated $CuFe_2O_4$ samples disappeared tetragonality and appeared cubic single phase after quenching.

Table 6D.7 shows the value of the activation energies for the system under consideration calculated by fitting the data points of the curve in Fig. 6D.7 according to Arrhenius equation. The activation energy before and after irradiation for all the composition in the order of ~ 0.2 eV, is greater than the ionization energy 0.1 eV of donor or accepter but the smaller than the polaron hopping energy ~0.5 eV. This suggests that the conduction phenomena in the present systems are due to the electron transition such as $Fe^{3+} \Leftrightarrow Fe^{2+}$ and $Cu^{2+} \Leftrightarrow Cu^{1+}$. The obtained data of E_f and E_p show that the activation energy of electric conduction in paramagnetic region (E_p) is higher than that in the ferrimagnetic region (E_f). This could be related to the disordered state in the paramagnetic region with respect to the ordered in the ferrimagnetic region. The value of activation energy (E_f and E_p) for all the samples is found to higher than the unirradiated ones, apart from x = 0.0 and 0.6 (SC) samples.

The irradiation by Li-ion generates some vacancies at different depth and localized defects, which acts as trapping centers. The enhancement of dc resistivity and activation energy after irradiation may be attributed to the hindering of $Fe^{3+} \Leftrightarrow Fe^{2+}$ and $Cu^{2+} \Leftrightarrow Cu^{1+}$ conduction process by trapping centers. The transition temperature is increased is results of increasing the ordered region after irradiation. This is the arrangement of the magnetic dipoles takes place due to energy of irradiation on expanse of paramagnetic region, though increasing Nèel temperature (T_N).

The calculated values of Fermi energy E_F as a function of temperature for two values of A (A = 0, 2) are depicted in Fig. 6D.8. The extrapolated values of Fermi energy $|E_F|$ to T = 0K give up the values of E_F (0) (Table 6D.7), which are comparable with those of the activation energy of ferrimagnetic region (E_f). The Fermi energy $|E_F|$ of SC samples are increased with increasing Al-Cr concentration (x) before and after irradiation but there is no systematic variation observed in QC samples with Al-Cr concentration (x). All SC and QC irradiated samples show higher values of Fermi energy $|E_F|$ with respect to the unirradiated ones, except for x = 0.6 (SC) and 0.2, 0.6 (QC) samples. This suggests alteration in effective density state of electrons in conduction bands by irradiation.

The compositional variation of the Seebeck coefficient (α) as a function of temperature for unirradiated and irradiated $CuAl_xCr_xFe_{2-2x}O_4$ (SC and QC) ferrites are shown in Fig. 6D.9. The present system have established all the samples except those with x = 0.0 QC unirradiated as well as irradiated are n-type semiconductors, whereas QC sample x = 0.0 shows a p-type semiconductor before and after irradiation. It is reported that copper ferrite acts both as n- and p-type semiconductor [6D. 31, 6D.32]. In general in the present system following types of conduction may be expected:

(i) $Fe^{2+} \Leftrightarrow Fe^{3+}$ (n-type)

(ii) $Cu^{2+} \Leftrightarrow Cu^{1+}$ (n-type)

(iii) $Fe^{4+} \Leftrightarrow Fe^{3+}$ (p-type)

(iv) $Cr^{3+} \Leftrightarrow Cr^{4+}$ (p-type)

Our results show a negative value of α confirms n-type charge carriers for both the set of samples, except a positive value of α confirm p- type charge carriers for samples QC x =0.0 before and after irradiation. This provides that the most probable mechanism for n-type conduction is electron hopping between $Fe^{3+} \Leftrightarrow Fe^{2+}$ and $Cu^{2+} \Leftrightarrow Cu^{1+}$ ions. There is also possibility of conduction due to the holes between $Fe^{3+} \Leftrightarrow Fe^{4+}$ and $Cr^{3+} \Leftrightarrow Cr^{4+}$ ions in the system. The observed positive value for x = 0.0 composition of QC system suggests that the conduction process no. (iii) and (iv) are responsible, on the hand in this composition Cr^{3+} ions are absent, thus the responsible conduction process is between $Fe^{3+} \Leftrightarrow Fe^{4+}$ ions. These processes are expected to take place between two adjacent octahedral sites of a spinel lattice. It was also interpreted in copper ferrites that Cu^{2+} on A-site might have acted occur p-type conduction [6D.33].

It is observed that the rate of $|\alpha|$ increases within the temperature range studied is lower for SC-$CuFe_2O_4$ unirradiated samples as compared to QC-$CuFe_2O_4$ unirradiated sample, while it is found to higher for all Al-Cr substituted SC unirradiated samples with respect to QC unirradiated ones. The magnitude of $|\alpha|$ shows random behaviour with Al-Cr content (x) for both set of samples before and after irradiation. The first phenomena suggest that quenching hinders the accumulation of charges and second phenomenon may be due to random formation of Cr^{4+} and Fe^{4+}. The Seebeck coefficient $|\alpha|$ increases gradually with increasing temperature for both sets of the samples before and after irradiation. The variation of $|\alpha|$ with temperature can be explained on the basis of the fact that in the case of n-type

of semiconducting materials, the hot surface becomes positively charged, as it loses some of its electrons. The cold surface of the semiconductors becomes negatively charged due to the diffusion of free electrons from the hot portion. On increasing temperature conduction mechanism $Cu^{1+} + Fe^{3+} \leftrightarrow Cu^{2+} + Fe^{2+}$ become more probable, generate electrons, accumulated on cold surface, as a result potential difference (ΔV) developed, which increases $|\alpha|$ with temperature. The rate of $|\alpha|$ within the temperature range studied is decreased for SC-QC irradiated samples than the unirradiated samples; suggest that the generation of defects by irradiation hinders the accumulation of charges.

The charge carrier concentration (n_c) calculated from Seebeck coefficient values as a function of temperature is shown in Fig. 6D.10. It is interesting to note that the nature of n_c for x = 0.0 (SC-QC) concentration is different to that of x > 0.0 (SC-QC) samples. For x = 0.0 (SC-QC), n_c remain almost constant and independent of temperature, while for x = 0.2-0.8 (SC-QC) n_c decreases with increasing temperature. The value of n_c is found to higher for all SC and QC irradiated samples as compared to unirradiated samples may be due to the more charge carriers developed by electronic rearrangement of cation under irradiation.

The temperature dependence of dielectric constant (ε'), complex dielectric constant (ε'') and dielectric loss tangent (tanδ) at different applied frequency (10kHz-1MHz) for all the compositions of unirradiated and irradiated $CuAl_xCr_xFe_{2-2x}O_4$ (SC and QC) ferrite system are shown in Figs. 6D.11a-11e, 6D.13a-13e and 6D.14a-14e, respectively. It is seen that the general trends of ε' and ε'' appreciably increase when the temperature is increased for both SC and QC $CuFe_2O_4$ sample, which is due to the polarization effect. The space charge polarization is governed by the number of space charge carriers. With the rise in temperature the number of charge carriers increases, resulting in enhanced build-up space charge polarization and hence an increase in the ε' and ε''.

It can be noticed that the dielectric constant (ε') continuously increases with temperature until a maximum is reached. Afterward, on further increase in temperature, the dielectric constant (ε') shows a sharp decreases for the SC and QC unirradiated samples with x = 0.4, 0.8 and 0.6 (SC) in the particular higher frequency range 100kHz-1MHz. As the frequency of the applied field is increased, the temperature at which a drop in ε' occurs shifts towards higher temperatures. Such an

abnormal (peak) behaviour of ε' against T was observed in Cu-Zn, Cu-Mn and Cu-Ni ferrites [6D.19], where ε' increases with increasing temperature having a maximum peak (hump) that shifts towards higher temperature with increasing frequency. Besides at higher frequencies, ε' attain a stable value for unirradiated samples x = 0.2 (SC-QC) and x = 0.6 (QC), after which ε' starts to decrease with increasing temperature. For the lower frequencies, the polarization is increased by electric field and also by the increase in the number of charge carriers with increasing temperature. Both effects (increasing temperature and frequency) tend to increase ε'. For the higher frequencies, the electric field will have more effect than will the temperature. This means that saturation in the generation of charge carriers was reached at high temperature and high frequency. Therefore, the electronic exchange cannot follow the field variation and hence the dielectric constant (ε') decreases accordingly [6D.34]. The value of dielectric constant (ε') for QC unirradiated and irradiated samples x = 0.0 and 0.2 is found to lower and higher for the samples with x > 0.2 than the SC unirradiated and irradiated samples in the measured temperature range at different frequencies.

The variation of ε' as a function of temperature at different frequency for SC and QC irradiated $CuAl_xCr_xFe_{2-2x}O_4$ ferrites is also illustrated in Fig. 6D.11a-11e. In SC irradiated $CuFe_2O_4$ shows same behaviour as like unirradiated sample, ε' increases with increasing temperature up to 600K then becomes temperature and frequency independent but the magnitude of ε' is increased than the SC unirradiated $CuFe_2O_4$. Furthermore, QC irradiated $CuFe_2O_4$ sample also exhibits general increasing trend in ε' with temperature up to frequency 500kHz. At frequencies 800kHz and 1MHz, ε' achieve a stable value up to 400K after that ε' starts to decrease with increasing temperature.

The magnitude ε' of QC irradiated $CuFe_2O_4$ sample is also found to higher with compared to unirradiated ones. The value of dielectric constant (ε') for Al-Cr substituted SC-QC irradiated $CuFe_2O_4$ (x > 0.0) is found to decrease with respect to unirradiated samples, except those with x = 0.2 (SC) sample. The irradiated samples x = 0.2 (SC), 0.4 (SC) and 0.8 (SC & QC) also exhibit abnormal behaviour (peak or hump) in the measured temperature range at different frequencies 50kHz to 1MHz. After irradiation this peak (hump) is shifted towards lower values of temperature as the frequency increases. The QC irradiated samples x = 0.2, 0.4 and 0.6 also attain a

stable value in ε' with temperature up to 450K then it starts to decrease with increasing temperature.

The frequency dependence of ε' at different temperature for unirradiated and irradiated $CuAl_xCr_xFe_{2-2x}O_4$ (SC and QC) ferrites is shown in Fig. 6D.12a-12e. The figure illustrate that, for SC unirradiated and irradiated $CuFe_2O_4$ samples, the dispersion peak in the dielectric constant ε'_{max} (abnormal behaviour) is observed at room temperature (approximately at the lower range of the measured frequency) and shifted towards higher frequency as temperature increases 303K, 373K, 473K and 573K. This kind of dielectric peak ε'_{max} is disappeared and the normal dielectric behaviour become predominant for the QC unirradiated $CuFe_2O_4$ sample. In normal dielectric behaviour the dielectric constant decreases with increasing frequency until it reaches a nearly constant value because, beyond a fixed frequency of the electric filed, the electronic exchange cannot follow the alternating field, so it reaches a constant value. For QC irradiated $CuFe_2O_4$ sample also show normal dielectric behaviour at selected temperatures 288K and 373K but there is anomaly again observed at higher temperatures 473K and 573K in the measured frequency range. The SC and QC irradiated $CuFe_2O_4$ samples are found to higher magnitude of dielectric constant ε' at room temperature (303K) and lower magnitude at higher temperatures (373K, 473K and 573K) with corresponding to unirradiated samples. The dielectric dispersion peak ε'_{max} (abnormal behaviour) is also observed in all Al-Cr substituted $CuFe_2O_4$ samples, apart from QC unirradiated and irradiated sample x = 0.4 (at T = 301K) and QC irradiated sample x = 0.6 (at T = 298K, 373K and 473K). After irradiation, All Al-Cr substituted $CuFe_2O_4$ irradiated samples show lower magnitude in ε' with respect to unirradiated ones, except for x = 0.8 (QC) sample. The peaking behaviour of the dielectric constant with frequency and temperature was observed for Cu-Ni, Cu-Mn and Cu-Zn ferrites [6D.19] and Cu-Cr ferrites [6D. 22].

Our results show abnormal behaviour before and after irradiation, which can be explained in the light of the Rezlescu model [6D.19]. According to this model in the ferrites containing copper, just like present system under investigation, an exchange $Cu^{1+} \leftrightarrow Cu^{2+}$ exists. There is an amount of Cu^{1+} ions, which causes an important modification of electrical and magnetic properties of ferrites [6D.35, 6D.36]. It is reported that copper ferrite acts both as n- and p-type semiconductors [6D.31, 6D.32]. It is known that the copper ferrites exhibit p-type electrical

conduction obtained by removing holes. The appearance of p- carriers can be ascribed to the reduction tendency of the $Cu^{1+} \leftrightarrow Cu^{2+}$ ions at about 900-950^{o}C during the sintering process [6D.31]. They assumed that for the formation of each pair of Cu^{1+} ions an oxygen atom is eliminated, an equivalent quantity of metal ions must occupy the interstitial sites. The simple presence of Cu^{1+} ions dose not explain the p-conduction since they act as n-carriers. But by assuming that the interstitial cations act as acceptor centers, the p-carriers may be identified as holes on oxygen ion sites. They also supposed that the local displacements of p-carriers in the direction of the external electric field take part in the polarization.

The abnormal dielectric behaviour of the ferrites containing copper is due to the collective contribution of the two types of carriers, p- and n, to the polarization. The contribution of the p-carriers is lower than that obtained by the electronic exchange and it has opposite sign. In addition, since the mobility of p-type carriers is lower than that of n-type carriers, their contribution to polarization will decrease more rapidly. The maximum of the ε' is shifted towards higher frequency with increasing temperature due to the increasing hopping frequency of charge carriers.

The abnormal behaviour of the temperature dependence of ε' is probably due to same reason. The contribution of the two types carriers, n- and p- to polarization depend on temperature. Since the influence of temperature on electronic exchange $Fe^{2+} \leftrightarrow Fe^{3+}$ and $Cu^{1+} \leftrightarrow Cu^{2+}$ is more pronounced than that on the displacement of p-carriers ($Fe^{3+} \leftrightarrow Fe^{4+}$ and $Cr^{3+} \leftrightarrow Cr^{4+}$), ε' will increase rapidly with increasing temperature. But above certain temperature, which naturally depends on the copper content, the p-transitions become important and thus ε' will begin to decrease as a result of two contribution with opposite signs [6D.26]. Murthy et al [6D.37] have been reported that the temperature dependence anomaly also can be ascribed to the diffused tetragonal to cubic phase transitions normally observed in Cu-ferrites in the temperature range 423-573K.

The thermal variation of complex dielectric constant (ε'') and dielectric loss tangent (tanδ) of unirradiated and irradiated samples for the compositions x = 0.0 to 0.8 (SC-QC system) at different frequencies 10kHz to 1MHz are represented in Figs. 6D.13a-13e, 6D.14a-14e, respectively. It is observed that for all the compositions and applied frequencies ε'' and tanδ increases with increasing temperature before and after irradiation. It is notice that the ε'' for the QC unirradiated sample with x = 0.8,

initially decrease up to 375K then increases with increasing temperature. The value of ε'' is decreased for all the composition of SC and QC irradiated samples with compared to unirradiated samples, except for x = 0.0 (QC), 0.4 (SC-QC) samples.

The temperature dependence tanδ also increase with increasing temperature, this is natural character of semiconductors. It is observed that the tanδ of SC-$CuFe_2O_4$, initially decrease up to 600K subsequently increases with increasing temperature at different frequencies 500kHz, 800kHz and 1MHz before and after irradiation. Similar behaviour also recognized for QC unirradiated sample with x = 0.8 in the frequency range 50kHz to 1MHz.

The irradiated samples with compositions x = 0.0 (QC), 0.2 (SC-QC), 0.4 (SC-QC), 0.6 (SC) exhibit higher values of tanδ, while for x = 0.0 (SC), 0.6 (QC) and 0.8 (QC) lower values with corresponding to unirradiated samples. There is no remarkable change in tanδ is observed for the irradiated sample x = 0.8 (SC) with respect to unirradiated ones. After irradiation, there is also remarkable peak form in the temperature dependence tanδ curve for sample x = 0.4 (QC) in the frequency range 10kHz to 500kHz. As frequency increases, the intensity of this peak is increased and shifts toward higher temperatures. As mention above the dielectric polarization is increased with increasing temperature, as a result ε'' and tanδ increase. The observed increase in tanδ with temperature suggests that material becomes more and lossy on increasing temperature. The rate of dielectric loss within the temperature studied is lower for x = 0.0, 0.4 and 0.6 (SC) and higher for x = 0.2, 0.8 (SC) as compared to QC samples before and after irradiation.

The plot of complex dielectric constant ε'' against frequency for unirradiated and irradiated samples is shown in Fig. 6D.15a-15e. As ε'' is associated with the dielectric losses that occurs in materials. It is clear that for both SC and QC systems the dielectric loss in form of ε'' (ε''= ε'tanδ) shows continuously decreasing trend with rise in frequency. This behaviour of the dielectric may be explained qualitatively by the supposition that of the mechanism of the polarization process in ferrite is similar to that of the conduction process. By the electronic exchange $Fe^{2+} \Leftrightarrow Fe^{3+} + e^-$, $Cu^{2+} + e^- \Leftrightarrow Cu^{1+}$, one obtain local displacement of electron in the direction of the applied field. These displacements determine the polarization of the ferrite. It is known that the effect of polarization is to reduce the field inside the medium. The decrease in the polarization (the dielectric constant ε') with increasing frequency is

due to the fact that, beyond a certain frequency of electric field, the electronic exchange $Fe^{2+} \Leftrightarrow Fe^{3+}$ and $Cu^{2+} \Leftrightarrow Cu^{1+}$ ions cannot fellow the alternating field. Therefore, the dielectric constant (ε') and complex dielectric constant (ε'') of a substance may decrease substantially as the frequency is increased [6D.38, 6D.34]. The value of ε'' is found to lower for all irradiated samples, excluding for irradiated samples with x = 0.0 (SC-303K, 373K), 0.4 (SC-QC) and which is more pronounced in the measured frequency range 100Hz to 10kHz with compared to unirradiated specimens. The value of ε'' for unirradiated and irradiated samples are found to coincide each other above 10kHz at all different temperatures. After irradiation, there is no remarkable change observed in ε'' for sample x = 0.6 (SC).

Fig. 6D.16a-16e correlates the a. c. resistivity in term of $\log_{10}\rho_{ac}$ and the reciprocal of the absolute temperature for different frequencies of the investigated samples. The figure shows that the a. c. resistivity of all the samples are decreased by increasing both applied frequency and measuring temperature, except for QC unirradiated sample x = 0.8. For the composition with x = 0.8 (QC-unirradiated sample), the a. c. resistivity initially increases with increasing temperature within the lower temperature range 300K- 420K; thereafter it follows the conventional behaviour of decreasing resistivity with increase in temperature. This is characterized by the metallic conductivity in the temperature range 300K- 420K. The change of slope at Curie temperature is general observation in ferrites, in present case the temperature at which change in slope takes place is corresponding to Curie temperature before and after irradiation. The large number of charge carriers (electron/holes) that are generated during the transformation process of valences of both Fe^{3+} and Cu^{2+} to Fe^{2+} and Cu^{1+}, Fe^{3+} to Fe^{4+} and Cr^{3+} to Cr^{4+} respectively will raise the conduction state of the present system. This means that the resistivity of the systems will decrease with increasing temperature due to generation of such electrons/holes. After irradiation, All samples are found higher value of ρ_{ac} with respect to unirradiated samples in the measured temperature range at different frequencies, apart from x = 0.0 (QC), 0.4 (SC-QC) and 0.6 (SC).

Fig. 6D.17a-17e shows the variation of a. c. resistivity ($\log_{10}\rho_{ac}$) with frequency measured at different temperatures of present samples. All the unirradiated and irradiated samples show decrease in ρ_{ac} with the increasing frequency from 100Hz to 1MHz, which is the normal behaviour of ferrites. Initially, the ρ_{ac} remain

constant up to 10kHz then it is start to decrease at high frequencies. The conduction mechanism in the present system on the basis of hopping of charge carriers between Fe^{3+} - Fe^{2+}, Cu^{2+} - Cu^{1+}, Fe^{3+}- Fe^{4+} and Cr^{3+}- Cr^{4+} ions on octahedral sites. The increase in frequency of the applied field enhances the hopping of charge carriers resulting in an increase in the conduction process thereby decreasing resistivity. At high frequencies ρ_{ac} becomes small because the hopping frequency no longer follows the external applied field and lags behind it. From the figure, it is clear that all irradiated samples have the same trend as described before but the a. c. resistivity values for irradiated samples at all rate are higher than the unirradiated ones, excluding irradiated samples with x = 0.0 (SC-303K and 373K, QC-473K and 573K), 0.4 (SC-QC) and 0.6 (SC) in the same measured frequencies.

The increase in a. c. resistivity ρ_{ac} after irradiation is due to the formation of point/clusters of defects, which act as trapping centers for the charge carriers. It is also possibility to the formation of Cu^{1+}-defects leads to decrease of the conductivity value due to the smaller rate of electron exchange between Cu^{1+}/Fe^{2+} or Cu^{1+}/Fe^{3+} compared to that between Fe^{2+}/Fe^{3+}, according to the orbital consideration [6D.39]. On the other hand, the irradiation energy helps the alignment of charge carriers (hopping electrons/holes) which are disturbed due to thermal energy and applied field and accordingly ρ_{ac} is found to decrease with compared to unirradiated some of the samples. A drastic change in ε', ε'' and tanδ after irradiation can be explained in the view of the structural changes as well as redistribution of cation under irradiation, which may be modify the ratio of Fe^{2+}/Fe^{3+}, Cu^{1+}/Cu^{2+}, Cr^{3+}/Cr^{4+} on the octahedral sites as a consequences of the hopping process and polarizability.

The variation of real (M') and imaginary (M'') part of dielectric modulus with frequency at different temperature are shown in Fig. 6D.18a-18e. It can be seen that the M' and M'' increases with increasing frequency indicating change in interaction between charge carriers and relaxation rate with frequency at different temperatures before and after irradiation. Irradiated samples with x = 0.0, 0.6 (QC) exhibit a pronounced relaxation hump (peak) for M''(f) curve that moves towards higher frequencies on heating with respect to unirradiated samples. Similar relaxation hump (peak) observed only in M''(f) curve unirradiated sample x = 0.4 (QC) and shifted towards higher frequencies as the temperature increases, which means an increase in relaxation rate because of the thermal activation of the charge carriers. The non-

occurrence of the M''(f) peak for another samples may be due to the fact that it occurs above the frequency range studied. The dielectric modulus spectra of M'(f) versus M''(f) at different temperature for SC and QC both the system are depicted in Fig. 6D.19a-19e. All the samples show a straight line with large slope, which do not obtain complete single semicircular arc in the measured frequency range. It is observed that with increase in temperature the slope of lines decrease before and after irradiation.

The plot of Z' versus Z'' of SC and QC samples before and after irradiation are represented in Fig. 6D.20. At room temperature, Z' versus Z'' plots indicate that the contributions are from the grain (at high frequency side) and the grain boundaries (on low frequency side) respectively for all SC unirradiated sample, apart from x = 0.0 (SC). It is observed that the SC irradiated samples with x = 0.0, 0.4 and 0.8 exhibit half semicircular arc at lower frequencies with grain boundary effect, whereas x = 0.2 and 0.6 give straight line rather than semicircular arc at higher frequencies with grain effect. The QC samples exhibit half single semicircular arc in low frequency side with only contribution of grain boundaries before and after irradiation, except for QC irradiated sample x = 0.6. The QC irradiated sample x = 0.6 gives both grain and grain boundary contributions, respectively.

Fig. 6D.21 shows the variation of real (Z') and imaginary (Z'') part of impedances as a function of frequency at room temperature for both SC and QC samples. It is clear that the Z'' (f) curve do not exhibit maximum peak Z''_{max} for SC and QC unirradiated $CuFe_2O_4$ sample in the studied frequency range, whereas maximum peak (Z''_{max}) appeared for the same samples after irradiation. The SC unirradiated samples with x > 0.0, maximum peak Z''_{max} again appeared with Al-Cr concentration (x) increases, which is disappeared for the samples with x = 0.2 and 0.6 (SC) after irradiation. The QC unirradiated samples x = 0.2, 0.8 and irradiated samples x = 0.2 to 0.8 also show maximum peak Z''_{max} of Z'' (f) curve in studied frequency range.

Conclusion

To study on the influence of thermal history and 50 MeV Li ion irradiation on the structural, magnetic, electric and dielectric properties of diamagnetic Al^{3+} and magnetic Cr^{3+} co-substituted Cu-ferrite, i.e. the system with generic formula $CuFe_{2-2x}Al_xCr_xO_4$ are summarized as under.

The investigations on the influence of thermal history of the spinel system $CuFe_{2-2x}Al_xCr_xO_4$ showed that the slow cooled (SC) and quenched (QC) samples exhibit Jahn-Teller structural tetragonal deformation owing to the presence of Cu^{2+} and Cr^{3+} ions at octahedral sites of the spinel lattice. The study also showed that the distribution of cations is sensitive to the heat treatment of the materials. The swift heavy ion irradiation (SHII) reduces the tetragonal distortion in both the cases and significantly modifies the cation distribution in case of the QC sample. The lattice parameters are found to decrease after the SHII in both the specimens indicated overall unit cell contraction after the SHII. The QC samples show higher values of saturation magnetization compared to the SC ones. No remarkable change has been observed in the magnetization after the specimens subjected to the SHII. The Mössbauer parameters like linewidths and isomer shift values are influenced by both heat treatment and irradiation. Thus, the SHII affects the micro-magnetic properties like "hyperfine interactions" significantly compared to the bulk properties like saturation magnetization. The fluctuation in Curie temperature (T_c) values after the SHII in case of both the SC and QC samples are due to micro-structure disorder.

The remarkable electrical behaviour of QC-$CuFe_2O_4$ and QC irradiated sample x = 0.4 at high temperature is due to the change in the electronic states of Cu^{2+} increasing the degeneracy of the orbital. The activation energy in order to ~ 0.2 eV supported the conduction phenomena in the present systems are due to the electron transition such as $Fe^{3+} \Leftrightarrow Fe^{2+}$ and $Cu^{2+} \Leftrightarrow Cu^{1+}$ rather than ionization or polaron hopping. The present system have established all the samples except those with x = 0.0 QC unirradiated as well as irradiated are n-type semiconductors, whereas QC sample x = 0.0 shows a p-type semiconductor before and after irradiation.

The ferrites containing copper exhibit an abnormal behaviour of dielectric constant ε' as a function of temperature and frequency before and after irradiation and this can be explained on the basis of two types of carriers n- and p- in the polarization process.

References

6D.1 V. A. M. Barbers, Progress in Spinel Ferrites, Elsevier, Amsterdam (1995)

6D.2 A. Hauet, J. Teilet, B. Hannoyer and M. Lenglet, Phys. Status Solidi A **103** (1987) 257

6D.3 J. Chappet and R. B. Frankel, Phys. Rev. **19** (1967) 570

6D.4 U. V. Chhaya, B. S. Trivedi, R. G. Kulkarni and D. R. S. Somayajulu, J. Mater. Sci. Lett. **18** (1999) 1177

6D.5 U. N. Trivedi, K. B. Modi and H. H. Joshi, Pramana **58** (2002) 1031

6D.6 B. S. Trivedi, N. N. Jani, H. H. Joshi and R. G. Kulkarni, J. Mater. Sci. **35** (2000) 5523

6D.7 V. D. Murumbar, K. B. Modi, K. M. Jadhav, G. K. Bichile and R. G. Kulkarni, Mater. Lett. **32** (1997) 281

6D.8 U.N.Trivedi, K.B.Modi, D.S.Kundaliya, A.G.Joshi, S.K.Malik and H.H.Joshi, J. Alloys and Comp. **369** (2004) 58

6D.9 M. A. Amer, M. A. Ahmed, M. K. El-Nimr and M. A. Mostafa, Hyper. Inter. **96** (1995) 91

6D.10 S. A. Mazen, M. H. Abdallah, B. A. Sabrah and H. A. M. Hashem, Phys. Stat. Sol. (a) **134** (1992) 262

6D.11 M. C. Chhantbar, U.N. Trivedi, P. V. Tanna, H. J. Shah, R. P. Vara, H. H. Joshi and K. B. Modi, Ind. J. Phys. **78A(3)** (2004) 321

6D.12 V. A. Potakova, N. D. Zverv and V. P. Romanov, Phys. Stat. Sol. (a) **12** (1972) 623

6D.13 X. X. Tang, A. Manthiram and I. B. Goodenough, J. Sol. Stat. Chem. **79** (1989) 250

6D.14 D. Ravinder, K. Sathi Reddy, P. Mahesha, T. Bhaskar Rao and Y. C. Venudhar, J. Alloys and Comp. **370** (2004) L17

6D.15 D. Ravinder, J. Alloys and Comp. **291** (1999) 208

6D.16 V. R. Kulkarni, M. M. todkar and A. S. Vaingankar, Ind. J. Pure & Appl. Phys. **24** (1986) 294

6D.17 A. M. Sankpal, S. R. sawant and A. S. Viangankar, Ind. J. Pure & Appl. Phys. **26** (1988) 459

6D.18 S. M. Otari, V. B. Kadam, S. R. Sawant and S. A. Patil, Ind. J. Pure & Appl. Phys. **28** (1990) 248

6D.19 N. Rezlescu and E. Rezlescu, Phys. Stat. Sol. (a) **23** (1974) 575,

6D.20 M. A. Ahmed, M. K. El Nimr, A. Tawfik and A. M. El Hasab, J. Magn. Magn. Mater. **98** (1991) 33

6D.21 S. S. Ata-Allah and M. K. Fayek, Hyper. Inter. **128** (2000) 467

6D.22 M. A. El-Hiti, M. A. Ahmed, M. M. Mosaad and S. M. Attia, J. Mag. Mag. Mater. **150** (1995) 399

6D.23 V. R. Kulkarni and A. S. Vaingakar, J. Mater. Sci. **2** (1987) 408

6D.24 C. B. Kolekar, P. N. Kamble, S. G. Kulkarni and A. S. Vaingankar, J. Mater. Sci. **150** (1995) 399

6D.25 K. B. Modi and H. H. Joshi, Ind. J. Phys. **76A(6)** (2002) 543

6D.26 M. C. Chhantbar, K. B. Modi and H. H. Joshi, J. Mater. Sci. **42** (2007) 6989

6D.27 J. Smit, H. J. P. Wijn, Ferrites, Cleaver-Hume Press, London, (1959)

6D.28 S. A. Patil, B. L. Patil, S. R. Sawant, A. S. Jambhale and R. N. Patil, Ind. J. Pure & Appl. Phys. **31** (1993) 904

6D.29 A. A. Ghani, A. I. Eatah and A. A. Mohamed, ICF-3, Japan (1980) 216

6D.30 A. B. Naik, S. A. Patil & J. I. Pawar, Indian Journal of Pure and Applied Physics **27** (1989) 149

6D.31 M. R. Rosenberg, P. Nicoloau, I. Bunget, Phys. Stat. Sol. **15** (1966) 521

6D.32 K. K. Tatankar, V. L. Mathe and K. V. Siva Kumar, Mater. Chem. Phys. **72** (2001) 23

6D.33 N. Nanba and S. Kobayashi, Japanese J. Appl. Phys. **17(10)** (1978) 1819

6D.34 S. A. Mazen, F. Metawe and S. F. Mansour, J. Phys. D: Appl. Phys. **30** (1997) 1799

6D.35 N. Rezlescu and E. Cuciureanu, Phys. Stat. Sol (a) **3** (1971) 1096,

6D.36 N. Rezlescu and E. Cuciureanu, Phys. Stat. Sol (a) **3** (1970) 73

6D.37 K. S. Murthy, R. C. S. Murthy and J. Ghose, Mater. Res. Bull. **104** (1987) 793

6D.38 K. Iwavchi, J. Appl. Phys. **10** (1971) 1520

6D.39 M. A. Mousa, J. Radioanal. Nucl. Chem. Letters **118(1)** (1987) 33

Table 6D.1: Chemical compositions and molecular weight of each specimen of the spinel system: $CuAl_xCr_xFe_{2-2x}O_4$

Content (x)	Compositions	Molecular Weight (amu)
0.0	$CuFe_2O_4$	239.24
0.2	$CuAl_{0.2}Cr_{0.2}Fe_{1.6}O_4$	232.69
0.4	$CuAl_{0.4}Cr_{0.4}Fe_{1.2}O_4$	226.15
0.6	$CuAl_{0.6}Cr_{0.6}Fe_{0.8}O_4$	219.61
0.8	$CuAl_{0.8}Cr_{0.8}Fe_{0.4}O_4$	213.07

Table 6D.2: Lattice constant (a), tetragonality (c/a), Bulk density (d), X-ray density (ρ_x) and percentage of porosity (P) for the unirradiated and irradiated samples of $CuAl_xCr_xFe_{2-2x}O_4$ (SC-QC) systems

Slow-Cooled- $CuAl_xCr_xFe_{2-2x}O_4$							
x	sample	Lattice parameter			Bulk density (d) $(kg/m^3)x10^3$	X-ray density (ρ_x) $(kg/m^3)x10^3$	Porosity (%)
		a (Å)	c (Å)	c/a			
0.0	Unirr	8.404	8.620	1.026	3.6377	5.2221	30.3407
	Irr	8.380	8.401	1.003	3.7577	5.3890	30.2709
0.2	Unirr	8.367	8.585	1.026	4.1904	5.1451	18.5551
	Irr	8.331	8.351	1.002	4.4598	5.3350	16.4057
0.4	Unirr	8.342	8.542	1.024	3.3681	5.0558	33.3815
	Irr	8.310	Cubic	---	3.5896	5.2371	31.4576
0.6	Unirr	8.309	8.517	1.025	2.5106	4.9632	49.4157
	Irr	8.284	8.301	1.002	2.3403	5.1231	54.3189
0.8	Unirr	8.279	8.481	1.024	2.3446	4.8709	51.8656
	Irr	8.258	8.281	1.003	2.0221	5.0140	59.6708
Quenched- $CuAl_xCr_xFe_{2-2x}O_4$							
0.0	Unirr	8.413	Cubic	---	3.7653	5.3392	29.4779
	Irr	8.401	---	---	4.2955	5.3621	19.8914
0.2	Unirr	8.389	8.448	1.007	3.606	5.2011	30.6688
	Irr	8.381	8.398	1.002	3.2054	5.2421	38.8525
0.4	Unirr	8.366	Cubic	Cubic	3.9177	5.1326	23.6701
	Irr	8.359	---	---	3.7524	5.1455	27.0741
0.6	Unirr	8.342	8.400	1.007	2.6581	4.9926	46.7591
	Irr	8.331	8.348	1.002	2.2685	5.0370	54.9630
0.8	Unirr	8.318	8.385	1.008	2.3062	4.8806	52.7478
	Irr	8.299	8.324	1.003	2.0187	4.9389	59.1267

Table 6D.3: Results of XRD intensity analysis and Cation distributions for the unirradiated and irradiated samples of $CuAl_xCr_xFe_{2-2x}O_4$ (SC-QC) systems

Slow-Cooled- $CuAl_xCr_xFe_{2-2x}O_4$								
x	sample	Cation Distribution	I220/I440		I440/I422		I220/I400	
		A-site - B-site	Cal.	Obs.	Cal.	Obs.	Cal.	Obs.
0.0	Unirr	$(Cu_{0.21}Fe_{0.79})[Cu_{0.79}Fe_{1.21}]O_4$	0.91	1.35	1.87	2.12	1.56	2.63
	Irr	$(Cu_{0.214}Fe_{0.786})[Cu_{0.786}Fe_{1.214}]O_4$	0.70	0.73	1.90	1.62	1.54	1.83
0.2	Unirr	$(Cu_{0.29}Fe_{0.71})[Cu_{0.71}Al_{0.2}Cr_{0.2}Fe_{0.89}]O_4$	0.90	1.01	1.70	1.78	1.71	1.63
	Irr	$(Cu_{0.25}Al_{0.02}Fe_{0.73})[Cu_{0.75}Al_{0.18}Cr_{0.2}Fe_{0.87}]O_4$	0.81	0.82	1.63	1.69	1.80	1.89
0.4	Unirr	$(Cu_{0.2}Al_{0.2}Fe_{0.6})[Cu_{0.8}Al_{0.2}Cr_{0.4}Fe_{0.6}]O_4$	0.89	1.18	1.48	1.57	2.98	3.18
	Irr	$(Cu_{0.2}Al_{0.22}Fe_{0.58})[Cu_{0.8}Al_{0.18}Cr_{0.4}Fe_{0.62}]O_4$	0.90	1.01	1.41	1.47	1.99	2.24
0.6	Unirr	$(Cu_{0.30}Al_{0.19}Fe_{0.51})[Cu_{0.70}Al_{0.41}Cr_{0.6}Fe_{0.29}]O_4$	0.86	1.03	1.49	1.45	1.92	1.89
	Irr	$(Cu_{0.40}Al_{0.125}Fe_{0.475})[Cu_{0.6}Al_{0.475}Cr_{0.6}Fe_{0\cdot325}]O_4$	0.74	1.24	2.01	2.10	1.46	1.41
Quenched- $CuAl_xCr_xFe_{2-2x}O_4$								
0.0	Unirr	$(Cu_{0.35}Fe_{0.65})[Cu_{0.65}Fe_{1.35}]O_4$	1.21	1.23	2.51	2.46	1.61	1.87
	Irr	$(Cu_{0.30}Fe_{0.70})[Cu_{0.70}Fe_{1.30}]O_4$	0.55	0.75	2.16	1.98	0.98	0.90
0.2	Unirr	$(Cu_{0.30}Al_{0.05}Fe_{0.65})[Cu_{0.70}Al_{0.15}Cr_{0.2}Fe_{0.95}]O_4$	0.95	1.21	2.33	2.02	1.26	1.02
	Irr	$(Cu_{0.25}Al_{0.10}Fe_{0.65})[Cu_{0.75}Al_{0.10}Cr_{0.2}Fe_{0.95}]O_4$	0.81	0.85	1.45	1.54	2.01	2.25
0.4	Unirr	$(Cu_{0.10}Al_{0.34}Fe_{0.56})[Cu_{0.90}Al_{0.06}Cr_{0.4}Fe_{0.64}]O_4$	0.87	1.06	2.25	2.40	1.30	1.46
	Irr	Not found	-	-	-	-	-	-
0.6	Unirr	$(Cu_{0.40}Al_{0.12}Fe_{0.48})[Cu_{0.60}Al_{0.48}Cr_{0.6}Fe_{0.32}]O_4$	0.75	1.30	1.94	2.01	1.53	1.61
	Irr	$(Cu_{0.42}Al_{0.10}Fe_{0.48})[Cu_{0.58}Al_{0.50}Cr_{0.6}Fe_{0\cdot32}]O_4$	0.76	1.41	1.92	2.06	1.52	1.68

Table 6D.4: Saturation magnetization (σ_s), Magneton number (η_B) and Curie Temperature (T_c) for the unirradiated and irradiated samples of $CuAl_xCr_xFe_{2-2x}O_4$ (SC-QC) systems

Slow-Cooled- $CuAl_xCr_xFe_{2-2x}O_4$					
Content (x)	Sample	σ_s (emu/gm)	η_B^N (μ_B)	η_B^{obs} (μ_B)	T_c(K) ±5K
0.0	Unirr	61.48	2.68	2.63	612
	Irr	63.18	2.71	2.70	666
0.2	Unirr	41.32	1.92	1.72	525
	Irr	40.76	1.80	1.70	484
0.4	Unirr	20.47	1.80	0.83	489
	Irr	22.72	2.00	0.92	513
0.6	Unirr	12.50	1.10	0.49	423
	Irr	12.19	1.25	0.47	441
Quenched- $CuAl_xCr_xFe_{2-2x}O_4$					
0.0	Unirr	84.71	3.80	3.63	555
	Irr	84.51	3.40	3.62	580
0.2	Unirr	57.17	2.50	2.38	482
	Irr	59.39	2.60	2.47	475
0.4	Unirr	29.90	2.40	1.21	420
	Irr	30..00	-	1.22	430
0.6	Unirr	17.92	1.20	0.71	348
	Irr	16.97	1.16	0.67	357

Table 6D.5: Various physical parameters: Lattice constant (a), tetragonality (c/a), Saturation magnetization (σ_s), magneton number (n_B), Nèel temperature (T_N), Nuclear Hyperfine field (H_n), Isomer shift (IS) and Mössbauer line width (Γ) for two compositions x = 0.2 and 0.6 of the unirradiated and irradiated $CuAl_xCr_xFe_{2-2x}O_4$ (SC-QC) systems

Parameter	x = 0.2				x = 0.6			
	Slow-cooled		Quenched		Slow-cooled		Quenched	
	Unirr	Irr	Unirr	Irr	Unirr	Irr	Unirr	Irr
a (Å)	8.367	8.331	8.389	8.381	8.309	8.284	8.342	8.331
c/a	1.026	1.002	1.007	1.002	1.025	1.002	1.007	1.002
σ_s (emu/g)	41.32	40.76	57.17	59.39	12.50	12.19	17.92	16.97
$n_{B\ obs}$ (μ_B)	1.72	1.70	2.38	2.47	0.49	0.47	0.71	0.67
$n_{B\ Nèel}$ (μ_B)	1.92	1.80	2.50	2.60	1.10	1.25	1.20	1.16
T_N (K)	525	484	482	475	423	441	348	357
H_nA-site (T)	37.4	32.2	30.1	27.1	26.9	15.0	12.04	13.5
H_nB-site (T)	39.0	43.3	33.7	39.1	31.3	38.0	27.72	21.4
IS A-site (mm/S)	0.21	0.26	0.24	0.30	0.25	0.30	0.24	0.27
IS B-site (mm/S)	0.24	0.29	0.26	0.34	0.27	0.36	0.29	0.38
QS (B) (mm/sec)	----	0.26	----	0.17	----	0.16	----	0.43
Γ A-site (mm/S)	0.40	1.29	0.43	1.53	0.42	0.64	0.53	-----
Γ B-site (mm/S)	0.45	1.47	0.89	1.76	1.02	1.41	1.49	-----

Table 6D.6a: Positions of IR main absorption bands (ν_1,ν_2) with sholulders/spllitings bands ($\nu_{sh/sp}$) for the slow-cooled (SC) unirradiated and irradiated $CuAl_xCr_xFe_{2-2x}O_4$ system

x	Sample	$\nu_{1sh/sp}(m^{-1})$ x 10^2	$\nu_1(m^{-1})$ x 10^2	$\nu_{1sh/sp}(m^{-1})$ x 10^2	$\nu_{2sh/sp}(m^{-1})$ x 10^2	$\nu_2\,(m^{-1})$ x 10^2	$\nu_{2sh/sp}\,(m^{-1})$ x 10^2
0.0	Unirr	---	568.8	---	411.1	398.7	378.7, 369.1, 352.5, 338.3, 315.4
	Irr	---	559.4	---	---	398.2	379.2, 358.7, 335.9, 319.0, 309.1
0.2	Unirr	---	575.6	---	---	463.8	426.5
	Irr	697.3, 590.6	579.1	---	483.1	466.2	456.7, 426.1, 418.7
0.4	Unirr	---	576.7	---	---	448.7	422.7
	Irr	665.6	577.4	524.4	468.0	449.9	441.5, 426.6, 412.8, 405.5
0.6	Unirr	---	580.9	---	---	463.7	---
	Irr	658.5	608.1	549.4	498.9	454.1	426.8
0.8	Unirr	---	589.0	---	---	512.8	---
	Irr	719.2	604.8	---	---	512.6	483.8, 449.2, 408.9

Table 6D.6b: Positions of IR main absorption bands (ν_1,ν_2) with sholulders/spllitings bands ($\nu_{sh/sp}$) for the quenched (QC) unirradiated and irradiated $CuAl_xCr_xFe_{2-2x}O_4$ system

x	Sample	ν_{1sh} (m^{-1}) x 10^2	ν_1(m^{-1}) x 10^2	ν_{1sh} (m^{-1}) x 10^2	ν_{2sh}(m^{-1}) x 10^2	ν_2 (m^{-1}) x 10^2	ν_{2sh} (m^{-1})x10^2
0.0	Unirr	---	567.3	---	412.4, 397.4	380.6	369.9, 356.2, 338.3, 314.2
	Irr	---	566.1	---	467.3, 417.9, 389.7	382.2	366.4, 344.0, 334.8, 318.7, 308.7
0.2	Unirr	---	573.0	558.8, 540.6	---	471.4	455.7, 434.7
	Irr	605.4, 591.1	570.6	553.3, 537.4, 521.6	497.9, 482.1	466.4	447.3, 418.9
0.4	Unirr	---	579.4	---	---	479.9	464.0, 442.3, 424.7
	Irr	659.8, 609.6	580.9	553.8, 529.3, 503.5	---	475.0	455.9, 426.1, 405.7
0.6	Unirr	---	592.8	---	---	500.6	---
	Irr	698.8	593.5	579.6, 541.4	---	506.3	468.1, 452.1, 413.9
0.8	Unirr	725.0	620.0	---	---	509.3	---
	Irr	703.6	661.3	579.9	---	516.4	488.9, 470.9, 455.1, 441.3, 425.5, 406.5

Table 6D.7: Compositional variation of dc resistivity ($\log_{10}\rho_{dc}$), activation energy (ΔE), Fermi energy ($E_F(0)$) and Nèel temperatures (T_N) for the unirradiated and irradiated samples of $CuAl_xCr_xFe_{2-2x}O_4$ (SC-QC) systems

Slow Cooled-$CuAl_xCr_xFe_{2-2x}O_4$								
x	**Sample**	**$\log_{10}\delta_{dc}$ (ohm.cm) (RT)**	**Activation Energy (eV)**			**Fermi Energy $\lvert E_F\rvert$ eV**	**T_N(K) ± 5K (Resi.)**	**T_N(K) ± 5K (Sus)**
			E_f	**E_p**	**ΔE**			
0.0	Unirr	5.3198	0.253	0.264	0.011	0.006	603	612
	Irr	3.9918	0.144	0.182	0.038	0.041	623	666
0.2	Unirr	2.8191	0.098	0.117	0.019	0.037	533	525
	Irr	4.7549	0.213	0.263	0.050	0.048	473	484
0.4	Unirr	3.9595	0.167	0.247	0.080	0.011	483	489
	Irr	4.2917	0.168	0.229	0.061	0.144	503	513
0.6	Unirr	4.4629	0.159	0.189	0.030	0.687	403	423
	Irr	3.6651	0.141	0.162	0.021	0.268	413	441
0.8	Unirr	4.8304	-	0.165	-	0.128	-	-
	Irr	7.1439	-	0.298	-	0.284	-	-
Quenched-$CuAl_xCr_xFe_{2-2x}O_4$								
0.0	Unirr	3.2266	0.138	0.200	0.062	0.063	563	555
	Irr	3.5438	0.149	0.272	0.123	0.115	600	580
0.2	Unirr	3.3150	0.101	0.212	0.111	0.059	543	482
	Irr	5.2505	0.186	0.190	0.004	0.001	523	475
0.4	Unirr	3.2877	0.110	0.117	0.007	0.007	433	420
	Irr	6.4351	0.178	0.197	0.019	0.062	453	430
0.6	Unirr	3.8549	0.072	0.082	0.010	0.145	353	348
	Irr	7.1768	0.282	0.296	0.014	0.065	375	357
0.8	Unirr	3.7948	-	0.164		0.058	-	-
	Irr	4.0743	-	0.204		0.168	-	-

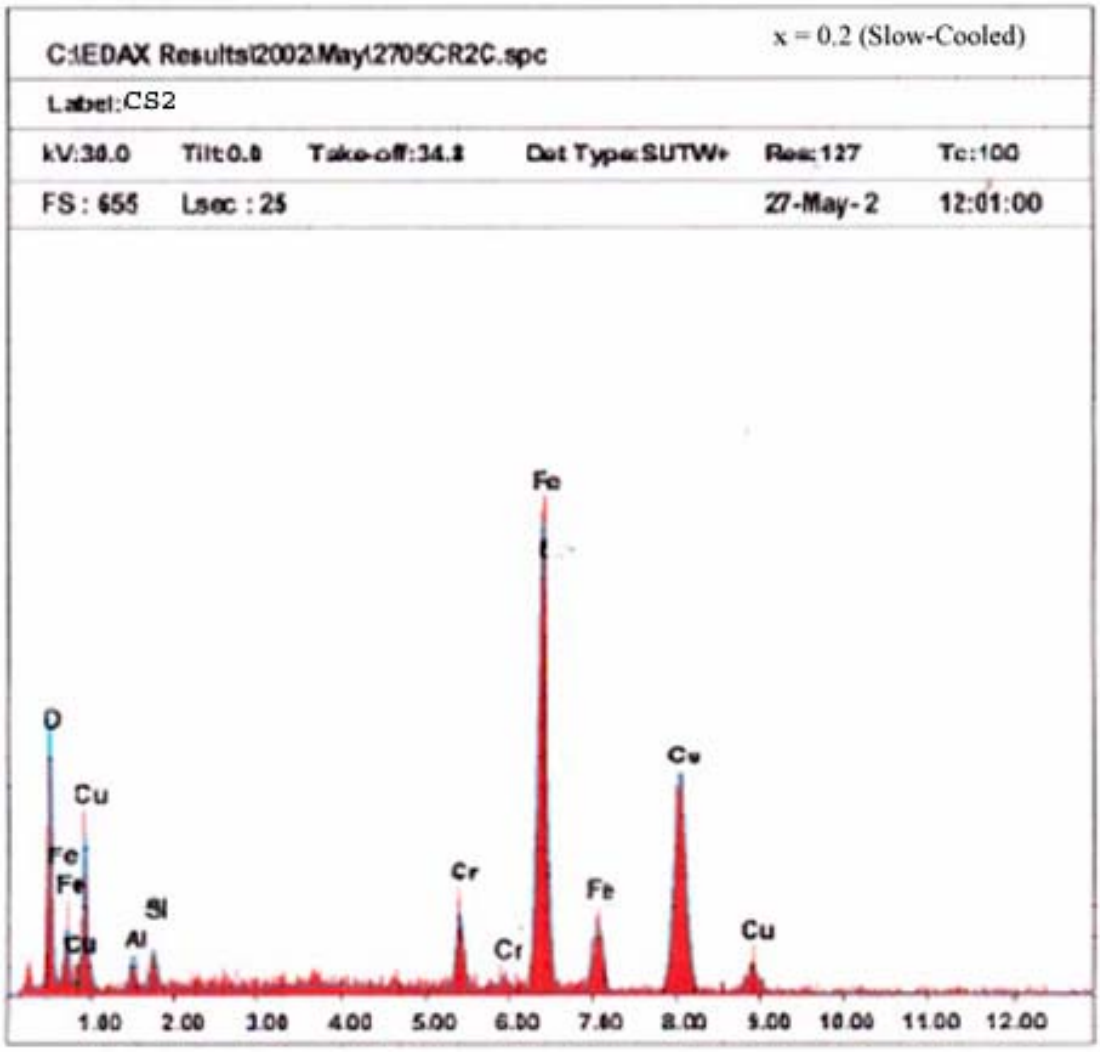

Fig. 6D.1a EDAX pattern for slow-cooled sample x = 0.2 of $CuAl_xCr_xFe_{2-2x}O_4$ system

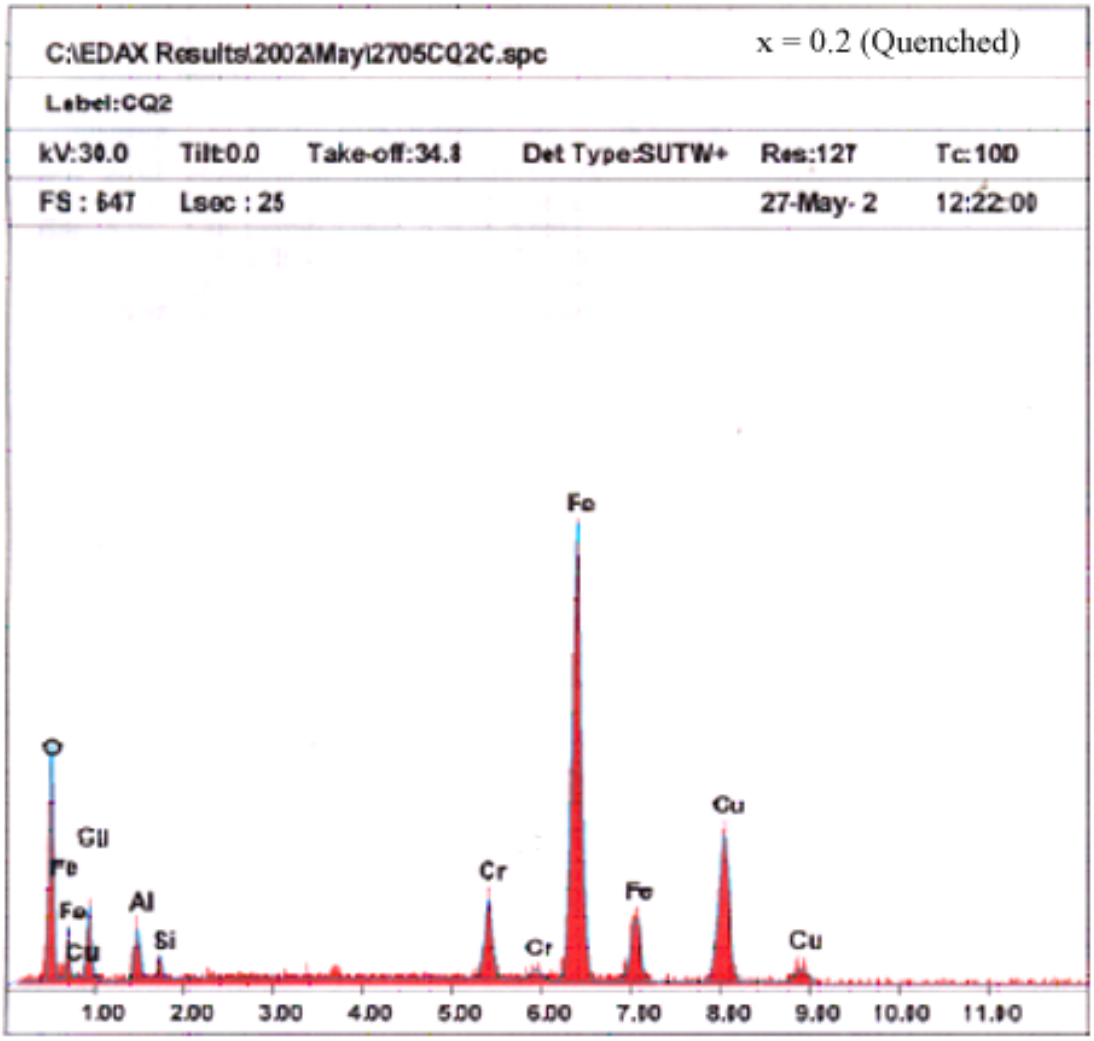

Fig. 6D.1b EDAX pattern for quenched sample x = 0.2 of $CuAl_xCr_xFe_{2-2x}O_4$ system

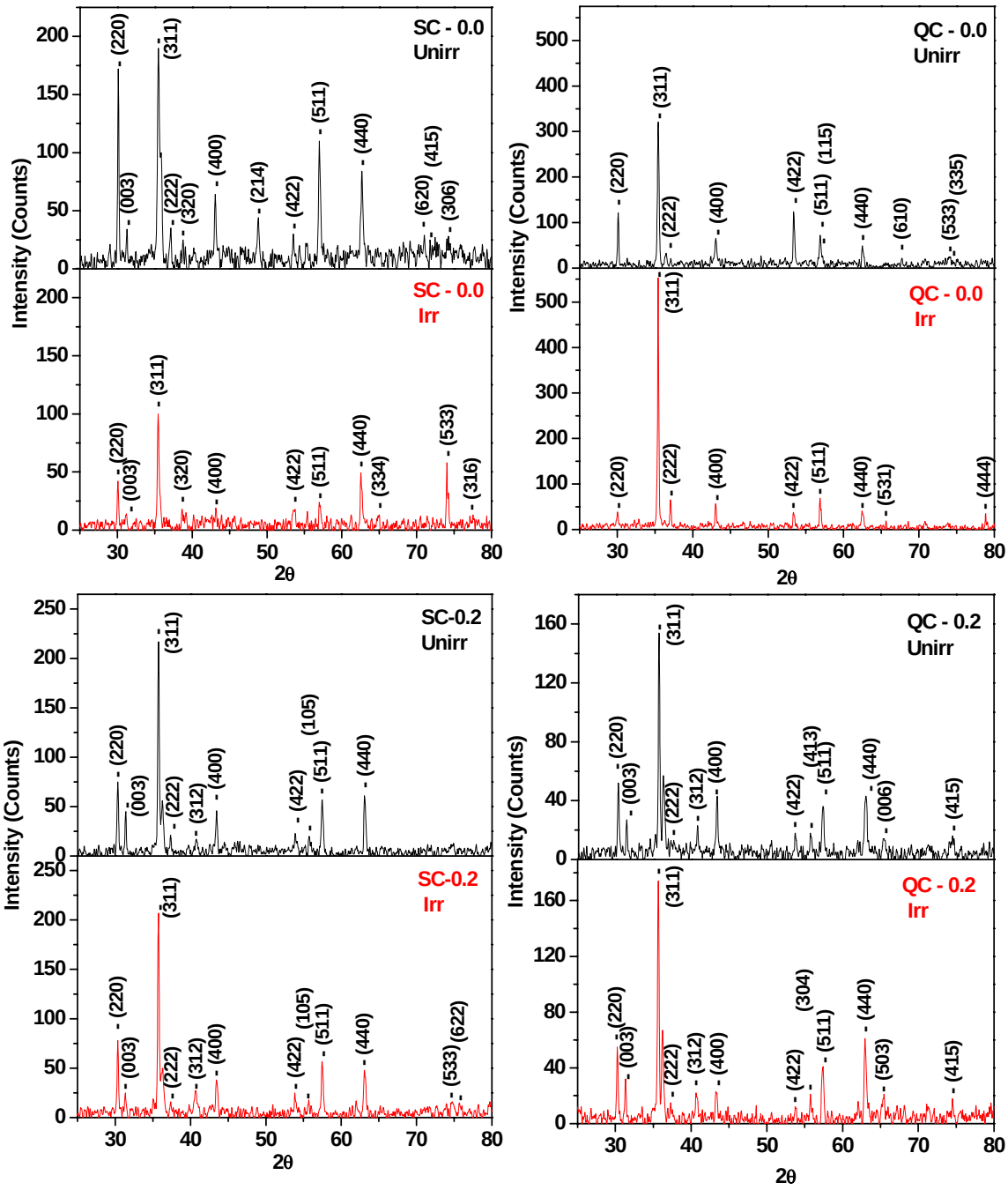

Fig. 6D.2a X-ray diffraction patterns for the unirradiated and irradiated samples x = 0.0 and 0.2 of $CuAl_xCr_xFe_{2-2x}O_4$ (SC-QC) systems

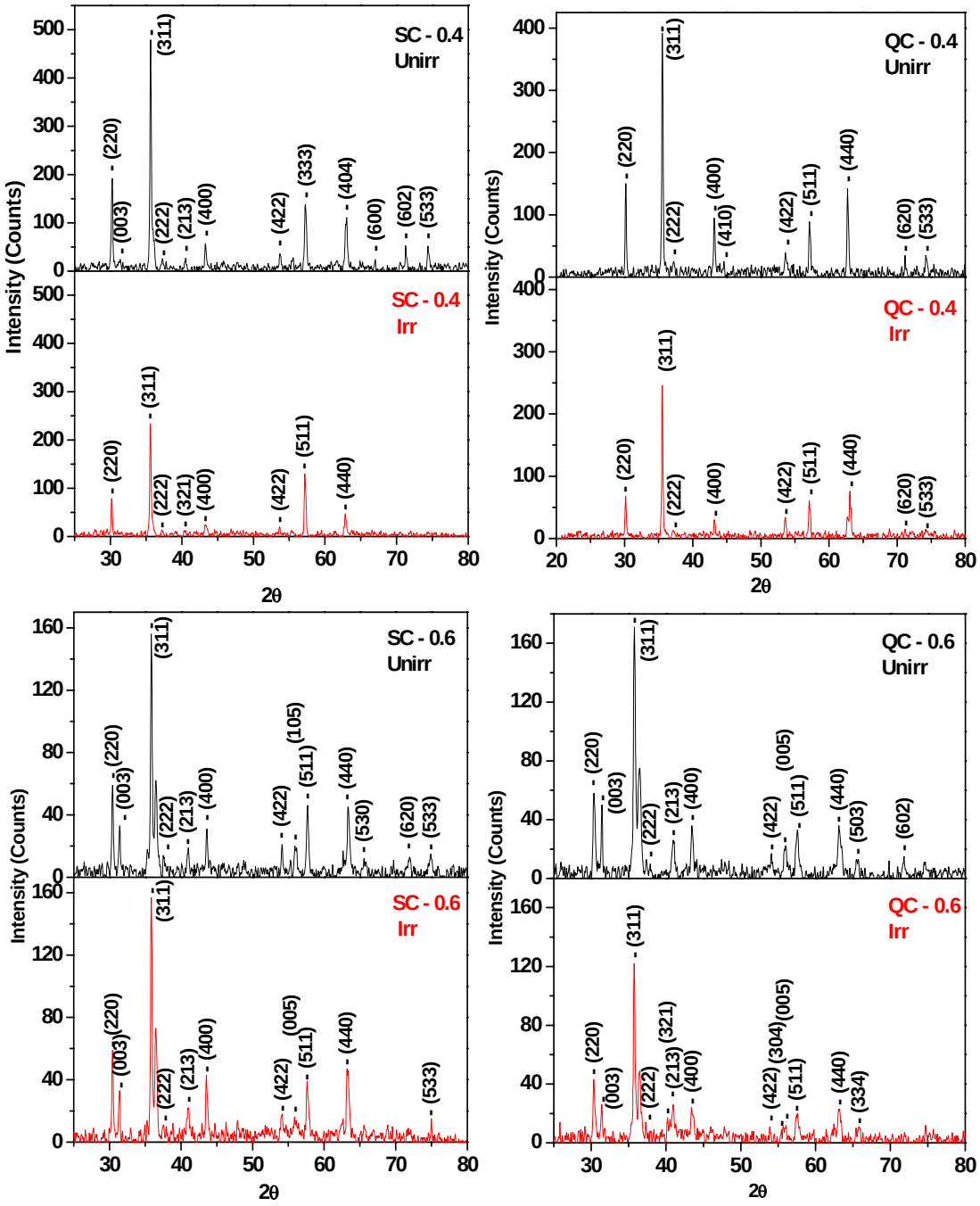

Fig. 6D.2b X-ray diffraction patterns for the unirradiated and irradiated samples x = 0.4 and 0.6 of $CuAl_xCr_xFe_{2-2x}O_4$ (SC-QC) systems

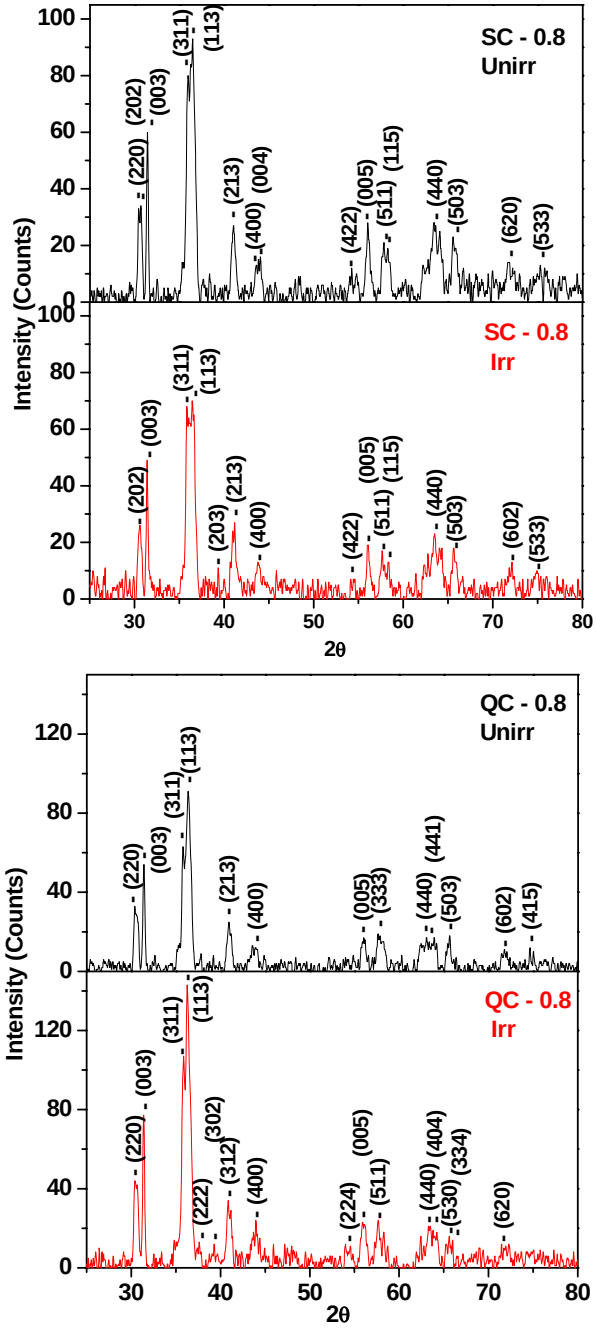

Fig. 6D.2c X-ray diffraction patterns for the unirradiated and irradiated sample x = 0.8 of $CuAl_xCr_xFe_{2-2x}O_4$ (SC-QC) systems

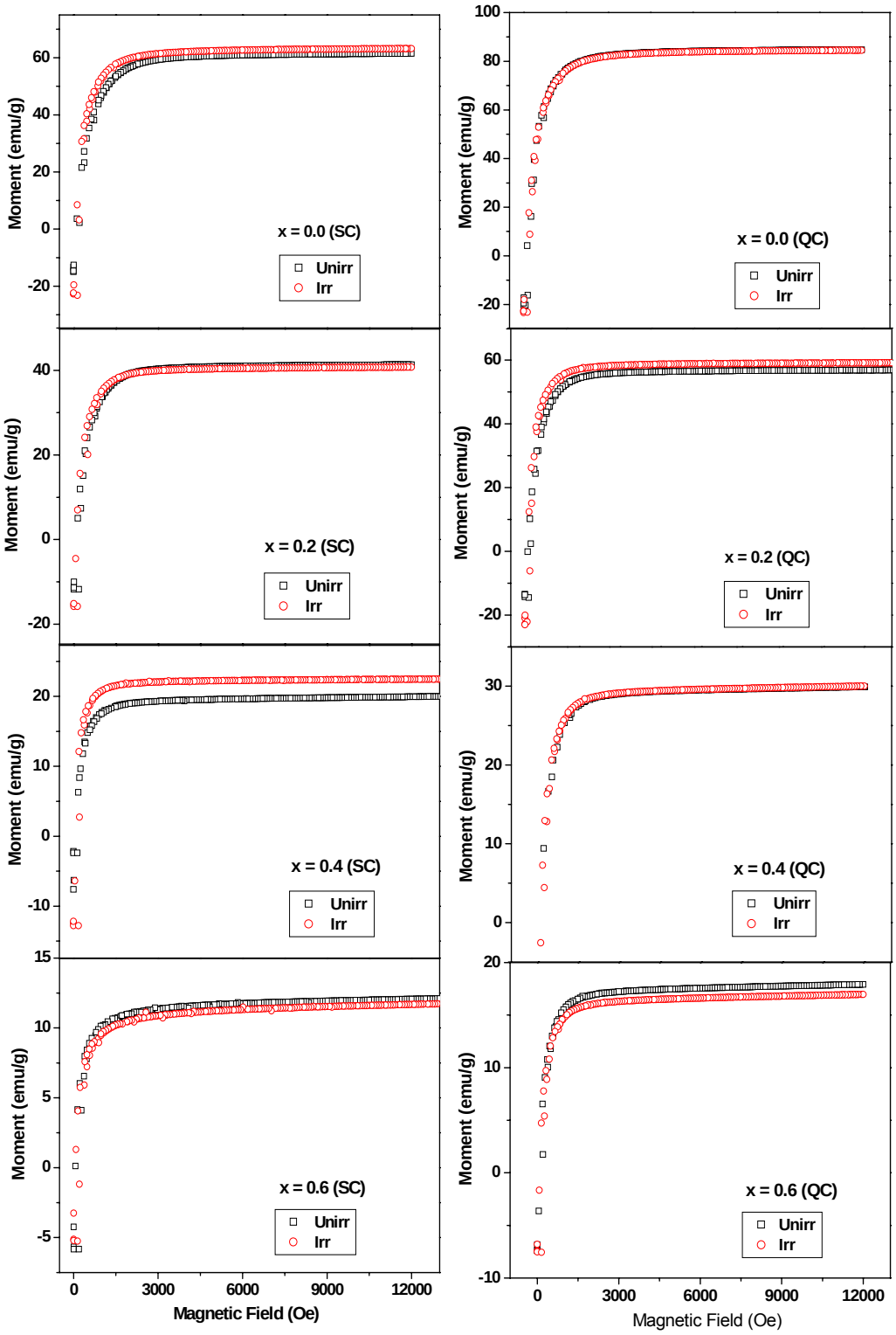

Fig. 6D.3 High field (1.2 Tesla) magnetization plots (M vs H) at 77K for the unirradiated and irradiated samples of $CuAl_xCr_xFe_{2-2x}O_4$ (SC-QC) systems

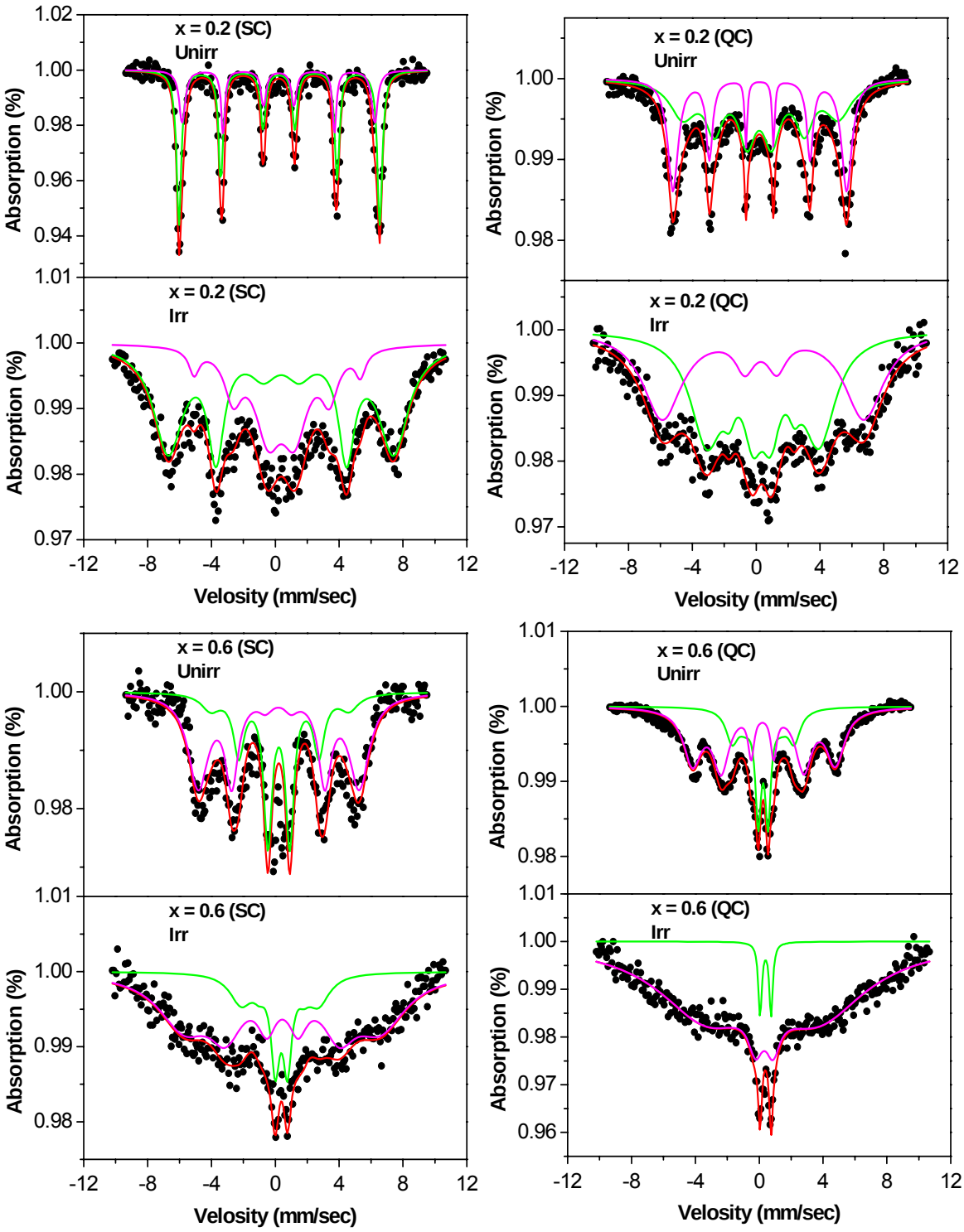

Fig. 6D.4 Mössbauer spectrum at 300K for the unirradiated and irradiated samples x = 0.2 and 0.6 of $CuAl_xCr_xFe_{2-2x}O_4$ (SC-QC) systems

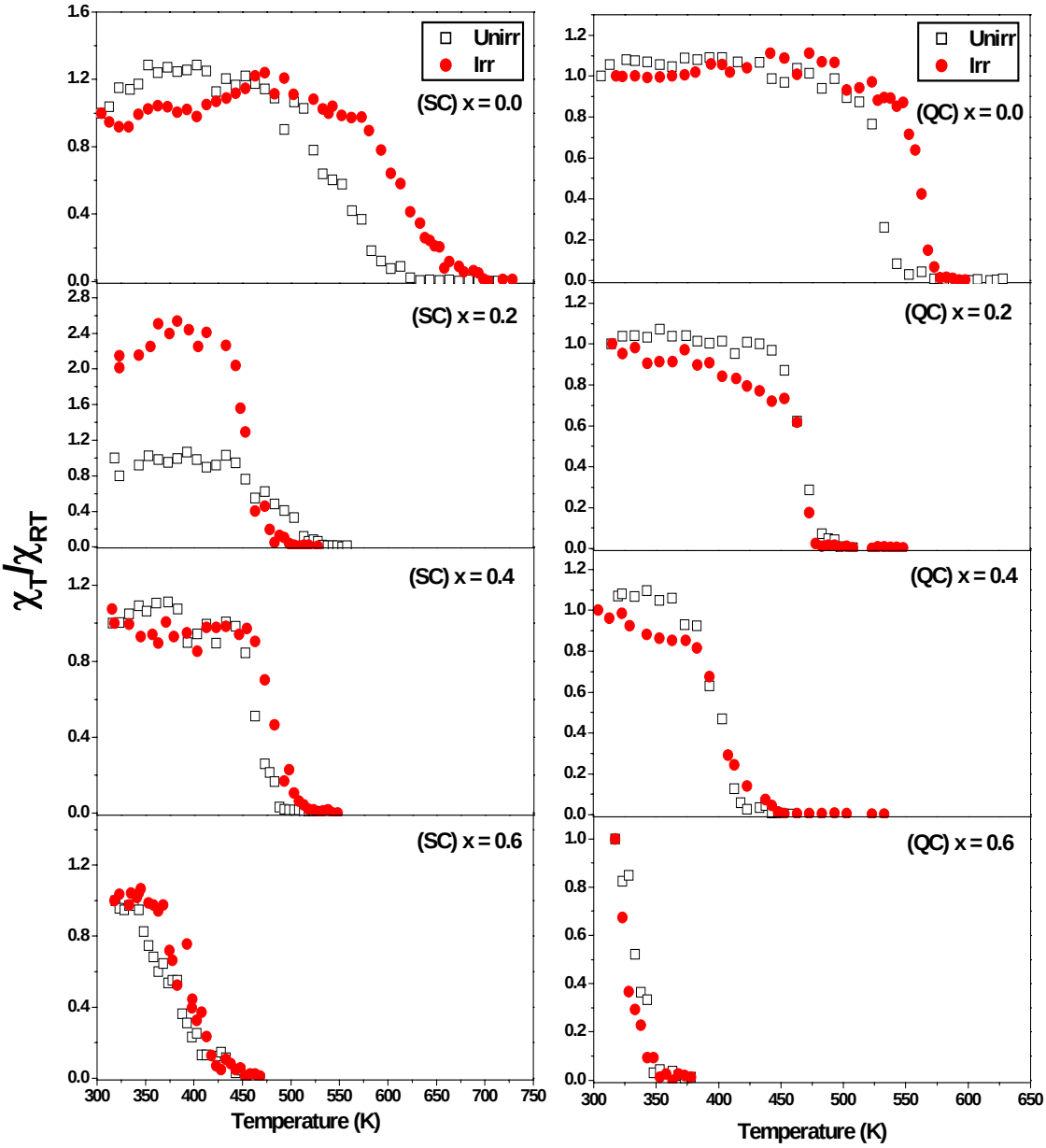

Fig. 6D.5 Thermal variation of low field (0.5 Oe) AC susceptibility for the unirradiated and irradiated samples of $CuAl_xCr_xFe_{2-2x}O_4$ (SC-QC) systems

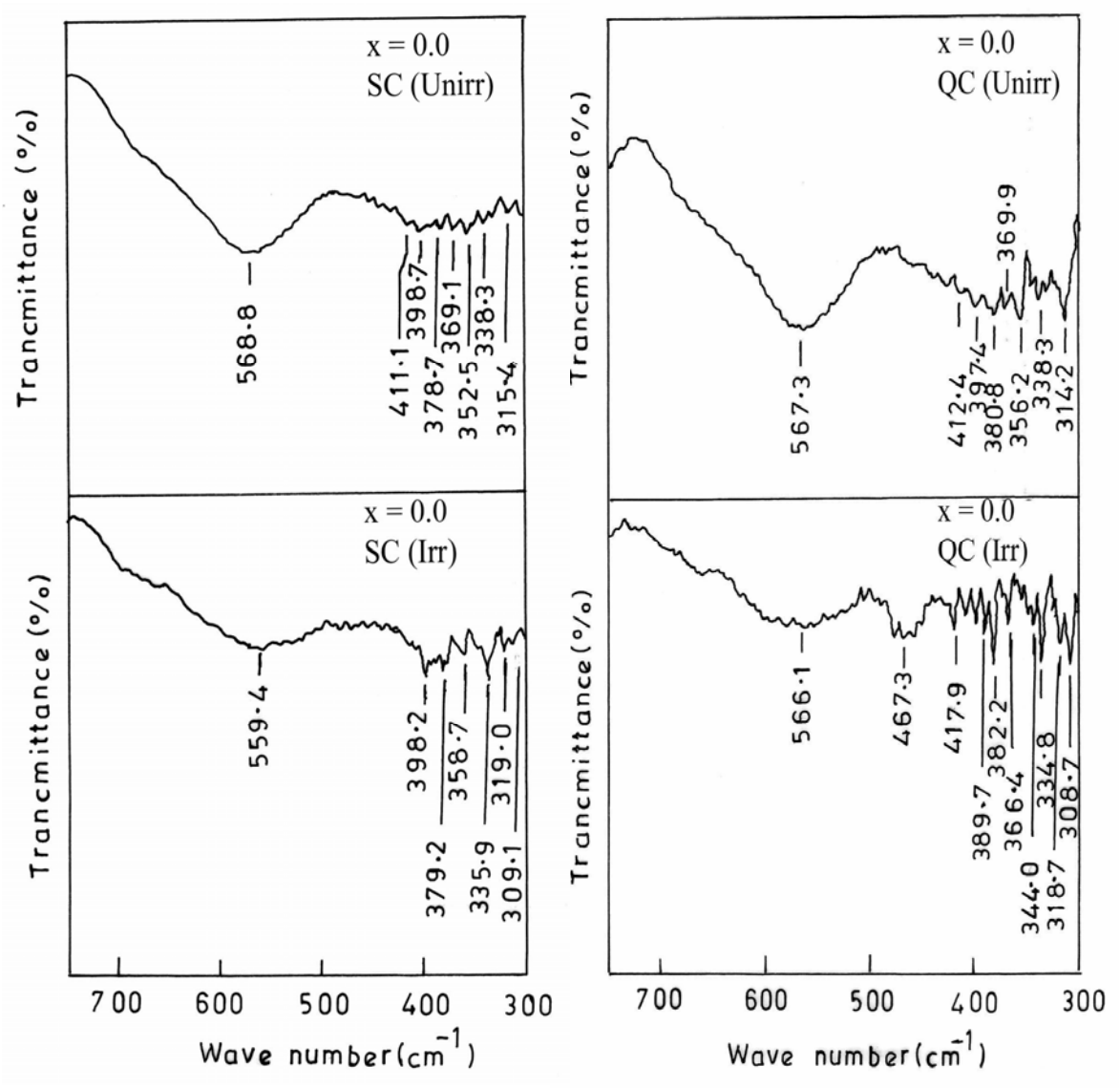

Fig. 6D.6a Infrared spectra for the unirradiated and irradiated sample x = 0.0 of $CuAl_xCr_xFe_{2-2x}O_4$ (SC-QC) systems

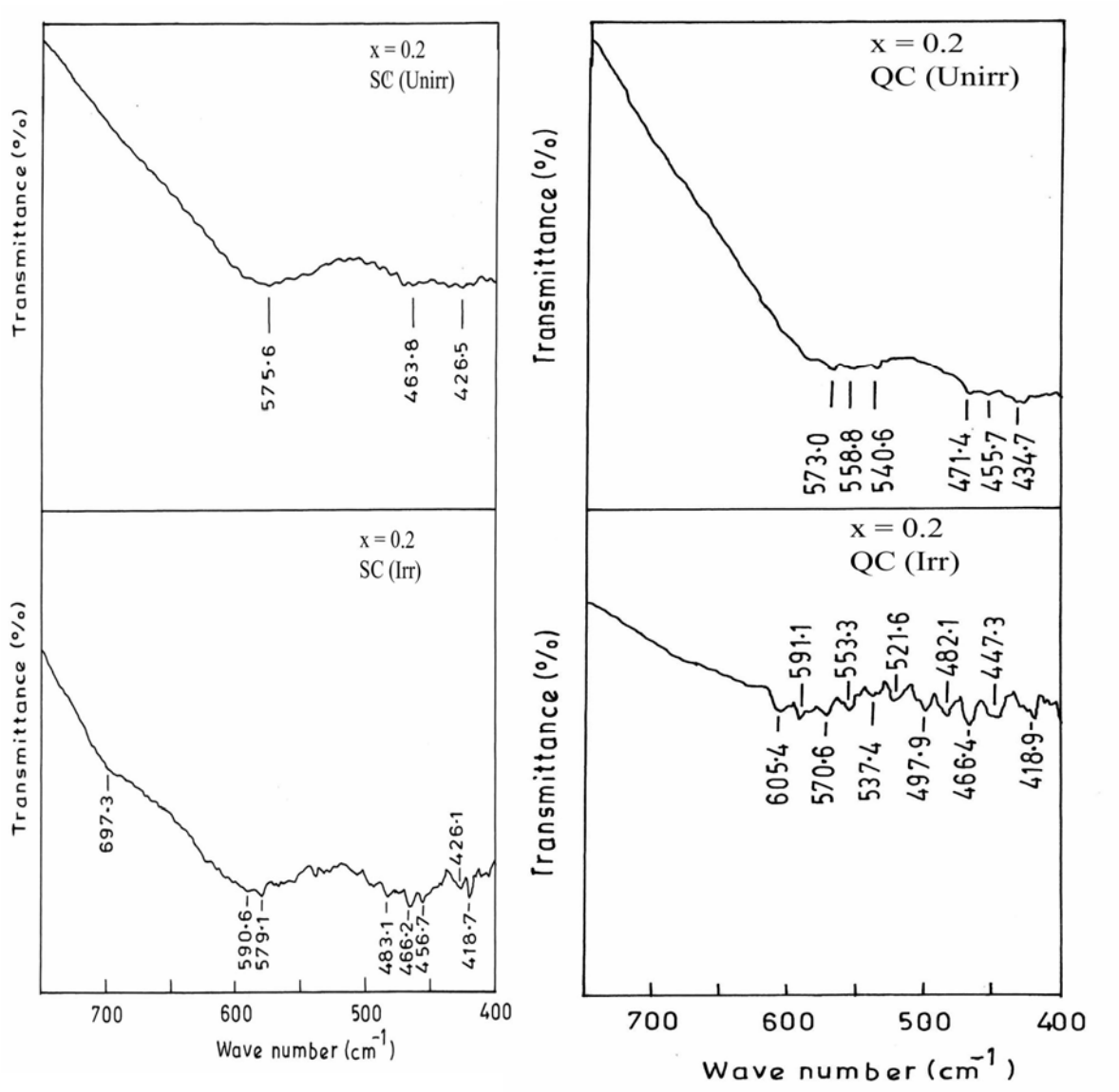

Fig. 6D.6b Infrared spectra for the unirradiated and irradiated sample x = 0.2 of $CuAl_xCr_xFe_{2-2x}O_4$ (SC-QC) systems

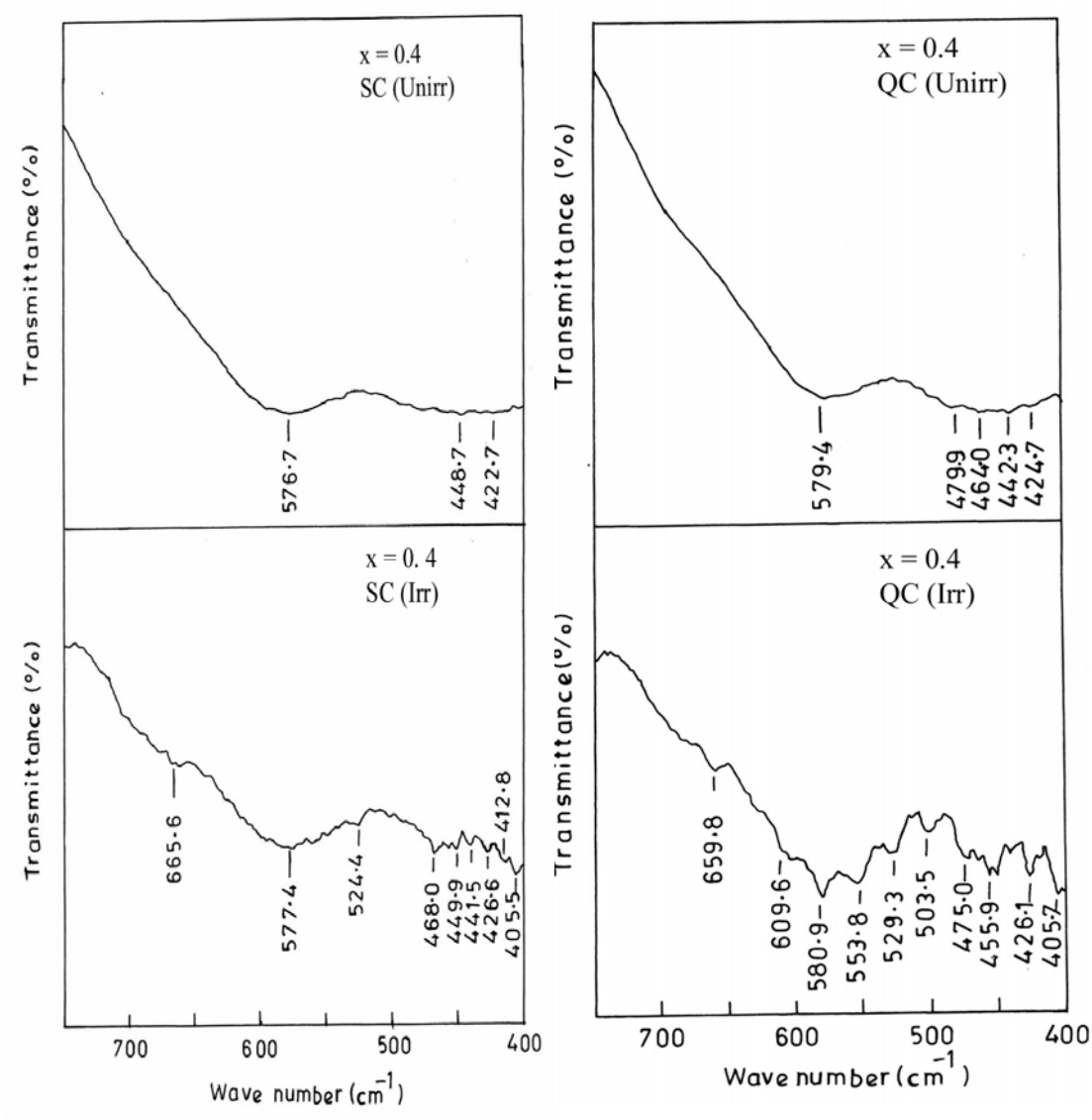

Fig. 6D.6c Infrared spectra for the unirradiated and irradiated sample x = 0.4 of $CuAl_xCr_xFe_{2-2x}O_4$ (SC-QC) systems

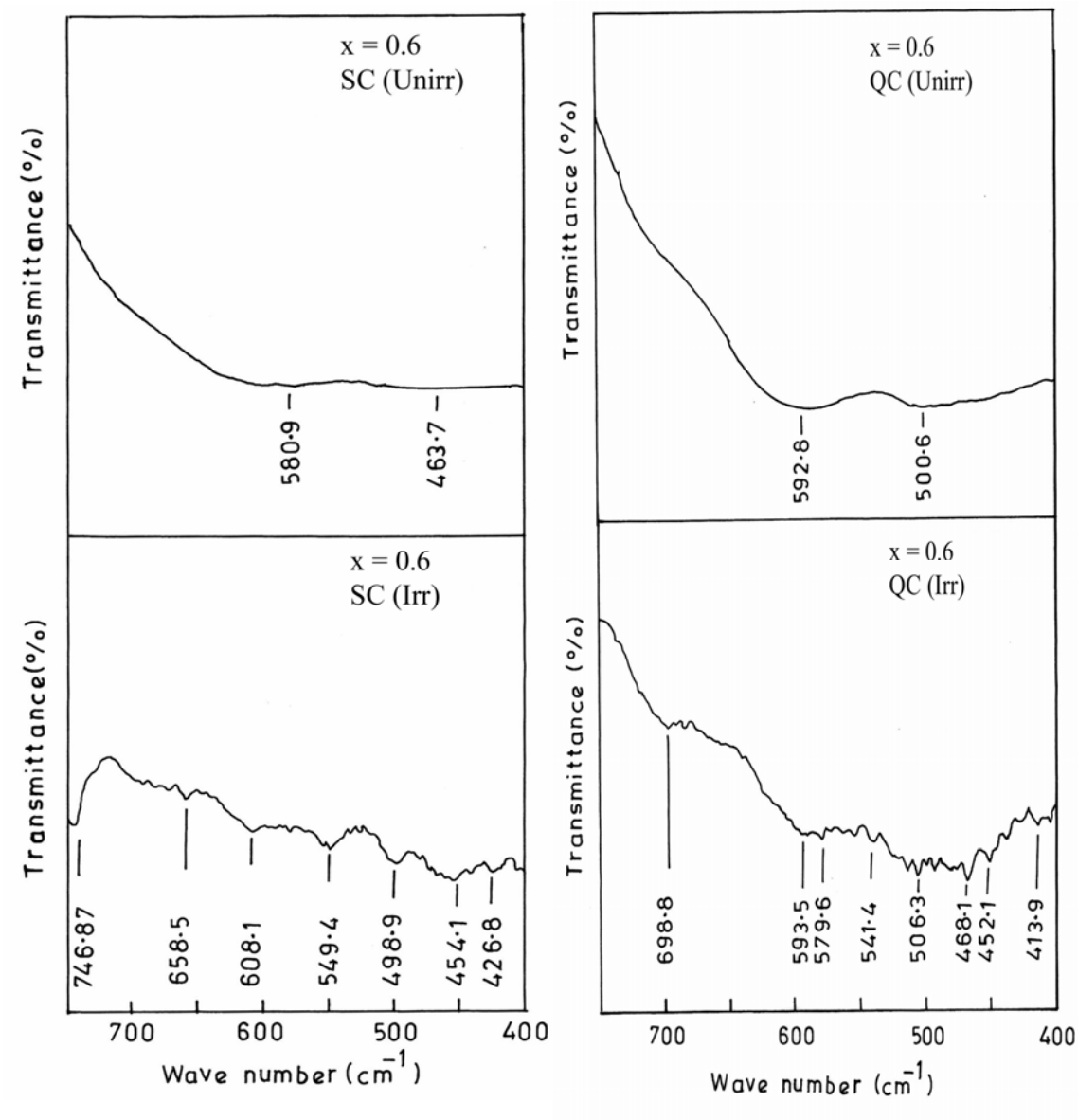

Fig. 6D.6d Infrared spectra for the unirradiated and irradiated sample x = 0.6 of $CuAl_xCr_xFe_{2-2x}O_4$ (SC-QC) systems

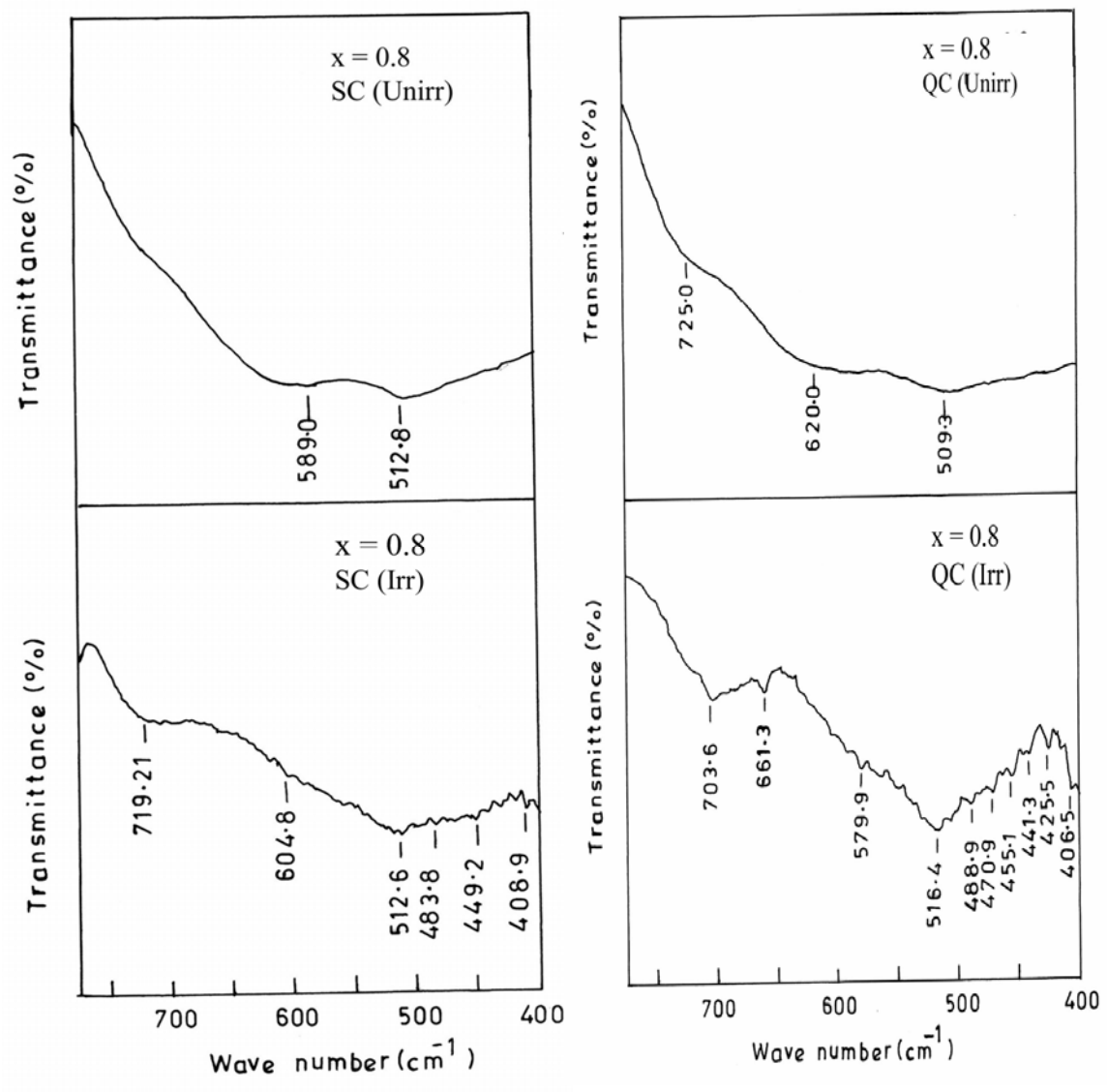

Fig. 6D.6e Infrared spectra for the unirradiated and irradiated sample x = 0.8 of $CuAl_xCr_xFe_{2-2x}O_4$ (SC-QC) systems

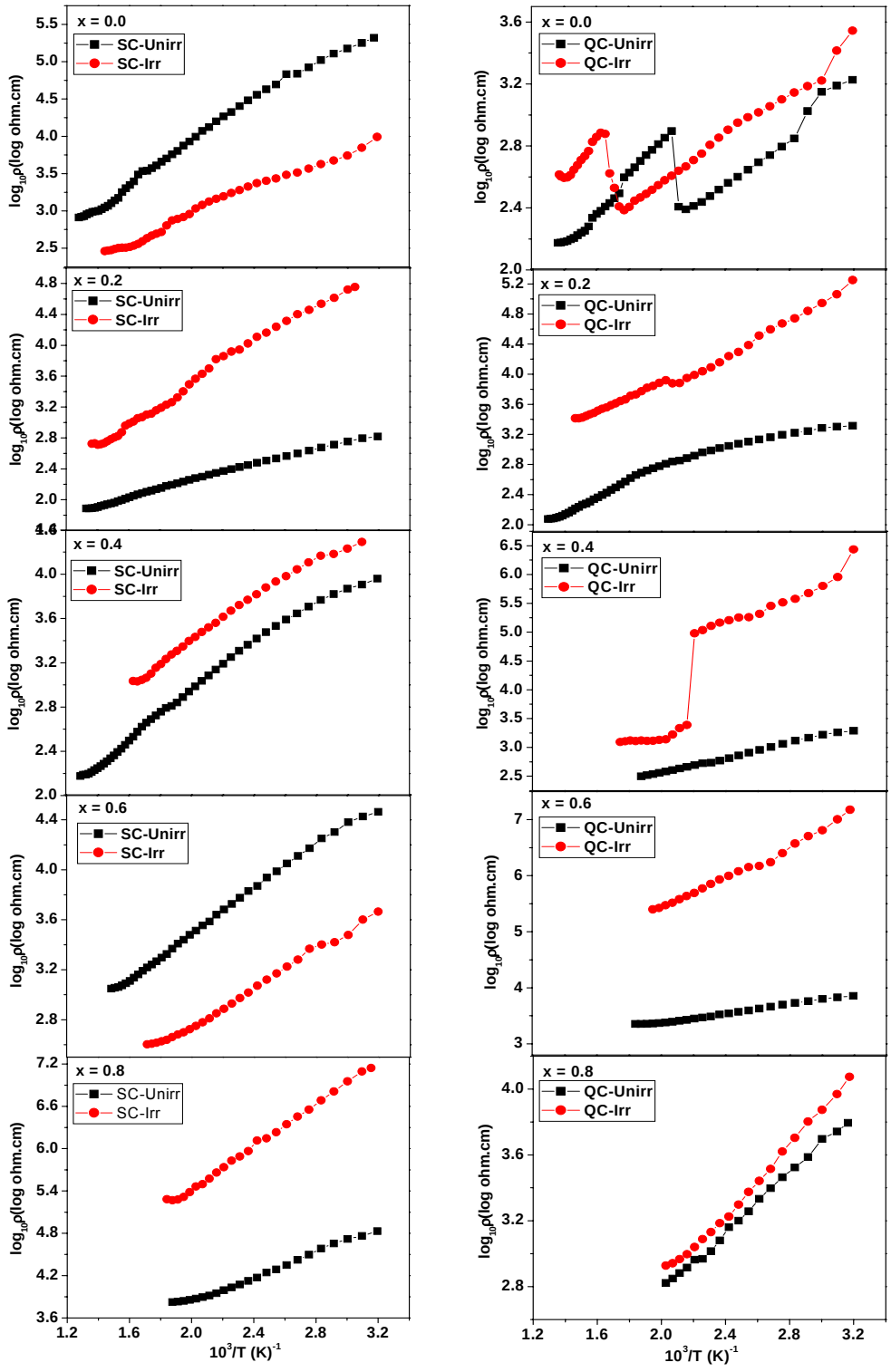

Fig. 6D.7 Thermal variation of dc resistivity ($\log_{10}\rho_{dc}$) for the compositions x = 0.0, 0.2, 0.4, 0.6 and 0.8 of unirradiated and irradiated $CuAl_xCr_xFe_{2-2x}O_4$ (SC- QC) systems

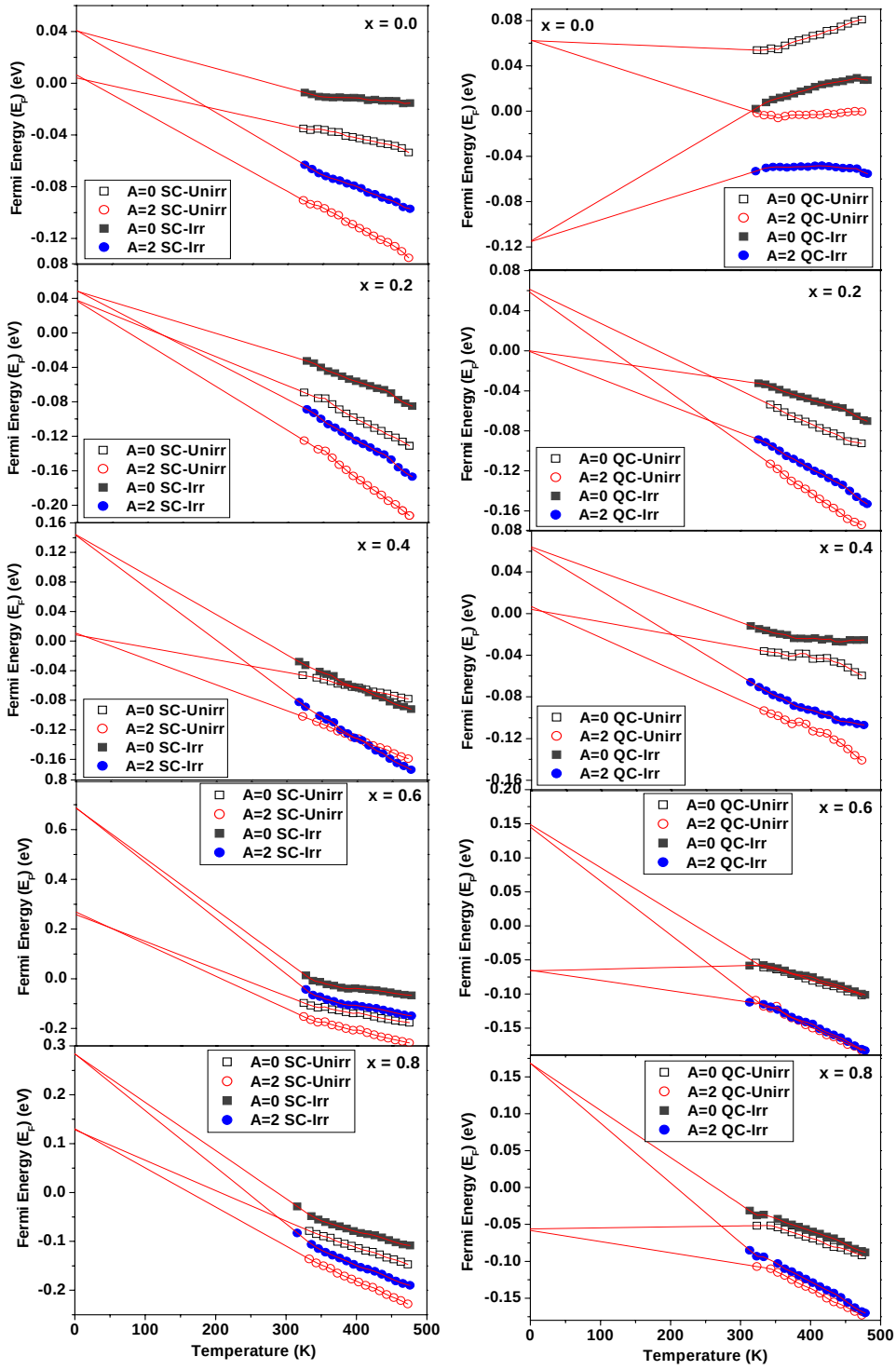

Fig. 6D.8 Temperature dependence of Fermi energy (E_F) for the compositions x = 0.0, 0.2, 0.4, 0.6 and 0.8 of unirradiated and irradiated $CuAl_xCr_xFe_{2-2x}O_4$ (SC- QC) systems

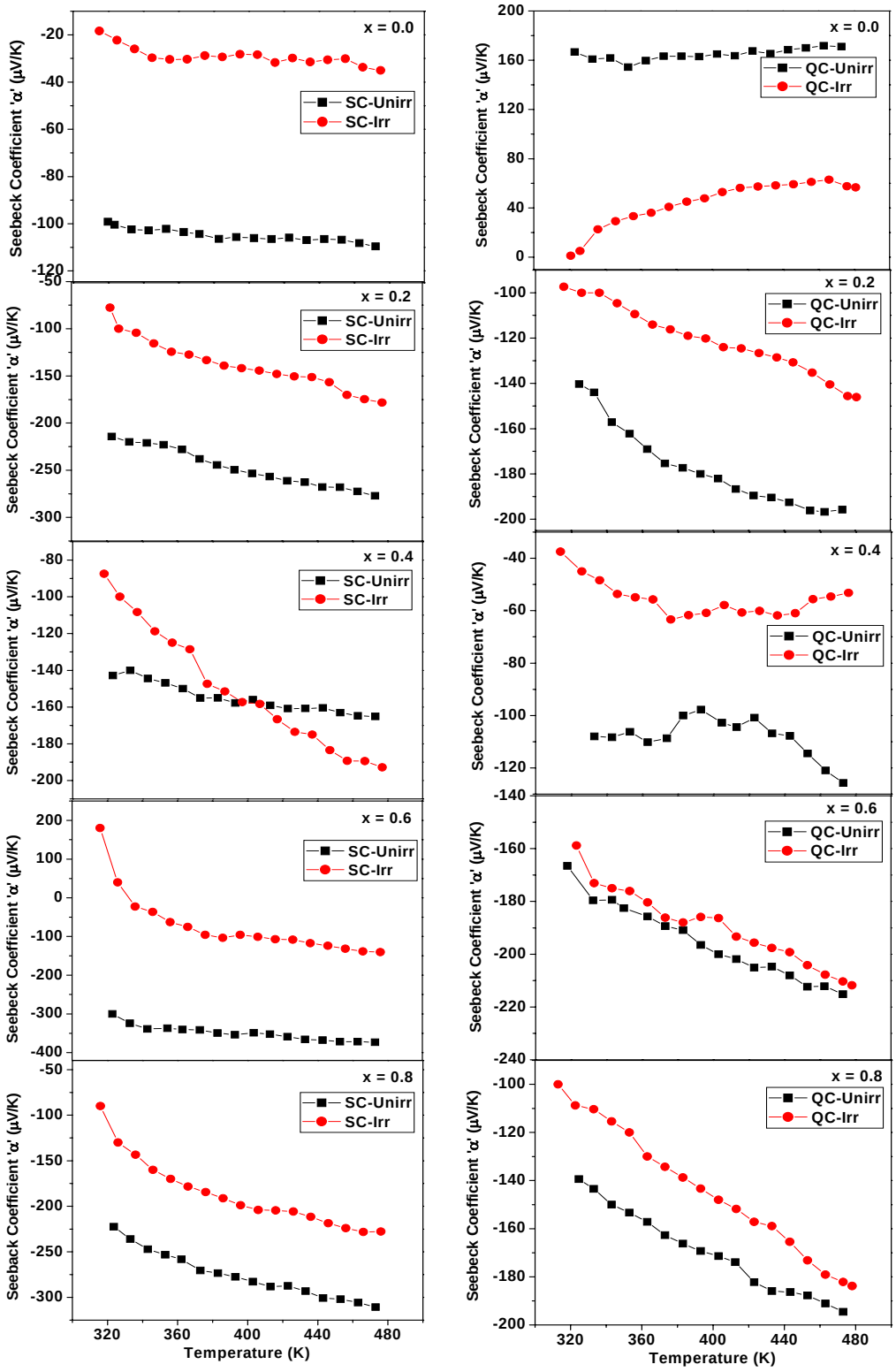

Fig. 6D.9 Thermal variation of Seebeck coefficient for the compositions x = 0.0, 0.2, 0.4, 0.6 and 0.8 of unirradiated and irradiated $CuAl_xCr_xFe_{2-2x}O_4$ (SC- QC) systems

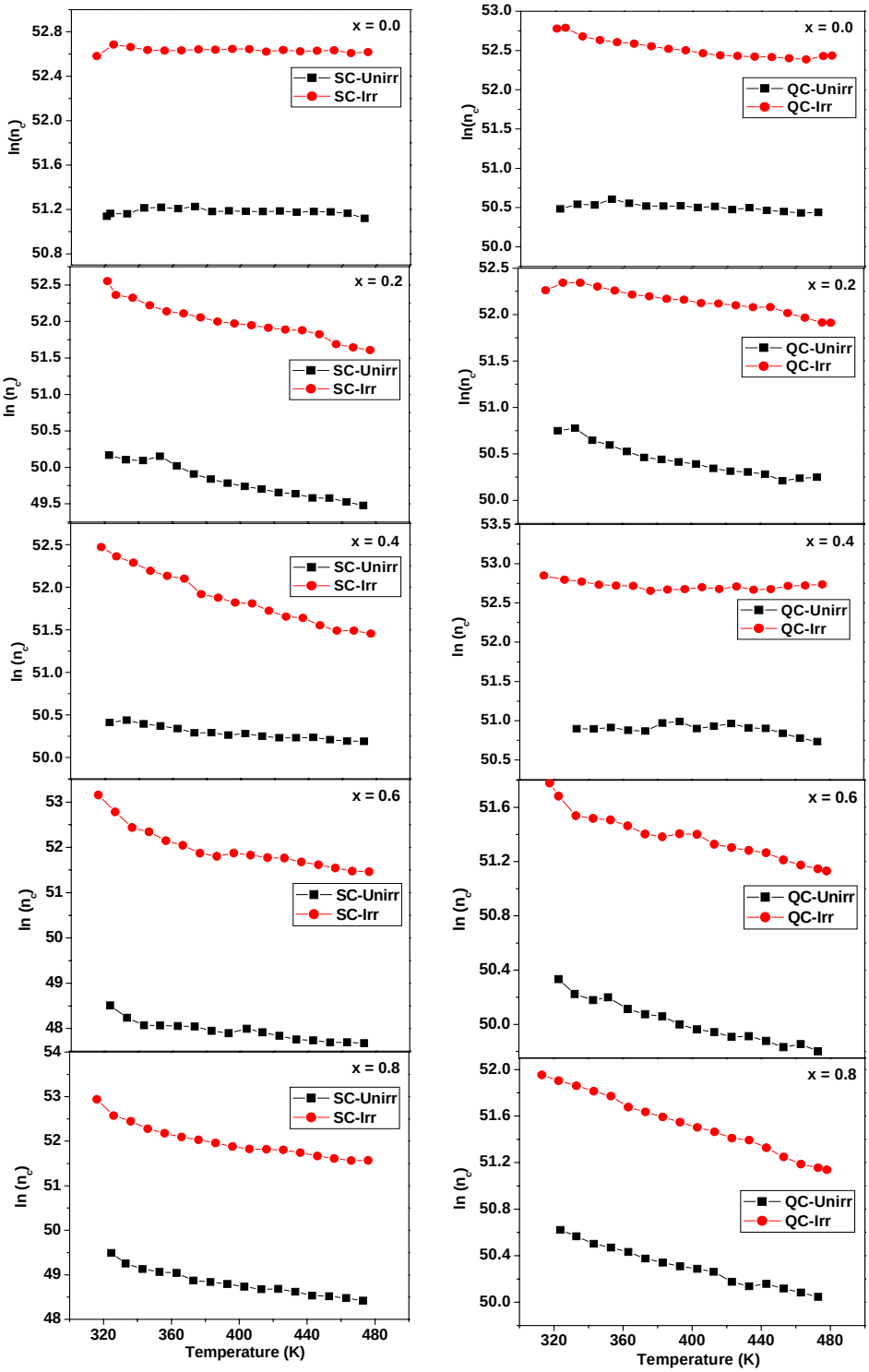

Fig. 6D.10 Variation of charge carrier concentration with temperature for the compositions x = 0.0, 0.2, 0.4, 0.6 and 0.8 of unirradiated and irradiated $CuAl_xCr_xFe_{2-2x}O_4$ (SC- QC) systems

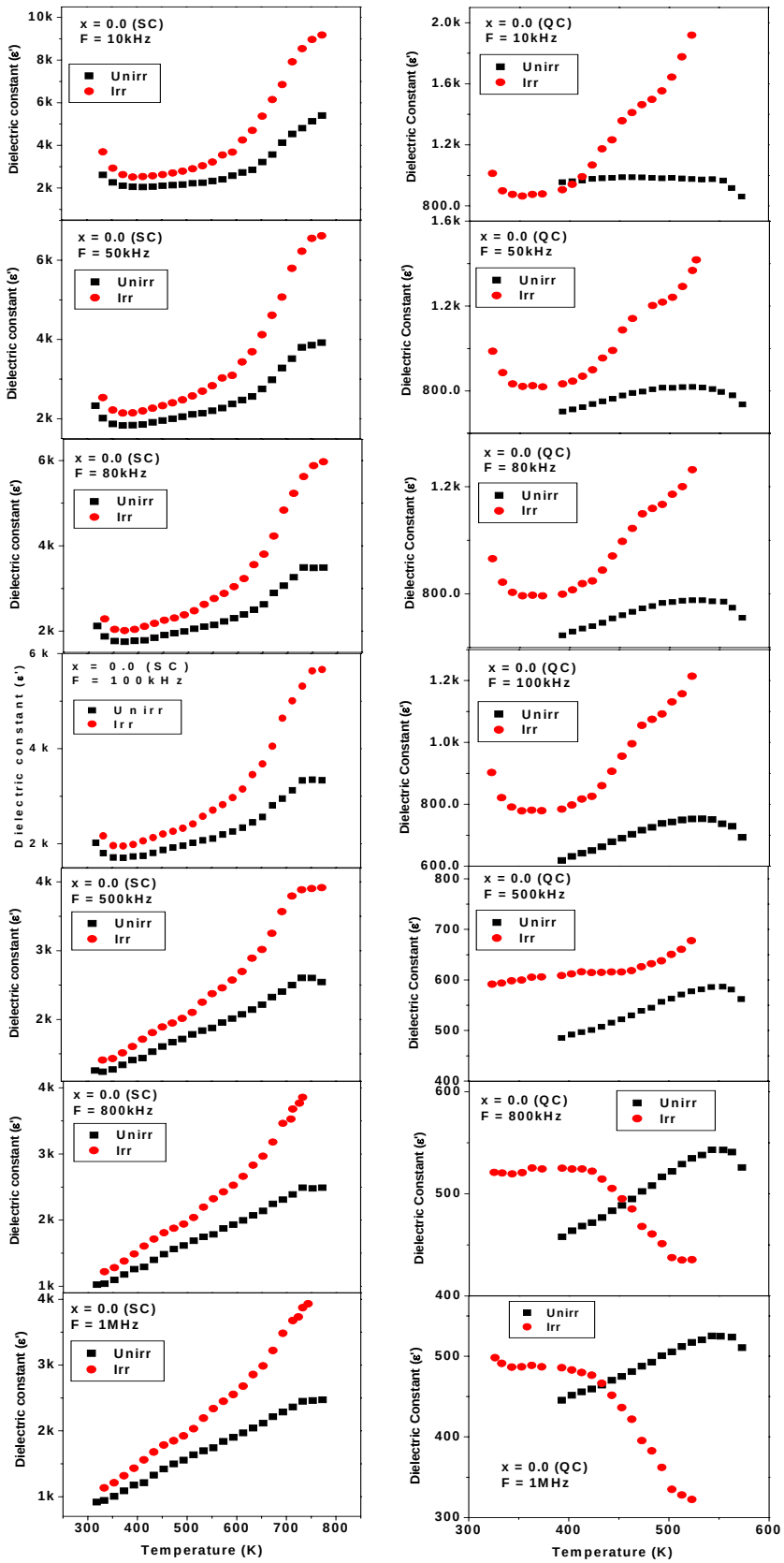

Fig. 6D.11a Thermal variation of Dielectric Constant (ε') at different frequencies for the composition x = 0.0 of unirradiated and irradiated $CuAl_xCr_xFe_{2-2x}O_4$ (SC-QC) systems

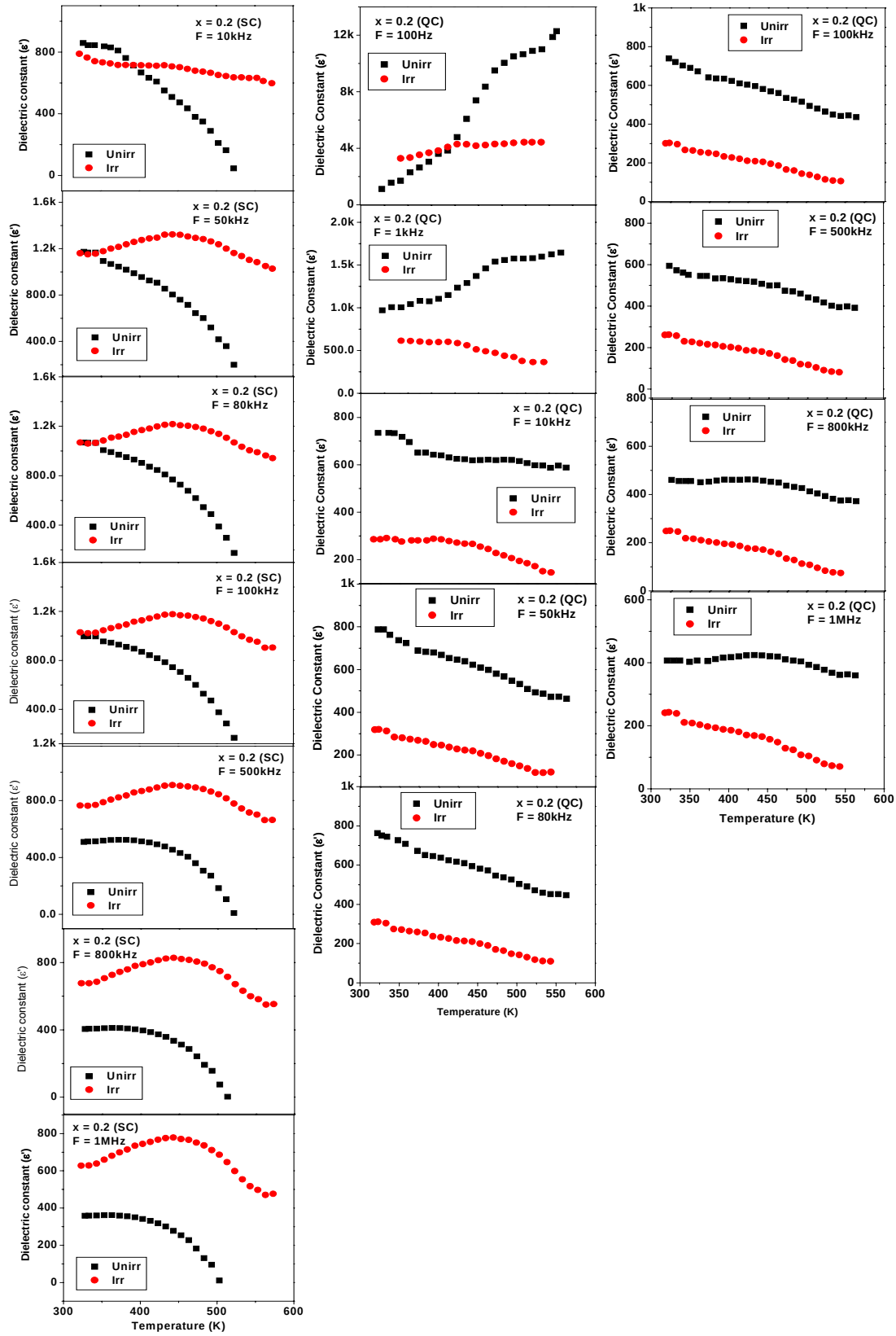

Fig. 6D.11b Thermal variation of Dielectric Constant (ε') at different frequencies for the composition x = 0.2 of unirradiated and irradiated $CuAl_xCr_xFe_{2-2x}O_4$ (SC-QC) systems

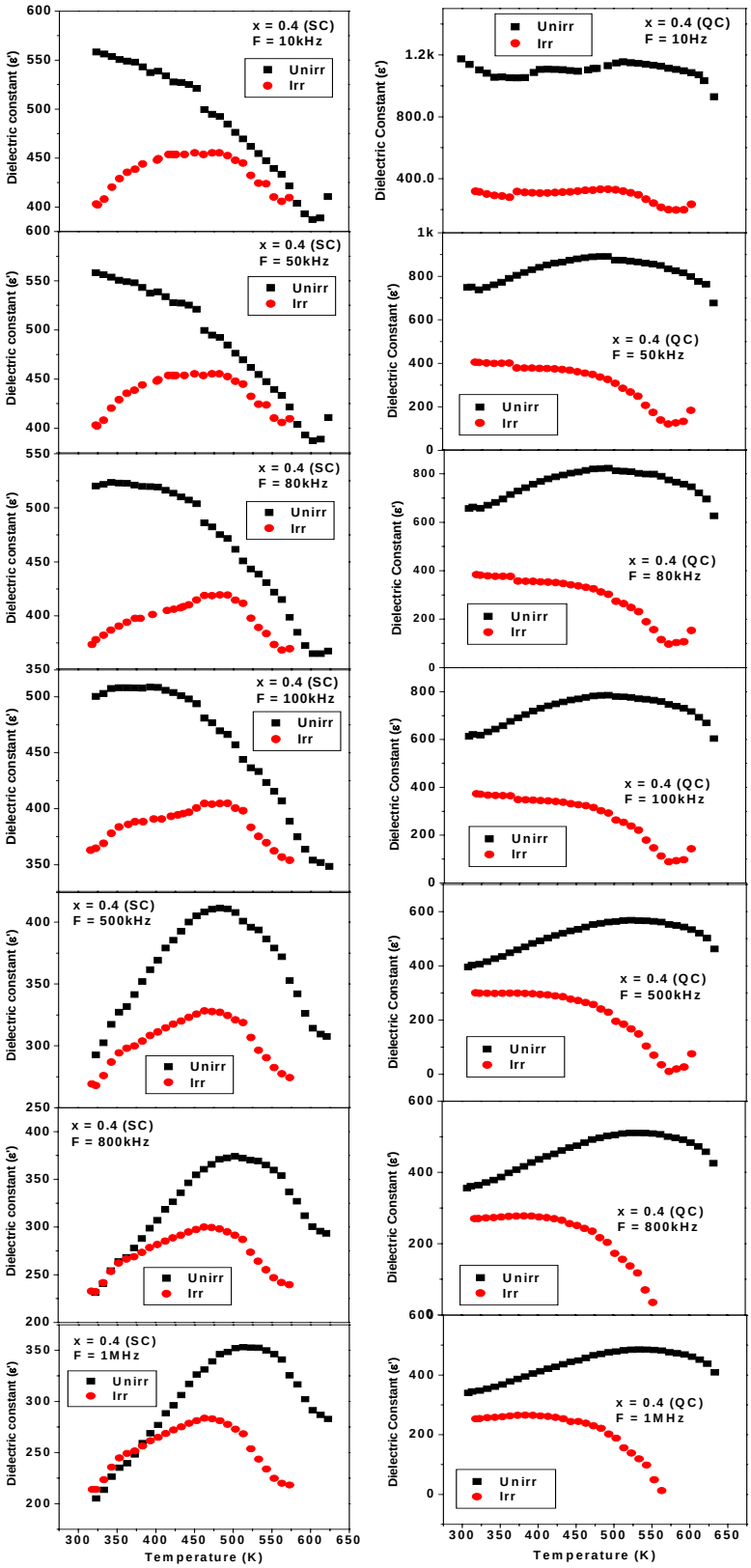

Fig. 6D.11c Thermal variation of Dielectric Constant (ε') at different frequencies for the composition x = 0.4 of unirradiated and irradiated $CuAl_xCr_xFe_{2-2x}O_4$ (SC-QC) systems

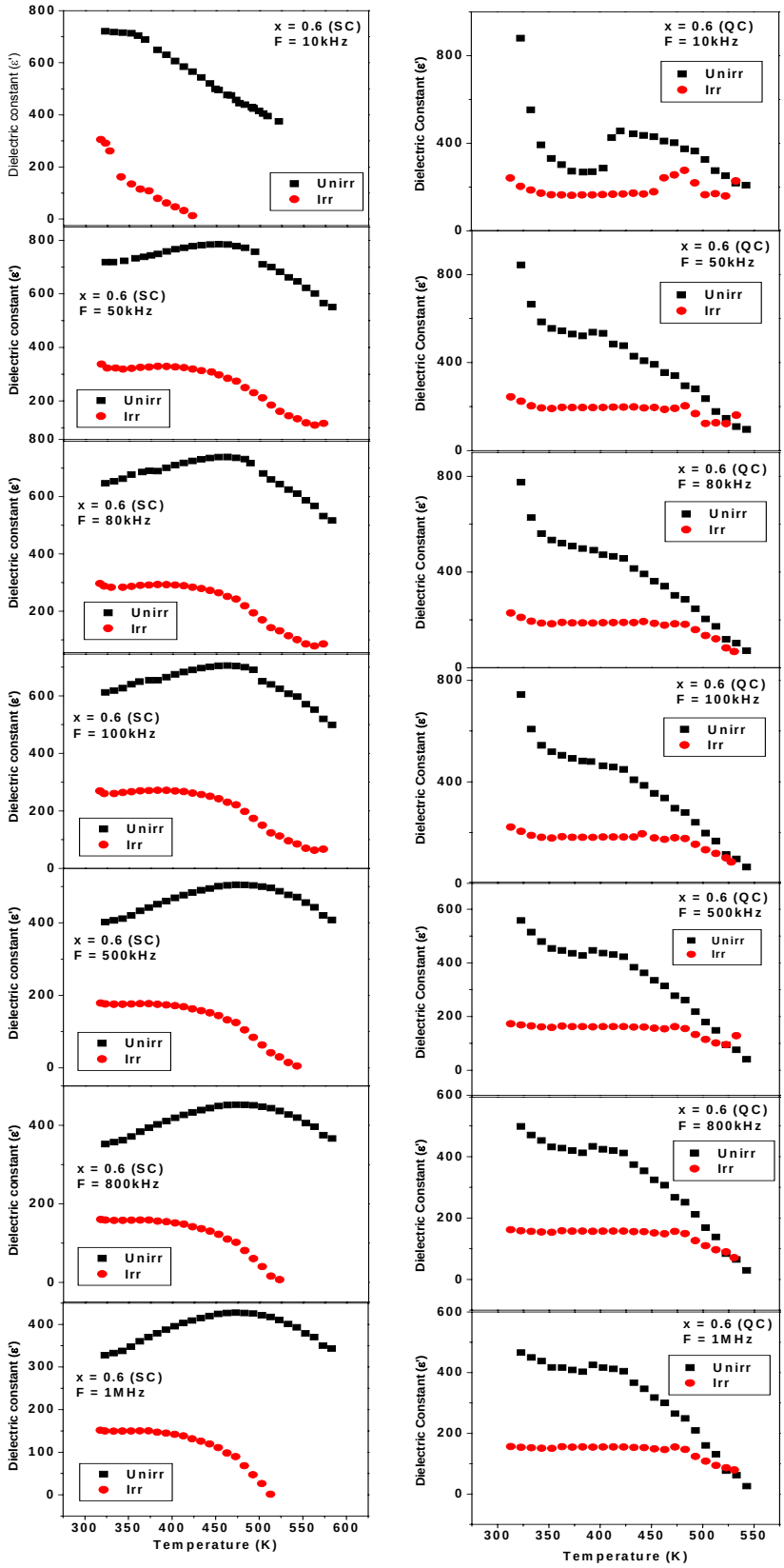

Fig. 6D.11d Thermal variation of Dielectric Constant (ε') at different frequencies for the composition x = 0.6 of unirradiated and irradiated $CuAl_xCr_xFe_{2-2x}O_4$ (SC- QC) systems

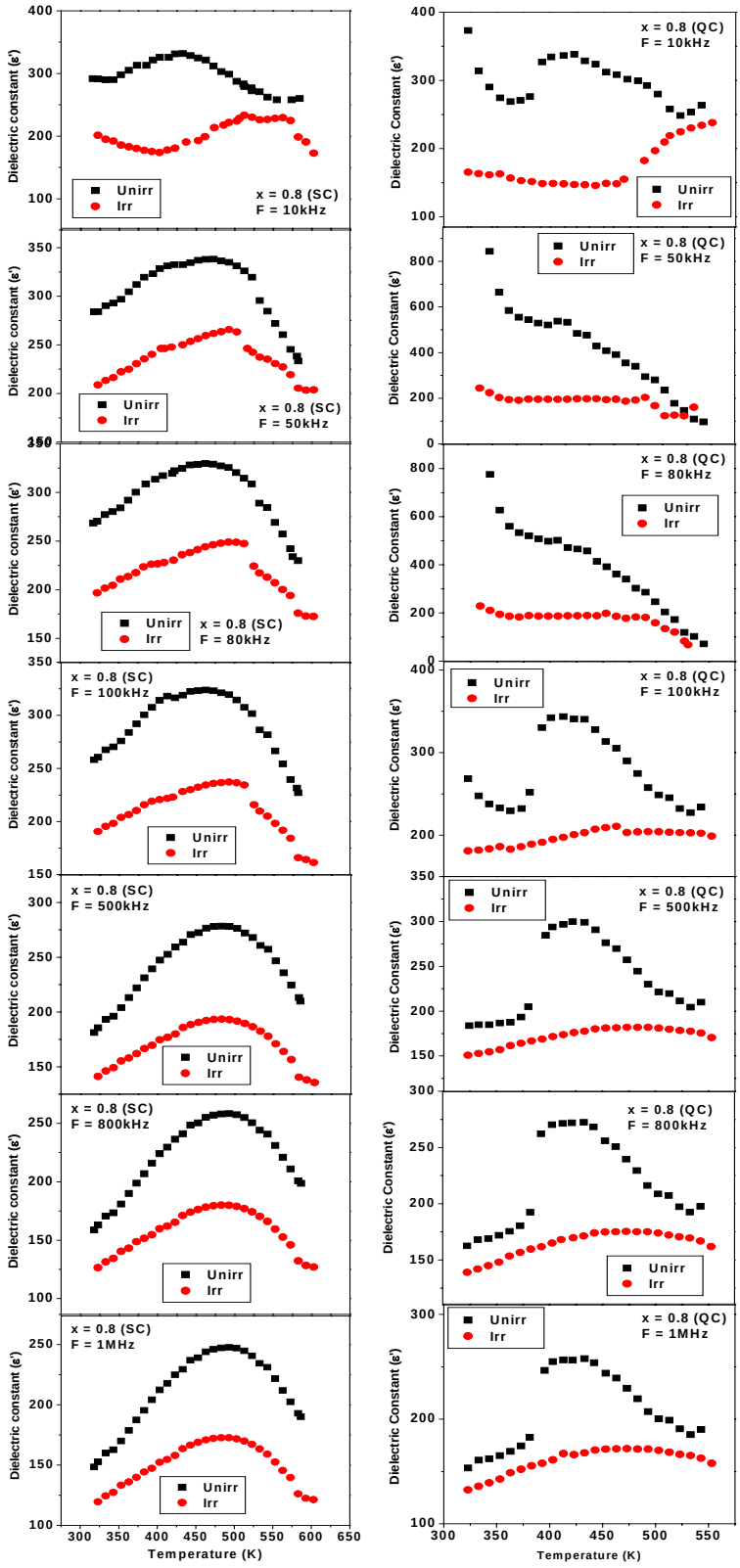

Fig. 6D.11e Thermal variation of Dielectric Constant (ε') at different frequencies for the composition x = 0.8 of unirradiated and irradiated $CuAl_xCr_xFe_{2-2x}O_4$ (SC- QC) systems

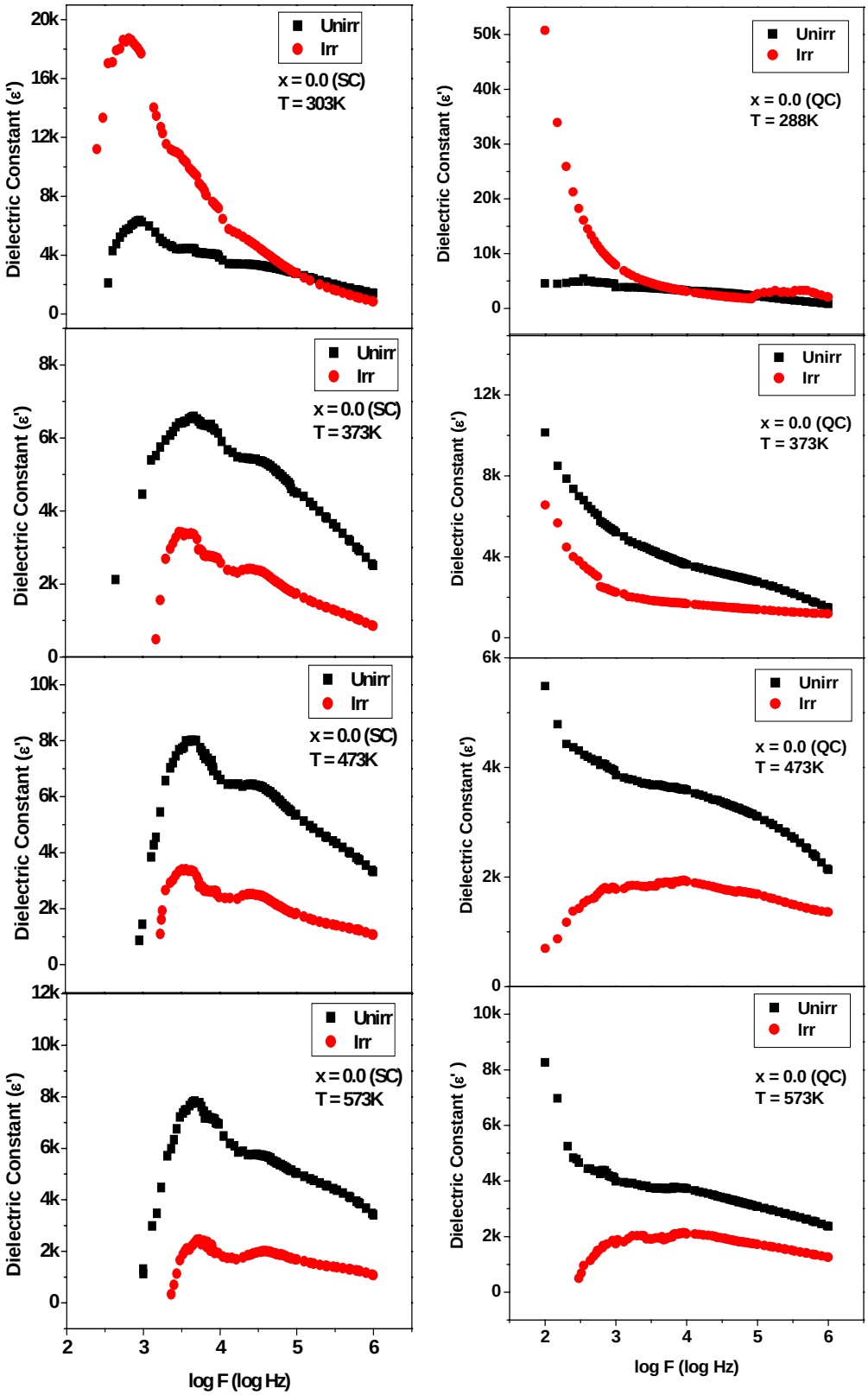

Fig. 6D.12a Dielectric Constant (ε') versus Frequency (log F) at selected temperatures for the composition x = 0.0 of unirradiated and irradiated $CuAl_xCr_xFe_{2-2x}O_4$ (SC-QC) systems

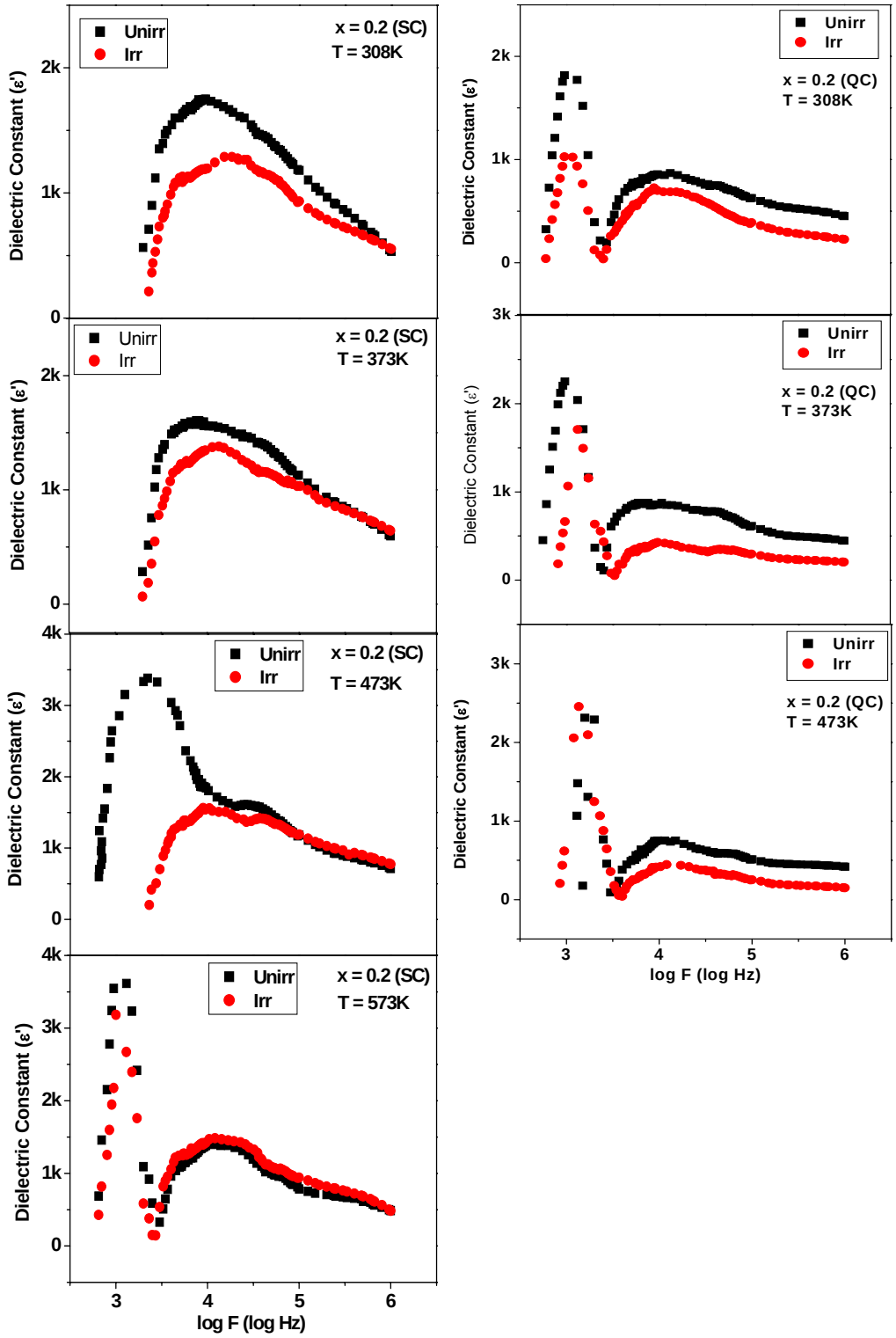

Fig. 6D.12b Dielectric Constant (ε') versus Frequency (log F) at selected temperatures for the composition x = 0.2 of unirradiated and irradiated $CuAl_xCr_xFe_{2-2x}O_4$ (SC-QC) systems

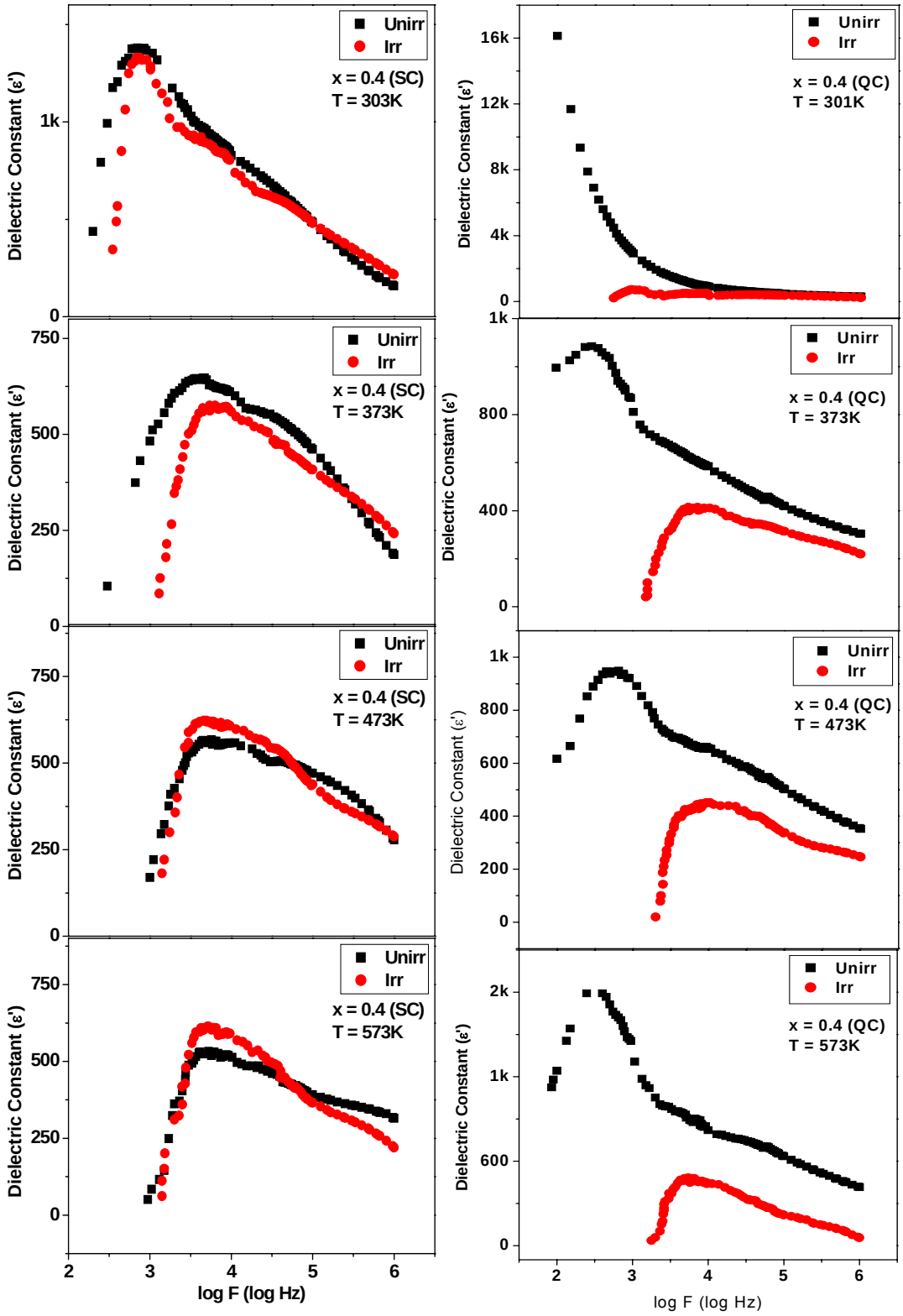

Fig. 6D.12c Dielectric Constant (ε') versus Frequency (log F) at selected temperatures for the composition x = 0.4 of unirradiated and irradiated $CuAl_xCr_xFe_{2-2x}O_4$ (SC-QC) systems

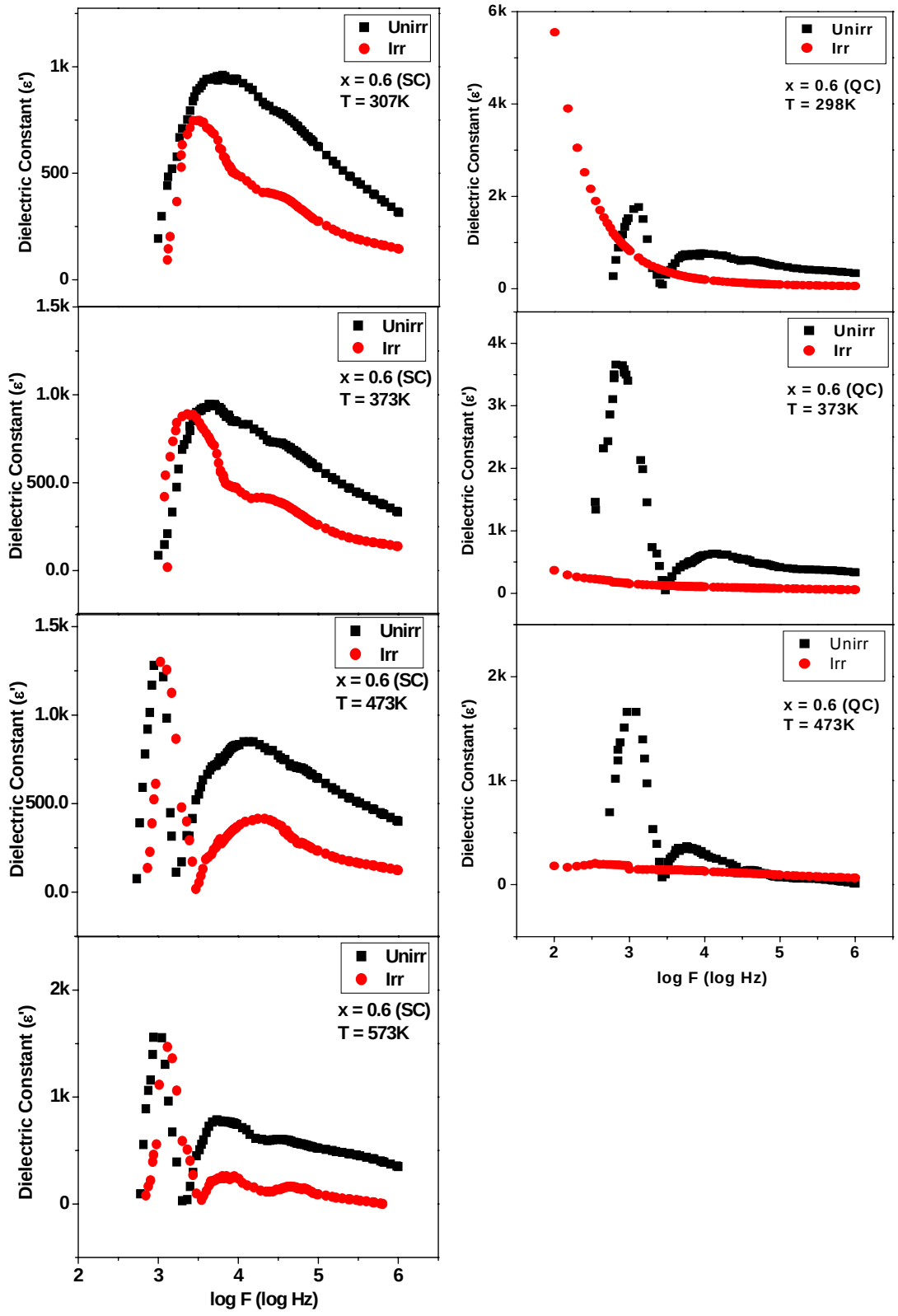

Fig. 6D.12d Dielectric Constant (ε') versus Frequency (log F) at selected temperatures for the composition x = 0.6 of unirradiated and irradiated $CuAl_xCr_xFe_{2-2x}O_4$ (SC-QC) systems

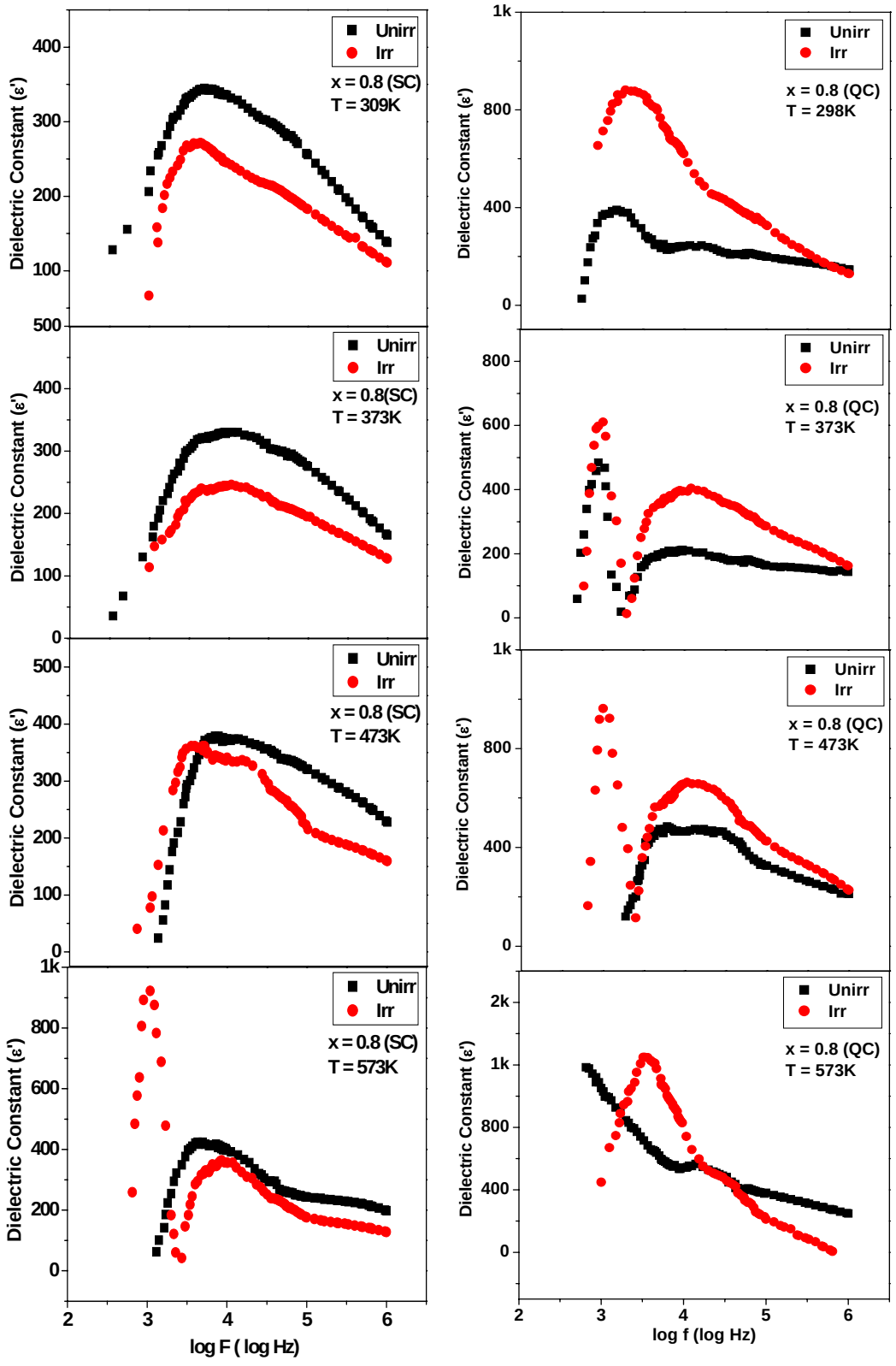

Fig. 6D.12e Dielectric Constant (ε') versus Frequency (log F) at selected temperatures for the composition x = 0.8 of unirradiated and irradiated $CuAl_xCr_xFe_{2-2x}O_4$ (SC-QC) systems

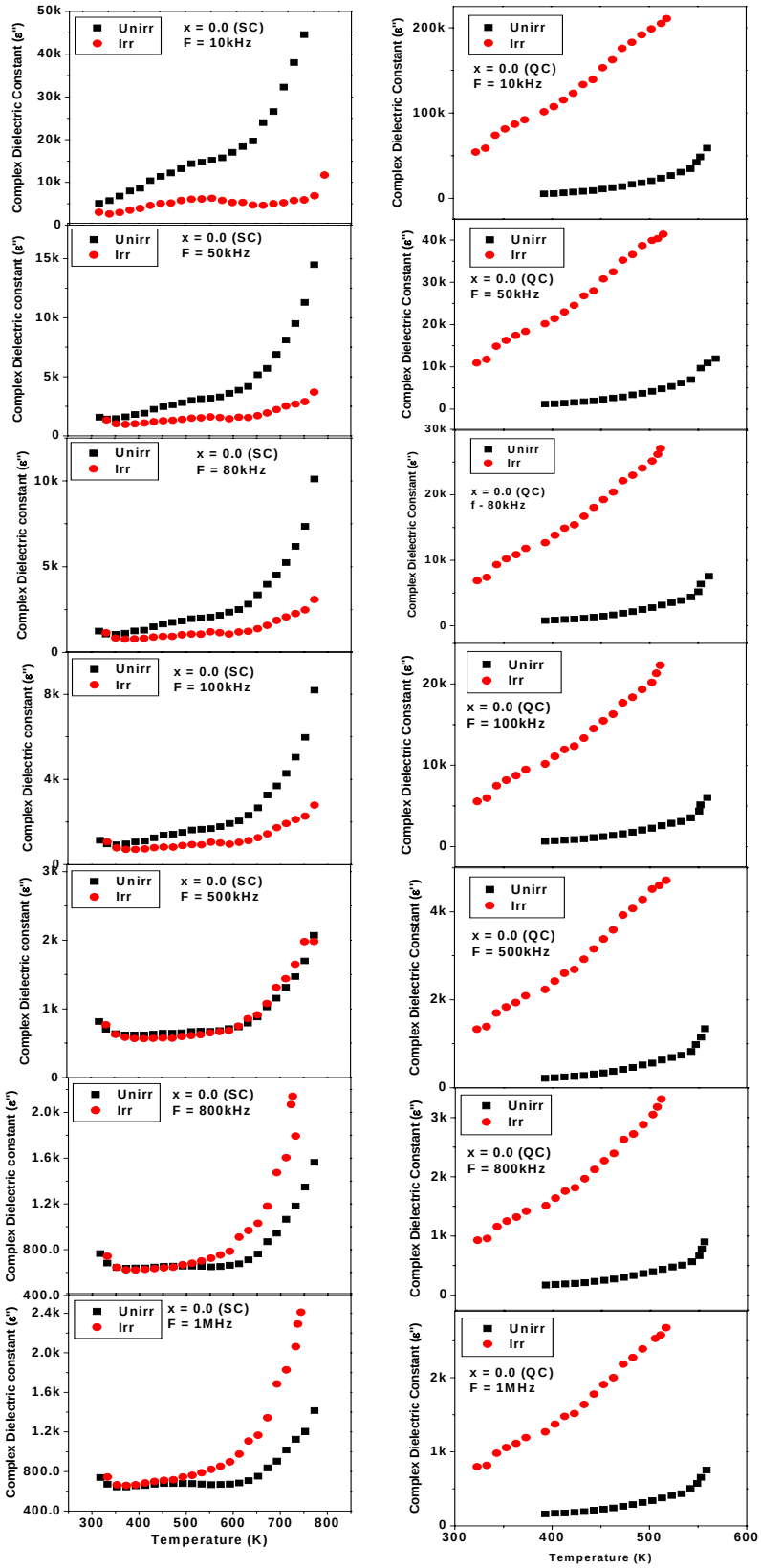

Fig. 6D.13a Thermal variation of Complex Dielectric Constant (ε'') at different frequencies for the composition x = 0.0 of unirradiated and irradiated $CuAl_xCr_xFe_{2-2x}O_4$ (SC-QC) systems

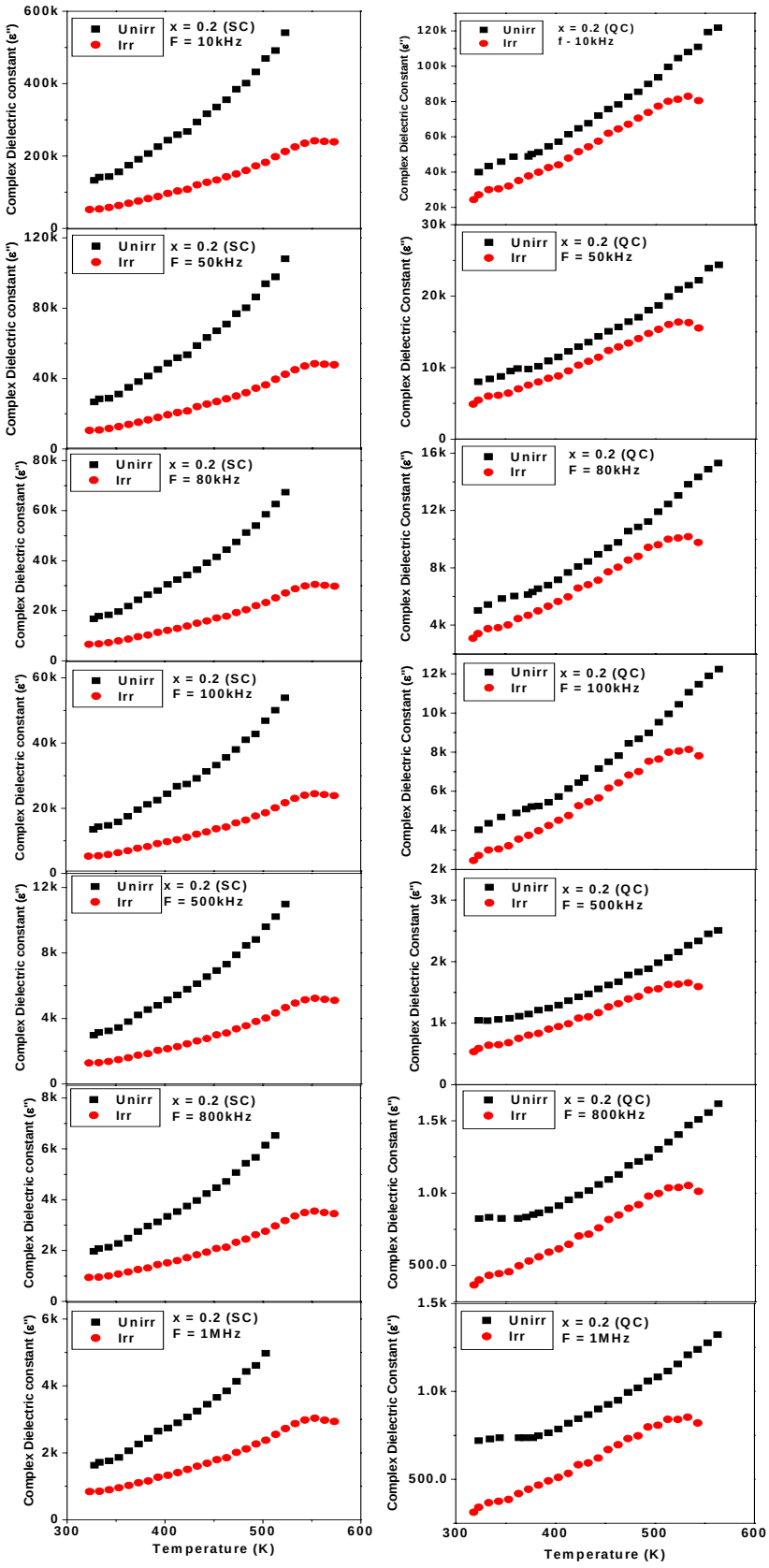

Fig. 6D.13b Thermal variation of Complex Dielectric Constant (ε'') at different frequencies for the composition x = 0.2 of unirradiated and irradiated $CuAl_xCr_xFe_{2-2x}O_4$ (SC-QC) systems

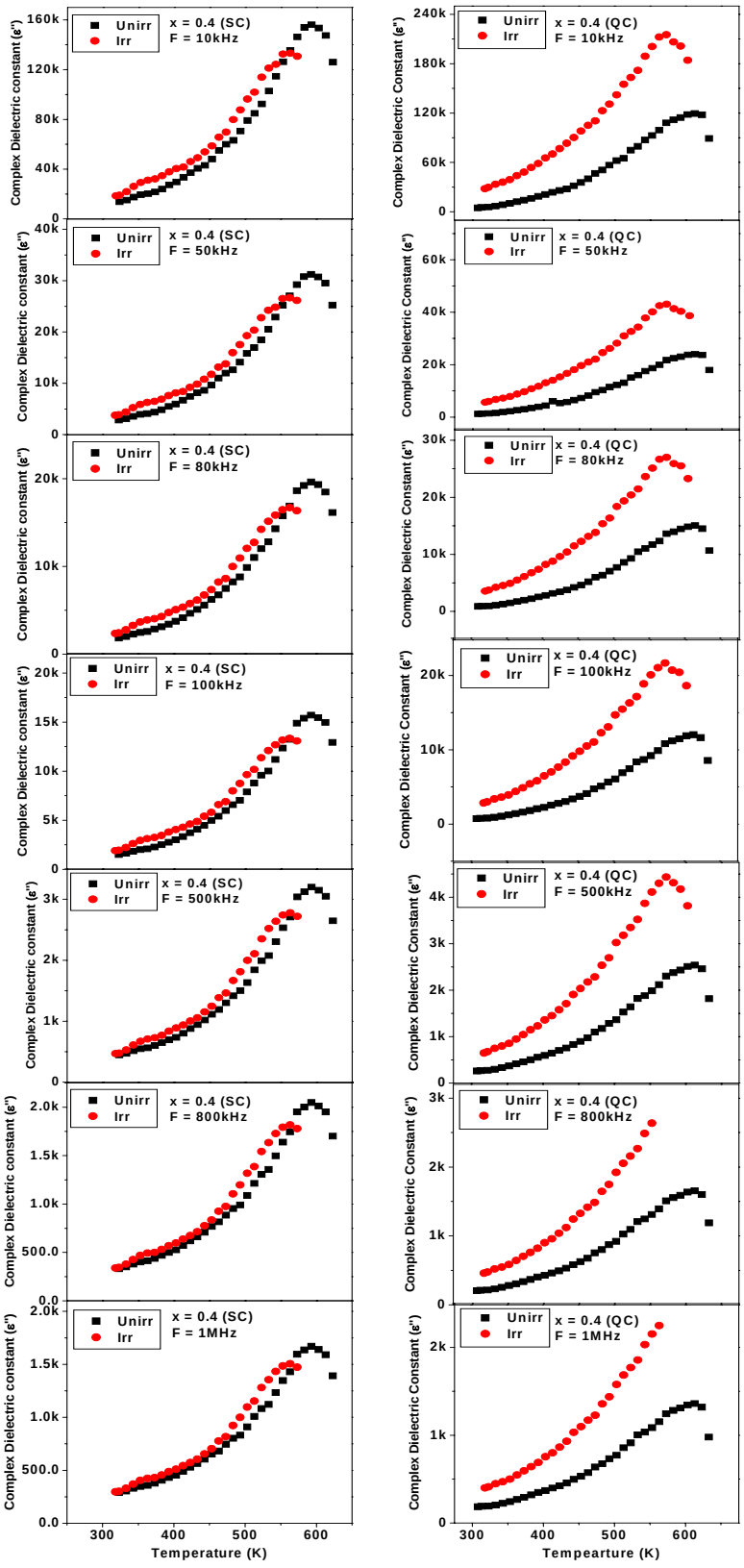

Fig. 6D.13c Thermal variation of Complex Dielectric Constant (ε'') at different frequencies for the composition x = 0.4 of unirradiated and irradiated $CuAl_xCr_xFe_{2-2x}O_4$ (SC-QC) systems

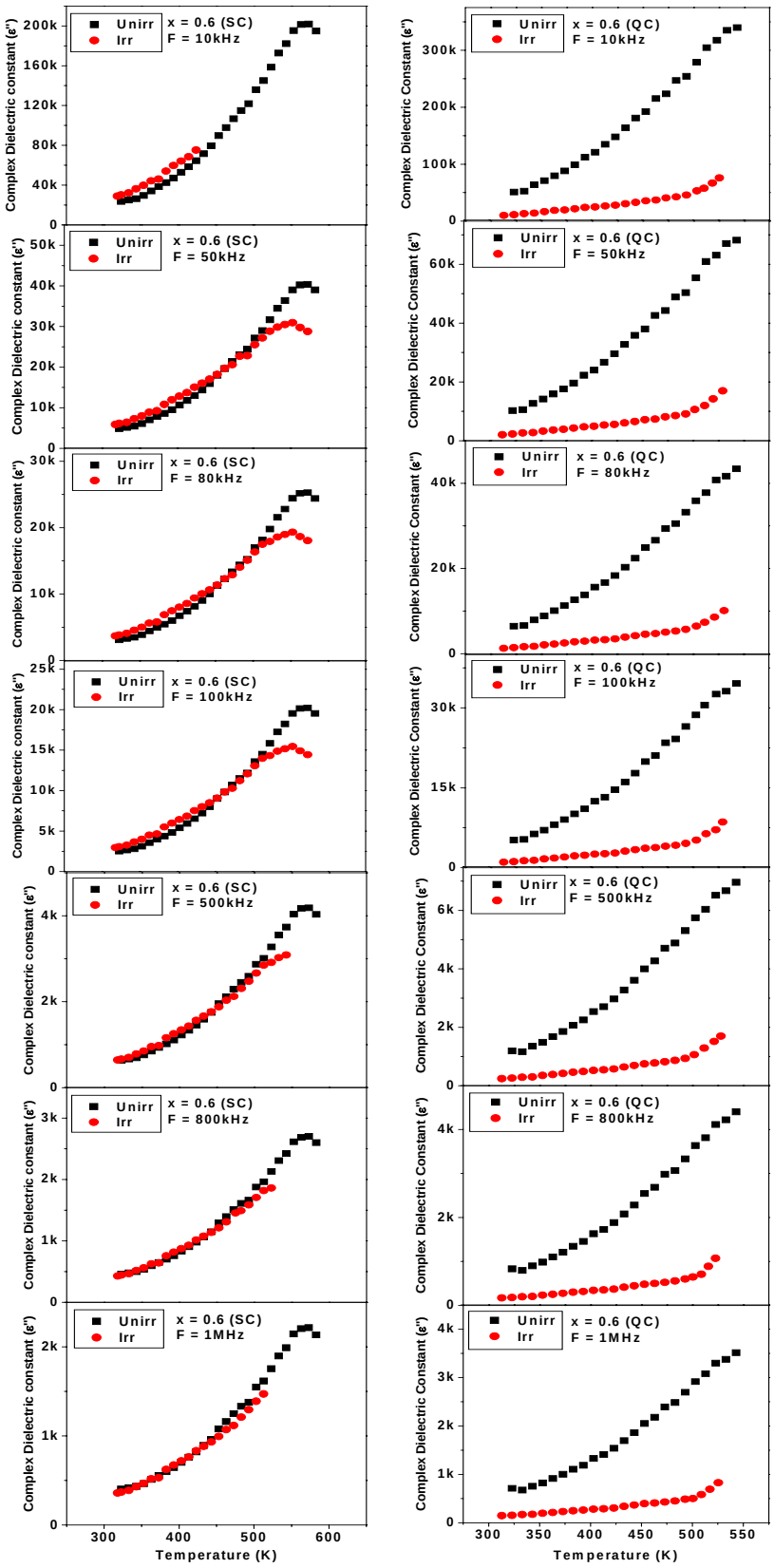

Fig. 6D.13d Thermal variation of Complex Dielectric Constant (ε'') at different frequencies for the composition x = 0.6 of unirradiated and irradiated $CuAl_xCr_xFe_{2-2x}O_4$ (SC-QC) systems

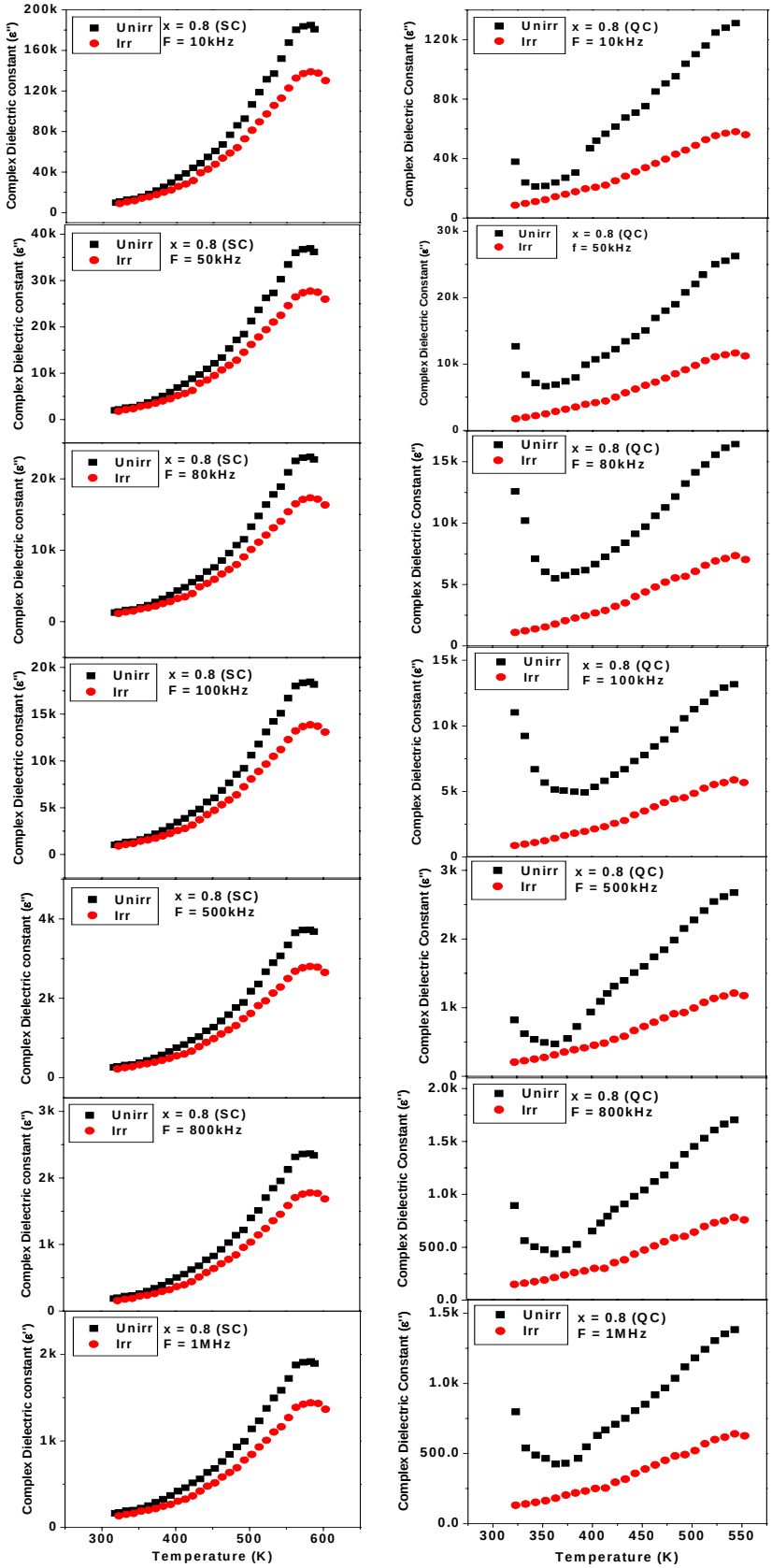

Fig. 6D.13e Thermal variation of Complex Dielectric Constant (ε'') at different frequencies for the composition x = 0.8 of unirradiated and irradiated $CuAl_xCr_xFe_{2-2x}O_4$ (SC-QC) systems

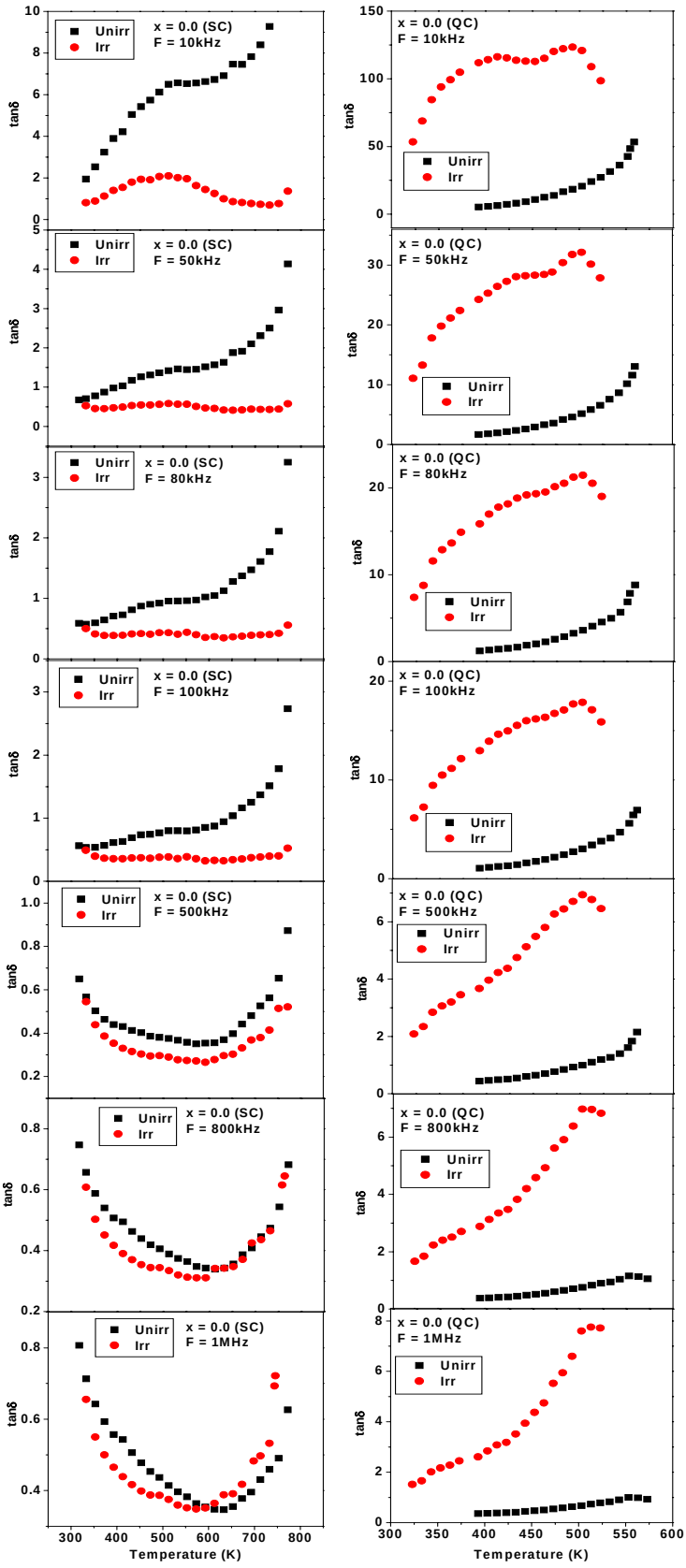

Fig. 6D.14a Thermal variation of Dielectric loss tangent (tanδ) at different frequencies for the composition x = 0.0 of unirradiated and irradiated $CuAl_xCr_xFe_{2-2x}O_4$ (SC-QC) systems

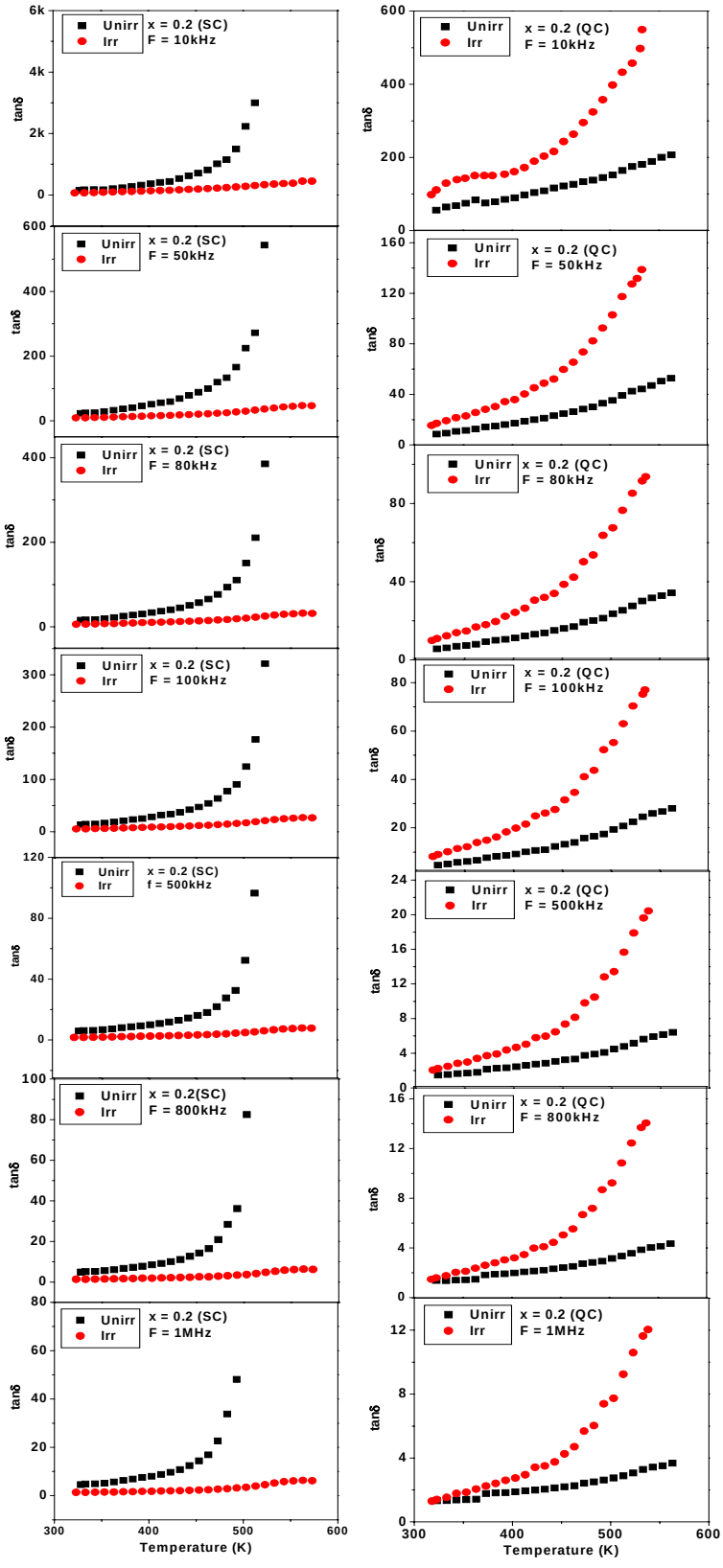

Fig. 6D.14b Thermal variation of Dielectric loss tangent (tanδ) at different frequencies for the composition x = 0.2 of unirradiated and irradiated $CuAl_xCr_xFe_{2-2x}O_4$ (SC-QC) systems

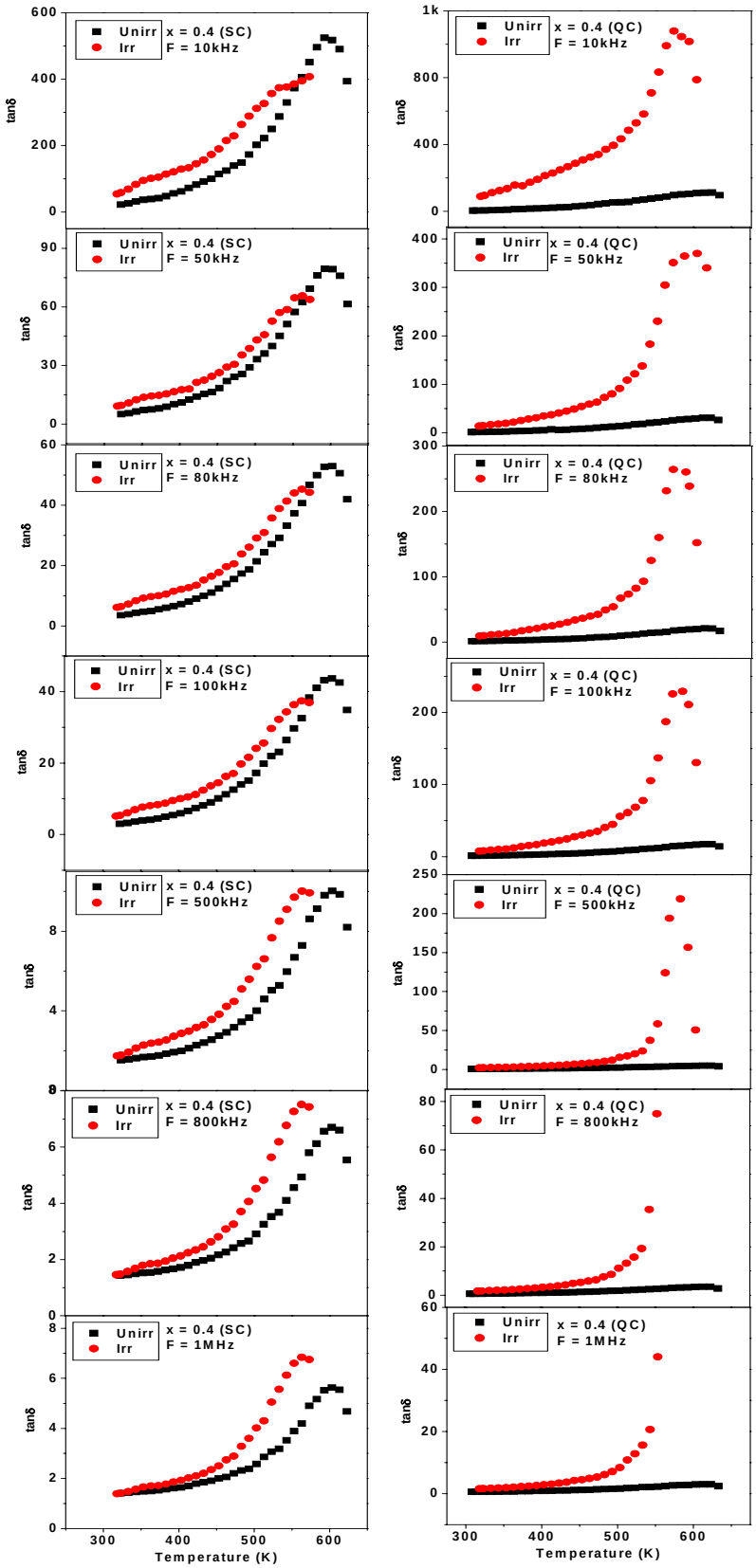

Fig. 6D.14c Thermal variation of Dielectric loss tangent (tanδ) at different frequencies for the composition x = 0.4 of unirradiated and irradiated $CuAl_xCr_xFe_{2-2x}O_4$ (SC-QC) systems

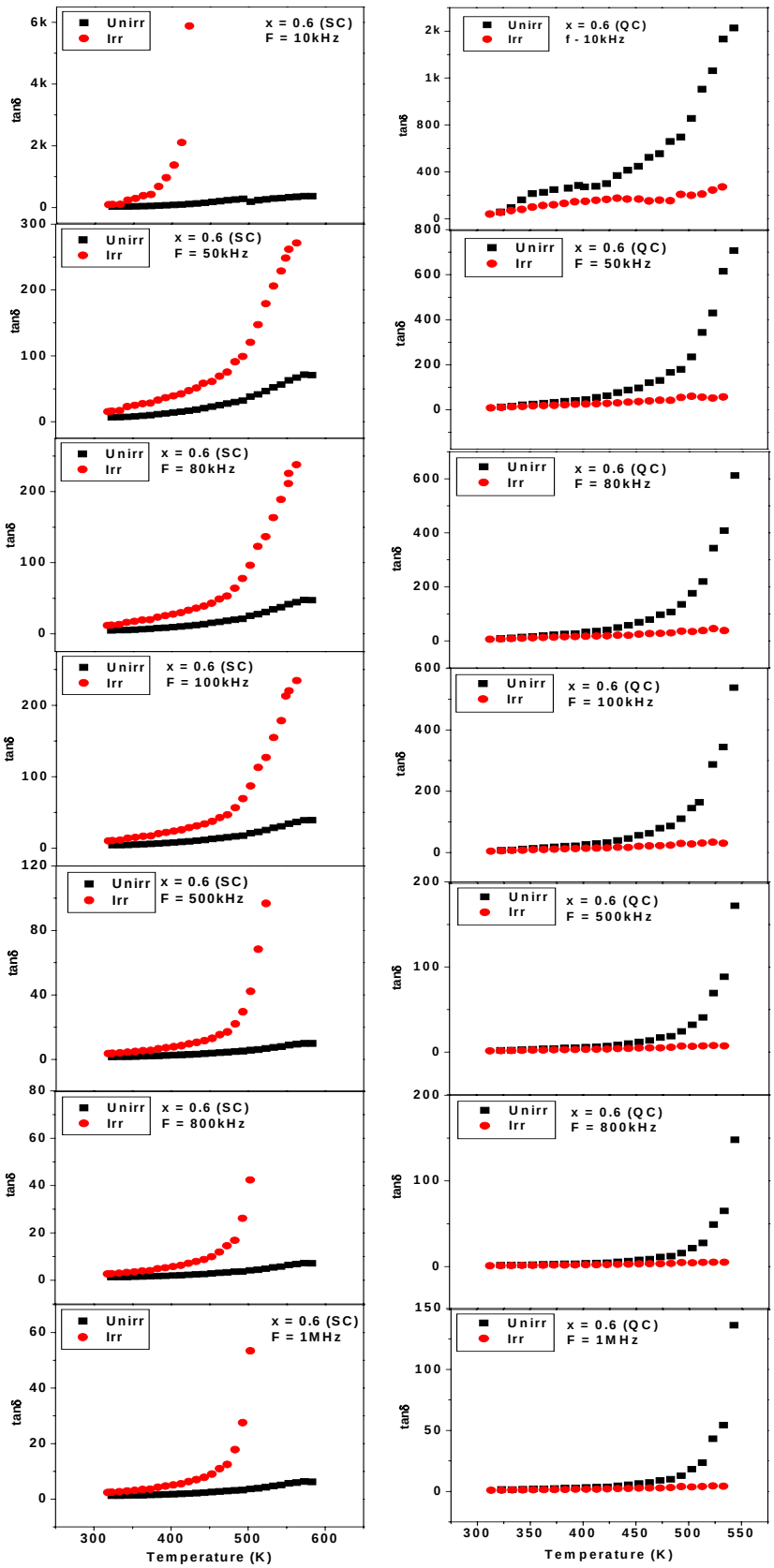

Fig. 6D.14d Thermal variation of Dielectric loss tangent (tanδ) at different frequencies for the composition x = 0.6 of unirradiated and irradiated $CuAl_xCr_xFe_{2-2x}O_4$ (SC-QC) systems

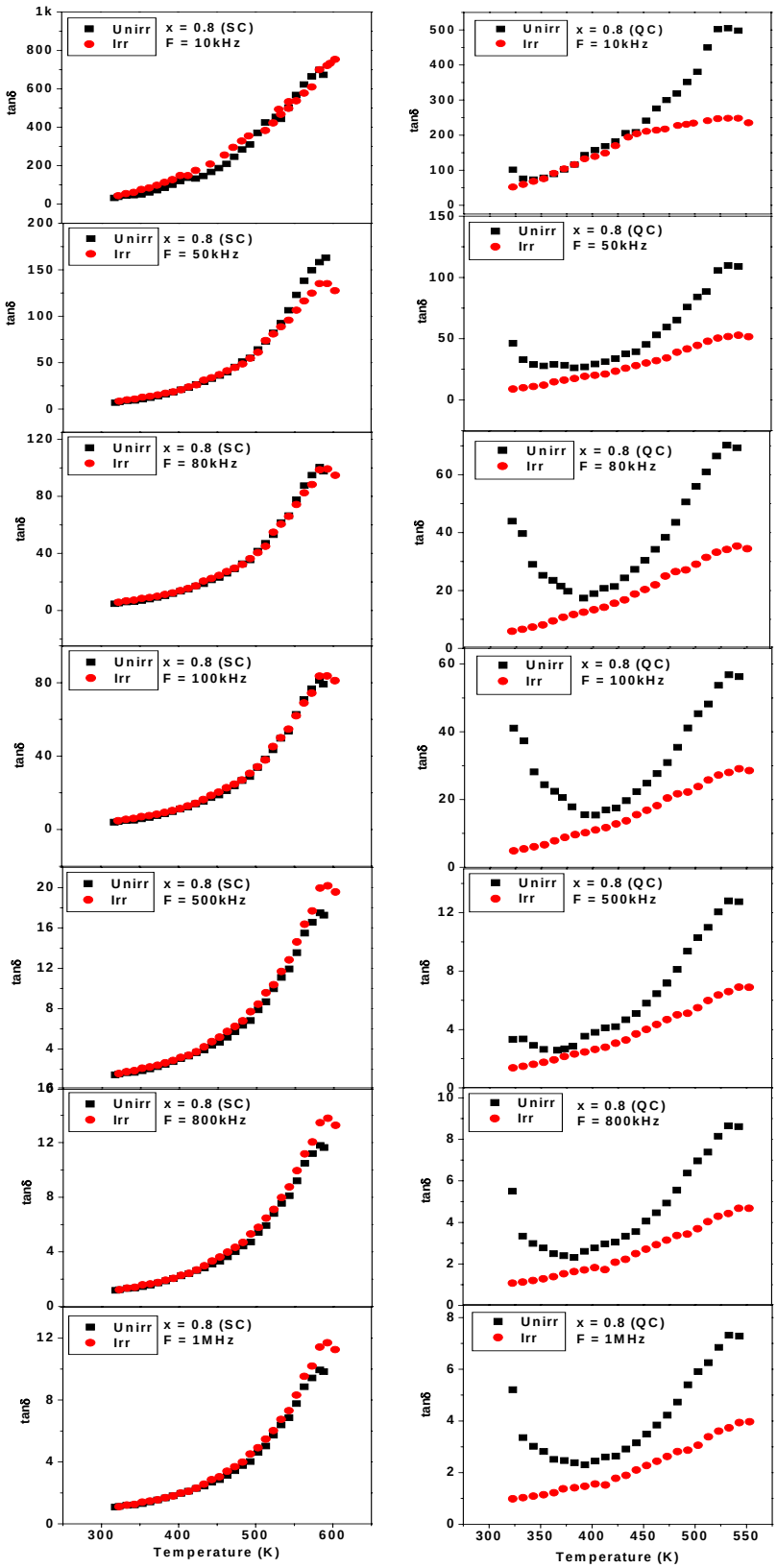

Fig. 6D.14e Thermal variation of Dielectric loss tangent (tanδ) at different frequencies for the composition x = 0.8 of unirradiated and irradiated $CuAl_xCr_xFe_{2-2x}O_4$ (SC-QC) systems

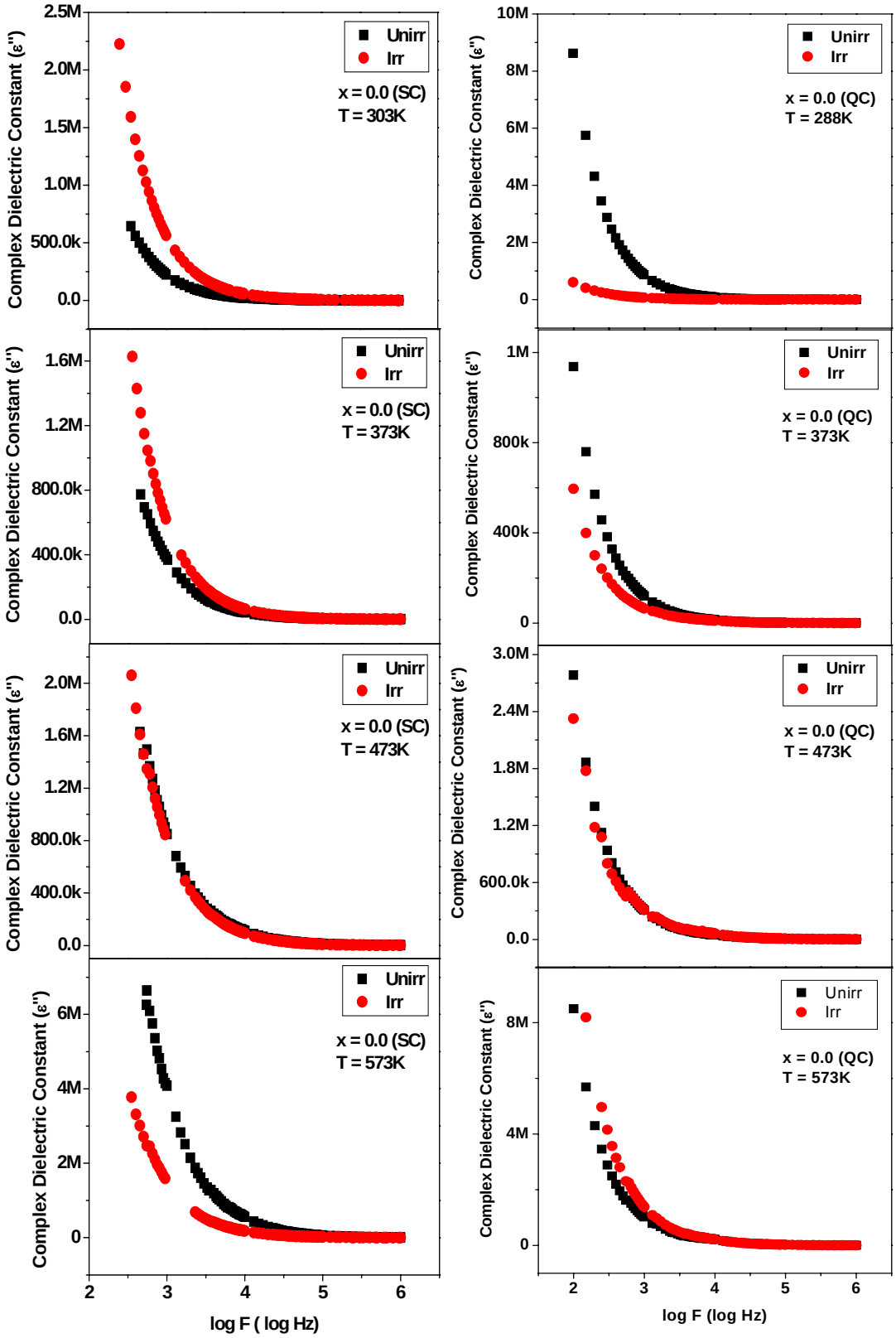

Fig. 6D.15a Complex Dielectric Constant (ε”) versus Frequency (log F) at selected temperatures for the composition x = 0.0 of unirradiated and irradiated $CuAl_xCr_xFe_{2-2x}O_4$ (SC-QC) systems

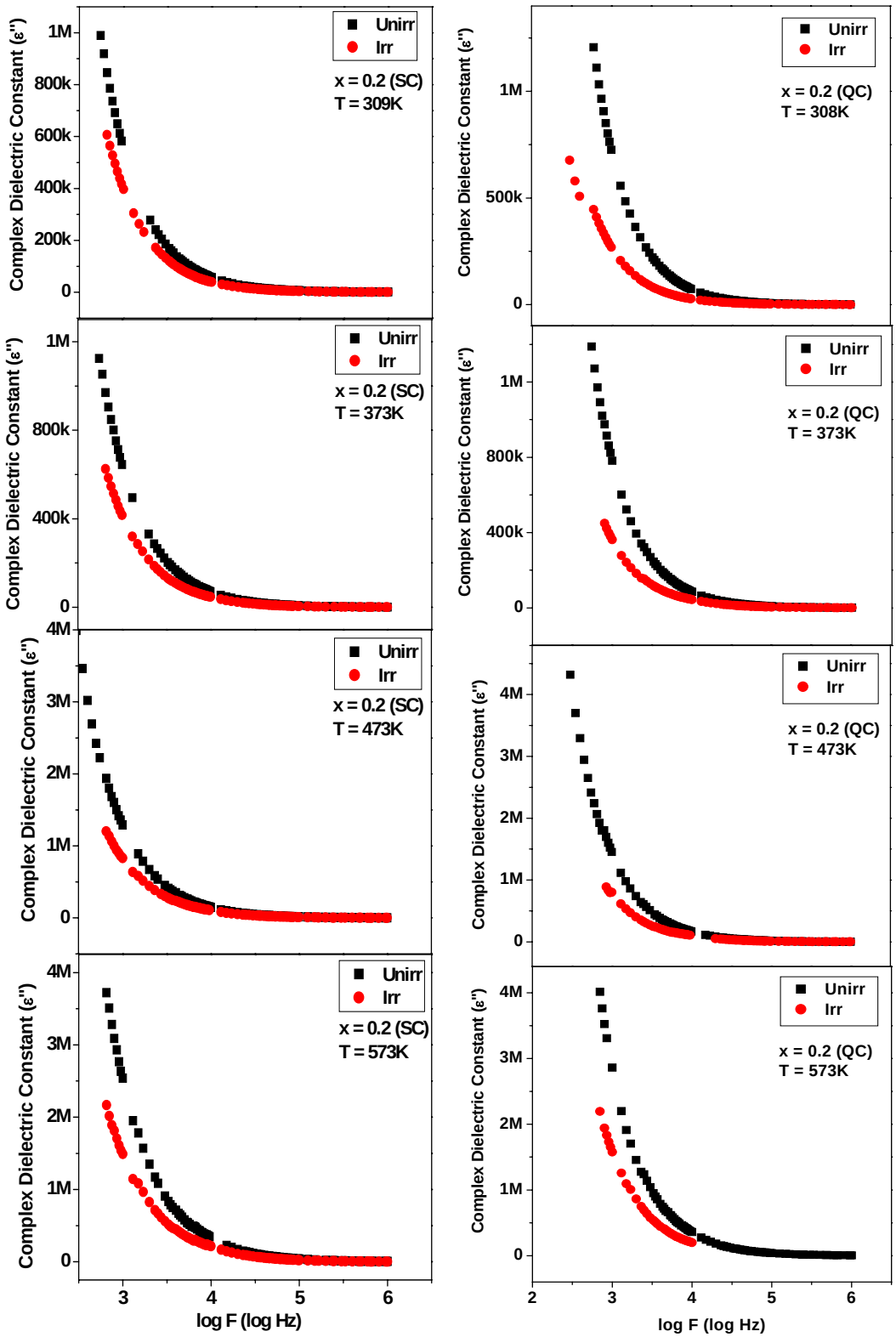

Fig. 6D.15b Complex Dielectric Constant (ε”) versus Frequency (log F) at selected temperatures for the composition x = 0.2 of unirradiated and irradiated $CuAl_xCr_xFe_{2-2x}O_4$ (SC-QC) systems

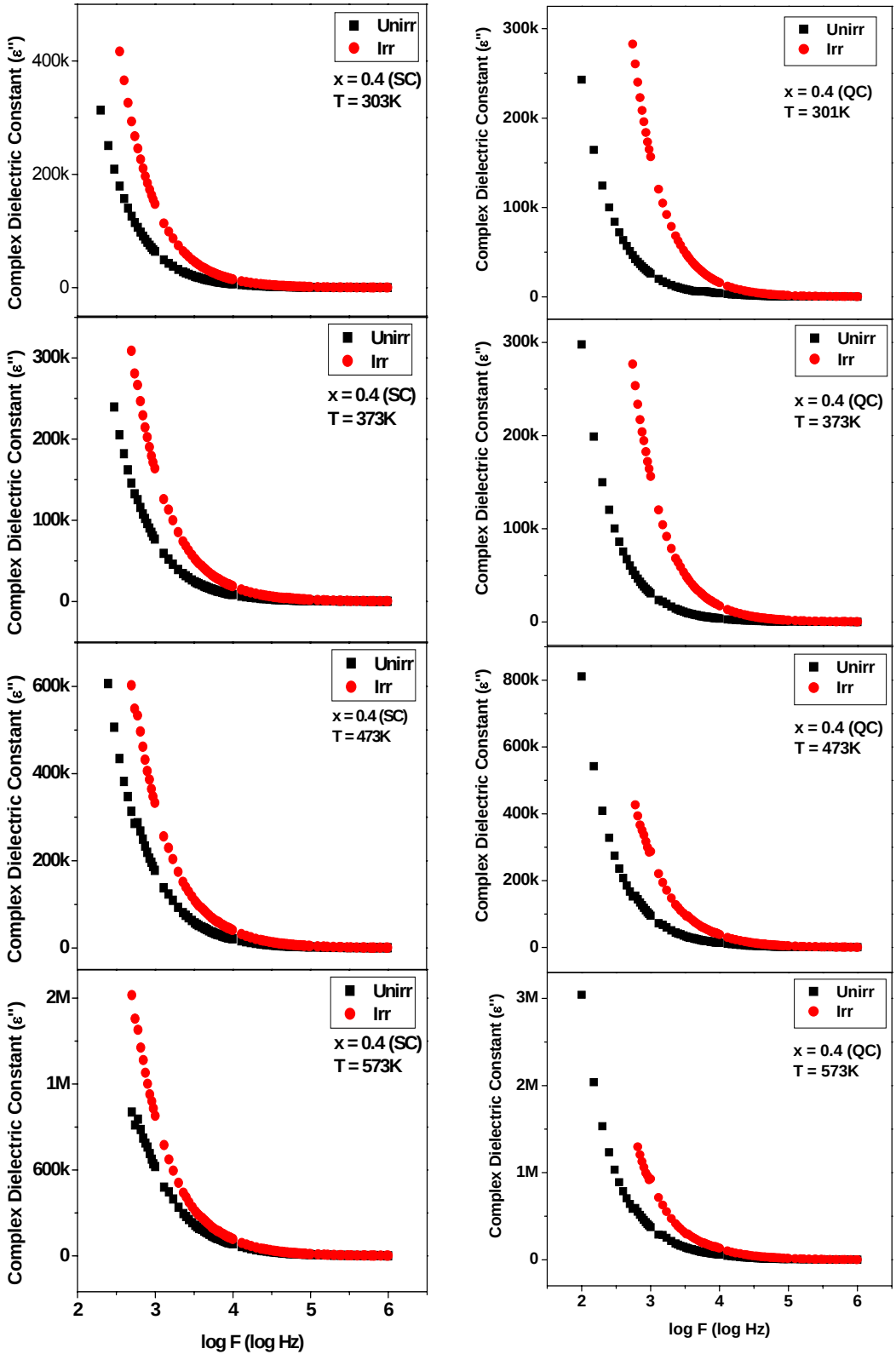

Fig. 6D.15c Complex Dielectric Constant (ε") versus Frequency (log F) at selected temperatures for the composition x = 0.4 of unirradiated and irradiated $CuAl_xCr_xFe_{2-2x}O_4$ (SC-QC) systems

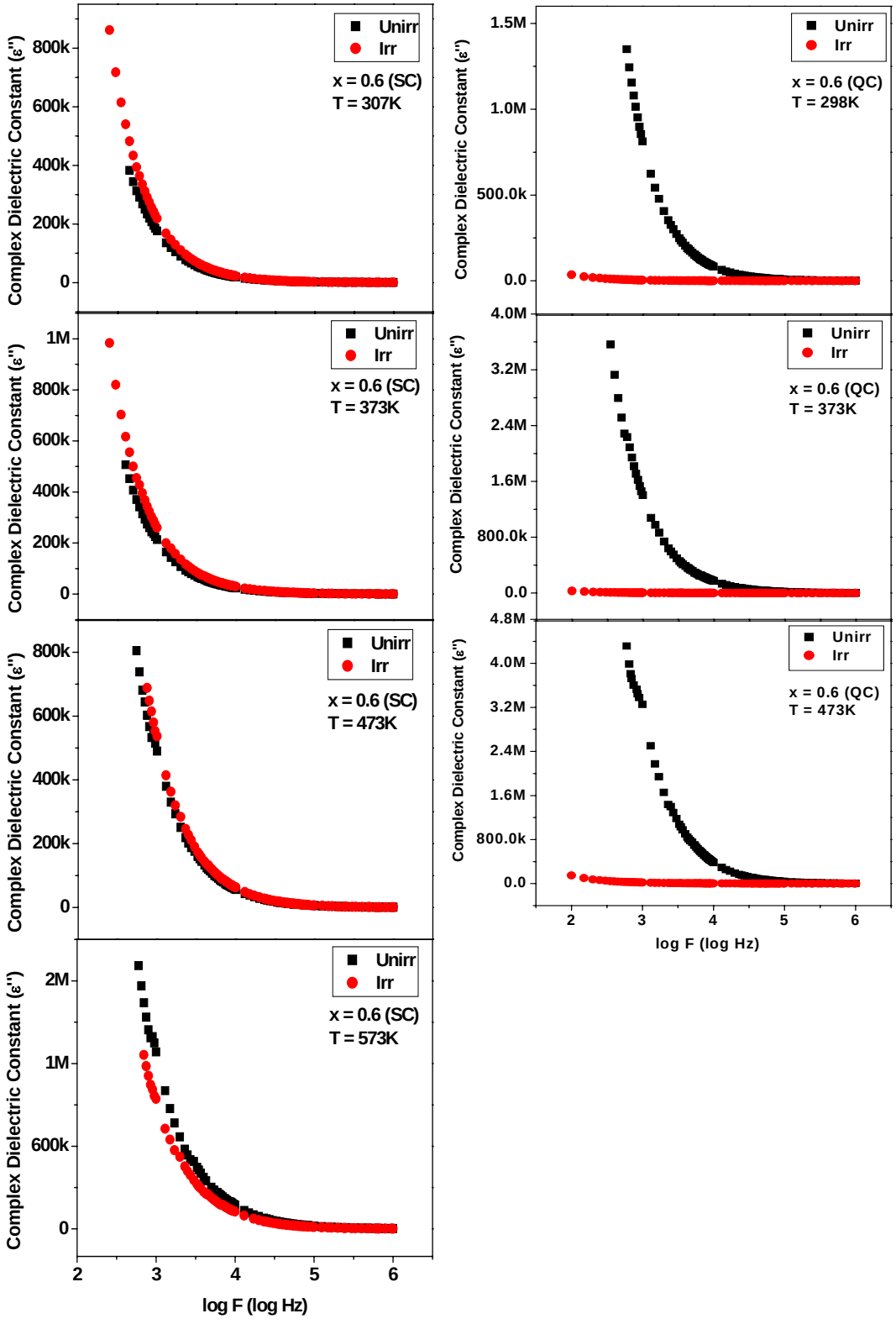

Fig. 6D.15d Complex Dielectric Constant (ε") versus Frequency (log F) at selected temperatures for the composition x = 0.6 of unirradiated and irradiated $CuAl_xCr_xFe_{2-2x}O_4$ (SC-QC) systems

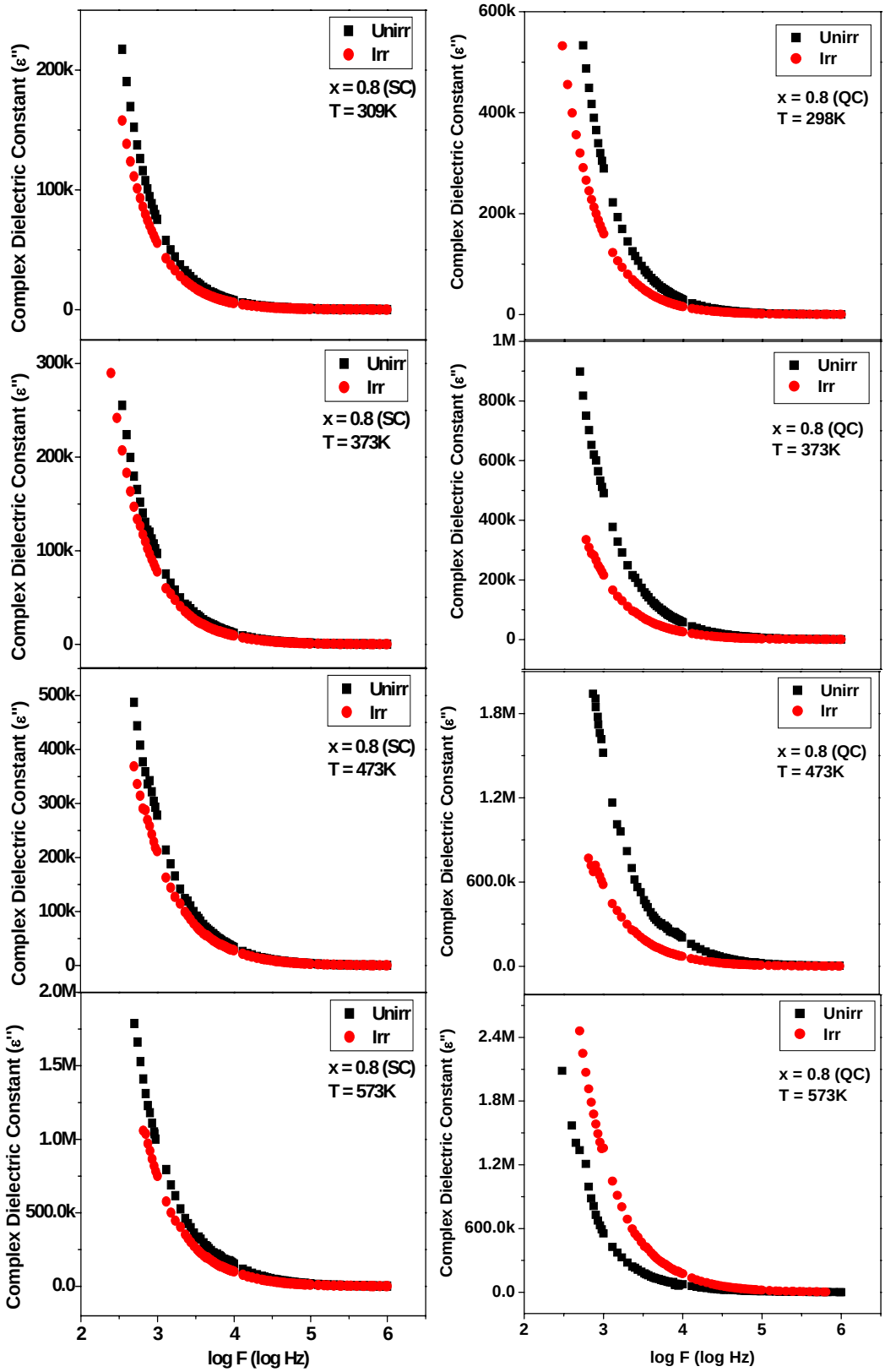

Fig. 6D.15e Complex Dielectric Constant (ε") versus Frequency (log F) at selected temperatures for the composition x = 0.8 of unirradiated and irradiated $CuAl_xCr_xFe_{2-2x}O_4$ (SC-QC) systems

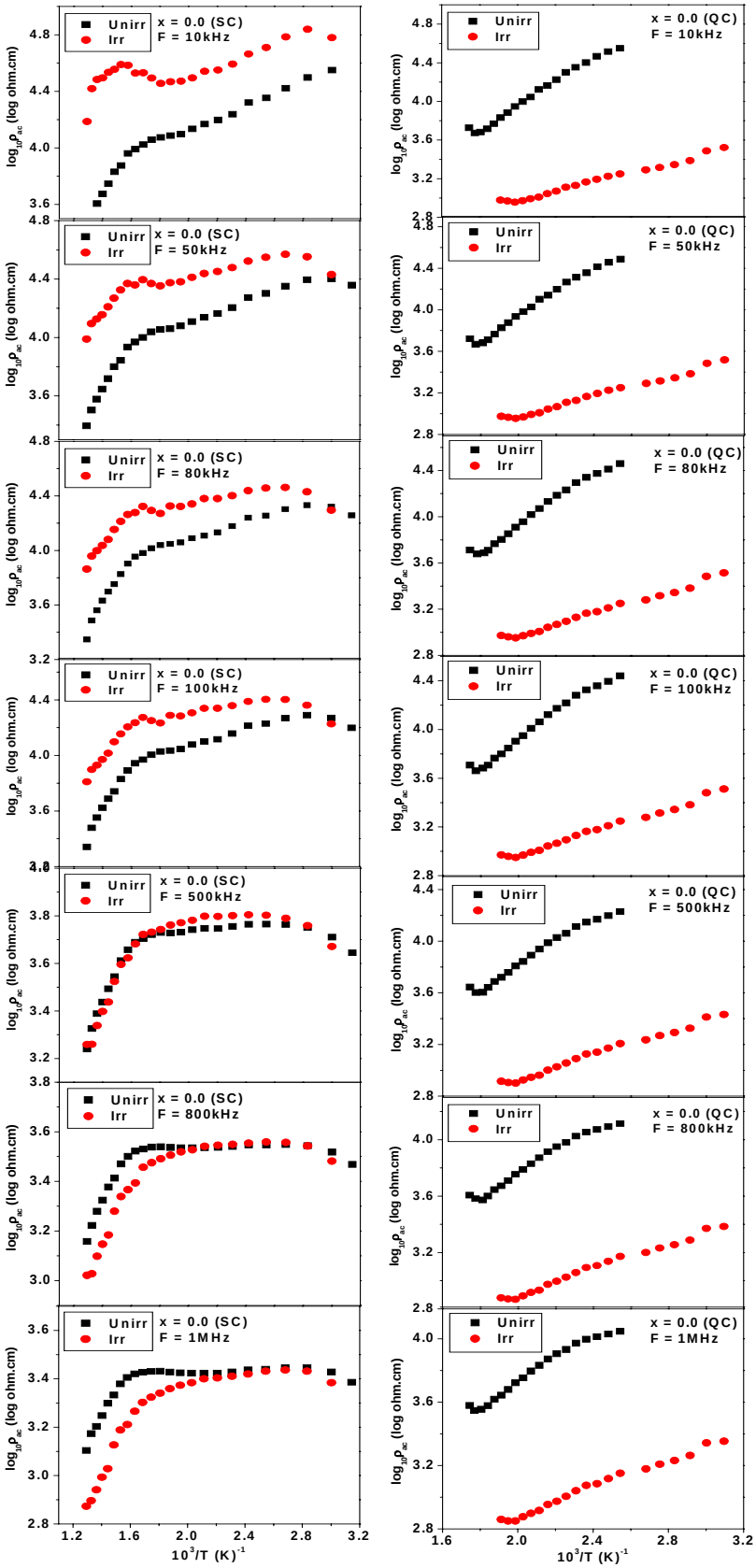

Fig. 6D.16a Thermal variation of AC resistivity ($\log_{10}\rho_{ac}$) at different frequencies for the composition x = 0.0 of unirradiated and irradiated $CuAl_xCr_xFe_{2-2x}O_4$ (SC-QC) systems

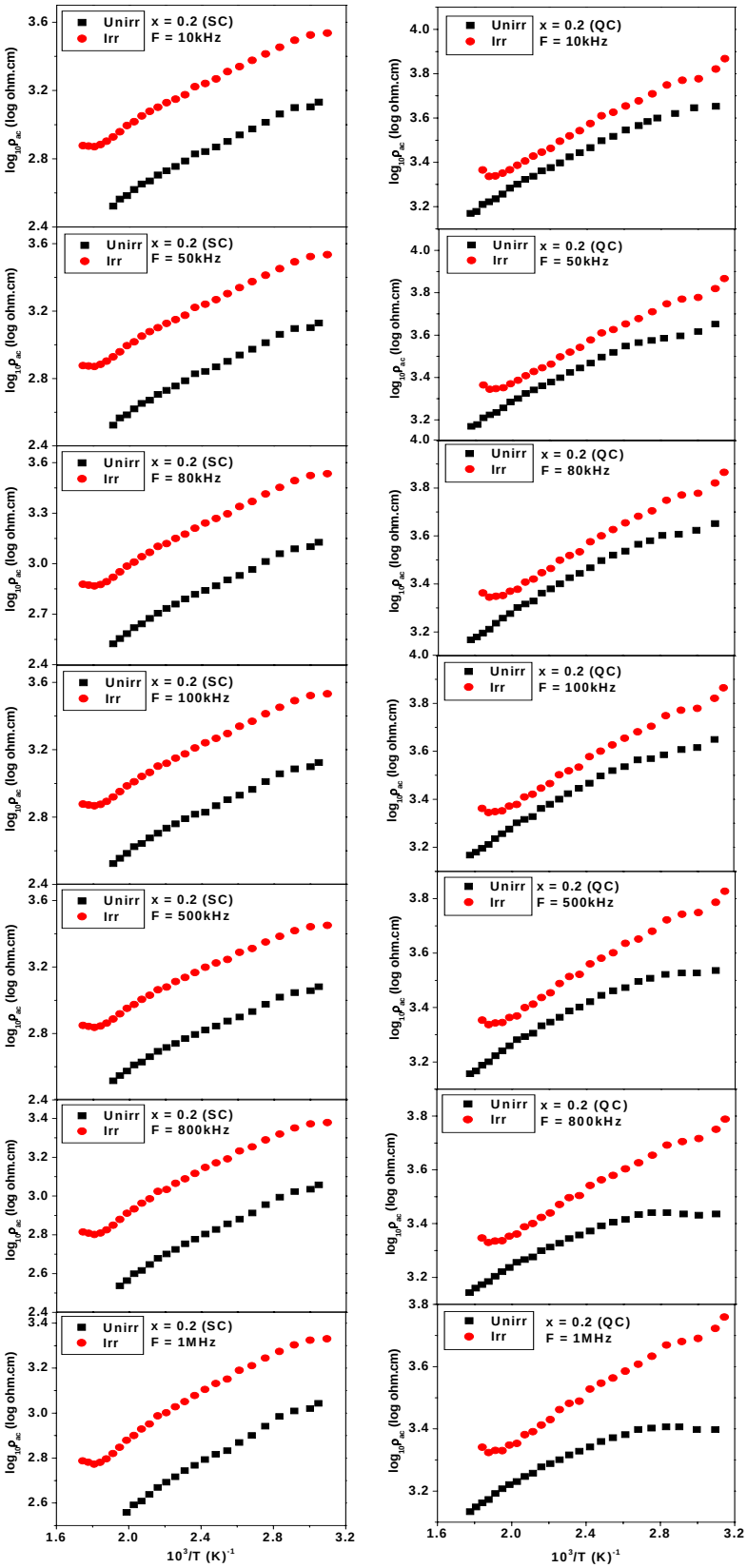

Fig. 6D.16b Thermal variation of AC resistivity ($log_{10}\rho_{ac}$) at different frequencies for the composition x = 0.2 of unirradiated and irradiated $CuAl_xCr_xFe_{2-2x}O_4$ (SC-QC) systems

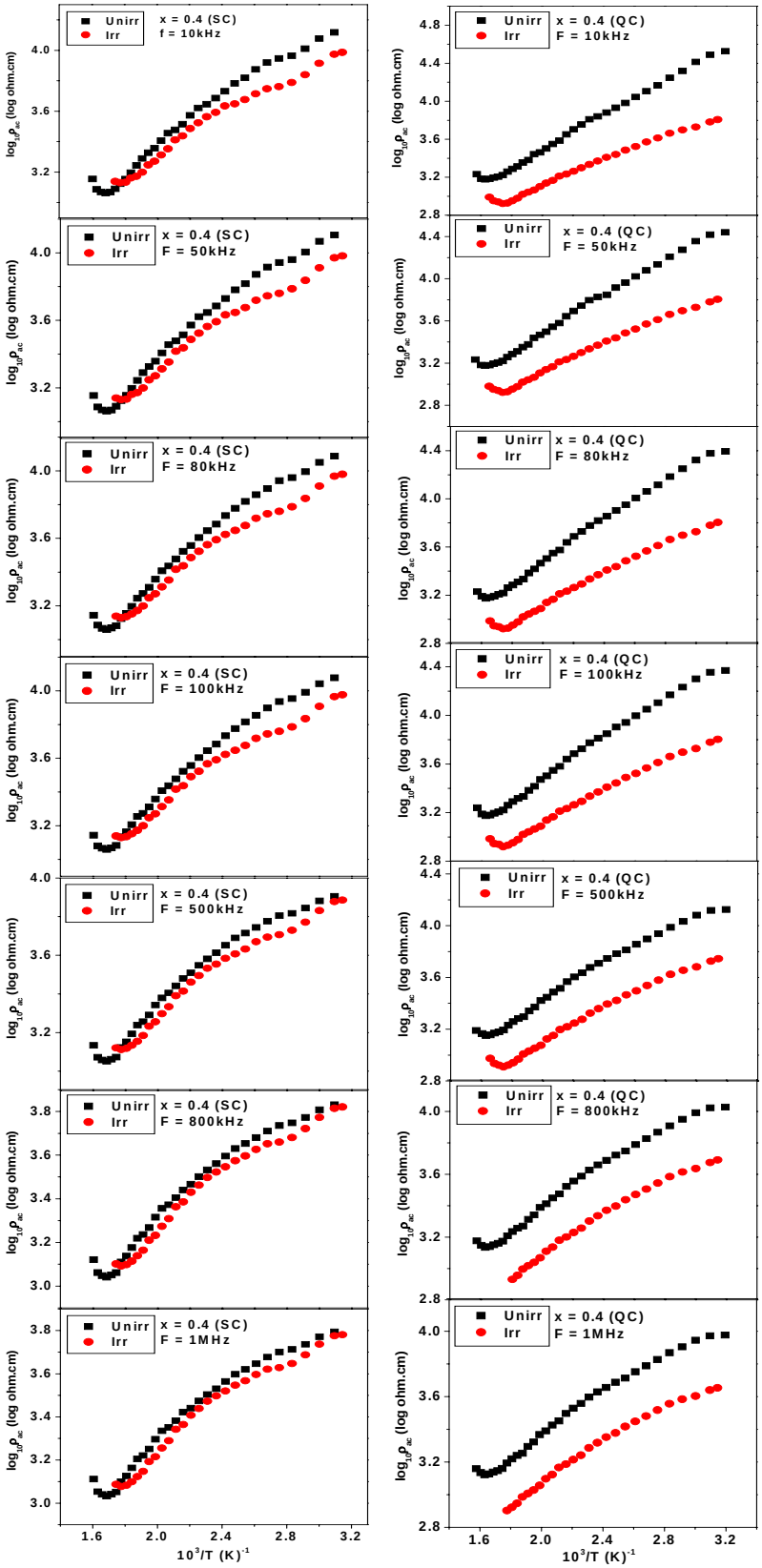

Fig. 6D.16c Thermal variation of AC resistivity ($\log_{10}\rho_{ac}$) at different frequencies for the composition x = 0.4 of unirradiated and irradiated $CuAl_xCr_xFe_{2-2x}O_4$ (SC-QC) systems

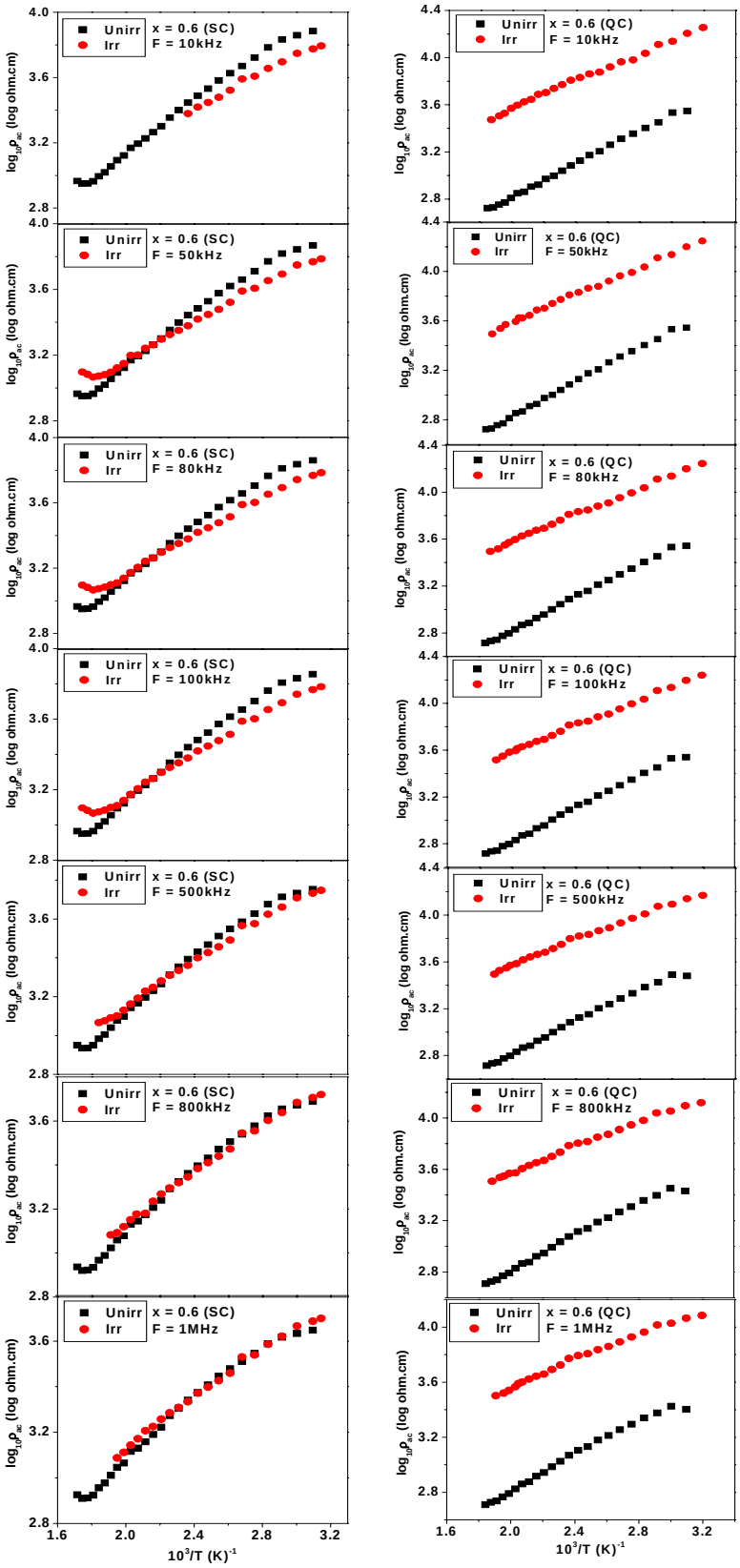

Fig. 6D.16d Thermal variation of AC resistivity ($\log_{10}\rho_{ac}$) at different frequencies for the composition x = 0.6 of the unirradiated and irradiated $CuAl_xCr_xFe_{2-2x}O_4$ (SC-QC) systems

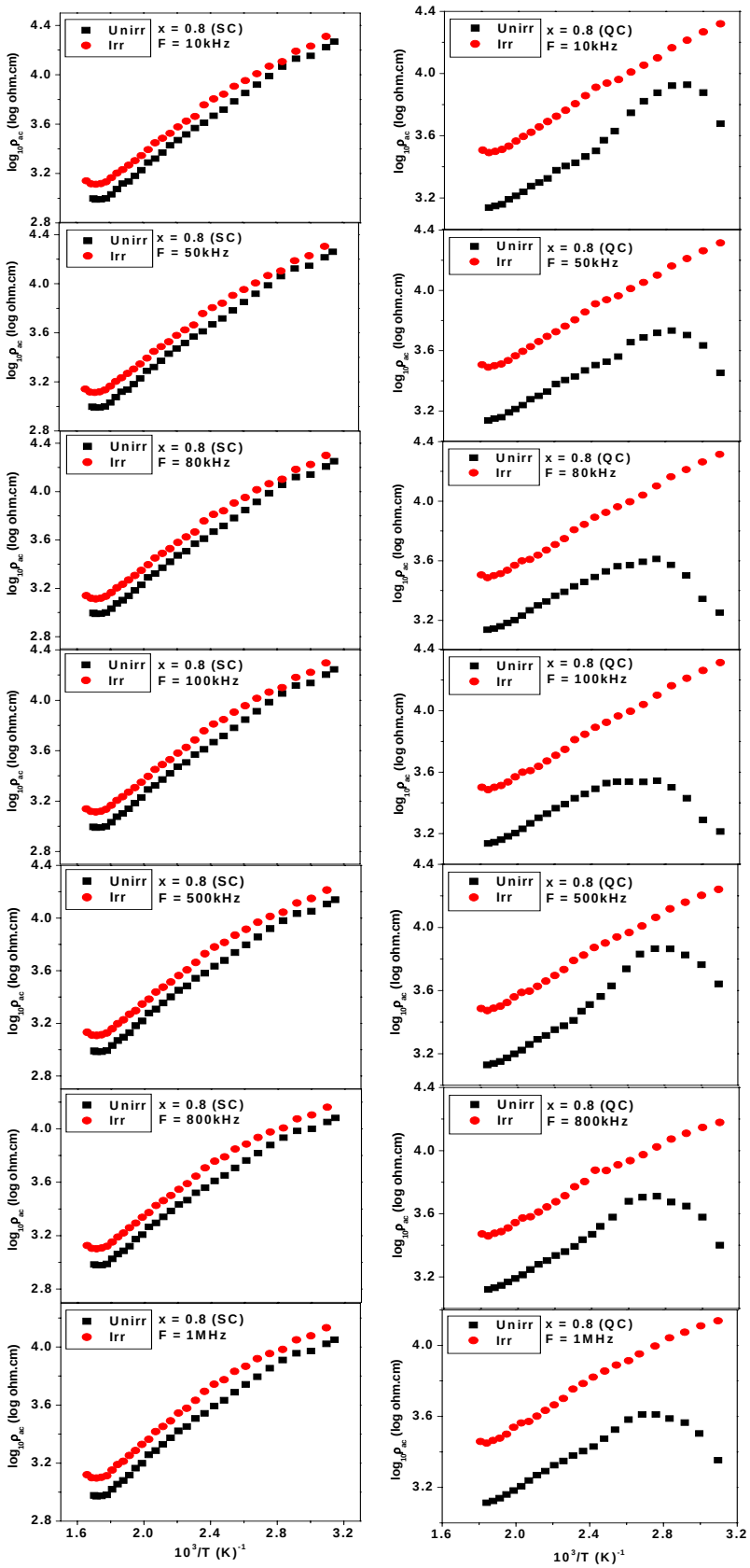

Fig. 6D.16e Thermal variation of AC resistivity ($\log_{10}\rho_{ac}$) at different frequencies for the composition x = 0.8 of unirradiated and irradiated $CuAl_xCr_xFe_{2-2x}O_4$ (SC-QC) systems

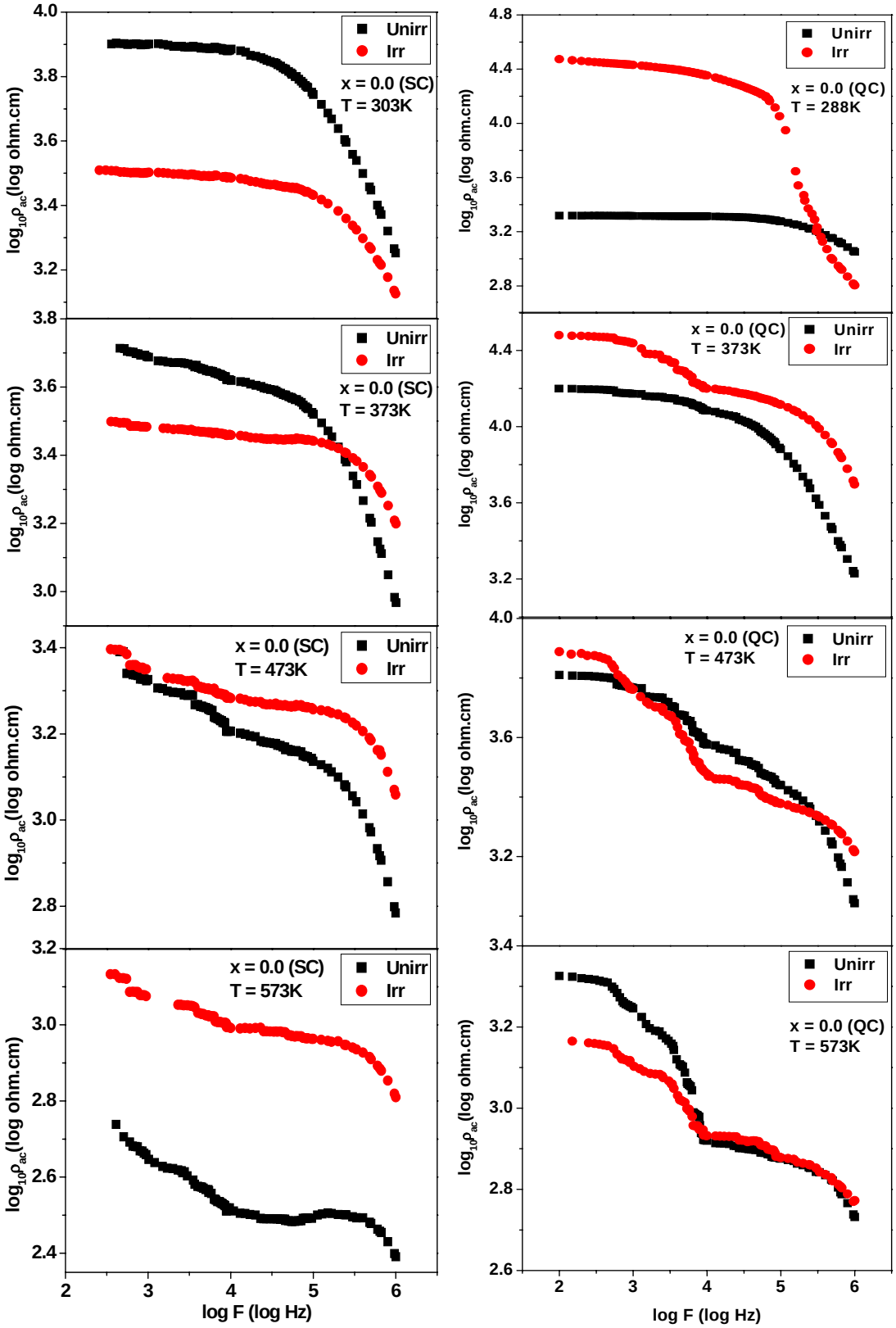

Fig. 6D.17a AC resistivity ($\log_{10}\rho_{ac}$) versus Frequency (log F) at selected temperatures for the composition x = 0.0 of unirradiated and irradiated $CuAl_xCr_xFe_{2-2x}O_4$ (SC-QC) systems

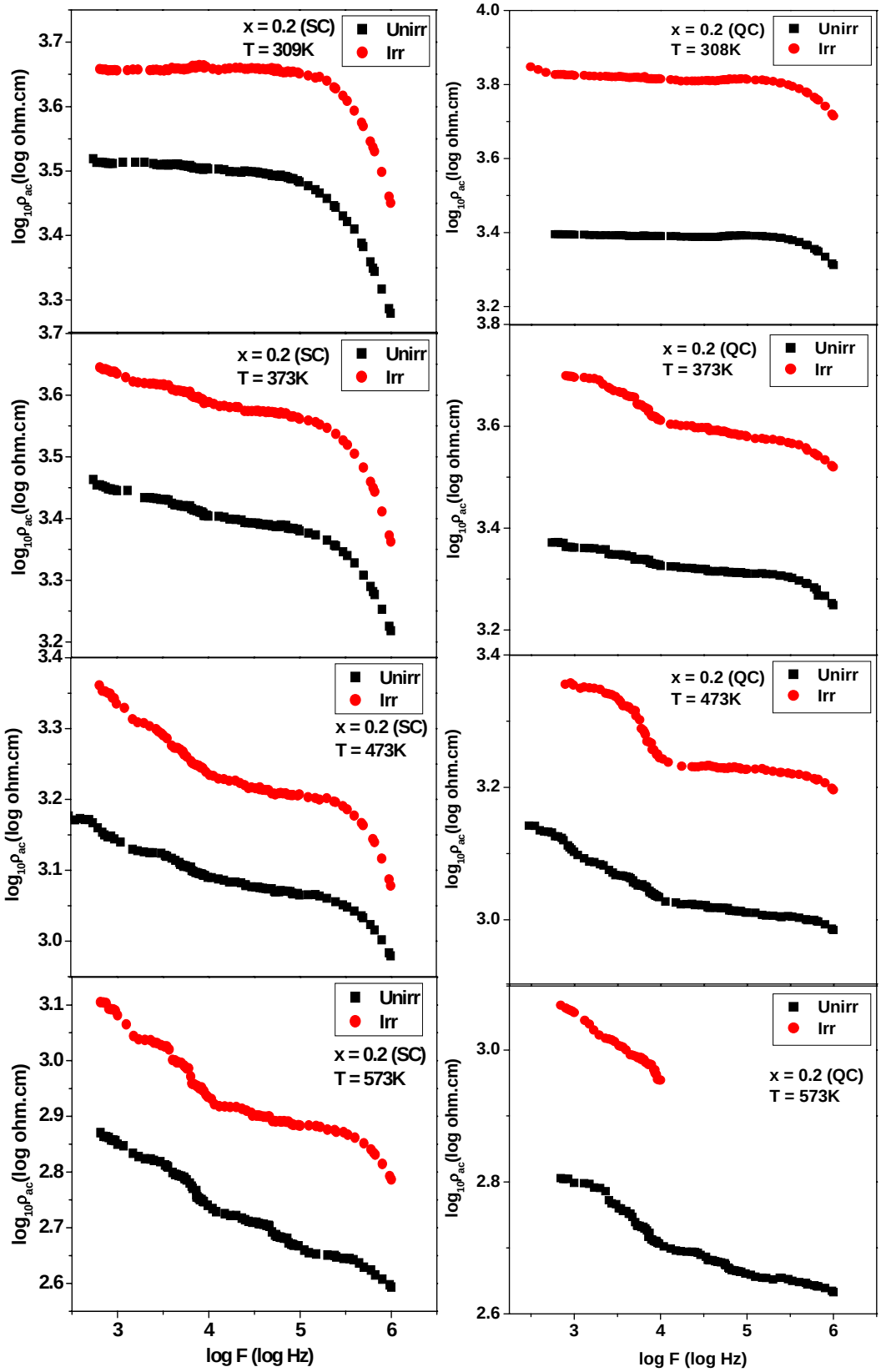

Fig. 6D.17b AC resistivity ($\log_{10}\rho_{ac}$) versus Frequency (log F) at selected temperatures for the composition x = 0.2 of unirradiated and irradiated $CuAl_xCr_xFe_{2-2x}O_4$ (SC-QC) systems

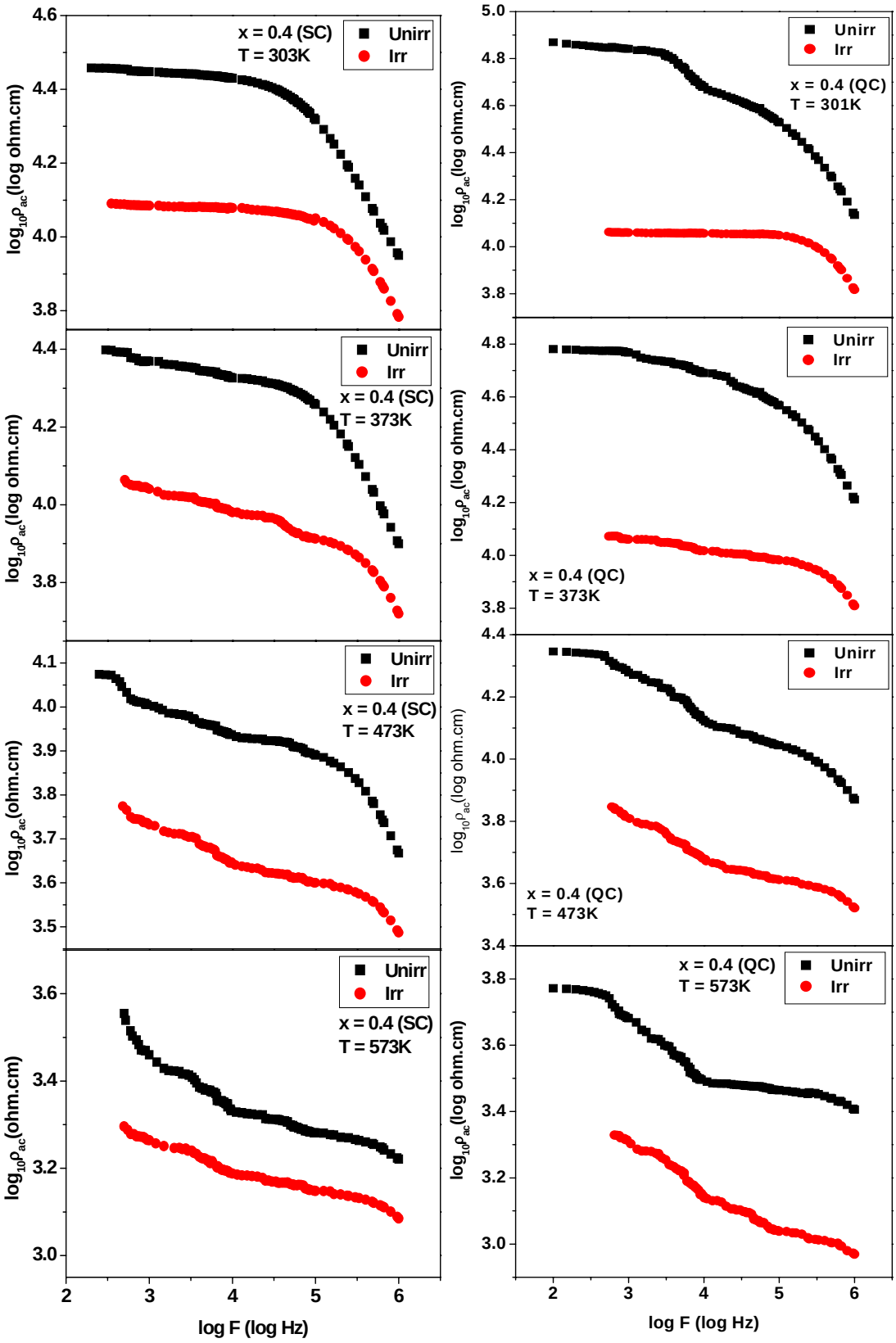

Fig. 6D.17c AC resistivity ($\log_{10}\rho_{ac}$) versus Frequency (log F) at selected temperatures for the composition x = 0.4 of unirradiated and irradiated $CuAl_xCr_xFe_{2-2x}O_4$ (SC-QC) systems

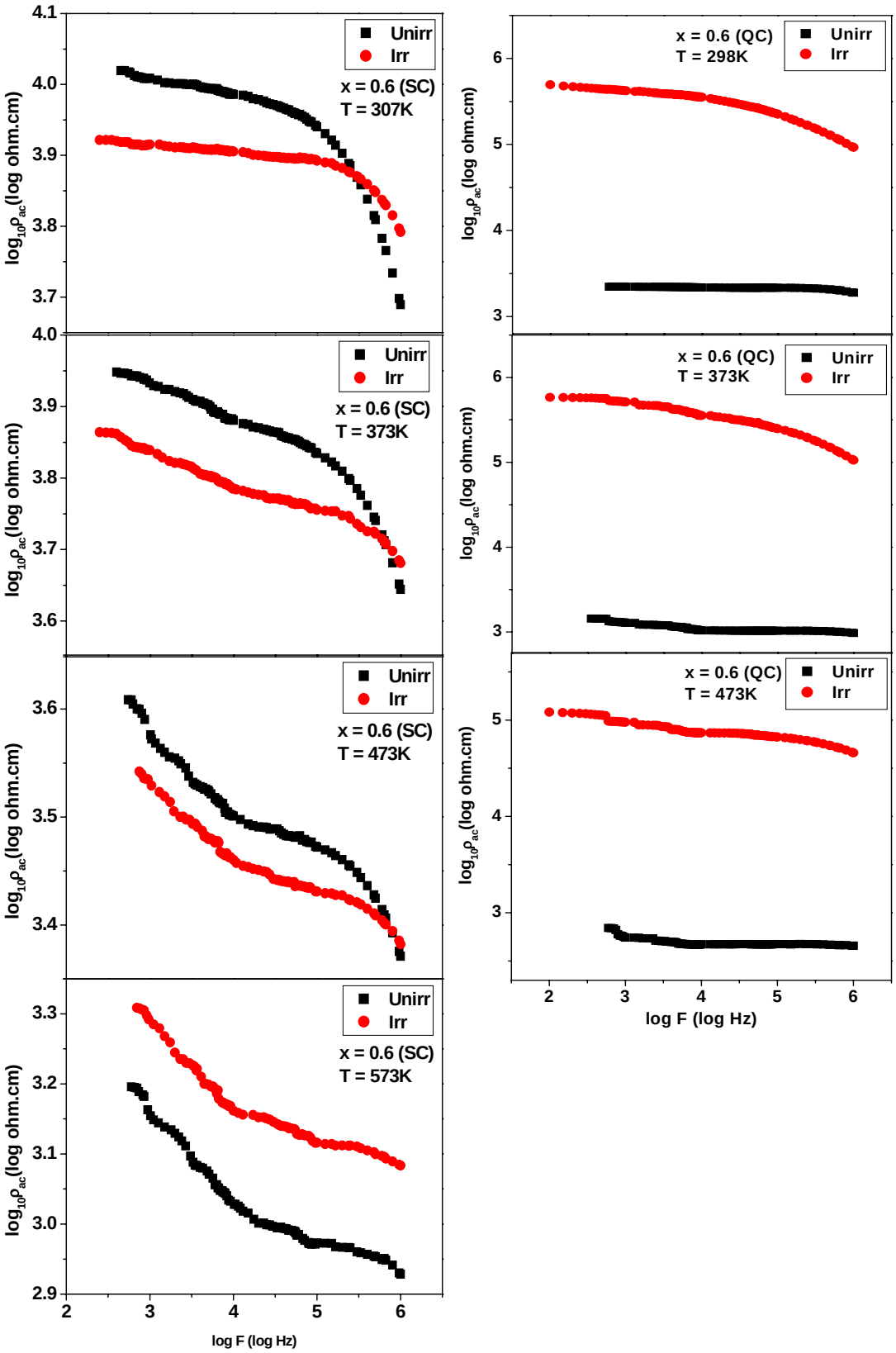

Fig. 6D.17d AC resistivity ($\log_{10}\rho_{ac}$) versus Frequency (log F) at selected temperatures for the composition x = 0.6 of unirradiated and irradiated $CuAl_xCr_xFe_{2-2x}O_4$ (SC-QC) systems

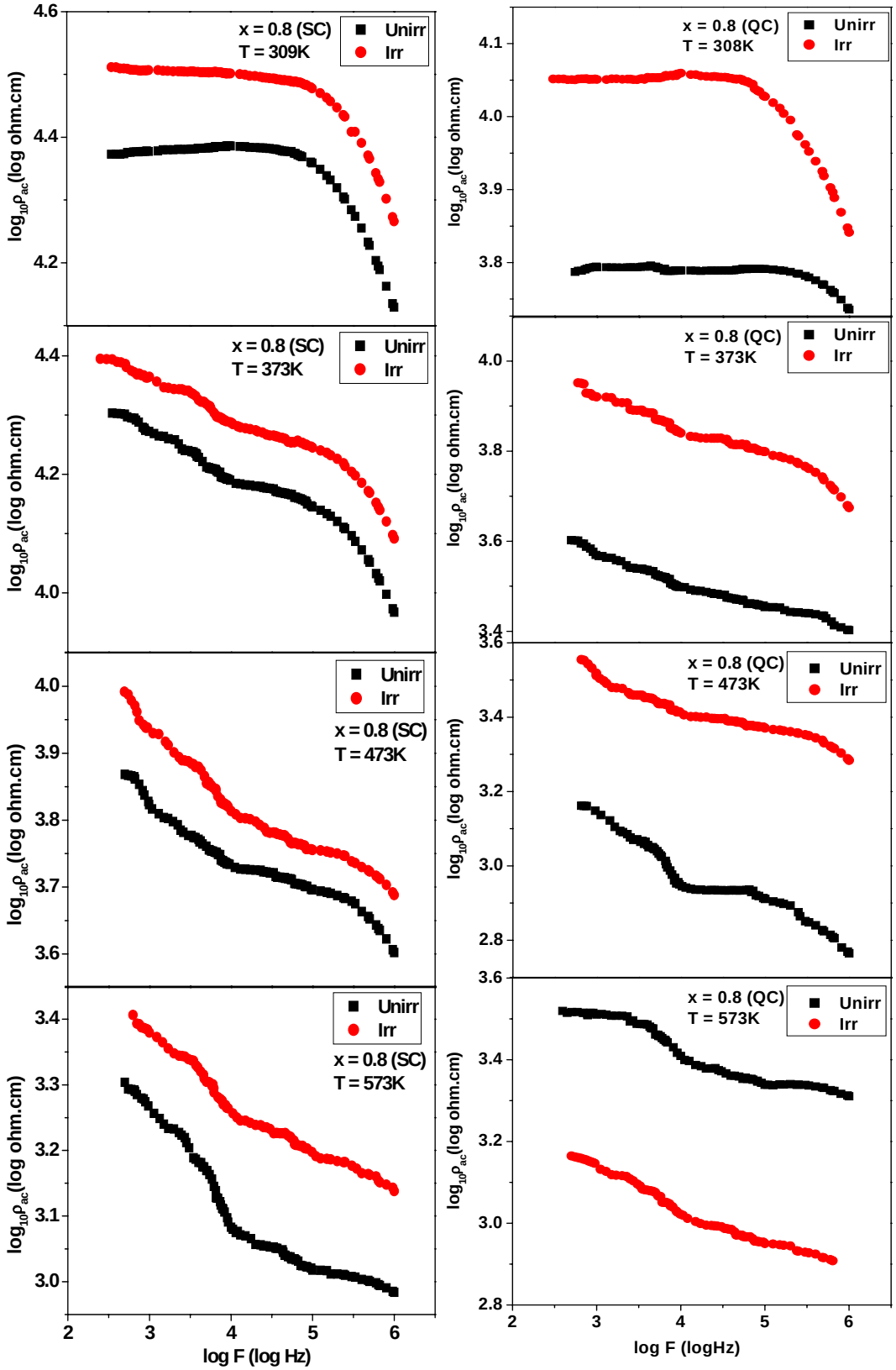

Fig. 6D.17e AC resistivity ($\log_{10}\rho_{ac}$) versus Frequency (log F) at selected temperatures for the composition x = 0.8 of unirradiated and irradiated $CuAl_xCr_xFe_{2-2x}O_4$ (SC-QC) systems

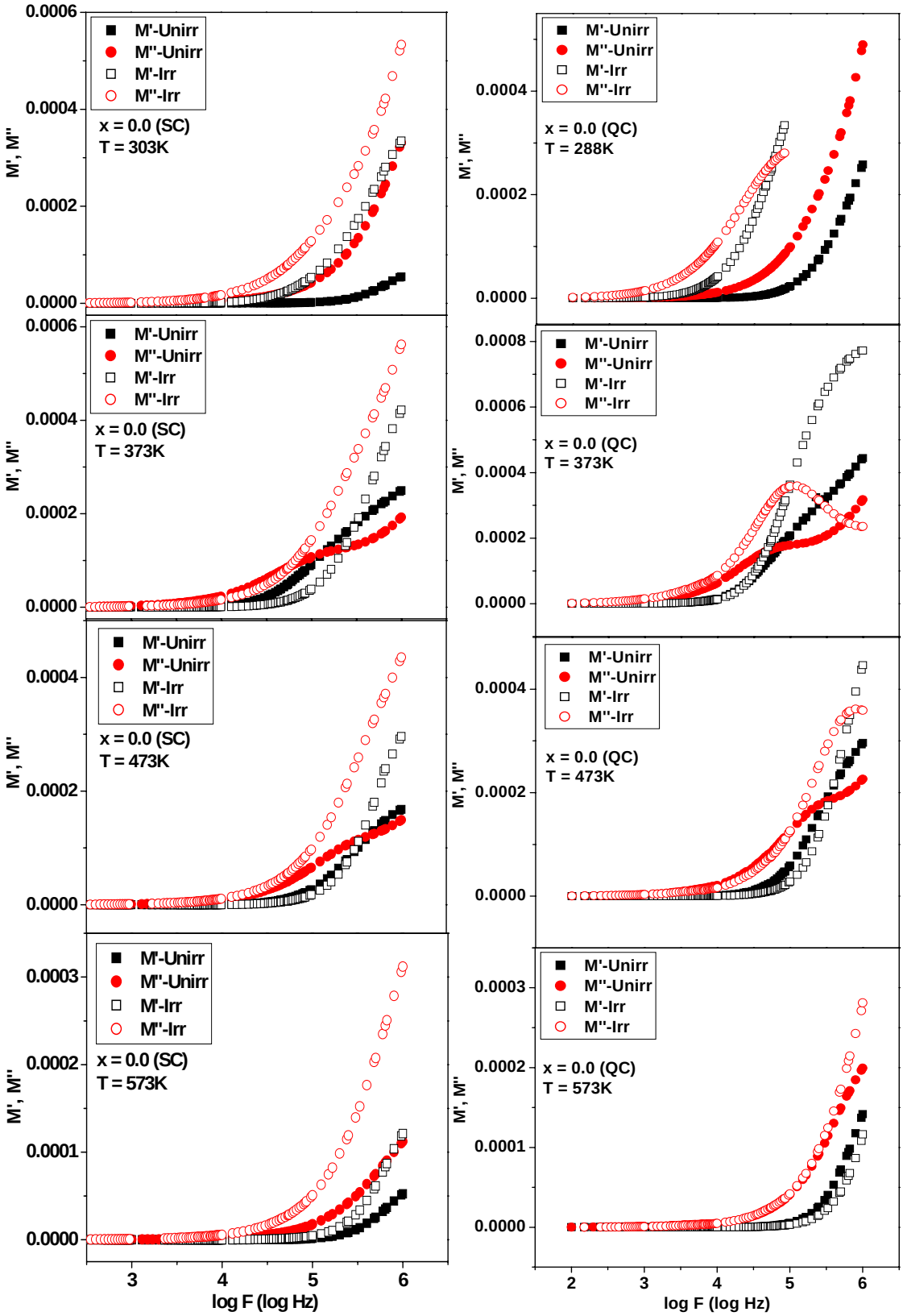

Fig. 6D.18a Real (M') and imaginary (M'') part of the dielectric modulus versus frequency at selected temperatures for the composition x = 0.0 of unirradiated and irradiated $CuAl_xCr_xFe_{2-2x}O_4$ (SC-QC) systems

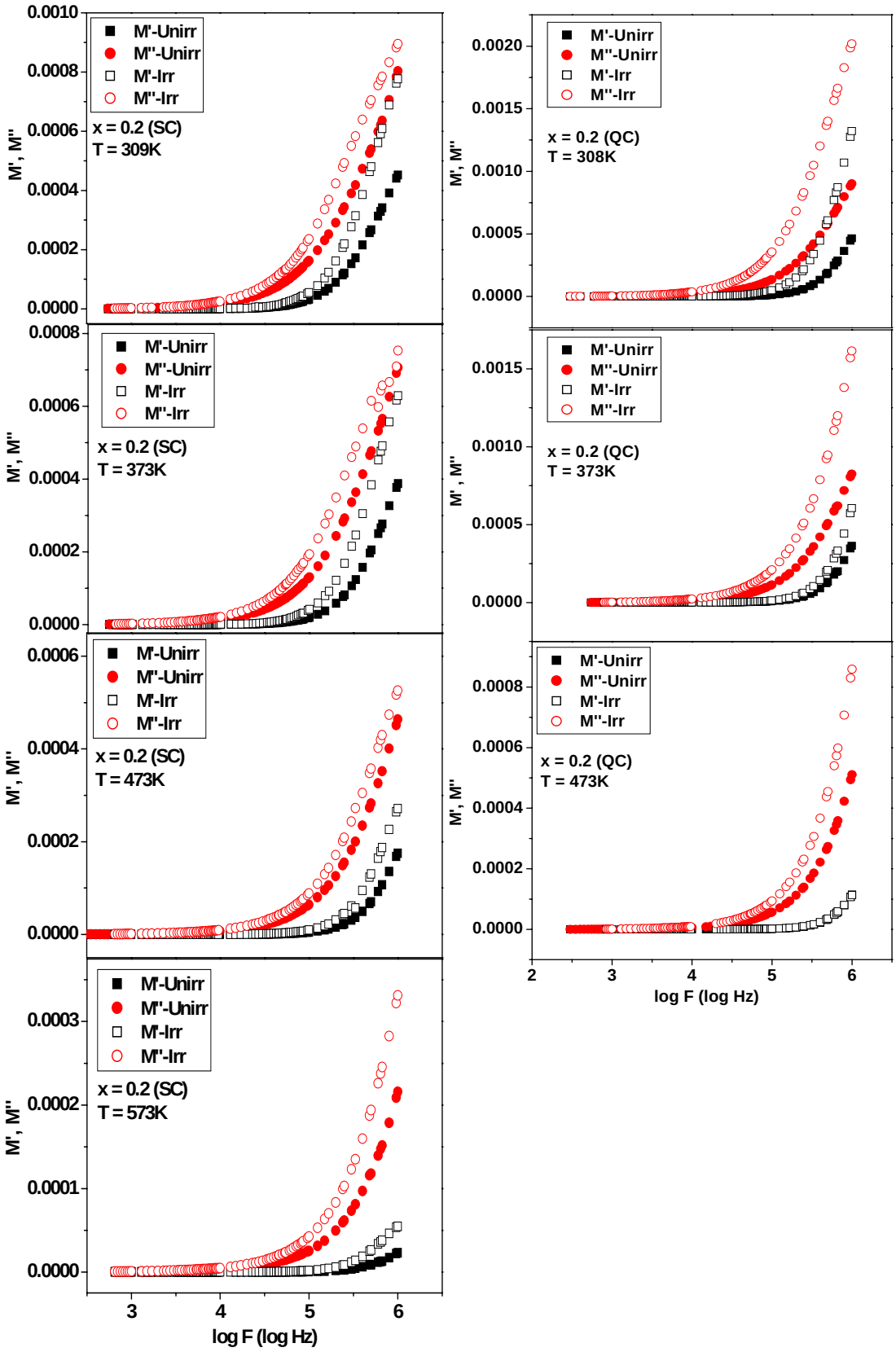

Fig. 6D.18b Real (M') and imaginary (M'') part of the dielectric modulus versus frequency at selected temperatures for the composition x = 0.2 of unirradiated and irradiated $CuAl_xCr_xFe_{2-2x}O_4$ (SC-QC) systems

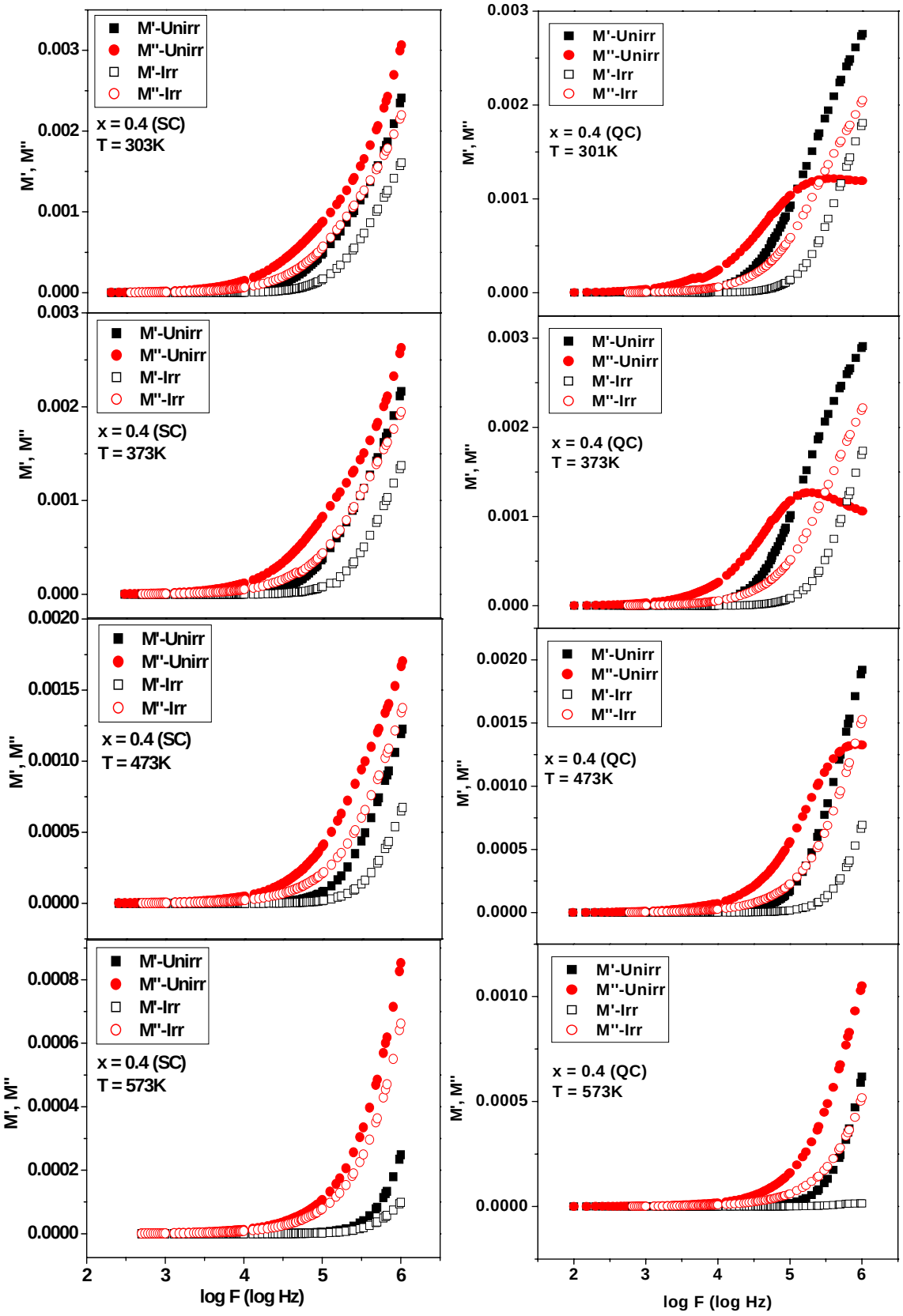

Fig. 6D.18c Real (M') and imaginary (M'') part of the dielectric modulus versus frequency at selected temperatures for the composition x = 0.4 of unirradiated and irradiated $CuAl_xCr_xFe_{2-2x}O_4$ (SC-QC) systems

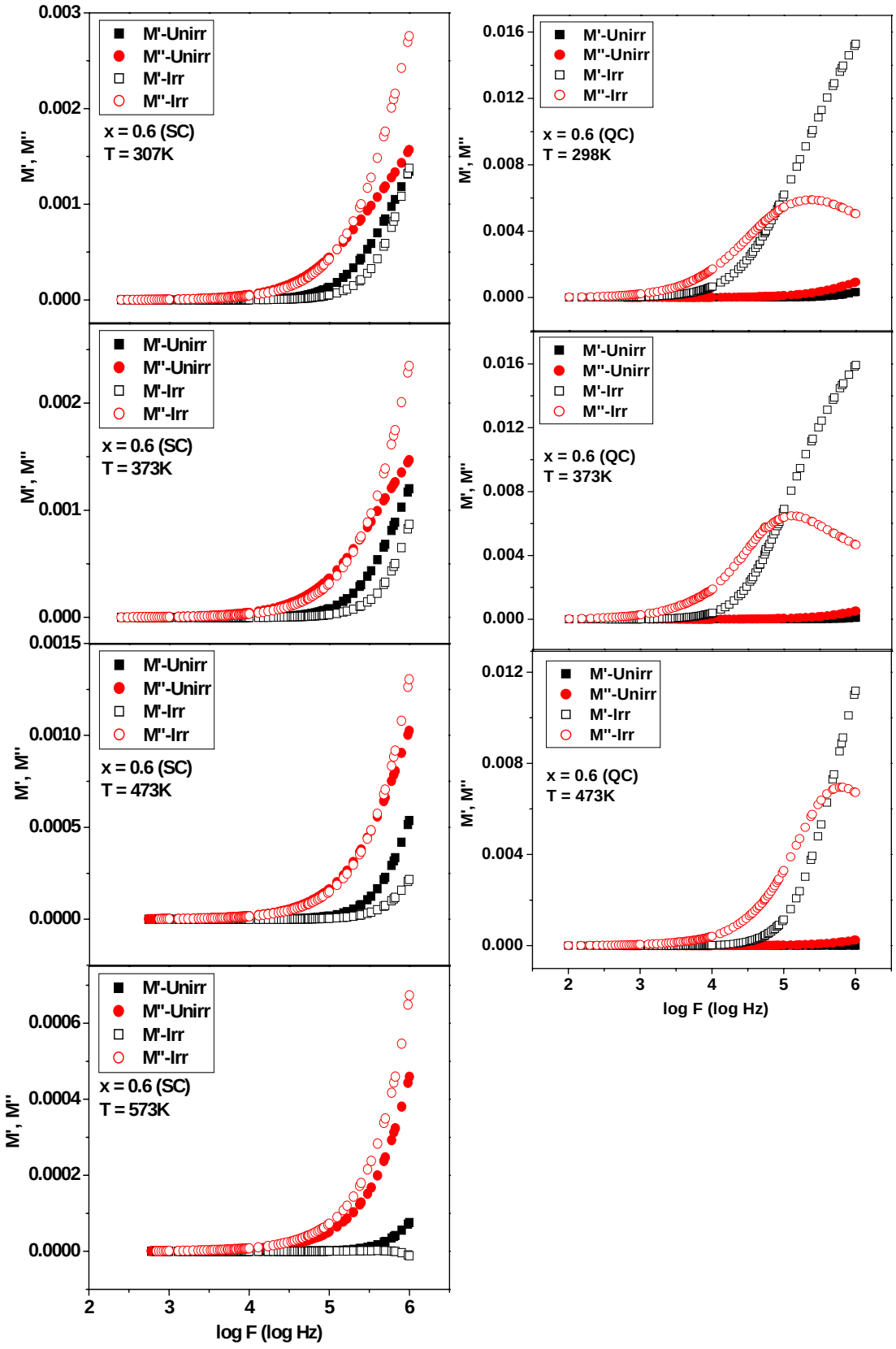

Fig. 6D.18d Real (M') and imaginary (M'') part of the dielectric modulus versus frequency at selected temperatures for the composition x = 0.6 of unirradiated and irradiated $CuAl_xCr_xFe_{2-2x}O_4$ (SC-QC) systems

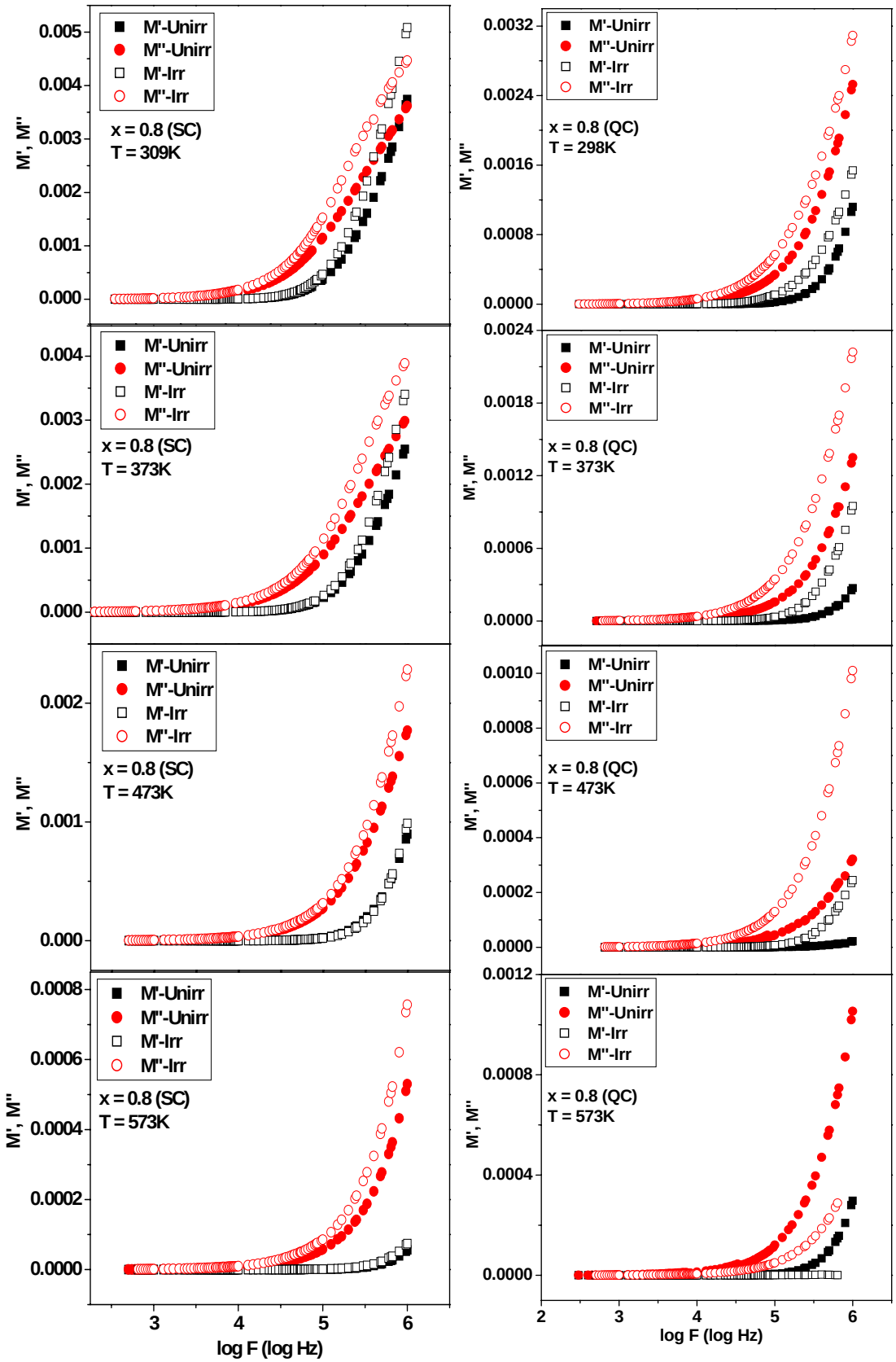

Fig. 6D.18e Real (M') and imaginary (M'') part of the dielectric modulus versus frequency at selected temperatures for the composition x = 0.8 of unirradiated and irradiated $CuAl_xCr_xFe_{2-2x}O_4$ (SC-QC) systems

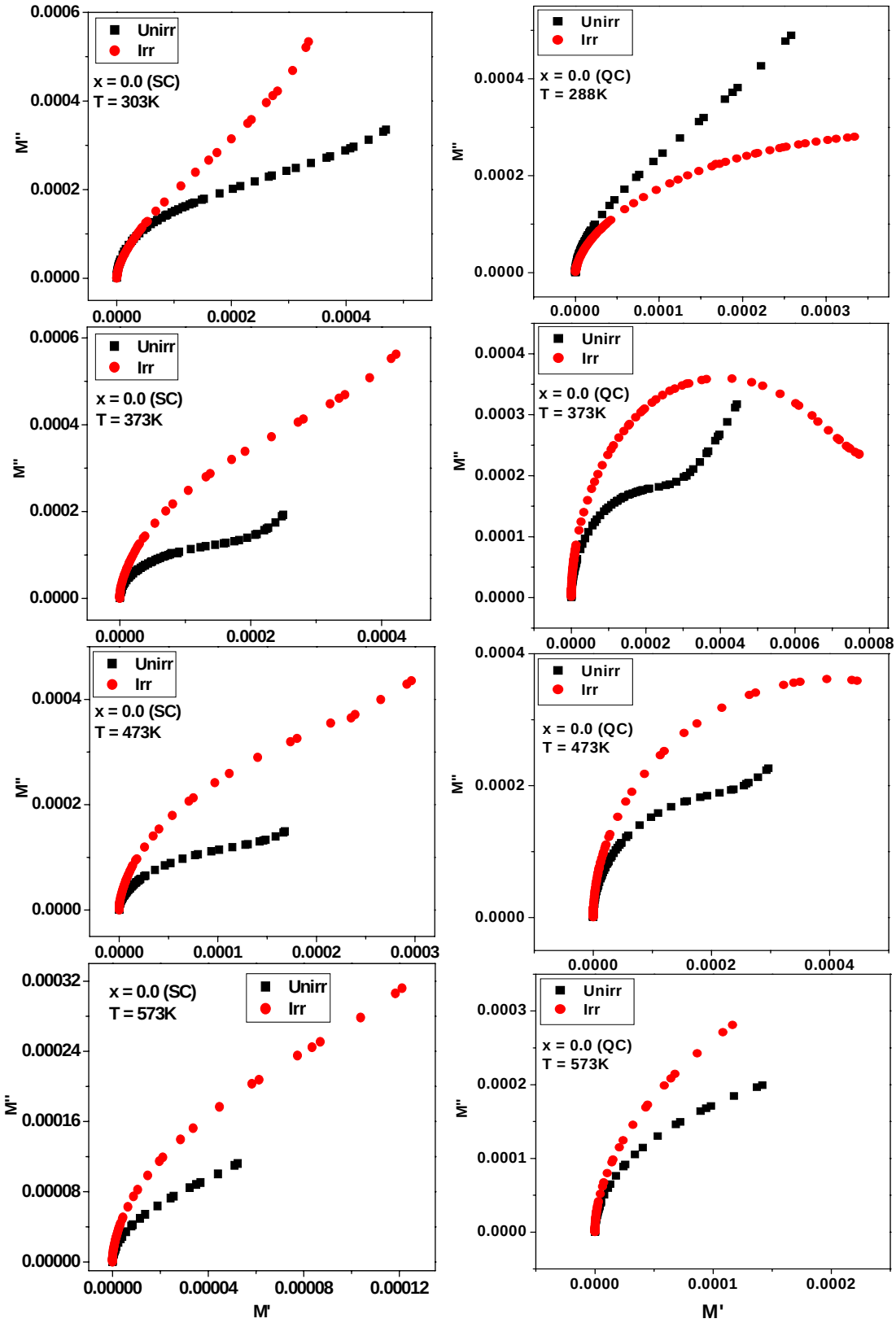

Fig. 6D.19a Real (M') versus imaginary (M'') parts of the dielectric modulus, Cole-Cole plots at selected temperatures for the composition x = 0.0 of unirradiated and irradiated $CuAl_xCr_xFe_{2-2x}O_4$ (SC-QC)systems

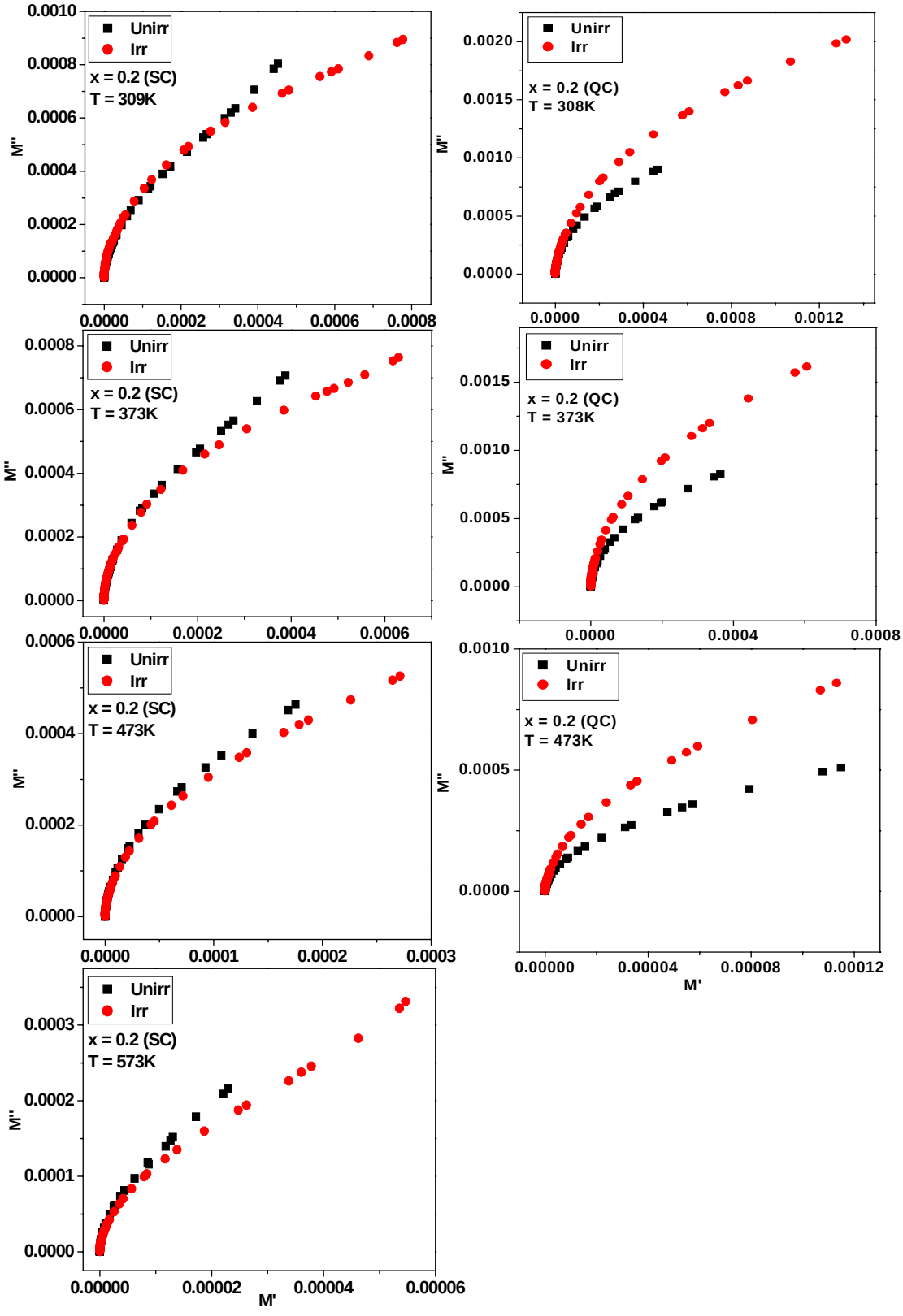

Fig. 6D.19b Real (M') versus imaginary (M'') parts of the dielectric modulus, Cole-Cole plots at selected temperatures for the composition x = 0.2 of unirradiated and irradiated $CuAl_xCr_xFe_{2-2x}O_4$ (SC-QC) systems

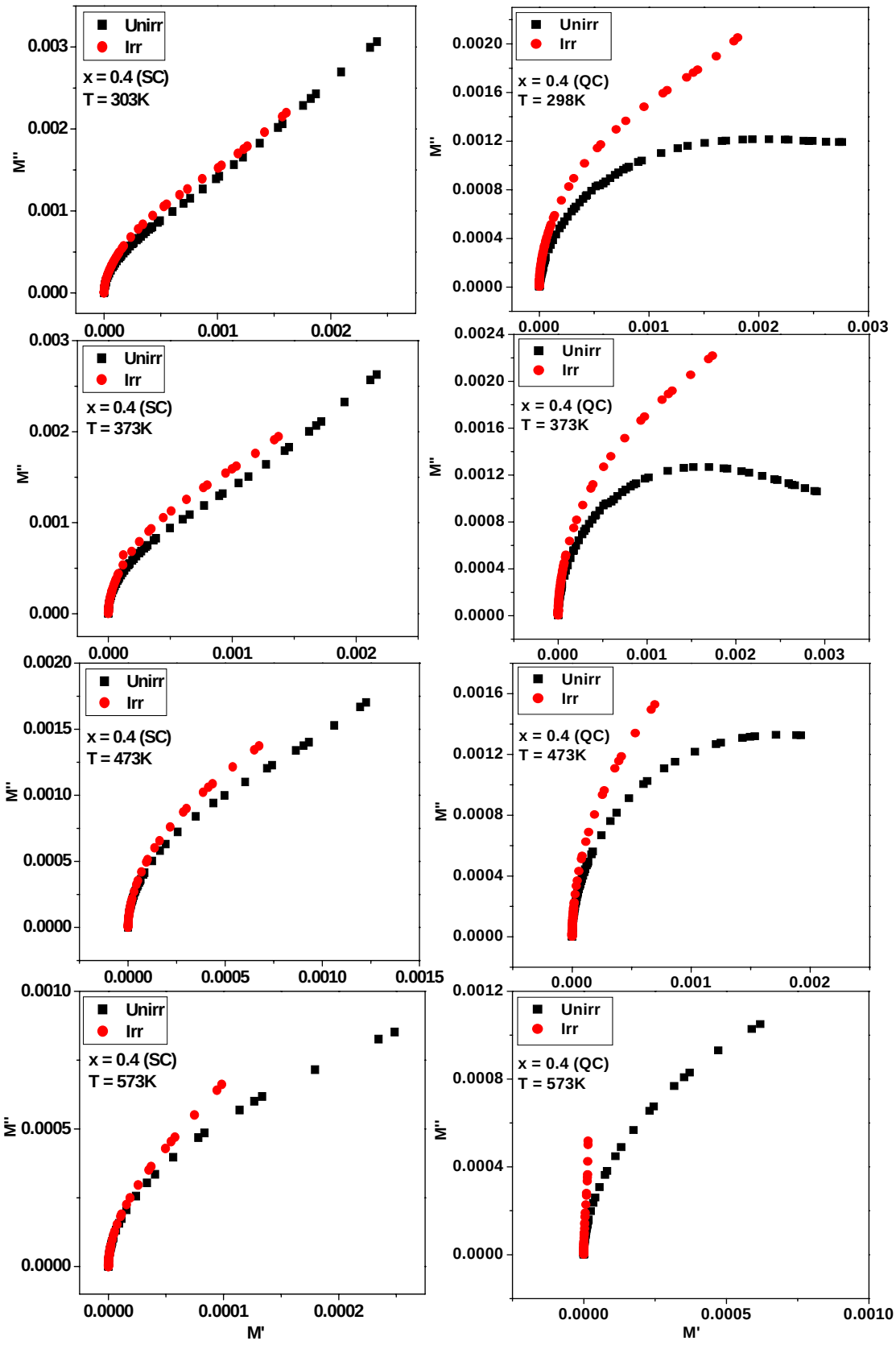

Fig. 6D.19c Real (M') versus imaginary (M'') parts of the dielectric modulus, Cole-Cole plots at selected temperatures for the composition x = 0.4 of unirradiated and irradiated $CuAl_xCr_xFe_{2-2x}O_4$ (SC-QC) systems

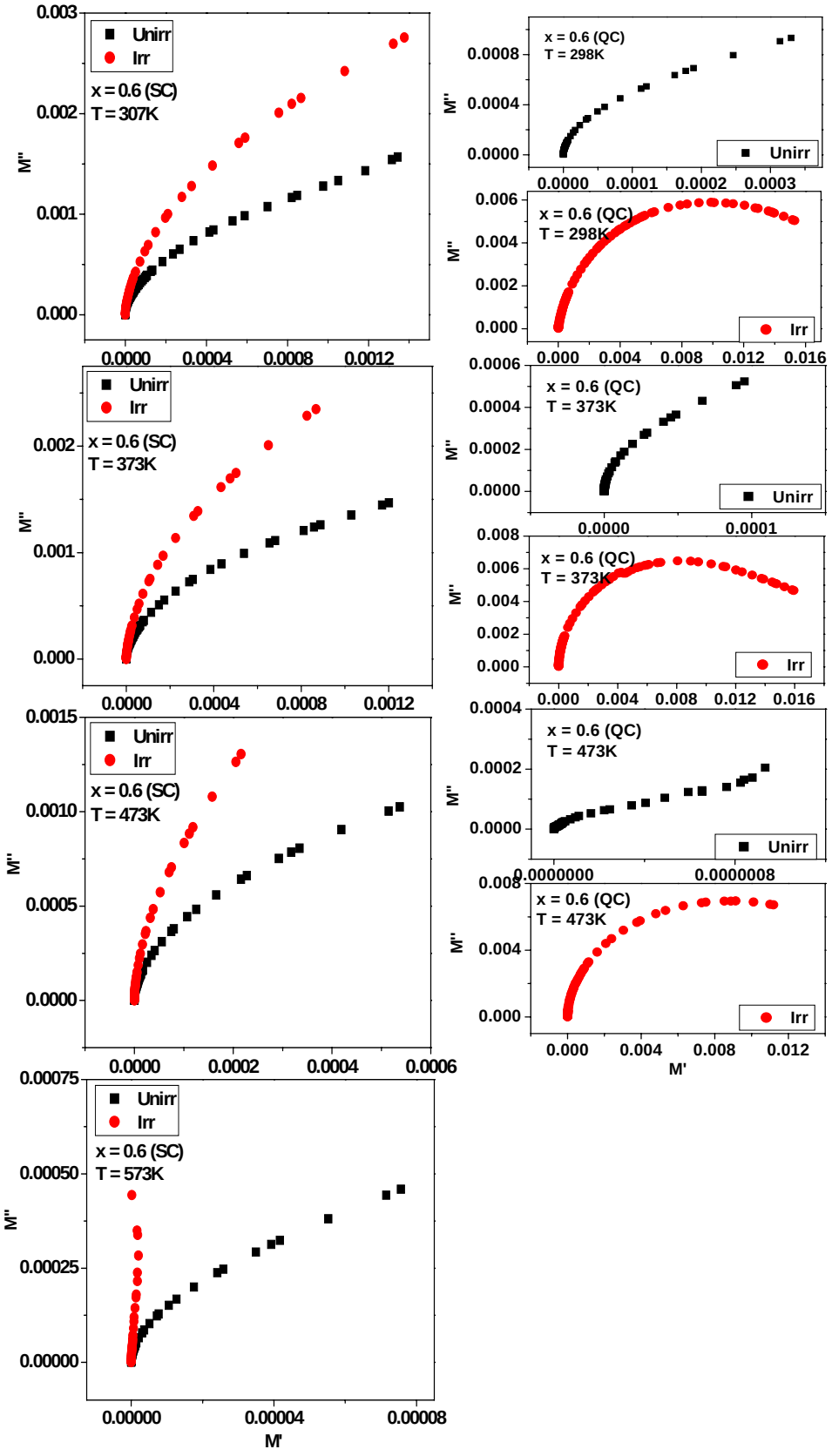

Fig. 6D.19d Real (M') versus imaginary (M'') parts of the dielectric modulus, Cole-Cole plots at selected temperatures for the composition x = 0.6 of unirradiated and irradiated $CuAl_xCr_xFe_{2-2x}O_4$(SC-QC) systems

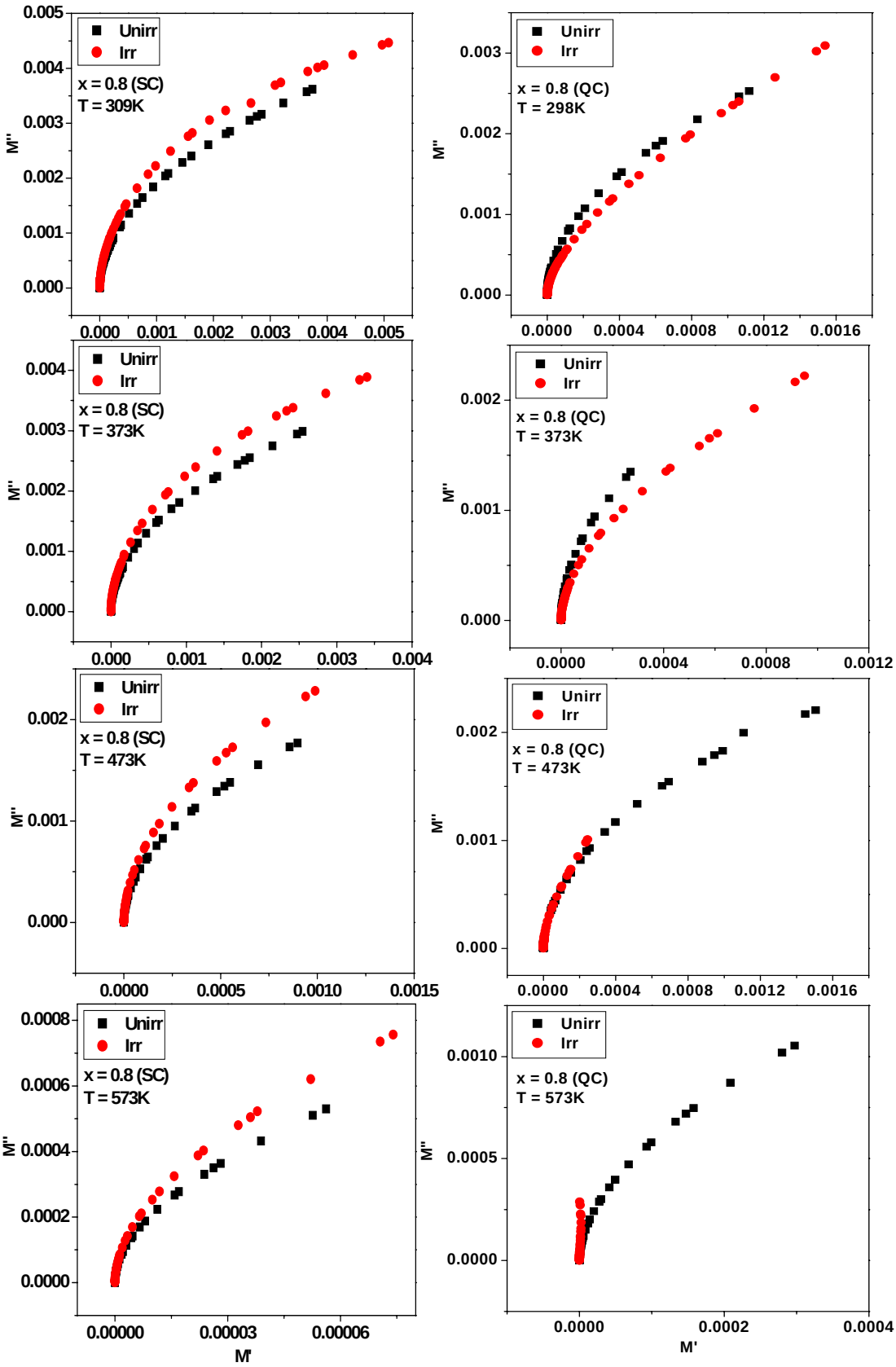

Fig. 6D.19e Real (M') versus imaginary (M'') parts of the dielectric modulus, Cole-Cole plots at selected temperatures for the composition x = 0.8 of unirradiated and irradiated $CuAl_xCr_xFe_{2-2x}O_4$ (SC-QC) systems

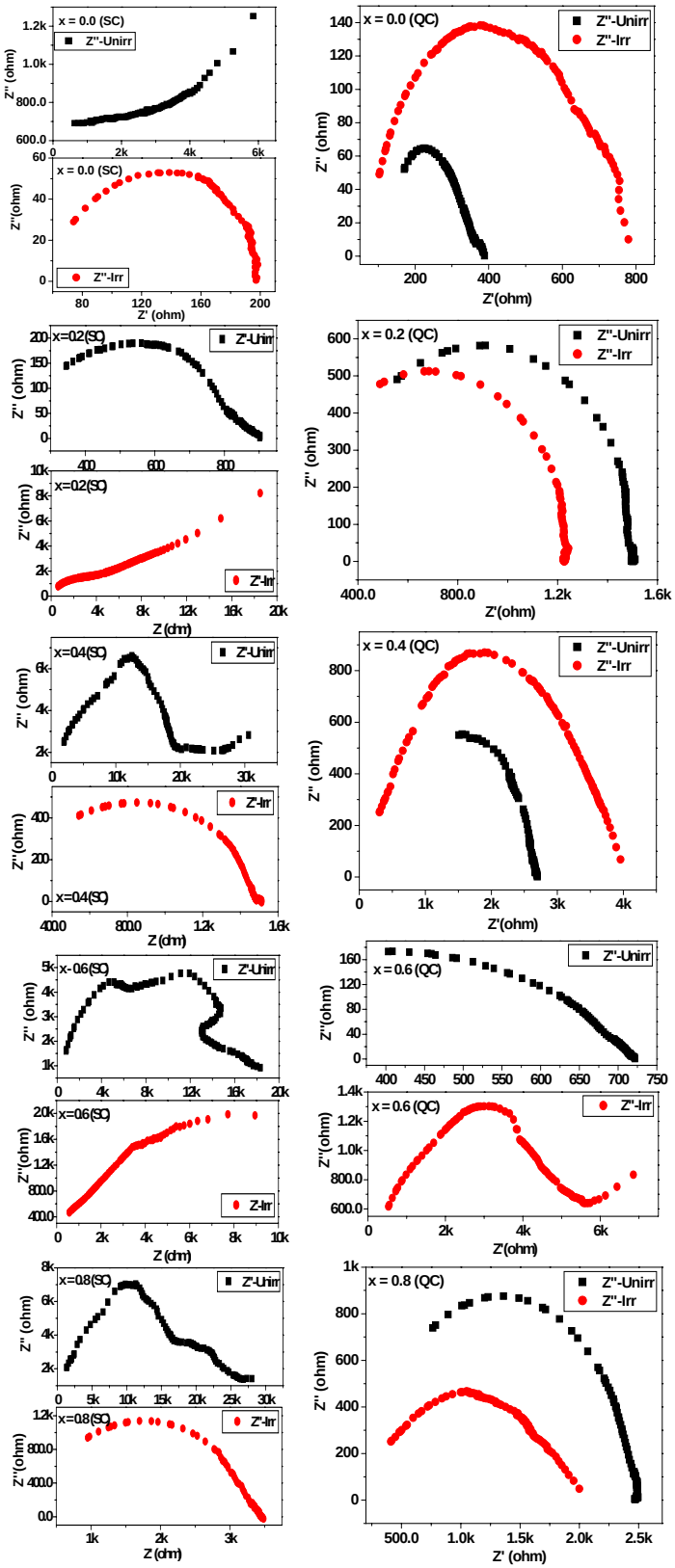

Fig. 6D.20 Real (Z') versus imaginary (Z'') parts, Cole-Cole plots at room temperature for the compositions x = 0.0, 0.2, 0.4, 0.6 and 0.8 of unirradiated and irradiated $CuAl_xCr_xFe_{2-2x}O_4$ (SC-QC) systems

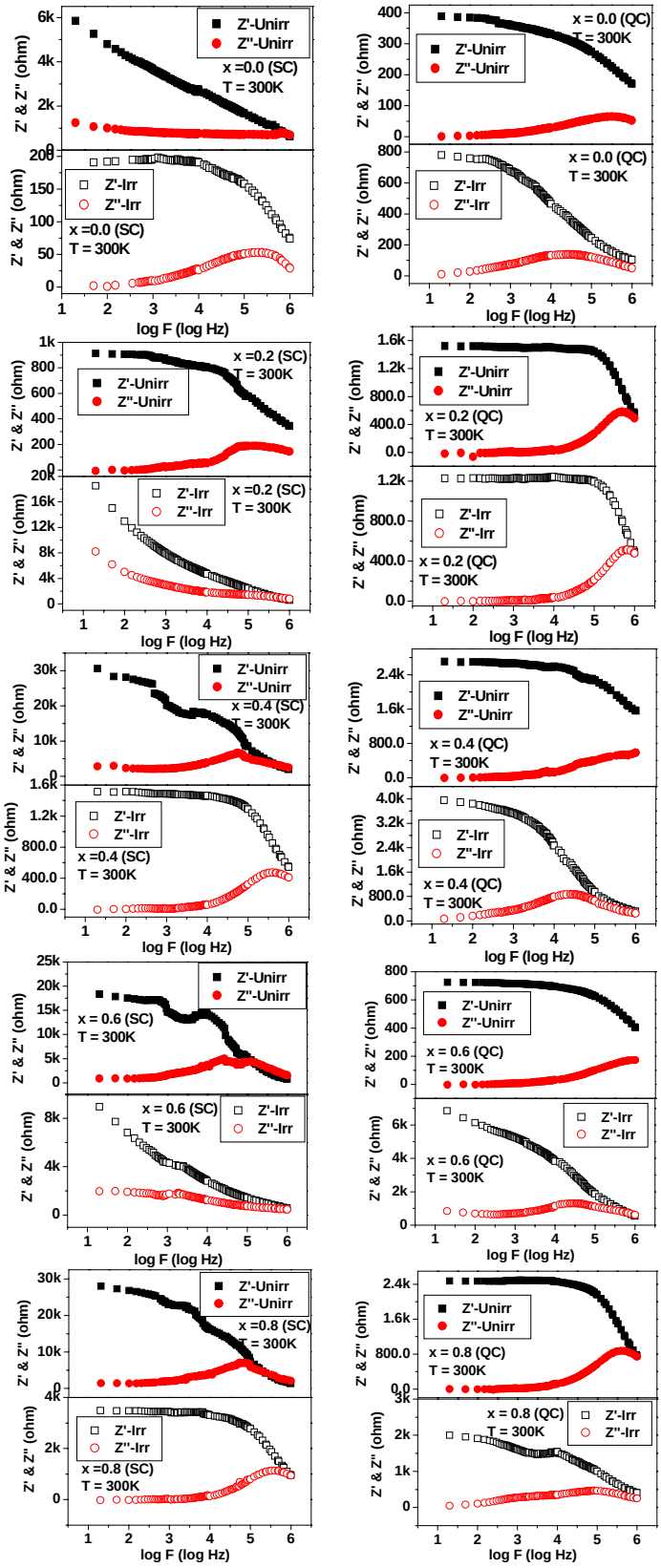

Fig. 6D.21 Variation of real part (Z') and imaginary part (Z'') of the impedance with frequency at room temperature for the compostions x = 0.0, 0.2, 0.4, 0.6 and 0.8 of unirradiated and irradiated $CuAl_xCr_xFe_{2-2x}O_4$ (SC-QC) systems

❖ The Comparative study of the spinel ferrite systems $Li_{0.5(1+x)}Ti_xAl_{0.1}Fe_{2.4-1.5x}O_4$ and $Li_{0.5(1+x)}Ti_xCr_{0.1}Fe_{2.4-1.5x}O_4$ with effect of Swift Heavy Ions Irradiation

Using 50 MeV Li^{3+} ion irradiation, the change induced in polycrystalline ferrites $Li_{0.5(1+x)}Ti_xAl_{0.1}Fe_{2.4-1.5x}O_4$ [LTAF] (x = 0.0 to 0.3, step – 0.1) and $Li_{0.5(1+x)}Ti_xCr_{0.1}Fe_{2.4-1.5x}O_4$ [LTCF] (x = 0.0 to 0.3, step – 0.1) in the electronic stopping power regime is studied. Both the systems were irradiated with the same fluence of 5 x 10^{13} ions/cm^2. The modifications of the structural and magnetic properties are studied by means of X-ray diffraction (XRD), magnetization, ^{57}Fe Mössbauer spectroscopy and low field AC susceptibility.

XRD patterns show all the Bragg reflections could be indexed for the fcc spinel structure and the peak positions in the case of irradiated samples are shifted to lower Bragg angle (2θ) values indicating expansion of the unit cell for both the systems. The cell edge parameter is found to increase after SHI-irradiation in both the systems, which is attributable to the rearrangement of the cations. It is also interesting to note that the observed saturation moment for unirradiated samples agrees well with the Néel moment (η_B^N) but at the same time the saturation moment is found to be reduced for all the samples after SHI-irradiation in both the systems. For the irradiated samples the observed saturation moment (η_B^{obs}) is found to be lower compared to the predicted value by the Néel theory (η_B^N), reduction being more pronounced in the LTAF system.

The Mössbauer spectra at 295K for the entire specimen exhibit two superimposed asymmetric A and B-site Zeemann sextets. The spectra for irradiated samples of LTAF system exhibit central paramagnetic doublet superimposed on magnetic sextet which is attributed to the partial formation of paramagnetic centres and rearrangement of the cations in the lattice due to SHI-irradiation. No appreciable influence of SHI-irradiation has been observed in the Mössbauer spectra of LTCF ferrites. In case of LTAF system, the generation of point/clusters of defects inhibits the long range ferrimagnetic order through redistribution of cations in the localized defected regions leading to the formation of paramagnetic centres which gives rise to the central paramagnetic doublet in the Mössbauer spectra of the LTAF system.

In contrast, the Mössbauer spectra of the irradiated samples of LTCF system with the same fluence as used for the LTAF do not show a slightest sign of central paramagnetic doublet. This suggests that the presence of magnetic ion Cr^{3+} ($3\mu_B$) in the lattice seems to play an important role of keeping the long range order intact in spite of SHI induced defected regions/rearrangement of the cations while the coexistence of non-magnetic cations Al^{3+} and Ti^{4+} gives rise to SHI induced localized paramagnetic centres.

The nuclear hyperfine fields (H_nf) for LTAF system are found very low compared to pure $Li_{0.5}Fe_{2.5}O_4$ which is ascribed to the non-magnetic Al^{3+}-substitution, while the hyperfine field values for LTCF are almost near to the pure Li-ferrite. In both the cases, H_nf reduces due to Ti^{4+} substitution. Similarly, Isomer shift values are found to be much lower for LTAF compared to LTCF. No effect of SHII is observed on these parameters for all the specimen. The line width for the LTAF is not much influenced by SHII but it gives rise to central enhancement, while no central enhancement is observed but the line widths are much influenced in case of LTCF. The Curie temperature (T_c) for irradiated specimens is lower than their unirradiated counterparts for both the systems.

In conclusion, the contrast in the role of Ti^{4+} in the presence of Al^{3+} and Cr^{3+} causing the formation of paramagnetic centres through SHII induced cation rearrangement has been revealed through the comparative Mössbauer signatures of both the systems. The observed reduction in the saturation magnetic moment and Curie temperature after irradiation is attributed to the partial formation of paramagnetic centres and rearrangement of cations in the lattice.

The same systems are investigated by means of infrared spectroscopy, elastic properties and results are apprised as under: The IR spectra of all the compositions of unirradiated and irradiated LTAF and LTCF system show the presence of two absorption bands along with some shoulders in the range of 400-800 cm^{-1}. The high frequency band ν_1 for unirradiated and irradiated LTAF system is in the range 518-599 cm^{-1} and for LTCF system is in the range 501-589 cm^{-1} which is assigned to intrinsic vibrations of the tetrahedral group and the lower frequency band ν_2 for unirradiated and irradiated LTAF system is in the range 408-488 cm^{-1} and for LTCF system is in the range 405-490 cm^{-1} which is assigned to the intrinsic vibrations of the octahedral group.

It is important to note that on increasing Ti-content (x) in both the systems, the intensity of all absorption bands and their shoulders decrease whereas bands become broader. This is ascribed to the chemical disorder brought about by the Ti^{4+} substitution. No systematic variation is observed in the principal bands except slight shift in the band positions with concentration (x).

On comparing the IR signatures of both the pre-irradiated systems the following observations are made: In contrast to LTAF (x=0.0), the IR spectrum of LTCF (x=0.0) sample indicates new two bands at 710.7 and 675.0 cm^{-1} around the first primary band ν_1 and gets disappeared on increasing the Ti-content (x). The influence of Ti^{4+} in causing the chemical disorder in the presence of Cr^{3+} is seen to be more pronounced compared to the Al^{3+} substituted system as evidenced by quick merger of absorption bands for LTCF with content(x).

In case of post-irradiated specimens, it is noticed that the irradiation causes the splitting of main absorption bands ν_1 and ν_2 for all the samples. It is also important to note that around main absorption band (ν_1) new subsidiary band (ν^*) come into sight with the shoulders or splitting in the range of 601 – 670 cm^{-1} with the compositions x = 0.1, 0.2, and 0.3 for the LTCF system while the new subsidiary band ν^* with splitting observed for only one composition x = 0.1 in the LTAF system. In accordance with the XRD results, the observed shifting of main absorption bands towards higher frequency side after irradiation is attributed to the expansion of unit cell dimensions. The growing subsidiary band (ν^*) with shoulders which may be assigned to the destruction of the Fe^{3+}- O^{-2}- Fe^{3+} bonds and the corresponding generation of the Fe^{2-} - O^{2-} complexes at the tetrahedral site causing the migration of Ti^{4+} ion to octahedral side after the irradiation. Furthermore, the increase in splitting of the main absorption bands ν_1 and ν_2 is due to the vibrations A-sites Fe^{2+}-O^{2-} and B-site Fe^{2+}-O^{2-}, Cr^{4+}-O^{2-} complexes, respectively. The B-sites complexes arise due to electron hopping process $Cr^{3+} + Fe^{3+} \leftrightarrow Cr^{4+} + Fe^{2+}$. The presence of Fe^{2+} ions in ferrites can produce splitting of IR absorption bands. This may be because the local lattice deformation can occur due to the Jahn-Teller effect in Fe^{2+}, which can lead to a non- cubic component in the crystal field potential and to the splitting of the bands.

The IR spectra of irradiated samples of LTAF system exhibit the shifting of main absorption bands to higher frequency side whereas new absorption bands are

generated in LTCF system. The increase in splitting of the main absorption bands is observed after SHI- irradiation in both the systems.

The force constant (k) is found to decrease with increasing Li-Ti content (x) in LTAF system that suggests the weakening of interatomic bonding but in contrary for LTCF system which is found to increase with Li-Ti content (x) suggesting strengthen of interatomic bonding. The values of longitudinal elastic wave velocity (υ_l), transverse elastic wave velocity (υ_s), mean elastic wave velocity (υ_m) and Debye temperature (θ_D) are found to decrease with increasing Li-Ti content (x) for LTAF system whereas it is observed to increase for LTCF system. After irradiation, the values of υ_l, υ_s, υ_m and θ_D are decreased from that of the unirradiated samples in both the systems. The values of bulk modulus (B), Young's modulus (E) and rigidity modulus (G) are decreased with increasing Li-Ti content (x) for LTAF system while the values of B, E and G are found to increase with increasing Li-Ti content (x) for LTCF system. After irradiation it is found that the value of B E and G are diminished from that of the unirradiated samples in both the system.

The dissimilarity in the role of Ti^{4+} in the presence of Al^{3+} causes the weakening of interatomic bonding and the presence of Cr^{3+} causes strengthening of interatomic bonding has been revealed through the comparative study of elastic properties of both the systems.

The results of electrical and dielectric properties of the systems are summarized as follows: The dc resistivity (ρ_{dc}) decreases linearly with increasing temperature, reflecting the semiconductor nature of ferrites for before and after irradiation in both the systems. The value of activation energy is supported the conduction phenomenon in present system is due to polaron hopping in the both systems. The polaron radius (r_p) and Jump length (L_A,L_B) increases with Li-Ti concentration (x) of the unirradiated and irradiated samples, which is followed trend of lattice parameter (a) for both the systems. The thermoelectric power 'α' is positive for the all samples indicating that the conduction is due to the majority charge carrier is hole. Thus, the conduction mechanism for the p-type semiconductor is due to the hole transfer from the Fe^{3+} to Fe^{4+} and Cr^{3+} to Cr^{4+} for LTCF system and Fe^{3+} to Fe^{4+} for LTAF system at octahedral sites.

The dielectric constant (ε') gradually increase by increasing temperature at each separate frequency for all unirradiated and irradiated specimens for both LTAF

and LTCF systems. As the temperature increases, the dc and ac conductivities increase due to increase in drift mobility of thermally activated holes. As a result, the dielectric polarization increases causing an increase in ε' in both systems.

After irradiation, an abnormal dielectric behaviour and the formation of maxima peak in temperature dependence ε' curves were observed in un-substituted sample LTAF (x = 0.0) while it is observed in Ti-substituted samples x = 0.1 and 0.2 for the LTCF system. The occurrence of peak was found to be broad as the frequency increases and no shifting observed in maxima peak for LTAF (x = 0.0) system. The peak formation at higher temperature region and shifted toward lower temperature side on the increasing frequency for the LTCF (x = 0.1 and 0.2) system. After irradiation, the peak formation at higher temperature region and shifted toward lower temperature side on the increasing frequency (at high frequency region) for the composition x = 0.1 and 0.2 in LTCF system is attributed to two competitive effects, the first of which is the increase of the mobility of charge carriers with increasing temperature leading to an increase in ε' because the conductivity and polarization of the same origin and the second opposing effect is the hindrance of charge carriers movements due to the thermal agitation as well as trapping centres. The shift in the peak position toward lower temperature with increasing frequency may be the applied frequency act a pumping force pushing the charge carriers from one conduction state to another or the applied frequency may be due to the strong effect of the field where the dipoles can easily orient themselves in the field direction which is hindrance by trapping centres.

No dielectric relaxation peak observed in temperature dependence tanδ curves for the concentration $x \leq 0.2$ while x= 0.3 appearance of the relaxation peak (a broad peak) in the low temperature range and this broad relaxation peak shift towards higher temperature with increasing frequency for the unirradiated samples in both systems. In the case of irradiated Ti^{4+} substituted Li-Cr (x > 0.0) ferrites the magnitude of loss factor (tanδ) is higher than that of the unirradiated samples in the whole temperature range and show relaxation broad peak at low temperature region. As increase the frequency, the intensity of observed relaxation broad peak is abridged and shifts towards higher temperature region after irradiation. All the irradiated LTAF samples show sharp and more pronounced broad peak at frequency range 500Hz to 100kHz as compared to unirradiated samples. The position of broad maxima (peak) shifts

towards higher temperature side or broad peak disappear as the frequency increases up to 500kHz to 1MHz, except for x = 0.2 irradiated sample. The temperature dependent dispersion exhibited by the irradiated samples is consistent with Debye-type of dispersion for loss for both the systems.

The frequency dependence dielectric properties reveal the dispersion due to Maxwell-Wagner type interfacial polarization in agreement with Koop's phenomenological theory in the both systems. The irradiated LTCF samples with x = 0.0 and 0.1 exhibit dielectric dispersion peak ε'_{max} (abnormal behaviour) in low frequency region and dispersion peak shifted towards higher frequency with increasing temperature. This anomaly in variation of dielectric constant after irradiation is due to point/clusters of defects creation, which results in collective contribution of p- and n-type of conduction. The small hump is found in tanδ curve after irradiation in the higher frequency region (at 298K) for the concentration x = 0.2 and 0.3 of irradiated LTCF samples.

The dielectric constant (ε') shows an anomalous (resonance peak) behaviour with frequency for irradiated samples x = 0.0 (at T = 573 K) and x= 0.2 (at T = 473K & 573K) with corresponding to unirradiated samples, even as tanδ shows same an anomalous behaviour for unirradiated sample x = 0.0 (at T= 773K) for LTAF system. The occurrence of anomaly (peak) in the variation of ε' and tanδ with frequency can be observed when the hopping frequency is approximately equal to that of the externally applied electric field; that means 'resonance phenomena'.

The impedance curve Z'' versus log f for LTAF system shows that Z'' (f) reveals the maximum value for the unirradiated samples x = 0.0 and 0.2 at particular frequency (Z''_{max}) and then decreases with further increase in frequency, whereas unirradiated samples for x = 0.1 and 0.3 are found to decrease continuously with increasing frequency. After irradiation, this peak (Z''_{max}) is disappeared or shifting to lower frequency side with corresponding to unirradiated samples x = 0.0 and 0.2, while irradiated sample x = 0.3 is appeared Z''_{max} with respect to unirradiated sample for the same measured frequency range. The observed presence of a single peak after irradiation for x = 0.0 and before irradiation for x = 0.1 in the imaginary spectra of impedance Z'' (f) suggest the relaxation and indicate change in conductivity with frequency for LTCF system.

The electrical modulus spectra shows the electrical relaxation with peak frequency in the imaginary M'' (f) part of the modulus spectra of unirradiated samples for all the compositions of LTCF system at different temperatures. The peak frequency is called relaxation frequency and it increases with temperature because of the thermal activation of localized electric charge carriers which form the electric dipoles. The M'' peak shifts towards higher frequency with increasing temperature suggests that the relaxation time decreases with the measuring temperature. After irradiation same electrical relaxation peak disappeared in imaginary part of the modulus spectra in the same studied frequency region is due to change the charge carrier hopping rate or change in the dipole-dipole interactions after irradiation in the LTCF system. Same behaviour also observed in LTAF system.

FUTURE SCOPE

In the present work, bulk samples of all the systems have been prepared using the solid state reaction method and the effect of swift heavy ion irradiation on structural, magnetic, electric, dielectric and impedance properties of the bulk samples have been studied using different techniques like XRD, Infrared Spectroscopy, Magnetization, Mössbauer spectroscopy, AC susceptibility, DC resistivity, thermoelectric power, dielectric measurements, impedance spectroscopy etc.

- In the same way there is a future scope for performing initial permeability of the unirradiated and irradiated samples in toroidal shape as a function of temperature and frequency in order to observe changes in relaxation frequency and an understanding of relaxation phenomena.
- To synthesize nano-particles and thin films of the present samples and irradiation with different energy, ions and fluence could also be interesting topic for further studies.
- Neutron diffraction and Synchrotron X-ray radiation study would be good source of understanding precise crystal structure, including point defects chemistry and cation disorder of the samples.
- There is a scope to obtain information of multiple oxidation states of the transition metal ions in mixed valence spinels by X-ray photoelectron spectroscopy (XPS).
- Using X-ray absorption fine structure (XAFS) including extended X-ray absorption fine structure (EXAFS) and near-edge extended X-ray absorption fine structure (NEXAFS) can be obtained inversion parameters of the spinel ferrites, because this techniques offer element specificity and local structure sensitivity, as well as inter ionic distances, coordination number and so on.
- Furthermore, site-specific X-ray Magnetic Circular Dichroism (XMCD) studies are needed for such magnetic ions occupying A and B sites and it would be helpful to discuss the origin of magnetic moments and overlapping electrons orbitals.

❖ The List of Research Publications

(a) National and Internatinal Journals

1. Structural properties of magnesium and aluminium Co-substituted lithium ferrite
K.B. Modi, J.D. Gajera, **M. C. Chhantbar**, K. G. Saija, G. J. Baldha, H. H. Joshi
Materials Letters **57** (2003) 4049-4053

2. Effect of Fe^{3+} substitution on structural and macro magnetic properties of Yttrium Iron Garnet
Kunal b Modi, H. J. Shah, U. N. Trivedi, R. P. Vara, **M. C. Chhantbar** & H. H. Joshi
Indian Journal of Engineering & Material Science **10** (Dec 2003) 502-506

3. Infrared spectral studies of Zn-substituted $CuFeCrO_4$ spinel ferrite system
M. C. Chhantbar, U.N. Trivedi, P. V. Tanna, R. P. Vara, H. H. Joshi, K. B. Modi
Indian Journal of Physics **78A (3)** (2004) 321 - 326

4. Structural properties of Fe^{3+} substituted Yttrium Ion Garnet
R. P. Vara, H. J. Shah, M. P. Pandya, **M. C. Chhantbar** & K. B. Modi
Indian Journal of Pure & Applied Physics **42** (February 2004) 117 – 120

5. Infrared spectroscopic study of Fe^{3+} substituted Yttrium Iron Garnet
K. B. Modi, R. P. Vara, H. G. Vora, **M. C. Chhantbar**, H. H. Joshi
Journal of Materials Science **39** (2004) 2187 – 2189

6. Study of Substitution limit, structural, bulk magnetic and electrical properties of Ca^{2+} substituted magnesium ferrite
S. D. Chhaya, M. P. Pandya, **M. C. Chhantbar**, K. B. Modi, G. J. Baldha, H. H. Joshi
Journal of Alloys & Compounds **377** (2004) 155-161

7. Localized canted spin behaviour in $Zn_xMg_{1.5-x}Mn_{0.5}FeO_4$ spinel ferrite system
K. P. Thummer, **M. C. Chhantbar**, K. B. Modi, G. J. Baldha, H. H. Joshi
Journal of Magnetism and Magnetic Materials **280** (2004) 23-30

8. ^{57}Fe Mössbauer studies on $MgAl_xCr_xFe_{2-2x}O_4$ spinel system
K. P. Thummer, **M.C. Chhantbar**, K. B. Modi, G. J. Baldha, H. H. Joshi
Materials Letters **58** (2004) 2248-2251

9. Effect of Mn^{4+} substitution on magnetic behaviour of cobalt ferrite
K. P. Thummer, **M. C. Chhantbar**, K. B. Modi, H. H. Joshi
Indian Journal of Physics **79(1)** (2005) 41-45

10. Elastic constants determination for Fe^{3+} substituted YIG through infrared-red spectroscopy and heterogeneous metal mixture rule
K. B. Modi, **M.C. Chhantbar**, P. U. Sharma, H. H. Joshi
Journal of Materials Science **40** (2005) 1247-1249

11. Frequency dependent dielectric behaviour of cadmium and chromium co-substituted nickel ferrite
U. N. Trivedi, **M. C. Chhantbar**, K. B. Modi, H. H. Joshi
Indian Journal of Pure & Applied Physics **43** (2005) 688-690

12. Study of elastic behaviour of magnesium ferri aluminates
K. B. Modi, **M. C. Chhantbar**, H. H. Joshi
Ceramics International **32** (2006) 111-114

13. Influence of 50 MeV Li^{3+} -ion irradiation on structural and magnetic properties of Ti^{4+} -substituted $Li_{0.5}Al_{0.1}Fe_{2.4}O_4$
M.C. Chhantbar, K.B. Modi, G. J. Baldha, H.H. Joshi, R.V. Upadhyay, RaviKumar,
Nuclear Instruments and Methods in Physics Research **B 244** (2006) 124-127

14. Study of elastic properties of fine particle copper-zinc ferrites through infrared spectroscopy
K. B. Modi, U. N. Trivedi, P. U. Sharma, V. K. Lakhani, **M. C. Chhantbar** & H. H. Joshi
Indian Journal of Pure & Applied Physics **44** (2006) 165-168

15. Study of infrared spectroscopy and elastic properties of fine and coarse grained nickel-cadmium ferrites
K. B. Modi, M. K. Rangolia, **M. C. Chhantbar**, H. H. Joshi
Journal of Material Science 41 (2006) 7308-7318

16. Compositional, temperature and frequency dependence of dielectric behaviour of zinc substituted copper-ferri-chromates
M. C. Chhantbar, K. B. Modi & H. H. Joshi
Journal of Material Science 42 (2007) 6989-6995

17. ^{57}Fe Mössbauer study of Ti^{4+}- substituted $Li_{0.5(1+x)}Cr_{0.1}Fe_{2.4-1.5x}O_4$ Spinels
M C Chhantbar, A Gismelseed*, K B Modi, G J Baldha, Ali Yousif* & H H Joshi
Indian Journal of Pure & Applied Physic **45** (October 2007) 856-859

18. Magnetic behaviour of nano-sized and coarse powders of Cd-Ni ferrites synthesized by wet-chemical route
M. K. Rangolia, **M. C. Chhantbar**, A. R. Tanna, K. B. Modi, G. J. Baldha & H. H. Joshi
Indian Journal of Pure and Applied Physics **46** (January -2008) 60-64

19. Study of magnetic ordering in $MnAl_xCr_xFe_{2-2x}O_4$
Kalpesh H. Jani, **M. C. Chhantbar** and H. H. Joshi
Journal of Magnetism and Magnetic Materials **320** (2008) 2208-2214

20. 50 MeV Li^{3+} ion irradiation induced modifications in structural and magnetic properties of Ti^{4+}-substituted Li-Al and Li-Cr ferrites
M. C. Chhantbar, Ali Yousif, Ravikumar and H. H. Joshi
Hyperfine Interaction **148** (2008) 1-8

(b) National and International Conferences

[1] Structural Properties of Fe^{3+} substituted Yttrium Iron Garnet
H.J. Shah, **M. C. Chhantbar**
One day Seminar on Condensed Matter Physics "Compose-2001"
on 17 March- 2001 organized by Department of Physics, Sardar Patel University,
Vallabh Vidyanagar.

[2] Bulk Modulus Determination through Electrical Measurements
K. B. Modi, H. J. Shah, **M. C. Chhantbar**, H. H. Joshi
DAE Solid State Physics (India) 43 (2000) 486-487

[3] Comparative study of Magnetic Behaviour of $Co_{1+x}R_xFe_{2-2x}O_4$ Spinel Ferrite system
M. C. Chhantbar, K. P. Thummer, U. N. Trivedi, S. S. Bhatu, V. K. Lakhani, A. R. Tanna, U. V. Chhaya
DAE Solid State Physics Symposium (26-30 December 2003), Jiwaji University, Gwalier.

[4] Effect of SHI irradiation on dielectric behaviour of Ti^{4+} substituted Cr^{3+} containing Lithium ferrite
M. C. Chhantbar, G. J. Baldha, K. B. Modi and H. H. Joshi
"Seminar on Condensed Matter Physics [DRS – SAP II (UGC) Programme]", at Department of Physics, Sardar Patel University, Vallabh Vidyanagar held on 21st February 2004.

[5] Structural modifications of Ti^{4+} substituted Li – Al ferrite by swift heavy ion irradiation
M. C. Chhantbar, K. B. Modi, R. Ravikumar* and H. H. Joshi
"XVIII Gujarat Science Congress" held at Department of Physics, Saurashtra University, Rajkot
on March 13, 2004.

[6] Study of Elastic Properties of Magnesium and Aluminum Co-substituted Lithium Ferrite Near Microwave Frequencies.
K. B. Modi, U. N. Trivedi, M. P. Pandya, S. S. Bhatu, **M. C. Chhantbar** and H. H. Joshi
"Microwaves and Optoelectronics" editors M.D. Shirsat, V. V. Nawarkhele, G. S. Raju and P. W. Khirade, Anamaya Publishers, New Delhi, India

[7] A mixed ternary spinel System: $(Cd\ Cr)_xNi_{1-x}Fe_{2-x}\ O_4$ Investigated by ^{57}Fe Mössbauer Spectroscopy
M. C. Chhantbar, U.N. Trivedi, K. B. Modi, G. J. Baldha, H. C. Verma, and H. H. Joshi
49th DAE Solid State Physics Symposium (December 26 – 30, 2004), at Guru Nanak Dev University, Amritsar, India.

[8] Elastic Constant Determination through submillimeter Elestic waves for magnesium
Ferri Aliminates
K. B. Modi, U. V. Chhaya, U. N. Trivedi, **M. C. Chhantbar** and H. H. Joshi
International Conference on submillimeter wave science and Technology, held during Oct 13-15, 2004 organized by Physical Research Lab. Ahmedabad, India

[9] Influence of 50 MeV Li^{3+} -ion irradiation on structural and magnetic properties of Ti^{4+} - substituted $Li_{0.5}Al_{0.1}Fe_{2.4}O_4$
M.C. Chhantbar, K.B. Modi, G. J. Baldha, H.H. Joshi, R.V. Upadhyay, RaviKumar,
INDO-GERMON WORKSHOP "Synthesis and Modification of Nano Structured Materials by Energetic Ion Beams" held during Feb. 20-24, 2005 organized by Nuclear Science Centre, New Delhi.

[10] Effect of SHII on Bulk and Microscopic Magnetic Properties of YIG
P.U. Sharma, **M. C. Chhantbar**, Ravi Kumar, H. C. Verma, M. K. Roy, H. H. Joshi and K. B. Modi
National Conference on "Recent Advances in Material Science (RAMS-2006)" held 27-29, 2006 organized by Department of Physics, Kurukshetra University, Kurukshetra.

[11] Contrast in the ^{57}Fe Mossbauer Spectroscopic signature of Swift Heavy Ion Irradiated Ti-substituted Li-Al and Li-Cr ferrites
M. C. Chhantbar, Ali Yousif, Ravikumar, H. H. Joshi
51 DAE Solid State Physics Symposium (December 26 – 30, 2006) at Barkatulah University, Bhopal

[12] 50 MeV Li^{3+} ion irradiation induced modifications in structural and magnetic properties of Ti^{4+}-substituted Li-Al and Li-Cr ferrites
M. C. Chhantbar, Ali Yousif, Ravikumar and H. H. Joshi
International Conference of the Applications of the Mössbauer effect (October 14-19, 2007) at Indian Institute of Technology, Kanpur, INDIA

[13] Influence of heat treatment and 50MeV Li-ion irradiation on structural and magnetic properties of the spinel ferrite system: $CuFe_{2-2x}Al_xCr_xO_4$
M.C. Chhantbar, U. N. Trivedi, S. Chattopadhyay, D. Jana, Alok Benerjee, Ravikumar and H.H.Joshi
"Indo-US workshop on Advanced Magnetic Materials and Their Applications" (March 1-4, 2009) jointly organized by Indian Institute of Technology, Bombay, India and Northeastern University, Boston, USA at Department of Physics, IIT, Bombay.

❖ The List of National and International Conferences/Workshop/ Special Training program attended

(a) Special Training School/Workshop/Symposium/Conferences attended in India

(1) 13th National Symposium on plasma science & Technology, "Plasma - 98", during 27-30 October- 1998 organized by Department of Physics, Saurashtra University, Rajkot.

(2) Mini User workshop on Engineering of Oxide Material by Swift Heavy Ion Irradiation, during 10-11 April- 2001 organized by Department of Physics, Saurashtra University, Rajkot and Nuclear Science Center, New Delhi.

(3) Workshop on "Operation, Maintenance and Utilization of electronic Instruments" during 7-13 October–2002, organized by Indian Association of Physics Teacher, Kanpur and Department of Physics, Saurashtra University, Rajkot.

(4) Workshop on "Material Science with Pulsed Heavy Ion Beam" on 29 November-2002 organized by Nuclear Science Centre, New Delhi.

(5) International workshop on "Nanomaterials, Magnetic Ions & Magnetic Semiconductors Studied Mostly by Hyperfine Interactions" during 10-14 February – 2004 organized by Physics Department, Faculty of Science, M. S. University of Baroda, India.

(6) National Workshop on "Prospects of Astronomy Research in Universities" held at Department of Physics, Saurashtra University, and Rajkot during 25-27 February 2004.

(7) ISTE sponsored workshop on "Matlab for Process Engineers" during 16^{th}-18^{th} July 2004 organized by Chemical Engineering Department, V.V.P. Engineering College,Rajkot, India.

(8) National Workshop on "Advanced Methods for Materials Characterization (NWMC)" at BARC TSH, Anusktinagar, Mumbai during October 11-15, 2004 under the auspices of Materials Research Society of India (MRSI).

(9) International School on EPR/ESR Spectroscopy and Free Radical Research (ISEPRSFRR-2004) held during November 17-20, 2004, at Bhabha Atomic Research Centre, Mumbai, India.

(10) "Gujarat region interchapter IPA meet & the world Year of Physics-2005" activities organized by the Department of Physics, Veer Narmad South Gujarat University, Surat during 3-4 December 2005.

(11) "National Conference on Condensed Matter and Material Physics (CMMP06)" held during 19-21 January 2006, organized by Department of Physics, Faculty of Science, The Maharaja Sayajirao University of Baroda, Vadodara, India.

(12) "National Symposium on Application of ^{57}Fe Mössbauer Spectroscopy" at Department of Physics, Jai Narain Vyas University, Jodhpur, India during February 6-8, 2006.

(13) One day acquaintance Programme jointly organized by Inter University Accelerator Centre, New Delhi and IPA Vallabh Vidyanagar Chapter at Department of Physics, Sardar Patel University, Vallabh Vidyanagar on 24 February 2006.

(14) One day National Seminar on "Recent Advances in Condensed Matter and Space Physics" at Department of Physics, Saurashtra University, Rajkot organized under UGC-Special Assistance Programme on 21st March 2006.

(15) The school on "X-ray Techniques in Material Science" at IUAC, hosted by Inter University Accelerator Centre held at New Delhi during June 12-16, 2006.

(16) Workshop on "Functional Oxide Materials" at Inter University Accelerator Centre, New Delhi, during the period 25- 26 September 2006.

(17) National workshop on "Nanoscience and Nanotechnology in Biomedical applications" organized by Department of Physics, Bhavnagar University, Bhavnagar, India during 29 Jan-1 Feb, 2007.

(b) Special Training School/Workshop/Symposium/Conferences attended in overseas

{1} "The school on Pulsed Neutron Sources: Enhancing the capacity for Material Science" held at the Abdus Salam International Centre for Theoretical Physics, Miramare, Trieste-Italy during 17-28 October 2005.

{2} "School on Pulsed Neutrons: Characterization of Materials" held at the Abdus Salam International Centre for Theoretical Physics, Miramare, Trieste-Italy during 15-26 October 2007.

{3} "Joint ICTP-IAEA Advanced Workshop on Model Codes for Spallation Reactions" held at the Abdus Salam International Centre for Theoretical Physics, Miramare, Trieste-Italy during 4-8 February 2008.

{4} "Joint ICTP-IAEA workshop on Advanced Simulation and Modelling for Ion Beam Analysis" held at the Abdus Salam International Centre for Theoretical Physics, Miramare, Trieste-Italy during 23-27 February 2009.

==========